Universität Ulm | 89069 Ulm | Germany

ulm university universität ulm

Fakultät für Naturwissenschaften
Institut für Elektrochemie

A Study of Photocatalytic 2D Semiconducting Polymeric Carbon Nitrides

Kumulative Dissertation zur Erlangung des akademischen Grades doctor rerum naturalium (Dr. rer. nat.) der Fakultät für Naturwissenschaften der Universität Ulm

Vorgelegt von:
Changbin Im
aus Gwangju, Südkorea
2024

This work was carried out in the period between October 2018 and November 2024 under the supervision of Prof. Dr. Timo Jacob at the Institute of Electrochemistry at Ulm University.

Amtierender Dekan
der Fakultät für Naturwissenschaften der Universität Ulm:
Prof. Dr. Kay-Eberhard Gottschalk
Institut für Experimentelle Physik,
Universität Ulm

Erstgutachter:
Prof. Dr. Timo Jacob
Institut für Elektrochemie,
Universität Ulm

Zweitgutachter:
Prof. Dr. Arnulf Latz
Institut für Technische Thermodynamik, Deutsches Zentrum für Luft- und Raumfahrt e.V. (DLR); Multiphysikalische Modellierung,
Mitglied beim Exzellenzcluster POLiS

Tag der mündlichen Prüfung: Ulm, 05. 05. 2025

Name: Changbin Im Matriculation number: 1039818

Declaration

I hereby declare that I have written the present dissertation independently and that I have not used any sources or resources other than those indicated. I also declare that any phrases taken from published or unpublished texts have been identified as such and that I have complied with the Ulm University Statutes for Safeguarding Good Scientific Practice.

Ulm, date .....

Changbin Im

Acknowledgements

First and foremost, I would like to express my deepest gratitude to Prof. Dr. Timo Jacob, who provided me with the opportunity to grow into a theoretical chemist. Above all, the remarkable freedom he afforded me allowed me to channel my diverse scientific curiosities into a cohesive, multidisciplinary research focus, helping me to mature into an independent researcher. His keen and insightful intuition has greatly expanded my understanding of phenomena, and I am confident it will remain one of my most valuable assets in my future research endeavors.

I am also profoundly grateful to Prof. Dr. Radim Beranek, with whom I engaged in numerous discussions. These conversations helped me to balance both theoretical and experimental perspectives, and his warm, personal advice was a powerful source of motivation for me.

My sincere thanks also go to Prof. Dr. Jaeyoung Lee at Gwangju Institute of Science and Technology (GIST). His support enabled me to begin my studies here, and his unwavering encouragement and assistance have been invaluable.

I extend my gratitude to Dr. Björn Kirchhoff, who has been a friend, colleague, and mentor. I am equally indebted to Dr. Felicitas Jansen, Dietmar Jansen, and Erika Jansen, whose support has been essential in sustaining my life here.

I would also like to thank Dr. Attila Farkas and Dr. Mohammad Al-Shakran, with whom I shared my early days here, which were important. Furthermore, I am especially grateful to Ms. Diemut Heinrich-Magon, who provided me with extensive

administrative assistance outside of my research.

To all theoretical and experimental members of the electrochemistry institute, as well as all my friends, I extend my heartfelt thanks. I am especially indebted to the colleagues who ensured a steady supply of quality coffee, which was greatly appreciated.

Finally, my sincerest gratitude goes to my beloved parents, my healthy grandmother, my late grandfather, and my brother and his family. Above all, I give thanks to God for everything.

Contents

List of Publications **xxvii**

1 Introduction **1**

1.1 Motivation and Outline 1

2 Theory **5**

2.1 The many-body Schrödinger Equation 5

2.2 Wavefunction method 7

2.2.1 Hartree method 7

2.2.2 Variational method 8

2.2.3 Hartree-Fock method 10

2.3 Density functional theory 13

2.3.1 Hohenberg–Kohn theorms 13

2.3.2 The Kohn–Sham equations 14

2.3.3 Exchange and correlation functionals 15

2.3.4 Local density approximation 16

2.3.5 Generalized gradient approximations 16

2.3.6 Hybrid functional 18

2.4 *GW* Approximation: A Many-Body Approach 20

2.4.1 Self-Energy and Quasiparticle Energy 21

2.4.2 *GW* Method and Hedins Equations 22

2.4.3 Bethe-Salpeter Equation 23

2.5 Photophysical Processes, Excitons, and Recombination 25
2.5.1 Atomistic thermodynamics for surfaces 25
2.6 Excited states 34
2.6.1 Time dependent Hartree-Fock 34
2.6.2 Linear Response Theory 36
2.6.3 Adiabatic Approximation in TDHF 37
2.6.4 Applications of TDHF 39
2.7 Plane wave basis set 39
2.8 Pseudopotentials 44
2.8.1 Norm-Conserving Pseudopotentials 46
2.8.2 Ultrasoft Pseudopotentials 47
2.8.3 Projector-Augmented Wave Method 48

3 Structure–property characteristics: the First-principles calculations 51
3.1 Thermochemistry 51
3.1.1 Abstract 51
3.1.2 Introduction 52
3.1.3 Methodology 55
3.1.4 Computational Details 55
3.1.5 Thermochemistry 56
3.1.6 Model Systems 58
3.1.7 Results 59
3.1.8 Formation Energy Trends for 1D Materials 59
3.1.9 Formation Energy Trends for 2D and 3D Materials 62
3.1.10 Optical Property Trends 62
3.1.11 The Influence of Hydrogen Bonding on the melon Structure . . 66
3.1.12 Discussion 67

3.1.13 Correlation between Degree of Condensation and Synthetic Conditions . . . 69
3.1.14 Interconversion . . . 71
3.1.15 Influence of Stacking *vs.* Lateral Condensation . . . 74
3.1.16 Influence of Corrugation . . . 75
3.1.17 Postulation of a More Complete Computational Carbon Nitride Model . . . 77
3.1.18 Conclusion . . . 80
3.2 Structural-electonic-optical properties . . . 82
3.2.1 Abstract . . . 82
3.2.2 Introduction . . . 83
3.2.3 Results and discussion . . . 85
3.2.4 Structural Models . . . 85
3.2.5 Dielectric Functions and Optical Properties . . . 92
3.2.6 Interlayer Interactions: Influence on Electronic and Optical Properties . . . 98
3.2.7 Conclusion . . . 101
3.2.8 Experimental and computational methods . . . 102
3.2.9 Computational details . . . 102
3.2.10 Sample preparation and diffuse reflectance spectroscopy . . . 103
3.2.11 Supplementary methods . . . 103
3.3 Optical properties: *GW*@BSE . . . 106
3.3.1 Abstract . . . 106
3.3.2 Introduction . . . 106
3.3.3 Method . . . 108
3.3.4 Models . . . 110
3.3.5 Optical spectra . . . 111

3.3.6 Exciton formation 115
3.3.7 Prolonged exciton lifetime and photocatalytic activity 117
3.3.8 Conclusion 121

4 Applications **123**
4.1 Motivation 123
4.2 Mechanistic Investigation of HER and ORR on PCNs 125
4.2.1 Introduction 125
4.2.2 Computational details 126
4.2.3 DFT calculations 126
4.2.4 Atomistic thermodynamics for surfaces 127
4.2.5 Computational hydrogen electrode 129
4.2.6 Results and Discussion 133
4.2.7 HER on monolayer and multilayer PCNs 133
4.2.8 ORR and HER-coupled ORR 139
4.2.9 H_2O_2 production on PCN monolayers 147
4.2.10 Conclusion 148
4.3 A Study in Red: The Overlooked Role of Azo-Moieties in Polymeric Carbon Nitride Photocatalysts with Strongly Extended Optical Absorption 149
4.3.1 Abstract 150
4.3.2 Conclusion 151
4.3.3 Contribution to the Conclusion 152
4.4 Water-Soluble Polymeric Carbon Nitride Colloidal Nanoparticles for Highly Selective Quasi-Homogeneous Photocatalysis 175
4.4.1 Abstract 176
4.4.2 Conclusion 176
4.4.3 Contribution to the Conclusion 177

4.5 Water-soluble ionic carbon nitride as unconventional stabilizer for highly catalytically active ultrafine gold nanoparticles 210
4.5.1 Abstract 211
4.5.2 Conclusion 212
4.5.3 Contribution to the Conclusion 213

A Appendix **263**
A.1 Structure–property characteristics: the First-principles calculations . . 263
A.1.1 Data Availability 263
A.1.2 Supplementary methods 263
A.2 Structural-electonic-optical properties 270
A.2.1 Supplementary data 270
A.3 Optical properties: *GW*@BSE 272
A.3.1 Supplementary data 272
A.3.2 Modifications of the VASP BSE.F file 292
A.4 Mechanistic Investigation of HER and ORR on PCNs 297
A.4.1 Supplementary Information 297

Bibliography **311**

List of Abbreviations **327**

Curriculum Vitae **331**

List of Figures

1 (a) Jablonski diagram illustrating excited-state processes, including charge generation and recombination, in an organic solar cell (S: singlet state, T: triplet state, CT: charge transfer state).[26] (b) Schematic illustrations of Förster resonance energy transfer and Dexter electron-exchange energy transfer. Solid and dash lines indicate radiative and nonradiative transitions, respectively[27]. These figures are taken from the corresponding literature. 25

2 A schematic illustration of the pseudo potential inside and outside the core region of an atom at position R_α. The black and red lines represent the exact and pseudopotential (wave function), respectively. This figure is taken from [28]. 44

3 Schematic illustration of additive augmentation in the PAW method: (a) Pseudized quantities are defined across the entire space using a regular plane wave grid. (b) Within specific spheres, pseudo-wave functions are reconstructed, and the corresponding one-center terms are removed. (c) The all-electron wave functions are then reconstructed, and the associated one-center energies are added.. 48

1 Illustration of molecular oligomer model systems investigated in this study. The models are named after a h_{xy} naming scheme, where x is the number of heptazine units and y is an increasing number that indexes the oligomers. 58

2 Illustration of periodic 2D surface and 3D crystal models investigated in this study. Structures are composed of s-melon, melon, PHI, $C_9N_{13}H_3$, cg-C_3N_4(corrugated), and pg-C_3N_4(planar) structural motifs. 59

3 The free energy of formation for all (a) trimer and (b) tetramer structures are shown as function of $\Delta\mu_{NH_3}$. The free energy of formation is normalized to eV/atom to be able to compare structures with different total number of atoms. Free energy results are then expanded into T-$p_{\mathrm{NH_3}}$-dependent phase diagrams for the most stable (c) trimer and (d) tetramer structures, respectively. The experimental temperature range for synthesis of these molecular structures is given between the dotted and the dashed line.[38, 39, 44, 87, 88] 61

4 The free energy of formation for all (a) 2D and (b) 3D structures is shown as a function of $\Delta\mu_{\mathrm{NH_3}}$. The free energy of formation is normalized to eV/atom to be able to compare structures with different total number of atoms. Then, free energy results are expanded into a T-$p_{\mathrm{NH_3}}$-dependent phase diagrams for the most stable (c) 2D and (d) 3D structures, respectively. The experimentally measured temperature range for the formation and the decomposition of PCNs are given as dotted black and yellow lines.[44, 87] The dotted grey line indicates the stability region for the fully flat pg-C_3N_4-2D/-3D phases which constitutes a local minimum structure and lays behind the more stable corrugated cg-C_3N_4-2D/-3D structure. 63

5 Summary of the calculated optical gap trends; HOMO-LUMO gaps are given for molecules and bandgaps are given for the periodic structures. For simplicity, the averaged HOMO-LUMO gaps are presented for the dimer up to tetramer structures. A color palate is given for reference to roughly indicate the energy range corresponding to visible light. 64

6 Calculated bandgap trends as a function of the number of heptazine monomers in hydrogen-terminated ribbon models of increasing width. Band gaps of key 2D structures are given in light red for reference (see Figure 5). The ribbon models neglect the influence of corrugation, see text for more details. As the number of heptazine units increases from 2 to 7, the bandgap decreases from 3.6 eV to 2.9 eV, with the most significant decrease observed already from 2 to 3 heptazine units (*ca.* 0.6 eV). 65

7 Formation free energy phase diagrams of 2D and 3D structures updated from Figure 4. The hydrogen-bonding stabilized melon-2D/-3D structure are excluded, instead the single-string s-melon-2D/-3D structures are shown. The dotted and the dashed line indicated the experimentally observed temperature where formation of 2D and 3D structures begins[35, 44, 87] and where the melon-3D structure was found to form,[31] respectively. 68

8 Free energy of formation for key 2D and 3D structures as a function of a selected set of μ_{NH_3} conditions. The free energy of formation is normalized to eV/atom to be able to compare structures with different total number of atoms. 69

9 Reaction flow chart connecting structures via the calculated reaction free energy, ΔG_{r}, which depends on $\Delta\mu_{\mathrm{NH_3}}$ (-2.6 eV $<$ $\Delta\mu_{\mathrm{NH_3}}$ $<$ -1.9 eV). Temperature is fixed to 628 °C, which constitutes the maximum temperature before carbonization of the material sets in, so that the reaction free energy trends depend solely on $p_{\mathrm{NH_3}}$. Two reaction mechanisms are suggested: i) The non-deamination pathway involving stacking and hydrogen bonding and ii) the deamination pathway involving release of NH_3. The structures are classified by their degree of condensation (DoC). The "pore-filling" route is suggested to connect PHI structure to cg-C_3N_4 structure; see text for more details. 72

10 (a) Illustration of the postulated "mixed" PCN model as well as the parent structures it is composed of. (b) Calculated bandgaps for the mixed structural motif as well as for the parent structures as a function of the DoC. The oval shape indicates the range of DoCs and bandgaps obtained for the four tested mixed models; the yellow star indicates the most promising model that is also depicted in (a). 79

11 The illustration of the PCN models used in this study. The upper is the 2D monolayer and the lower is the stacked 3D structure. 85

12 The projected density of states of (a, e) melon, (b, f) PHI, (c, g) pg–CN, and (d, h) cg–CN. The projection is performed on s, p orbitals corresponding to carbon and nitrogen atoms. The trivial contribution of hydrogen is omitted. Fermi energy referenced to 0 eV. 87

13 The band structure (left) and its orbital projection (right) of (a) melon-2D, (b) PHI-2D, (c) pg–CN-2D, and (d) cg–CN-2D. The projection is performed on s, p orbitals corresponding to carbon and nitrogen atoms. The trivial contribution of hydrogen is omitted. Fermi energy is referenced to 0 eV. 89

14 The band structure (left) and its orbital projection (right) of (a) melon-3D, (b) PHI-3D, (c) pg–CN-3D, and (d) cg–CN-3D. The projection is performed on s, p orbitals corresponding to carbon and nitrogen atoms. The trivial contribution of hydrogen is omitted. Fermi energy is referenced to 0 eV. The inset provides a comparison of energy levels near the VBM in the corresponding 2D structure, illustrating different degrees of interlayer interactions. 91

15 The imaginary part of the macroscopic dielectric functions of (a) melon, (b) PHI, (c) cg, and (d) pg on top of the HSE@Casida method. Imaginary parts corresponding to the respective cartesian direction (xx, yy, zz), obtained by Eq. (3.15) are shown. 93

16 The absorption spectra and oscillator strength were calculated for (a) melon, (b) PHI, (c) cg, and (d) pg in both 2D and 3D structures. The absorption spectra and oscillator strength of (e) mix1-3D and (f) mix2-3D, which depict the amorphous structure, are presented alongside the experimental values which is a dashed line. 95

17 The proposed photophysical process of the general PCN materials in (a) 2D monolayer and (b) 3D stacked structures. The electron density at the respective energy level is illustrated below. The red corresponds to the absorption process, the blue is the photoluminescence process, the black is the non-radiative internal conversion, and the magenta is the interlayer energy/electron transfer, respectively. 99

18 Structures of polymeric carbon nitrides. 110

19 Imaginary part of dielectric functions. The solid and the dashed lines are obtained by the *GW*@BSE and the *GW*@IP respectively. 111

20 Illustration of the calculated absorption spectra for 2D and 3D PCN models along averaged spatial directions. The oscillator strengths in relation to wavelength are presented in red. 113

21 Representaton of eigenvalues (BSE and IP) and coupling coefficients (radius of circles) of bright states for both 2D and 3D PCN structures, corresponding to the absorption edges (top) and interlayer interactions (bottom). 114

22 Calculated radiative exciton lifetimes of both 2D and 3D PCN structures. Bright states are denoted in blue, while dark states are represented in red. Their respective effective lifetimes at 300 K are indicated by dashed lines. 117

23 (left) Electron density of electron hole and the excited electrons and (right) the proposed mechanisms of photoexcitation process for (a) PHI and (b) c-gCN-3D structures, where π_{dist} and π^*_{dist} are the energy levels of distorted π electrons, π_{inter} is the π^* state at the other layer, and $\mathrm{E_b}$ is the exciton binding energy, respectively. 119

1 Illustration of thermodynamic-electrochemical system modeling. This figure demonstrates how surface (interface) reactions are approximated in the gas phase and solid phase using the proton-coupled electron transfer mechanism. 127

2 Free energy profiles of a typical HER with H intermediates on (a) PCN monolayers and (b) multilayered PCNs (4-layer). The mix1 and mix2 structures incorporate melon-like edges, corrugated graphitic features, and PHI motifs. The free energy of the intermediates is calculated at pH = 0. 133

3 (a) Free energy profiles of HER with additional H intermediates on melon monolayer. (b) Corresponding top-view and side-view images of the structures. The free energy profiles are shown under conditions of pH = 0 and $U = 0$ V. 135

4 (a) Free energy profiles of HER with additional H intermediates on PHI monolayer. (b) Corresponding top-view and side-view images of the structures. The free energy profiles are shown under conditions of pH = 0 and $U = 0$ V. 136

5 (a) Free energy profiles of HER with additional H intermediates on c-gCN monolayer. (b) Corresponding top-view and side-view images of the structures. The free energy profiles are shown under conditions of pH = 0 and $U = 0$ V. 137

6 (a) Free energy profiles of HER with additional H intermediates on p-gCN monolayer. (b) Corresponding top-view and side-view images of the structures. The free energy profiles are shown under conditions of pH = 0 and $U = 0$ V. 137

7 Free energy profiles of the typical ORR process on PCN monolayers at $U = 0$ V. 139

8 The structural images depict the corresponding reaction pathways for the ORR on (a) melon, (b) PHI, (c) c-gCN, and (d) p-gCN monolayers. 140

9 Free energy profiles of the typical 4-electron ORR process on PCN monolayers at $U = 1.23$ V and $U = 2.7$ V, respectively. 141

10 Free energy profiles of the typical 4-electron ORR process combined with 2-electron HER process on PCN monolayers at $U = 0$ V. 143

11 Free energy profiles of the typical 4-electron ORR process combined with 2-electron HER process on PCN monolayers at $U = 1.23$ V and $U = 2.7$ V, respectively. 144

12 The structural images depict the corresponding reaction pathways for the HER-coupled-ORR process on (a) melon, (b) PHI, (c) c-gCN, and (d) p-gCN monolayers. 145

13 Free energy diagram of H_2O_2 production via (a) typical 2-electron pathways and (b) HER-coupled 2-electron pathways on PCN monolayers. The free energy is plotted using CHE with $U = 0.68$ V and pH = 0 conditions. The selection of the best reaction pathways considers only the lowest overpotential for the oxygen intermediates. 147

S1 Proposed structures of the mixed motifs used in the study. The structures are composed of the PHI and cg-C_3N_4 structure because of their high DoC (79%–94%). The structures of Mixed1-3D and Mixed2-3D have the edge boundaries which reduce the corrugation. The both Mixed1-3D and Mixed2-3D are distinct from the sequence of the structural motifs. The Mixed3-3D is made of inclusion of PHI structure within cg-C_3N_4 domain to both layers and the Mixed4-3D is constructed of cg-C_3N_4 layer (upper) and PHI layer (bottom), respectively. 264

S2 The evaluation of the calculated chemical potential of ammonia used in this study. The reference plots are taken from the NIST-JANAF[194, 195] and the literature.[64, 196] The dotted points ($\mathrm{NH_3}$ NIST-JANAF and $\mathrm{NH_3}$ exp. data) and small dotted lines ($\mathrm{NH_3}$ ideal gas) are taken from the experimental and the literature, respectively. The bold dashed line illustrates the calculated $\Delta\mu_{\mathrm{NH_3}}(\mathrm{T}, p)$ in this study. Then we added two $p_{\mathrm{NH_3}}$ conditions of 0.001 MP and 50 MP to further trace the variations. 265

S3 The contour plot of $\Delta\mu_{\mathrm{NH_3}}$. The plot is derived from the equation (3.4). The black points is sampled the respective $\Delta\mu_{\mathrm{NH_3}}$. (See Figure 8 of red, green, blue, and purple.) 266

S4 The calculated phase diagram of the normalized free energy of formation between melon-3D and cg-C_3N_4-3D. The inclusion of the vibrational contributions increases the relative stability of of cg-C_3N_4-3D (blue area) to $\Delta\mu_{NH_3}$ direction. The phase diagram of melon structure from the literature is shown in gray area.[64] 267

S5 Free energy of formation for 2D and 3D structures with regards to various μ_{NH_3}. The μ_{NH_3} is differentiated from the combination of T and p_{NH_3}. The free energy of formation is normalized to eV/atom due to the different numbers of elements. 267

S6 Respective phase diagram of the free energy reaction for 2D and 3D structures. The contour map is used to find spontaneous $\Delta\mu_{NH_3}$ for temperature and p_{NH_3} conditions. 268

S7 The degree of condensation and RMSD value are plotted with 3D structures.The Mixed structures are composed of PHI and g-C_3N_4 structures (see Figure S1). The RMSD value of 3D structure is obtained from the average of the each layer. 269

S8 The depiction of electron density in (a) melon, (b) PHI, (c) cg, and (d) pg 2D structures corresponding to the respective energy level at Γ. . . 270

S9 The calculated imaginary part of the dielectric function for pg-2D structure using TD@Casida (black), GW@BSE (red)[125], and GW@IP[125] (blue) calculations. The scissor correction is applied based on the brightest state, which is commonly located around 4 eV. 271

S10 Illustration of the e–h coupling constants corresponding to the 32 excitation energy of melon-2D structure optimized CA (LDA) functionals. . 274

S11 Illustration of the e–h coupling constants corresponding to the 32 excitation energy of melon-3D structure optimized CA (LDA) functionals. . 275

S12 Illustration of the e–h coupling constants corresponding to the 32 excitation energy of PHI-2D structure optimized CA (LDA) functionals. . . . 276

S13 Illustration of the e–h coupling constants corresponding to the 32 excitation energy of PHI-3D structure optimized CA (LDA) functionals. . . . 276

S14 Illustration of the e–h coupling constants corresponding to the 32 excitation energy of c-gCN-2D structure optimized CA (LDA) functionals. . 277

S15 Illustration of the e–h coupling constants corresponding to the 32 excitation energy of c-gCN-3D structure optimized CA (LDA) functionals. . 278

S16 Illustration of the e–h coupling constants corresponding to the 32 excitation energy of p-gCN-2D structure optimized CA (LDA) functionals. . 279

S17 Illustration of the e–h coupling constants corresponding to the 32 excitation energy of p-gCN-3D structure optimized CA (LDA) functionals. . 280

S18 Imaginary part of dielectric functions of the PCN structure optimized with PBE-D3 functionals. The solid and the dashed lines are obtained by the *GW*@BSE and the *GW*@IP respectively. 281

S19 The illustration of the calculated absorption spectra for 2D and 3D PCN models, optimized PBE functionals, along averaged spatial directions. The oscillator strengths in relation to wavelength are presented in red. 282

S20 Representaton of eigenvalues (BSE and IP) and coupling coefficients (radius of circles) of bright states for both 2D and 3D PCN structures, optimized by PBE-D3 functionals, corresponding to the absorption edges (top) and interlayer interactions (bottom). 283

S21 Calculated radiative exciton lifetime of both 2D and 3D PCN structures optimized by PBE-D3 functionals. Bright states are denoted in blue, while dark states are represented in red. Their respective effective lifetime at 300 K are indicated by dashed lines. 284

S22 Illustration of the e–h coupling constants corresponding to the 32 excitation energy of melon-2D structure optimized PBE (GGA) functionals. 285

S23 Illustration of the e–h coupling constants corresponding to the 32 excitation energy of melon-3D structure optimized PBE (GGA) functionals. 286

S24 Illustration of the e–h coupling constants corresponding to the 32 excitation energy of PHI-2D structure optimized PBE (GGA) functionals. . . 287

S25 Illustration of the e–h coupling constants corresponding to the 32 excitation energy of PHI-3D structure optimized PBE (GGA) functionals. . . 287

S26 Illustration of the e–h coupling constants corresponding to the 32 excitation energy of c-gCN-2D structure optimized PBE (GGA) functionals. 288

S27 Illustration of the e–h coupling constants corresponding to the 32 excitation energy of c-gCN-3D structure optimized PBE (GGA) functionals. 289

S28 Illustration of the e–h coupling constants corresponding to the 32 excitation energy of p-gCN-2D structure optimized PBE (GGA) functionals. 290

S29 Illustration of the e–h coupling constants corresponding to the 32 excitation energy of p-gCN-3D structure optimized PBE (GGA) functionals. 291

S30 Illustrations of the first hydrogen adsorption sites for top-view (left) and side-view (right) on melon. 297

S31 Illustrations of the second hydrogen adsorption sites for top-view (left) and side-view (right) on melon. 298

S32 Illustrations of the first hydrogen adsorption sites for top-view (left) and side-view (right) on PHI. 299

S33 Illustrations of the first hydrogen adsorption sites for top-view (left) and side-view (right) on c-gCN. 299

S34 Illustrations of the first hydrogen adsorption sites for top-view (left) and side-view (right) on c-gCN. 300

S35 Illustrations of the first hydrogen adsorption sites for top-view (left) and side-view (right) on p-gCN. 301
S36 Illustrations of the first hydrogen adsorption sites for top-view (left) and side-view (right) on p-gCN. 301
S37 Illustrations of the second hydrogen adsorption sites for top-view (left) and side-view (right) on PHI. 301
S38 Free energy profiles for the typical ORR process on PCN monolayers: (a) melon, (b) PHI, (c) c-gCN, and (d) p-gCN. The free energy of the intermediates at the investigated active sites is analyzed under applied electrode potentials of $U = 0$, 1.23, and 2.7 V, respectively. 302
S39 Free energy profiles for the HER-coupled-ORR process on PCN monolayers: (a) melon, (b) PHI, (c) c-gCN, and (d) p-gCN. The free energy of the intermediates at the investigated active sites is analyzed under applied electrode potentials of $U = 0$, 1.23, and 2.7 V, respectively. . . 303

List of Tables

1 The calculated bandgap (HSE06) of PCN structures. 90

2 The assignment of calculated absorption peaks for the PCN structural features. 97

3 Bandgaps of 2D and 3D PCN structures (optimized using CA functionals) were calculated via independent particle approximations (G_0W_0@IP) and BSE (G_0W_0@BSE) methods, alongside the effective exciton lifetime at 300 K. (D) and (I) denote the direct and indirect bandgaps, respectively. 120

1 Values of G, ΔG, and the PDS for the typical 4-electron ORR intermediates on PCN monolayers as a function of U. 142

2 Values of G, ΔG, and the PDS for the typical 4-electron ORR intermediates including 2-electron HER steps on PCN monolayers as a function of U. 146

S1 Summary of Optical property 266

S2 Summary of Degree of Corrugation 269

S3 The lattice parameters of the PCN structures obtained by the CAPZ and PBE functionals. 272

S4 Bandgaps of 2D and 3D PCN structures (optimized using PBE functionals) were calculated via independent particle approximations (G_0W_0@IP) and BSE (G_0W_0@BSE) methods, alongside the effective exciton lifetime at 300 K. The (D) and (I) denote the direct and the indirect bandgap, respectively. 273

S5 Free energy of the intermediates for ORR at the active sites of melon monolayer. The ΔG and the potential-determining steps under the simulated electrode potential ($U = 0$ V) are illustrated. 304

S6 Free energy of the intermediates for ORR at the active sites of melon monolayer. The ΔG and the potential-determining steps under the simulated electrode potential ($U = 1.23$ V) are illustrated. 304

S7 Free energy of the intermediates for ORR at the active sites of melon monolayer. The ΔG and the potential-determining steps under the simulated electrode potential ($U = 2.7$ V) are illustrated. 305

S8 Free energy of the intermediates for ORR at the active sites of PHI monolayer. The ΔG and the potential-determining steps under the simulated electrode potential ($U = 0$ V) are illustrated. 305

S9 Free energy of the intermediates for ORR at the active sites of PHI monolayer. The ΔG and the potential-determining steps under the simulated electrode potential ($U = 1.23$ V) are illustrated. 306

S10 Free energy of the intermediates for ORR at the active sites of PHI monolayer. The ΔG and the potential-determining steps under the simulated electrode potential ($U = 2.7$ V) are illustrated. 306

S11 Free energy of the intermediates for ORR at the active sites of c-gCN monolayer. The ΔG and the potential-determining steps under the simulated electrode potential ($U = 0$ V) are illustrated. 307

S12 Free energy of the intermediates for ORR at the active sites of c-gCN monolayer. The ΔG and the potential-determining steps under the simulated electrode potential ($U = 1.23$ V) are illustrated. 307
S13 Free energy of the intermediates for ORR at the active sites of c-gCN monolayer. The ΔG and the potential-determining steps under the simulated electrode potential ($U = 2.7$ V) are illustrated. 308
S14 Free energy of the intermediates for ORR at the active sites of p-gCN monolayer. The ΔG and the potential-determining steps under the simulated electrode potential ($U = 0$ V) are illustrated. 308
S15 Free energy of the intermediates for ORR at the active sites of p-gCN monolayer. The ΔG and the potential-determining steps under the simulated electrode potential ($U = 1.23$ V) are illustrated. 309
S16 Free energy of the intermediates for ORR at the active sites of p-gCN monolayer. The ΔG and the potential-determining steps under the simulated electrode potential ($U = 2.7$ V) are illustrated. 309

List of Publications

The thesis is based on the following publications:

(*i*) **C. Im**, B. Kirchhoff, I. Krivtsov, D. Mitoraj, R. Beranek, and T. Jacob, Structure and optical properties of polymeric carbon nitrides from atomistic simulations, *Chemistry of Materials* 35, 15471559 (2023, front cover).

(*ii*) **C. Im**, M. M. Elnagar, B. Kirchhoff, D. Mitoraj, I. Krivtsov, A. Farkas, R. Beranek, and T. Jacob, Unraveling the optical signatures of polymeric carbon nitrides: insights into stacking-induced excitonic transitions, *Journal of Materials Chemistry C* 13, 86828693 (2025).

(*iii*) **C. Im**, R. Beranek, and T. Jacob, Structural influence on exciton formation and the critical role of dark excitons in polymeric carbon nitrides, *Advanced Energy Materials* 15. 13. 2405549 (2025, Inside Back Cover)

(*iv*) **C. Im**, J. Koenigsdorff, R. Beranek, and T. Jacob, The origin of catalytic reactivity in hydrogenation-coupled H_2O_2 production on polymeric carbon nitrides, (2025, *In preparation*).

(*v*) D. Mitoraj, I. Krivtsov, C. Li, A. Rajagopal, **C. Im**, C. Adler, K. KÍoble, O. Khainakova, J. Hniopek, C. Neumann, et al., A study in red: the overlooked role of azo-moieties in polymeric carbon nitride photocatalysts with strongly extended optical absorption, *ChemistryA European Journal* 27, 1718817202 (2021).

(*vi*) I. Krivtsov, D. Mitoraj, C. Adler, M. Ilkaeva, M. Sardo, L. Mafra, C. Neumann, A.

Turchanin, C. Li, B. Dietzek, R. Leiter, J. Biskupek, U. Kaiser, **C. Im**, B. Kirchhoff, T. Jacob, and R. Beranek, Water-soluble polymeric carbon nitride colloidal nanoparticles for highly selective quasi-homogeneous photocatalysis, *Angewandte Chemie International Edition* 59, 487495 (2020).

(*vii*) M. M. Elnagar, J. Liessem, **C. Im**†, D. Mitoraj, L. A. Kibler, C. Neumann, A. Turchanin, R. Leiter, U. Kaiser, T. Jacob, et al., Water-soluble ionic carbon nitride as unconventional stabilizer for highly catalytically active ultrafine gold nanoparticles, *Nanoscale* 15, 1926819281 (2023).

$\dagger =$ *Shared First Authorships*

Further publications:

(*viii*) A. Rajagopal, E. Akbarzadeh, C. Li, D. Mitoraj, I. Krivtsov, C. Adler, T. Diemant, J. Biskupek, U. Kaiser, **C. Im**, M. Heiland, T. Jacob, C. Streb, B. Dietzek, and R. Beranek, Polymeric carbon nitride coupled with a molecular thiomolybdate catalyst: exciton and charge dynamics in light-driven hydrogen evolution, *Sustainable Energy & Fuels* 4, 60856095 (2020).

(*ix*) S. Kang, **C. Im**, I. Spanos, K. Ham, A. Lim, T. Jacob, R. Schlĺogl, and J. Lee, Durable nickel-iron (oxy) hydroxide oxygen evolution electrocatalysts through surface functionalization with tetraphenyl- porphyrin, *Angewandte Chemie International Edition*, e202214541 (2022, front cover).

1 Introduction

1.1 Motivation and Outline

The rapid advancement of artificial intelligence (AI), coupled with urgent global crises such as pandemics and climate change, has significantly accelerated the search for innovative material structures to address these challenges. Computational modeling and simulation have emerged as indispensable tools in materials science, not only for explaining observed phenomena but also for designing new materials with enhanced performance. In particular, simulations based on first-principles calculations offer a powerful approach to describing material properties at the atomic level, providing insights into their fundamental physical and chemical characteristics. Moreover, these simulations are becoming increasingly valuable as databases for AI applications, facilitating data-driven discoveries and optimizations using the machine-learning force field in material science.

Recent advancements in high-performance computing (HPC) clusters have enabled larger and more complex computational models, which were previously impractical due to computational limitations. The improved capability to accurately describe electronic structures has expanded the utility of first-principles calculations beyond traditional boundaries. This development has made it possible to go beyond simple unit cell models used decades ago, allowing the exploration of supercell structures with diverse geometries and complex environments, including amorphous materials and disordered systems that were previously challenging to model accurately.

In addition, the extension from basic ground-state calculations to more sophisticated methods, such as time-dependent approaches, has facilitated the description of excited states and interactions with external stimuli. These methods are crucial for simulating the behavior of complex electronic structures under non-equilibrium conditions. Consequently, the development of computational techniques has become increasingly relevant for studying complex systems in photochemistry, photophysics, photovoltaics, and optoelectronics, such as organic light-emitting diodes (OLEDs) and photocatalysts.

Amid these advancements, two-dimensional (2D) materials, such as graphene and MXenes, have garnered significant attention due to their exceptional properties and wide-ranging potential applications. Research on these materials has flourished, driven by their unique electronic, mechanical, and thermal properties, which make them suitable for numerous technological applications. Among the various 2D materials, carbon nitride structures have attracted particular interest as organic semiconductors composed of carbon and nitrogen. These materials have demonstrated promising photocatalytic capabilities, with early reports highlighting their potential for applications in solar energy conversion and environmental remediation.[1–15]

Despite extensive experimental and theoretical investigations, research on carbon nitrides has been limited by their inherently high degree of disorder and non-crystallinity. This has made it challenging to systematically study their microstructural variations beyond the interlayer spacing. Understanding the impact of these structural characteristics on their photocatalytic behavior remains a largely unexplored area in the field.

In my doctoral research, I focused on the photocatalytic potential of 2D carbon nitride materials, also known as polyermic carbon nitrides (PCN)s. This work involved a detailed investigation of their structural, electronic, and optoelectronic properties,

aiming to uncover the relationships between these characteristics and their catalytic performance. By leveraging advanced computational techniques, I sought to provide a deeper understanding of the complex interactions within these materials, contributing to the development of more efficient and versatile photocatalytic systems.

In Chapters 1-3, the thermodynamic properties of various reported 2D carbon nitride structures, along with the resulting changes in electronic structures and optical properties, were described using methods ranging from the Local Density Approximation (LDA) to the GW approximation. This comprehensive analysis provided a detailed understanding of the material characteristics at different levels of theoretical accuracy.

Chapter 4 builds on this foundation to investigate the reaction mechanisms of the oxygen reduction reaction (ORR) and hydrogen evolution reaction (HER), offering insights into how the structural and electronic features influence catalytic performance.

Chapters 5-7 extend these findings through collaborative experimental studies, aiming to establish correlations between the observed properties and the actual atomic structures. The experimentally observed characteristics were shown to align well with the features predicted by computational studies, thus validating the theoretical models and offering a deeper understanding of the experimental observations.

Additional details and extended discussions of these results, including code modifications, further computational trials, and additional results for comparison that are not discussed in the main text, are provided in the Appendix, where the authors related publications are included.

2 Theory

The following sections cover the fundamentals of Hartree-Fock methods and time-independent density functional theory, which are used to describe the electronic structure of the ground state. Additionally, we discuss GW methods, Casida and Bethe-Salpeter equations, and related techniques employed to approximate accurate electronic structures beyond the ground state. Furthermore, this chapter explores the basics of photochemistry, illustrating how theoretical simulations can be linked to experimental observations. This comprehensive chapter is grounded in the existing literature. [16–20] For simplicity, atomic units are employed in the equations.

2.1 The many-body Schrödinger Equation

In order to describe the electronic structure of materials, it is essential to address many-body problems involving electrons and nuclei interacting through Coulombic forces. Specifically, solving the non-relativistic Schrödinger equation for many-electron systems is crucial for accurately handling particles as lightweight as electrons.

$$i\hbar\frac{d}{dt}|\Psi(\mathbf{r},t)\rangle = H|\Psi(\mathbf{r},t)\rangle \tag{2.1}$$

, where H is the Hamiltonian operator, Ψ is the wavefunction of a system (many-particle), t and **r** is time at each spatial point of particles. The Hamiltonian includes the operators corresponding to the kinetic and potential energy. from the electrons

and nuclei.

$$H = T_n + T_e + V_{nn} + V_{en} + V_{ee} + V_{e-ext} + V_{n_e xt} \tag{2.2}$$

, where the kinetic energy of nuclei T_n and electrons T_e are given by:

$$T_n = \sum_I -\frac{1}{2M_I}\nabla_I^2,\ T_e = \sum_i -\frac{1}{2}\nabla_i^2 \tag{2.3}$$

, where M_I is the mass of nuclei. The Coulombic energy between the nuclei V_{nn}, the electrons V_{ee}, and the electron–nuclei V_{en} are given by:

$$V_{nn} = \sum_{I,J} \frac{Z_I Z_J}{|\mathbf{R}_I - \mathbf{R}_J|},\ V_{ne} = \sum_{i,I} \frac{Z_I}{|\mathbf{R}_I - \mathbf{r}_i|},\ V_{ee} = \sum_{i,j} \frac{1}{|\mathbf{r}_i - \mathbf{r}_j|} \tag{2.4}$$

, where Z is the charge, **R** and **r** are the spatial coordinates of nuclei and electrons, respectively. The potential contributions from the external electromagnetic field for the electron and the nuclei are V_{e-ext} and V_{n-ext}.

The time-independent form is approximated by the separation of the spatial wave-function and time-dependent phase part

$$\Psi(\mathbf{r}, \mathbf{R}, t) = \Psi(\mathbf{r}, \mathbf{R}) e^{-iEt} \tag{2.5}$$

, where **r** and **R** are now spatial points of electrons and nuclei, respectively. Then, we obtain the time-independent form of Schrödinger equation:

$$H\Psi(\mathbf{r}, \mathbf{R}) = E\Psi(\mathbf{r}, \mathbf{R}) \tag{2.6}$$

The Born-Oppenheimer approximation allows further simplification by assuming the static motion of nuclei, which now the wavefunction of the equation for the electrons

can be expressed by:

$$\left[T_e + V_{en}(\mathbf{r}) + V_{e-ext} + V_{ee}(\mathbf{r} - \mathbf{r}_j)\right] \Psi(\mathbf{r}) = E\Psi(\mathbf{r}) \tag{2.7}$$

However, solving the many-electron Schrödinger equation is not straightforward. Two successful numerical techniques were established the former is the wavefunction method and the latter is the electron density method.

2.2 Wavefunction method

2.2.1 Hartree method

The Hartree product, named after D. R. Hartree who first introduced atomic units, approximates the wavefunction of a system as a combination of wavefunctions of individual particles, which also includes a meaning of mean-field approximation:[21]

$$\Psi(\mathbf{r}_1, \cdots, \mathbf{r}_i) = \psi_1(\mathbf{r}_1) \cdots \psi_i(\mathbf{r}_i) \tag{2.8}$$

, where ψ is individual wavefunctions and the orthonormality of one-electron wavefunctions $\int d\psi_i^*(\mathbf{r})\psi_j(\mathbf{r}) = \delta_{ij}$ is assumed implicitly. From the equation 2.8, we assume that the wavefunction of each electron ψ is independent (non-interacting). Then, the total charge density at point **r** except for each electron i is given by:

$$\rho(\mathbf{r}) = -\sum_{i \neq j} |\psi_j(\mathbf{r})|^2 \tag{2.9}$$

This charge density yields a mean-field potential:

$$\nabla^2 V(\mathbf{r}) = -\frac{\rho(\mathbf{r})}{\epsilon_0} \tag{2.10}$$

This mean-field potential can be expressed by the Coulomb integral:

$$V(\mathbf{r}) = \int \frac{\rho(\mathbf{r}_j)}{|\mathbf{r}_i - \mathbf{r}_j|} d\mathbf{r}_j = -\sum_{i \neq j} \int \frac{|\psi_j(\mathbf{r}_j)|^2}{|\mathbf{r}_i - \mathbf{r}_j|} d\mathbf{r}_j \tag{2.11}$$

It constructs the time-independent Schrödinger equation of the non-interacting one-electron wavefunction:

$$\left[T_e + V_{en} + V_{e-ext} + V(\mathbf{r}_i)\right] \psi_i = \epsilon_i \psi_i \tag{2.12}$$

Finally, the Hartree equation is given by:

$$\left[T_e + V_{ext} + V(\mathbf{r}_i)\right] \psi_{_i} = \epsilon_i \psi_{_i} \tag{2.13}$$

, where the V_{ext} includes V_{en} and V_{e-ext}, and the ϵ_i is the Lagrange multipliers. This non-linear equation provides the basis that the solution can be obtained by the use of iteration and the following variational condition suggested by J. C. Slater and J. A. Gaunt:

$$\delta \left(\langle \prod_i \psi_i | H | \prod_i \psi_i \rangle - \sum_i \epsilon_i \langle \psi_i | \psi_i \rangle \right) = 0 \tag{2.14}$$

The detailed application for the variational condition will follow in Section 2.2.2.

2.2.2 Variational method

The energy can be given by the expectation value of trial wavefunctions:

$$E\left[\Phi\right] = \langle \Phi | H | \Phi \rangle \tag{2.15}$$

The energy can be minimized by the perturbation of the trial wavefunctions $\delta\Phi$

$$\begin{aligned} E\left[\Phi+\delta\Phi\right] &= \langle(\Phi+\delta\Phi|H|\Phi+\delta\Phi)\rangle \\ &= E\left[\Phi\right] + \langle(\delta\Phi|H|\Phi)\rangle + \langle(\Phi|H|\delta\Phi)\rangle + \cdots \\ &= E\left[\Phi\right] + \delta E + \cdots . \end{aligned} \tag{2.16}$$

The minimum energy min(E) can be found when $\delta E = 0$. It gives the lowest energy eigenstate (ground-state energy) E_0 of the Hamiltonian.

$$\begin{aligned} E_0 &= \frac{\langle\Phi|H|\Phi\rangle}{\langle\Phi|\Phi\rangle} \\ \delta E &= \left(\frac{\langle\delta\Phi|H|\Phi\rangle}{\langle\delta\Phi|\Phi\rangle} + \frac{\langle\Phi|H|\delta\Phi\rangle}{\langle\Phi|\delta\Phi\rangle}\right) \end{aligned} \tag{2.17}$$

This method also called the Rayleigh-Ritz method, is the way to find the wavefunctions for the ground-state energy using a linear combination of known basis functions Φ_i with unknown coefficients c_i:

$$\begin{aligned} \Phi &= \sum_i c_i \Phi_i \\ \delta\Phi_i &= \delta c_i \Phi \end{aligned} \tag{2.18}$$

With the constraint of the orthonomality of the trial wavefunctions $\langle\Phi_i|\Phi_j\rangle = \delta_{ij}$, we can minimize the energy when the δE is given by

$$\delta E = \sum_{ij}\left(\frac{\delta c_i^* c_j \langle\Phi_i|H|\Phi_j\rangle}{\delta c_i^* c_j \langle\Phi_i|\Phi_j\rangle} + \frac{\delta c_i c_j^* \langle\Phi_i|H|\Phi_j\rangle}{\delta c_i c_j^* \langle\Phi_i|\Phi_j\rangle}\right) = 0 \tag{2.19}$$

The E energy becomes minimum when each term goes to 0 and the secular equation is given by:

$$\sum_i c_i \left(H_{ij} - E S_{ij}\right) = 0 \tag{2.20}$$

, where the overlap matrix $S_{ij} = \langle \Phi_i | \Phi_j \rangle$ and $H_{ij} = \langle \Phi_i | H | \Phi_j \rangle$. Thus, the wavefunction of state i can be approximated by finding the corresponding coefficient c_i from the equation.

2.2.3 Hartree-Fock method

Indeed, the Hartree product cannot adequately describe fermions like electrons, which require antisymmetric wavefunctions. The solution for antisymmetric wavefunctions was introduced by J. C. Slater and V. A. Fock through the use of a Slater determinant, which is based on the simplest assumption for the many-electron wavefunction reproduced the Hartree equation.

$$\Psi^{\mathsf{HF}}(\mathbf{r}_1, \cdots, \mathbf{r}_N) = \frac{1}{\sqrt{N!}} det \begin{bmatrix} \psi_1(\mathbf{r}_1) & \psi_1(\mathbf{r}_2) & \cdots & \psi_1(\mathbf{r}_N) \\ \psi_2(\mathbf{r}_1) & \psi_2(\mathbf{r}_2) & \cdots & \psi_2(\mathbf{r}_N) \\ \vdots & \vdots & \ddots & \vdots \\ \psi_N(\mathbf{r}_1) & \psi_N(\mathbf{r}_2) & ... & \psi_N(\mathbf{r}_N) \end{bmatrix} \tag{2.21}$$

This so-called Hartree–Fock method including Pauli exclusion principles provides a more accurate picture than the case of the Hartree method which neglects the exchange of electrons.

In the Hartree-Fock method, the expectation value of the Hamiltonian for energy E_{HF} is given by:

$$E_{\mathsf{HF}}(\psi) = \langle \Psi^{\mathsf{HF}} | H | \Psi^{\mathsf{HF}} \rangle = \sum_i H_i + \frac{1}{2} \sum_{i,j(i \neq j)} (J_{ij} - K_{ij}) \tag{2.22}$$

, where

$$
\begin{aligned}
H_i &= \langle \psi_i | T_e + V_{ext} | \psi_i \rangle \\
J_{ij} &= \sum_{i,j(i \neq j)} \langle \psi_i(x_i) \psi_j(x_j) | \frac{1}{|x_i - x_j|} | \psi_i(x_i) \psi_j(x_j) \rangle \\
K_{ij} &= \sum_{i,j(i \neq j)} \langle \psi_i(x_i) \psi_j(x_j) | \frac{1}{|x_i - x_j|} | \psi_j(x_i) \psi_i(x_j) \rangle
\end{aligned}
\tag{2.23}
$$

The individual one-electron integrals are labeled as H_i, while the two-electron integrals encompass both the Coulomb integrals denoted as J_{ij}, and the exchange integrals represented as K_{ij}. The exchange term is a consequence of the anti-symmetry property of the spin-electrons. In order to allow spin polarization into the spatial coordinates, the spin-wavefunction $\psi(x) = \psi\{\mathbf{r}, \sigma\}$ is used in the equation 2.23 instead of the spatial wavefunction $\psi(\mathbf{r})$. The two-electron integral part still can be solved by the iteration. By the means of the variational method, we can approximate at least the lowest eigenstate or ground-state energy. (The equation 2.20 and the equation 2.22).

The Hartree-Fock equations of one-electron wavefunctions then can be given by:

$$
\begin{aligned}
F|\psi_i\rangle &= \left[H_i + \sum_j (j_j - k_j) \right] |\psi_i\rangle = \sum_j \epsilon_{ij} |\psi_j\rangle \\
F &= h + \sum_j (j_j - k_j) = h + U_{\mathsf{HF}}
\end{aligned}
\tag{2.24}
$$

, where F is Fock operator and U_{HF} is the Hartree energy. The equation 2.24 also yields the canonical Hartree-Fock equations of the independent individual electrons.

$$
F\psi_i = \epsilon_i \psi_i \tag{2.25}
$$

The Hartree-Fock-Roothaan method then reforms the Hartree-Fock equation into the coefficient matrix problems of the basis functions (The equation 2.18 and the equation

2.20):

$$\boldsymbol{FC} = \epsilon \boldsymbol{SC} \tag{2.26}$$

, where $\boldsymbol{S}$ is overlap matrix and $\boldsymbol{C}$ is the coefficient matrix. These Hartree-Fock-Roothaan equations allow us to construct Fock matrix using the coefficient matrix. The newly updated Fock matrix with the eigenvectors can be thereby obtained from the new coefficient matrix during the self-iterative field (SCF) method.

While the Hartree–Fock–Roothaan method, employing a linear combination of basis functions (atomic orbitals), provides numerical solutions via matrix diagonalization, it's crucial to acknowledge that the computation of the Fock matrix, encompassing the Coulomb and Exchange matrix, demands significant computational resources. Furthermore, the single Slater determinant Hartree-Fock method does not account for electron correlation, making it incapable of accurately describing the exact electronic structure. By considering multiple electron configurations, it is theoretically possible to approximate the exact electronic wavefunctions through a linear combination of all conceivable excited Slater determinants. This approach, known as the full configuration interaction (full CI) ansatz, can represent interacting electron wavefunctions with precise forms. Other wavefunction-based approaches such as coupled cluster and Møller-Plesset perturbation theory (MP) have also been developed. However, the exponential increase in computational costs limits their practical application to very small molecules. These limitations have led to the emergence of Kohn-Sham density functional theory (KS-DFT), which offers a substantially cost-efficient and accurate alternative method.

2.3 Density functional theory

2.3.1 Hohenberg–Kohn theorms

Density functional theory (DFT) employs the charge density rather than the many-body electron wavefunctions to describe the ground state energy of the system.

The formulation of the original DFT was started by P. Hohenberg and W. Kohn.[22] The Hohenberg–Kohn theorem states:

1. The electron density function of the ground state can be defined as the Hamiltonian and the corresponding wavefunction is determined from the unique external potential. This means that the external potential is also expressed as a unique functional of electronic density, therefore, the many particle ground state is also a unique functional of the electronic density.

2. The ground state energy can be obtained by the variational principle, where the electron density is the variable function.

Based on these theorems, Hohenberg and Kohn define a universal function $F[n]$ is given by:

$$F\left[n\right] \equiv \langle \Psi | T_e + V_{ee} | \Psi \rangle \equiv \int n(\mathbf{r}) d\mathbf{r} = N \tag{2.27}$$

, where N is the number of electrons in the system and $n(\mathbf{r})$ is the electronic density. It provided a groundbreaking foundation for simplifying the intricate many-body problem involving N electrons into the problem of handling $3N$ electron density functions. DFT is also considered the successor to the Thomas-Fermi model due to its utilization of the electron density model.

2.3.2 The Kohn–Sham equations

The Hohenberg–Kohn theorem was further developed by W. Kohn and L. J. Sham. The ground-state energy of an interacting inhomogeneous electron gas under the external potential is given by:[22]

$$E = \int V_{ext}(\mathbf{r}) n(\mathbf{r}) d\mathbf{r} + \frac{1}{2} \iint \frac{n(\mathbf{r}) n(\mathbf{r}')}{|\mathbf{r} - \mathbf{r}'|} d\mathbf{r} d\mathbf{r}' + F[n] \tag{2.28}$$

W. Kohn and L. J. Sham separated the universal function into two parts:[23]

$$F[n] \equiv T_e[n] + E_{xc}[n] \tag{2.29}$$

, where T_e is the kinetic energy of non-interacting electrons analogous to the Hartree method and $E_{xc}[n]$ is the exchange and correlation energy of an interacting system with density $n(\mathbf{r})$. Under the slowly varying electron density, $E_{xc}[n]$ can be given by:

$$E_{xc}[n] = \int n(\mathbf{r}) \epsilon_{xc}[n(\mathbf{r})] \, d\mathbf{r} \tag{2.30}$$

, where $\epsilon_{xc}(n)$ is the exchange and correlation energy per electron of a homogeneous electronic gas (HEG). This HEG assumption yields the equations:

$$\int \delta(\mathbf{r}) \Big\{ V_{\text{eff}} + \frac{\delta T_s[n]}{\delta n(\mathbf{r})} + \mu_{xc}[n(\mathbf{r})] \Big\} d\mathbf{r} = 0, \ \int \delta n(\mathbf{r}) = 0 \tag{2.31}$$

, where

$$V_{\text{eff}} = V_{ext}(\mathbf{r}) + \int \frac{n(\mathbf{r}')}{|\mathbf{r} - \mathbf{r}'|} d\mathbf{r}' \tag{2.32}$$

and

$$\mu_{xc}(n) = \frac{\delta}{\delta n(\mathbf{r})} E_{xc}[n(\mathbf{r})] \tag{2.33}$$

The equation 2.31 and the equation 2.33 allow us to approximate the interacting

and the slowly varying electronic density with non-interacting and homogeneous density. Thereby, these equations formulate the one-particle Schrödinger equation, also known as the Kohn-Sham equation, which uses the electron density functional $n(\mathbf{r})$ under the given potential $V_{\text{eff}} + \mu_{xc}\left[n(\mathbf{r})\right]$ given by

$$\left[T_e + V_{\text{eff}} + \mu_{xc}\left[n(\mathbf{r})\right]\right]\psi_i = \epsilon_i\psi_i,\ n(\mathbf{r}) = \sum_i |\psi_i(\mathbf{r})|^2 \tag{2.34}$$

The equations need to be solved by SCF method to approach the ground state energy: One starts with an initial guess of an electron density $n(\mathbf{r})$, constructs the effective potential V_{eff} and the exchange and correlated contribution of interacting particles μ_{xc}. Then, the ground state energy is given by

$$E_0 = \sum_i \epsilon_i - \frac{1}{2}\int\int \frac{n(\mathbf{r})n(\mathbf{r}')}{|\mathbf{r}-\mathbf{r}'|}d\mathbf{r}d\mathbf{r}' + \int n(\mathbf{r})\left[\epsilon_{xc}(n(\mathbf{r})) - \mu_{xc}(n(\mathbf{r}))\right]d\mathbf{r} \tag{2.35}$$

Within this framework, the formidable challenge of addressing interacting electrons in a stationary external potential is reformed into a manageable problem involving non-interacting electrons navigating within an effective potential.

2.3.3 Exchange and correlation functionals

The adoption of the universal density functional for the Kohn-Sham equation represented a groundbreaking direction for simplifying the many-electron problem. However, it bears inherent limitations in terms of accuracy, as it avoids providing an accurate description of the exchange and correlation energy for interacting electron densities. To address this limitation, several electronic models have been developed to more accurately approximate the exchange and correlation energy.

2.3.4 Local density approximation

The first one is the LDA originated from the Thomas-Fermi model. The LDA functionals approximate the exchange and correlation energy by directly borrowing from the HEG model, as shown in the following equation:

$$E_{xc}^{\mathsf{LDA}}[n] = \int d\mathbf{r}\; n(\mathbf{r})\epsilon_{xc}^{\mathsf{LDA}}(n(\mathbf{r})) \tag{2.36}$$

and

$$\epsilon_{xc}^{\mathsf{LDA}}(n(\mathbf{r})) = \epsilon_{x}^{\mathsf{LDA}}(n(\mathbf{r})) + \epsilon_{c}^{\mathsf{LDA}}(n(\mathbf{r})) \tag{2.37}$$

, where $\epsilon_{x}^{\mathsf{LDA}}(n(\mathbf{r})) = -\frac{3}{4}(\frac{3}{\pi}n(r))^{\frac{1}{3}}$ and $\epsilon_{c}^{\mathsf{LDA}}(n(\mathbf{r}))$ is fitted from the results of Quantum Monte Carlo simulation. As predicted by the Hohenberg-Kohn-Sham framework, this LDA functional, even when used in conjunction with the HEG, has shown success in describing the bulk structure of large atomic systems. Because the HEG model describes well near the nuclei and the main body of charge distribution. However, it tends to provide less accurate electronic descriptions by underestimating the exchange energy and overestimating the correlation energy. These limitations also stem from the lack of description of varying density at the surface or the overlap regions in the molecules. Furthermore, unlike the Hartree-Fock method, LDA does not consider the exchange energy explicitly. This leads to an issue of double counting of electrons which results in a significant underestimation of the band gap of the insulators.

2.3.5 Generalized gradient approximations

Actually, the model for the inhomogenous electron gas (IEG) is proposed by Hohenberg and Kohn. [22] Here, the expansion of the exchange and correlation energy for

the IEG model is given by

$$E_{xc}[n] = \int n(\mathbf{r})\epsilon_{xc}[n(\mathbf{r})]\, d\mathbf{r} + \int |\nabla n(\mathbf{r})|^2 \epsilon_{xc}^{(2)}[n(\mathbf{r})]\, d\mathbf{r} + \cdots \tag{2.38}$$

, where the second term of the exchange and correlation portion $\epsilon_{xc}^{(2)}[n(\mathbf{r})]$ is expressed by the energy expansion in powers of the gradient operator. Since the kinetic term T_e is based on the non-interacting homogeneous electron gas model, the updated T_e can be given by

$$T_e[n] = \int \frac{3}{10}(3\pi^2 n)^{\frac{2}{3}} n(\mathbf{r}) d\mathbf{r} + \int |\nabla n|^2 t^{(2)}(n) d\mathbf{r} + \cdots \tag{2.39}$$

The inclusion of the second term gives the generalized gradient approximation (GGA), where the GGA exchange-correlation energy is given by

$$E_{xc}^{\mathsf{GGA}}[n] = \int n(\mathbf{r})\epsilon_{xc}^{\mathsf{GGA}}[n(\mathbf{r}), |\nabla n(\mathbf{r})|]\, d\mathbf{r} \tag{2.40}$$

and here

$$\begin{aligned} \epsilon_{xc}^{\mathsf{GGA}}[n(\mathbf{r}), |\nabla n(\mathbf{r})|] &= \epsilon_x^{\mathsf{GGA}} + \epsilon_c^{\mathsf{GGA}} \\ \epsilon_x^{\mathsf{GGA}} &= \epsilon_x^{\mathsf{LDA}}(n(\mathbf{r}))F_x[n(\mathbf{r}), |\nabla n(\mathbf{r})|] \\ \epsilon_c^{\mathsf{GGA}} &= \epsilon_c^{\mathsf{LDA}}(n(\mathbf{r})) + G[n(\mathbf{r}), |\nabla n(\mathbf{r})|] \end{aligned} \tag{2.41}$$

, where both the enhancement factor F_x and the parameter sets G are diverse to the functional. Due to the incorporation of the inhomogeneous electron density component, GGA provides a more accurate description of binding energy. As a result, it demonstrates successful results in depicting chemical reactions. This significantly contributes to the broader utilization of DFT calculations. Even after the development of the Kohn-Sham equation and its associated models, various methods have been evolving in DFT, encompassing different functionals and addressing long-range inter-

actions such as van der Waals interactions. However, as the DFT-GGA method gains widespread use, there have been reports of material structures that are not easily described by simple gradients. To address this, other approaches like meta-GGA or Hubbard corrections have been proposed. Nonetheless, these methods involve the inclusion of additional parameters to refine the description of the electron density, making them not a universally applicable solution but rather empirical methods.

2.3.6 Hybrid functional

After the successful description of GGA functionals, there have been numerous studies regarding the development of the exchange and correlation functionals E_{xc}. In the series of publications, A. D. Becke proposed the consideration of the *exact-exchange* energy for the further improvement of the functionals.[24] In the Kohn–Sham DFT, the exchange correlation energy E_{xc} can be given as "adiabatic connection" formulation.[25]

$$E_{xc} = \int_0^1 U_{xc}^{\lambda} d\lambda \tag{2.42}$$

, where λ is an interatomic coupling-strength parameter to turn on the Coulomb repulsion between electrons, and U_{xc}^{λ} is the coupling-strength correlated the potential energy of the exchange-correlation. ($\lambda = 0$ means non-interacting Kohn–Sham system and $\lambda = 1$ is fully interacting real system) When the $\lambda = 0$, the Equation 2.42 gives the exact exchange energy solely. Therefore, the novel approximation of E_{xc} was proposed

$$E_{xc} = E_{xc}^{\text{LSDA}} + a_0(E_x^{\text{exact}} - E_x^{\text{LSDA}}) + a_x \Delta E_x^{\text{B88}} + a_c \Delta E_c^{\text{PW91}} \tag{2.43}$$

, where a_0, a_x, and a_c are semiempirical coefficients from the experiments, E_x^{exact} is the exact exchange energy, E_x^{B88} is the gradient correction for the exchange, E_x^{PW91}

is the gradient correction of the correlation, E_{xc}^{LSDA} and E_{x}^{LSDA} is the energy of the exchange-correlation and the exchange energy from the local-spin density approximation (LSDA) functional respectively. These hybrid functionals have proven successful in describing the properties of a wide range of molecular structures. This success is attributed to their ability to provide a more accurate energy description based on the electronic structure, as the incorporation of some degree of accurate exchange energy (E_{xc}) that is particularly successful in describing the properties of localized electrons. However, calculating the accurate exchange energy remains computationally demanding. As a result, adopting the idea of solid-state physics, more efficient hybrid functionals have been developed that screen long-range Coulomb interactions to make the process more efficient.

$$\frac{1}{|\mathbf{r}-\mathbf{r}'|} = \frac{\text{erfc}(\mu|\mathbf{r}-\mathbf{r}'|)}{|\mathbf{r}-\mathbf{r}'|} + \frac{\text{erf}(\mu|\mathbf{r}-\mathbf{r}'|)}{|\mathbf{r}-\mathbf{r}'|} \tag{2.44}$$

and

$$\text{erfc}(\mu|\mathbf{r}-\mathbf{r}'|) = 1 - \text{erf}(\mu|\mathbf{r}-\mathbf{r}'|) \tag{2.45}$$

, where erfc is the complementary error function, erf is the error function, and μ is the characteristic length of the short-lange exchange interaction. The first right term is the short-range and the second right term is the long-range component, respectively. Here, PBE0 functional is given by

$$E_{xc}^{\text{PBE0}} = aE_{x}^{\text{SR,HF}} + (1-a)E_{x}^{\text{PBE}} + E_{c}^{\text{PBE}} \tag{2.46}$$

and HSE functional is given by

$$E_{xc}^{\text{HSE}} = aE_{x}^{\text{SR,HF}} + (1-a)E_{x}^{\text{PBE,SR}} + E_{x}^{\text{PBE,LR}} + E_{c}^{\text{PBE}} \tag{2.47}$$

, where the PBE is the GGA functional suggested by Perdew, Burke, and Ernzerhof (PBE) and a is the mixing parameter. The use of these range separation parameters improved the efficiency of computational costs significantly. Consequently, the hybrid functional has proved that it provides not only a more accurate description of the properties of the ground state (lattice parameters, electronic structure, and cohesive energy) but also reasonable properties of the excited states (band gap and photoemission spectra). However, challenges persist, particularly in addressing the use of empirical parameters and the limitations of the single-determinant method, which need further improvements for hybrid functionals to evolve into purely *ab initio* methods.

2.4 *GW* Approximation: A Many-Body Approach

The GW approximation is a powerful method for calculating quasiparticle energy in many-body systems. In this approach, the self-energy Σ is approximated as the product of the Green's function G and the dynamically screened Coulomb interaction W. This approximation is named "GW" due to this factorization. The Green's function G is defined as:

$$G(r, r', \omega) = \sum_n \frac{\psi_n(r)\psi_n^*(r')}{\omega - \epsilon_n + i\eta} \tag{2.48}$$

where ψ_n and ϵ_n are the quasiparticle wave functions and energy, and η is a small positive constant. The Green's function describes electron propagation, including electron-electron interactions, while the self-energy $\Sigma(r, r', \omega)$ incorporates many-body effects beyond the mean-field approximation. In the GW approximation, the self-energy is given by:

$$\Sigma(r, r', \omega) = i \int G(r, r', \omega') W(r, r', \omega - \omega') d\omega' \tag{2.49}$$

where $W(r, r', \omega)$ is the dynamically screened Coulomb interaction, reflecting how electron interactions are screened by other electrons in the material.

2.4.1 Self-Energy and Quasiparticle Energy

In the GW approximation, the self-energy $\Sigma(r, r', \omega)$ adjusts the electronic energy levels from those obtained in simpler mean-field approximations, such as DFT or Hartree-Fock. The quasiparticle energy E_n is calculated using the following expression:

$$E_n = \epsilon_n + \langle \psi_n | \Sigma(E_n) - V_{xc} | \psi_n \rangle \tag{2.50}$$

where ϵ_n are the eigenvalues from a DFT or Hartree-Fock calculation, V_{xc} represents the exchange-correlation potential in DFT, and $\Sigma(E_n)$ is the self-energy evaluated at the quasiparticle energy E_n. This expression corrects the approximate eigenvalues by replacing the exchange-correlation potential with the more accurate GW self-energy.

In practice, the GW method is often used in a non-self-consistent form, called G_0W_0, where G and W are computed from a fixed DFT starting point without iterative updates. More accurate results can be obtained through self-consistent GW methods, which iteratively update G and W until convergence, though at a higher computational cost.

2.4.2 *GW* Method and Hedins Equations

The GW method is built upon Hedins equations, which describe many-body effects in terms of G, Σ, W, the irreducible polarizability χ, and the vertex function Γ. The equations are:

$$G(1,2) = G_0(1,2) + \int d(3,4) G_0(1,3) \Sigma(3,4) G(4,2) \tag{2.51}$$

$$\chi(1,2) = \int d(3,4) G(1,3) G(4,1) \Gamma(3;4,2) \tag{2.52}$$

$$W(1,2) = V(1,2) + \int d(3,4) V(1,3) \chi(3,4) W(4,2) \tag{2.53}$$

$$\Sigma(1,2) = \int d(3,4) G(1,3) \Gamma(3;2,4) W(4,1) \tag{2.54}$$

In practical GW calculations, Γ is often simplified as $\Gamma(1,2;3) = \delta(1,2)\delta(1,3)$, reducing the complexity. This leads to simplified forms for χ and Σ:

$$\chi(1,2) = G(1,2)G(2,1) \tag{2.55}$$

$$\Sigma(1,2) = G(1,2)W(2,1) \tag{2.56}$$

Finally, the Green function can also be represented spectrally as:

$$G(r,r',\omega) = \sum_i \frac{\psi_i(r)\psi_i^*(r')}{\omega - \epsilon_i(\omega)} \tag{2.57}$$

or, more generally,

$$G(r,r',\omega) = \int d\omega' \frac{A(r,r',\omega')}{\omega - \omega' - i\delta} + \int d\omega' \frac{A(r,r',\omega')}{\omega + \omega' + i\delta} \tag{2.58}$$

, where A is the spectral function.

2.4.3 Bethe-Salpeter Equation

The Bethe-Salpeter Equation (BSE) builds on the GW approximation to describe optical excitations, such as excitons, in materials. While the GW method provides an accurate description of quasiparticle energy, it does not account for electron-hole interactions, which are critical for understanding optical properties. The BSE formalism addresses this by describing the interactions between excited electrons and the holes they leave behind. The BSE is derived from the two-particle Green's function, which describes the propagation of an electron and a hole in the system. The equation takes the form:

$$H_{\text{BSE}}\Psi_{\text{exc}} = E_{\text{exc}}\Psi_{\text{exc}} \tag{2.59}$$

, where H_{BSE} is the BSE Hamiltonian, Ψ_{exc} is the electron-hole wave function (exciton wave function), and E_{exc} is the excitation energy. The BSE Hamiltonian includes both the quasiparticle energy obtained from the GW approximation and the electron-hole interaction term, which accounts for the Coulomb attraction between the excited electron and the hole. Therefore, the Hessian matrix from Equ. 2.68 need to update the matrix A and B from the Equ. 2.69 to the following:

$$\begin{aligned} A_{ai,bj} &= (\epsilon_a - \epsilon_i)\delta_{ab}\delta_{ij} + W_{ai,bj} \\ B_{ai,bj} &= W_{ai,bj} \end{aligned} \tag{2.60}$$

, where W is the screened Coulomb interaction from GW calculations. The BSE method is particularly important for calculating optical spectra in semiconductors, in-

sulators, and other materials where excitonic effects are significant. Excitons are bound states of an electron and a hole, and they can have energy below the quasiparticle band gap. The BSE method captures these excitonic states, providing a more accurate description of absorption spectra than the GW approximation alone.

GW-BSE Workflow

In practice, the GW and BSE methods are often used together in a sequential workflow to calculate the electronic and optical properties of materials. The typical steps are as follows:

1. **Ground State Calculation**: A ground state calculation is performed using DFT to obtain the initial wave functions and eigenvalues.

2. **Quasiparticle Energy Calculation**: The GW approximation is applied to correct the DFT eigenvalues and obtain more accurate quasiparticle energy.

3. **Exciton Calculation**: The BSE is solved using the GW-corrected quasiparticle energy to obtain the exciton wave functions and excitation energy.

4. **Optical Spectrum**: The optical spectrum is calculated by evaluating the absorption cross-section from the exciton wave functions and energy.

This workflow provides a comprehensive description of both quasiparticle and excitonic properties, making it suitable for studying optical and electronic excitations in materials.

2.5 Photophysical Processes, Excitons, and Recombination

2.5.1 Atomistic thermodynamics for surfaces

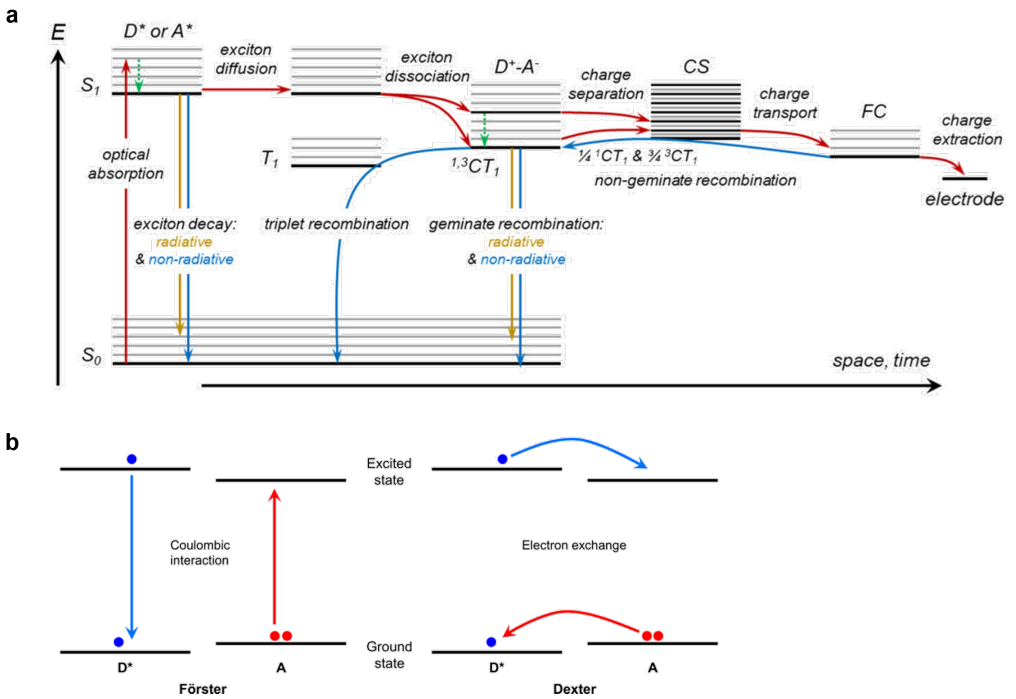

Figure 1: (a) Jablonski diagram illustrating excited-state processes, including charge generation and recombination, in an organic solar cell (S: singlet state, T: triplet state, CT: charge transfer state).[26] (b) Schematic illustrations of Förster resonance energy transfer and Dexter electron-exchange energy transfer. Solid and dash lines indicate radiative and nonradiative transitions, respectively[27]. These figures are taken from the corresponding literature.

Photophysical processes are central to understanding the interaction between light and matter, particularly in the context of semiconductors, photovoltaics, and light-emitting devices. These processes involve the absorption of photons, the generation of excited states (including excitons), energy transfer, and the eventual recombination of charge carriers.1 This section covers the fundamental concepts of photophysical

processes, focusing on excitons and the mechanisms that govern their formation, transport, and recombination.

Absorption of Light

The first step in any photophysical process is the absorption of light. When a material absorbs a photon, an electron is excited from a lower energy state (usually the valence band in semiconductors) to a higher energy state (typically the conduction band). This process creates an electron in the conduction band and a corresponding hole in the valence band. The energy of the absorbed photon must match the energy difference between the initial and final electronic states, which is typically the band gap in semiconductors or the energy difference between molecular orbitals in organic materials.

Excitons: Bound Electron-Hole Pairs

In many materials, particularly semiconductors and insulators, the excited electron and the hole it leaves behind can form a bound state known as an exciton. Excitons are quasiparticles that represent the correlated motion of the electron and the hole. They are bound by the Coulomb attraction between the negatively charged electron and the positively charged hole. Excitons can be classified into two types based on the distance between the electron and hole:

- **Frenkel Excitons**: In materials with strong Coulomb interactions and small dielectric constants, such as organic semiconductors and molecular crystals, the electron and hole remain close together. These excitons are highly localized, with binding energy typically on the order of 0.5 to 2.0 eV.

- **Wannier-Mott Excitons**: In materials with large dielectric constants, such as inorganic semiconductors, the electron and hole are more loosely bound. These excitons are more delocalized and have lower binding energy, typically on the order of a few meV to tens of meV.

The binding energy of an exciton is the energy required to separate the electron and hole into free charge carriers. In materials with low exciton binding energy, thermal energy at room temperature can dissociate excitons into free carriers, which can then contribute to electrical conductivity or other processes.

Exciton Transport

Once excitons are generated, they can move through the material by hopping or diffusion. The mobility of excitons depends on their nature (Frenkel or Wannier-Mott) and the specific properties of the material. In organic semiconductors, excitons typically move by hopping from molecule to molecule, while in inorganic semiconductors, they diffuse more freely due to the delocalized nature of Wannier-Mott excitons. Exciton transport is important for many applications, such as OLEDs and organic photovoltaics, where the efficient movement of excitons to specific regions *(e.g.*, the interface between donor and acceptor materials) is critical for device performance.

Energy Transfer

In addition to transport, excitons can also undergo **energy transfer** processes, where the excitation energy is transferred from one site to another without the movement of the exciton itself. Energy transfer can occur via several mechanisms:

- **Förster Resonance Energy Transfer (FRET)**: FRET is a long-range energy transfer process that occurs when the emission spectrum of a donor molecule

overlaps with the absorption spectrum of an acceptor molecule. This process is mediated by dipole-dipole interactions and is common in molecular systems, such as photosynthetic complexes.

- **Dexter Energy Transfer**: Dexter energy transfer is a short-range process that requires the overlap of molecular orbitals between the donor and acceptor. This process is typically less efficient than FRET and occurs over much shorter distances.

Exciton Recombination

Excitons eventually recombine, either radiatively or non-radiatively. In **radiative recombination**, the electron and hole recombine to emit a photon, resulting in processes like fluorescence and phosphorescence. The energy of the emitted photon corresponds to the energy difference between the electron and hole. In **non-radiative recombination**, the energy of the exciton is dissipated as heat rather than emitted as light. Non-radiative recombination processes (Auger recombination and Defect-mediated recombination)

Exciton Dissociation

In some materials, particularly in photovoltaic devices, excitons must be dissociated into free charge carriers (electrons and holes) to generate a photocurrent. This process typically occurs at the interface between two materials with different electron affinities, such as the donor-acceptor interface in organic solar cells. The efficiency of exciton dissociation depends on the exciton binding energy and the strength of the electric field at the interface. In organic photovoltaics, materials are chosen to ensure efficient exciton dissociation, enabling the generation of free carriers that contribute

to the photocurrent.

Charge Transport and Recombination

After exciton dissociation, the free electrons and holes must be transported to the electrodes to generate a current. Charge transport occurs through the conduction and valence bands in inorganic semiconductors or through hopping between molecules in organic materials. The mobility of the charge carriers depends on the materials properties, such as the level of disorder, the presence of impurities, and the strength of electron-phonon interactions. Charge carriers can also undergo recombination during transport. In **bimolecular recombination**, an electron and a hole recombine to emit a photon, while in **trap-assisted recombination**, charge carriers are captured by defects or impurities in the material. Reducing recombination is critical for improving the efficiency of devices like solar cells and LEDs.

Exciton Dissociation and Charge Generation

For applications like photovoltaics (PVs), such as organic photovoltaics (OPVs) and hybrid perovskite solar cells, the dissociation of excitons into free charge carriers (electrons and holes) is a critical step for converting absorbed light into electrical energy. In these devices, the exciton must be efficiently separated into its constituent electron and hole, which are subsequently transported to the electrodes to generate a photocurrent.

Exciton Dissociation Mechanism

Exciton dissociation occurs when the exciton encounters an interface or a region with a potential difference that can overcome the exciton binding energy. In organic

photovoltaic systems, for instance, excitons are dissociated at the **donor-acceptor interface**. The donor material (typically an organic molecule or polymer) absorbs the light, generating excitons. When the exciton diffuses to the interface between the donor and the acceptor material (usually a fullerene derivative or another organic semiconductor), the electron transfers to the acceptor material due to the difference in electron affinity, while the hole remains in the donor material. This process splits the exciton, producing free charge carriers.

The efficiency of exciton dissociation is primarily determined by:

- **Binding Energy**: Low exciton binding energy increase the likelihood that thermal energy at room temperature can dissociate the exciton into free charges.
- **Interface Engineering**: The energy difference between the donor and acceptor levels must be sufficient to drive the electron transfer and subsequent dissociation of the exciton.
- **Electric Field**: A strong internal electric field at the interface can aid in separating the electron-hole pair and reduce the likelihood of recombination.

Charge Generation and Transfer

After dissociation, free charges are generated: electrons in the acceptor phase and holes in the donor phase. These free charges must be efficiently transferred through their respective phases (donor and acceptor) to the electrodes to contribute to the photocurrent. The rate at which this transfer occurs affects the overall efficiency of devices like solar cells. In inorganic semiconductors like silicon, the exciton binding energy is typically very small (few meV), and excitons can thermally dissociate at room temperature. However, in organic semiconductors, exciton binding energy can be quite high (hundreds of meV), necessitating carefully engineered heterojunctions

to promote efficient exciton dissociation.

Charge Transport in Photovoltaic Devices

Charge transport is a critical phase in devices like solar cells and light-emitting diodes. Once free electrons and holes are generated, they must move through the device to reach the electrodes before they recombine. The efficiency of this process is dictated by several factors, including the materials electronic properties, the presence of defects, and the interaction between charge carriers and phonons (vibrations of the atomic lattice).

Charge Carrier Mobility

Charge carrier mobility is a measure of how quickly an electron or hole can move through a material under the influence of an electric field. It is influenced by factors such as:

- **Material Disorder**: Amorphous or disordered materials, common in organic semiconductors, tend to exhibit lower mobilities due to the presence of traps or barriers that impede carrier movement.
- **Impurities and Defects**: In real materials, defects such as vacancies or impurities can trap charge carriers, reducing their mobility and leading to non-radiative recombination.
- **Temperature Dependence**: In materials where charge transport is dominated by hopping between localized states (as in many organic materials), mobility increases with temperature as thermal energy aids the hopping process.

In organic photovoltaic devices, the mobility of charge carriers (both electrons and

holes) is typically lower than in inorganic semiconductors, which can limit the performance of these devices. Engineering strategies such as optimizing the morphology of donor-acceptor blends or using materials with higher inherent mobilities can help improve charge transport.

Drift and Diffusion of Charge Carriers

Charge transport in photovoltaic devices occurs through two main mechanisms: drift and diffusion. **Drift** refers to the motion of charge carriers under the influence of an electric field, while **diffusion** is the motion of carriers driven by concentration gradients. In organic solar cells, where the internal electric field is often weak, diffusion can play a significant role in charge transport. However, the presence of traps and recombination centers can impede both drift and diffusion, leading to losses in photocurrent and device efficiency.

Recombination Mechanisms

After charge carriers (electrons and holes) are generated and transported through the material, recombination can occur. Recombination is the process by which an electron in the conduction band (or the lowest unoccupied molecular orbital (LUMO) in molecular systems) recombines with a hole in the valence band (or highest occupied molecular orbital (HOMO)). Recombination can be either radiative, where light is emitted, or non-radiative, where the energy is lost as heat.

Radiative Recombination

Radiative recombination occurs when the energy released during recombination is emitted as a photon. This process is essential for light-emitting devices, where effi-

cient light emission is the desired outcome. The efficiency of radiative recombination is characterized by the **radiative quantum yield**, which is the fraction of recombination events that result in photon emission. In contrast, radiative recombination in solar cells represents a loss mechanism, as the energy of the absorbed photon is not converted into electrical energy but is instead re-emitted.

Non-Radiative Recombination

In non-radiative recombination, the energy from the recombining electron and hole is dissipated as heat, typically through lattice vibrations (phonons). Non-radiative recombination reduces the efficiency of both light-emitting and photovoltaic devices because it results in a loss of usable energy. There are several types of non-radiative recombination:

- **Shockley-Read-Hall (SRH) Recombination**: This occurs when defects or impurities in the material act as traps for electrons or holes. Once trapped, the carrier can recombine with a free carrier of the opposite charge, releasing energy as heat. SRH recombination is particularly prevalent in materials with a high density of defects, such as polycrystalline semiconductors.
- **Auger Recombination**: In this process, the recombination energy is transferred to another electron or hole, which is excited to a higher energy level. Auger recombination is common in materials with high carrier densities, such as in heavily doped semiconductors or under high excitation intensities (*e.g.*, in LEDs or lasers).
- **Bimolecular Recombination**: This occurs when an electron and hole recombine directly without the involvement of defects or impurities. In ideal, defect-free semiconductors, bimolecular recombination is the dominant recombination pathway.

2.6 Excited states

The application of DFT in ground-state energy calculations has significantly expanded the versatility of computing the chemical properties of various materials. Building on this success, methods are being developed to describe not only the ground state but also non-ground states, such as excited states.

Like ground state calculations, there are two main approaches for computing excited states: one using wave functions and the other using electron density. The wave function-based methods include CI, Multireference CI, Multireference MP, Multi-Configurational Self-Consistent Field (MCSCF) methods, Complete Active Space Perturbation Theory, as well as Equation-of-Motion and Linear-Response Coupled Cluster theories (EOM-CC and LR-CC, respectively). However, a drawback of these methods is their high computational cost, making them impractical for large molecules.

Due to the practical issue of computational expense associated with the size of the basis set, more feasible methods, such as Time-Dependent Density Functional Theory (TD-DFT) and Time-Dependent Hartree-Fock (TDHF), have been used in most cases. In this dissertation, the details of TD-DFT are excluded due to the lack of the exact exchange energy which follows the limitations of DFT, that it underestimates the energy of localized electrons, which are the main properties of PCN materials.

2.6.1 Time dependent Hartree-Fock

An approximation for the time-dependent Schrödinger equation can start with a single determinant

$$\Psi(r,t) = |\psi_1(r,t)\psi_2(r,t)\cdots\psi_{N-1}(r,t)\psi_N(r,t)| \tag{2.61}$$

, where each electron orbital varies with time-dependent Hartree-Fock equations

$$i\frac{\delta\psi_i}{\delta t} = F(t)\psi_i \tag{2.62}$$

It can be expressed by the Hartree–Fock–Roothaan form in 2.26

$$i\frac{\delta}{\delta t}C = F(t)C \tag{2.63}$$

and its adjoint is given by

$$-i\frac{\delta}{\delta t}C^\dagger = C^\dagger F(t) \tag{2.64}$$

, where C is the coefficient matrix of the orthonormal basis functions. Here we can apply a small perturbation with time $-f(t)$ and then, the ground state orbitals slightly alter

$$\Phi(t) = \Phi_0 + \sum_{i,a} C_{ia}(t)\Phi(i \to a) \tag{2.65}$$

, where one electron moves from ψ_i to ψ_a. The contributions of the first order of the perturbation give the occupied-unoccupied(virtual) and the unoccupied(virtual)-occupied terms, while all the other terms go to zero. The Hartree–Fock equations of motion give

$$\begin{aligned} i\frac{\delta}{\delta t}C_{ai} &= (\epsilon_a - \epsilon_i)C_{ai} + \langle aj|ib\rangle C_{jb} + \langle ab|ij\rangle C^\dagger_{jb} - f_{ai}(t) \\ -i\frac{\delta}{\delta t}C^\dagger_{ai} &= (\epsilon_a - \epsilon_i)C^\dagger_{ai} + \langle ij|ab\rangle C_{jb} + \langle ib|aj\rangle C^\dagger_{jb} - f_{ia}(t) \end{aligned} \tag{2.66}$$

, where the occupied orbitals are $i, j, \cdots$ and the unoccupied orbitals $a, b, \cdots$. The coefficient matrix with time factor can be given by

$$\begin{aligned} C_{ai} &= X_{ai}e^{-i\omega t} + Y^\dagger_{ai}e^{-i\omega t} \\ C^\dagger_{ai} &= X^\dagger_{ai}e^{-i\omega t} + Y_{ai}e^{-i\omega t} \end{aligned} \tag{2.67}$$

Therefore, the Hessian matrix can be expressed as

$$\begin{bmatrix} \mathbf{A} & \mathbf{B} \\ \mathbf{B}^* & \mathbf{A}^* \end{bmatrix} \begin{bmatrix} \mathbf{X} \\ \mathbf{Y} \end{bmatrix} = \omega \begin{bmatrix} 1 & 0 \\ 0 & -1 \end{bmatrix} \begin{bmatrix} \mathbf{X} \\ \mathbf{Y} \end{bmatrix} \tag{2.68}$$

, where ω is the corresponding excitation energy and the matrix elements are given by

$$\begin{aligned} A &= (\epsilon_a - \epsilon_i)\delta_{ai,jb} + \langle aj|ib\rangle \\ B &= \langle ij|ab\rangle \end{aligned} \tag{2.69}$$

The primary element found along the main diagonal of the **A** matrix corresponds to the dissimilarity in energy between orbitals i and a, which is the initial and final states to which the electron is excited. The second component of the **A** matrix, along with the elements of the **B** matrix, arise from how the Coulomb and exchange operators respond linearly to the initial perturbations in single-particle orbitals.

The key idea behind TDHF is that, in the presence of a weak external field, the response of the system can be described by small time-dependent changes in the molecular orbitals. This approach forms the basis of **linear response theory**.

2.6.2 Linear Response Theory

Linear response theory is used to calculate how a system responds to small perturbations. In the context of TDHF, we apply a weak external field and calculate how the wave function of the system evolves in time. More precisely, how it responds in the frequency domain. The goal is to determine the induced dipole moment, which provides information about the absorption spectrum of the system.

The key quantity in linear response theory is the dynamic polarizability $\alpha(\omega)$, which

describes how the system responds to an oscillating external electric field at frequency ω. This can be obtained from the time-dependent induced dipole moment:

$$\mathbf{d}(t) = \langle \Psi(t) | \hat{\mathbf{d}} | \Psi(t) \rangle \tag{2.70}$$

The polarizability $\alpha(\omega)$ is related to the absorption spectrum through the imaginary part of $\alpha(\omega)$:

$$\sigma(\omega) \propto \mathrm{Im}[\alpha(\omega)] \tag{2.71}$$

The absorption spectrum provides insight into the electronic excitation energy of the system. In TDHF, these excitations correspond to the energy differences between occupied and virtual orbitals, corrected for exchange interactions.

2.6.3 Adiabatic Approximation in TDHF

In practical implementations of TDHF, the **adiabatic approximation** is often employed. This approximation assumes that the time-dependent perturbation varies slowly enough that the system can be treated as if it is in a quasi-static state at each instant in time. In other words, the system is assumed to evolve through a sequence of static Hartree-Fock states, each of which is in equilibrium with the external field at that moment. The adiabatic approximation simplifies the TDHF equations by treating the time-dependent Fock operator as if it were the static Fock operator at each time step. This allows the time evolution of the molecular orbitals to be calculated efficiently without solving the entire time-dependent Schrödinger equation.

Excitation energy and Transition Dipoles

The main output of TDHF linear response calculations is the excitation energy and transition dipole moments of the system. The excitation energy corresponds to the eigenvalues of the time-dependent Hartree-Fock equations, while the transition dipole moments determine the strength of the oscillator strengths.

The excitation energy obtained from TDHF is typically larger than those from more accurate methods (*e.g.* Post-Hartree-Fock method) because TDHF neglects electron correlation. However, TDHF provides a qualitatively correct description of the excitation spectrum and is a useful starting point for more advanced time-dependent methods, such as TDDFT. The excitation energy ΔE_{fi} represents the energy difference between the ground state and an excited state, which corresponds to the eigenvalues of the time-dependent Hartree-Fock equations. The transition dipole moment $\vec{\mu}_{fi}$ determines the strength of the interaction between electronic states and an electromagnetic field, specifically during optical transitions. In TDHF, the oscillator strength f_{fi} for a transition from an initial state i to a final state f can be calculated from the transition dipole moment $\vec{\mu}_{fi}$ using:

$$f_{fi} = \frac{2}{3} \frac{\Delta E_{fi}}{\hbar} |\vec{\mu}_{fi}|^2 \tag{2.72}$$

, where f_{fi} is the oscillator strength, ΔE_{fi} is the excitation energy (difference between the initial and final states), $\vec{\mu}_{fi}$ is the transition dipole moment, and $\hbar$ is the reduced Planck's constant.

Thus, oscillator strength f_{fi} quantifies the intensity of an optical transition and is directly proportional to the square of the transition dipole moment $\vec{\mu}_{fi}$. Calculating transition dipole moments in TDHF effectively provides the oscillator strengths, representing the strength of each optical transition.

2.6.4 Applications of TDHF

TDHF has been widely used to study the optical and electronic properties of molecules and materials. Some of the main applications include:

- **Absorption Spectra**: TDHF can be used to calculate the absorption spectra of molecules and materials, providing information about their electronic excitations and optical properties.
- **Nonlinear Optical Properties**: TDHF can also be used to study nonlinear optical properties, such as second-harmonic generation and two-photon absorption, by going beyond the linear response regime.
- **Photodissociation and Charge Transfer**: TDHF has been applied to study photoinduced processes, such as photodissociation and charge transfer, in molecules and clusters.

Despite its limitations, TDHF remains a useful tool for studying time-dependent processes in quantum systems, particularly when combined with other methods like TDDFT or many-body perturbation theory.

2.7 Plane wave basis set

In computational chemistry, solving the many-electron Schrödinger equation for molecular or periodic systems often requires a suitable approximation of the electronic wave functions. One of the most widely used methods in simulations of periodic systems, such as crystalline materials or surfaces, is the plane wave basis set approach. This section delves into the fundamentals of plane wave basis sets, providing a clear foundation for their role in computational methods such as DFT and Hartree-Fock.

Introduction to Basis Sets

In quantum chemistry, the wave function of a system, which describes the probability distribution of electrons, is a complex entity that requires appropriate mathematical representation for computational modeling. Basis sets, in this context, are used to express the wave function as a linear combination of predefined functions. The choice of basis set can have a significant impact on the accuracy and efficiency of the calculations. While Gaussian-type orbitals (GTOs) are frequently used for molecular systems, plane wave basis sets are preferred for systems with inherent periodicity, such as crystalline solids.

Definition and Properties of Plane Waves

A plane wave is a mathematical function of the form:

$$\psi(\mathbf{r}) = e^{i\mathbf{k}\cdot\mathbf{r}} \tag{2.73}$$

, where $\mathbf{r}$ is the position vector, and $\mathbf{k}$ is the wave vector that defines both the magnitude and direction of the wave. The wave vector is related to the periodic boundary conditions imposed by the lattice, and each wave function is characterized by a specific wavelength (or momentum) determined by $\mathbf{k}$. The principal advantage of plane waves is their simplicity. Since the form of a plane wave is uniform and does not depend on the specific properties of the atoms or the molecular environment, they provide a universal and systematic basis for expanding the wave functions of electrons in periodic systems. This feature makes them particularly well-suited to materials science and solid-state physics, where systems often exhibit long-range periodic order.

Plane Waves and Periodicity

Plane wave basis sets exploit the periodicity of the systems they are designed to model. In periodic systems, the potential and electron density exhibit a repeating pattern, consistent with the underlying crystal lattice. This allows for the application of **Bloch's theorem**, which states that the wave function in a periodic potential can be expressed as the product of a plane wave and a function with the periodicity of the lattice. Bloch's theorem simplifies the description of electrons in a crystal, and plane wave basis sets provide a natural framework for this description. The periodic boundary conditions also help limit the range of wave vectors that need to be considered in the simulation. Due to the translational symmetry, it is only necessary to consider wave vectors within the first Brillouin zone, which represents the fundamental domain of the reciprocal lattice. This reduces the computational cost significantly compared to methods that require localized basis functions.

Energy Cutoff: Truncation of the Basis Set

While the plane wave basis set is conceptually simple and elegant, the practical implementation requires a truncation. In principle, an infinite number of plane waves are needed to represent an arbitrary wave function. However, in computational simulations, a cutoff energy is introduced to limit the number of plane waves included in the basis set. This energy cutoff defines the maximum kinetic energy of the plane waves, which is related to the magnitude of the wave vector $\mathbf{k}$:

$$E_{\text{cut}} = \frac{\hbar^2 \mathbf{k}^2}{2m} \tag{2.74}$$

Only plane waves with kinetic energy less than E_{cut} are included in the calculation, which effectively truncates the basis set. The choice of the energy cutoff is critical

for balancing accuracy and computational efficiency. A higher cutoff increases the accuracy of the wave function approximation but at the expense of increased computational cost. In practice, convergence tests are performed to determine the minimum cutoff energy that provides sufficient accuracy for a given system.

Advantages and disadvantages of Plane Wave Basis Sets

Plane wave basis sets offer several significant advantages over other types of basis sets, particularly for periodic systems:

- System Independence: Unlike localized basis sets, plane waves are not tied to specific atoms or bonding environments. T his makes them ideal for periodic systems, where the repeating nature of the lattice means that any localized feature is inherently spread over the system.
- **Systematic Convergence**: The accuracy of a plane wave basis set can be systematically improved by increasing the energy cutoff. This provides a straightforward path to ensure convergence, as opposed to localized basis sets, which may require more careful tuning to achieve accuracy.
- **Ease of Use in Periodic Systems**: Plane wave basis sets are inherently compatible with periodic boundary conditions, which are standard in calculations of crystalline materials. The use of Blochs theorem and reciprocal space sampling allows for efficient calculations of large systems.
- **Simplification of Mathematical Operations**: Many mathematical operations, such as differentiation and integration, are simpler in the plane wave formalism. The plane waves are eigenfunctions of the Laplace operator, which means that kinetic energy terms in the Hamiltonian can be evaluated analytically in reciprocal space. This property leads to efficient computation of kinetic energy

terms.

The plane wave basis sets also have limitations that must be considered:

- **Inefficiency for Localized Electrons**: Plane waves are non-localized and spread uniformly across the entire simulation cell. This characteristic makes them inefficient for describing tightly bound or highly localized electrons, such as core electrons in atoms. To address this, pseudopotentials (discussed in the next section) are often used to remove the need to explicitly treat core electrons, allowing the plane wave basis set to focus on the valence electrons.

- **Large Basis Set for Complex Systems**: While plane wave basis sets are efficient for periodic systems, they can become computationally expensive for large or complex systems with multiple elements and atoms per unit cell. As the number of atoms increases, so does the required number of plane waves, which can make simulations more resource-intensive.

- **Limited Use in Molecular Systems**: Plane waves are not well-suited for non-periodic systems, such as isolated molecules or clusters, without significant modification (such as the use of supercells or artificial periodicity). For molecular systems, localized basis sets, such as Gaussian-type orbitals, are typically more efficient.

2.8 Pseudopotentials

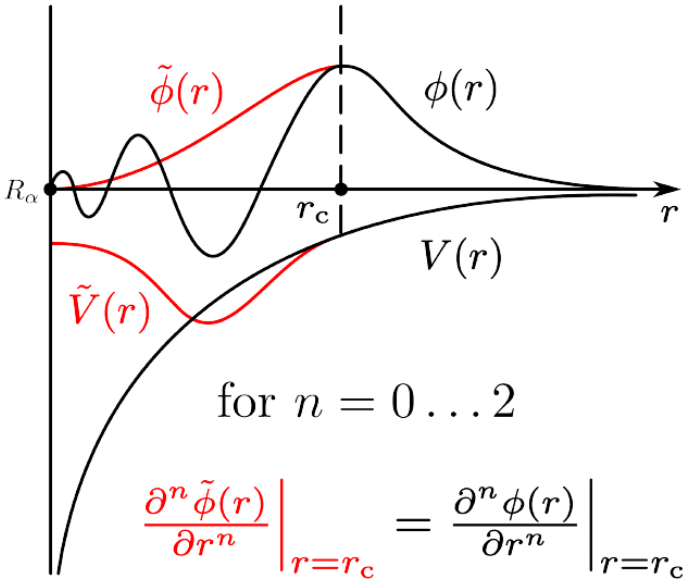

Figure 2: A schematic illustration of the pseudo potential inside and outside the core region of an atom at position R_α. The black and red lines represent the exact and pseudopotential (wave function), respectively. This figure is taken from [28].

In conjunction with plane wave basis sets, pseudopotentials are a fundamental concept in computational chemistry, particularly in the field of electronic structure calculations for periodic systems. Pseudopotentials help alleviate the computational burden associated with modeling core electrons while maintaining the accuracy needed for describing valence electrons, which are more chemically active. This section will delve into the role and construction of pseudopotentials, their application in quantum chemical calculations, and their advantages and limitations.

Motivation for Pseudopotentials

The primary motivation for using pseudopotentials arises from the difficulty and inefficiency of treating core electrons explicitly in quantum chemical calculations. Core electrons, which are tightly bound to the nucleus, generally do not participate in chemical bonding and have wave functions that oscillate rapidly near the nucleus. Modeling these electrons requires a high level of precision, leading to the inclusion of a large number of plane waves (in the case of plane wave basis sets) to accurately capture these rapid oscillations. This significantly increases the computational cost without a corresponding gain in accuracy for the properties of interest, such as chemical reactivity, which is primarily determined by valence electrons. To address this, pseudopotentials are used to replace the effect of the core electrons and the strong nuclear potential with a smoother, less oscillatory potential that acts on the valence electrons.2 The pseudopotential essentially "freezes out" the core electrons, allowing the valence electrons to be described using a much simpler wave function that requires fewer plane waves to represent accurately.

Basic Concept of Pseudopotentials

A pseudopotential is a potential function that mimics the combined effect of the nucleus and core electrons on the valence electrons. In this approximation, the core electrons are no longer treated explicitly, and their influence is incorporated into an effective potential that acts on the valence electrons. This approximation is based on the idea that core electrons shield the valence electrons from the full nuclear potential, so the valence electrons experience an effective potential that is weaker and smoother than the actual Coulomb potential near the nucleus. The general form of a pseudopotential can be written as:

$$V_{\text{pseudo}}(r) = V_{\text{local}}(r) + \sum_{l} V_l(r) P_l \tag{2.75}$$

, where $V_{\text{local}}(r)$ is the local part of the pseudopotential that acts uniformly on all angular momentum states, and $V_l(r)$ represents the non-local part that depends on the angular momentum quantum number l. The projector P_l ensures that the pseudopotential correctly accounts for the angular momentum-dependent behavior of the valence electrons.

Construction of Pseudopotentials

There are different strategies for constructing pseudopotentials, but the basic principles remain consistent: they must reproduce the behavior of the valence electrons both inside and outside the core region while significantly simplifying the representation of the wave functions near the nucleus. Two of the most commonly used methods for constructing pseudopotentials are **norm-conserving pseudopotentials** and **ultrasoft pseudopotentials**.

2.8.1 Norm-Conserving Pseudopotentials

Norm-conserving pseudopotentials were introduced to ensure that the total charge inside a given radius (the core region) is conserved when transitioning from the all-electron description to the pseudopotential description. In this approach, the pseudopotential is constructed so that the pseudo-wave function matches the true wave function both outside the core region and within the core, up to a certain distance from the nucleus, ensuring the same integrated electron density. The key features of norm-conserving pseudopotentials include:

- **Norm Conservation**: The integrated charge density inside a chosen cutoff radius is the same for the true and pseudo wave functions.
- **Smoothness**: The pseudo-wave function is much smoother within the core region compared to the true wave function, which allows for a significant reduction in the number of basis functions needed for accurate calculations.
- **Transferability**: The pseudopotential is designed to work across different environments, meaning it can be used to model the same atom in a variety of chemical contexts with minimal adjustment.

Norm-conserving pseudopotentials are widely used in DFT calculations, particularly when high accuracy is required, but they tend to require a relatively high plane wave cutoff energy to achieve convergence.

2.8.2 Ultrasoft Pseudopotentials

Ultrasoft pseudopotentials are a more recent development that allow for even greater reduction in the plane wave cutoff energy by relaxing the norm-conservation constraint. In this method, the pseudo-wave functions are allowed to differ more significantly from the true wave functions inside the core region, which results in a much smoother pseudo-wave function and a corresponding reduction in the number of plane waves required for accurate representation. The relaxation of the norm-conservation condition is compensated by introducing augmentation functions that correct the charge density within the core region. This allows ultrasoft pseudopotentials to achieve high accuracy with a lower computational cost compared to norm-conserving pseudopotentials, especially in systems containing transition metals or other elements with complex electron configurations. Ultrasoft pseudopotentials are particularly useful for large-scale simulations of materials where computational efficiency is a key consideration, and they are widely employed in plane-wave-based

DFT codes.

2.8.3 Projector-Augmented Wave Method

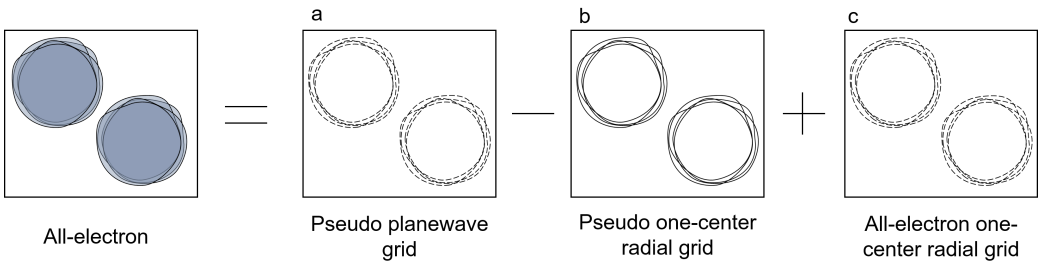

Figure 3: Schematic illustration of additive augmentation in the PAW method: (a) Pseudized quantities are defined across the entire space using a regular plane wave grid. (b) Within specific spheres, pseudo-wave functions are reconstructed, and the corresponding one-center terms are removed. (c) The all-electron wave functions are then reconstructed, and the associated one-center energies are added..

An alternative to traditional pseudopotentials is the projector-augmented wave (PAW) method, which combines aspects of both pseudopotentials and all-electron methods.3 In PAW, the true all-electron wave function is decomposed into a smooth pseudo-wave function and a set of projector functions that restore the correct behavior near the nucleus. The PAW method provides a more accurate representation of the electronic wave functions compared to traditional pseudopotentials while retaining the computational efficiency of plane wave calculations. It is particularly useful for systems where core-valence interactions play a significant role, such as in transition metals and heavier elements.

Advantages and disadvantages of Pseudopotentials

Pseudopotentials offer several advantages that make them indispensable in large-scale simulations of materials and molecules, especially when combined with plane wave basis sets:

- **Reduction in Computational Cost**: By removing the need to explicitly treat core electrons, pseudopotentials drastically reduce the number of plane waves required to represent the wave function accurately. This reduction leads to significant savings in computational resources.
- **Focus on Chemically Relevant Electrons**: Since valence electrons are primarily responsible for chemical bonding and reactivity, pseudopotentials allow the focus of the calculation to be placed on the electrons that matter most for these properties.
- **Simplified Potential Energy Surfaces**: The pseudopotential smooths out the rapidly oscillating behavior of the true potential near the nucleus, which simplifies the calculation of forces and total energy.
- Transferability: Well-constructed pseudopotentials can be used to model atoms in a variety of chemical environments, making them versatile tools in materials science and solid-state chemistry.

Despite their advantages, pseudopotentials also have some inherent limitations:

- **Accuracy**: While pseudopotentials work well for many systems, they are an approximation. In some cases, particularly where core-electron effects are important, pseudopotentials may not capture the true physics of the system as accurately as an all-electron method.
- **Transferability Issues**: Not all pseudopotentials are equally transferable across different chemical environments. A pseudopotential that works well in one sys-

tem (*e.g.*, bulk material) may not be as accurate in another (*e.g.*, surface or molecule) unless specifically designed for that purpose.

- **Incompatibility with Strongly Correlated Systems**: Pseudopotentials can struggle in systems where strong electron correlations, particularly involving core electrons, play a significant role, as these effects are typically not captured well by the smooth pseudopotential approximation.

3 Structure–property characteristics: the First-principles calculations

3.1 Thermochemistry

3.1.1 Abstract

Computational investigation of the structural and photophysical properties of polymeric carbon nitride (PCN) materials can help to establish understanding-driven material optimization strategies. However, the plethora of structural motifs found in synthesized PCNs complicates atomistic simulations. Performing hybrid DFT studies, we systematically investigate formation energy trends and optical properties of PCNs as a function of dimensionality. Thermochemical calculations predict that a mixture of structural motifs including the melon string structure, poly(heptazine imide), and g-C_3N_4 motifs is stable under typical synthetic conditions. Lateral condensation and stacking reduce the bandgap while out-of-plane corrugation increases both stability and the bandgap. The key result of this work is that already small domains of strongly condensed PCN embedded in a less condensed framework can give rise to desirable optical properties. This result reconciles conflicting literature reports indicating that the calculated bandgap of the thermodynamically favorable melon structure is too large compared to experiments, while the g-C_3N_4 structure, for which bandgap calculations are in better agreement with experiments, does not agree with the measured chemical composition of PCNs. Finally, we postulate a new computational model for

PCNs which combines the most important structural motifs and for which we calculate a bandgap of *ca.* 2.9 eV.

3.1.2 Introduction

Polymeric carbon nitrides (PCNs) have recently gained considerable attention as a class of non-metallic photocatalytic materials.[1] Among many potential applications, this new material class is currently being explored in particular for photo-induced hydrogen production,[6–11] alcohol oxidation,[12–15] and the CO_2 reduction reaction[29, 30] due to their intriguing photo-physical properties. PCNs feature optical gaps of *ca.* 2.8 eV.

Typical PCN materials obtained by straight-forward thermal synthesis are semi-crystalline and contain a multitude of micro-structural motifs.[31–35] This lack of crystallinity complicates structural characterization. However, if controlled reaction conditions can be enforced, certain motifs can become more prominent. For example, the "melon" structure, first described by Berzelius and Liebig[36, 37] consisting of strands of linearly polycondensed melamine monomers interconnected via hydrogen bonds, was successfully synthesized by Lotsch *et al.* by thermal treatment of melamine in a closed reaction vessel at 630 °C.[31, 38, 39] A mesoporous, non-hydrogenated graphitic carbon nitride (g-C_3N_4) was postulated and explored for photocatalytic hydrogen production.[40, 41] High condensation g-C_3N_4 model systems, where heptazine units are linked by tertiary amines into a 2D sheet structure, were suggested as theoretical models for PCNs by Lie and Cohen as early as 1989.[42] Since then, calculations explored models based on g-C_3N_4 that exhibit desirable optical properties which are in good agreement with experimentally measured PCN samples.[35] However, the low hydrogen content of this structure is incompatible with elemental analysis of PCN samples, which are usually in better agreement with melon-type

model systems. To this date, the idealized g-C_3N_4 structure has not been unambiguously identified in any synthesized samples. As a result, the exact structural characterization of PCNs is still an open question, and no single computational model on its own so far was able to fully explain the measured properties.

Combined theoretical and experimental efforts were able to shed light on some of the structural parameters of PCNs. Gracia *et al.* for example found that corrugation can stabilize heptazine-based PCNs.[43] Li *et al.* found that micro-structural features of PCNs such as H-bonding, interlayer spacing, and stacking configuration are susceptible to temperature variations during synthesis.[44] Salt melts were explored for PCN synthesis and the templating effect from these salts was found to facilitate the synthesis of PCN structures with large cavities, such as poly(triazine imide) (PTI) and poly(heptazine imide) (PHI).[45–47]

Uncertainty with respect to the structure of PCNs is one of several issues that theoreticians face when simulating this new material class. Further complications include the importance of accurately describing the optical properties, which necessitates the use of costly hybrid density functional theory (DFT) methods that augment regular generalized-gradient approximation (GGA) calculations with exact exchange contributions derived from Hartree-Fock wave function theory calculations on the Kohn-Sham orbitals.[48, 49] Unfortunately, large system sizes are often required to model PCNs, which can make hybrid DFT calculations computationally unfeasible. Finally, PCNs are characterized by a multitude of intricate structural features such as stacking, edge boundaries, and corrugation which further increases the complexity of model systems.[49–52] The structural complexity of PCNs therefore hampers computational efforts aimed at improving our understanding of their fascinating properties, including strong excitonic effects,[53] charge accumulation,[54–58] and tuning of the optical properties towards more efficient visible light absorption.[33, 59]

Most notably, there is significant disagreement in literature between theoretical bandgap predictions and experimentally measured bandgaps. In particular, models for which bandgaps of 3 eV and lower are calculated typically feature a high degree of condensation while elemental analyses of synthesized materials with similar bandgaps show hydrogen contents that are incompatible with the theoretical models.[60–63] The authors are convinced that this discrepancy is the result of the structural complexity of PCNs which is hard to represent properly in simulations.

In this study, we aim at postulating a more complete model system for PCNs. To this end, the relationship between structures and optical properties of PCNs are systemically investigated. Calculations initially focus on exploring individual parameters such as the degree of condensation, increase of dimensionality, and corrugation. To investigate these parameters and to model the polycondensation reaction from monomer to various PCN structures, the thermochemical approach introduced by Botari *et al.*[64] is adopted and extended by incorporating vibrational enthalpy and entropy contributions of the solid-state materials. By varying the chemical potential of NH_3, $\Delta\mu_{\mathrm{NH_3}}$, refined thermochemical maps are obtained and reveal a thermodynamic route for the formation of the fully-deaminated PCN structure, typically referred to as g-C_3N_4, via PHI as an intermediate.

The key finding of the present work is that already small domains of g-C_3N_4 embedded in less condensed PCN structures are sufficient to obtain bandgaps of 3 eV and lower. Thus, a comprehensive model system is postulated from a combination of the most important structural features explored in this work that affect the stability and optical properties of PCNs. This structure is thermodynamically feasible, shows a bandgap of *ca.* 2.9 eV while retaining a low degree of condensation, and is predicted to form under experimentally accessible conditions. This model constitutes an important step towards a more holistic description of this fascinating material class in atomistic simulations.

3.1.3 Methodology

3.1.4 Computational Details

All calculations were performed using the Vienna Ab initio Simulation Package (VASP) version of 5.4.4 which employs the projector-augmented wave (PAW) method.[65–69] A plane wave energy cut-off of 400 eV was used and the wavefunction was optimized to an accuracy of 10^{-6} eV. Atomic coordinates were relaxed until forces reached below 5×10^{-2} eV/Å. Gaussian-type finite-temperature smearing was employed with a smearing width of 0.01 eV. Long range interactions were treated with DFT-D3 dispersion correction.[70, 71]

The atomic and cell coordinates were relaxed using the exchange-correlation functional by Perdew, Burke, and Ernzerhof (PBE) within the generalized gradient approximation (GGA).[72] Accurate final energy results were then obtained by performing single-point calculations on the PBE-optimized structures using the hybrid functional by Heyd, Scuseria, and Ernzerhof with 25 % exact exchange and a screening factor of 0.2 $Å^{-1}$ (HSE06).[73] The HSE06 functional was found to deliver a good description of the electronic properties of PCNs.[48, 49, 52]

Atomic coordinates of molecular models were optimized using the ORCA package version 4.21[74, 75] using the PBE0 functional,[72, 76, 77] def2-TZVP basis set, def2/J auxiliary basis set, and DFT-D3 dispersion correction. Then, single point calculations were performed in VASP using the HSE06 functional to obtain final energy results. The pre-optimization in ORCA was found to be necessary because geometry relaxations in VASP regularly did not find the energetic minimum structures for molecules. In particular, corrugation is more pronounced in the ORCA optimized structures, which in fact also give lower total energy results after subsequent HSE06 single-point calculations in VASP. We assume that ORCA, with which we used fi-

nite basis sets and a hybrid functional for the relaxation, enabled symmetry breaking more easily compared to the GGA-based VASP plane wave calculations. To avoid spurious interactions between molecules and in case of 2D surface calculations, a vacuum layer of ($\sim$ 20 Å) was used and dipole correction was enabled in the relevant directions (molecules: all directions, surfaces: perpendicular to surface). The Monkhorst-Pack scheme was adopted to create *k* point grids for Brillouin zone integration.[78] A single, Γ-centered *k* point was used for molecular structures. The vibrational contribution was calculated from force constant matrices using the VASP-Phonopy interface.[79–81] A data set of atomic coordinate files of the investigated structures in the VASP-POSCAR file format has been made available.[82]

3.1.5 Thermochemistry

For thermochemical analysis, we consider a simple thermal synthesis which uses melamine as the monomer. The thermochemical stability for each structure is assessed by the formation free energy $\Delta G_{\mathsf{F}}(T, p)$ using the following equation:

$$\Delta G_{\mathsf{F}}(T, \boldsymbol{p}) = G_{\mathsf{structure}}(T, p) - (n\, G_{\mathsf{melamine}}(T, p) - m\, \mu_{\mathrm{NH_3}}(T, p)). \tag{3.1}$$

Temperature (T) and pressure (p) are taken into account for the solid-state structures. The free energy of any particular structure under investigation, $G_{\mathsf{structure}}$, and of a melamine monomer, G_{melamine}, are calculated as follows:

$$G = E^{\mathsf{total}} + F^{\mathsf{vib}} + pV \tag{3.2}$$

where E^{total} is total energy, F^{vib} is vibrational free energy. The contribution of vibra-

tional degree of freedom can be obtained from phonon density of states $\sigma(\omega)$.

$$\begin{aligned} F^{\text{vib}}(T,\omega) &= \int d\omega F^{\text{vib}}(T,\omega)\sigma(\omega) \\ &= \frac{1}{2}\hbar\omega + k_{\text{B}}T\ln\left[1-\exp\left(\frac{-\hbar\omega}{k_{\text{B}}T}\right)\right] \end{aligned} \tag{3.3}$$

The gas phase chemical potential of ammonia, $\mu_{\text{NH}_3}(T,p)$, which depends on temperature and partial pressure, is an important term to connect simulations with experimental conditions. We adopt the expression for $\Delta\mu_{\text{NH}_3}(T,p)$ from Botari *et al.*[64] This expression for the calculated $\mu_{\text{NH}_3}(T,p)$ is based on the polyatomic ideal gas approximation composed of translational, rotational, vibrational terms:[83–85]

$$\mu(T,p) = E^{\text{total}}_{\text{NH}_3} + E^{\text{ZPE}}_{\text{NH}_3} + \Delta\mu(T,p) + pV \tag{3.4}$$

$$\begin{aligned} \Delta\mu(T,p) &= \mu_{\text{trans}} + \mu_{\text{rot}} + \mu_{\text{vib}} \\ &= -\frac{1}{2}k_{\text{B}}T\Big\{\ln\left[\left(\frac{2\pi m}{h^2}\right)^{\frac{3}{2}}\frac{(k_{\text{B}}T)^{\frac{5}{2}}}{p}\right] && (3.5) \\ &\quad + \ln\left(\frac{k_{\text{B}}T}{\sigma^{\text{sym}}B_0}\right) && (3.6) \\ &\quad - \ln\left[1-\exp\left(-\frac{\hbar\omega}{k_{\text{B}}T}\right)\right]\Big\} && (3.7) \end{aligned}$$

, where k_{B} is the Boltzmann constant, m is the mass of ammonia, σ^{sym} is the symmetry number, B_0 is the rotational constant, ω is the fundamental modes of the particle, $\hbar$ is the reduced Planck constant.

To validate our approach, we successfully reproduced published formation free energy trends for PCNs, see Figure S2 and S3.[64] The published trends, however, neglect the influence of vibrational contributions on the free energy of both oligomers and solids. Significant changes can be observed when vibrational contributions are included (see Figure S4).

Finally, the degree of condensation (DoC) is used as a descriptor throughout this

work. It is calculated as the percentage quotient between the number of condensation points found in a particular structure and the product of the number of melem units - which are stable intermediates formed from the precursor melamine - that the structure is made up of times the maximum number of condensations that each melem unit in the structure can support (6):

$$\text{DoC} = \frac{\text{\# of condensations}}{N_{\text{melem}} \times 6} \times 100 \tag{3.8}$$

3.1.6 Model Systems

In order to simulate the thermodynamics of PCN formation, we simulate the polycondensation thermodynamics from the melamine monomer up to the tetramer phase. The investigated model systems are illustrated in Figure 1. The investigated 2D-

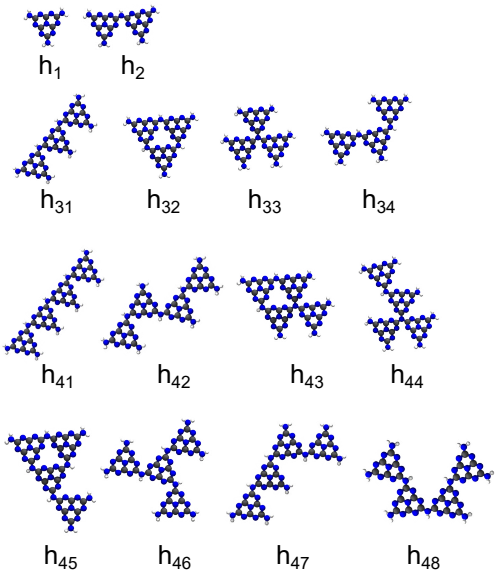

Figure 1: Illustration of molecular oligomer model systems investigated in this study. The models are named after a h_{xy} naming scheme, where x is the number of heptazine units and y is an increasing number that indexes the oligomers.

and 3D-periodic models are illustrated in Figure 2, while the mixed-motif structures postulated in section 3.1.17 are shown in Figure S1. The atomic coordinates of all

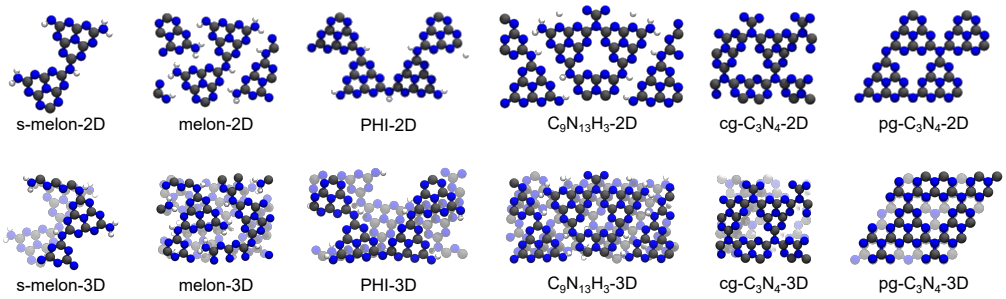

Figure 2: Illustration of periodic 2D surface and 3D crystal models investigated in this study. Structures are composed of s-melon, melon, PHI, $C_9N_{13}H_3$, cg-C_3N_4(corrugated), and pg-C_3N_4(planar) structural motifs.

structures were relaxed using the methodology outlined in section 3.1.4. Even though no constraints or restraints were placed on the models, the melon, pg-C_3N_4, and $C_9N_{13}H_3$ structures retained an idealized flat configuration, which is known to be a local minimum.[43, 51, 86] The other periodic structures show various degrees of corrugation. Corrugation is notorious due to the large number of local minima in the coordinate space. While this limitation affects our ability to predict absolute stability values with high confidence, it is only of minor importance when looking at larger scale stability trends, which is the focus of the present work.

3.1.7 Results

3.1.8 Formation Energy Trends for 1D Materials

To understand the condensation process, formation free energy (ΔG_F) phase diagrams are constructed using the melamine monomer and NH_3 molecules as reference. Since there is only one possible configuration to form a dimer, different trimer

and tetramer configurations are explored first. All calculated molecular structures are illustrated in Figure 1. The relative stability trends for the trimer and tetramer phases are shown in Figure 3(a) and 3(b), respectively. The phase diagram reveals that two competing condensation processes exist during the molecular oligomerization stage: non-cyclic and cyclic condensation. Non-cyclic condensation is the dominant process at more positive values of $\Delta\mu_{\mathrm{NH_3}}$ while cyclic condensation is dominant below $\Delta\mu_{\mathrm{NH_3}}$ values of *ca.* -1.0 eV, both in case of trimers and tetramers.

In case of the tetramer structures, the cyclic h_{45} and the h_{43} configurations (see Figure 1) are found to be similarly favorable. Both of these structures contain a condensed ring of three heptazine units (h_{32}) with an additional dangling heptazine unit, which is either attached at a terminal ($-\mathrm{NH}R$, where $R =$ heptazine, h_{45}) or at a bridging group (−NR, h_{43}). On the other hand, among the non-cyclic configurations, h_{42} and h_{48} compete as the most stable configurations with only small deviations of ΔG_{F} of $10^{-4} - 10^{-3}$ eV/atom. These structures as well as h_{41} and h_{42} actually constitute rotamers which can be converted into each other by rotation around bridging *R*−NH−*R* moieties. Structure h_{48} appears to be slightly more stable at $\Delta\mu_{\mathrm{NH_3}}$ values close to zero, likely due to stabilizing van-der-Waals interactions that result from this configuration. Both of the angled structures (h_{42} and h_{48}) are more stable than the linear structure h_{41}. However, the energy differences are small enough that a mixture of all of the discussed configurations may be formed from a thermodynamic point of view.

The ΔG_{F} differences between the most stable trimer and tetramer structures can be illustrated in a more practically-oriented way by expanding $\mu_{\mathrm{NH_3}}$ into T-p phase diagrams, see Figures 3(c) and (d). At reported synthetic conditions,[38, 39, 88] the formation of melem (h_1) begins at *ca.* 350–370 °C (Figure 3 (c) and (d)). From gravimetric analysis it is commonly assumed that formation of molecular oligomer structures is the dominant process until a temperature of *ca.* 500 °C.[87] At higher temperature, more condensed structures (*i.e.*, 2D-condensed polymers) are expected to

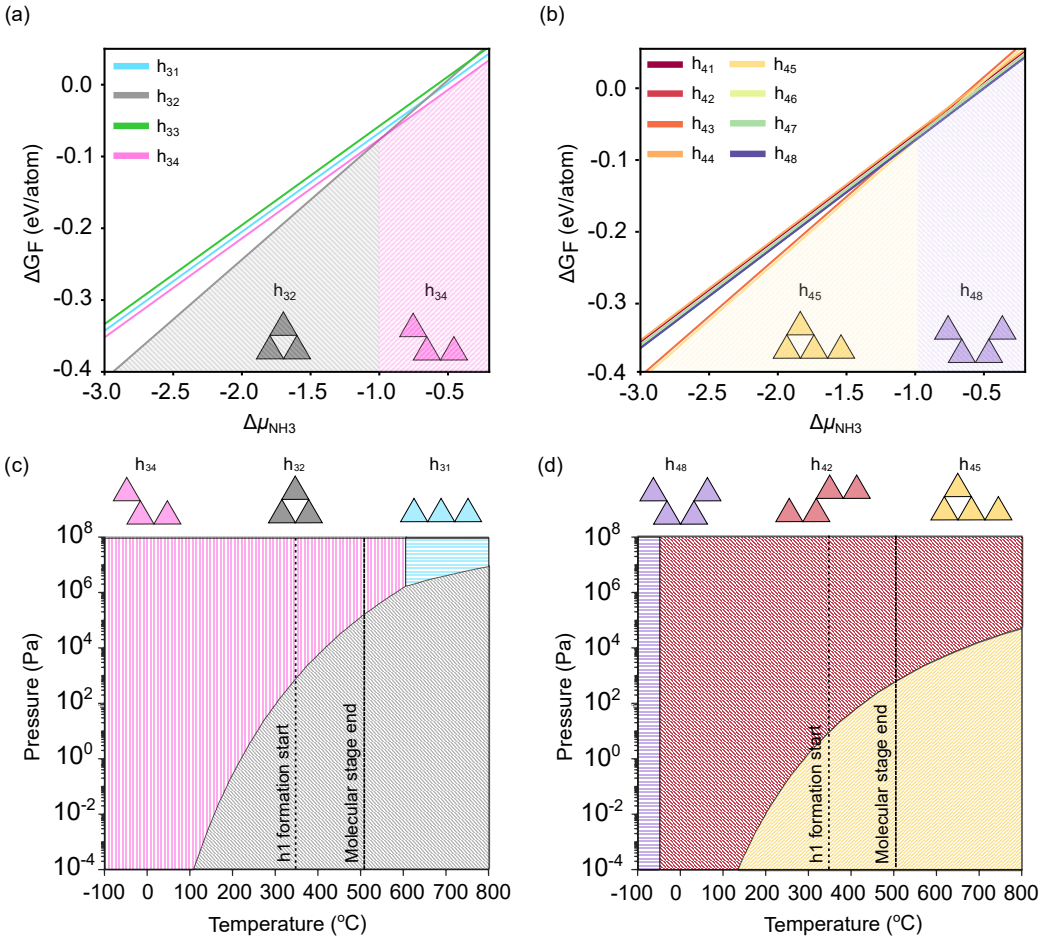

Figure 3: The free energy of formation for all (a) trimer and (b) tetramer structures are shown as function of $\Delta\mu_{\mathrm{NH_3}}$. The free energy of formation is normalized to eV/atom to be able to compare structures with different total number of atoms. Free energy results are then expanded into T-$p_{\mathrm{NH_3}}$-dependent phase diagrams for the most stable (c) trimer and (d) tetramer structures, respectively. The experimental temperature range for synthesis of these molecular structures is given between the dotted and the dashed line.[38, 39, 44, 87, 88]

form. From this analysis, it can be inferred that the more condensed structures h_{32} (trimer) and h_{45} (tetramer) are most likely to form in the typical experimental temperature regime (500–630 °C)[31] and low NH_3 partial pressure (p_{NH_3}), whereas the non-cyclic h_{34} and h_{42} structures are thermodynamically preferred at higher p_{NH_3}.

3.1.9 Formation Energy Trends for 2D and 3D Materials

The formation free energy trends for 2D and 3D structures are shown in Figure 4. The melon-2D structure accounts for the most stable structure up to $\Delta\mu_{NH_3} = -1.49$ eV. The PHI-2D structure appears as an intermediary phase between $\Delta\mu_{NH_3} = -1.49$ and -1.68 eV. For more negative $\Delta\mu_{NH_3}$, the highly-condensed cg-C_3N_4-2D structure becomes the most stable phase. By deconvoluting $\Delta\mu_{NH_3}$ into a T-p diagram, Figure 4 (c), a similar trend regarding the p_{NH_3} is obtained as for the molecular phases, *i.e.*, higher degree of condensation (DoC) can be achieved by reducing p_{NH_3} at the experimental temperature conditions (500–630 °C).[31]

In the 3D phase, cg-C_3N_4-3D is the most stable structure at $\Delta\mu_{NH_3} \leq -1.33$ eV. At more positive values of $\Delta\mu_{NH_3}$, the melon-3D structure becomes more stable. The T-p phase diagram (Figure 4 (d)) reveals that there is thermodynamic competition between the formation of the cg-C_3N_4-3D and melon-3D structures - or, in fact, their coexistence - in the experimental temperature range (500–630 °C) and at a p_{NH_3} of 1 atm. This phase border shows that lowering p_{NH_3} will make the more condensed cg-C_3N_4-3D structure thermodynamically more favourable.

3.1.10 Optical Property Trends

Calculated trends of the HOMO-LUMO gaps for the molecular structures as well as bandgap trends for the periodic structures are listed in Table S1. Figure 5 summarizes

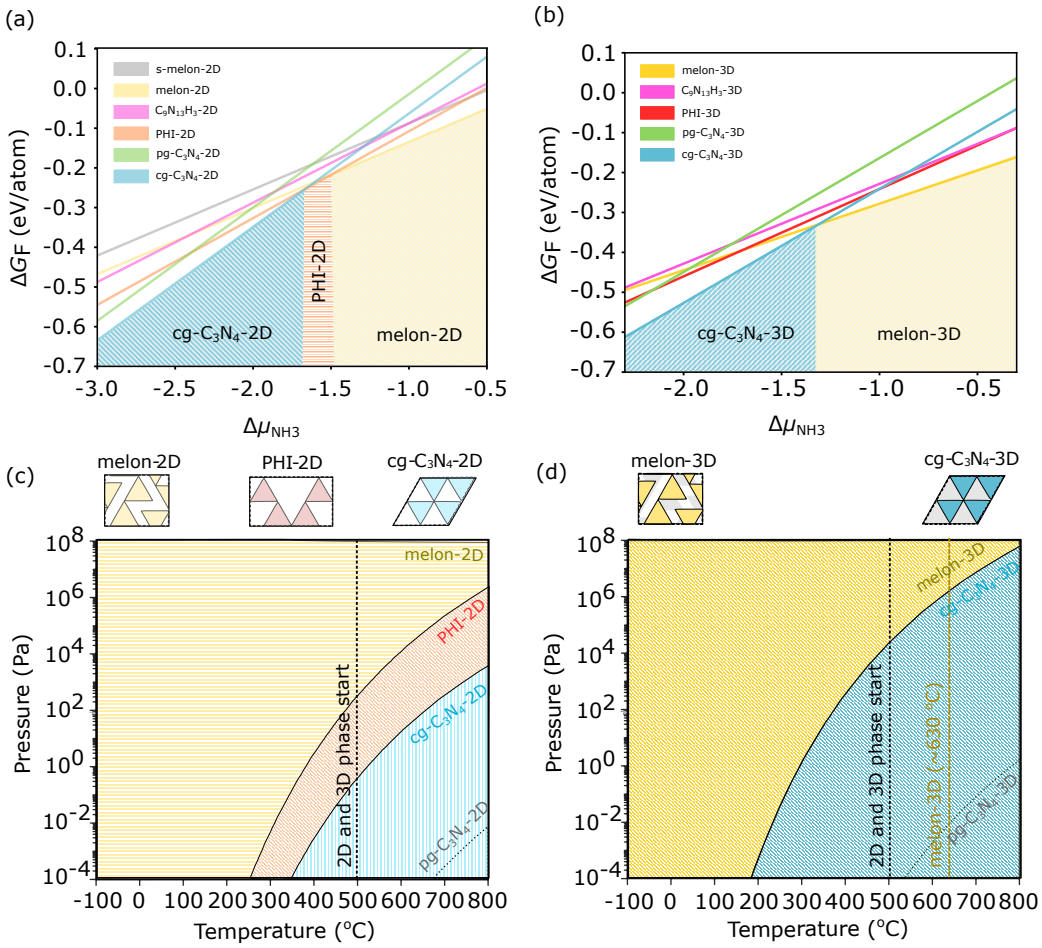

Figure 4: The free energy of formation for all (a) 2D and (b) 3D structures is shown as a function of $\Delta\mu_{\mathrm{NH_3}}$. The free energy of formation is normalized to eV/atom to be able to compare structures with different total number of atoms. Then, free energy results are expanded into a T-$p_{\mathrm{NH_3}}$-dependent phase diagrams for the most stable (c) 2D and (d) 3D structures, respectively. The experimentally measured temperature range for the formation and the decomposition of PCNs are given as dotted black and yellow lines.[44, 87] The dotted grey line indicates the stability region for the fully flat pg-C_3N_4-2D/-3D phases which constitutes a local minimum structure and lays behind the more stable corrugated cg-C_3N_4-2D/-3D structure.

the calculated values. Note that HOMO-LUMO gaps for the molecular models are

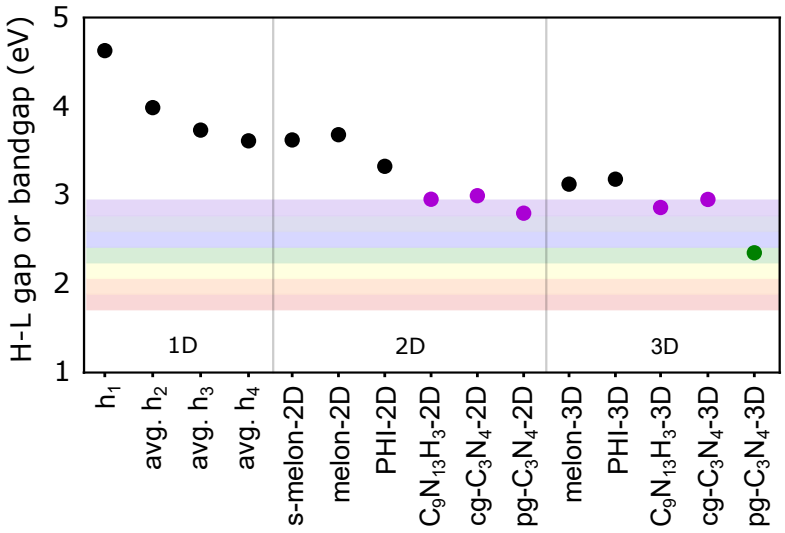

Figure 5: Summary of the calculated optical gap trends; HOMO-LUMO gaps are given for molecules and bandgaps are given for the periodic structures. For simplicity, the averaged HOMO-LUMO gaps are presented for the dimer up to tetramer structures. A color palate is given for reference to roughly indicate the energy range corresponding to visible light.

given as average values over all dimers, trimers, and tetramers, respectively.

The optical property results give rise to several noteworthy trends: first, the optical gap decreases as the DoC increases. This trend is particularly apparent for the 2D periodic models. For instance, the melon-2D model, which shows a DoC of 50%, has a *ca.* 0.7 eV larger bandgap than the highly-condensed cg-C_3N_4-2D model (DoC = 100%).

Second, as the dimensionality of the system increases from 1D molecules to 2D sheet models to 3D crystal models, the optical gap decreases. This trend is noteworthy in particular for the 2D to 3D transition where the growth mechanism is stacking of the 2D layers, *i.e.* no additional covalent bonds are formed.

Third, corrugation of the structures increases the optical gap slightly. For example, the

completely-flat pg-C_3N_4-2D model, which constitutes a local minimum configuration of the system, has a *ca.* 0.2 eV smaller bandgap than the corrugated and thermodynamically more stable ($\Delta E = 0.7$ eV/heptazine unit) cg-C_3N_4-2D system. This effect is even more pronounced for the 3D crystal models, where the non-corrugated system has a narrower bandgap of *ca.* 0.6 eV. At the same time, the interlayer spacing of the non-corrugated model decreases by *ca.* 0.17 Å compared to the corrugated model, indicating significantly stronger interaction between layers.

Lastly, we studied the bandgap as function of an increasing number of heptazine units for hydrogen-terminated nanoribbons. The studied model systems, bandgap results, and a comparison to the optical properties of some key structures investigated above are given in Figure 6. Calculations show that bandgaps converge to a value close to

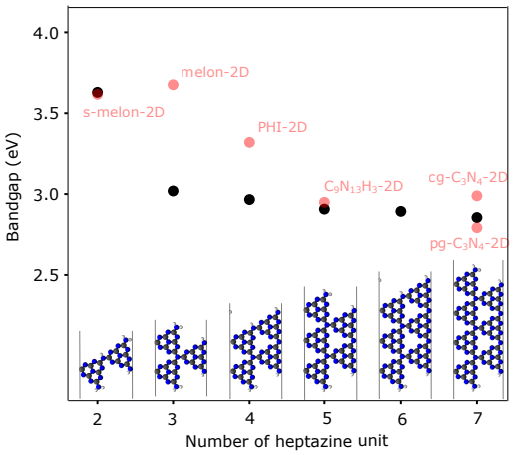

Figure 6: Calculated bandgap trends as a function of the number of heptazine monomers in hydrogen-terminated ribbon models of increasing width. Band gaps of key 2D structures are given in light red for reference (see Figure 5). The ribbon models neglect the influence of corrugation, see text for more details. As the number of heptazine units increases from 2 to 7, the bandgap decreases from 3.6 eV to 2.9 eV, with the most significant decrease observed already from 2 to 3 heptazine units (*ca.* 0.6 eV).

that of the 100 % DoC pg-C_3N_4-2D model for ribbons that are $5-7$ heptazine units

wide. Already at a width of 3 heptazine units, a significant reduction of the bandgap from *ca.* 3.6 to 3.0 eV is observed. This result suggests that already small areas of g-C_3N_4 are sufficient to produce the bandgaps observed for the fully-condensed 2D materials.

Note that corrugation is not taken into account in this test set and thus, values are closer to the flat pg-C_3N_4-2D model rather than the corrugated cg-C_3N_4-2D model. For larger ribbons ($5-7$ units), it is expected that bandgap values would shift to larger values if corrugation was accounted for, analoguous to the difference between cg- and pg-C_3N_4-2D.

3.1.11 The Influence of Hydrogen Bonding on the melon Structure

The melon-2D and melon-3D models are set apart from the other structures because their individual strings interact via hydrogen bonds exclusively rather than via any bridging covalent bonds. The investigated melon structures exhibit high thermodynamic stability both in the literature[52, 64] and our calculations, as shown in Figure 4. However, the formation energy trends were obtained by optimizing the atomic configurations at a temperature of 0 K; any temperature dependence of the calculated Gibbs free energy values is accounted for using the approximations described in the method section. Notably, it is known from atomistic and experimental studies on the structure of water that hydrogen bond lengths elongate quadratically as a function of increasing temperature.[89] The calculations presented here therefore likely underestimate the separation distance between the hydrogen-bonded melon strings and overestimate their stability at ambient temperature and particularly at elevated temperature during synthesis.

To account for this shortcoming, another melon-based periodic model is investigated: the single-stringed model, s-melon-2D, as presented in Figure 2. This structure con-

stitutes an extreme case, *i.e.* where melon strings are separated far enough that no more interaction via hydrogen bonds takes place between them. This model is therefore likely more representative for the string separation distance at high temperatures, such as during synthesis. Figure 7 compares the T-p-dependent stability of the favourable PHI and cg-C_3N_4 structures with the s-melon structure instead of the hydrogen-bonded melon-2D structure shown in Figure 4.

By comparing Figure 7 and Figure 4, it becomes clear that hydrogen bonding significantly contributes to the stability of the melon models. The exclusion of this contribution shifts the stability region of s-melon-2D structure in Figure 7 a) to a lower temperature and the PHI-2D structure now appears to be the most favourable configuration at reported experimental synthetic conditions as indicated by the dotted line.[35, 44, 87] In case of the 3D models, Figure 7 (b) shows that now, the cg-C_3N_4-3D and PHI-3D structural motifs are in thermodynamic competition, which means that a mixture of both structure can be expected to form under typical synthetic temperature conditions (500–630 °C).

3.1.12 Discussion

The purpose of this study is to elucidate the relationship between the structure of PCN materials and the corresponding optical properties from a thermodynamic point of view and as a function of material dimensionality. In the following, three key structural parameters that greatly affect the optical properties will be discussed in more detail based on the presented calculation results: (i) degree of condensation, (ii) stacking, and (iii) corrugation.

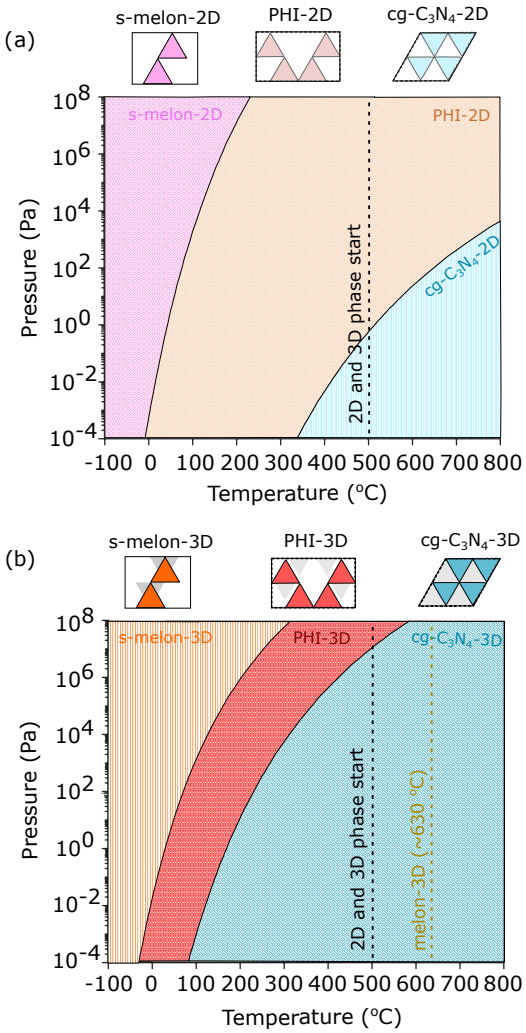

Figure 7: Formation free energy phase diagrams of 2D and 3D structures updated from Figure 4. The hydrogen-bonding stabilized melon-2D/-3D structure are excluded, instead the single-string s-melon-2D/-3D structures are shown. The dotted and the dashed line indicated the experimentally observed temperature where formation of 2D and 3D structures begins[35, 44, 87] and where the melon-3D structure was found to form,[31] respectively.

3.1.13 Correlation between Degree of Condensation and Synthetic Conditions

This section discusses in detail how different synthetic conditions can facilitate different degrees of condensation (DoC) of the synthesized material, according to the calculated formation energy trends. Figure 8 summarizes the formation free energy trends for the most stable structures presented in Figures 3, 4, and 7. An unfiltered overview containing all structures is shown in Figure S5. In this depiction, emphasis is placed on highlighting the change of trends of the thermodynamically preferred structure as a function of $\Delta\mu_{NH_3}$, *i.e.* at various T and p conditions.

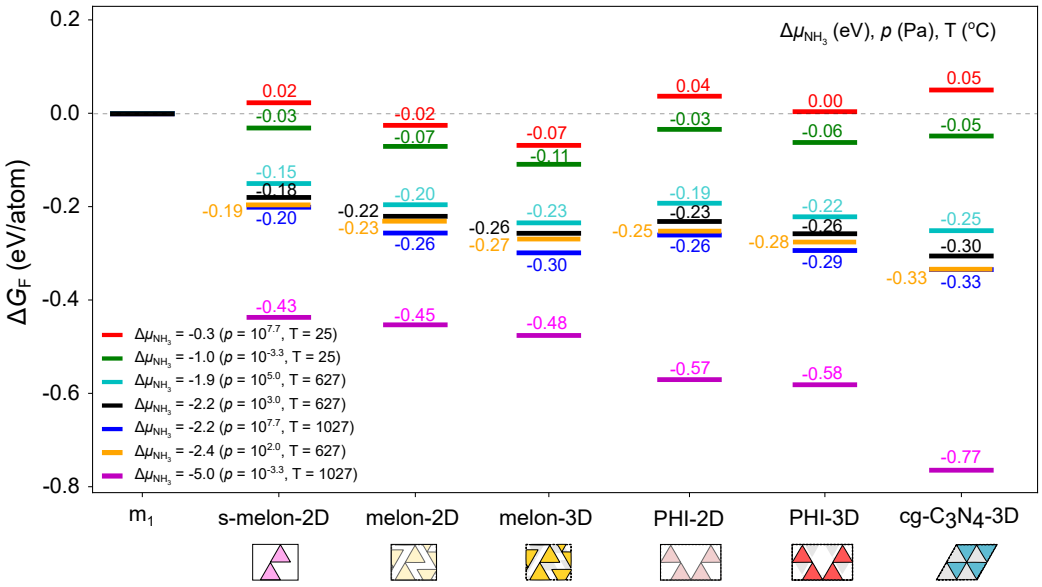

Figure 8: Free energy of formation for key 2D and 3D structures as a function of a selected set of μ_{NH_3} conditions. The free energy of formation is normalized to eV/atom to be able to compare structures with different total number of atoms.

The formation free energy, ΔG_F, is calculated for each structure from NH_3 and melamine as the educts. The middle-ranged cyan, black, yellow, blue, and orange lines represent the T-p parameter space that can be achieved under typical laboratory conditions.

From the formation energy trends, it is evident that the DoC is proportional to $\Delta\mu_{NH_3}$; structures with a higher DoC become more favourable as $\Delta\mu_{NH_3}$ becomes more negative. In the aforementioned middle range (blue to cyan lines), all structure show similar thermodynamic stability. We can therefore conclude that from a thermodynamic perspective, the experimentally synthesized material most probably is a mixture of these different structural motifs with no strong preference for any one particular motif.

In addition, the results suggest that certain structural motifs may become dominant when specific synthetic conditions are enforced. On one extreme end of the T-p spectrum, we predict that the less-condensed melon string structures can be enforced by performing the synthesis at low temperature conditions and high p_{NH_3}, for example in a closed reaction vessel (red and green lines). On the other extreme end, if the synthesis is performed at high temperature and low p_{NH_3}, for example in a reaction vessel with an applied vacuum (magenta line), the more condensed cg-C_3N_4 and PHI structures become favourable. While these extreme cases are not representative of conditions that can be readily achieved in the laboratory, they serve to illustrate the influence of the parameters of temperature and pressure on the expected composition of the PCN material.

Therefore, in order to obtain a PCN with a high DoC and a optical gap of 3 eV or less, these computational trends suggest that high temperature and low p_{NH_3} conditions should be maintained during the synthesis. These calculated trends are corroborated by experiments by Inoki *et al.*[90], who reported successful synthesis of a g-C_3N_4 structure under controlled low p_{NH_3} (*ca.* 9.0×10^3 Pa) at 550 °C. Their synthesized material shows a bandgap of 2.03 eV with an average crystal size of less than 3 nm. On the other hand, Lotsch *et al.* showed that formation of the melon structural motif can be promoted by conducting synthesis in a closed ampule at 630 °C.[31] Further condensation of the melon strings is likely hindered by the relatively high NH_3 p_{NH_3} within the ampule. Both of these experimental observations are in good agreement

with the predicted trends presented in this work (Figure 4(d)).

Finally, the presented results may help to reconcile conflicting observations from theory and experiments. While published theoretical results predict that high DoC is a requirement to achieve the desired bandgap, experiments measure bandgaps of 2.6–2.7 eV for materials where elemental analysis shows high H content that would indicate a low DoC.[35, 39, 91] According to the presented trends, the synthesized material likely contains a mixture of different more or less condensed structural motifs, giving rise to desirable optical properties in g-C_3N_4-like domains embedded in a matrix of less-condensed PCN such as the melon string motif. Consequently, this conclusion raises a follow-up question: how large do these highly-condensed domains need to be in order to exhibit the desired properties? This question will be addressed in section 3.1.15.

3.1.14 Interconversion

It is clear from the presented computational trends that there is thermodynamic competition between the melon-3D structure and the idealized, fully-condensed cg-C_3N_4-3D structure for the end product. Consequently, the question arises if and how interconversion can take place between these structure. More specifically, in this section we discuss whether a thermodynamic pathway exists to convert these phases into each other, for example by annealing the synthesis product under specific conditions.

From a structural point of view, direct conversion from melon to the fully-condensed structure is not straightforward (DoC = 50% for melon, DoC = 100% for cg-C_3N_4). It is therefore reasonable to assume that the PHI structure (DoC = 75%) may be an intermediate structure connecting them. In fact, the PHI structure has already been successfully synthesized, indicating that this structure is at least metastable, if not thermodynamically favourable under specific conditions.[92–97] We therefore hypoth-

esize that the large pores in the PHI structure may be filled with heptazine monomers under certain conditions to give the cg-C_3N_4 structure. Selected hypothetical pathways and their associated reaction free energy trends at different T-p conditions are summarized in Figure 9. More detailed p-T phase diagrams from which these trends

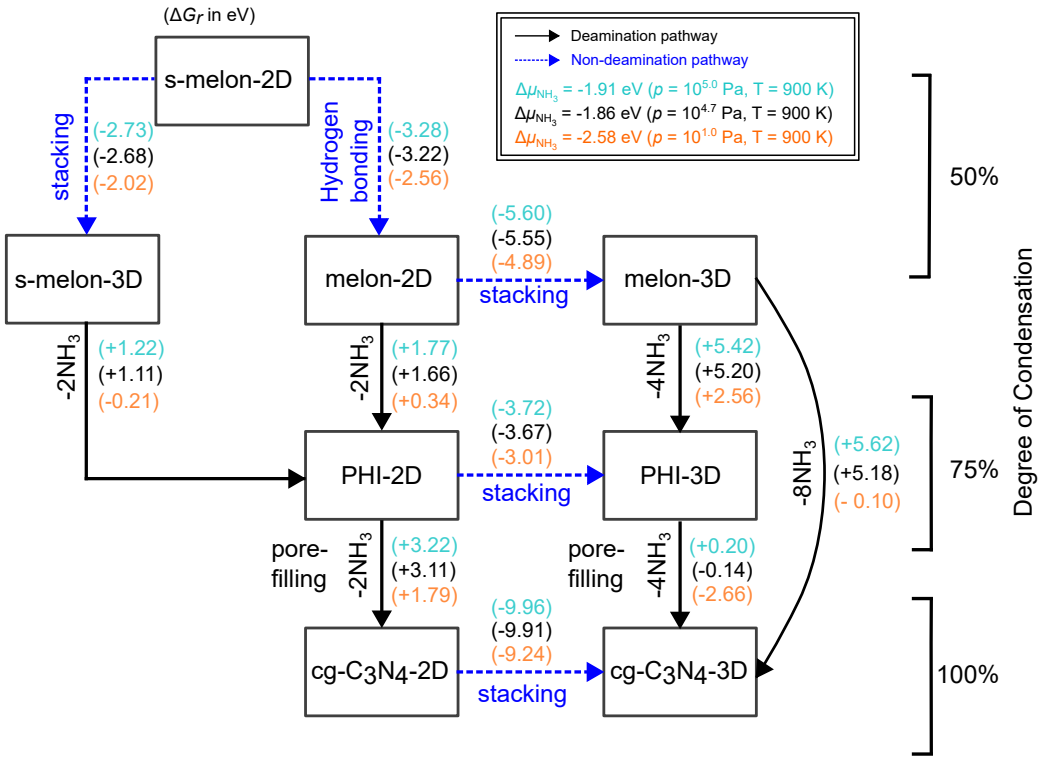

Figure 9: Reaction flow chart connecting structures via the calculated reaction free energy, ΔG_r, which depends on $\Delta\mu_{NH_3}$ (-2.6 eV $<\Delta\mu_{NH_3}<$ -1.9 eV). Temperature is fixed to 628 °C, which constitutes the maximum temperature before carbonization of the material sets in, so that the reaction free energy trends depend solely on p_{NH_3}. Two reaction mechanisms are suggested: i) The non-deamination pathway involving stacking and hydrogen bonding and ii) the deamination pathway involving release of NH_3. The structures are classified by their degree of condensation (DoC). The "pore-filling" route is suggested to connect PHI structure to cg-C_3N_4 structure; see text for more details.

were summarized are shown in Figure S6.

Here, the reaction free energy ΔG_r between any product and an educt state is calculated as

$$\Delta G_\mathrm{r}(T,p) = n\, G^{\text{product}}(T,p) - m\, G^{\text{educt}}(T,p)\; - o\, G^{\mathrm{NH_3}} \tag{3.9}$$

, where $G^{\text{product}}(T,p)$, $G^{\text{educt}}(T,p)$, and $G^{\mathrm{NH_3}}(T,p)$ constitute the Gibbs free energy of the product and educt configurations as well as the NH_3 molecule, respectively, and n, m, and o are stoichiometric factors.

The trends shown in Figure 9 were calculated at 628 °C, which is close to the decompostion temperature of *ca.* 630 °C.[87] The reaction profile can then be controlled by $p_{\mathrm{NH_3}}$. The proposed reaction profile conveys two important thermodynamic factors that determine the end structure at the respective conditions:

1. The non-deamination pathway is thermodynamically more favourable than the deamination pathway because stabilization occurs via hydrogen bonds and/or stacking. However, this process does not increase the DoC.

2. $p_{\mathrm{NH_3}}$ plays a pivotal role in controlling the reaction free energy of the deamination pathways, which increases the DoC.

From these trends, it is clear that the melon structure represents a thermodynamic sink. The conversion from melon-3D to the idealized cg-C_3N_4-3D structure only becomes exothermic at drastic conditions of $p_{\mathrm{NH_3}} = 10$ Pa. The same is true for the deamination pathway leading from s-melon-3D to PHI-2D. However, if the PHI-2D stage can be reached, which will likely be in equilibrium with the melon-2D structure due to similar formation free energy trends from s-melon-2D, the subsequent stacking to PHI-3D and pore filling reaction to cg-C_3N_4-3D, which already becomes spontaneous close to atmospheric pressure, are significantly downhill.

To develop a conversion strategy, it is crucial to determine from which point in this

flowchart one starts. For example, if synthesis of a PHI material has already succeeded, for example with the help of templating effects,[94, 95] further condensation due to pore filling is possible at comparatively mild conditions. However, converting a melon-3D material into cg-C_3N_4-3D may require drastic conditions. When synthesis starts from the educts, a mixture of melon-3D and more condensed material, as signified by the idealized cg-C_3N_4-3D system, can be expected due to thermodynamic competition of the s-melon-2D $\rightarrow$ s-melon-3D and the s-melon-2D $\rightarrow$ melon-2D pathway.

3.1.15 Influence of Stacking *vs.* Lateral Condensation

The presented results show that stacking, *i.e.* the 2D $\rightarrow$ 3D transition, is thermodynamically more favorable than condensation or pore filling reactions. Furthermore, a central conclusion of sections 3.1.13 and 3.1.14 is that the synthesized material is most likely a mixture of structures, particularly of the melon-3D structure and partially pore-filled PHI-3D. As mentioned at the end of section 3.1.13, we now face an important question: how big do these highly-condensed domains, which are likely interspersed throughout a host matrix of less strongly condensed melon- or PHI-type structures, need to be in order for the material to exhibit the bandgaps commonly measured in experiments?

In order to investigate this question, we performed a convergence study for strongly condensed carbon nitride nanoribbons of increasing width, see Figure 6. Results show that the optical gap of a ribbon structure composed of 7 or more heptazine units ($E_{\text{gap}} = 2.85$ eV) has reached that of the fully-condensed structures (cg-C_3N_4-2D: 2.99 eV, pg-C_3N_4-2D: 2.79 eV). This result underlines that small domains of strongly-condensed PCN of *ca.* 3–4 nm^2 can already exhibit the desired optical properties. Even though our computational predictions show that the material prefers to grow

via stacking rather than laterally, condensation of only 7 heptazine units should be readily possible. This extrapolated minimum crystalline size is in good agreement with experiments by Inoki *et al.*, who calculated a bandgap of 2.06 eV for PCN crystals of *ca.* 3 nm size.[90]

Furthermore, the average HOMO-LUMO gap of all studied tetramers was computed to be 3.61 eV, which is comparable to that of the melon 2D structures (3.62 eV and 3.68 for s-melon-2D and melon-2D, respectively; see Table S1). While the absolute values of molecular HOMO-LUMO gaps and bandgaps from periodic calculations are not directly comparable, this trend is still noteworthy. It is also corroborated by a combined experimental−theoretical study by Li *et al.*, who report that the optical gap of heptazine oligomers rapidly converges with size.[44] Therefore, this result not only emphasizes again that a high DoC is a key driving force for red shifting of the optical gap, but is also in a good agreement with the ribbon model convergence study which shows that only small domains of high condensation PCNs are required to produce a desirable bandgap.

3.1.16 Influence of Corrugation

Corrugation of carbon nitride materials is a significant factor in terms of thermodynamic stability and optical properties. Using GGA-DFT and MP2 methods, Gracia and Kroll found that corrugation enhances the thermodynamic stability of condensed carbon nitride structures by relieving the repulsive interaction between adjacent lone-pair electrons of the nitrogen atoms.[43] This conclusion is in agreement with many other published studies[43, 51, 86, 98] as well as the simulation results presented here. For example, our calculations show that the corrugated fully-condensed cg-C_3N_4-2D model is more stable than its fully flat counterpart pg-C_3N_4-2D ($\Delta E = 0.7$ eV/heptazine unit). In terms of optical properties, corrugation in-

creases the bandgap, see Table S1. For example, the flattened pg-C_3N_4-3D structure has a 0.6 eV narrower bandgap compared to the corrugated — and thermodynamically more stable — cg-C_3N_4-3D structure.

Out-of-plane corrugation of the material occurs in order to minimize repulsive interactions between adjacent N atoms.[43] Here, structural factors contributing to corrugation are examined in more detail, namely the DoC, lateral crystallite size, and stacking. To this end, we compare the calculated root-mean-square deviations (RMSD) of the out-of-plane shift of atomic coordinates for different 1D, 2D, and 3D structures, see Table S2.

First, lateral crystallite size is examined. The RMSD shift increases from 0.01 Å for the heptazine monomer (h_1) up to 0.25 Å for the pentamer (h_{51}). This result suggests that larger structures corrugate more easily. Section 3.1.13 already established that the experimental material is most likely a mixture of different structural motifs and section 3.1.15 established that already small areas of g-C_3N_4 can exhibit bandgaps of 3 eV and less. In light of these trends, the present results suggest that in order to achieve a desirable bandgap, a material with only small connected patches of the same structural motif, thereby avoiding corrugation, is desirable. A recent study by Mitoraj *et al.* has used this principle to good effect.[34] The group employed functionalization with a small fraction of azo-linkers in the inner domain to trigger local flattening of the material, thereby redshifting the absorption spectrum.

The DoC can have an even more profound impact on corrugation compared to crystallite size. For example, comparing RMSD shifts for the melon-2D (0.00 Å), PHI-2D (0.57 Å), and cg-C_3N_4-2D (0.80 Å) structures in Table S2, it becomes apparent that corrugation increases as the DoC increases, which counteracts the trend of narrowing bandgaps with increasing DoC (see Table S1). This result once again emphasizes that if the goal is to obtain a PCN material with low bandgap, connected areas of

the same structural motif should be kept small since corrugation becomes more pronounced as these areas increase in size.

Finally, stacking appears to inconsistently affect the RMSD shift of the atomic coordinates. For example, the out-of-plane RMSD shifts of atoms in the 2D and 3D cg-C_3N_4 models are close to identical (see Table S2). The bandgaps of these models are close to identical, see Table S1. On the other hand, the bandgap of the fully-flattened pg-C_3N_4 model is reduced by 0.44 eV due to stacking. Going from PHI-2D to PHI-3D, the extent of corrugation decreases, thereby slightly reducing the bandgap. This result indicates that at least based on the present data set, there is no obvious systematic trend connecting stacking and corrugation. Therefore, any new model system requires detailed investigation in this regard.

To summarize, corrugation has a profound impact on the stability and electronic structure of carbon nitride materials. In calculations, corrugation is found to stabilize structures thermodynamically and to increase the bandgap. The latter point is two-pronged: corrugation weakens the π-π interactions in the lateral direction but also weakens interlayer interactions perpendicular to the layers. From these results, we hypothesize that if the goal is to achieve a material with a small bandgap, synthetic conditions should be optimized to yield a PCN consisting of small domains of the same structural motif since corrugation becomes more pronounced with increasing domain size. As discussed in section 3.1.15, small domains of g-C_3N_4 material interspersed in a host matrix of less-condensed material are sufficient to obtain a desirable bandgap.

3.1.17 Postulation of a More Complete Computational Carbon Nitride Model

In this final section, we aim to combine the insights gained throughout this study to postulate a more complete model for the computational investigation of PCNs. While

the experimental material is arguably too complex to be treated with any one separate model, we are convinced that there is nevertheless great value in taking steps towards representing as many of the intricacies of this fascinating material class as possible in simulations.

The new model, herein referred to as the "mixed" model, should satisfy the following conditions:

1. The melon structure (50% DoC) should be represented in the model as it constitutes one of the thermodynamically most stable structures found in the present study.
2. The PHI model (75% DoC) is another thermodynamically stable candidate structure that warrants representation, also because successful synthesis of this motif has been reported using a templating method with salt melts.[45, 97, 99]
3. From bandgap results in this study, only the fully condensed cg- and pg-C_3N_4 structures can sufficiently explain the experimental bandgap. The planarized pg-C_3N_4-3D structure gives a bandgap as low as 2.35 eV. Calculated free energy trends suggest that these structures form under low p_{NH3} conditions. This 100% DoC structure should therefore be represented as well.
4. Results on the influence of corrugation as well as the presented lateral size *vs.* bandgap data show that small domains of g-C_3N_4 with low corrugation are sufficient to achieve a narrower bandgap. The model size, therefore, can remain overall small, with rapid alternations between the above structural motifs.

The resulting model as well as a comparison between its DoC and optical properties with those of its three parent structures is illustrated in Figure 10. Shown here is only the most promising mixed model with 57% DoC. Three other structures with DoC up to 71 % were investigated as well and are shown in the Supporting Information, see Figure S1 for illustrations of their structures and Table S1 for the optical properties.

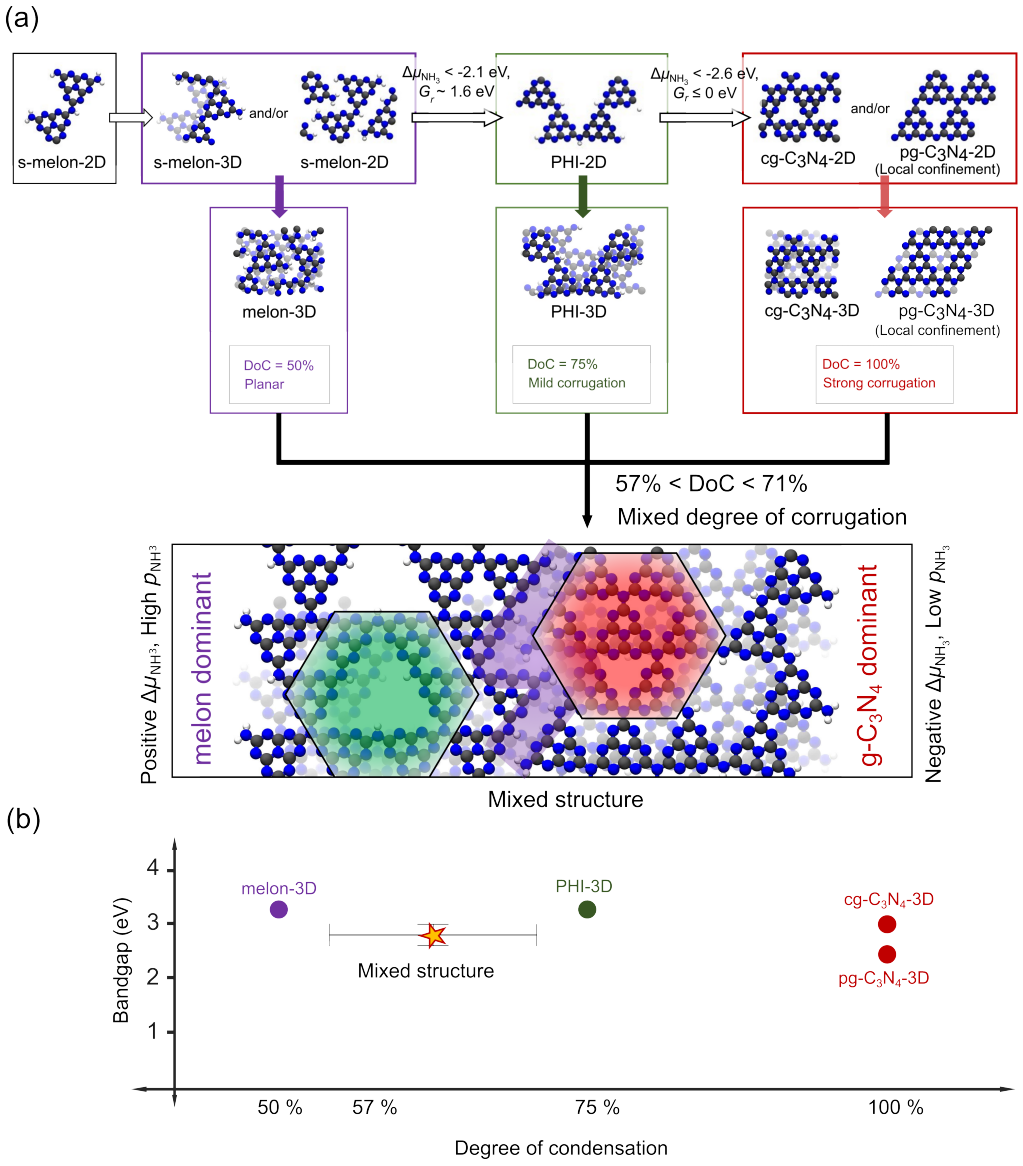

Figure 10: (a) Illustration of the postulated "mixed" PCN model as well as the parent structures it is composed of. (b) Calculated bandgaps for the mixed structural motif as well as for the parent structures as a function of the DoC. The oval shape indicates the range of DoCs and bandgaps obtained for the four tested mixed models; the yellow star indicates the most promising model that is also depicted in (a).

Because the fully-condensed structural motif (red hexagon) is confined in a small domain, only mild corrugation occurs (0.573 Å *vs.* 0.804 Å for cg-C_3N_4) and the resulting optical bandgap is *ca.* 2.9 eV, see Table S1. It is noteworthy that the optical bandgap of the mixed structures is lower than that of cg-C_3N_4-3D, likely due to the aforementioned encapsulation and local flattening. This result confirms the initial hypothesis that extended condensed structures are not necessary to achieve a desirable bandgap, and highlights that mixed structures can easily give rise to low bandgaps.

To the best of our knowledge, this is the first time that a model system capturing this many important facets of PCNs at once is presented in literature. This study, however, is limited to the structure of the pure PCN materials and does not take into account functional end groups such as –N–H and –N–CN which may be able to further adjust the local electronic structure.[100] The influence of functional groups on electronic properties and reactivity will be explored in the future using this model system as basis.

3.1.18 Conclusion

The thermodynamic stability and the optical properties of heptazine-based carbon nitride materials were investigated using accurate hybrid density functional theory calculations. Three structural parameters were identified that strongly affect the optical properties:

1. degree of condensation (DoC; decreases bandgap and decreases stability),
2. stacking (decreases bandgap and increases stability),
3. and corrugation (increases bandgap and increases stability).

Materials with a high DoC also show pronounced corrugation, which presents a

dilemma if material optimization towards narrow bandgaps is the goal. Materials with high DoC and pronounced corrugation form at conditions where the chemical potential of NH_3, μ_{NH_3}, is strongly negative, *i.e.* at high temperature and low p_{NH_3}. The melon string structure is preferred at less negative μ_{NH_3} but exhibits a large bandgap. We identified interconversion pathways starting from the melon string structure towards more condensed structures. However, from the relatively small differences in thermochemical stability between these structures, it is expected that materials synthesized under typical experimental conditions consist of a mixture of more and less condensed structural motifs. The thermodynamic preference for stacking over lateral condensation likely further discourages formation of extended areas of the same motif.

From the calculated trends, we postulate a complex computational model that combines features of the melon string, poly(heptazine imide) (PHI), and g-C_3N_4 model systems. This mixed structure shows a similar thermodynamic stability region as its parent molecules and exhibits, despite its lower DoC of 57%, a narrower bandgap of 2.9 eV compared to the fully condensed but strongly corrugated cg-C_3N_4-3D model. The bandgap is likely a result of local flattening of the small, encapsulated, strongly-condensed motif featured in the model.

The present study therefore illustrates that the experimentally well established favorable optical properties of PCNs can emerge from comparatively small g-C_3N_4 domains embedded in a framework of thermodynamically more stable and less condensed motifs like the melon string or PHI structures. In future studies, the presented computational model will be used to explore the effects of functionalization and templating ions on the stability, catalytic activity, and optical properties of PCNs.

3.2 Structural-electonic-optical properties

3.2.1 Abstract

Two-dimensional (2D) materials have attracted considerable attention due to their unique physicochemical properties and significant potential in energy-related applications. Polymeric carbon nitrides (PCNs) with 2D stacked architecture show promise as photocatalysts for solar-to-fuel conversion and as versatile 2D semiconductors. However, the lack of a clear definition of the exact structural model of these materials limits our fundamental understanding of their unique properties. Here, we investigate the structure-induced optical properties of PCNs through *ab initio* calculations. Our study on the electronic and optical properties of PCNs highlights the significant influence of structure on their behavior, especially near band edges. The analysis reveals that the degree of condensation and corrugation influences the electron/hole localization and the energy levels of π electrons, which are crucial for the optical behavior. In addition, the microstructures of 2D configurations lead to divergent optical properties in 3D configurations, with characteristic peaks identified at 350 nm and interlayer interactions at 400–500 nm, depending on the specific microstructures. Through observations over 2D and 3D structures, we elucidate exciton photophysical processes in PCN materials. This highlights the substantial differences in optical properties between actual 2D and 3D structures, while also demonstrating the potential for carrier and energy transport mechanisms to occur perpendicular to the plane. Finally, our results provide deep insights into the understanding of previously hidden microstructural, electronic, and optical properties of PCNs, paving the way for further performance and property enhancements in this class of materials.

3.2.2 Introduction

Quantum confinement effects of single-atom catalysts, 1D and 2D nanostructured materials have attracted considerable attention due to their unique physicochemical properties and significant potential in energy-related applications.[101–104] Among them, intensive investigations have aimed to control the 2D layered structures and to harness the exceptional properties for practical applications.[105] In particular, research on 2D semiconductor materials has received considerable interest in artificial photocatalysis due to the tunability of the electronic structure. [106, 107]

In particular, 2D backbone materials composed of heptazine and *s*-triazine, collectively referred to as PCN, have gained significant attention due to their ease of synthesis and versatility in (photo-)catalytic performance and applications such as CO_2 conversion, oxygen evolution/reduction, hydrogen peroxide production, and hydrogen generation, all under UV and/or near-visible irradiation. [108–120]

The detailed classification of PCN materials depends on their intricate structures and properties. Among these classifications, the conventional PCN structures such as melon and graphitic carbon nitride exhibit a suitable bandgap (2.7 eV), which can extend the light absorption to visible light[34, 90]. Moreover, ionic carbon nitrides such as poly(heptazine imide) (PHI) have attracted attention owing to their unique properties, such as charge accumulation capabilities for the delayed catalysis[121], or very low photocurrent onset in photoelectrodes[122, 123], showcasing the material's potential in numerous applications.

Despite the heightened interest in PCN materials, we still have a limited understanding of their photophysical and chemical properties and how these are connected to their structures. Therefore, it is difficult to explain their photochemical properties, which often depend heavily on synthesis conditions.[119, 120] Additionally, the relationship between charge carrier dynamics and photocatalytic efficiency is barely

reported.[124]

Computational simulations, particularly those utilizing *ab initio* calculations, are a promising tool for understanding the atomic-level properties of materials, including their electronic structure. The calculations have been performed in order to identify the desirable model structure for PCN in order to reveal its unique properties. It is expected that PCN exhibits strong exciton binding, similar to other organic semiconductors, in a Frenkel-type excitation.[125–127] However, due to the uncertainty of the structural models representing PCN and their calculated results differing from actual experiments, there is a need for better structural models that can accurately represent the properties of PCN. In our previous studies, we calculated the thermochemical stability of reported PCN models and concluded that the actual PCN configuration is closer to a linear structure rather than a 2D structure, coexisting with melon and graphitic structures. Furthermore, the energetic preference for stacking over size expansion allowed us to provide valuable insights into the shape of the real PCN structure.[128]

In this study, we explore the intricate relationship between the structural properties of PCN and their impact on the optical behavior through *ab initio* calculations. Our research elucidates common characteristics inherent to both 2D and 3D PCN materials, notably the localization of electrons/holes and the significant role of π electrons associated with carbon-nitrogen bonds. This study reveals that microstructural variations significantly impact the π electron energy levels in 2D PCNs, thereby defining their optical signatures. Moreover, we have identified intricate interlayer interactions within these structures, which are integral to the unique configuration of each 2D layer.

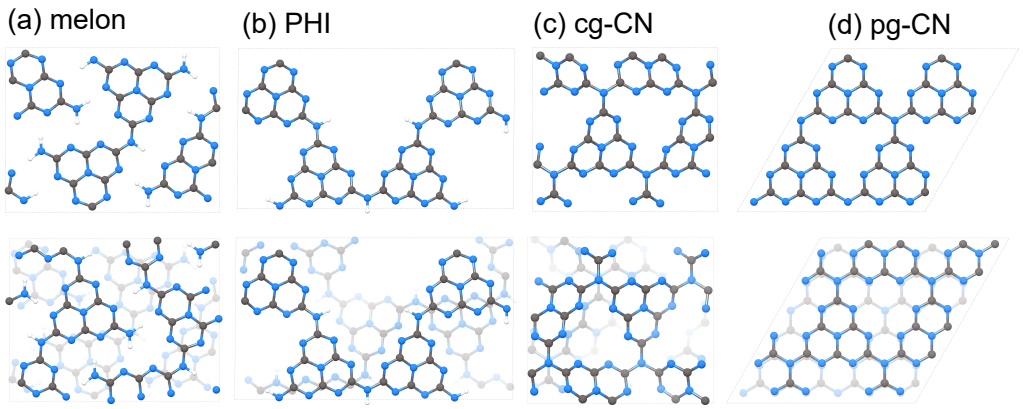

Figure 11: The illustration of the PCN models used in this study. The upper is the 2D monolayer and the lower is the stacked 3D structure.

3.2.3 Results and discussion

3.2.4 Structural Models

The elucidation of PCN structures has been a recurring topic for a decade, beginning with the proposal of melon and graphitic carbon nitride structures.[1, 5, 91, 129] The discovery of the PHI structure, also known as ionic carbon nitride, synthesized through the molten salt method, further contributed to the diversity of PCN architectures. [130, 131] However, the absence of the exact structure model for PCN still presents a challenge in establishing the structure–electronic (optical) relationship, impeding a thorough understanding. Previous research has mainly focused on investigating the electronic and optical structures of 2D monolayers and their respective configurations.[125, 132, 133] In our previous research, we successfully established the thermodynamic conditions governing the PCN structural motifs under practical synthetic conditions. [128] This thermochemical stability suggests that the narrow and highly stacked heptazines locally possess melon (linear) and graphitic (fully condensed) regimes. The main objective of the present study is now to identify and

characterize the optical-electronic properties depending on the structural features.

Figure 11 illustrates the 2D monolayer and 3D stacked models of the heptazine-based carbon nitrides used in the present study, representing melon (linear structure), PHI, and both the corrugated (cg–CN) and planar graphitic carbon nitride (pg–CN) structures, respectively. While the graphitic structure (100% degree of condensation) is regarded as "ideal," both theory and experiment suggest the partial presence of the graphitic domains within less condensed matrics.[1, 90, 128, 134, 135] This study excludes the effect of structural inhomogeneity, since the electronic contribution of the dangling triazine or heptazine moiety near the band edges is negligible.[34] Due to the robust exciton binding energy and a compact exciton radius of the Frenkel exciton, commonly assumed for heptazine-based carbon nitrides, the model structures employed in this study satisfactorily describe the localized electronic nature and sufficiently include the comprehensive properties of the general PCN structure. [136]

In Figure 12, we analyzed the projected density of states (PDOS) of both 2D monolayer and 3D stacked structures using DFT with the HSE06 hybrid exchange-correlation functional. This analysis was conducted to characterize the orbital distribution of the elements, based on structural effects such as the degree of condensation, the degree of corrugation, and stacking. It is commonly observed in both the 2D monolayer and 3D stacked models that nitrogen orbitals largely contribute to the occupied orbitals near the valence band maximum (VBM). The unoccupied orbitals near the conduction band minimum (CBM) are shared by both carbon and nitrogen atoms. This common configuration indicates that the typical electronic transition near the Fermi level in PCNs occurs between the occupied N-p orbitals and the unoccupied C-p and N-p shared orbitals. This finding strongly supports the conclusion that π–π^* transitions are the prevalent electronic transitions in PCN materials.[137] To provide more specific details, the PDOS analysis of both 2D and 3D structures reveals a significant alteration in the primary contribution of the VBM orbitals, shifting from Np_z orbitals

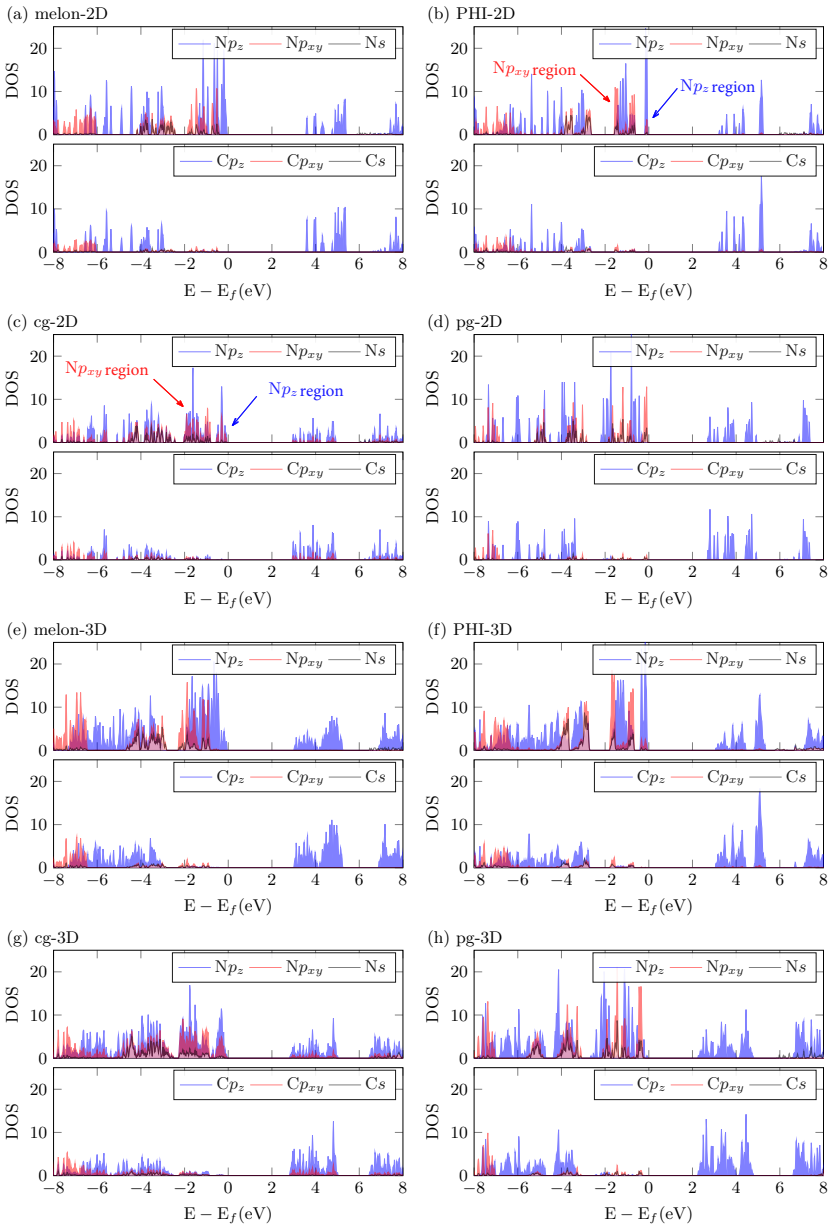

Figure 12: The projected density of states of (a, e) melon, (b, f) PHI, (c, g) pg–CN, and (d, h) cg–CN. The projection is performed on s, p orbitals corresponding to carbon and nitrogen atoms. The trivial contribution of hydrogen is omitted. Fermi energy referenced to 0 eV.

to Np_{x+y} orbitals as the degree of condensation increases (melon $\rightarrow$ PHI $\rightarrow$ g-CN). Notably, the Np_{x+y} orbital contribution becomes the most prominent in the graphitic and planar structures (pg–CN). In these structures, the projected electron density of Np_{x+y} can represent both π bonding and non-bonding electron pairs due to the distorted p_z orientation caused by the buckled structure, which is not accounted for in simple spatial projections. For clarity, we present the actual electron density corresponding to the respective energy level in Figure S8. The electron density clearly illustrates that in flat structures (melon and pg–CN), the actual lone-pair electrons correspond to the Np_{x+y} orbitals. In corrugated structures (PHI and cg–CN), the lone-pair electron density is limited to energy levels where the density of states of Np_{x+y} is higher than that of p_z (see Figure 12, marked with arrows). This lower energy profile of the lone-pair electrons in corrugated structures, approximately $0.5-1$ eV lower compared to the p_z orbitals, indicates that the utilization of lone-pair electrons is less favorable than that of π electrons. The elevated energy levels of the lone-pair electrons in pg–CN can be attributed to the substantial confinement of electrons resulting from the highly symmetrical structure. [125] This symmetry enhances interactions among Np_{x+y} orbitals, maintaining the locally stable structure. [138] We have also observed that the impact of stacking on the electronic structure differs between planar structures (melon and pg–CN) and buckled structures (PHI and cg–CN). In planar structures, the emergence of small Np_z peaks at the VBM can be attributed to the overlapping p_z orbitals between the layers (Figure 12). These energy levels indicate the presence of interactions between the layers, occupying the band edge. On the other hand, in buckled structures, the peaks in the stacked 3D structures exhibit almost the same pattern as the 2D monolayer, indicating minimized interaction between different layers. Importantly, both the overlapping p_z orbitals are situated near the Fermi level. This suggests that interlayer interactions in 3D structures have a significant influence on the bandgap.

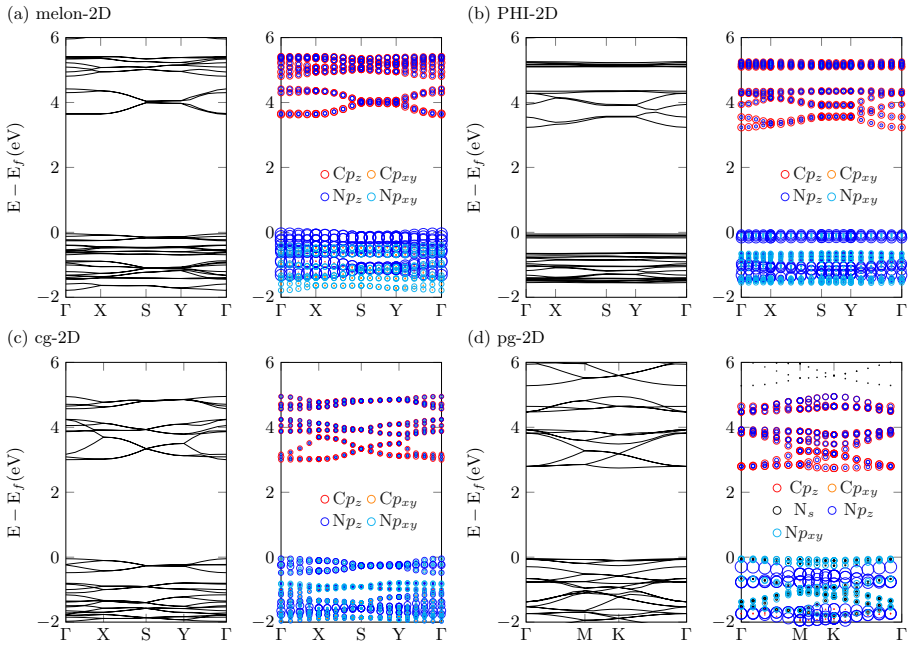

Figure 13: The band structure (left) and its orbital projection (right) of (a) melon-2D, (b) PHI-2D, (c) pg–CN-2D, and (d) cg–CN-2D. The projection is performed on s, p orbitals corresponding to carbon and nitrogen atoms. The trivial contribution of hydrogen is omitted. Fermi energy is referenced to 0 eV.

In Figure 13 and 14, we present the band structure and its elemental/orbital projection for both the monolayer and stacked structures, respectively. Firstly, a flat band structure is evident at the band edges and other energy levels, indicating localized electrons resulting from discontinuous potentials. [125, 133, 139] The pg–2D structure exclusively exhibits an indirect bandgap, whereas the other 2D and 3D structures have direct bandgaps. However, the disparity between the direct and indirect gap could be negligible not only in the pg–2D structure but also the others due to the observed flat band nature throughout the highly symmetric k-point. These small deviations between the indirect and direct transitions may give rise to various shallow trapping levels due to the strongly localized electrons and holes.[140–143] The calculated bandgap energy of the 2D and 3D structures is provided in Table 1.

The bandgap tends to decrease as the 2D monolayer evolves into the stacked 3D structure. This decrease can be attributed to the quantum size effect of confined electrons. [17] Specifically, the bandgap reduction in PCNs is a consequence of the discrete arrangement of energy levels, resulting from the interplay of localized electrons within each layer. This interaction of localized electrons leads to a rearrangement of energy levels, the energy levels of occupied orbitals become relatively elevated while the unoccupied orbitals are lowered accordingly. The bandgap reduction due to stacking is more pronounced in the planar structures (melon: 0.56 eV and pg–CN: 0.44 eV), whereas it is relatively suppressed in the corrugated structures (PHI: 0.14 eV and cg–CN: 0.04 eV). Hence, we can comprehend the role of corrugation in the

Table 1: The calculated bandgap (HSE06) of PCN structures.

Structure	bandgap (eV)	Structure	bandgap (eV)
melon-2D	3.68	melon-3D	3.12
PHI-2D	3.32	PHI-3D	3.18
cg-2D	2.99	cg-3D	2.95
pg-2D	2.79	pg-3D	2.35

electronic structure, which minimizes interlayer interaction by distorting the structure.

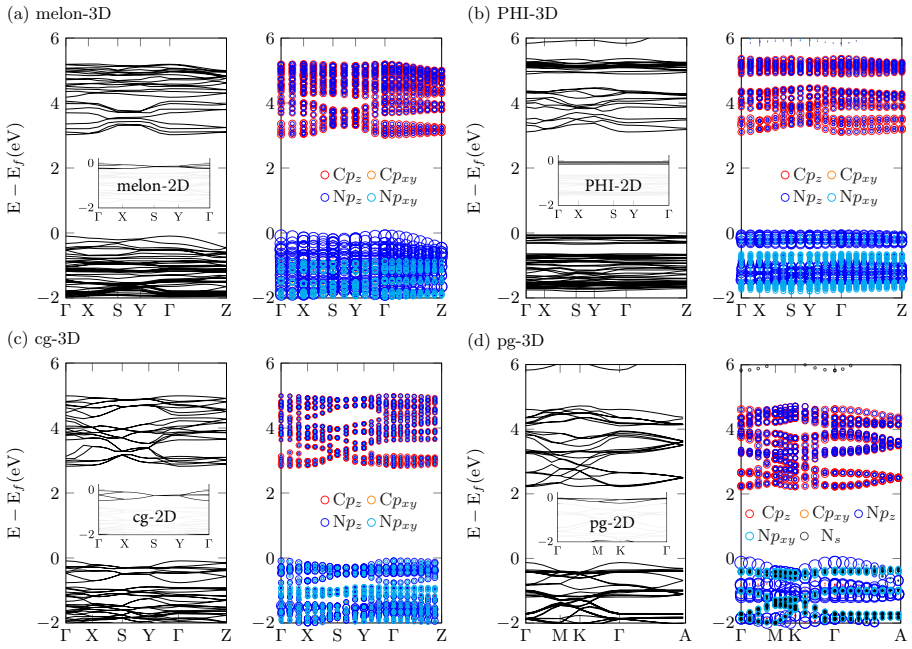

Figure 14: The band structure (left) and its orbital projection (right) of (a) melon-3D, (b) PHI-3D, (c) pg–CN-3D, and (d) cg–CN-3D. The projection is performed on s, p orbitals corresponding to carbon and nitrogen atoms. The trivial contribution of hydrogen is omitted. Fermi energy is referenced to 0 eV. The inset provides a comparison of energy levels near the VBM in the corresponding 2D structure, illustrating different degrees of interlayer interactions.

Particularly in the 3D stacked structures, we observe that as the degree of condensation increases, the structure becomes more corrugated, except for the pg–CN structure, which is a local minimum structure. However, this pronounced corrugation does not lead to a substantial decrease in the bandgap. This suggests that for PCN structures where the degree of condensation[128] exceeds that of PHI (75%), the local flattening significantly influences the effective bandgap. In brief, our findings underscore the significance of interlayer interactions and depth-related π electrons as the principal contributors to the bandgap of conventional PCN structures. Furthermore,

we emphasize that the calculated bandgap from the ground state should correspond to the positions of the absorption peaks in the absorption spectra, rather than the main peaks in the emission spectra at 2.7 eV or the bandgap obtained from the absorption coefficient using the Kubelka–Munk theory.[144] In calculating the bandgap of the periodic PCN models using *ab initio* methods, it is crucial to strictly adhere to the Franck–Condon principle, due to the current absence of methods to obtain the excited geometry. Therefore, determining the actual bandgap corresponding to the 2.7 eV emission necessitates further calculations that consider both the excited geometry and vibrational contributions. This also indicates that the major peak position near the band edge from the experimentally observed absorption spectra (*ca.* 400 nm, approximately 3.09 eV) should align with either the calculated bandgap or the position of the calculated absorption spectra.[145] Our computed bandgaps for PCNs, which consistently group at approximately 3 eV for 3D structures, such as the linear melon and PHI configurations, align seamlessly with this interpretation (cf. Table.1). Further discussions on detailed optical–electronic characteristics depending on structures will be addressed in the following section.

3.2.5 Dielectric Functions and Optical Properties

In this section, we discuss the dielectric function and optical properties of both 2D and 3D PCN structures (see Figure 15). Our primary emphasis is on the imaginary part of the dielectric function, which closely correlates with absorption spectra. To establish the validity of our calculations, we compared the imaginary parts of the dielectric functions of pg–CN–2D between the TDHF@Casida method in our study and the GW@BSE method acquired from literature (Figure S9). We observed systematic shifts between the TDHF@Casida and GW@BSE results, indicating the potential applicability of a scissor correction. Thus, we have accordingly applied the scissor

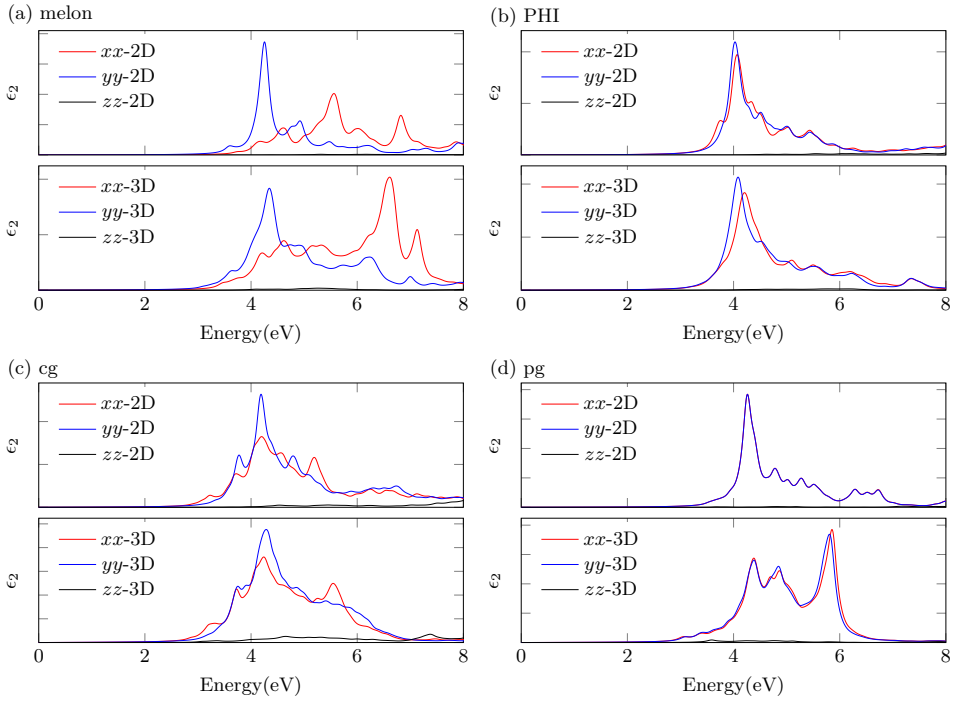

Figure 15: The imaginary part of the macroscopic dielectric functions of (a) melon, (b) PHI, (c) cg, and (d) pg on top of the HSE@Casida method. Imaginary parts corresponding to the respective cartesian direction (xx, yy, zz), obtained by Eq. (3.15) are shown.

correction to other 2D structures to approximate the GW level of theory, which includes electron–hole interactions. However, it is important to note that for 3D structures, the precision of the scissor correction is constrained by limitations in existing literature. [125, 133] Nonetheless, the consistent and systematic shift in energy levels observed from 2D to 3D structures (both cg and pg) supports the continued validity of the scissor correction, even for the evaluated 3D structures.[146, 147]

In the calculated imaginary parts, a prominent bright exciton emerges, consistently appearing near 4 eV in both 2D and 3D PCNs. Below 4 eV (310 nm), we observe multiple bright states with relatively weak intensities, which are related to structural variations within the PCNs. Interestingly, when transitioning from 2D to 3D PCN structures, we discern an overall similarity of the imaginary parts, especially near the band edges. While interlayer interactions induce distinct changes in the band structure, the changes in optical properties remain minor due to their relatively weaker intensities compared to the absorption peaks near 4 eV. This observation illustrates that, despite the pronounced structural differences in PCN, the absorption behavior near the band edge can yield only minor variations. Consequently, this explains the challenges of characterizing PCN microstructures from absorption spectra alone. Figure 15(a) shows the imaginary part of dielectric functions for 2D and 3D melon structures, revealing distinct optical anisotropy. [148, 149] This distinctive feature reflects the linear structure characteristic of melon, raising considerations regarding its directional polarizability and potential limitations in optical efficiency.

In Figure 16, we present average absorption spectra polarized in the respective spatial direction for 2D and 3D PCNs. We also provide the oscillator strength corresponding to the optical transition probability plotted with regard to wavelength. Notably, a discrepancy between absorption spectra and oscillator strength indicates that calculated absorption encompasses transitions from different energy levels.[150]

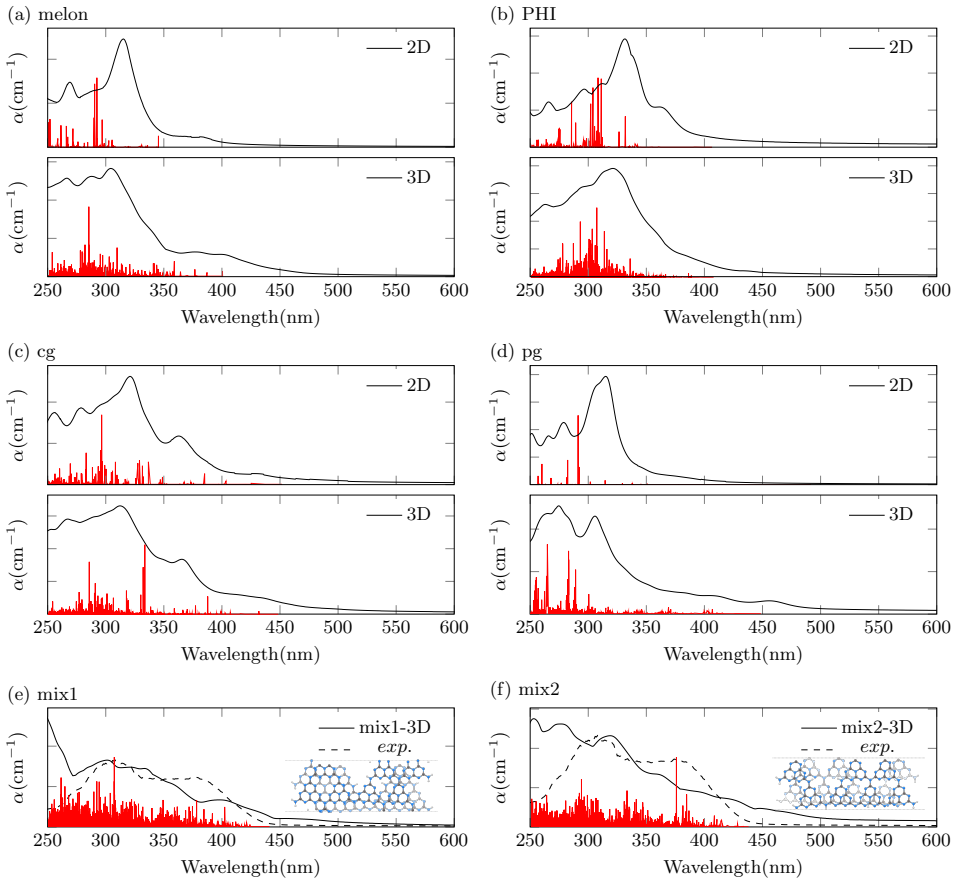

Figure 16: The absorption spectra and oscillator strength were calculated for (a) melon, (b) PHI, (c) cg, and (d) pg in both 2D and 3D structures. The absorption spectra and oscillator strength of (e) mix1-3D and (f) mix2-3D, which depict the amorphous structure, are presented alongside the experimental values which is a dashed line.

This misalignment most likely contributes to the major disparity between the calculated absorption spectra of PCNs and experimental observations. In line with the imaginary part of dielectric functions in Figure 15, strong oscillator strength consistently manifests around 300 nm (approximately 4.1 eV) in models of 2D and 3D structures. We found that this peak reflects the highest degenerate state of excited π electrons in C–N bonds within PCN structures (cf. Figure S8). Additionally, the absorption peak and oscillator strength around 350 nm are linked to structural features. The intensity of this peak is pronounced in the buckled structures (PHI, cg) and shifts across structures, correlating with the degree of condensation within the PCN. Lastly, the absorption peak appearing around 400 nm (3.09 eV) is a consequence of interlayer interactions. This wavelength for the interlayer interactions is in good agreement with the literature observing the interplanar electron hopping in melon from transient absorption spectroscopy and transient photoluminescence using the pump wavelength of 388 nm. [151] The peak intensity and patterns are also in agreement with the aforementioned PDOS results regarding the variation in interlayer interactions due to corrugations. Additionally, the absorption edge in each 2D structure undergoes a red shift in 3D structures. This red shift caused by interlayer overlap results in the formation of new peaks in melon (400 nm), cg (400–450 nm), and pg (450–500 nm), but it is not observed in the PHI structure.[152] It is noteworthy that the subtle red shift observed in PHI can be attributed to the minimized interlayer interactions resulting from its structural flexibility. This structural adaptability allows the PHI structure to mitigate interactions, including interlayer interactions and the lone-pair repulsion of nitrogen atoms, by controlling interlayer spacing and local corrugation, respectively. Consequently, the PHI structure exhibits remarkable independence between layers and heptazine units, simultaneously. The suggested independence between the different layers can be confirmed by the band structure in Figure 13 and 14. When the PHI structure becomes 3D (from 2D), the simple overlap

Table 2: The assignment of calculated absorption peaks for the PCN structural features.

Absorption feature	Attribution	
$\sim$300 nm	degenerated π electrons	
around 350 nm	structural feature	weak at melon and pg, PHI (365 nm), cg (375 nm)
around 400 nm	interlayer interaction	melon (400 nm), cg (400-450 nm), and pg (450-500 nm)

of energy levels is exhibited near band edges, while in the corrugated structure, it can be seen that one energy level moves upwards, and the others shift downward. It indicates that stronger interlayer interaction exists in the cg structure than in the case of the PHI structure. Additionally, the peaks ranging from 400–500 nm may provide the theoretical explanation that the forbidden transition, known as n–π transition, can be attributed to the graphitic regions. It is noted that these absorption peaks are specific to pure PCNs. This study does not consider interactions with other chemical species, such as radicals, charged, or heteroatom species, which might alter the behavior. The calculated absorption peaks for the PCN structural features are summarized in Table 2.

In our prior research, we introduced two microstructure patterns for PCNs, representing more amorphous configurations.[128] Figure 16(e) and (f) illustrate the amorphous structures (inset) and their absorption spectra and oscillator strength. These two structures are virtual models that partially incorporate microstructures from melon (at the edge boundary), PHI, and graphitic structures. The mix1–3D structure contains minimal graphitic structures, positioned on both sides, while the mix2–3D structure features a larger graphitic region. Although neither structure fully replicates the experimental absorption spectra, our analysis suggests that the proportion of

graphitic regions in the mixed model structures is significantly lower than that in the actually measured structure. However, the absorption edge extending to 450 or 500 nm can be easily found in the literature, due to the variety of synthetic conditions .[153, 154] Notably, by combining the oscillator strength from both structures, we can closely reproduce the absorption spectra observed in the experiment. This finding suggests the presence of stacking patterns within these two mixed structures, revealing the stacking patterns of the mixed microstructures. These patterns are distinct from the typical AB stacking arrangements found in crystallites of the respective PCN microstructures.

3.2.6 Interlayer Interactions: Influence on Electronic and Optical Properties

Our results have consistently revealed the significant impact of interlayer interactions within PCN structures on their electronic structure and optical behavior near the band edge. Additionally, we have established that fundamental features, common to both 2D and 3D PCN structures, including the degenerate π–π^* transition peak associated with C–N bonds, the structural characteristic peaks dependent on the degree of condensation, and interlayer overlap peaks, are consistently present in typical PCN materials. These observations indicate potential photophysical processes occurring in 2D and 3D PCNs, which are depicted in Figure 17(a) and (b), respectively. In 2D PCNs, the electronic structure of a monolayer near the band edges can be categorized into two π states: π_1 (localized π electron) and π_2 (delocalized π electron), with a non-bonding (lone-pair) state positioned between them. The bright excitation near 300 nm can be explained by π–π^* transitions governed by the Franck–Condon principle for vertical transitions. Corresponding energy transitions can exist in two forms, Case 1 and Case 3 in Figure 17(a), encompassing a wider energy range than the bandgap. We claim that excitons formed in this range represent hot carriers, sup-

ported by the fact that PCN absorption prominently occurs around 300 nm and 400 nm, while the primary emission converges at 450 nm. However, generic 2D PCN structures have limitations in explaining the discrepancy between the absorption and emission profiles of PCNs. This limitation occurs due to the absence of factors facilitating the relaxation of hot carriers. Instead, this energy range actually corresponds to bound exciton states, which enhance hot emission. This indicates that the 2D PCN structure can show not only the direct hot emissions (Case 1 and Case 3) but also the emission after the cooling of hot excitons (Case 2 and Case 4) simultaneously.[17, 155] This discrepancy implies that a single layer of PCN can exhibit substantially different exciton behavior when compared to multilayered PCNs. [156]

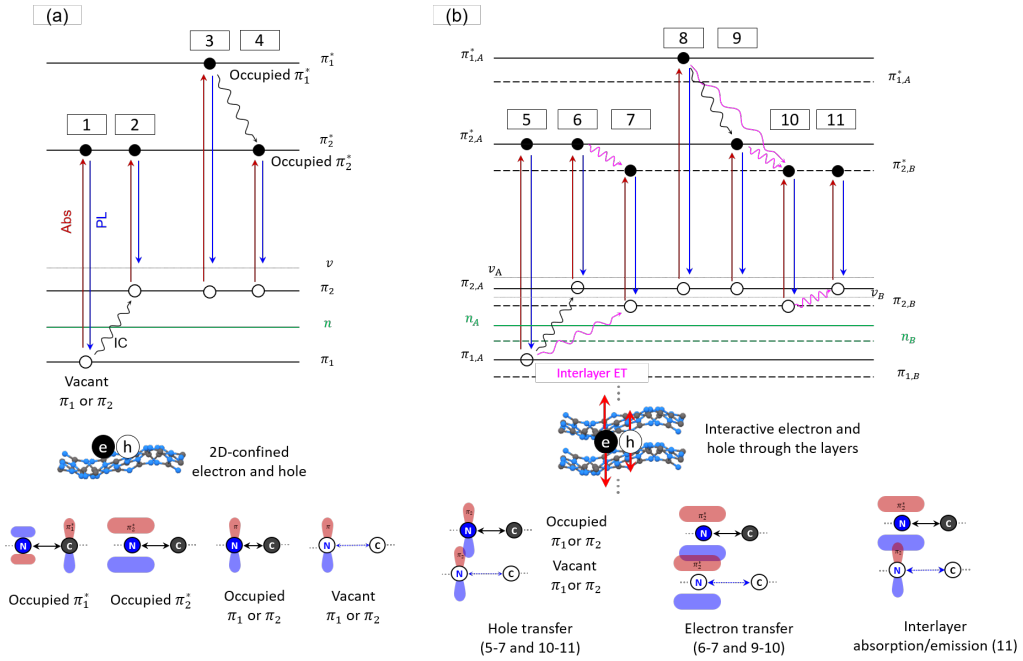

Figure 17: The proposed photophysical process of the general PCN materials in (a) 2D monolayer and (b) 3D stacked structures. The electron density at the respective energy level is illustrated below. The red corresponds to the absorption process, the blue is the photoluminescence process, the black is the non-radiative internal conversion, and the magenta is the interlayer energy/electron transfer, respectively.

Consequently, the reported absorption patterns of PCNs so far suggest the presence of PCNs in a multilayered form. This is consistent with our previous study, which suggested that stacking processes are thermodynamically favored over graphitic processes during the condensation reaction of PCN precursors.[128] In the stacked 3D PCN structure, a more discrete energy structure can emerge, owing to the interplay between the 2D layers and the alignment of energy levels (Figure 17(b)). This characteristic indicates that the interlayer interactions within 3D structures can give rise to more complex excitonic processes. The proposed absorption profile exhibits a similar pattern to the 2D materials, with minor energy shifts attributed to the independence of each layer. Notably, in 3D PCN structures, the cooling processes of hot carriers can gain prominence, derived by the overlaid π orbitals from the stacking. The orbital shapes corresponding to the respective energy levels are represented in Figure 17(a). In the absorption spectra, the electrons and holes generated around 300 nm can undergo internal conversion more readily in the stacked 3D structure compared to the 2D structure. This phenomenon is attributed to the stabilization of the generated holes through Coulombic interactions with electron orbitals in other layers. Consequently, Auger relaxation (Case 6) and the relaxation of excited electrons due to screened holes (Case 9) can be boosted in 3D structures. [17] These factors offer fundamental insights into why PCNs exhibit multiple absorption peaks while displaying a prominent emission peak. Interlayer interactions are expected to lead to lower exciton binding energy in 3D structures compared to 2D counterparts, although a precise determination of exciton binding energy in 3D PCN structures necessitates further taking exact electron–hole interactions into account *e.g.*, GW@BSE.

Based on the results so far, we assert that interlayer interactions play a pivotal role in the band edge properties of real PCN materials. Our calculations, in particular, highlight that the stacking indeed enables excited electrons, holes, and energy transport perpendicular to the layers. Thus, it is anticipated that tuning the interlayer interac-

tions, such as modifying interlayer distances by introducing alkali ions, could indeed influence the exciton dynamics and also the related catalytic activity. This is supported by the fact that the generated electron/hole has sufficient orbital overlap with adjacent layers, and the interlayer spacing for electron transfer falls within the range of 3.2–3.4 Å, suggesting the potential for Förster or Dexter-type energy transfer, in accordance with Fermi's golden rule, as well as electron transfer. [17]

Furthermore, the 3D band structure in Figure 14 reveals that the energy at Γ–Z or Γ–A directions (both are perpendicular to the plane) requires only 0.1–0.2 eV higher energy than the direct bandgap. These small energy barriers can be less meaningful if the cooling process of hot excitons is actually more pronounced in 3D structures. Significantly, this overlap of vertical orbitals selectively occurs at lone-pair N atoms in PCNs, implying that interlayer transitions can occur more effectively in the structures showing highly ordered crystallinity, rather than in strongly amorphous PCNs. This could result in a slight blue shift in absorption/emission peaks. Additionally, the possibility of such interlayer interactions provides a basis for explaining cascade phenomena, electronic or ionic conductivity, recombination, and charge accumulation (particularly in the presence of cations) in PCNs. [157, 158] For a more meticulous understanding of the electronic structure and corresponding optical properties in 3D structures, further studies at a higher theoretical level are warranted, encompassing electron–hole interactions. However, our present studies already underscore the importance of interlayer interactions in PCNs and opens up avenues for future investigations for this intriguing class of materials.

3.2.7 Conclusion

In our study, we conducted *ab initio* DFT calculations to unravel the complex relationship between the microstructural attributes of PCN materials and their optical behav-

ior. This methodological approach allowed us to uncover distinctive electronic properties, underscoring the influence of condensation and corrugation degrees within PCN microstructures on their electronic and optical characteristics. Our analysis distinctly highlighted the correlation between absorption spectrum peaks and microstructural nuances, alongside the critical role of interlayer interactions in shaping these properties. Notably, our findings illuminate the stark differences in optical behavior between 2D and 3D PCN structures, pointing to the pivotal role of interlayer interactions in modulating properties near the band edges. This research underscores the presence of localized electrons and the predominance of π electrons, associated with carbon-nitrogen bonds, as fundamental determinants of optical properties near the band edge in both 2D and 3D PCNs. The results of this study underscore the significant influence of interlayer interactions on the near band edge properties of generic PCNs, which paves the way for manipulating the electronic and/or optical properties as well as charge dynamics in PCNs through rational microstructural engineering.

3.2.8 Experimental and computational methods

3.2.9 Computational details

Calculations were conducted using the Vienna *Ab initio* Simulation Package (VASP) version 6.3.2, which utilizes the projector-augmented wave (PAW) method.[65–69] A plane wave energy cut-off of 400 eV was employed, and the wavefunction was optimized to an accuracy of 10^{-6} eV. Atomic coordinates were relaxed until the forces reached below 5×10^{-2} eV/Å. Gaussian-type finite-temperature smearing with a width of 0.01 eV was applied. DFT-D3 dispersion correction was utilized to account for long-range interactions.[70, 71] The atomic and cell coordinates were relaxed using the Perdew, Burke, and Ernzerhof (PBE) exchange–correlation functional within the generalized gradient approximation (GGA).[72] Accurate final energy results were ob-

tained by performing single-point calculations on the PBE-optimized structures using the Heyd–Scuseria–Ernzerhof (HSE06) hybrid functional, which includes 25% exact exchange and a screening factor of 0.2 $Å^{-1}$.[73] The HSE06 functional was found to provide a good description of the electronic properties of PCNs. For the monolayer, a vacuum layer with a thickness of 20 Å was added to avoid interactions between the periodic images, and dipole correction was applied. The Brillouin zone integration for periodic models was performed using Gamma-centered *k* grids. The excitonic effects were calculated including the frequency-dependent dielectric functions and the oscillator strength by the time-dependent Hartree–Fock (TDHF) implanted in VASP.[159, 160] The details are described in the Supporting Information and all data used in this study is available via Zenodo.[161]

3.2.10 Sample preparation and diffuse reflectance spectroscopy

The conventional yellow coloured polymeric carbon nitride was prepared by thermal polycondensation of 30 g melamine at 530 °C for 4 h in a lid-covered crucible. Diffuse reflectance UV–vis spectra of solid was recorded using a Shimadzu UV2600 UV–vis spectrophotometer.

3.2.11 Supplementary methods

The optical excitation energy is obtained from the transition matrix within the adiabatic linear response theory:[162]

$$\begin{bmatrix} A & B \\ -B^* & -A^* \end{bmatrix} \begin{bmatrix} \mathbf{X}_s \\ \mathbf{Y}_s \end{bmatrix} = E_s \begin{bmatrix} \mathbf{X}_s \\ \mathbf{Y}_s \end{bmatrix} \tag{3.10}$$

where E_s is the excitation eigenvalues, X_s and Y_s are corresponding wavefunctions, A and $-A^*$ are the resonant transition and antiresonant transitions from occupied

orbitals to unoccupied orbitals, and B and $-B^*$ are the coupling between the excitations and de-excitations, respectively. In the HSE@Casida formulation, the matrices A:

$$A_{vc}^{v'c'} = (\varepsilon_v^{\mathrm{HSE}} - \varepsilon_c^{\mathrm{HSE}v})\delta_{vv'}\delta_{cc'} + \langle cv'|V|vc'\rangle - \langle cv'|f_{\mathrm{xc}}|c'v\rangle \tag{3.11}$$

, and the matrices B:

$$B_{vc}^{v'c'} = \langle vv'|V|cc'\rangle - \langle vv'|f_{\mathrm{xc}}|c'c\rangle \tag{3.12}$$

, where the occupied v, v' and unoccupied c, c' states, include that interactions between electrons and holes are described by an effective nonlocal frequency-dependent kernel f_{xc}. [163] The Tamm-Dancoff approximation (TDA) neglects the off-diagonal coupling elements. Hence, the Eq. (3.10) reduces to $AX_s = E_sX_s$.[164] The macroscopic dielectric matrix $\epsilon_{\mathsf{M}}(\mathbf{q},\omega)$ is obtained by an inversion of the full microscopic dielectric matrix in giving long–wavelength limit $\mathbf{q} \to 0$. It gives $\epsilon_{\mathsf{M}}(\mathbf{q},\omega) = (\epsilon_{0,0}^{-1}(\mathbf{q},\omega))^{-1}$. Exploiting the TDA approximation, the solution of HSE@Casida (E_s and X_s) can be used to obtain the macroscopic dielectric function:

$$\epsilon_{\mathsf{M}}^{\alpha\alpha}(\mathbf{q},\omega) = 1+\frac{2}{\Omega}\frac{e^2\hbar^2}{\epsilon_0 m_0^2}\sum_s\left(\left|\sum_{c,v,\mathbf{k},m}\frac{\langle c\mathbf{k}m|p_\alpha|v\mathbf{k}m\rangle}{\epsilon_{c\mathbf{k}}^m - \epsilon_{v\mathbf{k}}^m}^* X_s^{c,v,\mathbf{k}}\right|^2 \times \sum_{\beta=\pm1}\frac{1}{E_s - \beta\hbar(\omega+i\eta)}\right) \tag{3.13}$$

, where p is the momentum operator with Cartesian coordinates α, m is z-component quantum number, Ω is the lattice volume, and η is an infinitesimal number related to the exciton lifetime.[165, 166] The oscillator strength f_α^s of state s is given by

$$f_\alpha^s \propto E_s\left|\sum_{c,v,\mathbf{k},m}\frac{\langle c\mathbf{k}m|p_\alpha|v\mathbf{k}m\rangle}{\epsilon_{c\mathbf{k}}^m - \epsilon_{v\mathbf{k}}^m}^* X_s^{c,v,\mathbf{k}}\right|^2. \tag{3.14}$$

The imaginary part of the dielectric function for 3×3 Cartesian tensor is given by

$$\epsilon_{\mathrm{M}}^{2,\alpha\alpha}(\omega) = \frac{4\pi^2 e^2}{\Omega} \lim_{q\to 0} \frac{1}{q^2} \sum_{c,v,\mathbf{k},m} 2w_{\mathbf{k}} \delta(\varepsilon_{c\mathbf{k}+\mathbf{q}} - \varepsilon_{v\mathbf{k}} - \omega) \times \langle u_{c\mathbf{k}+q\mathbf{e}_\alpha} | u_{v\mathbf{k}} \rangle \langle u_{v\mathbf{k}} | u_{c\mathbf{k}+q\mathbf{e}_\alpha} \rangle \tag{3.15}$$

, where the $\mathbf{e}_\alpha$ is unit vectors for cartesian coordinates, $w_{\mathbf{k}}$ is *k*-point weights, and *u* is the Bloch vector, respectively. The real part of the dielectric tensor $\epsilon_{\mathrm{M}}^{\mathrm{real},\alpha\alpha}(\omega)$ is obtained by Kramers–Kronig relations:

$$\epsilon_{\mathrm{M}}^{\mathrm{real},\alpha\alpha}(\omega) = 1 + \frac{2}{\pi} P \int_0^\infty \frac{\epsilon_{\mathrm{M}}^{\mathrm{img},\alpha\alpha}(\omega')\omega'}{\omega'^2 - \omega^2}\, d\omega \tag{3.16}$$

From the real and the imaginary parts of dielectric functions, the absorption coefficient is calculated.[167]

3.3 Optical properties: *GW*@BSE

3.3.1 Abstract

Polymeric carbon nitrides (PCNs) exhibit intriguing optical properties and exceptional performance in (photo)catalysis, optoelectronics, and energy storage. Nevertheless, the intricate phenomena involving light absorption, formation of long-lived excitons, photo-charging, and photochemical processes observed in PCNs remain poorly understood. Our theoretical investigation elucidates the origin of distinct dark and bright excitons, their stability and lifetimes, and their correlation with the microstructural attributes of PCNs. Furthermore, we identify the decisive role of dark excitons in catalytic reactivity, which underlies the differences in the photocatalytic performance of different PCN derivatives.

3.3.2 Introduction

Polymeric carbon nitrides (PCNs), commonly referred to as graphitic carbon nitrides or melon, along with their (semi)crystalline derivatives such as poly(heptazine imide) (PHI) have emerged as compelling materials for photocatalysis, optoelectronics, and energy storage applications.[1–5] This can be attributed to their straightforward synthesis, robust chemical stability, and optical properties that span from the UV to visible light range.[5] Research on PCNs has demonstrated their efficacy in photocatalytic applications such as hydrogen production under near-visible light, water splitting, CO_2 reduction, and H_2O_2 production.[62] Highly crystalline forms of carbon nitrides are typically obtained using molten salt methods, resulting in highly ordered 2D structures.[95] Particularly, these derivatives, containing cations, are of significant interest due to enhanced photocatalytic activity and the photo-charging behavior that can be utilized in time-delayed photocatalysis or boosted photocurrent response.[57,

168, 169] Despite the plethora of useful and intriguing properties, the knowledge of the relationship between the structural and optical properties in PCN materials is still largely underdeveloped.[5] Merschjann *et al*. reported that charge transport in PCN structures occurs between interplanar layers.[170] Godin *et al*. discussed the charge trapping phenomena in conventional PCNs, and Yang *et al*. reported that the excess electron accumulation in ionic PCNs leads to lower quantum yields due to accelerated electron–hole (e–h) recombination.[54, 55] However, any clear conclusions from experimental studies of exciton dynamics in PCNs using time-resolved spectroscopy remain limited due to the lack of detailed understanding of the structure-induced excited state properties.[54, 55, 148] For example, the frequently observed trapped excitons in PCNs are typically attributed to structural defects. Nonetheless, there is a notable absence of detailed discussion on the nature of these structural defects or their impact on photocatalytic activity. Utilizing many-body perturbation theory based on Green's function formalism can provide accurate descriptions of excited state properties such as accurate bandgap, exciton energy, and absorption spectra. Our previous studies reported strong exciton binding energy,[125] and have examined the effects of PCN microstructures, such as corrugation, degree of condensation, and stacking, focusing on their thermodynamic stability, electronic structure, and optical properties.[128] We particularly noted that the interlayer interactions in PCNs play a significant role in both thermodynamic and electronic properties.[171] Herein, we perform first-principles calculations based on *GW* and the Bethe–Salpeter equation (*GW*-BSE),[160] to elucidate the crucial link between the various structural motifs in PCNs and the corresponding optical properties, formation of bright and dark excitons, exciton stability and lifetime, as the resulting factors governing the photocatalytic activity. We demonstrate that the strongly localized electrons in PCNs induce active interlayer transitions due to the stacked structure of PCNs. Furthermore, we show that the interactions between heptazine units vary with the microstructure of PCNs,

affecting the formation and the lifetimes of the dark excitons more significantly than of the bright excitons. Our findings thus establish the pronounced structure-related variations of the dark excitons as a key factor determining the experimentally encountered optical properties and photocatalytic performance of different types of PCNs.

3.3.3 Method

All *ab initio* calculations were performed using VASP (6.4.1), which uses the projector augmented wave potentials (PAWs).[172] We considered PCN structures optimized by the local density approximation (LDA) and generalized gradient approximation (GGA) functionals, respectively, to compare the description of the highly-localized π-electrons within the heptazine units.[171] The Perdew–Zunger parametrization of Ceperley–Alder Monte-Carlo correlation (CA) functional[173, 174] with the many-body dispersion energy method (MBD@rsSCS)[175, 176] is used within LDA, while PBE-D3 is adopted for the GGA calculations.[70, 72] To describe the single-particle excitations of the PCN structure, we conduct a single-shot *GW* calculation to avoid bandgap overestimation.[177, 178] In brief, the *GW* approximation neglects the vertex functions in Hedin's formalisms, and the self-energy (Σ) is given as the product of the Green function (G) with the screened self interactions (W). Then, the quasi-particle energy is given by:

$$E_{n\mathbf{k}}^{\mathrm{QP}} = E_{n\mathbf{k}} + Z_{n\mathbf{k}}\langle\psi_{n\mathbf{k}}|\Sigma - V_{\mathrm{xc}}|\psi_{n\mathbf{k}}\rangle, \tag{3.17}$$

where **k** and n are the wave vector and band index, $Z_{n\mathbf{k}}$ is the renormalization function obtained from the self-energy with DFT eigenvalues.[179] In the G_0W_0 calculations, we include 256 bands for the 2D PCN-structure and 512 bands for 3D PCN-structure, respectively. For the 2D and 3D PCN structures, Γ-centered $2 \times 2 \times 1$ and $2 \times 2 \times 2$ **k**-space meshes are used, respectively. The quasi-particle energy is updated by using BSE to include *e–h* interactions within the Tamm–Dancoff approxi-

mation (TDA)[164], given by:

$$(E^{\mathrm{QP}}_{c\mathbf{k}} - E^{\mathrm{QP}}_{v\mathbf{k}})A_{vc\mathbf{k}} + \sum_{v'c'\mathbf{k}'} \langle vc\mathbf{k}|K_{e-h}|v'c'\mathbf{k}'\rangle A_{v'c'\mathbf{k}'} = \Omega A_{vc\mathbf{k}}, \tag{3.18}$$

where c and v are indices of conduction and valance bands, respectively, $A_{vc\mathbf{k}}$ are e–h coupling coefficients, Ω are the BSE eigenvalues, and K_{e-h} is the e–h interaction kernel.[180, 181] For the BSE calculations we considered 32 eigenvalues. Then, the independent quasi-particle (IP) energy considering electron–electron (*e*–*e*) interactions is obtained as *GW*@IP, and the BSE is used to include *e*–*h* interactions, finally denoted as *GW*@BSE. The real and the imaginary parts of the macroscopic dielectric functions are computed including local field effect.[159] From the calculated oscillator strengths, the bright excitons are selected having the 5% of the highest intensity, and the rest are classified as the dark states. We modified the VASP source code to obtain the transitional dipole momentum kernel (μ_{S}) (See Appendix A) to calculate the radiative decay rate of the exciton state S (γ_{S}) at wavevector $\mathbf{Q} = 0$ using the equation, given by:[182]

$$\gamma_{\mathrm{S}}(0) = \tau_{\mathrm{S}}(0)^{-1} = \frac{8\pi e^2 E_{\mathrm{S}}(0)}{\hbar^2 c}\frac{\mu^2_{\mathrm{S}}}{A}, \tag{3.19}$$

where E_{S} is the exciton energy at $\mathbf{Q}$, A is the area of the unit cells, c is the speed of light, and τ_{S} is the exciton lifetime. Furthermore, we calculate the effective radiative lifetime $\langle\tau_{\mathrm{eff}}\rangle$ at temperature (T) assuming a neglectable exciton momentum in PCN structures at high symmetry points.[183] Therefore, the effective radiative lifetime using the Boltzmann average of τ_{S} is given by:

$$\langle\tau_{\mathrm{eff}}\rangle^{-1} = \frac{\sum_{\mathrm{S}} \tau_{\mathrm{S}}^{-1} e^{-E_{\mathrm{S}}(0)/k_{\mathrm{B}}T}}{\sum_{\mathrm{S}} e^{-E_{\mathrm{S}}(0)/k_{\mathrm{B}}T}} \tag{3.20}$$

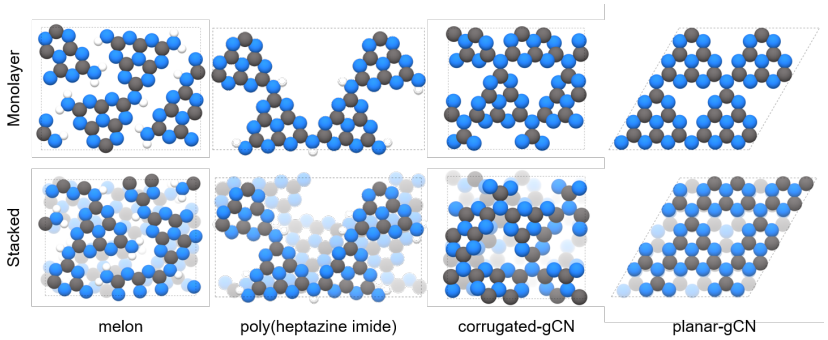

Figure 18: Structures of polymeric carbon nitrides.

3.3.4 Models

Figure 18 illustrates the different PCN structures considered in this work. These models encompass variations in the degree of poly-condensation of heptazine units, corrugations, and stacking configurations.[128] Increased poly-condensation leads to higher carbon and nitrogen contents, but a reduced hydrogen ratio. The planar-gCN (p-gCN) is known to be energetically less stable compared to corrugated-gCN (c-gCN), which represents a local minimum in the energy landscape.[184] PCN structures, composed of these heptazine units, typically exhibit highly-localized π electrons. Thus, we primarily present results for optimized geometries using CA (LDA) functionals. These functionals provide an efficient description of structures with highly-localized electrons, considered as key properties. To address the limitations of the MBD@rsSCS dispersion correction, which depends on the exchange–correlation energy from the LDA functionals, we also included results obtained with the PBE-D3 *xc*-functional. This approach offers a better description of interlayer properties. Results of the optimized geometry with PBE-D3 are available in the supplementary information (SI) for comparison (Figs. S9–S20). The lattice parameters of the optimized geometries obtained with both functionals are summarized in Table S1.

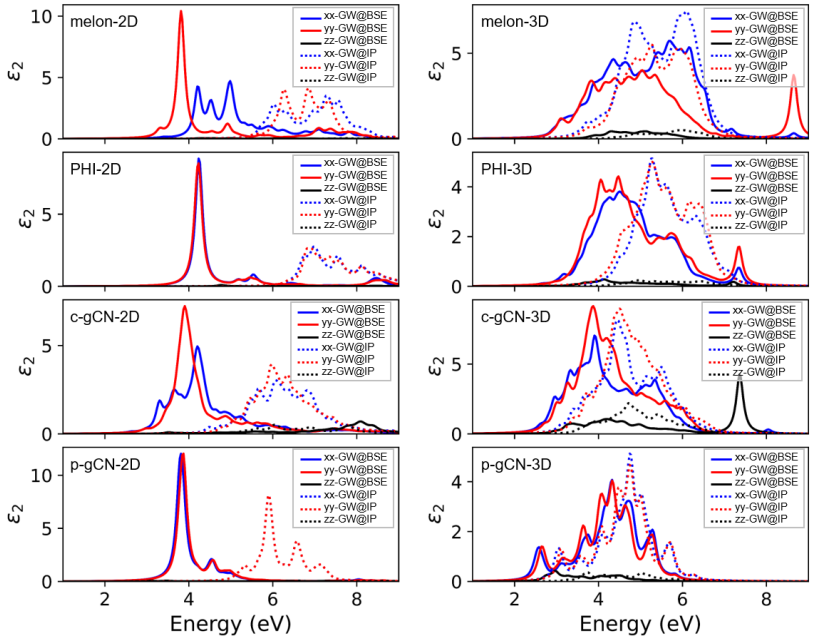

Figure 19: Imaginary part of dielectric functions. The solid and the dashed lines are obtained by the *GW*@BSE and the *GW*@IP respectively.

3.3.5 Optical spectra

The sole use of density functional theory (DFT) to accurately describe optical properties has numerous limitations.[159, 177] To address these challenges, we use the BSE to address the energy originating from *e*–*h* interactions on top of the quasi-particle energy derived from GW calculations. This GW-based quasi-particle energy incorporates precisely screened *e*–*e* interactions, thereby enhancing the accuracy of single excitation property predictions. Notably, the quasi-particle energy adjusted by the BSE correction typically exhibits a red shift compared to those predicted by the IP approximation, which omits *e*–*h* interactions. By analyzing the imaginary part of the macroscopic dielectric functions from both *GW*@BSE and *GW*@IP calculations, we can estimate the exciton binding energy in 2D and 3D PCN structures, as illus-

trated in Figure 19. Spatially-projected absorption coefficients reveal distinct patterns: 2D PCN structures show strong exciton binding energy (> 2 eV).[125] However, this significant exciton binding energy diminishes to less than 1 eV in 3D stacked structures. Moreover, the transition from a 2D monolayer to a stacked 3D configuration alters the absorption edges and reduces the optical anisotropy observed in PHI-2D and c-gCN-2D structures. Since the optical anisotropy is attributed to the in-plane joint patterns of the heptazine units formed during poly-condensation, the reduced optical anisotropy implies that the fractions of the 2D PCN micro-structure can indeed interact with each other throughout the 3D assembly. In brief, this means that diverse forms of PCN fragments within the PCN structure interact electronically and optically through their stacking configurations, regardless of size or shape. Our findings provide clear evidence of strong interlayer interactions, resulting in dramatically decreased exciton binding energy and changes in absorption patterns including altered optical anisotropy and absorption edges.

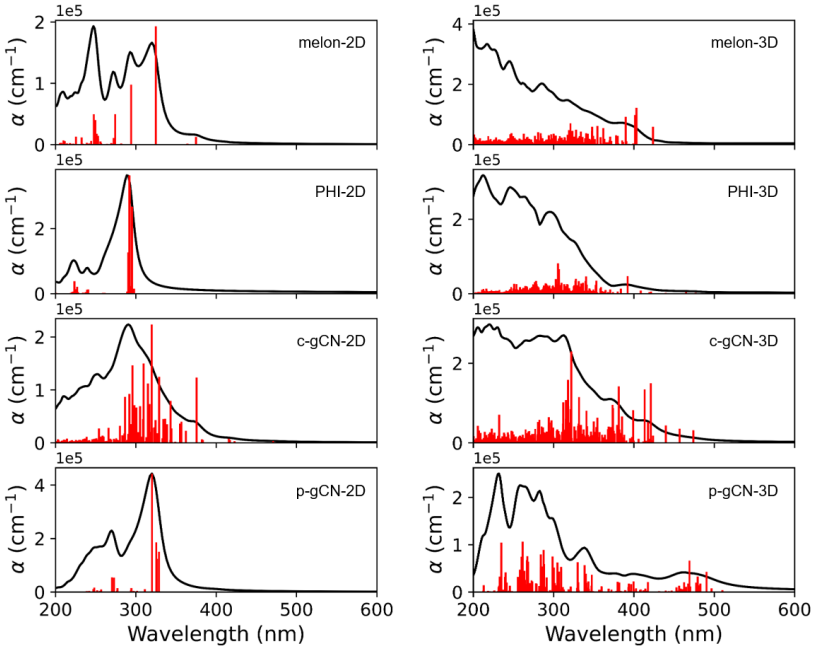

Figure 20: Illustration of the calculated absorption spectra for 2D and 3D PCN models along averaged spatial directions. The oscillator strengths in relation to wavelength are presented in red.

To better elucidate the origins of the absorption features near the absorption edge, in Figure 20 we depict the oscillator strengths and averaged absorption spectra along spatial directions for PCN 2D and 3D structures obtained from *GW*@BSE calculations. Firstly, we observed that each 2D structure of PCNs exhibits distinct absorption spectra patterns. When these structures are stacked to form a 3D structure, additional peaks arise due to interlayer interactions. These emergent peaks are more pronounced in flat structures (melon and p-gCN), where interlayer interactions result in more absorption patterns. In contrast, in buckled structures (PHI and c-gCN), small absorption peaks appear due to interlayer interactions with the red-shifted 2D peaks. The strong intensity of absorption peaks near 200 nm in 3D PCNs is due to the stacking of infinite 2D models, indicating that finite-sized ribbon structures exhibit a reason-

able decrease in the intensity of these absorption peaks[171] The peaks appearing beyond 400 nm originate from the interactions between layers and the in-plane π–π^* transitions, which will be discussed below. The absorption edges of the different PCN structures are obtained as 2.93 eV for melon-3D, 2.60 eV for PHI-3D, 2.62 eV for c-gCN-3D, and 1.69 eV for p-gCN-3D. These PCN structures and bandgaps are completely in line with the experimentally observed bandgaps of PCNs, which range from 2.6 to 2.8 eV.[5, 127, 185, 186] Especially, the frequently observed long absorption tails can not only be attributed to thermal vibrational motion, but can have a distinct structural origin, primarily from the graphitic (*i.e.* fully condensed) domains.[187]

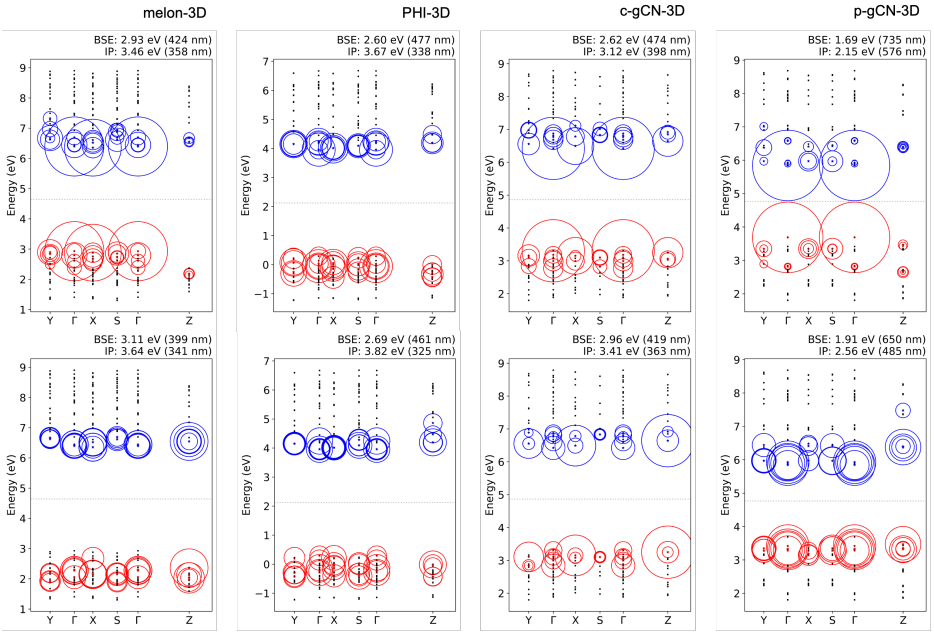

Figure 21: Representaton of eigenvalues (BSE and IP) and coupling coefficients (radius of circles) of bright states for both 2D and 3D PCN structures, corresponding to the absorption edges (top) and interlayer interactions (bottom).

3.3.6 Exciton formation

Figure 20 demonstrates the oscillator strengths that, according to the Franck–Condon principle, represent the probability of electronic transitions at each energy level. Cases of high oscillator strengths with relatively low absorption peaks occur in the absorption spectrum due to consideration of the dipole momentum and selection rules. Therefore, by comparing absorption spectra with oscillator strengths, we can predict the types of electronic transitions. Notably, most electronic transitions near the absorption edge in PCN 3D structures are combined with the dark states. Our results from the BSE calculations provide the coupling coefficients corresponding to transitions between energy levels at each high symmetry point, as shown in Figure 21. The coupling constants of the other lowest 32 excited states are presented in the Supplemental Material. The coupling coefficients (radius of circles) at the band edges for each PCN 3D structure are displayed at the top line of the figure, and the coupling coefficients that are most pronounced for interlayer interactions are displayed at the bottom line. At the absorption edges, stable excitons are related to transitions between the band edges in melon, c-gCN, and p-gCN structures while relatively more degenerate excitons are formed in the PHI structure. The coupling constants at the bottom line of Figure 21 represent the exciton formation at the Z-point in each structure, indicating a direction toward the other layer from the Γ-point. These interlayer transitions are identified as the electron transitions from the sub-levels of the valence band to near the conduction band edge, indicating that these transitions involve different π electrons than those associated with band edge transitions. Our previous study found that absorption peaks of PCN structure can be sorted as in-plane π–π^* transitions and π–π^* interlayer transitions.[171] When comparing the relative stability of excitons formed in the PCN structures at the interlayer, the c-gCN structure exhibits the most stable exciton with an energy gap of 2.96 eV. Melon and PHI also show stabilization of interlayer excitons at 3.11 eV and 2.97 eV, respectively, each showing roughly a 0.3

eV difference from their absorption edges. The differences in exciton stability at the interlayer are determined by the degree of overlap between orbitals of different layers, specifically being regulated by the magnitude of the transition momentum off-diagonal components. These off-diagonal components turn out to be the degree of interaction of the nitrogen non-bonding (n) electrons, which impact the π electrons at the interlayers. This explains how the interlayer distances are related to the configurations of PCN structures. This is more clearly understood when comparing the coupling constant plots of LDA-optimized geometries with different interlayer distances (see Table S1) to those of GGA-optimized geometry results (Figs. S11, S13–S20). Furthermore, our previous study found that the thermodynamic contributions from vibrational motion due to the flexible layered structure of PCNs are non-negligible.[128] Thus, we expect that enhanced interlayer interactions may be evident due to interlayer vibration modes.

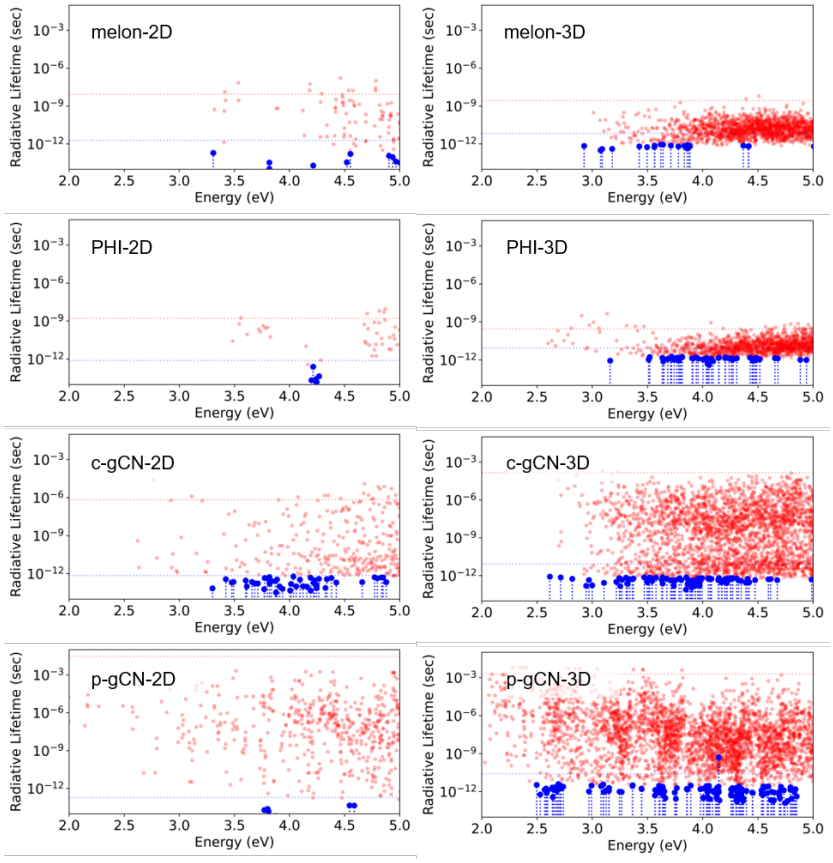

Figure 22: Calculated radiative exciton lifetimes of both 2D and 3D PCN structures. Bright states are denoted in blue, while dark states are represented in red. Their respective effective lifetimes at 300 K are indicated by dashed lines.

3.3.7 Prolonged exciton lifetime and photocatalytic activity

We have calculated the exciton lifetimes and effective lifetimes at 300 K based on the energy required for each excited state, transition probability, and transition dipole momentum. The obtained behavior is shown in Figure 22 and summarized in Table 3. Here, we define the energy states with the top 5% oscillator strengths as bright states (blue) and the rest as dark states (red) (see Method section). Firstly, the effective lifetimes of bright excitons in 3D PCN structures are slightly increased compared to

those in 2D structures. This suggests that most bright excitons in PCN structures are formed by the direct in-plane transitions of strongly localized π electrons and the interlayer π transitions. Therefore, the stacking configuration helps stabilize these bright excitons. In contrast, the dark excitons formed in 3D structures are destabilized by interlayer interactions. Most dark excitons are related to in-plane n–π^* or distorted π–π^* transitions and interlayer interactions cannot sufficiently stabilize these states due to the lack of interaction. Notably, the effective lifetime of dark excitons increases dramatically in graphitic structures (c-gCN and p-gCN). This indicates that a new form of excitons, different from those in melon and PHI structures, exists in gCN. We propose that these long-lived excitons are closely related to the trapped excitons reported in the literature[54]. Furthermore, we suggest that the calculated lifetimes of dark excitons shed light on the photo-charging phenomenon observed in ionic-PHI.[55, 57, 148, 168, 169, 188] Notably, the photocharging phenomenon persists in the proton-exchanged structure (H-PHI), indicating that the phenomenon is more attributed to the high symmetry crystalline regions rather than the influence of existing cations. However, the principle and the nature of electron accumulation in PHIs have not been elucidated so far. Our results demonstrate that the extended lifetime of excitons is observed in both 3D stacked and 2D graphitic structures (c-gCN and p-gCN), indicating that these long lifetimes are primarily due to structural features rather than interlayer interactions. In contrast, the PHI structures exhibit the shortest dark exciton lifetime even shorter than those of melon structures. This might explain the general experimental observation that the photo(electro)catalytic activity and photoinduced electron accumulation in ionic (PHI-type) PCNs are enabled only in the presence of effective electron donors, such as alcohols, that can quickly extract the hole from the short-lived excitons in PHI-type PCNs.[55, 57, 143, 148, 168, 169]

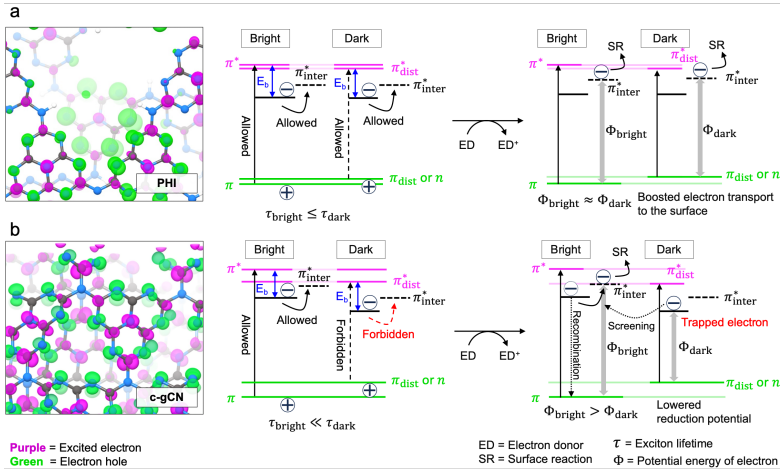

Figure 23: (left) Electron density of electron hole and the excited electrons and (right) the proposed mechanisms of photoexcitation process for (a) PHI and (b) c-gCN-3D structures, where π_{dist} and π^*_{dist} are the energy levels of distorted π electrons, π_{inter} is the π^* state at the other layer, and $\mathrm{E_b}$ is the exciton binding energy, respectively.

In order to further elucidate the nature of these dark states, Figure 23 shows the electronic density corresponding to the electron and the electron hole for the dark excitons of the longest lifetime in the PHI and the c-gCN structure. It clearly shows that these dark excitons are different in PHI and c-gCN structures. This suggests that the repulsive force between heptazine units causes a distorted orientation of the n or π orbitals. The varying degrees of this distortion control the selection rules, resulting in allowed transitions in PHI and forbidden transitions in c-gCN for dark excitons. This forbidden in-plane transition further hinders the interlayer interaction due to the lack of orbital overlaps. Moreover, this distortion also affects the energy levels of π states, resulting in a larger energy gap between π^* and π^*_{dist} in c-gCN than in the case of PHI. Therefore, the larger distortion of the orbitals can exhibit prolonged exciton lifetimes and lower energy gaps for the dark states. (See Table 3) In the case of melon, the presence of hydrogen bonding slightly alters one of the π electrons, resulting in dark states with lifetimes similar to but slightly longer than those in PHI.[171] In p-

Table 3: Bandgaps of 2D and 3D PCN structures (optimized using CA functionals) were calculated via independent particle approximations (G_0W_0@IP) and BSE (G_0W_0@BSE) methods, alongside the effective exciton lifetime at 300 K. (D) and (I) denote the direct and indirect bandgaps, respectively.

	Structure	G_0W_0@IP (eV)	G_0W_0@BSE (eV)	Exiton lifetime <$\tau_{300\mathrm{K}}$>	
				bright	dark
2D	melon	5.50 (D)	3.31	1.96 ps	8.70 ns
	PHI	5.83 (I)	3.48	0.78 ps	1.65 ns
	c-gCN	4.48 (D)	2.62	8.36 ps	141.00 μs
	p-gCN	4.26 (I)	1.95	0.20 ps	28.73 ms
3D	melon	3.46 (I)	2.93	6.96 ps	2.72 ns
	PHI	3.67 (D)	2.60	8.77 ps	277.34 ps
	c-gCN	3.12 (D)	2.62	8.36 ps	141.00 μs
	p-gCN	2.15 (I)	1.69	26.04 ps	1.92 ms

gCN, the strongly forced forbidden n–π^* transitions due to the high symmetry lead to the detrimental effect of dark states, similar to those in c-gCN. Furthermore, these findings shed light on the experimentally observed detrimental effects of deep charge trap states on photocatalytic activity in both conventional and ionic (PHI) carbon nitrides.[54, 55] The significant distortion of π or n orbitals can create deeply trapped dark excitons compared to the bright states (Fig. 23b). Due to their longer exciton lifetimes, these trapped excitons are less affected by hole-quenching rates and can effectively accumulate electrons. However, these electrons, being spatially distorted and trapped, can not directly contribute to the interlayer interactions for the carrier transport, resulting in significantly reduced quantum yields due to their strongly diminished reductive potential, as reported in the literature.[54] Moreover, the presence of these trapped electrons might shield interlayer charge transport of the bright states, which could further promote the recombination of bright excitons. The presence of these deeply trapped electrons also suggests that they can be used as a descriptor to indicate whether conventional or ionic (PHI) carbon nitrides obtained from the

synthesis process contain graphitic domains. On the other hand, in PHI structures (Fig. 23a), the dark states of the less affected π electrons exhibit similar energy levels to the bright states, forming shallow trapped states. Due to this similarity, these dark states can have lifetimes as short as the bright states. Although a fast electron donor rate is required for hole-quenching due to these short lifetimes, once the hole of the dark exciton is filled, the nearly undistorted orientation of the π electrons enables efficient interlayer carrier transport, leading to effective surface catalytic reactions. We assume that these dark-state-induced phenomena (enhanced photocatalytic activity or time-delayed photocatalysis) in PHI can be more pronounced in the presence of cations, as the stabilization of these excess electrons is also a key factor in preventing recombination.[57, 168, 188] We note that, although the model structures used in our simulations cannot fully account for the complex and still not fully resolved structure of real-life PCN materials, our results are in excellent agreement with experimental observations, and elucidate the crucial role of dark states in photocatalytic activity of PCN materials.

3.3.8 Conclusion

Our study elucidates the principles underlying the exciton formation, transitions, and lifetimes within PCN structures. The results establish a valuable link between the structural and optical properties of PCN materials, which is a key prerequisite for rational tuning of their electronic structures for optimal performance. Utilizing *GW*@BSE calculations, we find the decisive role of dark excitons for effective photocatalytic performance. The structure-dependent mechanisms of dark exciton formation elucidate the electron accumulation phenomena and subsequent surface reactions in different types of carbon nitrides. Our study thus establishes a valuable theoretical framework for further spectroscopic studies, and paves the way for the knowledge-driven design

of PCN-based materials with tuned properties.

4 Applications

4.1 Motivation

In the preceding chapters, I employed the first-principles calculations to uncover the fundamental relationship of structure-electronic-optical properties PCN materials. Building on these foundational insights, the following chapter aims to contextualize those findings by addressing more complex phenomena and their practical implications. Specifically, the focus is on how the structural, electronic, and chemical properties explored earlier can be applied to understand and explain the following:

- **Understanding Multilayer Interactions and Hydrogenation in PCNs**: This work explores the role of multilayer interactions in PCN microstructures and mixed PCN models on the hydrogen evolution reaction (HER) and oxygen reduction reaction (ORR). By leveraging theoretical insights, I analyze how interlayer interactions stabilize hydrogen adsorption, the implications of hydrogen coverage, and how hydrogenation significantly alters ORR energetics in H-PCN compared to genuine PCNs. These findings emphasize the need for precise models to accurately describe reduction reactions and reveal the potential of H-PCN structures in HER and H_2O_2 production.
- **Exploring Azo-Moieties in Red PCNs for Enhanced Photocatalysis**: The impact of thermal treatment on PCNs is investigated, demonstrating how azo-moieties formed during high-temperature processes extend the visible light absorption beyond 600 nm. These structural modifications lower the bandgap, en-

abling effective photocatalytic hydrogen evolution under low-energy light. However, the trade-offs introduced by network fragmentation, such as recombination centers, are also analyzed, providing a pathway to balance optical absorption, charge separation, and catalytic performance.

- **Water-Soluble PCNs for Photocatalytic H_2O_2 Production**: By examining K,Na-PHI, a water-soluble ionic polymeric carbon nitride, I analyze how functional groups such as cyamelurate enhance colloidal stability and photocatalytic efficiency. These insights demonstrate the materials suitability for selective H_2O_2 production and its robustness under repeated use, providing a scalable approach for quasi-homogeneous photocatalysis in aqueous systems.
- **Stabilizing Ultrafine Nanoparticles with K,Na-PHI**: K,Na-PHI's role as an effective stabilizer for ultrafine gold nanoparticles (Au NPs) is elucidated through theoretical and experimental analyses. I show how charge delocalization within the ionic framework enhances stabilization against aggregation without impeding catalytic activity. This work highlights the versatility of K,Na-PHI as a nanocatalyst capping agent and its broader implications for developing stable, high-performance nanoparticles.

By applying the findings of previous chapters, this chapter seeks to bridge the gap between theory and application, providing deeper insights into PCN-based systems and their practical use in catalysis and photocatalysis. These studies not only expand the understanding of PCN structure-property-reactivity relationships but also pave the way for innovations in sustainable and efficient material applications.

4.2 Mechanistic Investigation of HER and ORR on PCNs

4.2.1 Introduction

Photo-induced catalytic reactions on PCNs, such as the HER, the ORR, and CO_2 reduction (CO2RR), have garnered significant attention in both experimental and theoretical studies due to their potential in hydrogen gas and H_2O_2 production. Most studies have focused on modifying PCN structures through cation doping and functionalization to investigate the effects of heterogeneous configurations. However, from a fundamental perspective, the reaction mechanisms at the surface and the underlying photo-induced phenomena remain unclear, primarily due to the lack of detailed understanding of the intrinsic PCN structures. In the previous chapters, we have explored the thermochemical properties (Chapter 3.1), as well as the structural–electronic–optical relationships (Chapter 3.2) and detailed electronic behavior (Chapter 3.3). Building on these results, this chapter investigates the detailed reduction reactions related to hydrogen production and the oxygen reduction processes, primarily under electrochemical conditions, using computational approaches. We will discuss the thermodynamics of these reaction profiles, focusing on varying proton coverage on PCN monolayers and their correlation to active sites in the ORR. Additionally, we simulate the potential energy profiles for photo-excited reactions by modeling electrode potentials. PCNs are layered structures composed of conjugated carbon-nitrogen π electrons. Due to their highly charged surfaces, nucleophilic species like oxygen molecules often face difficulty interacting with the electronic structure. Nonetheless, experimental studies under aqueous conditions have demonstrated remarkable H_2O_2 production capabilities via photocatalytic reactions. This suggests that O_2 on the surface engages in a reaction mechanism that remains unknown. Previous studies have attempted to explain the reaction mechanism by considering only the intermediates in the well-known 4-electron or 2-electron ORR pathways.[189]

However, these approaches fall short of a complete explanation, as they overlook the initial adsorption of O_2 specieskey for progressing the reaction. Even the *OOH intermediate, crucial in ORR, does not adequately adhere to these models. Given the thermodynamic stability, electronic structure, and optical properties studied in earlier chapters, a clearer understanding of the reduction reaction mechanisms is essential. In this chapter, we first examine the active sites and reaction mechanisms for H_2, followed by an investigation into the role of hydrogen coverage in the ORR. Finally, we explore the feasibility of 4-electron pathways for the ORR.

4.2.2 Computational details

4.2.3 DFT calculations

Calculations were performed using the Vienna *Ab initio* Simulation Package (VASP) version 6.4.1, implementing the projector-augmented wave (PAW) method.[65–69] A plane wave energy cutoff of 400 eV was applied, with wavefunction convergence achieved to an accuracy of 10^{-6} eV. Atomic coordinates were relaxed until forces were reduced below 5×10^{-2} eV/Å. A gamma-centered $4 \times 4 \times 1$ k-point grid was used. Gaussian smearing with a finite-temperature width of 0.01 eV was applied to ensure accurate electronic convergence. To model long-range interactions, DFT-D3 dispersion correction was used.[70, 71] For multilayer systems, a total of four layers were modeled, and the performance of PBE-TS and PBE-D3 methods was compared, with D3 showing interlayer spacing values closer to experimental observations. The bottom layer was fixed to approximate bulk properties, while the top three layers were fully relaxed. Additionally, a vacuum layer of over 12 Åwas introduced to prevent spurious interactions. The atomic and cell coordinates were optimized using the Perdew, Burke, and Ernzerhof (PBE) exchangecorrelation functional within the generalized gradient approximation (GGA).[72] All calculations included spin polarization

considerations.

4.2.4 Atomistic thermodynamics for surfaces

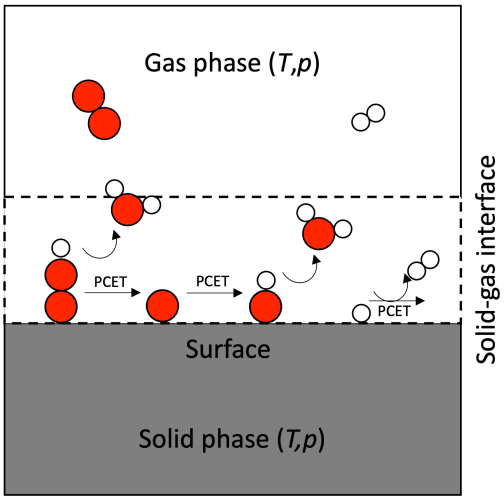

Figure 1: Illustration of thermodynamic-electrochemical system modeling. This figure demonstrates how surface (interface) reactions are approximated in the gas phase and solid phase using the proton-coupled electron transfer mechanism.

Figure 1 illustrates the free energy profiles for the HER and ORR as modeled in this study. The red atoms represent oxygen, and the white atoms represent hydrogen. For an accurate atomic model, particularly at the solid-liquid interface, parameters such as molecular orientation and solvation energy at the interface need to be considered. However, the essential intermediates and known reaction mechanisms can be successfully predicted using simplified models like those shown in Figure 1, demonstrating the effectiveness of this approach for reaction mechanism analysis. To build such atomic models, the Gibbs free energy for different segments of the structure can

be expressed as follows:

$$\mathrm{G} = G_{\text{solid}} + G_{\text{gas}} + G_{\text{surface}} \tag{4.1}$$

The solid-gas interface consists of the surface structure, adsorbed species, and charged molecules that, while not directly participating in the reaction, play a role in defining the system. In real electrochemical reactions, electrochemical double layers (Helmholtz and diffusion layers) encompass these charged molecules. Due to the computational limitations of first-principles calculations, the analysis often focuses on the Gibbs free energy differences between surface structures and intermediates, rather than modeling the full system. Thus, the reaction mechanisms are inferred through the free energy differences between a clean surface and the surface containing adsorbed species. The Gibbs free energy of the surface, including the adsorbed species, is given by:

$$G_{\text{surface}} = \gamma A + \theta \cdot N \cdot \mu_{\text{ads}} \quad \text{with} \quad \theta = \begin{cases} 1 & \text{if the adsorbate exists,} \\ 0 & \text{if the adsorbate does not exist.} \end{cases} \tag{4.2}$$

Here, γ is the surface free energy per unit area, μ_{ads} is the chemical potential of the adsorbate, N is the number of adsorbed species, and A is the surface area.

The Gibbs free energy of adsorption is calculated as:

$$\Delta G_{\text{ads}} = G^{\text{ads}}_{\text{surface}} - G^{\text{clean}}_{\text{surface}} \tag{4.3}$$

The chemical potential of the adsorbate is determined by the thermodynamic equilibrium conditions of the surrounding gas phase reservoir. For a given temperature T

and pressure p, the chemical potential of the adsorbate in the gas phase is:

$$\mu_{\text{ads, gas}}(T,p) = \frac{-k_{\text{B}}T\ln Q^{\text{tot}}_{\text{ads, gas}} + pV}{N} \tag{4.4}$$

when $Q^{\text{tot}}_{\text{ads, gas}}$ is given by

$$Q^{\text{tot}}_{\text{ads, gas}} = \frac{1}{N!}(q^{\text{trans}}q^{\text{rot}}q^{\text{vib}})^N \tag{4.5}$$

where Q^{tot}ads, gas is the total partition function of the adsorbate gas phase, defined as:

$$Q^{\text{tot}}_{\text{ads, gas}} = \frac{1}{N!}(q^{\text{trans}}q^{\text{rot}}q^{\text{vib}})^N \tag{4.6}$$

Here, V is the volume, and q represents the partition functions of the gas phase corresponding to translational, rotational, and vibrational free energy, respectively.

Using Equation 4.4, the chemical potential of a single gas phase molecule is expressed as:

$$\mu_{\text{ads, gas}}(T,p) = E^{\text{total}}_{\text{ads, gas}} + E^{\text{ZPE}}_{\text{ads, gas}} + \Delta\mu_{\text{ads, gas}}(T,p) \tag{4.7}$$

By utilizing Equations 4.2, 4.4, and 4.7, the free energy of adsorption ΔG_{ads} for reaction intermediates can be calculated under thermodynamic conditions from atomistic models.

4.2.5 Computational hydrogen electrode

The Computational hydrogen electrode (CHE) model is a computational approach to simulate the electrochemical reaction, relating the concept of the proton-coupled electron transfer (PECT) to the chemical potential of hydrogen molecules. The general

reduction reaction in the half-cell is given by

$$(\textit{oxidant}) + ze^- \rightleftharpoons (\textit{reductant}) \tag{4.8}$$

, where z is the number of electrons for the reduction reaction. In standard conditions pH $= 0$ conditions, the $2\mathrm{H}^+/\mathrm{H}_2$ redox couple is in equilibrium as

$$2\mathrm{H}^+_{\mathrm{aq}} + 2e^- \rightleftharpoons \mathrm{H}_{2,\,\mathrm{gas}} \tag{4.9}$$

Then, the dissociation of a hydrogen molecule with finite pH and electrode potential can be expressed as:[190]

$$\frac{1}{2}\mu(\mathrm{H}_{2,\,\mathrm{gas}}) = \mu(\mathrm{H}^+_{\mathrm{aq}} + e^-) + e(U_{\mathrm{elec}} - U_{\mathrm{redox}}) + k_{\mathrm{B}}T\ln(10)\mathrm{pH} \tag{4.10}$$

Using this CHE model, we can investigate the free energy of reaction intermediates during the HER or the ORR, correlating the finite pH condition and the applied electrode potentials. The mechanism of the electrochemical HER involves the following reactions:

$$\begin{aligned} &\mathrm{H}^+ + e^- + * \rightarrow \mathrm{H}^* && (\text{Volmer step}) \\ &\mathrm{H}^* + \mathrm{H}^+ + e^- \rightarrow \mathrm{H}_{2,\,\mathrm{gas}} && (\text{Heyrovsky step}) \\ &\mathrm{H}^* + \mathrm{H}^* \rightarrow \mathrm{H}_{2,\,\mathrm{gas}}\ \text{or}\ \mathrm{H}^*_2 && (\text{Tafel step}). \end{aligned} \tag{4.11}$$

These suggest 2-electron reaction mechanisms (1) Volmer-Heyrovsky reaction and (2) Volmer-Tafel reaction. The 4-electron steps suggested the mechanism of oxygen

reduction in the acidic solution:

$$\mathrm{O_2} + * \rightarrow \mathrm{O_2^*} \tag{4.12}$$

$$\mathrm{O_2^*} + (\mathrm{H^+} + e^-) \rightarrow \mathrm{HOO^*} \tag{4.13}$$

$$\mathrm{HOO^*} + (\mathrm{H^+} + e^-) \rightarrow \mathrm{O^*} + \mathrm{H_2O} \tag{4.14}$$

$$\mathrm{O^*} + (\mathrm{H^+} + e^-) \rightarrow \mathrm{HO^*} \tag{4.15}$$

$$\mathrm{HO^*} + (\mathrm{H^+} + e^-) \rightarrow * + \mathrm{H_2O} \tag{4.16}$$

The 2-electron pathway for the peroxide H_2O_2 production in acidic medium is given by:

$$\mathrm{O_2} + * \rightarrow \mathrm{O_2^*} \tag{4.17}$$

$$\mathrm{O_2^*} + (\mathrm{H^+} + e^-) \rightarrow \mathrm{HO_2^*} \tag{4.18}$$

$$\mathrm{HO_2^*} + (\mathrm{H^+} + e^-) \rightarrow \mathrm{H_2O_2} \tag{4.19}$$

The intermediates are used to investigate the profile of the free energy diagram to estimate the reaction barrier and to compare the structural effect accordingly. The redox potentials are +1.23 V $(vs.$ SHE at pH = 0$)$ for the 4-electron ORR and +0.682 V$(vs.$ SHE at pH = 0$)$ for the 2-electron pathway to produce hydrogen peroxide, respectively. The thermodynamic potential-determining step can be max$[\Delta G]$ and the overpotential for each intermediate is given by:

$$\eta = \frac{\Delta G}{e} - U_{\text{redox}} \tag{4.20}$$

Therefore, the overpotential from the potential-determining step (PDS) can be obtained when $\Delta G = \max[\Delta G]$ for the reaction.

This redox potential of the water production from the oxygen reduction is derived from

the half-cell electrochemical reaction is represented by:

$$\mathrm{O_2} + 4\mathrm{H_2} \rightleftharpoons 2\mathrm{H_2O} - 4.92\,\mathrm{eV} \tag{4.21}$$

It refers to the reaction as highly exothermic. This 4-electron step reaction can be converted to the standard potential for the reaction $E^\circ = 1.23\,\mathrm{V}\,vs.$ RHE per one proton-coupled electron transfer. To adapt these thermodynamic results to the computational way, one can calculate the formation energy of water from the combination of each molecule. In this case, the error comes from the computational value from the isolated $\mathrm{O_2}$ molecule causing the ΔG especially for the $\mathrm{O_2}$ adsorption. By correcting this error manually we could get the ideal energy profile for the reaction steps.[191, 192] Therefore, $\epsilon_{\mathrm{O_2}} = -0.466\,\mathrm{eV}$ is applied in this study to correct the total energy of $\mathrm{O_2}$. To this end, we investigated the effect of HER on the ORR energetics. We assume that the active site for the HER differs from that of the ORR, and that the HER can occur independently and precede the ORR, as it occurs at a lower potential. Thus, we define the ORR steps, incorporating the HER, as follows:

$$\mathrm{O_2} + * + (\mathrm{H^+} + e^-) \rightarrow \mathrm{H^*} + \mathrm{O_2} \tag{4.22}$$

$$\mathrm{H^*} + \mathrm{O_2} + * + (\mathrm{H^+} + e^-) \rightarrow \mathrm{H^*} + \mathrm{O_2^*} \tag{4.23}$$

$$\mathrm{H^*} + \mathrm{O_2^*} + (\mathrm{H^+} + e^-) \rightarrow \mathrm{H^*} + \mathrm{HO_2^*} \tag{4.24}$$

$$\mathrm{H^*} + \mathrm{HO_2^*} + (\mathrm{H^+} + e^-) \rightarrow \mathrm{H^*} + \mathrm{O^*} + \mathrm{H_2O} \tag{4.25}$$

$$\mathrm{H^*} + \mathrm{O^*} + (\mathrm{H^+} + e^-) \rightarrow \mathrm{H^*} + \mathrm{HO^*} \tag{4.26}$$

$$\mathrm{H^*} + \mathrm{HO^*} + (\mathrm{H^+} + e^-) \rightarrow \mathrm{H^*} + * + \mathrm{H_2O} \tag{4.27}$$

$$\mathrm{H^*} + (\mathrm{H^+} + e^-) \rightarrow \mathrm{H_2} + * \tag{4.28}$$

4.2.6 Results and Discussion

4.2.7 HER on monolayer and multilayer PCNs

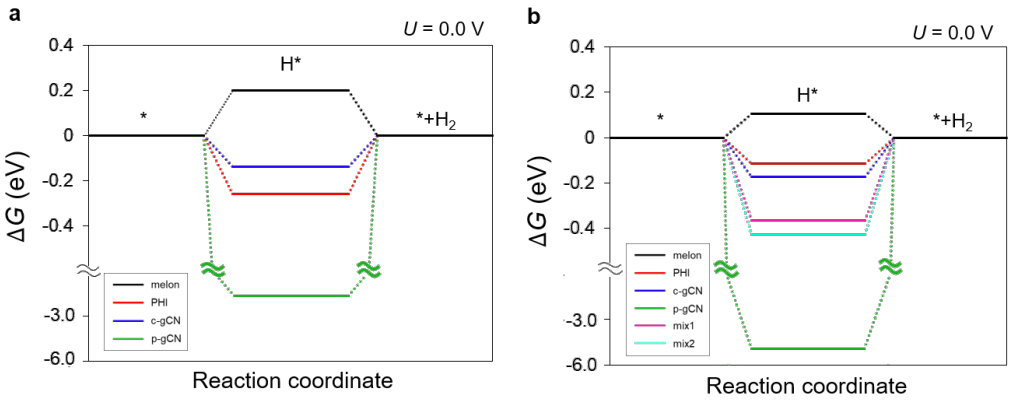

Figure 2: Free energy profiles of a typical HER with H intermediates on (a) PCN monolayers and (b) multilayered PCNs (4-layer). The mix1 and mix2 structures incorporate melon-like edges, corrugated graphitic features, and PHI motifs. The free energy of the intermediates is calculated at pH = 0.

The PCN structures (melon, PHI, c-gCN, p-gCN) exhibit diverse electronic structures (3.2 and adsorption sites for hydrogen. First, we examine the possible C and N adsorption sites in each monolayer structure. As shown in Figure 12 of Chapter 3.2, both π orbitals and non-bonding orbitals are located near the Fermi level across all PCN structures. Therefore, we anticipate that the initial hydrogen adsorption for HER occurs at the nitrogen sites, driven by the π or non-bonding (n) electrons. Based on this assumption, we calculated the hydrogen adsorption free energy on the surfaces of the PCN monolayers. The lowest adsorption energy for each PCN monolayer is shown in Figure 2a. The melon structure exhibits a positive H^* adsorption energy of 0.2 eV, while the other structures show negative adsorption energy: -0.26 eV (PHI), -0.14 eV (c-gCN), and -2.04 eV (p-gCN), respectively. These results clearly indicate that HER activity can vary significantly depending on the PCN microstruc-

ture. As predicted from the electronic structure analysis, the most favorable H^* site is consistently the lone-pair N. This suggests that structures with a higher degree of condensation tend to exhibit more spontaneous and stronger hydrogen adsorption. The relatively low degree of condensation (50%) in the melon structure, combined with the hydrogen bonds connecting the melon strings, stabilizes the surface electronic structure. On the other hand, PHI and c-gCN, with relatively higher degrees of condensation (75% and 100%, respectively), exhibit similar adsorption energy. This observation suggests that, in addition to the degree of condensation, the level of corrugation plays a key role in stabilizing surface electrons. These findings are further supported by the adsorption energy of -2.04 eV in p-gCN, which has a 100% degree of condensation and a planar structure.

These results are more clearly observed in the HER free energy profiles of multilayered PCNs shown in Figure 2b. The multilayered PCNs are composed of 4 layers, based on the PCN microstructure utilized in Chapter 3.1. The free energy of hydrogen adsorption in these multilayer structures shows a different trend compared to monolayer PCNs. The adsorption free energy of the hydrogen intermediates is calculated as 0.10 eV (melon), -0.11 eV (PHI), -0.17 eV (c-gCN), and -5.06 eV (p-gCN), as shown in Figure 2b. In flat structures like melon and p-gCN, interlayer interactions tend to stabilize hydrogen adsorption more than in monolayers. Conversely, in buckled structures like PHI and c-gCN, there is little change in hydrogen adsorption free energy compared to monolayers (-0.14 eV $\rightarrow -0.17$ eV for c-gCN), or the adsorption is less stabilized (-0.26 eV $\rightarrow -0.11$ eV for PHI). Additionally, in the mixed structures (mix1 and mix2) introduced in the previous chapter, the hydrogen adsorption free energy was found to be -0.43 eV and -0.37 eV, respectively. This suggests that real PCN structures, which are likely to consist of various combined microstructures, may exhibit different hydrogen adsorption energy (*ca.* -0.4 eV). In summary, the free energy of hydrogen adsorption decreases as the degree of condensation

and corrugation increases. Given that p-gCN represents a local minimum structure, the low limiting potentials of monolayer melon, PHI, and c-gCN (≤ 0.26 eV) closely correspond to the electrochemical overpotential of approximately 0.2 eV for Pt(111) under acidic conditions, as reported in the literature [193]. However, when factors such as multilayered structures or various microstructures, which are closer to real structures, are considered, the hydrogen adsorption free energy alters. This indicates that interlayer interactions and different degrees of polycondensation reactions significantly influence hydrogen adsorption, implying that estimates based solely on single microstructures or monolayer structures have limitations in fully explaining the actual hydrogen evolution process. Figure 3–6 illustrate the pathways where ΔG_2 and ΔG_3 are minimized, shown in black and red, respectively. The path with the lowest overpotential among all active sites is shown in blue. The other pathways and the corresponding PCN structures are provided in Figure S30–S36. The HER, assuming the formation of two hydrogen intermediates, is presented as follows:

$$* \xrightarrow[(\mathrm{H}^+ + e^-)]{\Delta G_1} {}^*\mathrm{H} \xrightarrow[(\mathrm{H}^+ + e^-)]{\Delta G_2} {}^*\mathrm{H} + {}^*\mathrm{H} \xrightarrow[(\mathrm{H}^+ + e^-)]{\Delta G_3} {}^*\mathrm{H} + \mathrm{H}_2 \tag{4.29}$$

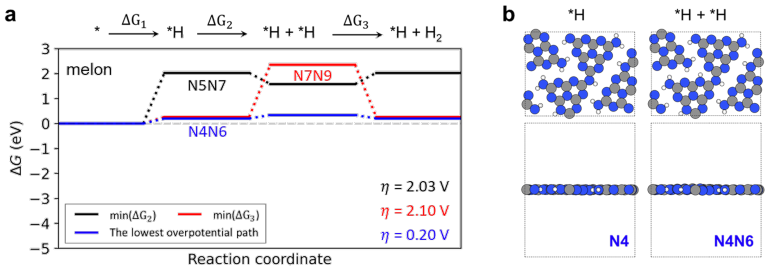

Figure 3: (a) Free energy profiles of HER with additional H intermediates on melon monolayer. (b) Corresponding top-view and side-view images of the structures. The free energy profiles are shown under conditions of pH = 0 and $U = 0$ V.

Figure 3a depicts the HER pathway with the lowest ΔG_2, ΔG_3, and overpotential for the melon structure. When the first hydrogen adsorption occurs with a high free energy (pyridine N, N5), the second hydrogen adsorption can proceed with a relatively low overpotential (black). In contrast, if the first hydrogen adsorption requires the lowest energy, the second adsorption can encounter an energy barrier as high as 2.1 eV (red). For the min(ΔG_2) pathway, it is energetically favorable for hydrogen evolution to occur at the second active site after the first hydrogen adsorption, while in the min(ΔG_3) pathway, sequential desorption occurs after hydrogen adsorption at both active sites. Both reactions can proceed at the potential energy of 2.7 eV, which corresponds to the excited electron's potential energy in PCN. In the pathway with the lowest overpotential, both active sites are pyridine N (N4, N6), allowing for consecutive adsorption and desorption within a very low limiting potential of 0.2 eV.

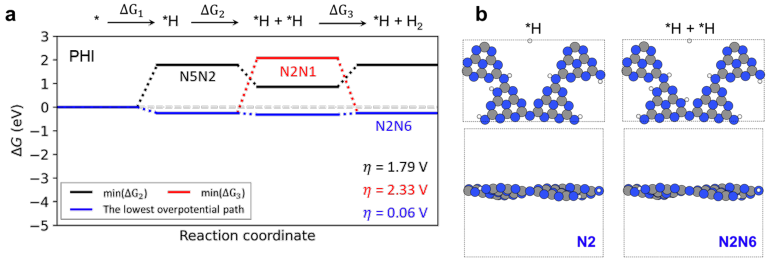

Figure 4: (a) Free energy profiles of HER with additional H intermediates on PHI monolayer. (b) Corresponding top-view and side-view images of the structures. The free energy profiles are shown under conditions of pH = 0 and $U = 0$ V.

In the case of PHI, a similar pattern to melon is observed. (Figure 4) The key difference is that the lowest overpotential path (blue) has a $\Delta G < 0$, unlike melon. Additionally, with a limiting potential of $\eta = 0.06$ eV, a highly efficient HER is expected.

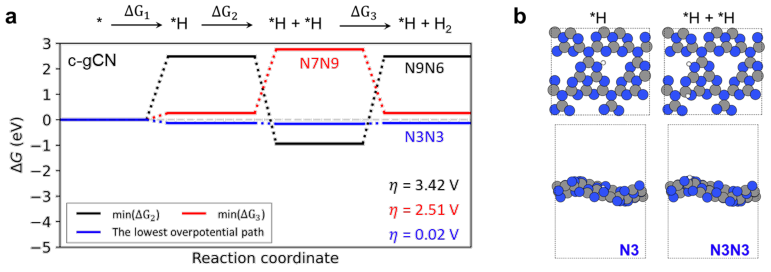

Figure 5: (a) Free energy profiles of HER with additional H intermediates on c-gCN monolayer. (b) Corresponding top-view and side-view images of the structures. The free energy profiles are shown under conditions of pH = 0 and $U = 0$ V.

For c-gCN, the adsorption at N9 (tertiary N) results in a high overpotential of 2.5 eV, with the second hydrogen adsorption site located on the carbon next to pyridine N.(Figure 5) However, hydrogen adsorbed on the carbon requires a desorption energy barrier of 3.42 eV, suggesting that hydrogen coverage on carbon may be related to degradation reactions. In the lowest overpotential pathway, similar to PHI, $\Delta G < 0$ is achieved with a very low overpotential of $\eta = 0.02$ eV.

[hbp]

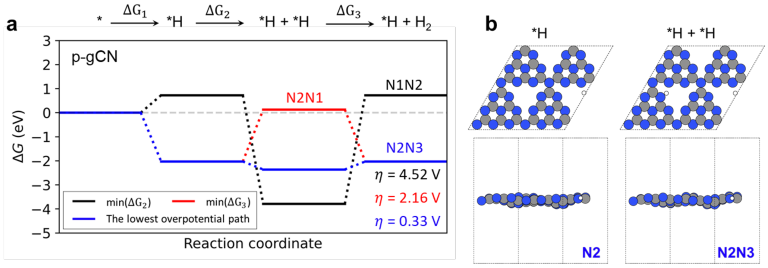

Figure 6: (a) Free energy profiles of HER with additional H intermediates on p-gCN monolayer. (b) Corresponding top-view and side-view images of the structures. The free energy profiles are shown under conditions of pH = 0 and $U = 0$ V.

In the case of p-gCN, degradation was observed in many pathways, and significant corrugation occurred after hydrogen adsorption (Figure S35 and Figure S36). Ad-

ditionally, as with the other PCN structures, the hydrogen adsorption sites located at pyridine N exhibited the lowest overpotential, with $\Delta G < 0$ and a highly negative free energy (< -2 eV), indicating that hydrogen adsorption is thermodynamically highly spontaneous. Upon examining the reaction pathways up to the second hydrogen adsorption site for the four structuresmelon, PHI, c-gCN, and p-gCNwe identified pathways with very low limiting potentials in all structures, which align well with the literature, confirming that these structures hold great promise for HER. However, depending on the microstructure, the free energy of reaction intermediates can vary significantly, showing either highly negative or positive values. Furthermore, considering that multilayered structures generally exhibit lower first hydrogen adsorption energy than PHI and c-gCN, the reaction pathway in real PCN structures likely involves $\Delta G < 0$ and very low limiting potentials. This indicates that these materials are highly promising not only as photocatalysts but also as electrochemical hydrogen evolution catalysts. However, the low electrical conductivity, due to their semiconductor nature, remains a significant challenge. In photocatalytic hydrogen evolution, the relatively high potential energy of excited electrons may allow for multiple reaction pathways to occur simultaneously, potentially compromising the stability of PCN catalysts. Therefore, designing PCNs with extremely low bandgaps could be highly advantageous for photo-induced HER.

4.2.8 ORR and HER-coupled ORR

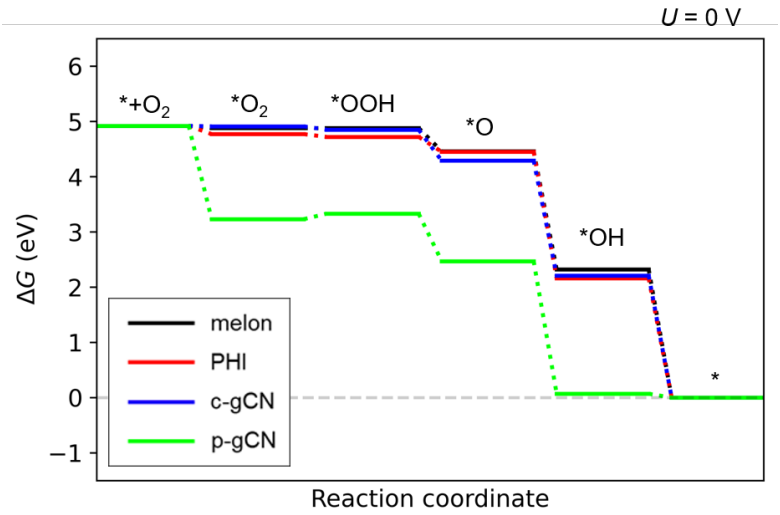

Figure 7: Free energy profiles of the typical ORR process on PCN monolayers at $U =$ 0 V.

The reaction energy profiles of the active sites for the general 4-electron ORR reaction in each genuine PCN monolayer structure were investigated. Among the free energy profiles of various active sites, those with the lowest limiting potentials for the oxygen intermediates were considered the optimal cases.

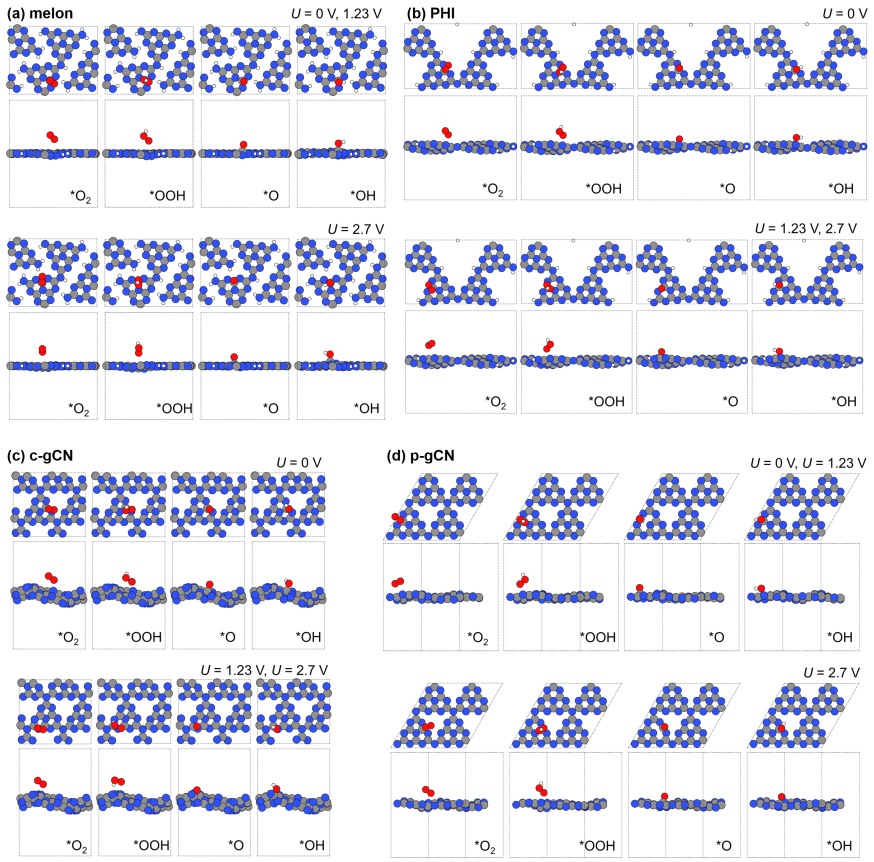

Figure 8: The structural images depict the corresponding reaction pathways for the ORR on (a) melon, (b) PHI, (c) c-gCN, and (d) p-gCN monolayers.

First, the energy profile of the 4-electron ORR in PCN monolayer structures at $U = 0$ V is shown in Figure 7, and the corresponding structures of each intermediate are presented in Figure 8. The free energy and potential-limiting steps for the reaction pathways on all surfaces are provided in Table S5-S16. All the energetics at the surveyed active sites and the simulated potentials are exhibited in Figure S38. The *U* = 0 V free energy profiles (Figure 7) show that melon, PHI, and c-gCN structures exhibit similar trends. However, p-gCN shows a significant decrease in the adsorption energy of intermediates, likely due to the buckling of its planar structure as a result of

interactions with oxygen intermediates, which lowers the overall energy of the system (Figure 8d). This suggests that p-gCN, being a local minima structure, becomes more stable upon buckling during intermediate adsorption. In all structures, the *O_2 and *OOH intermediates do not form chemical bonds with the surface. This could be due to the electronic structure of PCNs, which is highly localized within each heptazine unit but also significantly delocalized within the unit. This prevents the intermediates from inducing sufficient polarization on the surface. However, the long-range electron transfer (LR-EF) mechanism reported in the literature suggests that chemical reactions can proceed without direct chemical adsorption. Based on this, it is assumed that weak van der Waals interactions, or physisorption, retain the intermediates on the surface, stabilizing energy from -0.01 to -0.15 eV in most structures except p-gCN (Table 1).

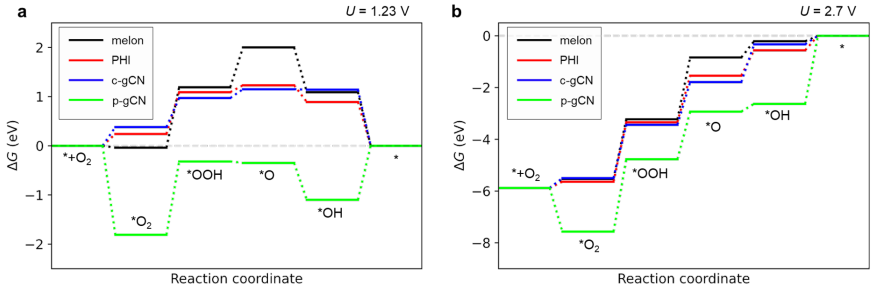

Figure 9: Free energy profiles of the typical 4-electron ORR process on PCN monolayers at $U = 1.23$ V and $U = 2.7$ V, respectively.

Assuming the LR-EF mechanism, the configuration of oxygen intermediates at $U = 0$ V is similar across the structures, with carbon being the active site. The *O_2 and *OOH intermediates are the potential-determining steps, and the reaction pathway is configured to minimize the free energy of these intermediates. The free energy profile at $U = 1.23$ V is shown in Figure 9a. At this potential, only p-gCN demonstrates a favorable reaction pathway, as intermediates on the other surfaces exhibit $\Delta G > 0$,

indicating that the ORR would not proceed. This suggests that ORR can occur only under mild conditions in planar structures, as shown in Figure 8, where different reduction sites may become active at $U = 1.23$ V compared to $U = 0$ V. ORR in genuine PCN monolayers is likely dominated by LR-EF, and reactions can occur at different sites depending on the applied potential. Under photo-induced catalytic conditions ($U = 2.7$ V, considering the typical PCN bandgap of 2.7 eV), ORR could occur in all PCN structures (Figure 9b). However, the uphill free energy profiles suggest that the reaction may not proceed smoothly, considering both kinetic and thermodynamic barriers.

Table 1: Values of G, ΔG, and the PDS for the typical 4-electron ORR intermediates on PCN monolayers as a function of U.

	Free energy (eV)											
	$U = 0$ V				$U = 1.23$ V				$U = 2.7$ V			
	melon	PHI	c-gCN	p-gCN	melon	PHI	c-gCN	p-gCN	melon	PHI	c-gCN	p-gCN
*+O_2	4.92	4.92	4.92	4.92	0.00	0.00	0.00	0.00	-5.88	-5.88	-5.88	-5.88
*O_2	4.88	4.77	4.91	3.23	-0.04	0.24	0.38	-1.81	-5.53	-5.64	-5.50	-7.57
*OOH	4.88	4.72	4.85	3.33	1.19	1.09	0.97	-0.32	-3.23	-3.34	-3.44	-4.77
*O	4.46	4.45	4.29	2.47	2.00	1.23	1.15	-0.35	-0.84	-1.54	-1.79	-2.93
*OH	2.32	2.16	2.21	0.07	1.09	0.89	1.14	-1.10	-0.21	-0.56	-0.33	-2.63
*+H_2O	0.00	0.00	0.00	0.00	0.00	0.00	0.00	0.00	0.00	0.00	0.00	0.00
ΔG_1	-0.04	-0.15	-0.01	-1.69	-0.04	0.24	0.38	-1.81	0.35	0.24	0.38	-1.69
ΔG_2	0.00	-0.05	-0.06	0.10	1.23	0.85	0.59	1.49	2.30	2.31	2.06	2.80
ΔG_3	-0.42	-0.27	-0.55	-0.86	0.81	0.13	0.18	-0.03	2.39	1.79	1.65	1.84
ΔG_4	-2.14	-2.29	-2.08	-2.40	-0.91	-0.33	-0.01	-0.75	0.63	0.99	1.46	0.30
ΔG_5	-2.32	-2.16	-2.21	-0.07	-1.09	-0.89	-1.14	1.10	0.21	0.56	0.33	2.63
max(ΔG)	0.00	-0.05	-0.01	0.10	1.23	0.85	0.59	1.49	2.39	2.31	2.06	2.80
Potential-determining step	ΔG_2	ΔG_2	ΔG_1	ΔG_2	ΔG_2	ΔG_2	ΔG_2	ΔG_2	ΔG_3	ΔG_2	ΔG_2	ΔG_2

The free energy values of the intermediates for ORR at different electrode potentials and the potential-limiting steps for each genuine PCN structure are summarized in Table 1.

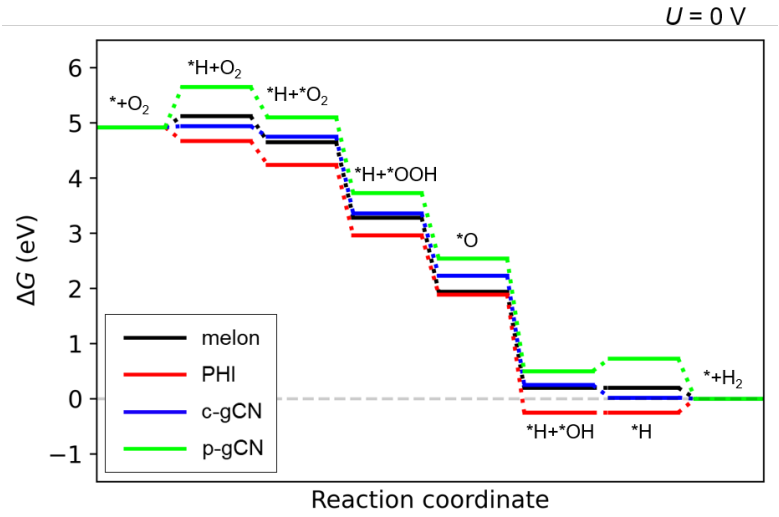

Figure 10: Free energy profiles of the typical 4-electron ORR process combined with 2-electron HER process on PCN monolayers at $U = 0$ V.

In the previous HER section, we observed that hydrogenation of heptazine units in PCN monolayer structures is energetically favorable. The mixed structural motifs and multilayer effects in PCN microstructures led to low adsorption energy of hydrogen intermediates, around -0.4 eV. Based on these findings, it is assumed that some hydrogen intermediate coverage exists at the potential before ORR occurs. Additionally, this hydrogenation would likely influence the highly localized π electronic structure within the heptazine units. Therefore, we further investigated the ORR free energy profile, including HER (Figures 10 and Figure 13). Since the actual sites for HER and ORR are independent, aside from the initial and final hydrogen adsorption/desorption reactions, ORR can be understood as occurring on a single explicit H-adsorbed PCN. Given that hydrogen adsorption/desorption free energy varies with position, the free energy of the hydrogen intermediates was included in our analysis. Figure S39 shows all the energetics at the surveyed active sites and the simulated potentials. The $U = 0$ V profile in Figure 10 reveals that the optimal reaction pathway occurs when

the hydrogen adsorption energy is high and the adsorption energy of the *O_2 and *OOH intermediates is low. This indicates that hydrogen adsorption significantly alters the electronic structure of the heptazine unit, facilitating the adsorption of oxygen intermediates (Figure 8). In particular, the energy of the *OOH, *O, and *OH intermediates decreases significantly compared to when protonation is not considered. Additionally, the adsorption/desorption energy of *H becomes the limiting potential step, suggesting the possibility that the ORR cycle could proceed without actual hydrogen desorption occurring.

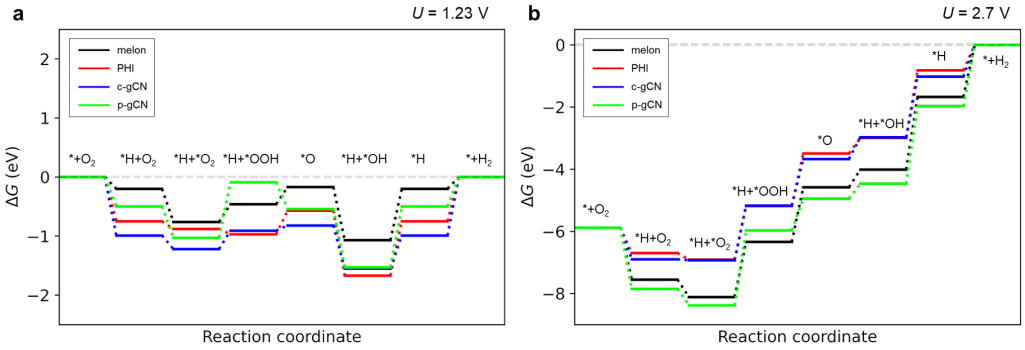

Figure 11: Free energy profiles of the typical 4-electron ORR process combined with 2-electron HER process on PCN monolayers at $U = 1.23$ V and $U = 2.7$ V, respectively.

The differences in reaction energetics become more pronounced at $U = 1.23$ V (Figure 11), where all intermediates exhibit $\Delta G < 0$. This highlights the importance of considering protonation in PCN structures for accurately predicting the ORR mechanism. Notably, the scaling relation of intermediates may differ depending on protonation; for example, while *OOH is more stable than *OH in genuine PCN, the order is reversed in H-PCN. This suggests that explicit protonation and electrode potential can alter intermediate stability and reaction sites. Hence, more precise model structures, such as those incorporating H-coverage, are necessary to study the reaction mechanisms accurately.



Figure 12: The structural images depict the corresponding reaction pathways for the HER-coupled-ORR process on (a) melon, (b) PHI, (c) c-gCN, and (d) p-gCN monolayers.

Unlike in genuine PCNs, where *OOH does not chemically adsorb, it does in H-PCNs, as shown in Figure 12.

Table 2: Values of G, ΔG, and the PDS for the typical 4-electron ORR intermediates including 2-electron HER steps on PCN monolayers as a function of U.

	Free energy (eV)											
	$U = 0$ V				$U = 1.23$ V				$U = 2.7$ V			
	melon	PHI	c-gCN	p-gCN	melon	PHI	c-gCN	p-gCN	melon	PHI	c-gCN	p-gCN
*+O_2	4.92	4.92	4.92	4.92	0.00	0.00	0.00	0.00	-5.88	-5.88	-5.88	-5.88
*H+O_2	5.12	4.67	4.94	5.65	-0.20	-0.75	-0.99	-0.50	-7.55	-6.70	-6.90	-7.85
H+O_2	4.65	4.24	4.75	5.10	-0.76	-0.88	-1.22	-1.03	-8.11	-6.91	-6.93	-8.38
*H+*OOH	3.28	2.96	3.36	3.73	-0.46	-0.97	-0.91	-0.09	-6.34	-5.18	-5.17	-5.97
*H+*O	1.94	1.89	2.23	2.54	-0.17	-0.57	-0.82	-0.54	-4.58	-3.49	-3.67	-4.95
*H+*OH	0.20	-0.25	0.25	0.50	-1.07	-1.67	-1.55	-1.53	-4.01	-2.99	-2.97	-4.47
*H+H_2O	0.20	-0.25	0.02	0.73	-0.20	-0.75	-0.99	-0.50	-1.67	-0.82	-1.02	-1.97
*+H_2	0.00	0.00	0.00	0.00	0.00	0.00	0.00	0.00	0.00	0.00	0.00	0.00
ΔG_1	0.20	-0.25	0.02	0.73	-0.20	-0.75	-0.99	-0.50	-1.67	-0.82	-1.02	-1.97
ΔG_2	-0.47	-0.43	-0.19	-0.55	-0.56	-0.13	-0.23	-0.53	-0.56	-0.21	-0.03	-0.53
ΔG_3	-1.37	-1.28	-1.39	-1.37	0.30	-0.09	0.31	0.94	1.77	1.73	1.77	2.41
ΔG_4	-1.34	-1.06	-1.13	-1.19	0.29	0.39	0.09	-0.45	1.76	1.69	1.50	1.02
ΔG_5	-1.74	-2.14	-1.97	-2.04	-0.90	-1.10	-0.73	-0.99	0.57	0.50	0.70	0.48
ΔG_6	0.00	0.00	-0.23	0.23	0.88	0.92	0.56	1.03	2.35	2.17	1.95	2.50
ΔG_7	-0.20	0.25	-0.02	-0.73	0.20	0.75	0.99	0.50	1.67	0.82	1.02	1.97
max(ΔG)	0.20	0.25	0.02	0.73	0.88	0.92	0.99	1.03	2.35	2.17	1.95	2.50
Potential-determining step	ΔG_1	ΔG_7	ΔG_1	ΔG_1	ΔG_6	ΔG_6	ΔG_7	ΔG_6	ΔG_6	ΔG_6	ΔG_6	ΔG_6

The free energy of the intermediates and their potential-limiting steps for ORR at various electrode potentials in H-PCN structures is provided in Table 2.

4.2.9 H_2O_2 production on PCN monolayers

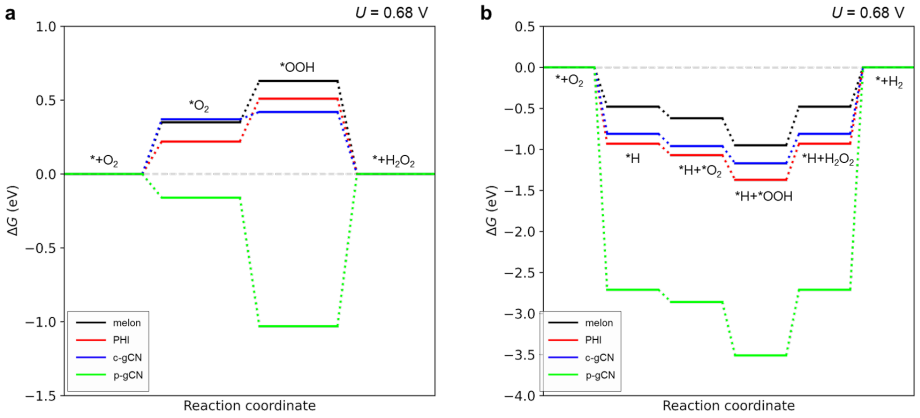

Figure 13: Free energy diagram of H_2O_2 production via (a) typical 2-electron pathways and (b) HER-coupled 2-electron pathways on PCN monolayers. The free energy is plotted using CHE with $U = 0.68$ V and pH = 0 conditions. The selection of the best reaction pathways considers only the lowest overpotential for the oxygen intermediates.

Recently, PCNs have shown great promise for photocatalytic H_2O_2 production. Thus, we also investigated the reaction pathway for the 2-electron H_2O_2 production in detail (Figure 13). In contrast to genuine PCN, where *OOH intermediates have $\Delta G > 0$, in H-PCN the free energy of the *OOH intermediate is $\Delta G < 0$. Additionally, the desorption of adsorbed hydrogen acts as a potential-limiting step, potentially suppressing hydrogen evolution. However, the free energy up to the *OOH intermediate remains entirely downhill, suggesting a high *OOH coverage and making H_2O_2 formation the second potential-limiting step. While hydrogen adsorption facilitates the formation of the *OOH intermediate, the thermodynamic barriers make the rapid formation of $*H_2O_2$ unlikely. Nevertheless, these free energy profiles, considering hydrogen adsorption, offer a more accurate prediction of H_2O_2 formation as observed experimentally. By linking HER and ORR, we achieved a more refined free energy profile for PCNs, which may better explain the catalytic activity of structures with highly local-

ized electronic structures. The multilayer effects observed in HER, which stabilize the free energy of adsorbed species, suggest that updated energy profiles for ORR in multilayered and mixed PCN structures are also necessary. Moreover, because the scaling relation of intermediates can change, more precise models like H-PCN are essential for accurate mechanistic studies.

4.2.10 Conclusion

We explored the effects of multilayer interactions in PCN microstructures and more realistic mixed PCN models on HER, as well as the impact of energetically spontaneous hydrogenation on the ORR mechanism. Our study demonstrates that simple PCN models, which do not consider the complexity of multilayers and microstructures, are limited in explaining the reduction reactions of hydrogen and oxygen. For hydrogen evolution, multilayer structures stabilize hydrogen adsorption energy through varying degrees of interlayer interaction, presenting a distinct behavior compared to monolayers. Furthermore, our study on consecutive hydrogen adsorption reveals that additional hydrogen adsorption energy within a single heptazine unit in PHI and g-CN structures is not significantly different, suggesting the possibility of high hydrogen coverage in PCN structures. This is consistent with the observation that the ORR adsorption energy profile can change in H-PCN compared to genuine PCN. Our study emphasizes the need for precise PCN models to study HER and ORR. Ultimately, we conclude that H-PCN structures may be advantageous for hydrogen evolution and H_2O_2 production. However, further research is essential to overcome the inherent semiconducting properties of PCNs and improve electron conductivity for their use as electrochemical catalysts. Our study provides clearer insight into the previously unexplored mechanisms of HER and ORR in PCN structures and contributes to a better understanding of the structure-property-reactivity relationship in PCNs.

4.3 A Study in Red: The Overlooked Role of Azo-Moieties in Polymeric Carbon Nitride Photocatalysts with Strongly Extended Optical Absorption

The following article is reprinted without changes from Dariusz Mitoraj, Igor Krivtsov, Chunyu Li, Ashwene Rajagopal, **Changbin Im**, Christiane Adler, Kerstin Köble, Olena Khainakova, Julian Hniopek, Christof Neumann, Andrey Turchanin, Ivan da Silva, Michael Schmitt, Robert Leiter Tibor Lehnert, Jürgen Popp, Ute Kaiser,Timo Jacob, Carsten Streb, Benjamin Dietzek and Radim Beranek.

"A Study in Red: The Overlooked Role of AzoMoieties in Polymeric Carbon Nitride Photocatalysts with Strongly Extended Optical Absorption." *ChemistryA European Journal* 27.68 (2021): 17188-17202, DOI:10.1002/chem.202102945.

Copyright 2021 The Authors. Chemistry - A European Journal published by Wiley-VCH GmbH

This is an open access article under the terms of the Creative Commons Attribution License, which permits use, distribution and reproduction in any medium, provided the original work is properly cited. (CC BY 4.0, https://creativecommons.org/licenses/by/4.0)

Author contributions: Changbin Im performed all the calculations. The manuscript was written through contributions of all authors. All authors discussed the results and commented on the manuscript.

A Study in Red: The Overlooked Role of Azo-Moieties in Polymeric Carbon Nitride Photocatalysts with Strongly Extended Optical Absorption

4.3.1 Abstract

The unique optical and photoredox properties of heptazine-based polymeric carbon nitride (PCN) materials make them promising semiconductors for driving various productive photocatalytic conversions. However, their typical absorption onset at ca. 430-450 nm is still far from optimum for efficient sunlight harvesting. Despite many reports of successful attempts to extend the light absorption range of PCNs, the determination of the structural features responsible for the red shift of the light absorption edge beyond 450 nm has often been obstructed by the highly disordered structure of PCNs and/or low content of the moieties responsible for changes in optical and electronic properties. In this work, we implement a high-temperature (900°C) treatment procedure for turning the conventional melamine-derived yellow PCN into a red carbon nitride. This approach preserves the typical PCN structure but incorporates a new functionality that promotes visible light absorption. A detailed characterization of the prepared material reveals that partial heptazine fragmentation accompanied by de-ammonification leads to the formation of azo-groups in the red PCN, a chromophore moiety whose role in shifting the optical absorption edge of PCNs has been overlooked so far. These azo moieties can be activated under visible-light (470 nm) for H_2 evolution even without any additional co-catalyst, but are also responsible for enhanced charge-trapping and radiative recombination, as shown by spectroscopic studies.

4.3.2 Conclusion

We report a simple post-synthetic approach involving a brief high-temperature treatment under vacuum that effec- tively turns the typically yellow PCN into a red PCN by extending significantly its visible light absorption to > 600 nm. Most importantly, we provide evidence that the extended optical absorption edge of PCNs subjected to high-temperature treatment is due to the formation of azo- moieties that act as linkages between the heptazine units inherent to PCN structure and/or between heptazine and triazine units formed upon partial fragmentation of PCN. Our present understanding is that the formation of planar- R-CNx units comprising the azo-linkages and embedded in the yellow carbon nitride framework is responsible for the reduction of the overall bandgap and the red colour of the material. Notably, the azo moieties effectively sensitize the red PCN for photocatalytic H2 evolution even under low energy (470 nm) light where conventional yellow PCN is inactive. Moreover, the red carbon nitride clearly contains moieties that can act as metal-free catalytic sites for H_2 as evidenced by effective operation even without any additional co-catalyst. The downside of the high-temperature treatment of PCN is the partial fragmentation of the heptazine network creating large number of recombination centres and decreasing the overall photocatalytic activity of the resulting photocatalyst. We assume that our findings on the so far overlooked role of azo moieties in PCNs with strongly extended absorption edge might not only be valid for this particular case, but also for other cases in which a strong shift of the PCN absorption edge has been observed upon thermal treatment procedures at temperatures leading to the heptazine fragmentation and formation of cyanogen species. The present work thus highlights the importance of a careful determination of structural features governing the complex interplay between the light absorption, charge separation and catalytic turnover in PCN-based polymers tailored for visible light-driven photocatalysis.

4.3.3 Contribution to the Conclusion

In this study, I contributed to the all computational investigation of electronic structures and optical properties using periodic density functional theory (DFT) calculations. My work involved performing extensive screening to identify key configurations of carbon nitride systems, including R-CNx and Y-CNx, and analyzing their stability, electronic band structures, and optical absorption characteristics. Specifically, I discovered the distinct planar-R-CNx and step-like R-CNx configurations, highlighting their energy differences and unique bandgap properties. Additionally, I elucidated the optical behavior of Y-CNx systems and their structural impact on confined planar-R-CNx units, which align with experimentally observed properties. Through this contribution, I was able to uncover the critical role of structural confinement in stabilizing less favorable configurations, providing new insights into the design of advanced two-dimensional materials with tunable optical properties.

Check for updates

Chemistry–A European Journal
Full Paper
doi.org/10.1002/chem.202102945
Chemistry Europe
European Chemical Societies Publishing

Special Issue

A Study in Red: The Overlooked Role of Azo-Moieties in Polymeric Carbon Nitride Photocatalysts with Strongly Extended Optical Absorption

Dariusz Mitoraj,[a] Igor Krivtsov,*[a, b] Chunyu Li,[c, d] Ashwene Rajagopal,[e] Changbin Im,[a] Christiane Adler,[a] Kerstin Köble,[a] Olena Khainakova,[b] Julian Hniopek,[c, f] Christof Neumann,[c, g] Andrey Turchanin,[c, g] Ivan da Silva,[h] Michael Schmitt,[c, f] Robert Leiter,[i] Tibor Lehnert,[i] Jürgen Popp,[c, f] Ute Kaiser,[i] Timo Jacob,[a, j, k] Carsten Streb,[e, j, k] Benjamin Dietzek,*[c, d, g] and Radim Beranek*[a]

Abstract: The unique optical and photoredox properties of heptazine-based polymeric carbon nitride (PCN) materials make them promising semiconductors for driving various productive photocatalytic conversions. However, their typical absorption onset at ca. 430–450 nm is still far from optimum for efficient sunlight harvesting. Despite many reports of successful attempts to extend the light absorption range of PCNs, the determination of the structural features responsible for the red shift of the light absorption edge beyond 450 nm has often been obstructed by the highly disordered structure of PCNs and/or low content of the moieties responsible for changes in optical and electronic properties. In this work, we implement a high-temperature (900 °C) treatment procedure for turning the conventional melamine-derived yellow PCN into a red carbon nitride. This approach preserves the typical PCN structure but incorporates a new functionality that promotes visible light absorption. A detailed characterization of the prepared material reveals that partial heptazine fragmentation accompanied by de-ammonification leads to the formation of azo-groups in the red PCN, a chromophore moiety whose role in shifting the optical absorption edge of PCNs has been overlooked so far. These azo moieties can be activated under visible-light (470 nm) for H_2 evolution even without any additional co-catalyst, but are also responsible for enhanced charge-trapping and radiative recombination, as shown by spectroscopic studies.

[a] *Dr. D. Mitoraj, Dr. I. Krivtsov, C. Im, C. Adler, K. Köble, Prof. T. Jacob, Prof. R. Beranek*
Institute of Electrochemistry Chemistry
Ulm University
Albert-Einstein-Allee 47, 89081 Ulm (Germany)
E-mail: igor.krivtsov@uni-ulm.de
radim.beranek@uni-ulm.de

[b] *Dr. I. Krivtsov, O. Khainakova*
Department of Organic and Inorganic Chemistry
University of Oviedo
33006 Oviedo (Spain)

[c] *C. Li, J. Hniopek, Dr. C. Neumann, Prof. A. Turchanin, Prof. M. Schmitt, Prof. J. Popp, Prof. B. Dietzek*
Institute of Physical Chemistry and Abbe Center of Photonics
Friedrich Schiller University Jena
Lessingstr. 10, 07743 Jena (Germany)
E-mail: benjamin.dietzek@uni-jena.de

[d] *C. Li, Prof. B. Dietzek*
Department Functional Interfaces
Leibniz Institute of Photonic Technology (IPHT)
Albert-Einstein-Str. 9, 07745 Jena (Germany)

[e] *Dr. A. Rajagopal, Prof. C. Streb*
Institute of Inorganic Chemistry I
Ulm University
Albert-Einstein-Allee 11, 89081 Ulm (Germany)

[f] *J. Hniopek, Prof. M. Schmitt, Prof. J. Popp*
Department Spectroscopy/Imaging
Leibniz Institute of Photonic Technology (IPHT)
Albert-Einstein-Str. 9, 07745 Jena (Germany)

[g] *Dr. C. Neumann, Prof. A. Turchanin, Prof. B. Dietzek*
Center for Energy and Environmental Chemistry Jena (CEEC Jena)
Philosophenweg 7a, 07743 Jena (Germany)

[h] *Dr. I. da Silva*
ISIS Neutron and Muon Source
Rutherford Appleton Laboratory
Harwell Oxford, Didcot, OX11 0QX (UK)

[i] *R. Leiter, Dr. T. Lehnert, Prof. U. Kaiser*
Electron Microscopy of Materials Science
Central Facility for Electron Microscopy
Ulm University
Albert-Einstein-Allee 11, 89081 Ulm (Germany)

[j] *Prof. T. Jacob, Prof. C. Streb*
Helmholtz-Institute-Ulm (HIU)
Helmholtzstr. 11, 89081 Ulm (Germany)

[k] *Prof. T. Jacob, Prof. C. Streb*
Karlsruhe Institute of Technology (KIT)
P.O. Box 3640, 76021 Karlsruhe (Germany)

Supporting information for this article is available on the WWW under https://doi.org/10.1002/chem.202102945

Special Issue *Part of a Special Issue on Contemporary Challenges in Catalysis.*

© 2021 The Authors. Chemistry - A European Journal published by Wiley-VCH GmbH. This is an open access article under the terms of the Creative Commons Attribution License, which permits use, distribution and reproduction in any medium, provided the original work is properly cited.

Introduction

Heptazine-based polymeric carbon nitride (PCN) materials[1] stand out from a range of other typical, mostly metal oxide-based photocatalysts mainly by their unique optical (i.e., bandgap and intra-gap states)[2] and photoredox (i.e., *quasi*-Fermi levels of electrons and holes) properties.[3] Nevertheless, the typical absorption onset of PCN is around 430–450 nm, which is far from making it an ideal absorber of solar radiation. This motivated significant research efforts directed towards shifting the optical absorption and the corresponding photocatalytic activity to the red. In general, one can distinguish two basic strategies for achieving this goal. Firstly, modified synthetic protocols aim at incorporating additional light absorbing moieties already during the synthesis of PCN, for example, by introducing sulfur species,[4] aromatic carbon moieties,[5] creating co-polymeric precursors with other N-containing molecules,[6] or by varying the condensation conditions, especially the temperature[7] or reaction medium composition.[8] Secondly, post-synthetic approaches comprise chemical surface modification of conventional PCN, for instance, by hydrogenation or oxidation,[9] sensitization with light harvesting compounds such as organic dyes,[10] carbon dots or fullerenes,[11] or various forms of post-synthetic thermal treatment.[12]

Although the condensation of PCN precursors at high temperatures (above 600 °C)[7] and the post-synthetic annealing of PCNs under similar conditions[12] might seem alike, the essential difference lies in the lower ammonia gas evolution from the material in the latter case. While the two approaches have somewhat similar effects on the material's optical properties if carried out under inert or reductive (NH_3, H_2) conditions[7,13] or under vacuum,[14] the reports on the performance of the resulting photocatalysts in terms of activity or visible-light response are contradictory and show little consensus regarding the optimal thermal treatment conditions. For example, Wang et al. reported a continuous increase of the photocatalytic H_2 evolution rate with increasing temperature of PCN condensation up to 700 °C.[12] In accord with this result, P. Niu et al. demonstrated an activity enhancement of PCN post-treated at 750 °C.[15] Nevertheless, other authors observed a maximum activity at intermediate heat-treatment (condensation or post-treatment) temperatures of 500 °C,[14] 550 °C,[7] and 580 °C,[16] 600 °C[10] or 680 °C,[17] followed by a significant drop in photocatalytic activity. These discrepancies in the reported photocatalytic performance of PCNs with extended visible-light absorption are clearly due to the lack of our knowledge on the nature of the colour centres that are responsible for the activation beyond wavelengths of ~450 nm in various PCNs. A number of plausible suggestions have been made to explain the red shift of the optical absorption edge, including increased condensation degree due to a partial residual NH_2-groups removal,[7] improved stacking allowing normally forbidden n-π^* transitions,[12] and creation of N-[17–18] or C-vacancies.[13a,19] Nonetheless, given the disordered nature of PCN polymers, it is difficult to unambiguously prove the distinct type of colour centres in the material, so that they often remain rather hypothesised than proven. However, the determination of the moieties or structural features responsible for the red shift is crucial for developing an appropriate synthetic or post-synthetic technique for the preparation of efficient visible-light active PCNs.

Herein, we report a post-synthetic approach involving a brief (3 min) high-temperature (above 900 °C) treatment under vacuum that effectively turns the typically yellow PCN into a red PCN by significantly extending its visible light absorption down to >600 nm. Interestingly, we demonstrate that the dramatic shift of the absorption edge is due to the formation of azo-linkages in the PCN structure, an aspect that has been largely overlooked so far. Finally, we elucidate and discuss the effects of the azo moieties on the charge transfer dynamics and photocatalytic activity of the obtained photocatalysts. This sheds some critical light on the general applicability of PCN photocatalysts with drastically extended visible-light absorption prepared by methods comprising a high-temperature treatment.

Materials and Methods

Synthesis of polymeric carbon nitride: The sample of conventional yellow PCN (Y-CN_x) was prepared by thermal polycondensation of 30 g melamine at 530 °C for 4 h in a lid-covered crucible. The red PCN materials (R-CN_x) were prepared by a heat treatment of Y-CN_x in a quartz tube initially having a reduced pressure of 1.8×10^{-2} mbar using a tube furnace operating at 900 °C for 3 min. After the treatment the samples were cooled down, brought to ambient pressure and powdered.

The dissolution of the synthesized samples was carried out by a modified method proposed by Horvarth-Bordon et al.[20] 1.0 g of the Y-CN_x or R-CN_x samples was suspended in 50 mL of 1 M aqueous KOH solution and transferred into a Teflon-lined stainless steel autoclave with a total volume of 100 mL. The autoclaves were heated at 100 °C for 16 h, then the obtained solution was filtered first through a paper filter and then through a 0.25 μm PES syringe filter. Tri-potassium cyamelurate crystals were produced from the above-mentioned solutions by evaporation and precipitation. The needle shaped tri-potassium cyamelurate crystals formed in both cases were filtered, washed with ethanol and dried. In order to analyse the presence of minor products of dissolution in KOH of Y-CN_x (Y-CN_x-K) and R-CN_x (R-CN_x-K), the solutions were subjected to several cycles of evaporation, tri-potassium cyamelurate crystals separation and subsequent concentration of the supernatant. The supernatant was subsequently analysed. The solid crystalline powder was obtained from the R-CN_x-K solution (R-CN_x-KS) by slow evaporation of water from the R-CN_x-K solution, then it was washed with deionized water and dried overnight at 70 °C.

Deposition of co-catalysts for photocatalytic H_2 reactions: The preparation of photocatalysts modified with Pt nanoparticles or $[Mo_3S_{13}]^{2-}$ (={Mo_3}) clusters was described in detail in our previous work.[21] Briefly, the platinized Y-CN_x and R-CN_x

© 2021 The Authors. Chemistry - A European Journal published by Wiley-VCH GmbH

15213765, 2021, 68, Downloaded from https://chemistry-europe.onlinelibrary.wiley.com/doi/10.1002/chem.202102945 by KIZ der Universitat Ulm, Wiley Online Library on [19/08/2024]. See the Terms and Conditions (https://onlinelibrary.wiley.com/terms-and-conditions) on Wiley Online Library for rules of use; OA articles are governed by the applicable Creative Commons License

samples were prepared using photodeposition method. For this, the Y/R-CN_x powder (0.2 g) was suspended in 20 mL H_2O: MeOH (9:1, v:v) containing hexachloroplatinic acid (4 mg), ultrasonicated for 1 h, bubbled with argon gas and irradiated for 30 min with a 150 W Xe-lamp equipped with a KG3 (Schott) heat filter (intensity ca. 1 sun). Subsequently, the powder was washed by centrifugation and dried overnight at 60 °C.

The {Mo_3} clusters were synthesized using $(NH_4)_2[Mo_3S_{13}]\times 2H_2O$ produced by the method described by Müller et al.[21–22] Then $Na_2[Mo_3S_{13}]\times 5H_2O$ (={Mo_3}) was obtained from $(NH_4)_2[Mo_3S_{13}]\times 2H_2O$ by its reaction in aqueous NaOH solution under reduced pressure (20 mbar) for 2 h. The resulting dark red solution was filtered into an aqueous NaCl solution, the precipitated product was isolated by filtration, washed with 2-propanol and diethyl ether, and dried *in vacuo* at room temperature to give red-brown {Mo_3}. The Y-CN_x-{Mo_3} and R-CN_x-{Mo_3} hybrids were synthesized through a two-step deposition process at room temperature. In a typical procedure, 20 mg of as-prepared Y/R-CN_x was dispersed in 20 mL of methanol by ultrasonication for 3 h to prepare a homogenous suspension. Then, a measured amount of {Mo_3} (soluble in methanol) was added and stirred for 24 h. The solid was collected by centrifugation and three times washed with methanol to remove the excess of {Mo_3}. Finally, the obtained precipitates were dried at room temperature under ambient conditions yielding Y-CN_x-{Mo_3} and R-CN_x-{Mo_3}.

Characterization

FTIR spectroscopy was performed on a Shimadzu FTIR-8400S spectrometer. Samples were prepared as KBr pellets. X-ray powder diffraction (XRD) data were collected on a Rigaku XRD-6000 and a Pananalytical X'pert PRO diffractometers using Cu Kα radiation (λ = 0.154 nm). **X-ray photoelectron spectroscopy (XPS)** measurements were performed from the samples deposited on a gold support using a UHV Multiprobe system (Scienta Omicron, Germany) with a monochromatic X-ray source (Al K_α) and an electron analyzer (Argus CU) with 0.6 eV energy resolution. Charge compensation during data acquisition was realized by an electron flood gun (NEK 150SC, Staib, Germany) at 6 eV and 50 μA. The background was subtracted and spectra were calibrated using the Au $4f_{7/2}$ peak (84.0 eV) before undergoing fitting using Voigt functions (30:70).

UV Raman spectroscopy was performed on a custom modified (to allow UV excitation) LabRAM HR 800 Raman System (Horiba Jobin Yvon, Bensheim, Germany) with an excitation wavelength of 244 nm provided by frequency doubling the 488 nm line of an Ar-Ion-Laser (Innova 300 C Moto-FRED, Coherent Inc., Santa Clara, CA, United States of America). The laser power was attenuated from 13 mW to 5 mW or 10 mW via a neutral density filter depending on the photothermal stability of the samples. The samples were illuminated through a microscope (BX 41, Olympus Corporation, Tokyo, Japan) through a 15×/0.2NA UV objective (LMU UVB, Thorlabs Inc., Newton, NJ, United States of America) with UV optimized antireflection coating. The scattered light is collected in 180° geometry via the same objective, filtered through two long-pass filters to remove the Rayleigh scattered light, passed through an entrance slit (width = 300 μm) and diffracted by a 2400 lines/mm blazed grating to a liquid N_2-cooled CCD (T_{op} = 160 K). All spectra were recorded with an integration time of 300 s and 12 averaged accumulations (i.e., 1 h of summed integration time). All samples were measured as manually compacted powders in a small stainless-steel mold. The Raman spectra were processed using R 3.5.1 by applying SNIP based baseline correction (100 iterations) and normalizing the spectra using Euclidean vector norm.[23]

FT Raman spectroscopy was performed on a Multispec FT-Raman spectrometer (Bruker Inc., Billerica, Massachusetts, United States of America). The excitation light at 1064 nm was provided by a Nd:YAG laser (Klastech DeniCAFC-LC-3/40, Dortmund, Germany). The spectra were recorded up to 4000 cm^{-1} with a spectral resolution of 4 cm^{-1}. The laser power at the samples was set to 200 mW for R-CN_x and 500 mW for Y-CN_x. R-CN_x-KS could not be measured using FT-Raman spectroscopy due to excessive photoluminescence.

The Raman spectra were processed using R 3.5.1 by applying SNIP based baseline correction (60 iterations) and normalizing the spectra to the ring-breathing mode at 980 cm^{-1} for visualization.

Neutron total scattering measurements: Time-of-flight powder neutron diffraction experiments were conducted using the GEM diffractometer at the ISIS pulsed neutron and muon source, Rutherford Appleton Laboratory, UK.[24] Powder samples of Y-CN_x and R-CN_x were loaded into 6 mm diameter cylindrical vanadium sample holders. Data collection consisted of ~6 h duration (1000 μA h) data sets, acquired at 300 K for total scattering analysis. MantidPlot software[25] was used for data reduction and normalisation. Total scattering data (covering a scattering range $0.5 < Q < 50$ $Å^{-1}$ when using the final processed files from the six GEM detector banks) were corrected and the pair distribution function was generated using the GUDRUN software.[26]

Transmission electron microscopy (TEM): The samples were dispersed in ethanol (supersonic bath) and drop-cast on holey carbon TEM grids. The TEM investigations were carried out using the chromatic (Cc) and spherical (Cs) aberration - corrected Sub-Ångström Low-Voltage Electron (SALVE) microscope operating at 80 kV. Values for Cc and Cs were in the range of −10 μm to −20 μm. Imaging included diffraction pattern from selected areas and high resolution (HR) TEM, recorded on a Ceta 16 M camera. Energy-filtered imaging exploiting absorption edges for elemental mapping was acquired on an Ultrascan 1000 XP camera using a Quantum ERS low-voltage Gatan imaging filter (GIF), attached to the SALVE microscope.

Diffuse reflectance spectroscopy (DRS) UV-vis spectra of solids were taken by a Shimadzu UV2600 UV-vis spectrophotometer. **UV-vis spectra** of the dissolved in KOH carbon nitride samples were recorded using a Cary 60 (Agilent Technologies) spectrophotometer.

© 2021 The Authors. Chemistry - A European Journal published by Wiley-VCH GmbH

15213765, 2021, 68, Downloaded from https://chemistry-europe.onlinelibrary.wiley.com/doi/10.1002/chem.202102945 by KIZ der Universitat Ulm, Wiley Online Library on [19/08/2024]. See the Terms and Conditions (https://onlinelibrary.wiley.com/terms-and-conditions) on Wiley Online Library for rules of use; OA articles are governed by the applicable Creative Commons License

15213765, 2021, 68, Downloaded from https://chemistry-europe.onlinelibrary.wiley.com/doi/10.1002/chem.202102945 by KIZ der Universitat Ulm, Wiley Online Library on [19/08/2024]. See the Terms and Conditions (https://onlinelibrary.wiley.com/terms-and-conditions) on Wiley Online Library for rules of use; OA articles are governed by the applicable Creative Commons License

Thermal decomposition of the carbon nitride samples was studied using a Mettler Toledo TGA/SDTA 851e at a heating rate of 10 °C min^{-1} in O_2 flow (50 mL min^{-1}) from 30 °C to 850 °C.

CHN analysis was performed using an Elementar Vario MICRO cube.

The EDX analysis was carried out using a Scanning electron microscope (Supra 55VP, SmartSEMTM, Zeiss) equipped with an Oxford Instruments EDX detector.

The solid-state ^{1}H, ^{13}C, MAS NMR, ^{1}H-^{13}C and ^{1}H-^{15}N CPMAS NMR spectra were registered at the spinning rates of 12 kHz for ^{1}H and 5 kHz for all other measurements using a Bruker Avance III 400WB spectrometer. ^{1}H, ^{13}C and ^{15}N chemical shifts are quoted in ppm from: TMS (0 ppm) and α-glycine (secondary reference, C=O at 176.0 ppm and NH_3^+ at 347.6 ppm on the nitromethane scale, respectively).

Liquid state ^{13}C NMR characterization of the products of the dissolution of carbon nitride samples in aqueous KOH (1.0 M) was carried out in a Bruker Avance II 400 MHz spectrometer at a 100 MHz frequency using TMS (0 ppm) standard. The samples were diluted in D_2O prior to analysis.

Gas chromatography: Gas-chromatography was performed on a Bruker Scion GC/MS, with a thermal conductivity detector 15 (column: molecular sieve 5 A 75 m × 0.53 mm, oven temperature 70 °C, flow rate 25 ml min^{-1}, detector temperature 200 °C) with Argon as carrier gas. The GC was calibrated by direct injection of known amounts of H_2 gas.

Emission spectroscopy: Polymeric carbon nitride suspensions for spectroscopic study were prepared by sonicating the carbon nitrides in deionized water (2 mg/mL) for 15 min. The supernatant liquid was collected after centrifugation (10 min, 7500 rpm) and used for steady-state emission and time-ressolved emission spectroscopy. Steady-state emission spectra (λ_{ex} = 380 nm) were recorded with a FLS980 spectrometer (Edinburgh Instruments) in a 1 cm quartz cell. Time resolved emission data were recorded using a Hamamatsu HPDTA streak camera. A Ti:sapphire laser (Tsunami, Newport Spectra-Physics GmbH) was used as the light source and a pulse selector (model 3980, Newport Spectra-Physics GmbH) was used to reduce the repetition rate of the fundamental to 400 kHz. The emission was collected from a 1 cm cuvette in a 90° angle between the pump beam and a CHROMEX spectrograph detector. Analysis of the time-resolved emission data was performed using DecayFit software.

Photocatalytic studies

The photocatalytic hydrogen production experiments were carried out using a custom-built air-cooling apparatus for maintaining room temperature (22 °C) and constant irradiation of the sample. Experiments were carried out in 21 mL Schlenk tubes capped with rubber septa. 10 mg of the CN_x-based catalysts, which had been found to be the optimal loading determined in our previous study,[21] was added to the Schlenk tube equipped with magnetic stirrer. The tube was evacuated and filled with argon. An H_2O:MeOH (9:1, v/v) solution, with or without addition of additional sacrificial electron donor, was purged with argon. 10 mL of the degassed solution was added to the photocatalyst in the Schlenk tube under inert conditions and kept under constant irradiation from an LED source (λ = 420 nm; 51.3 mW cm^{-2} or λ = 470 nm; ca. 40 mW cm^{-2}) in air-cooled photoreactors. The gas phase above the solution was probed by inserting a gas-tight GC syringe through the septum and the amount of hydrogen in the gas phase was quantified using headspace gas chromatography.

Computational studies

All periodic density functional theory (DFT) calculations were performed with the Vienna Ab initio Simulation Package (VASP 5.4.4),[27] utilizing the projector-augmented wave (PAW) method to describe the core electrons, while valence states were expanded by plane waves up to an energy cut-off of 400 eV. Geometries were pre-optimized (up to a force criterion of 5·10^{-2} eV·Å^{-1}) with the Perdew -Burke -Ernzerhof (PBE)[28] generalized-gradient-approximation (GGA) exchange-correlation functional, followed by a fine-optimization using the Heyd -Scuseria -Ernzerhof (HSE06)[29] hybrid functional (with the range separation parameter of 0.2 Å^{-1}) and 25% exact exchange. Van der Waals interactions were treated with Grimme's D3 dispersion correction scheme.[30] Self-consistency in the electronic structures were set to a limit of 10^{-6} eV, utilizing a Gaussian smearing of 0.01 eV. Periodic images of the two-dimensional systems were separated by a vacuum layer of at least 20 Å, together with dipole corrections. Integrations in the reciprocal space were evaluated on a Monkhorst-Pack[31] grid of 5 × 5 × 1 *k*-points.

Results and Discussion

Materials characterization

A schematic representation of the synthetic procedures implemented in this work is depicted in Figure 1a. The change of colour from yellow to nearly red is observed if Y-CN_x is heated at temperatures above 900 °C for a brief time interval (3 min) and under reduced pressure. The increase of the thermal treatment temperature or prolongation of this procedure do not lead to any further observable changes of the material's appearance and only result in lower yields (Figure 1a). The Y-CN_x sample has a typical UV-vis diffuse reflectance spectrum (Figure 1b) with an absorption edge of around 2.9 eV (Figure 1c), while R-CN_x shows another visible-light absorption band centred at ca. 483 nm (Figure 1b). Apparently, the new absorption peak in the visible region observed for the R-CN_x sample (Figure 1b) is an additional feature and can hardly be considered as shifted Y-CN_x absorption edge, which remains visible and manifests itself at an electronic transition energy of 2.9 eV, while the new contribution has an onset at ca. 2.2 eV (Figure 1d).

Notably, R-CN_x and Y-CN_x possess very similar elemental composition of $C_{2.88}N_{4.19}H_{1.69}$ and $C_{2.89}N_{4.28}H_{1.84}$, respectively, with

© 2021 The Authors. Chemistry - A European Journal published by Wiley-VCH GmbH

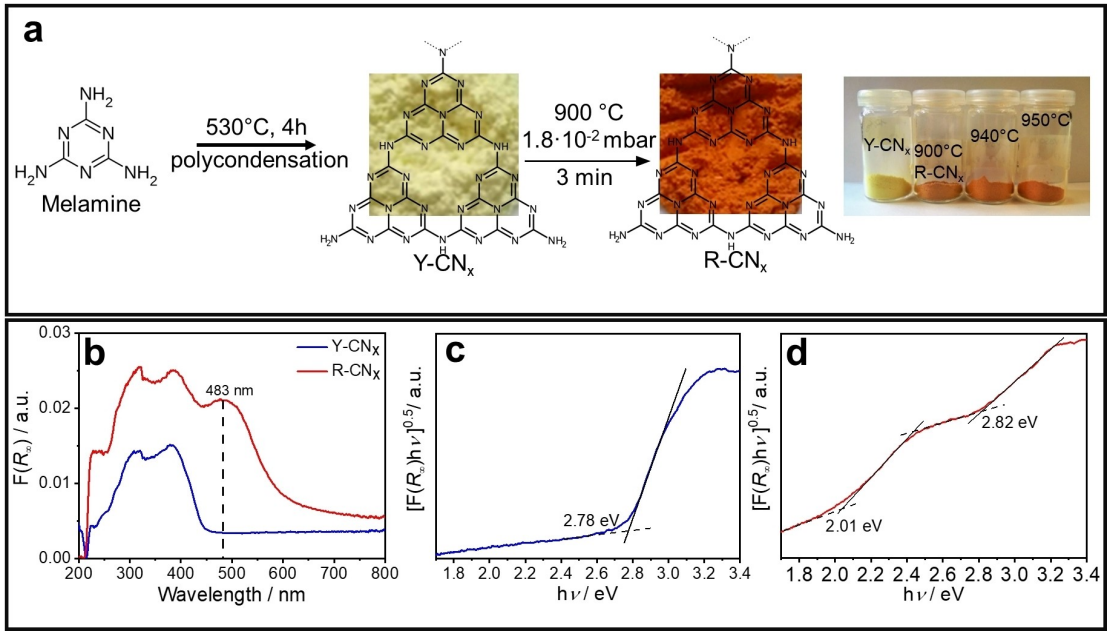

Figure 1. (a) Schematic representation of the synthetic procedures for conventional yellow Y-CN_x and low-bandgap reddish R-CN_x; diffuse reflectance spectra (b) and corresponding Tauc plots (assuming direct nature of the optical transition) for Y-CN_x (c) and R-CN_x (d).

only a small reduction of N and H content in the red materials as compared to the yellow one. The thermal behaviour of the both samples is also alike, the R-CN_x sample, though showing slightly lower degradation onset, reaches the maximum decomposition rate ca. 30 °C higher than Y-CN_x (see Supporting Information Figure S1). As evidenced by TEM, the microstructure and morphology of the Y-CN_x and R-CN_x samples are also practically identical, thus not allowing to draw any definite conclusions regarding the high-temperature induced modifications (see Supporting Information Figure S7).

XRD data manifest that the typical PCN structure persists in the R-CN_x material also after the high temperature treatment (Figure 2a). The reflections corresponding to the typical for PCN (100), (002) and even the less intense (300) and (004) planes[32] are clearly distinguishable in the R-CN_x diffractogram, although having somewhat lower intensity owing to partial amorphization of PCN under thermal treatment at 900 °C (Figure 2a). FTIR data also point to similar structure of Y-CN_x and R-CN_x as all the typical bands characteristic of PCN are also found in the spectrum of R-CN_x (Figure 2b), which is not the case, for instance, when PCN is treated in NaCl melt at high temperatures.[8] Although no definite conclusion can be made from it, the appearance of another band at around 3400 cm^{-1} in the spectrum of R-CN_x suggests the modification of H-bonding in the treated material (Figure 2b). The FT-Raman spectra of these two materials confirm the observations obtained by the IR- and XRD-measurements. According to the Raman spectra, the structure of Y-CN_x and R-CN_x are practically the same with only minor changes in intensity ratios in the fingerprint region (Figure 2c). The most noticeable difference between the two spectra is the stark decrease of intensity of the broad band between 2300 and 2500 cm^{-1} in R-CN_x. This band can be assigned to a second-order vibration of graphite-like carbon nitride and can only be observed in ordered structures, which supports the XRD-observed amorphization of the PCN.[33] The band at 806 cm^{-1} can be assigned to the ring-breathing mode of the triazines present in the CN_x structure while the band at 1235 cm^{-1} is specific to the ν(C–N) stretching vibration of the bridging amine moieties in the heptazine structure.[34] FT-Raman spectroscopy shows that the ratio of bridging amine to the sym-triazine breathing mode decreases in R-CN_x when comparing to Y-CN_x. This could indicate a replacement of the bridging amine moieties by some other bridging functionality, which is further supported by the intensity increase of the shoulder located at 1662 cm^{-1} relative to the main band at 1618 cm^{-1} (aromatic ring stretching). This increase in intensity could indicate an increase in *exo* unsaturated functionalities. Due to the complicated spectra and the possible loss of unpolymerized triazine impurities during the heat-treatment, the Raman spectra do not allow for definitive conclusions regarding the precise chemical structure, but can at least confirm changes to the binding conditions and offer a hint that amine bridges are replaced by unsaturated functionalities. Neutron diffraction, possibly the most adequate tool for structural characterization of carbon nitrides composed of low electron density atoms,[32] was further employed as a sensitive technique to detect the structural changes in PCN caused by the thermal treatment. The structure function F(Q) (Figure S3) as well as the calculated pair distribution function (PDF) data (Figure 2d) obtained from the neutron diffraction, however, show no significant differences in the analysed samples. This suggests that the PCN structure is mostly preserved in the R-CN_x material and no significant changes of the interlayer distances corresponding to the corrugation or planarization can be evidenced, which were

© 2021 The Authors. Chemistry - A European Journal published by Wiley-VCH GmbH

15213765, 2021, 68, Downloaded from https://chemistry-europe.onlinelibrary.wiley.com/doi/10.1002/chem.202102945 by KIZ der Universitat Ulm, Wiley Online Library on [19/08/2024]. See the Terms and Conditions (https://onlinelibrary.wiley.com/terms-and-conditions) on Wiley Online Library for rules of use; OA articles are governed by the applicable Creative Commons License

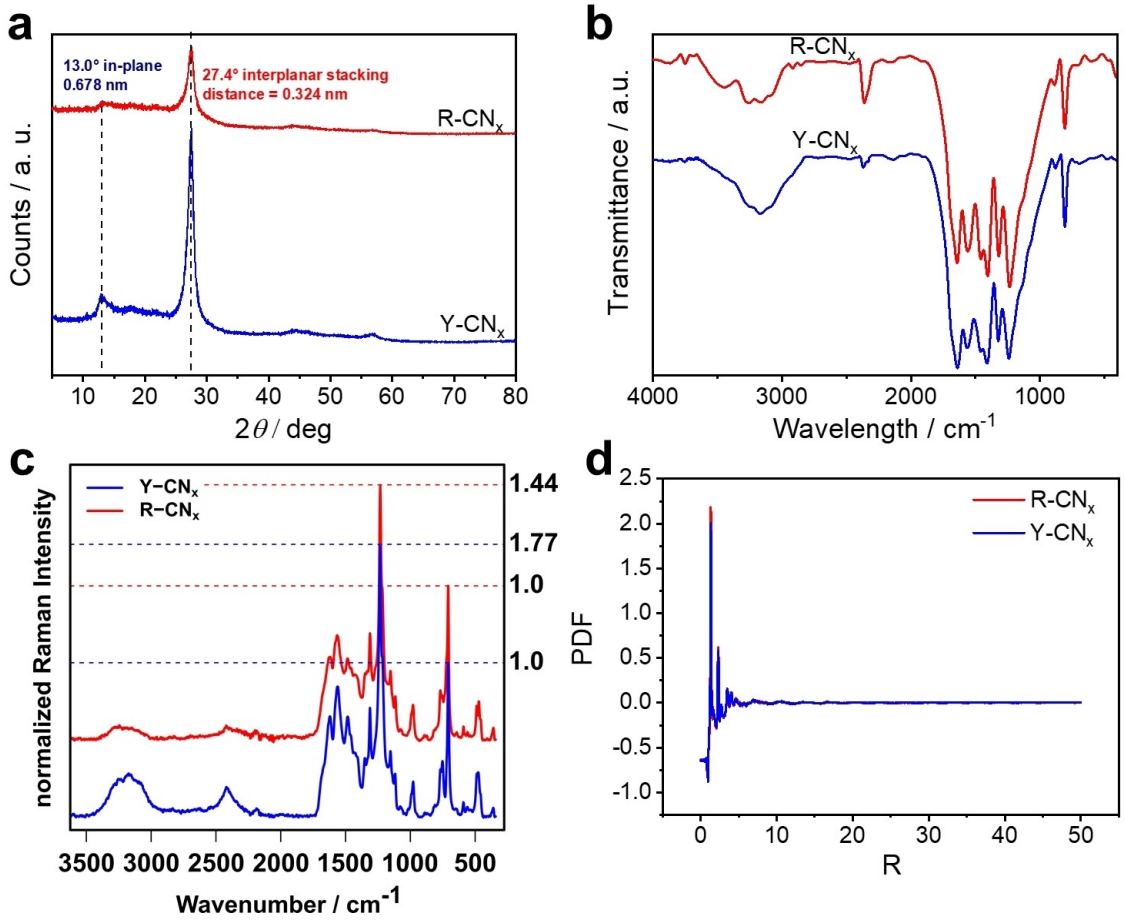

Figure 2. (a) powder XRD, (b) FTIR, (c) Raman and (d) neutron diffraction PDF calculated data obtained for Y-CN_x and R-CN_x.

previously suggested to be responsible for the colour change.[7,12]

The C 1s XP spectra for both materials are dominated by the peak at 283.8 eV attributed to adventitious carbon, while the maxima at 285.7, 287.3 and 290.1 eV are assigned to C-NH_x, N=C–N, and COOH species respectively (Figure S4). The N 1s spectrum of Y-CN_x can be fitted with four peaks having their maxima at binding energy values typical of PCN 397.8, 399.7, 401.5 and 404.1 eV, the latter one being ascribed to π-π excitation in the aromatic polyheptazine system (Figure S5a). The peak at 401.5 eV corresponds to the nitrogen in C-NH_x groups[35] and the maximum 397.8 eV is attributed to the C–N=C aromatic species. The contribution centred at 399.7 eV, usually assigned to N–C_3 groups,[36] should be rather assigned to the sum of these species and the triazine impurities, since the ratio between the maxima at 397.8 and 399.7 eV is far below 6, the value one might expect to obtain for the heptazine structure. We assume that the Y-CN_x sample contains certain amount of non-condensed impurities, which is in agreement with the XPS data obtained for melamine, which shows equal contributions at 398.4 and 399.7 eV in its XP N 1s spectrum.[37] The respective spectrum of the R-CN_x sample has, on the other hand, a more conventional profile, where the peaks corresponding to C–N=C, N–C_3 and C–NH_x are clearly distinguished at 398.1, 399.5 and 400.5 eV respectively (Figure S5b).

The direct ^{13}C NMR excitation spectra show a typical profile for heptazine based PCN materials with maxima in the range of 157–156 ppm and 165–164 ppm corresponding to the carbon atoms in N–C=N and –C–NH_x groups, respectively (Figure 3a). The reduction of the peak intensity and its slight shift from 156.7 to 157.4 ppm with respect to that of Y-CN_x is evident in the spectrum of R-CN_x (Figure 3a). This shift might be attributed either to a higher degree of disorder due to heptazine fragmentation in R-CN_x caused by the thermal treatment or to the formation of some new species in the material. According to the tabulated data of ^{13}C NMR chemical shifts,[38] the appearance of imine-like or azomethine groups (>C=N–) formed as the result of heptazine fragmentation is one of the conceivable possibilities. Another possibility is the formation of –C–N=N–C– azo functions that are known to promote visible-light absorption of tuned carbon nitrides.[39] The ratio between the peaks assigned to N–C=N to that of C–NH_x in the ^{13}C spectra is around 1.1 for Y-CN_x and 0.8 for R-CN_x. We assume that this might be attributed to a partial fragmentation of the heptazine structure in the thermally treated material, hence the loss of aromatic carbon-species. The ^{1}H-^{13}C CPMAS spectra show the enhancement of the peak intensity at 165–164 ppm

© 2021 The Authors. Chemistry - A European Journal published by Wiley-VCH GmbH

15213765, 2021, 68, Downloaded from https://chemistry-europe.onlinelibrary.wiley.com/doi/10.1002/chem.202102945 by KIZ der Universitat Ulm, Wiley Online Library on [19/08/2024]. See the Terms and Conditions (https://onlinelibrary.wiley.com/terms-and-conditions) on Wiley Online Library for rules of use; OA articles are governed by the applicable Creative Commons License

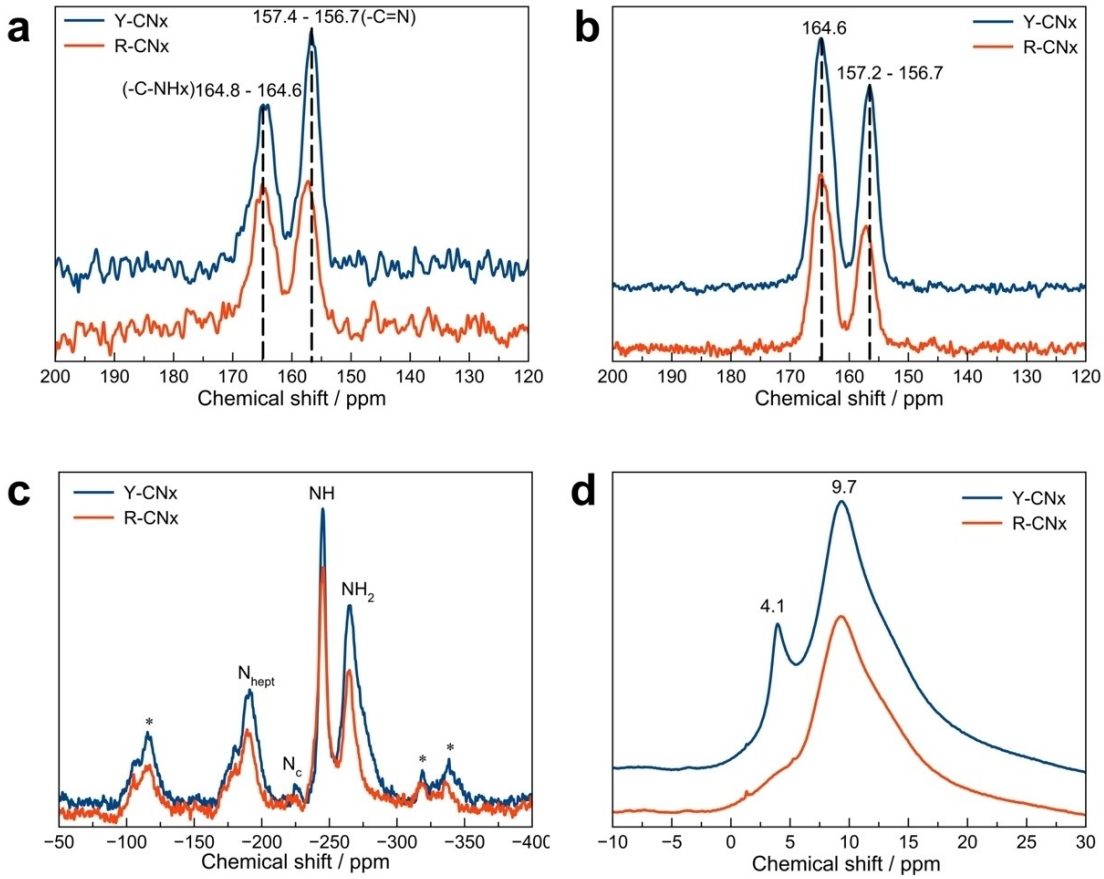

Figure 3. SS NMR (a) ^{13}C MAS, (b) ^{1}H-^{13}C CPMAS, (c) ^{1}H-^{15}N CPMAS and (d) ^{1}H MAS spectra of Y-CN_x and R-CN_x.

confirming its assignment to the C-NH_x moieties (Figure 3b). The intensity of the peak at around 157.4 ppm in the spectrum of R-CN_x is not increased significantly, suggesting that the new species formed after the treatment is not in the immediate proximity to any H atoms. This leads us to the conclusion that the formation of –C–N=N–C– azo linkages is more likely (Figure 3b). The ^{1}H-^{15}N CPMAS spectra show the same set of peaks at −191, −224, −245 and −265 ppm for both samples, which can be assigned to the peripheral heptazine N atoms, central heptazine nitrogen, nitrogen of NH– groups and of NH_2 species, respectively (Figure 3c).[35] A reduction of the FWHM and the intensity of the peak ascribed to the NH_2 functions can be observed for R-CN_x compared to Y-CN_x (Figure 3c). The peak fitting shows that the contribution centred at about −274 ppm is significantly reduced in the case of the R-CN_x sample (Figure S6). The amino-groups can manifest themselves in a large range of chemical shifts from −267 to −291[40] depending on their environment. Thus, we assume that the reduction of the NH_2 peak contribution at −274 ppm might be due to the elimination of more volatile carbon nitride constituents or impurities during the thermal treatment. The ^{1}H spectra are composed of two main contributions at 9.7 and 4.1 ppm which correspond to the hydrogens of hydrogen-bonded amino-groups and adsorbed water molecules, respectively (Figure 3d).[41]

The comparative analysis of R-CN_x and Y-CN_x presented above shows that the structural modifications produced by the high-temperature treatment are not easily detectable by conventional solid-state characterization approaches, although they clearly have a great impact on the light absorption properties of the materials (Figure 1). Therefore, further attempts to characterize the R-CN_x material were carried out starting by its dissolution in an appropriate solvent. The dissolution of PCN in KOH proceeds via hydroxyl attack on amino-groups of the polymer replacing them and forming water-soluble tri-potassium cyamelurate. Crucially, this approach enabling us to dissolve melon polymer has a potential to spectroscopically separate the contribution from species which possibly endow R-CN_x with extended light-absorption in the visible range. Notably, the dissolution of the Y-CN_x and R-CN_x samples resulted in colourless and yellow-green coloured solutions, respectively (Figure 4a). The evaporation and slow cooling of these solutions lead in both cases to the formation of needle-shaped single-crystals of different colour (Figure4a). In spite of that, the ^{13}C NMR analysis of the crystals dissolved in D_2O shows identical signals at 158.2 and 168.7 ppm for both samples with the integrated areas ratio of ca. 1:1 and assigned to CN_3 of the heptazine and N–C–O^- species, respectively, which is typical for potassium salts of cyameluric acid (Figures 4b and c).[20] In order to evaluate the presence of minor

© 2021 The Authors. Chemistry - A European Journal published by Wiley-VCH GmbH

15213765, 2021, 68, Downloaded from https://chemistry-europe.onlinelibrary.wiley.com/doi/10.1002/chem.202102945 by KIZ der Universitat Ulm, Wiley Online Library on [19/08/2024]. See the Terms and Conditions (https://onlinelibrary.wiley.com/terms-and-conditions) on Wiley Online Library for rules of use; OA articles are governed by the applicable Creative Commons License

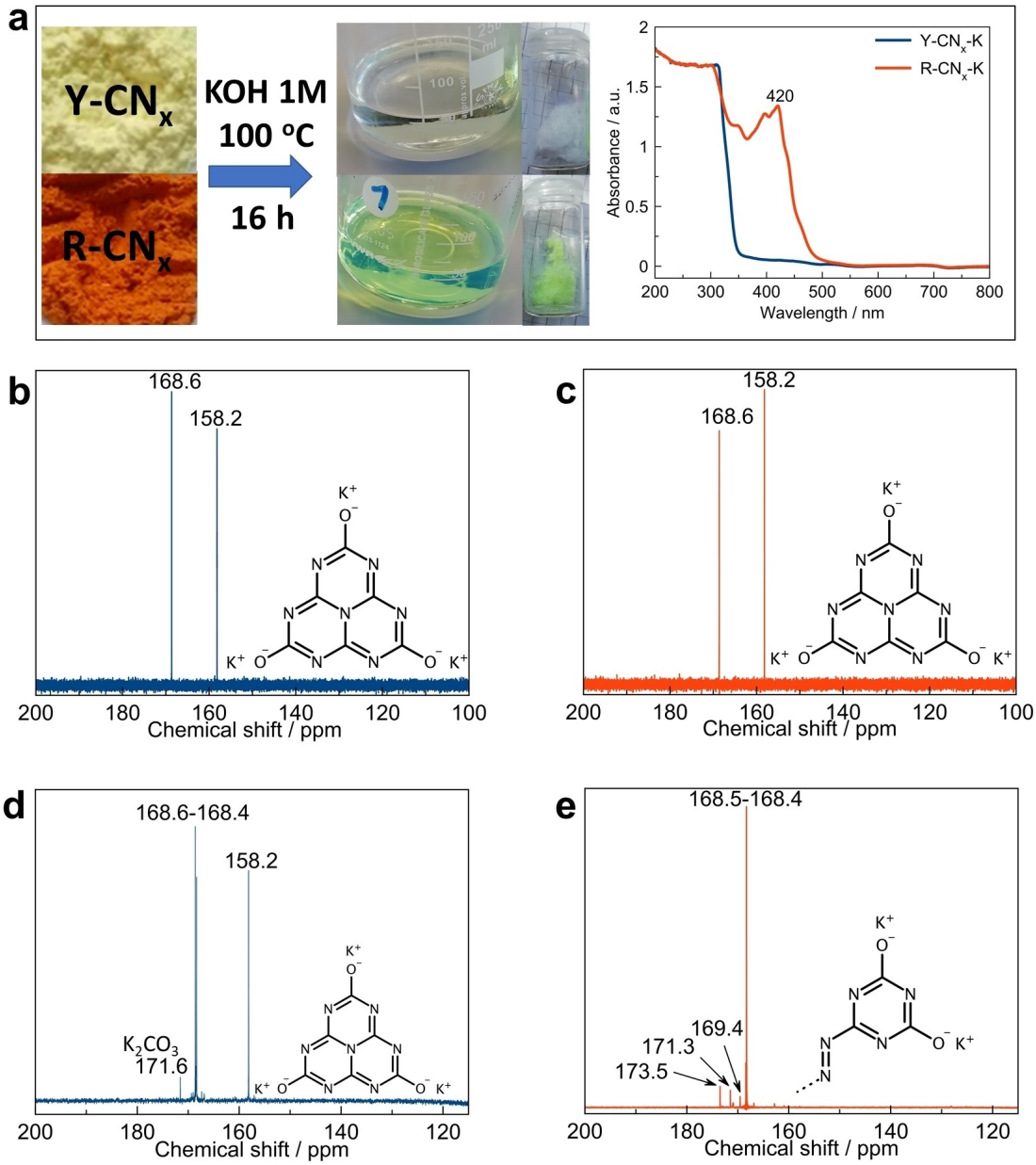

Figure 4. (a) The products of the Y-CN_x and R-CN_x dissolution in KOH and their UV-vis spectra; ^{13}C NMR spectra in D_2O of the crystals obtained from the dissolved in KOH (b) Y-CN_x and (c) R-CN_x samples; ^{13}C NMR spectra of the minor products of the (d) Y-CN_x and (e) R-CN_x samples dissolution in KOH with addition of D_2O.

components in the solutions, which might be responsible for the R-CN_x coloration, the obtained solutes of the PCN samples in KOH were concentrated by evaporation, while the formed tri-potassium cyamelurate crystals were removed from the system. The solution of Y-CN_x sample still showed the presence of a nearly pure potassium salt of cyameluric acid (Figure 4d), having only one additional peak at 171.6 ppm, which we attribute to the C of potassium carbonate. In the ^{13}C NMR spectrum of the solution of R-CN_x in KOH, on the other hand, the signal ascribed to carbon atoms in CN_3 environment of the heptazine is absent, instead the intense peaks at the chemical shifts of 168.6-168.4 ppm suggest the presence of triazine species bearing fully deprotonated N–C–O^- groups[42] (Figure 4e). Additionally, a peak at 173.5 ppm is observed, which can be ascribed to the presence of C–N=N–C inter-triazine linkages (Figure 4e).[43]

After tri-potassium cyamelurate crystals were extracted from the concentrated product of the R-CN_x dissolution in KOH, the slow evaporation of the solution yielded a yellow powder (R-CN_x-KS) with the composition $C_{1.00}N_{1.90}O_{0.90}K_{0.01}$, according to EDX elemental analysis, which is insoluble in water and DMSO. According to the XRD analysis (Figure 5a) and considering the presence of only triazine species in the initial solution, the crystalline phase of the separated compound might be ascribed

© 2021 The Authors. Chemistry - A European Journal published by Wiley-VCH GmbH

15213765, 2021, 68, Downloaded from https://chemistry-europe.onlinelibrary.wiley.com/doi/10.1002/chem.202102945 by KIZ der Universitat Ulm, Wiley Online Library on [19/08/2024]. See the Terms and Conditions (https://onlinelibrary.wiley.com/terms-and-conditions) on Wiley Online Library for rules of use; OA articles are governed by the applicable Creative Commons License

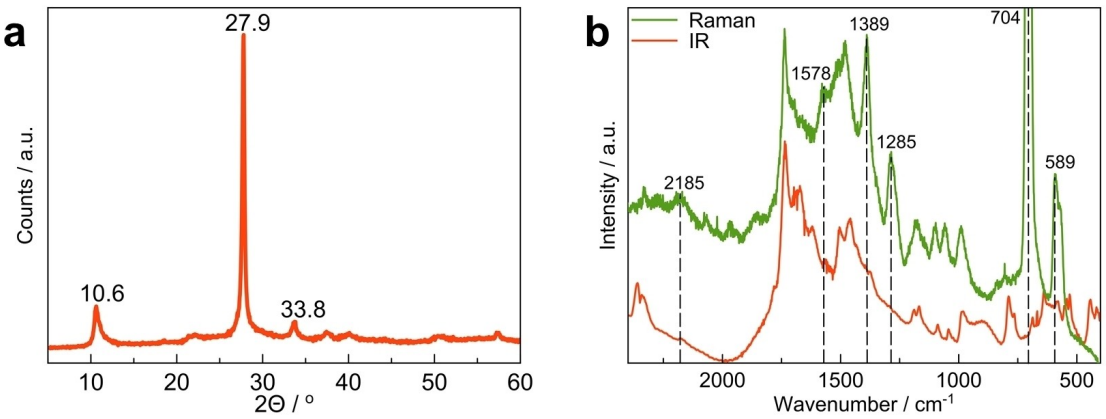

Figure 5. (a) XRD pattern and (b) comparative analysis of FTIR and Raman spectra of the insoluble R-CN_x-KS powder obtained by slow evaporation of R-CN_x-K solution.

to the poly(triazine imide) phase.[44] FTIR and Raman spectra reveal a wide absorption region in 1400–1660 cm^{-1} ascribed to C=N stretching of the heterocycle and a very intense Raman band at 704 cm^{-1} accompanied by a weaker band at 989 cm^{-1} (Figure S8a,b) attributed to triazine breathing modes,[45] thus corroborating the polytriazine nature of the material. The intense absorption peak at 1736 cm^{-1} coincides with the C=O bond stretching vibrations in alkali isocyanurates (Figure S8a,b), while the absorption in the 3145–3340 cm^{-1} range and at ca. 2850 cm^{-1} is attributed to free and H-bonded NH_x-moieties, respectively.[46] This suggests that the fully deprotonated cyanurate mono or oligomeric species in the solution undergo tautomeric transformation producing insoluble polymerized isocyanurate fragments. A comparative analysis of UV Raman and FTIR spectra shows multiple strongly Raman active modes that are not visible in the IR spectrum 1578, 1389, 1285 and 589 cm^{-1}. These can be attributed to N=N stretching,[47] N=N in trans-aromatic azo compounds, azoxy groups[34a] and C–N=N stretching combined with a C–N deformation vibrations,[48] respectively. The observed bands at 1389 and 589 cm^{-1} are especially indicative of a *trans*-azo moiety inside the R-CN_x-KS (i.e., in the solid obtained by slow evaporation of the R-CN_x-K solution that was obtained after filtering off the tri-potassium cyamelurate crystals from the concentrated product solution of the R-CN_x dissolution in KOH). Considering that it is very unlikely that azo groups are formed during KOH treatment of R-CN_x, we conclude that they were a part of its structural units in the solid-state, linking the heptazine or triazine moieties and being responsible for the visible-light absorption. Indeed, the type of the linkage between the structural units of polymeric carbon nitride determines the materials optical properties to a greater extent than the substitutional doping of the heptazine itself, as it defines the symmetry, planarity or corrugation of the polymeric system.[49] Notably, a band in the visible-light absorption region is still present in the UV-vis spectrum of the R-CN_x-KS, though blue-shifted with respect to that observed for R-CN_x (Figure S9).

To summarize, we suggest that the high-temperature treatment of Y-CN_x induces partial heptazine fragmentation accompanied by NH_3, CNH_2 and C_2N_2 fragments evolution, as previously confirmed by mass-spectroscopic analysis.[50] The produced C_2N_2 species can exist in several isomeric forms, such as cyanogen (N≡C–C≡N), the most thermodynamically stable one, isocyanogen (N≡C–N=C) or diisocyanogen (C=N–N=C). Diisocyanogen was detected in the products of norbornadienonazine thermolysis at temperatures exceeding 500 °C.[51] This isomer should have a higher reactivity than the rest of cyanogen isomeric forms making its isolation and investigation difficult.[52] Therefore, we speculate that the thermal decomposition of melon at high temperatures could yield diisocyanogen species that immediately react with the polymer backbone producing C=N–N=C linkages between the separate heptazine or triazine units, which subsequently isomerize to C–N=N–C forming the azo-link. In other words, a PCN material with strongly extended visible light absorption is obtained that contains, apart from typical PCN structural features, also poly (heptazine/triazine) azo-linked fragments that are chiefly responsible for the red shift of the optical absorption edge.

In order to better understand the electronic structures and optical properties of the different systems, periodic density functional theory calculations have been performed on various systems. Figure 6a shows the most relevant systems that were obtained after an extensive screening for possible structures of R-CN_x and Y-CN_x. For the red carbon nitride system two different configurations were found (see Figure 6), one in a planar configuration (planar-R-CN_x), and a second one with an azo-linkage at the N=N group that leads to a step-like structure of the layer. Interestingly, the planar configuration is 0.42 eV less stable than the R-CN_x system (Figure S10). However, while the latter one has a bandgap of 3.5 eV, which is in the expected range of carbon nitrides, the planar-R-CN_x system has a direct bandgap of only 2.2 eV. Regarding the Y-CN_x, an idealized fully interconnected layer of g-C_3N_4[1c] (E_{gap} = 2.8 eV) as well as a melon-type polymer with hydrogenated amino end groups (E_{gap} = 3.6 eV) that leads to strand-like structures were considered. All band structures and projected density of states of the different systems can be found in the Supporting Information (Figure S10, S11), together with the charge density distributions

© 2021 The Authors. Chemistry - A European Journal published by Wiley-VCH GmbH

15213765, 2021, 68, Downloaded from https://chemistry-europe.onlinelibrary.wiley.com/doi/10.1002/chem.202102945 by KIZ der Universitat Ulm, Wiley Online Library on [19/08/2024]. See the Terms and Conditions (https://onlinelibrary.wiley.com/terms-and-conditions) on Wiley Online Library for rules of use; OA articles are governed by the applicable Creative Commons License

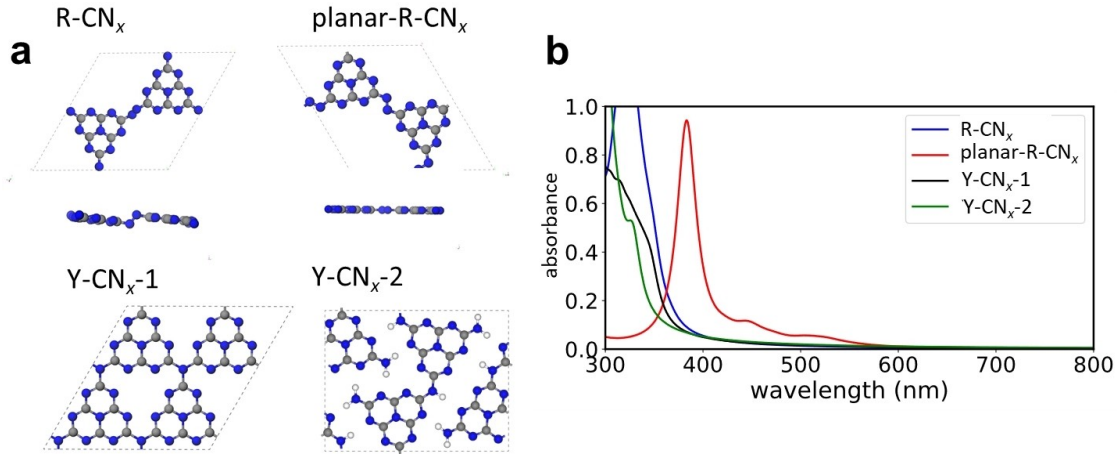

Figure 6. (a) Most relevant systems used for the in-depth analysis. For the R-CN_x systems both the top and side views are shown, while for the Y-CN_x systems only top views are shown. (b) Calculated absorption spectra for the four different systems.

at the corresponding valence band maxima (VBM) and conduction band minima (CBM) (Figure S12). The Figure 6b shows the calculated absorption spectra, which reveal the expected UV-absorbance for all CN_x structures, including the hypothetical fully condensed g-C_3N_4, except for planar-R-CN_x that shows absorption at longer wavelengths close to 400 nm.

The question remains why the experimentally observed optical properties of red carbon nitride conforms with the calculated behaviour of planar-R-CN_x, though this structure is less stable than the step-like R-CN_x configuration (see Figure 6). Our present hypothesis is that red carbon nitride is confined in a Y-CN_x framework (as shown in Figure 7a), which stabilizes the planar configuration, leading to localized planar-R-CN_x units. The azo-linkages in the planar-R-CN_x units then lead to reduction of the overall bandgap as depicted in the energy scheme shown in Figure 7b. Such confinement effects have also been observed for other two-dimensional systems (e.g., $TaSe_2$), where the embedding in a larger framework leads to a stabilization of the usually less preferred configuration.[53]

Photoluminescence spectroscopy

Photoluminescence (PL) spectra of drop-casted CN_x films are shown in Figure 8a. The PL of R-CN_x is spectrally broader and appears red-shifted compared to the benchmark material Y-CN_x. Fitting the steady-state PL spectra of both materials to a sum of two Gaussian peaks reveals that the apparent spectral broadening of the R-CN_x spectrum is due to the increase of a low-energy emission component (sub-peak B) below 2.5 eV. When monitoring the low-energy emission of R-CN_x, a distinct new peak (centered at 540 nm) becomes apparent in the PL excitation spectrum. This suggests the presence of distinct emissive states below the band edge of R-CN_x,[18] which are

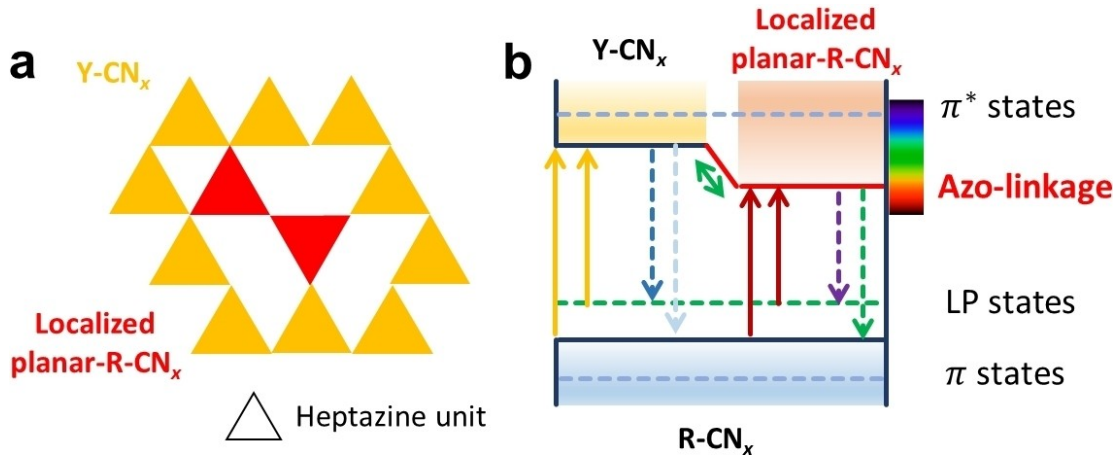

Figure 7. Proposed diagram of possible transitions for R-CN_x. The model (a) shows the confined localized planar-R-CN_x unit in the Y-CN_x framework, while the energy diagram (b) shows the corresponding energy states. Here the azo-linkage lowers the bandgap and leads to light absorption at wavelengths in the visible spectral range.

© 2021 The Authors. Chemistry - A European Journal published by Wiley-VCH GmbH

15213765, 2021, 68, Downloaded from https://chemistry-europe.onlinelibrary.wiley.com/doi/10.1002/chem.202102945 by KIZ der Universitat Ulm, Wiley Online Library on [19/08/2024]. See the Terms and Conditions (https://onlinelibrary.wiley.com/terms-and-conditions) on Wiley Online Library for rules of use; OA articles are governed by the applicable Creative Commons License

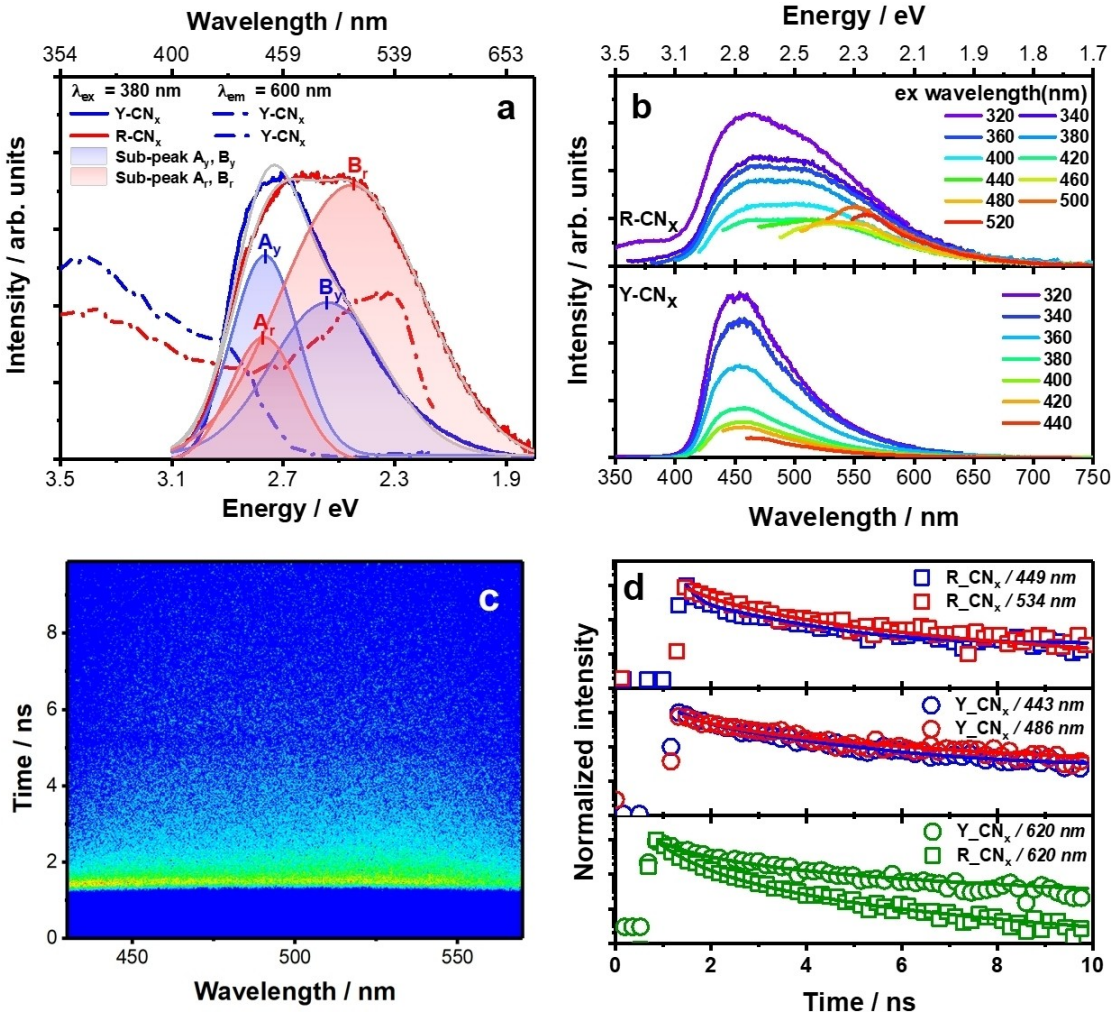

Figure 8. (a) PL and PL excitation spectra of drop casted Y-CN_x and R-CN_x. Emission upon excitation at 380 (solid lines) and PL excitation spectra recorded at 600 nm (dashed lines) spectra were taken at room temperature. Multi-peaks of the PL spectra for Y-CN_x (A_y, B_y) and R-CN_x (A_r, B_r) were fitted with a Gaussian function. (b) PL spectra of Y-CN_x and R-CN_x acquired at different excitation wavelengths. (c) Streak camera image showing the PL as a function of emission wavelength and time recorded for drop casted R-CN_x upon 385 nm excitation. The experimental time window was chosen to be 10 ns. (d) PL decay kinetics of R-CN_x after excited at 385 nm (upper panel) and 520 nm (lower panel). To derive the kinetics, the streak camera data has been integrated in a spectral range of ±5 nm with respect to the probe wavelengths indicated in panel (d). For comparison the respective PL decay kinetics of Y-CN_x are shown.

clearly visible also in the PL spectra recorded for different excitation wavelengths (Figure 8b). The sub-bandgap emission observed in R-CN_x is likely associated with an increased number of tail states due to the higher density of localized planar-R-CN_x units in the Y-CN_x framework (Figure 7) produced by heptazine fragmentation and azo-linkages formation after elevated temperature processing.[54]

To obtain more insight into the distinct PL properties of R-CN_x, time-resolved PL data were collected upon excitation at 380 and 520 nm. The choice of excitation wavelengths enables a comparison between bandgap excitation and direct excitation of the sub-band emission. Figure 8c exemplarily shows the streak camera data for R-CN_x upon excitation at 385 nm. The transient PL spectra can be fitted to a sum of two Gaussian peaks centered at 2.32 and 2.76 eV (Figure S13a). The corresponding time-resolved PL spectra for Y-CN_x yield emission contributions at 2.55 and 2.80 eV (see Figure S13a). Upon excitation at 520 nm a long-wave PL emission centered at 2.20 eV is visible (Figure S13b). To derive PL kinetics reflecting the lifetime of the emission upon excitation at 385 nm, the transient PL spectra are integrated in over 10 nm around the peak wavelength of the individual emission contributions (Figure 8d). The transient PL kinetics of R-CN_x (recorded at about 2.8 eV) are fitted by a bi-exponential decay yielding the characteristic time constants $\tau_1 = 0.17$ ns and $\tau_2 = 1.34$ ns. For Y-CN_x the equivalent data decay with slightly longer time constants, i.e. $\tau_1 = 0.39$ ns and $\tau_2 = 1.91$ ns. This comparison indicates somewhat faster exciton dissociation in R-CN_x, likely associated with higher defect density and the more localized excited state in the planar R-CN_x units (see Figure 7). The bi-exponential decay of the excitonic emission is related to different recombination centres in the material. If excitons are generated in proximity to such a recombination centre, they decay more rapidly on a sub-ns timescale, while excitons

© 2021 The Authors. Chemistry - A European Journal published by Wiley-VCH GmbH

15213765, 2021, 68, Downloaded from https://chemistry-europe.onlinelibrary.wiley.com/doi/10.1002/chem.202102945 by KIZ der Universitat Ulm, Wiley Online Library on [19/08/2024]. See the Terms and Conditions (https://onlinelibrary.wiley.com/terms-and-conditions) on Wiley Online Library for rules of use; OA articles are governed by the applicable Creative Commons License

generated distant from such recombination centres decay on a longer timescale. The decay of the sub-bandgap emission (recorded upon excitation at 520 nm and derived by integration over the entire PL band) is non-exponential decay, i.e. it follows a power law kinetic $I_{PL}(t) \sim t^{-\alpha}$ commonly used to account for reaction kinetics in diffusive systems.[55,56] Comparing R-CN_x to Y-CN_x, the value of the characteristic exponent decreases from $\alpha_{rCNx} \approx 2.2$ to $\alpha_{yCNx} \approx 1.3$. The more rapid decay in R-CN_x is attributed to an increased number of defect states serving as recombination centres.

Photocatalytic hydrogen evolution

Conventional Y-CN_x modified with appropriate co-catalysts is known for its ability to produce H_2 in presence of a sacrificial reducing agent under visible light irradiation.[1a] Pristine Y-CN_x is inactive for photocatalytic HER under monochromatic LED light irradiation at 420 nm (Figure 9a). However, after deposition of the {Mo_3} clusters and especially Pt nanoparticles, it demonstrates a very good performance reaching a H_2 production of around 0.04 mmol in 7 h (Figure 9a). Although the experimental data exposed and discussed above indicate that the basic structure of conventional yellow PCN is preserved also in the R-CN_x material, its photocatalytic behaviour is very different. The activity of the red R-CN_x modified with {Mo_3} clusters or Pt nanoparticles is lower by an order of magnitude compared to Y-CN_x, reaching only 0.005 mmol H_2 after 7 h of irradiation (Figure 9b). Similar to the conventional PCN counterpart, bare R-CN_x without a co-catalyst does not photocatalysed HER under 420 nm light irradiation (Figure 9b). Contrary to the case of Y-CN_x, R-CN_x shows higher photocatalytic activity if modified with the {Mo_3} clusters than with Pt nanoparticles (Figure 9b). A similar observation was reported by Wang et al. for protonated mesoporous carbon nitride materials.[57] These results suggest that the surface properties of the R-CN_x sample are different to a significant extent from those of Y-CN_x, affecting the interaction of the former with co-catalysts.

The photocatalytic activity of R-CN_x under 420 nm irradiation is inferior to that of its yellow counterpart, nonetheless the appearance of an additional absorption band in the visible-light range in the UV-vis spectrum of R-CN_x (Figure 1b and d) prompted us to study its performance also under excitation with lower energy light at the wavelength of 470 nm. Under these conditions, the Y-CN_x sample is, as expected, completely inactive in photocatalytic HER both with and without co-catalysts (Figure 10a), since it does not absorb in this spectral region (Figures 1b and c). Intriguingly, the red R-CN_x is not only capable of sacrificial H_2 evolution under irradiation at 470 nm when modified with {Mo_3} or Pt nanoparticles, but the pristine R-CN_x without any co-catalysts even shows a superior photocatalytic activity (Figure 10b). Therefore, the new functional groups in the red carbon nitride, the azo-linked poly (heptazine/triazines) formed as the result of the high-temperature treatment, are not only responsible for the strong red shift of the optical absorption edge of the material, but they also might possibly play an additional role of an active site for H_2 evolution. Despite the rather moderate activity of this material, its ability to absorb a significant portion of the visible light spectrum and the metal-free nature of its active site for photocatalytic HER represent intriguing aspects of R-CN_x with respect to solar light-driven photocatalysis. From the R-CN_x catalysed H_2 evolution plots one can observe an apparent deactivation trend (Figure 10b).

We hypothesized that this was due to the weak reductive power of methanol as a sacrificial reducing agent, hence some stronger reductants were added to the R-CN_x suspensions. The addition of ascorbic acid improved the photocatalytic performance of R-CN_x modified with {Mo_3} and Pt nanoparticles up to the level of the pristine catalyst, while leaving the activity of the co-catalyst modified samples unchanged (Figure 10c). The introduction of another strong reductant, triethanolamine (TEOA), affected the activity of bare R-CN_x only slightly, but had a strong impact on the activity of co-catalyst-modified R-CN_x (Figure 10d).

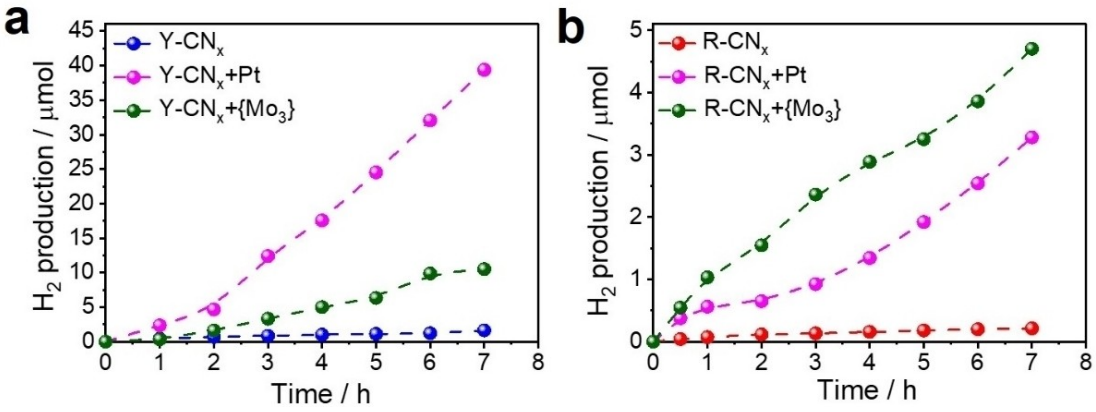

Figure 9. Photocatalytic HER performed using (a) Y-CN_x and (b) R-CN_x based materials under monochromatic 420 nm LED irradiation. Conditions: [catalyst]: 10 mg, Solvent: H_2O:MeOH (9:1, v:v), in absence of any additional electron donor.

© 2021 The Authors. Chemistry - A European Journal published by Wiley-VCH GmbH

15213765, 2021, 68, Downloaded from https://chemistry-europe.onlinelibrary.wiley.com/doi/10.1002/chem.202102945 by KIZ der Universitat Ulm, Wiley Online Library on [19/08/2024]. See the Terms and Conditions (https://onlinelibrary.wiley.com/terms-and-conditions) on Wiley Online Library for rules of use; OA articles are governed by the applicable Creative Commons License

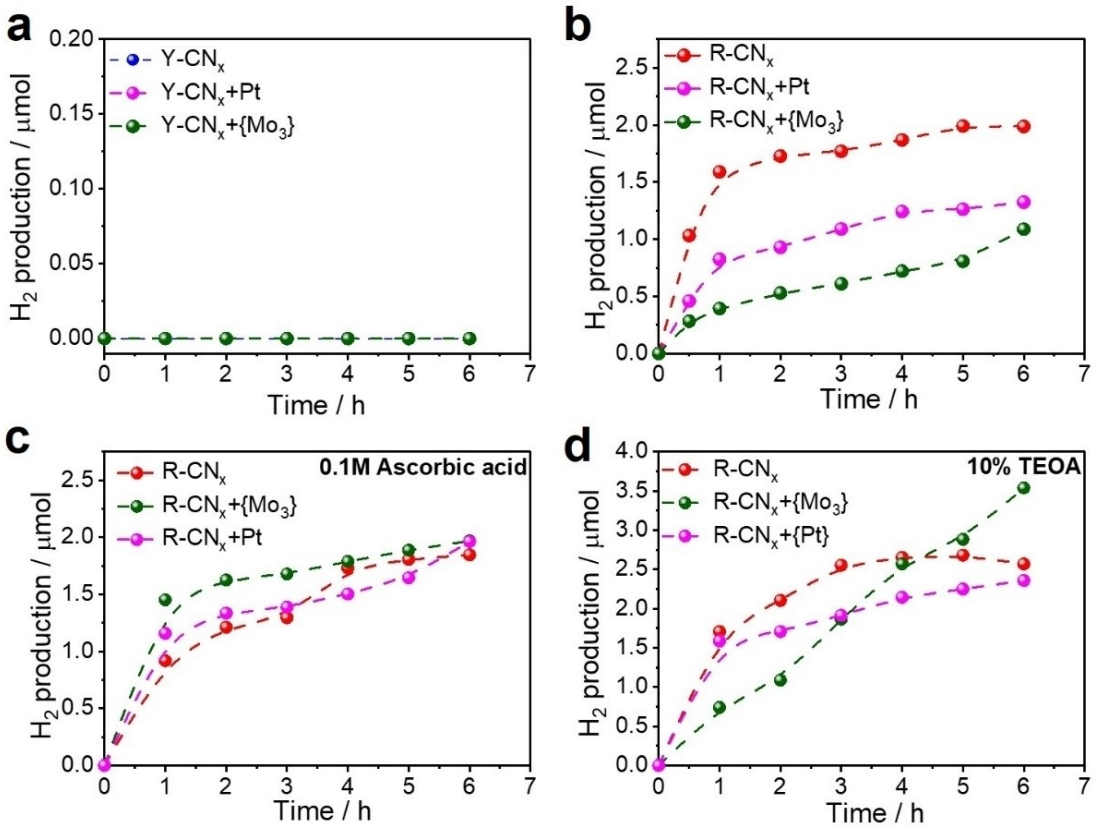

Figure 10. Photocatalytic HER performed using (a) Y-CN_x and R-CN_x based materials under 470 nm irradiation (b) in absence of any electron donor, (c) in presence of ascorbic acid (0.1 M; pH 2.4) and (d) 10% of TEOA (pH 10.5). Conditions: [catalyst] : 10 mg, Solvent: H_2O:MeOH (9:1, v:v).

Most notably, the strong deactivation trend could be reversed for the {Mo_3}-modified R-CN_x photocatalyst in the presence of TEOA, leading to a stable rate of H_2 evolution (green trace in Figure 10d). This might be attributed to a more effective oxidation of TEOA compared to ascorbic acid since positively charged TEOA at pH 10.5 ($pK_a = 7.9$) is expected to adsorb more effectively at the negatively charged R-CN_x than non-dissociated ascorbic acid ($pK_a = 4.3$) at pH 2.4.

Conclusions

We report a simple post-synthetic approach involving a brief high-temperature treatment under vacuum that effectively turns the typically yellow PCN into a red PCN by extending significantly its visible light absorption to >600 nm. Most importantly, we provide evidence that the extended optical absorption edge of PCNs subjected to high-temperature treatment is due to the formation of azo-moieties that act as linkages between the heptazine units inherent to PCN structure and/or between heptazine and triazine units formed upon partial fragmentation of PCN. Our present understanding is that the formation of planar-R-CN_x units comprising the azo-linkages and embedded in the yellow carbon nitride framework is responsible for the reduction of the overall bandgap and the red colour of the material. Notably, the azo moieties effectively sensitize the red PCN for photocatalytic H_2 evolution even under low energy (470 nm) light where conventional yellow PCN is inactive. Moreover, the red carbon nitride clearly contains moieties that can act as metal-free catalytic sites for H_2 as evidenced by effective operation even without any additional co-catalyst. The downside of the high-temperature treatment of PCN is the partial fragmentation of the heptazine network creating large number of recombination centres and decreasing the overall photocatalytic activity of the resulting photocatalyst. We assume that our findings on the so far overlooked role of azo moieties in PCNs with strongly extended absorption edge might not only be valid for this particular case, but also for other cases in which a strong shift of the PCN absorption edge has been observed upon thermal treatment procedures at temperatures leading to the heptazine fragmentation and formation of cyanogen species. The present work thus highlights the importance of a careful determination of structural features governing the complex interplay between the light absorption, charge separation and catalytic turnover in PCN-based polymers tailored for visible light-driven photocatalysis.

© 2021 The Authors. Chemistry - A European Journal published by Wiley-VCH GmbH

15213765, 2021, 68, Downloaded from https://chemistry-europe.onlinelibrary.wiley.com/doi/10.1002/chem.202102945 by KIZ der Universitat Ulm, Wiley Online Library on [19/08/2024]. See the Terms and Conditions (https://onlinelibrary.wiley.com/terms-and-conditions) on Wiley Online Library for rules of use; OA articles are governed by the applicable Creative Commons License

Acknowledgements

This work was funded by the Deutsche Forschungsgemeinschaft (DFG, German Research Foundation) – Projektnummer 364549901 – TRR 234 CataLight [Projects A5, B6, B7, C2, C3 and Z2] and BE 5102/5-1. We acknowledge also support by Spanish Ministerio de Ciencia e Innovación (PID2020-113558RB–C41). Computational resources were provided by the state of Baden-Württemberg through bwHPC and the German Science Foundation (DFG) under Grant No. INST 40/467-1 FUGG. C.N and A.T. acknowledge financial support of the DFG through the project TU 149/8-2 "Towards photo-active membranes for artificial photosynthesis" as well as the DFG through a research infrastructure grant INST 275/257-1 FUGG. I.K. acknowledges the support of the Alexander von Humboldt Foundation through the Humboldt Research Fellowship. We also acknowledge Christian Tontsch for NMR measurements and Samuel Blessing for XRD measurements. Open Access funding enabled and organized by Projekt DEAL.

Conflict of Interest

The authors declare no conflict of interest.

Keywords: carbon nitrides · hydrogen · photocatalysis · solar energy conversion · visible light

[1] a) X. Wang, K. Maeda, A. Thomas, K. Takanabe, G. Xin, J. Carlsson, K. Domen, M. Antonietti, *Nat. Mater.* **2009**, *8*, 76–80; b) Y. Wang, X. Wang, M. Antonietti, *Angew. Chem. Int. Ed.* **2012**, *51*, 68–89; *Angew. Chem.* **2012**, *124*, 70–92; c) F. Kessler, Y. Zheng, D. Schwarz, C. Merschjann, W. Schnick, X. Wang, M. Bojdys, *Nat. Rev. Mater.* **2017**, *2*; d) X. Wang, S. Blechert, M. Antonietti, *ACS Catal.* **2012**, *2*, 1596–1606; e) J. Barrio, M. Volokh, M. Shalom, *J. Mater. Chem. A* **2020**, *8*, 11075–11116.

[2] a) R. Godin, Y. Wang, M. A. Zwijnenburg, J. W. Tang, J. R. Durrant, *J. Am. Chem. Soc.* **2017**, *139*, 5216–5224; b) W. Yang, R. Godin, H. Kasap, B. Moss, Y. Dong, S. A. J. Hillman, L. Steier, E. Reisner, J. R. Durrant, *J. Am. Chem. Soc.* **2019**, *141*, 11219–11229; c) C. Li, E. Hofmeister, I. Krivtsov, D. Mitoraj, C. Adler, R. Beranek, B. Dietzek, *ChemSusChem* **2021**, *14*, 1728–1736.

[3] a) X. Wang, K. Maeda, X. Chen, K. Takanabe, K. Domen, Y. Hou, X. Fu, M. Antonietti, *J. Am. Chem. Soc.* **2009**, *131*, 1680–1681; b) S. Yang, Y. Gong, J. Zhang, L. Zhan, L. Ma, Z. Fang, R. Vajtai, X. Wang, P. Ajayan, *Adv. Mater.* **2013**, *25*, 2452–2456; c) C. Adler, S. Selim, I. Krivtsov, C. Li, D. Mitoraj, B. Dietzek, J. R. Durrant, R. Beranek, *Adv. Funct. Mater.* **2021**, https://doi.org/10.1002/adfm.202105369.

[4] G. Zhang, J. Zhang, M. Zhang, X. Wang, *J. Mater. Chem.* **2012**, *22*, 8083–8091.

[5] H. Kim, S. Gim, T. Jeon, W. Choi, *ACS Appl. Mater. Interfaces* **2017**, *9*, 40360–40368.

[6] a) G. Zhang, G. Li, Z. Lan, L. Lin, A. Savateev, T. Heil, S. Zafeiratos, X. Wang, M. Antonietti, *Angew. Chem. Int. Ed.* **2017**, *56*, 13445–13449; *Angew. Chem.* **2017**, *129*, 13630–13634; b) J. Zhang, G. Zhang, X. Chen, S. Lin, L. Mohlmann, G. Dolega, G. Lipner, M. Antonietti, S. Blechert, X. Wang, *Angew. Chem. Int. Ed.* **2012**, *51*, 3183–3187; *Angew. Chem.* **2012**, *124*, 3237–3241.

[7] A. Jorge, D. Martin, M. Dhanoa, A. Rahman, N. Makwana, J. Tang, A. Sella, F. Cora, S. Firth, J. Darr, P. McMillan, *J. Phys. Chem. C* **2013**, *117*, 7178–7185.

[8] Y. Yang, S. Wang, Y. Jiao, Z. Wang, M. Xiao, A. Du, Y. Li, J. Wang, L. Wang, *Adv. Funct. Mater.* **2018**, *28*.

[9] a) P. Niu, L. Yin, Y. Yang, G. Liu, H. Cheng, *Adv. Mater.* **2014**, *26*, 8046–8052; b) J. Li, B. Shen, Z. Hong, B. Lin, B. Gao, Y. Chen, *Chem. Commun.* **2012**, *48*, 12017–12019.

[10] J. Xu, Y. Li, S. Peng, G. Lu, S. Li, *Phys. Chem. Chem. Phys.* **2013**, *15*, 7657–7665.

[11] a) Y. Gao, F. Hou, S. Hu, B. Wu, Y. Wang, H. Zhang, B. Jiang, H. Fu, *ChemCatChem* **2018**, *10*, 1330–1335; b) B. Chai, X. Liao, F. Song, H. Zhou, *Dalton Trans.* **2014**, *43*, 982–989.

[12] Y. Chen, B. Wang, S. Lin, Y. Zhang, X. Wang, *J. Phys. Chem. C* **2014**, *118*, 29981–29989.

[13] a) Q. Liang, Z. Li, Z. Huang, F. Kang, Q. Yang, *Adv. Funct. Mater.* **2015**, *25*, 6885–6892; b) Y. Hou, J. Yang, C. Lei, B. Yang, Z. Li, Y. Xie, X. Zhang, L. Lei, J. Chen, *ACS Sustainable Chem. Eng.* **2018**, *6*, 6497–6506.

[14] Y. Cao, Z. Zhang, J. Long, J. Liang, H. Lin, H. Lin, X. Wang, *J. Mater. Chem. A* **2014**, *2*, 17797–17807.

[15] P. Niu, H. Li, Y. Ma, T. Zhai, *J. Phys. Chem. C* **2018**, *122*, 20717–20726.

[16] Y. Kang, Y. Yang, L. Yin, X. Kang, L. Wang, G. Liu, H. Cheng, *Adv. Mater.* **2016**, *28*, 6471–6477.

[17] P. Niu, M. Qiao, Y. Li, L. Huang, T. Zhai, *Nano Energy* **2018**, *44*, 73–81.

[18] Z. Gan, H. Xu, Y. Hao, *Nanoscale* **2016**, *8*, 7794–7807.

[19] S. Li, G. Dong, R. Hailili, L. Yang, Y. Li, F. Wang, Y. Zeng, C. Wang, *Appl. Catal. B* **2016**, *190*, 26–35.

[20] E. Horvath-Bordon, E. Kroke, I. Svoboda, H. Fuess, R. Riedel, S. Neeraj, A. K. Cheetham, *Dalton Trans.* **2004**, 3900–3908.

[21] A. Rajagopal, E. Akbarzadeh, C. Y. Li, D. Mitoraj, I. Krivtsov, C. Adler, T. Diemant, J. Biskupek, U. Kaiser, C. Im, M. Heiland, T. Jacob, C. Streb, B. Dietzek, R. Beranek, *Sustain. Energy Fuels* **2020**, *4*, 6085–6095.

[22] A. Muller, V. Wittneben, E. Krickemeyer, H. Bogge, M. Lemke, *Z. Anorg. Allg. Chem.* **1991**, *605*, 175–188.

[23] C. Ryan, E. Clayton, W. Griffin, S. Sie, D. Cousens, *Nucl. Instrum. Methods Phys. Res. Sect. B* **1988**, *34*, 396–402.

[24] A. C. Hannon, *Nucl. Instrum. Methods Phys. Res. Sect. A* **2005**, *551*, 88–107.

[25] *Manipulation and Analysis Toolkit for Instrument Data. Mantid Project* **2013**, https://www.mantidproject.org.

[26] A. K. Soper. *Programs for correcting raw neutron and X-ray diffraction data to differential scattering cross section. Gudrun and GudrunX*, **2010**, https://www.isis.stfc.ac.uk/Pages/Gudrun.aspx.

[27] a) G. Kresse, J. Hafner, *Phys. Rev. B* **1993**, *47*, 558–561; b) G. Kresse, J. Furthmuller, *Phys. Rev. B* **1996**, *54*, 11169–11186; c) G. Kresse, J. Furthmuller, *Comput. Mater. Sci.* **1996**, *6*, 15–50.

[28] J. P. Perdew, K. Burke, M. Ernzerhof, *Phys. Rev. Lett.* **1996**, *77*, 3865–3868.

[29] A. V. Krukau, O. A. Vydrov, A. F. Izmaylov, G. E. Scuseria, *J. Chem. Phys.* **2006**, *125*.

[30] S. Grimme, S. Ehrlich, L. Goerigk, *J. Comput. Chem.* **2011**, *32*, 1456–1465.

[31] H. J. Monkhorst, J. D. Pack, *Phys. Rev. B* **1976**, *13*, 5188–5192.

[32] F. Fina, S. Callear, G. Carins, J. Irvine, *Chem. Mater.* **2015**, *27*, 2612–2618.

[33] Y. Wang, D. C. Alsmeyer, R. L. Mccreery, *Chem. Mater.* **1990**, *2*, 557–563.

[34] a) G. Socrates, *Infrared and Raman Characteristic Group Frequencies*, Wiley, **2001**; b) T. Komatsu, *Macromol. Chem. Phys.* **2001**, *202*, 19–25.

[35] V. Lau, I. Moudrakovski, T. Botari, S. Weinberger, M. Mesch, V. Duppel, J. Senker, V. Blum, B. Lotsch, *Nat. Commun.* **2016**, *7*.

[36] E. Raymundo-Pinero, D. Cazorla-Amoros, A. Linares-Solano, J. Find, U. Wild, R. Schlogl, *Carbon* **2002**, *40*, 597–608.

[37] H. Ma, X. Jia, L. Chen, P. Zhu, W. Guo, X. Guo, Y. Wang, S. Li, G. Zou, G. Zhang, P. Bex, *J. Phys. Condens. Matter* **2002**, *14*, 11269–11273.

[38] NMR Frequency Tables, http://kodu.ut.ee/~laurit/AK2/NMR tables Bruker2012.pdf.

[39] P. Kumar, E. Vahidzadeh, W. K. Thakur, P. Kar, K. M. Alam, A. Goswami, N. Mandi, K. Cui, G. M. Bernard, V. K. Michaelis, K. Shankar, *J. Am. Chem. Soc.* **2019**, *141*, 5415–5436.

[40] B. Jurgens, E. Irran, J. Senker, P. Kroll, H. Muller, W. Schnick, *J. Am. Chem. Soc.* **2003**, *125*, 10288–10300.

[41] M. Ilkaeva, I. Krivtsov, E. Garcia-Lopez, G. Marci, O. Khainakova, J. Garcia, L. Palmisano, E. Diaz, S. Ordonez, *J. Catal.* **2018**, *359*, 212–222.

[42] E. Wirnhier, M. Doblinger, D. Gunzelmann, J. Senker, B. V. Lotsch, W. Schnick, *Chem. Eur. J.* **2011**, *17*, 3213–3221.

[43] X. T. Li, S. H. Li, S. P. Pang, Y. Z. Yu, Y. J. Luo, *Chin. Chem. Lett.* **2007**, *18*, 1037–1039.

[44] T. M. Suter, T. S. Miller, J. K. Cockcroft, A. E. Aliev, M. C. Wilding, A. Sella, F. Cora, C. A. Howard, P. F. McMillan, *Chem. Sci.* **2019**, *10*, 2519–2528.

[45] E. Quirico, G. Montagnac, V. Lees, P. F. McMillan, C. Szopa, G. Cernogora, J. N. Rouzaud, P. Simon, J. M. Bernard, P. Coll, N. Fray, R. D. Minard, F. Raulin, B. Reynard, B. Schmitt, *Icarus* **2008**, *198*, 218–231.

[46] P. Gross, H. A. Hoppe, *Z. Anorg. Allg. Chem.* **2019**, *645*, 257–266.

[47] Y. F. Xie, P. Li, J. Zhang, H. Y. Wang, H. Qian, W. R. Yao, *Spectrochim. Acta Part A* **2013**, *114*, 80–84.

 © 2021 The Authors. Chemistry - A European Journal published by Wiley-VCH GmbH

15213765, 2021, 68, Downloaded from https://chemistry-europe.onlinelibrary.wiley.com/doi/10.1002/chem.202102945 by KIZ der Universitat Ulm, Wiley Online Library on [19/08/2024]. See the Terms and Conditions (https://onlinelibrary.wiley.com/terms-and-conditions) on Wiley Online Library for rules of use; OA articles are governed by the applicable Creative Commons License

[48] L. L. Sun, C. S. Wang, Y. J. Pan, T. Y. Chen, Z. Y. Lv, *J. Raman Spectrosc.* **2020**, *51*, 756–763.
[49] Y. O. Wang, M. K. Bayazit, S. J. A. Moniz, Q. S. Ruan, C. C. Lau, N. Martsinovich, J. W. Tang, *Energy Environ. Sci.* **2017**, *10*, 1643–1651.
[50] M. J. Bojdys, *Analysis of Carbodeon's Nicanite®*, **2017**, https://doi.org/10.5281/zenodo.1119088.
[51] G. Maier, H. P. Reisenauer, J. Eckwert, C. Sierakowski, T. Stumpf, *Angew. Chem. Int. Ed.* **1992**, *31*, 1218–1220; *Angew. Chem.* **1992**, *104*, 1287–1289.
[52] L. S. Cederbaum, F. Tarantelli, H. G. Weikert, M. Scheller, H. Koppel, *Angew. Chem. Int. Ed.* **1989**, *28*, 761–762; *Angew. Chem.* **1989**, *101*, 770–771.
[53] M. K. Kinyaniui, J. Köster, U. Kaiser, Z. Chen, T. Jacob, *In preparation* **2021**.
[54] S. Chen, Y. Zhao, N. Ullah, Q. Wan, R. Zhang, *Carbon* **2019**, *150*, 439–445.
[55] C. Merschjann, S. Tschierlei, T. Tyborski, K. Kailasam, S. Orthmann, D. Hollmann, T. Schedel-Niedrig, A. Thomas, S. Lochbrunner, *Adv. Mater.* **2015**, *27*, 7993–7999.
[56] D. J. Huntley, *J. Phys. Condens. Matter* **2006**, *18*, 1359–1365.
[57] F. Guo, Y. Hou, A. Asiri, X. Wang, *Chem. Commun.* **2017**, *53*, 13221–13224.

Manuscript received: August 12, 2021
Accepted manuscript online: September 29, 2021
Version of record online: October 21, 2021

 © 2021 The Authors. Chemistry - A European Journal published by Wiley-VCH GmbH

15213765, 2021, 68, Downloaded from https://chemistry-europe.onlinelibrary.wiley.com/doi/10.1002/chem.202102945 by KIZ der Universitat Ulm, Wiley Online Library on [19/08/2024]. See the Terms and Conditions (https://onlinelibrary.wiley.com/terms-and-conditions) on Wiley Online Library for rules of use; OA articles are governed by the applicable Creative Commons License

Chemistry–A European Journal

Supporting Information

A Study in Red: The Overlooked Role of Azo-Moieties in Polymeric Carbon Nitride Photocatalysts with Strongly Extended Optical Absorption

Dariusz Mitoraj, Igor Krivtsov,* Chunyu Li, Ashwene Rajagopal, Changbin Im, Christiane Adler, Kerstin Köble, Olena Khainakova, Julian Hniopek, Christof Neumann, Andrey Turchanin, Ivan da Silva, Michael Schmitt, Robert Leiter, Tibor Lehnert, Jürgen Popp, Ute Kaiser, Timo Jacob, Carsten Streb, Benjamin Dietzek,* and Radim Beranek*

SUPPORTING INFORMATION

A Study in Red: The Overlooked Role of Azo-Moieties in Polymeric Carbon Nitride Photocatalysts with Strongly Extended Optical Absorption

Dariusz Mitoraj, Igor Krivtsov, Chunyu Li, Ashwene Rajagopal, Changbin Im, Christiane Adler, Kerstin Köble, Olena Khainakova, Julian Hniopek, Christof Neumann, Andrey Turchanin, Ivan da Silva, Michael Schmitt, Robert Leiter, Tibor Lehnert, Jürgen Popp, Ute Kaiser, Timo Jacob, Carsten Streb, Benjamin Dietzek,* Radim Beranek**

*Corresponding authors: igor.krivtsov@uni-ulm.de, benjamin.dietzek@uni-jena.de, radim.beranek@uni-ulm.de

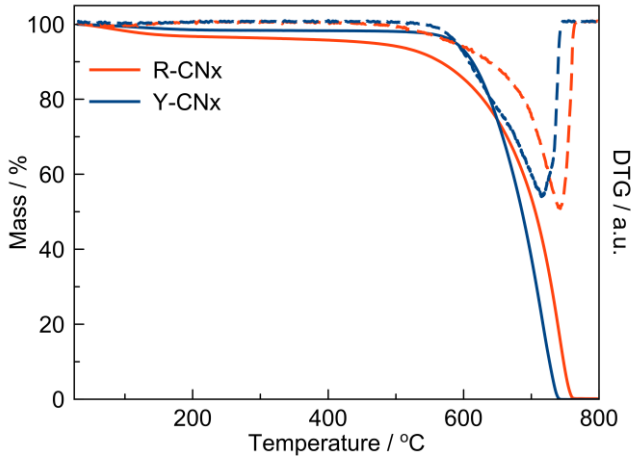

Figure S1. Thermogravimetric analysis of the Y-CN_x and R-CN_x samples

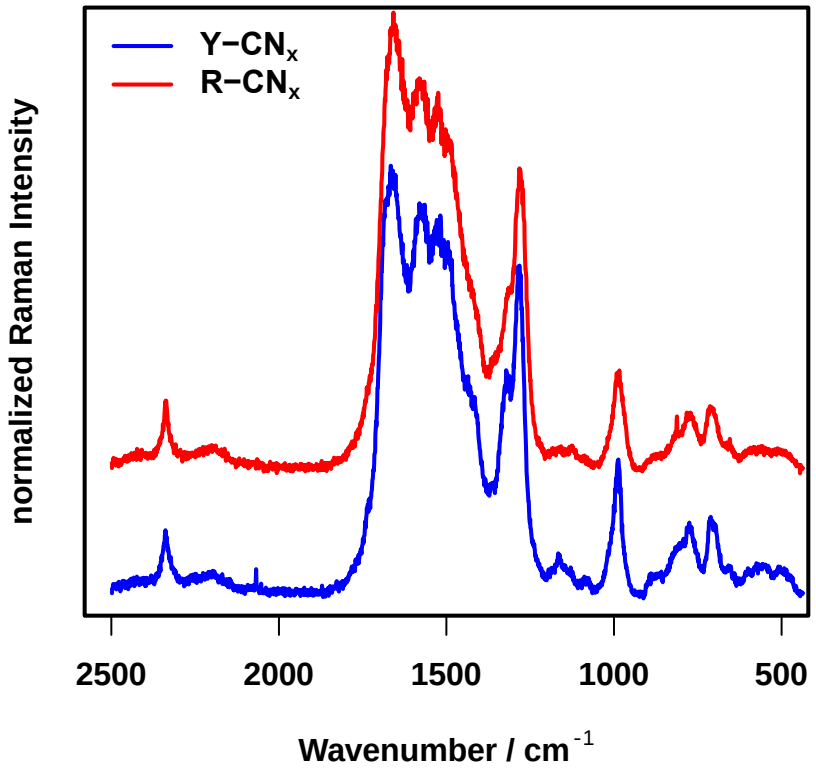

Figure S2. UV-Raman spectra of the Y-CN_x and R-CN_x samples

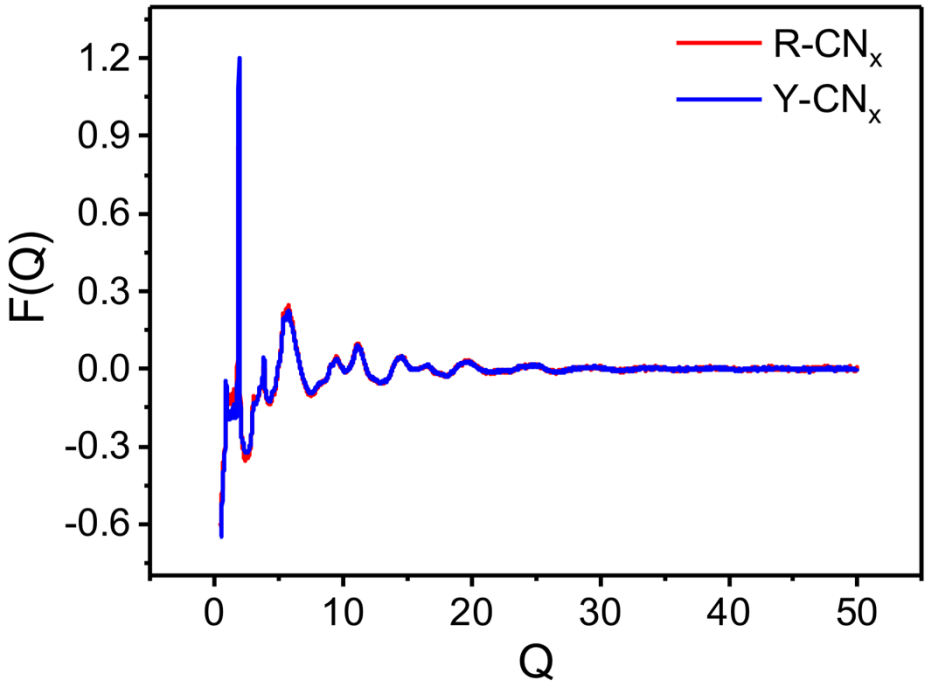

Figure S3. Neutron diffraction structure function obtained for Y-CN_x and R-CN_x

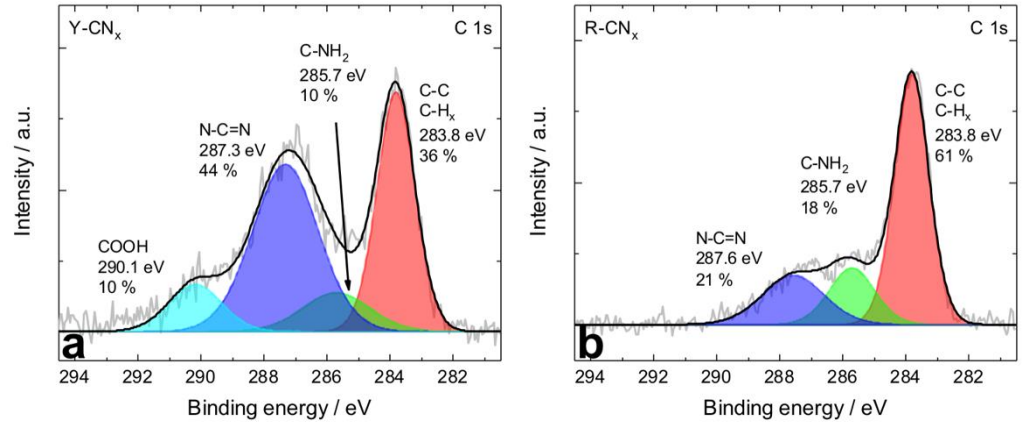

Figure S4. XP C 1s spectra of the Y-CN$_x$ (a) and R-CN$_x$ (b) samples

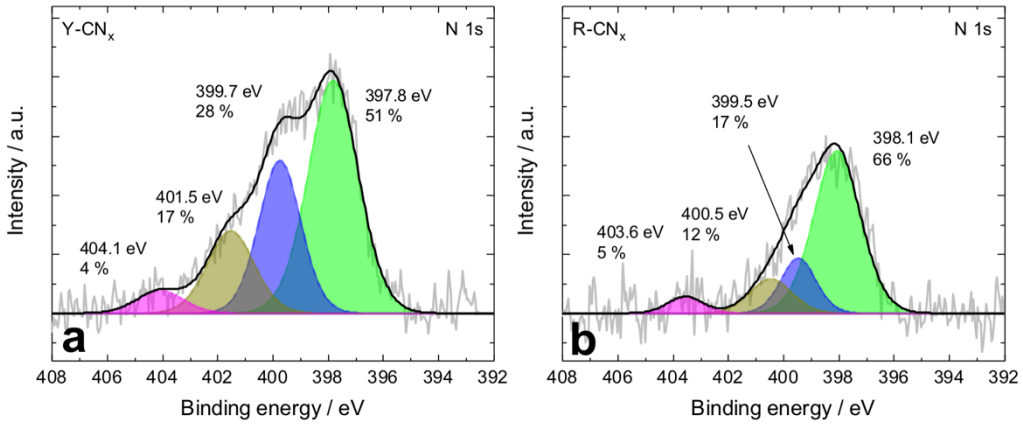

Figure S5. XP N 1s spectra of (a) Y-CN$_x$ and (b) R-CN$_x$ samples

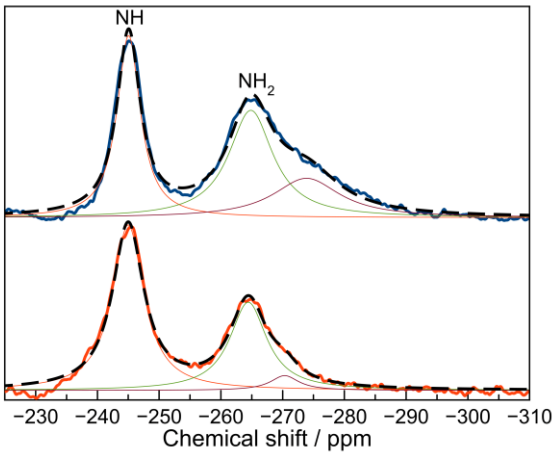

Figure S6. Deconvoluted ^{1}H-^{15}N SS NMR spectra of the Y-CN$_x$ and R-CN$_x$ samples

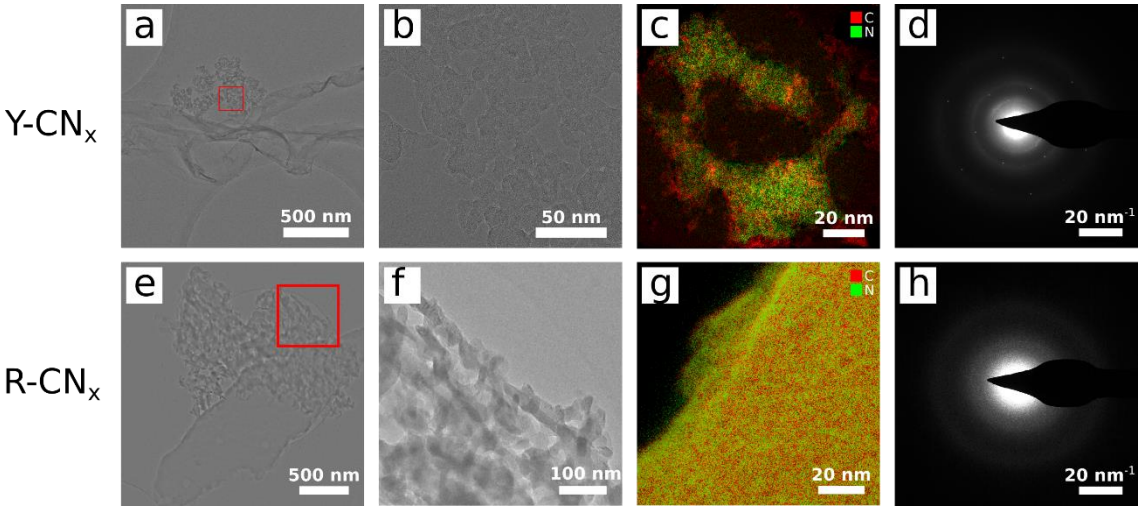

Figure S7. TEM data for Y-CN_x (a-d) and R-CN_x (e-h): Overview image (a) of the sample on amorphous carbon film with graphene as a support. The red marked area is further magnified in (b) showing agglomerated particles. Energy filtered TEM (EFTEM) mapping (c) of C- and N-K lines show homogeneous distribution of carbon and nitrogen in the particles. Electron diffraction pattern (d) shows amorphous rings in addition to the graphene spots. Overview image (e) for R-CNx shows similar agglomerations, further magnified from the red marked area in (f). EFTEM mapping (g) from the region shows homogeneous distribution of C and N. Diffraction pattern (h) shows amorphous rings.

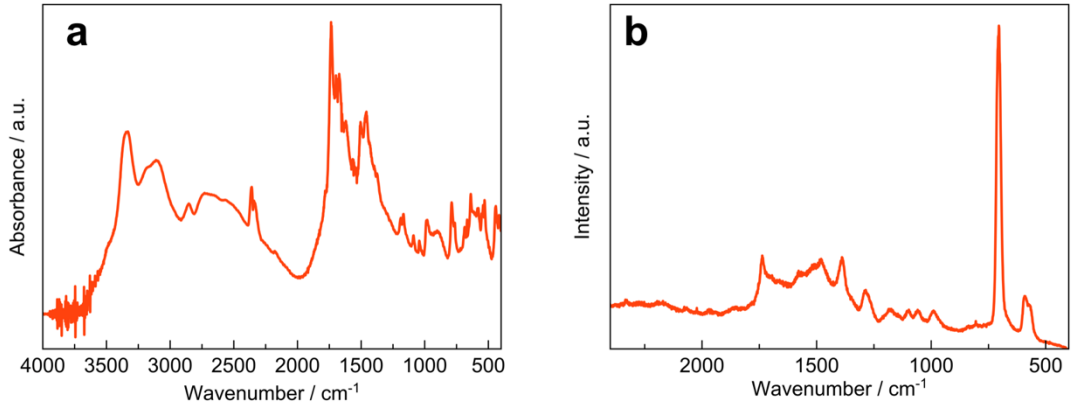

Figure S8. (a) FTIR and **(b)** Raman spectra of the R-CN_x-KS sample

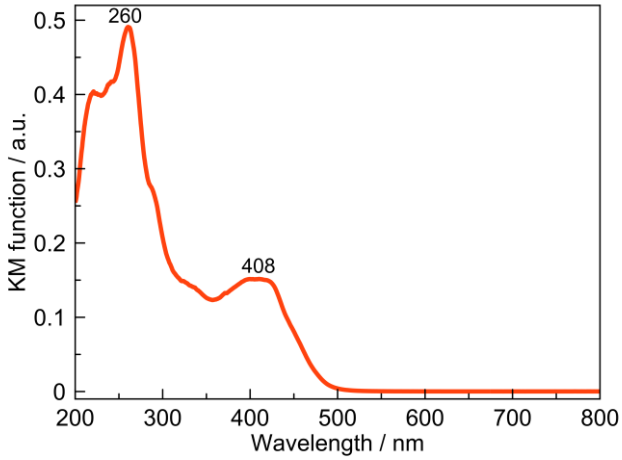

Figure S9. DRUV-vis spectrum of the R-CN_x-KS sample

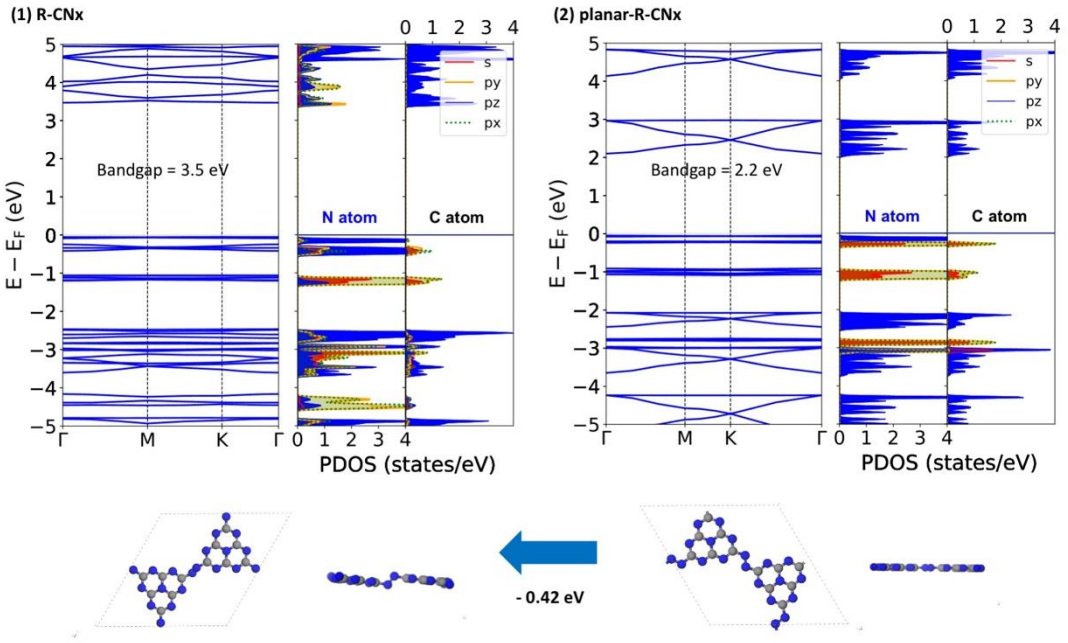

Figure S10. Electronic band structures, projected density of states and the structural images of the R-CN_x models.

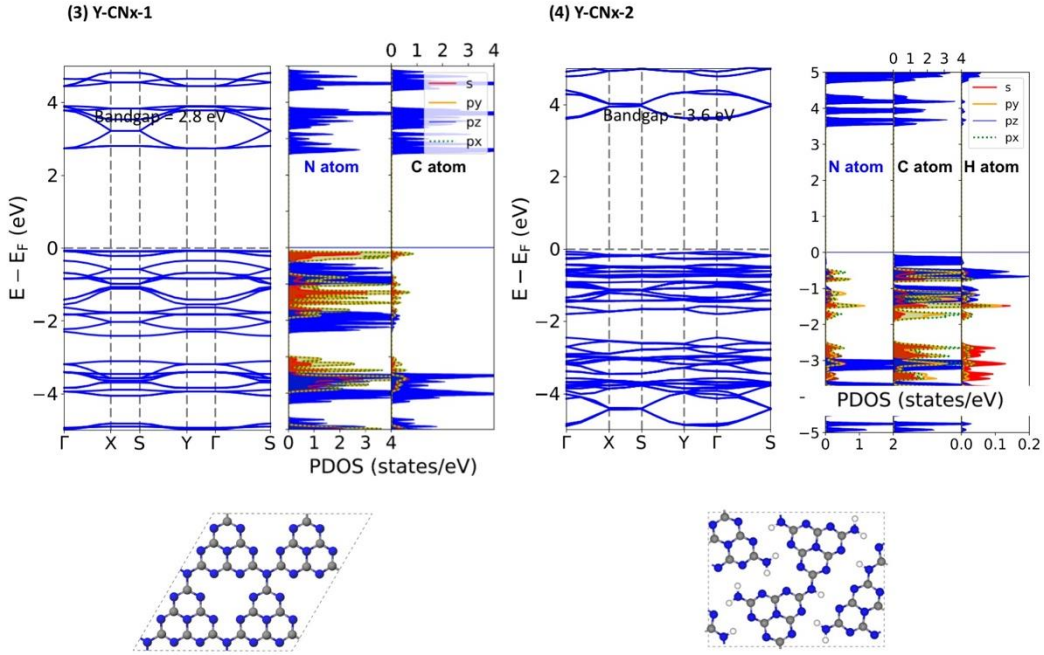

Figure S11. Electronic band structures, projected density of states and the structural images of the Y-CN_x models.

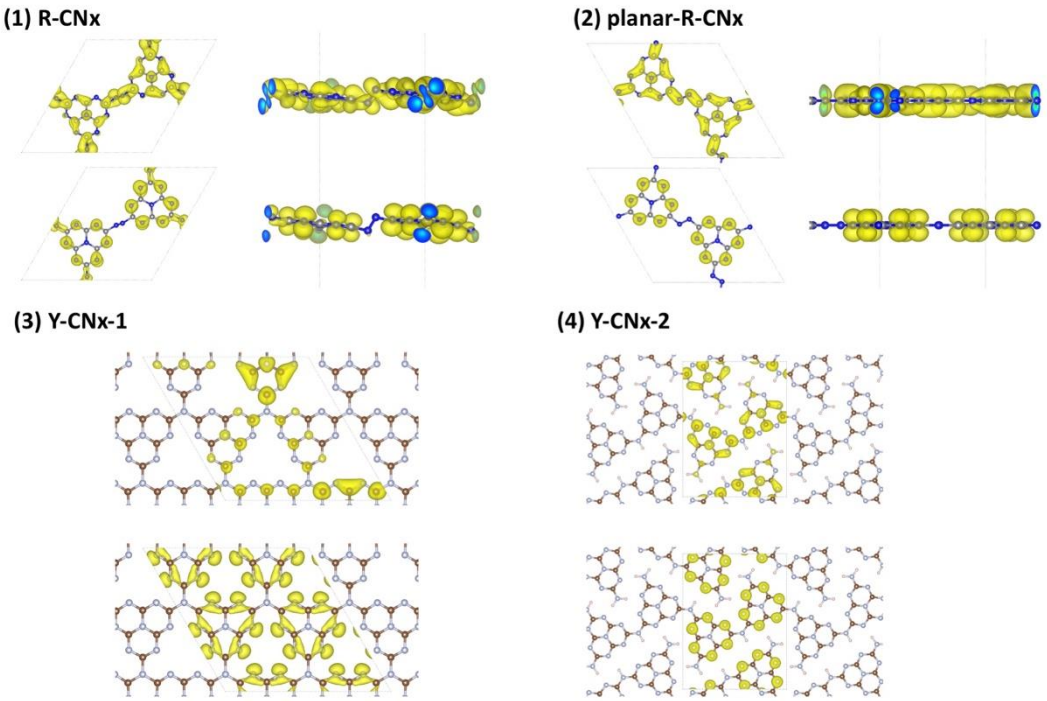

Figure S12. Charge densities at VBM (bottom) and CBM (top). The blue color is for nitrogen and the silver is for carbon.

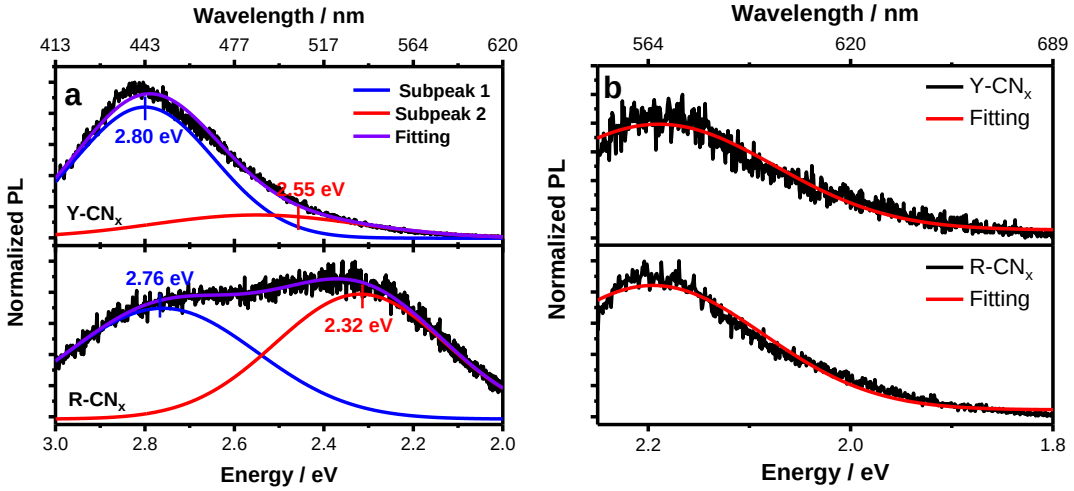

Figure S13. Gaussian fit of time-resolved emission spectra of dropcasted Y-CN$_x$ and R-CN$_x$ under 385 nm (a) with the high energy (blue line) and low energy (red line) PL centers and under 520 nm excitation.

4.4 Water-Soluble Polymeric Carbon Nitride Colloidal Nanoparticles for Highly Selective Quasi-Homogeneous Photocatalysis

The following article is reprinted without changes from Dr. Igor Krivtsov, Dr. Dariusz Mitoraj, Christiane Adler, Dr. Marina Ilkaeva, Dr. Mariana Sardo, Dr. Luís Mafra, Christof Neumann, Prof. Andrey Turchanin, Chunyu Li, Prof. Benjamin Dietzek, Robert Leiter, Dr. Johannes Biskupek, Prof. Ute Kaiser, **Changbin Im**, Björn Kirchhoff, Prof. Timo Jacob, Prof. Radim Beranek.

"Watersoluble polymeric carbon nitride colloidal nanoparticles for highly selective quasihomogeneous photocatalysis." *Angewandte Chemie International Edition* 59.1 (2020): 487-495, DOI:10.1002/anie.201913331.

Copyright 2019 The Authors. Published by Wiley-VCH Verlag GmbH & Co. KGaA.

This is an open access article under the terms of the Creative Commons Attribution License, which permits use, distribution and reproduction in any medium, provided the original work is properly cited. (CC BY 4.0, https://creativecommons.org/licenses/by/4.0)

Author contributions: Changbin Im performed all the calculations. The manuscript was written through contributions of all authors. All authors discussed the results and commented on the manuscript.

Water-Soluble Polymeric Carbon Nitride Colloidal Nanoparticles for Highly Selective Quasi-Homogeneous Photocatalysis

4.4.1 Abstract

Heptazine-based polymeric carbon nitrides (PCN) are promising photocatalysts for light-driven redox trans- formations. However, their activity is hampered by low surface area resulting in low concentration of accessible active sites. Herein, we report a bottom-up preparation of PCN nano- particles with a narrow size distribution (*ca.* 10 $\pm$3 nm), which are fully soluble in water showing no gelation or precipitation over several months. They allow photocatalysis to be carried out under quasi-homogeneous conditions. The superior per- formance of water-soluble PCN, compared to conventional solid PCN, is shown in photocatalytic H_2O_2 production via reduction of oxygen accompanied by highly selective photo-oxidation of 4-methoxybenzyl alcohol and benzyl alcohol or lignocellulose-derived feedstock (ethanol, glycerol, glucose). The dissolved photocatalyst can be easily recovered and re- dissolved by simple modulation of the ionic strength of the medium, without any loss of activity and selectivity.

4.4.2 Conclusion

A facile low-temperature bottom-up synthesis of water- soluble heptazine-based polymeric carbon nitride exhibiting high photocatalytic activity and selectivity is reported for the first time. Our structural investigations and theoretical calculations suggest that the water solubility and excellent stability of colloidal solutions of K,Na-poly(heptazine imide), in contrast to conventional insoluble PCN materials, is conditioned by a decreased number of terminal NHx-groups which are exchanged for cyamelurate moieties. These neg- atively charged surface functional groups interact preferen- tially with water, in particular with water molecules of the tight hydration shell of Na+ ions,

which, in turn, leads to formation of an effective hydration layer on the surface of K,Na-PHI nanoparticles and thus precludes the hydrogen- bonding between the heptazine units that would otherwise cause coagulation and precipitation. The superior performance of these K,Na-PHI nanoparticles compared to conven- tional solid PCN, is demonstrated in photocatalytic synthesis of H_2O_2, via reduction of oxygen accompanied by highly selective (up to 100 %) photoreforming of 4-methoxybenzyl alcohol, benzyl alcohol, and biomass-derived feedstocks (ethanol, glycerol, glucose). The dissolved photocatalyst can be easily separated from the reaction medium by increasing the ionic strength of the solution, and repeatedly used in consecutive reaction cycles without any change in particle size or any noticeable loss in activity or selectivity. This work thus establishes a new method of easily operable quasi-homoge- neous photocatalysis with carbon nitrides and paves the way for the use of water-soluble carbon nitrides in applications in which liquid aqueous processing or operation is mandatory.

4.4.3 Contribution to the Conclusion

In this study, I contributed to the theoretical investigation of the solvent-induced stabilization effects on PHI model systems by employing density functional theory (DFT) calculations with an implicit solvation approach. My work focused on comparing the stability of a periodic PHI model in various solvent environments, including water, acetonitrile, and methanol. The analysis revealed that water provides the highest stabilization compared to acetonitrile or methanol, as quantified in Table S5. Additionally, I identified a trend where the stabilization effect increases with the incorporation of oxygen-containing moieties in place of NH_2 groups. Through this contribution, I was able to validate the hypothesis that solvent environment and specific functional group modifications play a critical role in enhancing the stability of PHI systems, thereby advancing our understanding of their chemical behavior in different conditions.

Check for updates

Photocatalysis

International Edition: DOI: 10.1002/anie.201913331
German Edition: DOI: 10.1002/ange.201913331

Water-Soluble Polymeric Carbon Nitride Colloidal Nanoparticles for Highly Selective Quasi-Homogeneous Photocatalysis**

Igor Krivtsov, Dariusz Mitoraj, Christiane Adler, Marina Ilkaeva, Mariana Sardo, Luís Mafra, Christof Neumann, Andrey Turchanin, Chunyu Li, Benjamin Dietzek, Robert Leiter, Johannes Biskupek, Ute Kaiser, Changbin Im, Björn Kirchhoff, Timo Jacob, and Radim Beranek**

Abstract: *Heptazine-based polymeric carbon nitrides (PCN) are promising photocatalysts for light-driven redox transformations. However, their activity is hampered by low surface area resulting in low concentration of accessible active sites. Herein, we report a bottom-up preparation of PCN nanoparticles with a narrow size distribution (ca. 10 ± 3 nm), which are fully soluble in water showing no gelation or precipitation over several months. They allow photocatalysis to be carried out under quasi-homogeneous conditions. The superior performance of water-soluble PCN, compared to conventional solid PCN, is shown in photocatalytic H_2O_2 production via reduction of oxygen accompanied by highly selective photooxidation of 4-methoxybenzyl alcohol and benzyl alcohol or lignocellulose-derived feedstock (ethanol, glycerol, glucose). The dissolved photocatalyst can be easily recovered and redissolved by simple modulation of the ionic strength of the medium, without any loss of activity and selectivity.*

Introduction

Since the discovery of the photocatalytic activity of polymeric carbon nitride (PCN),[1] numerous top-down[2] and bottom-up[3] synthetic strategies aiming to disrupt the strong hydrogen bonding and van der Waals stacking in bulk-PCN have been reported. These efforts aim at improving the dispersibility of PCN in the reaction medium and to enhance the photocatalytic performance by increasing the number of accessible surface active sites. While top-down methods (e.g., sonication, heat and/or acid treatment) providing low-molecular weight materials were at least partially effective for achieving this goal, they unavoidably led to reduced yields of the catalyst due to losses occurring during exfoliation[4] or etching[5] and could not achieve truly homogeneous nanoparticles solutions. Another approach is based on breaking of H-bonds in bulk-PCN by dissolving it in appropriate solvents such as concentrated sulfuric acid[6] or sulfonic acid derivatives,[7] which destroys the polymeric structure leading to the formation of discrete PCN species (less than ca. 1 nm size) and limits the application of the dissolved photocatalyst to aggressive media. Highly alkaline conditions were also applied to obtain water-soluble PCN, however, no photocatalytic activity of the derived gels was reported.[8] Recent efforts regarding bottom-up synthesis of water-soluble or highly-dispersed PCN include templating,[9] high-temperature

[*] Dr. I. Krivtsov
Department of Organic and Inorganic Chemistry, University of Oviedo-CINN
33006 Oviedo (Spain)
E-mail: krivtsovigor@uniovi.es

Dr. I. Krivtsov, Dr. D. Mitoraj, C. Adler, C. Im, B. Kirchhoff, Prof. T. Jacob, Prof. R. Beranek
Institute of Electrochemistry Ulm University
Albert-Einstein-Allee 47, 89081 Ulm (Germany)
E-mail: radim.beranek@uni-ulm.de

Dr. M. Ilkaeva, Dr. M. Sardo, Dr. L. Mafra
CICECO—Aveiro Institute of Materials, Department of Chemistry University of Aveiro
Campus Universitário de Santiago, 3810-193 Aveiro (Portugal)

C. Neumann, Prof. A. Turchanin, C. Li, Prof. B. Dietzek
Institute of Physical Chemistry and Abbe Center of Photonics Friedrich Schiller University Jena
Lessingstrasse 10, 07743 Jena (Germany)

C. Neumann, Prof. A. Turchanin, Prof. B. Dietzek
Center for Energy and Environmental Chemistry Jena (CEEC Jena)
Philosophenweg 7a, 07743 Jena (Germany)

C. Li, Prof. B. Dietzek
Department Functional Interfaces, Leibniz Institute of Photonic Technology (IPHT)
Albert-Einstein-Strasse 9, 07745 Jena (Germany)

R. Leiter, Dr. J. Biskupek, Prof. U. Kaiser
Electron Microscopy of Materials Science, Central Facility for Electron Microscopy, Ulm University
Albert-Einstein-Allee 11, 89081 Ulm (Germany)

B. Kirchhoff
Science Institute, University of Iceland
Dunhaga 5, 107, Reykjavík (Iceland)

Prof. T. Jacob
Helmholtz-Institute-Ulm (HIU)
Helmholtzstrasse 11, 89081 Ulm (Germany)
and
Karlsruhe Institute of Technology (KIT)
P.O. Box 3640, 76021 Karlsruhe (Germany)

[**] A previous version of this manuscript has been deposited on a preprint server (https://doi.org/10.26434/chemrxiv.9879947.v1).

Supporting information and the ORCID identification number(s) for the author(s) of this article can be found under: https://doi.org/10.1002/anie.201913331.

© 2019 The Authors. Published by Wiley-VCH Verlag GmbH & Co. KGaA. This is an open access article under the terms of the Creative Commons Attribution License, which permits use, distribution and reproduction in any medium, provided the original work is properly cited.

synthesis in salt melts,[10] electrochemical poly(triazine imide) preparation,[11] sol-gel chemistry using self-induced gelation, occurring within several days, of poly(heptazine imide) hydrosols prepared by the KSCN-assisted condensation of melamine,[12] and formation of water-soluble PCN "quantum dots", which were highly luminescent, but found to be photocatalytically inactive[13] or their photocatalytic activity was not reported.[2b,3b,14]

Herein, we report, for the first time, a facile and high-yield preparation of PCN nanoparticles with a narrow size distribution (ca. 10 ± 3 nm), which are fully soluble in water showing no gelation or precipitation over several months, and allow carrying out highly efficient photocatalysis under quasi-homogeneous conditions. The enhanced performance of this material, as compared to the conventional solid PCN, is demonstrated in dual-product photocatalysis involving highly selective (up to 100%) photooxidation of one of the lignin model compounds 4-methoxybenzyl alcohol (4MBA)[15] to 4-methoxybenzaldehyde (4MBAL), concurrent with highly selective (≥ 70%) reduction of O_2 to H_2O_2, another highly valuable chemical feedstock with a market price higher than, for example, methanol. In addition, the superior photoactivity of water-soluble PCN is confirmed by enhanced H_2O_2 production rates using also benzyl alcohol and lignocellulose-derived feedstock as alternative reducing agents (ethanol, glycerol, glucose). Finally, we provide a very simple protocol for recovery and re-dissolution of the water-soluble photocatalyst, which enables easy handling and excellent recyclability of our photocatalyst under quasi-homogeneous operation conditions without any apparent loss of activity and selectivity.

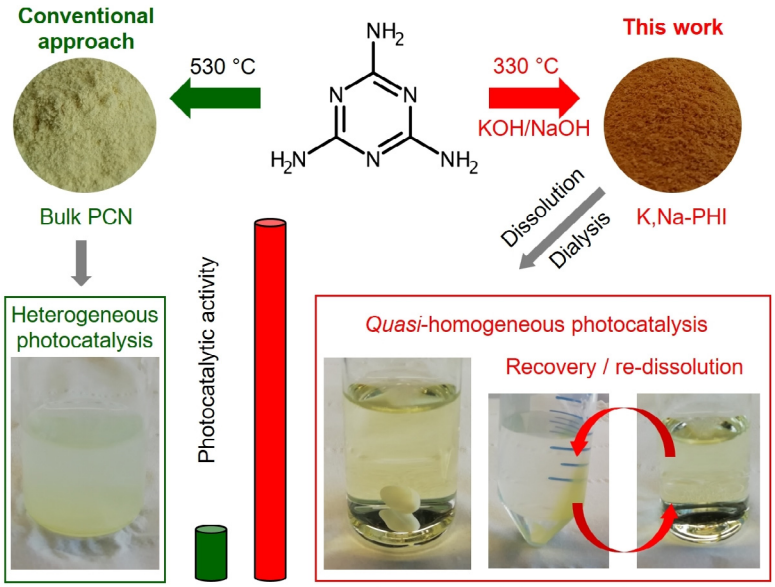

Figure 1. Alkali poly(heptazine imide) is synthesized at comparatively low temperature (330 °C) using a KOH/NaOH melt; after dissolution and dialysis the resulting material is a water-soluble photocatalyst, more active than the bulk PCN, and easily recovered (by increasing the ionic strength via addition of NaCl) and dissolved again, thus enabling recyclability without any loss of activity and selectivity.

Results and Discussion

Synthesis and Characterization

Figure 1 shows a schematic representation of the synthesis procedure resulting in a highly active water-soluble and recoverable PCN photocatalyst. Instead of using conventional metal halide-based solvents applied for the preparation of poly(triazine imides) and poly(heptazine imides),[16] or alkali-metal hydroxides at high temperature,[17] the use of a KOH/NaOH melt allowed us to reduce the temperature of melamine condensation to PCN structures from the usual range of 500–600 °C, or 450 °C reported by Wang et al. for the case of KSCN solvent,[12] down to 330 °C.

The use of KOH at loadings as low as 12.5 mmol (per 1.5 g ca. 12 mmol melamine) in the synthesis yields mostly insoluble potassium poly(heptazine imide) (K-PHI-S) (see Supporting Information, Table S1), while higher loadings (above 15 mmol) result in the formation of a pale-yellow potassium poly(heptazine imide) solution (K-PHI) with very low yield (< 9%). The use of NaOH leads to a water-soluble sodium poly(heptazine imide) (Na-PHI) even at low NaOH quantities (5 mmol), most likely due to its lower melting point, while higher concentrations in the melt induce the degradation of melamine and, consequently, a drastic decrease of the poly(heptazine imide) yield (< 4%; Table S1). The yields of the corresponding dialysed and dried material were highest for melamine condensation in a 10 mmol:5 mmol KOH/NaOH melt (yields up to 42%). The resulting mixed potassium/sodium poly(heptazine imide) (K,Na-PHI) material is water-soluble with a clearly observable Tyndall effect (Figure S1). Thermal analysis of the precursor mixture (melamine + KOH/NaOH) shows two main stages of mass loss at 150 and 280 °C assigned to H_2O evolution and to melamine deammonification, respectively (Figure S2). The presence of hydroxides in the melt catalyses the condensation of melamine, thus reducing the synthesis temperature of poly(heptazine imide) to 330 °C. This is, to our knowledge, the lowest temperature reported for the solid-state synthesis of heptazine-based PCN materials. The obtained solid (K-PHI-S) and dried solutions of the poly(heptazine imide) after dialysis (K,Na-PHI) show XRD patterns typical for conventional bulk melamine-derived PCN (melon, here designated as CN sample) and low-crystalline poly(heptazine imide) materials with an interlayer spacing of about 3.0 Å and a (100) reflection at 8.9 Å resulting from alkali metal cations incorporated into the poly(heptazine imide) structure[18] (Figure 2a, Figures S3, S4). The structure of the prepared solid K-PHI-S and dried K,Na-PHI samples is also confirmed by FTIR spectra showing a typical fingerprint of PCN materials in the range of 1200 to 1700 cm^{-1}, corresponding mostly to υ(C-NH-C) and υ(C=N) stretching vibrations, and a peak at 800 cm^{-1} attributed to the triazine ring breathing

 © 2019 The Authors. Published by Wiley-VCH Verlag GmbH & Co. KGaA, Weinheim

15213773, 2020, 1, Downloaded from https://onlinelibrary.wiley.com/doi/10.1002/anie.201913331 by KIZ der Universitat Ulm, Wiley Online Library on [19/08/2024]. See the Terms and Conditions (https://onlinelibrary.wiley.com/terms-and-conditions) on Wiley Online Library for rules of use; OA articles are governed by the applicable Creative Commons License

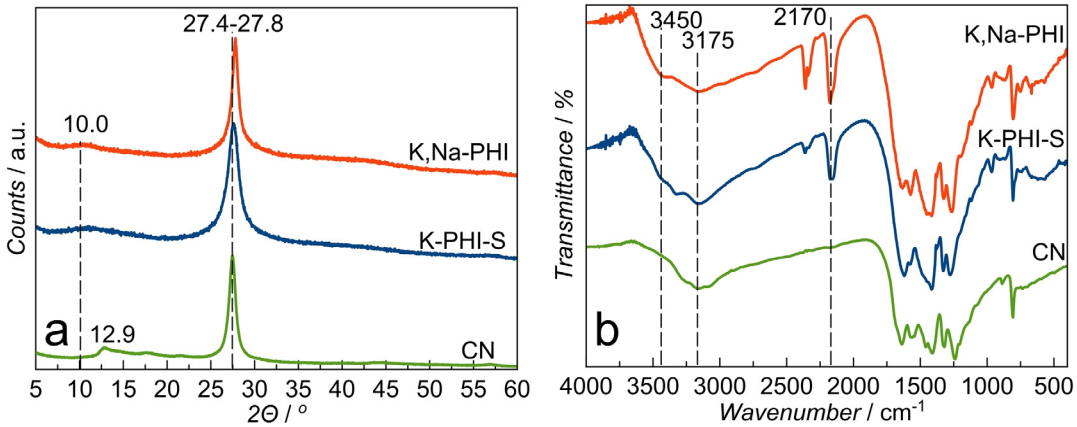

Figure 2. XRD patterns (a) and FTIR spectra (b) of the materials measured after dialysis and drying.

mode.[18] The peak at 3450 cm^{-1}, visible only for K,Na-PHI and K-PHI-S (Figure 2b), may be assigned to the stretching vibrations of OH-groups incorporated into the poly(heptazine imide) structure as a result of the alkali melt treatment. Additionally, in the range 2150–2175 cm^{-1}, υ(C≡N) vibrations are clearly present in the spectra of the samples prepared in hydroxide melts (Figure 2b). The same peak assignments can be made regarding the FTIR spectra of K-PHI and Na-PHI (Figure S5).

From all the synthesised series the samples K-PHI-S and K,Na-PHI were chosen for the detailed investigation as being the representatives of insoluble and soluble poly(heptazine imides; Table S1). These materials possess a high thermal stability typical for other PCNs, starting to decompose only at temperatures of about 600 °C (Figure S6). CHN elemental analysis of the K,Na-PHI and K-PHI-S samples shows C:N ratios of 0.67 and 0.72, respectively, which are typical for poly(heptazine imide) materials. The reduced concentration of H and the increased C:N ratio observed for K,Na-PHI might indicate a partial loss of NH_2-containing species due to polymer hydroxylation and/or lower fragmentation of the polyheptazine network (Table S2). The EDX elemental analysis reveals that the content of alkali metals and oxygen is doubled in K,Na-PHI with respect to K-PHI-S (Table S2). This might be attributed not only to the higher number of surface oxygen-containing functional groups, but also to increased amounts of chemisorbed water and CO_2, whose presence might be responsible for the formation of alkali-metal hydroxides or carbonates melting at high temperature (Figure S6).

To obtain further insight into the chemical structure of the materials, solid-state NMR analysis was carried out. ^{13}C NMR direct excitation of the K,Na-PHI sample shows a series of resonances at 122, 156, 163, 165, 168, and 169–174 ppm, which are assigned to the carbon atoms in C≡N (**1**), N–C=N (**3**), C-N_2(NH) (**4**), C-N_2(NH_2) (**5**), C-O^- (**6**) and C-N^- groups (**7**), likely found in different environments (Figures 3a,c, Figure S7).[16,19] The presence of CO_3^{2-} species cannot be excluded as its chemical shift coincides with resonances **6** and **7**. The presence of non-protonated N–C=N (**3**) groups suggests the poly(heptazine) nature of the material, although a possible admixture of poly(triazine) units cannot be ruled out completely. In ^1H-^{13}C cross-polarization (CP) magic-angle spinning (MAS) NMR spectra of K-PHI-S and K,Na-PHI the resonances ascribed to carbons **4** and **5** are significantly increased with respect to the other resonances (CPMAS and MAS, Figure 3a), while this is not the case for resonances **1**, **3**, **6**, and **7**. A new resonance emerges at 151 ppm (**2**) in the ^1H-^{13}C CPMAS spectrum of the K,Na-PHI sample, while it is less pronounced for the K-PHI-S sample (Figures 3a,c, Figure S7). This resonance is tentatively attributed either to the C-OH group of the aromatic poly(heptazine imide) structure or to the deprotonated analogous, that is, C-O^- moieties H-bonded to NH_x resulting from drying and polymerization. A similar observation was made for crystalline potassium cyamelurates and cyameluric acid.[20] A distinguishable shoulder, at 165 ppm (**5**), is observed at the left side of the ^{13}C resonance **4** (ca. 163 ppm) for K-PHI-S (Figure 3a), which corresponds to N_2C-(NH_2) and N_2C-(NH) species, respectively. Notably, the resonance at 165 ppm (**5**), observed in K-PHI-S, is drastically reduced for K,Na-PHI (Figures 3a,c, Figure S7). Resonance **6** at about 168 ppm, observed from the ^{13}C MAS spectrum of K,Na-PHI is not enhanced on the ^1H-^{13}C CPMAS spectrum, suggesting the lack of protons in the vicinity of this functional group. This supports the assignment of **6** to C-O^- stabilized by K^+ or Na^+, such as in the $[C_6N_7O_3]^{3-}$ groups of $K_3[C_6N_7O_3] \times H_2O$.[21] The ^1H-^{15}N CPMAS spectra of K,Na-PHI and K-PHI-S show three resonances at −275, −246, and −191 ppm assigned to NH_2, NH and heptazine secondary amines (N_{hept}), respectively. Although CPMAS is not quantitative, the NH_2/NH intensity ratio of the K,Na-PHI sample is much smaller than that of K-PHI-S; we hypothesize that NH_2 groups are consumed due to reaction with KOH/NaOH (Figure 3b,c). Also, a shoulder at −257 ppm, attributed to -N=C-OH(NH) can be observed in the spectrum of the K,Na-PHI sample (Figure S7). A quantitative estimation based on the ^{13}C direct excitation MAS spectra (Supporting Information, NMR study, Table S3, Figure S7) suggests that the formation of heptazine species (Figure S8) is favoured for the case of the K,Na-PHI sample, resulting in an increased number of N–C=N (**3**) carbons in K,Na-PHI as compared to K-PHI-S (Table S3, Figure S7). The lower concentration of terminal -NH_2 moieties in K,Na-PHI will likely lead to an overall decrease of the number of hydrogen bonds in the

 © 2019 The Authors. Published by Wiley-VCH Verlag GmbH & Co. KGaA, Weinheim

15213773, 2020, 1, Downloaded from https://onlinelibrary.wiley.com/doi/10.1002/anie.201913331 by KIZ der Universitat Ulm, Wiley Online Library on [19/08/2024]. See the Terms and Conditions (https://onlinelibrary.wiley.com/terms-and-conditions) on Wiley Online Library for rules of use; OA articles are governed by the applicable Creative Commons License

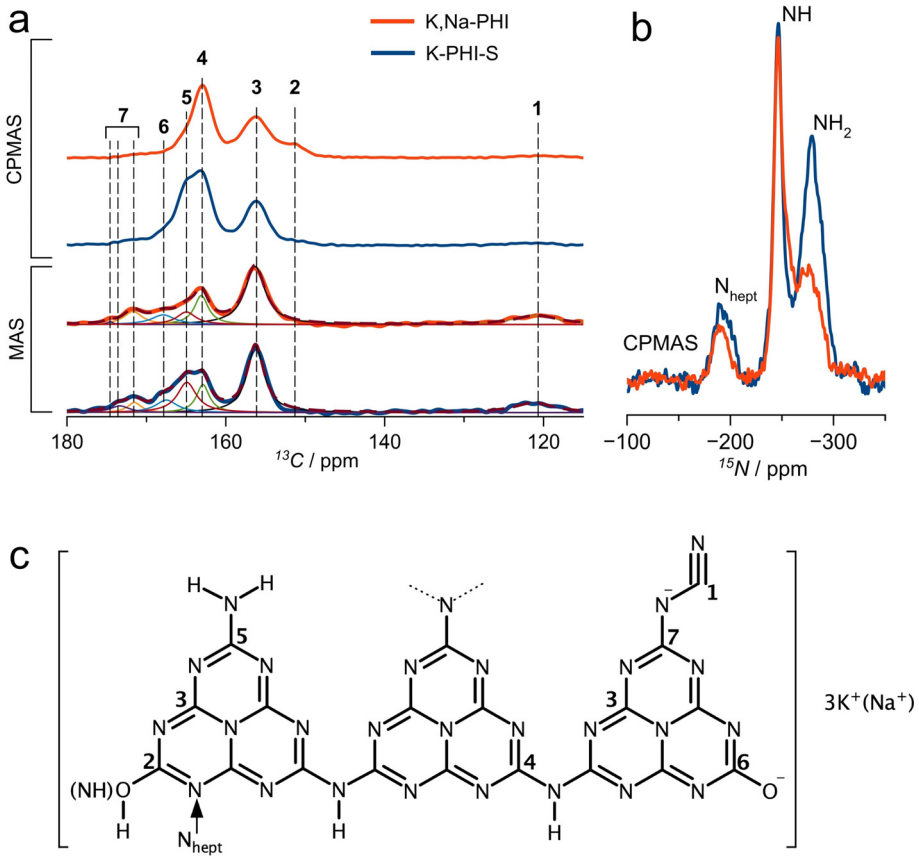

Figure 3. a) ^{13}C direct excitation MAS and ^{1}H-^{13}C CPMAS b) ^{1}H-^{15}N CPMAS NMR spectra of K-PHI-S and K,Na-PHI and c) schematic representation of the functionalized PCN and atom numbering scheme. ^{13}C MAS spectra (a) have been deconvoluted showing the different components assigned to the carbon atoms depicted in (c).

polymer network, thus exerting a direct influence on aggregation and solubility.

The X-ray photoelectron spectroscopy (XPS) data corroborate the presence of C-O$^-$ species in both analysed samples (Figure S9, Table S4) and indicate the redistribution of N-containing groups for the material prepared using KOH/NaOH mixture (Figure S9 e,f, Table S4). Although C1s XP spectra confirm the presence of N–C=N bonds, they do not allow unambiguous assignment of the peak at 286.2 eV that may be attributed to C-NH$_x$ and C-O$^-$ groups (Figure S9, Table S4). The N1s spectra reveal a different distribution of the N-containing species in K-PHI-S and K,Na-PHI. Based on integrated peak intensities, the increased contribution of the peak (C–N=C plus C≡N (N1)) with respect to those attributed to N-C$_3$ plus triazine C-NH$_x$ (N2) and heptazine C-NH$_x$ (N3) suggests a higher relative content of N belonging to the PCN aromatic structure in the K,Na-PHI material. This indicates a higher degree of condensation (Figure S9, Table S4). The O1s spectrum also exhibits an additional band at 531.0 eV in K,Na-PHI which can be tentatively assigned to CO$_2$ chemisorbed by the alkali metal ions present in higher quantities than in the K-PHI-S sample or to the hydroxylated carbon nitride species.

Summarizing, we hypothesize that the insoluble K-PHI-S material prepared in KOH melt has a poly(heptazine imide) structure bearing NH, -NH$_2$ groups, uncondensed NH$_x$-containing triazine species and oxygenated surface moieties in the form of cyamelurate fragments. The water-soluble K,Na-PHI prepared in KOH/NaOH mixture is also composed of a poly(heptazine imide) network. However, it is suggested to have a higher number of heptazine nitrogen atoms owing to a higher degree of triazine-to-heptazine condensation and a much smaller number of terminal amines resulting in weaker H-bonding between the poly(heptazine) layers. This, in combination with the presence of terminal cyamelurate functional groups in the material facilitating the formation of a solvent structure around the K,Na-PHI particles, rationalizes its high solubility in water. The dissolved K,Na-PHI has a zeta potential of −31 mV at pH of 7.5; this is a typical value for PCN-derived materials[22] which are prone to agglomeration in suspensions due to strong H-bonding between the terminal NH$_x$ species and the N atoms of the heptazine units. This means that electrostatic repulsion alone cannot be entirely responsible for the excellent dispersion of K,Na-PHI in water. We speculate that in K,Na-PHI, the cyamelurate C-O$^-$ groups are stabilized by H-bonds mainly with water molecules from the well-ordered hydration shell of the Na$^+$ ion. At low concentrations, Na$^+$ ions will therefore promote formation of a hydration layer at the PHI surface which improves solubility. With increasing Na$^+$ concentration the hydration layer will gradually be stripped causing coalescence due to positive van der Waals forces (see Figure S10). Notably, we have not found any appreciable solubility of K,Na-PHI in most of the common polar or non-polar organic solvents. This corroborates our assumption that the cyamelurate-functionalities of K,Na-PHI specifically interact with water creating a water solvation shell, which hinders the formation of H-bonds with other dissolved species and increases the electrostatic repulsion between nanoparticles due to the negative surface charge.

DFT calculations using an implicit solvation approach on a periodic PHI model are in agreement with this hypothesis (see Supporting Information, Theoretical study of K,Na-PHI). By comparing the stability of the model system (Figure S11) in water, acetonitrile, or methanol environments, we find that water will lead to a higher stabilization than acetonitrile, or methanol (Table S5). Further, we find that stabilization increases with the number of oxygen-containing (exchanged for –NH$_2$) moieties.

 © 2019 The Authors. Published by Wiley-VCH Verlag GmbH & Co. KGaA, Weinheim

15213773, 2020, 1, Downloaded from https://onlinelibrary.wiley.com/doi/10.1002/anie.201913331 by KIZ der Universitat Ulm, Wiley Online Library on [19/08/2024]. See the Terms and Conditions (https://onlinelibrary.wiley.com/terms-and-conditions) on Wiley Online Library for rules of use; OA articles are governed by the applicable Creative Commons License

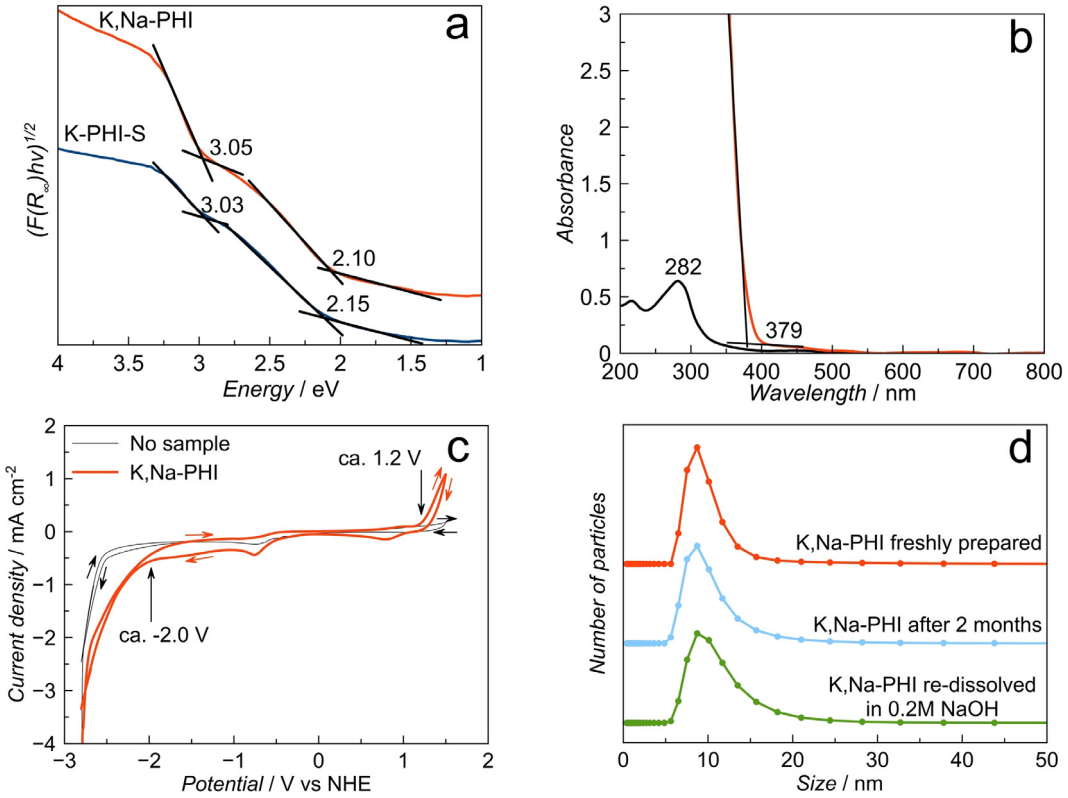

Figure 4. a) Diffuse reflectance UV/Vis spectra of the solid K-PHI-S and dried K,Na-PHI samples transformed using the Tauc formalism for the determination of absorption edges. b) UV/Vis electronic absorption spectra of K,Na-PHI dissolved in water at concentrations of 0.005 and 0.75 g L^{-1}. c) Cyclic voltammetry (50 mV s^{-1}, 0.1 M $TBAPF_6$ in acetonitrile) of the K,Na-PHI sample deposited on a glassy carbon electrode. d) Particle size distribution of the K,Na-PHI samples measured by DLS.

The analysis of electronic absorption properties of the dried poly(heptazine imide) samples using diffuse reflectance spectroscopy shows the presence of two optical absorption edges at 2.1–2.2 and 3.0 eV (Figure 4a). In contrast, the electronic absorption UV/Vis spectra taken from dissolved K,Na-PHI in water do not exhibit any significant light absorption in the visible range (Figure 4b). However, it is clear that a maximum absorption edge appears in the UV range (285 nm) under dilute conditions, while in concentrated solution the absorption edge shifts to 379 nm corresponding to about 3.3 eV (Figure 4b). The absorption at 285 nm can be attributed to the cyamelurate species present in K,Na-PHI.[20a] The slightly lower-energy absorption edge value of 3.0 eV measured in the solid-state as well as the appearance of the additional absorption edge at 2.1 eV might be attributed to the stacking or coalescence of the poly(heptazine imide) units, contrary to what is observed for the well-separated nanoparticles in a colloidal solution. The cyclic voltammetry study of the K,Na-PHI sample is in agreement with the energy gap determined by the optical method, showing the HOMO and LUMO positions at 1.2 V and −2.0 V versus normal hydrogen electrode (NHE), respectively (Figure 4c). The water-soluble K,Na-PHI nanoparticles prepared in this work show a relatively narrow size distribution (ca. 6–20 nm) as determined by dynamic light scattering (DLS; Figure 4d). The mean particle size of the sample is around 10 ± 3 nm (Figure 4d). The alkali poly(heptazine imide) materials prepared using only NaOH or only KOH (Na-PHI or K-PHI) demonstrate slightly broader size distribution (Figure S12). The Na,K-PHI particles are stable in water-based media for several months without suffering agglomeration. Notably, the dried material can also be redissolved in 0.2 M NaOH exhibiting a nearly identical particle size distribution, which confirms that the water-soluble PCN nanoparticles retain their morphological and structural integrity (Figure 4d).

The coalescence of dissolved particles after drying results in almost featureless SEM images, not showing any definite morphology (Figure S13). Although we were unable to obtain high-resolution TEM images due to significant beam damage to the samples, fibre-like morphology of the sample prepared from a dilute solution of K,Na-PHI dried on the microscope grid is noted (Figure S14). The thickness of the fibres is estimated to be about 10 nm, which is in agreement with the data from dynamic light scattering (Figure 4d). Note, however, that it cannot be ruled out that the observed morphology results from coalescence of the particles during the drying on the grid. We speculate that fibre net observed in TEM image is a result of the anisotropy of the original PHI particles causing directional agglomeration.

 © 2019 The Authors. Published by Wiley-VCH Verlag GmbH & Co. KGaA, Weinheim

15213773, 2020, 1, Downloaded from https://onlinelibrary.wiley.com/doi/10.1002/anie.201913331 by KIZ der Universitat Ulm, Wiley Online Library on [19/08/2024]. See the Terms and Conditions (https://onlinelibrary.wiley.com/terms-and-conditions) on Wiley Online Library for rules of use; OA articles are governed by the applicable Creative Commons License

15213773, 2020, 1, Downloaded from https://onlinelibrary.wiley.com/doi/10.1002/anie.201913331 by KIZ der Universitat Ulm, Wiley Online Library on [19/08/2024]. See the Terms and Conditions (https://onlinelibrary.wiley.com/terms-and-conditions) on Wiley Online Library for rules of use; OA articles are governed by the applicable Creative Commons License

Photocatalytic studies

Pristine and modified PCNs are well-known photocatalysts for partial photooxidation of organic molecules,[23] and methoxy-substituted aromatic alcohols in particular,[24] which opens the route for synthesis of high-value chemicals from low-value feedstock using only sunlight or cost-effective light sources (e.g., LED arrays) and easily available oxidizing agents such as aerial oxygen. The water-soluble colloidal PCN nanoparticles prepared in this work allow, for the first time, photocatalysis to be performed with PCN under quasi-homogeneous conditions. The optimization of the photocatalyst concentration in the reaction mixture was carried out for the solid K-PHI-S and the water soluble K,Na-PHI samples, resulting in optimal loadings of 0.5 $g\,L^{-1}$ and 0.75 $g\,L^{-1}$, respectively (Figures S15, S16). The photocatalytic performance of other water-soluble samples (K-PHI and Na-PHI) was lower or equal to that of K,Na-PHI (Figure S17), henceforth we focus on the photocatalytic properties of K,Na-PHI, which can be obtained in much higher synthetic yields. Initial tests for selective photooxidation of 4MBA to 4MBAL in water have demonstrated increased activity of K-PHI-S and K,Na-PHI with respect to the conventional PCN (CN sample) by factors of 2.1 and 2.8 under heterogeneous and quasi-homogeneous conditions, respectively (Figure 5a, Figure S18, Table S6). Notably, formation of the aldehyde is accompanied by two-electron reduction of O_2, producing hydrogen peroxide,[25] another highly valuable compound. The control experiments in the dark, with the K,Na-PHI and CN photocatalysts as well as 4MBA photolysis in the absence of any photocatalysts, showed that 4MBA oxidation was negligible under such conditions, and no formation of H_2O_2 was observed (see Supporting information). Additional control experiments under the flow of argon (to avoid the presence of oxygen) showed, as expected, that the H_2O_2 production was negligible (Figure S19). The 4MBAL production dropped significantly (by $>60\,\%$) and was clearly accompanied by reduction of the photocatalyst as its colour turned from yellow to brown, whereby this colour change disappeared after the exposure to air. This is an indication of photogenerated electrons being stored in the form of K,Na-PHI radicals, which was reported earlier for this type of materials.[26]

Using a purely aqueous solvent, the selectivity towards both target molecules after 4 h of irradiation is lower for the most active K,Na-PHI sample as compared to the benchmark CN photocatalyst (Figure 5a, Figure S18, Table S6). Addition of acetonitrile (MeCN), whereby the quasi-homogeneous reaction conditions are retained below 50 vol% of MeCN (Figures S20, S21), was found to significantly increase both activity and selectivity. We hypothesise that addition of MeCN accelerates desorption of the less polar aldehyde from the K,Na-PHI surface (Figure 5a, Figure S18, Table S6). The heterogenization of the reaction medium occurring at concentrations of MeCN >50 vol% (Figures S20, S21) is detrimental for the photocatalytic activity (Figure 5a, Figure S18, Table S6), which confirms the beneficial effect of running the reaction under quasi-homogeneous conditions. Under optimal reaction conditions (40 vol% of MeCN), the pseudo-first order rate constant (k) of 4MBA oxidation was increased by a factor of 2.3 and 6.5 compared to the results for K,Na-PHI and for a conventional CN photocatalyst in H_2O, respectively. Furthermore, selectivities towards the reaction products 4MBAL (91 %) and H_2O_2 (76 %) were enhanced (Figure 5a, Figure S18, Table S6). We point out that at lower conversion degrees (50 %) of 4MBA the selectivity is about 97 % and at even lower conversion levels it reaches up to 100 % (Figure S18, Table S6). It should also be noted that the catalytic performance of the solid heterogeneous photocatalysts, conventional CN and K-PHI-S, is practically not affected by the presence of the organic solvent in the reaction mixture (Figure S22).

Interestingly, the quasi-homogeneous nature of the photocatalytic systems allows to reduce the scattering effects on the suspended particles compared to conventional heterogeneous photocatalysis, improving the reliability of quantum yield estimations for this system (see the Supporting Information). The K,Na-PHI photocatalysts exhibited a quantum yield of about 10 % at 365 nm towards the 4MBAL formation, which is a rather respectable value as compared to common heterogeneous photocatalysts that typically show quantum yields of few per cent.[27]

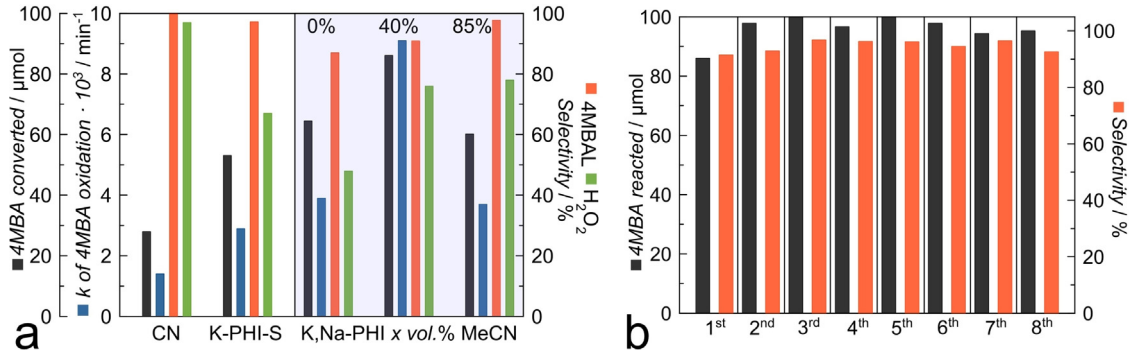

Figure 5. a) Photocatalytic oxidation of 4MBA with simultaneous H_2O_2 formation in H_2O (20 mL, 4MBA 0.1 mmol, pH 6.5–7.0, LED 365 nm, 4 h) and in H_2O/MeCN mixture in the presence of K,Na-PHI (20 mL, x vol% of MeCN, 4MBA 0.1 mmol, LED 365 nm, 4 h) b) recyclability test of the K,Na-PHI samples for 4MBA oxidation (20 mL, H_2O/MeCN(40 vol%), 4MBA 0.1 mmol, pH 6.5–7.0, LED 365 nm, 4 h, 0.125 g of NaCl is added for the photocatalyst recovery).

 © 2019 The Authors. Published by Wiley-VCH Verlag GmbH & Co. KGaA, Weinheim

A typical shortcoming of the practical implementation of homogenous or quasi-homogeneous photocatalysts concerns difficult recovery for reuse. We find that our water soluble K,Na-PHI photocatalyst can be easily recovered by increasing the ionic strength of the solution which causes coagulation and precipitation of K,Na-PHI. This can be achieved by addition of a salt such as NaCl (Figure 1, Figure S10). The photocatalyst can then be centrifuged, separated from the liquid phase, and re-dissolved. With this protocol, the photocatalyst can be reused in water as well as in H_2O/MeCN(40 vol. %) medium for at least eight reaction cycles without any deterioration of its activity or selectivity (Figure 5b, Figure S23).

Note that the superior photocatalytic performance of the water-soluble K,Na-PHI photocatalyst, compared to conventional solid PCN, is not limited to oxidation of 4MBA. Also, benzyl alcohol and lignocellulose-derived feedstocks, such as ethanol, glycerol, and glucose,[28] can act as effective hole scavengers. Using our water-soluble PCN photocatalyst, the H_2O_2 production was enhanced, as compared to the conventional solid PCN, by the factors of 3.9, 3.2, 2.8, and 6.8 in reactions with benzyl alcohol, ethanol, glycerol, and glucose as reducing agents, respectively (Figures S24, S25).

In situ absorption and emission spectroscopy was performed to gain further insight into the photocatalytic performance of the water-soluble K,Na-PHI photocatalyst. Figure 6a shows stable absorption spectra of K,Na-PHI over 4 h, when dissolved in degassed water. Under ambient atmosphere, a slight change of the absorption band at around 280 nm is apparent during the first hour of irradiation. Subsequently, the photoinduced changes in the colloidal solution level off, reaching a state in which the absorption spectrum changes no further. Similar changes are observed in in situ emission spectroscopy, in which the sample is continuously irradiated by an LED at 365 nm, while the fluorescence is intermittently (every 5 min) excited at 275 nm (Figure 6b). In the absence of atmospheric oxygen (spectra recorded at 0, 5, and 10 min) the emission intensity is stable. Upon exposing the sample to air, the emission intensity drops in the course of the first hour, after which the changes level off. These data point to the colloidal nanoparticles solution being a dynamic system in which a stable stationary state develops over time when the system is irradiated while in contact with air. Figure 6c shows a fluorescence titration of K,Na-PHI in water upon addition of 4MBA. Upon addition of the substrate, the emission band associated with the alcohol itself (at 300 nm) increases, while the emission of the K,Na-PHI decreases, indicating interaction of the photoexcited photocatalyst with the substrate. The fact that both dioxygen and 4MBA quench effectively the emission of the photoexcited K,Na-PHI corroborates its high activity in simultaneous photooxidation of 4MBA and reduction of O_2 to H_2O_2.

The high photocatalytic activity of the K,Na-PHI photocatalyst along with its solubility in water represent a great promise for its use in light-driven valorization of low-value feedstock such as insoluble lignocellulosic substrates,[29] where conventional solid-state CN materials would be inefficient due to their low surface area hampering the accessibility of substrates to the active sites. In this context, it is noteworthy that catalysts of PCN family are not only capable of oxidation of benzylic C-OH, but also of benzylic -CH_3 oxidation reactions in model lignin compounds.[30] Finally, we note that while the K,Na-PHI is fully water-soluble in a wide pH range (5–13), it can be converted into a gel simply by adding a strong acid, such as HCl. Therefore, we anticipate that the here presented water-soluble carbon nitrides can be utilized not only in any applications requiring aqueous liquid processing of carbon nitride, but also as building blocks in fabrication of further novel photocatalytic architectures with tailored morphology and porosity using sol-gel chemistry.

Conclusion

A facile low-temperature bottom-up synthesis of water-soluble heptazine-based polymeric carbon nitride exhibiting high photocatalytic activity and selectivity is reported for the first time. Our structural investigations and theoretical calculations suggest that the water solubility and excellent stability of colloidal solutions of K,Na-poly(heptazine imide), in contrast to conventional insoluble PCN materials, is

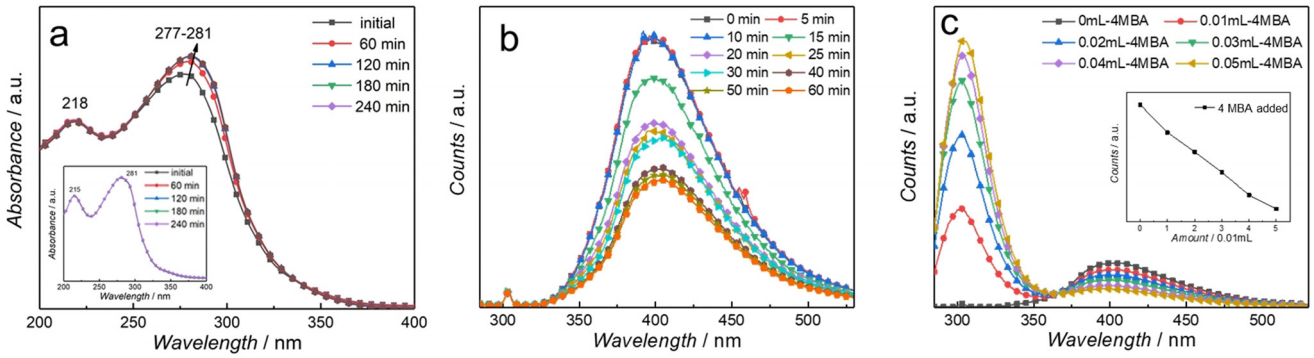

Figure 6. a) in situ UV/Vis spectra of the K,Na-PHI in H_2O recorded during illumination at 365 nm under aerobic and O_2-free (inset) conditions. b) in situ steady-state emission spectra of K,Na-PHI recorded upon fluorescence excitation at 275 nm during external illumination at 365 nm every 5 min in water before (0–10 min) and after applying O_2 (10–60 min). c) in situ steady-state emission spectra of K,Na-PHI (λ_{ex} = 275 nm) dissolved in water with addition of 4MBA (5 mM) during 365 nm illumination. Inset: maximum intensity of the emission band at 402 nm (associated with K,Na-PHI emission) upon addition of various amounts of 4MBA.

 © 2019 The Authors. Published by Wiley-VCH Verlag GmbH & Co. KGaA, Weinheim

15213773, 2020, 1, Downloaded from https://onlinelibrary.wiley.com/doi/10.1002/anie.201913331 by KIZ der Universitat Ulm, Wiley Online Library on [19/08/2024]. See the Terms and Conditions (https://onlinelibrary.wiley.com/terms-and-conditions) on Wiley Online Library for rules of use; OA articles are governed by the applicable Creative Commons License

conditioned by a decreased number of terminal NH_x-groups which are exchanged for cyamelurate moieties. These negatively charged surface functional groups interact preferentially with water, in particular with water molecules of the tight hydration shell of Na^+ ions, which, in turn, leads to formation of an effective hydration layer on the surface of K,Na-PHI nanoparticles and thus precludes the hydrogen-bonding between the heptazine units that would otherwise cause coagulation and precipitation. The superior performance of these K,Na-PHI nanoparticles compared to conventional solid PCN, is demonstrated in photocatalytic synthesis of H_2O_2, via reduction of oxygen accompanied by highly selective (up to 100%) photoreforming of 4-methoxybenzyl alcohol, benzyl alcohol, and biomass-derived feedstocks (ethanol, glycerol, glucose). The dissolved photocatalyst can be easily separated from the reaction medium by increasing the ionic strength of the solution, and repeatedly used in consecutive reaction cycles without any change in particle size or any noticeable loss in activity or selectivity. This work thus establishes a new method of easily operable quasi-homogeneous photocatalysis with carbon nitrides and paves the way for the use of water-soluble carbon nitrides in applications in which liquid aqueous processing or operation is mandatory.

Acknowledgements

This work was funded by the Deutsche Forschungsgemeinschaft (DFG, German Research Foundation)—Projektnummer 364549901—TRR 234 [Projects B6, B7, C3 and Z2] and BE 5102/3-1. We acknowledge also support by Spanish MINECO (MAT2016-78155-C2-1-R) and Gobierno del Principado de Asturias (GRUPIN-ID2018-170), and the project CICECO-Aveiro Institute of Materials, FCT Ref. UID/CTM/50011/2019, financed by national funds through the FCT/MCTES. L.M., M.S., and M.I. also acknowledge the National NMR Network (PTNMR), partially supported by Infrastructure Project N° 022161, and FCT/MCTES for funding (Project PTDC/QEQ-QAN/6373/2014). B.K. acknowledges the University of Iceland Research Fund for support through a PhD fellowship. Computational resources were provided by the state of Baden-Württemberg through bwHPC and the German Science Foundation (DFG) under Grant No. INST 40/467-1 FUGG. C.N. and A.T. acknowledge financial support of the DFG through the project TU 149/8-2 "Towards photoactive membranes for artificial photosynthesis" as well as the DFG through a research infrastructure grant INST 275/257-1 FUGG. I.K. acknowledges the support of the Alexander von Humboldt Foundation through the Humboldt Research Fellowship.

Conflict of interest

The authors declare no conflict of interest.

Keywords: carbon nitride · chemoselectivity · nanoparticles · photocatalysis · quasi-homogeneous catalysis

How to cite: *Angew. Chem. Int. Ed.* **2020**, *59*, 487–495
Angew. Chem. **2020**, *132*, 495–503

[1] X. Wang, K. Maeda, A. Thomas, K. Takanabe, G. Xin, J. M. Carlsson, K. Domen, M. Antonietti, *Nat. Mater.* **2009**, *8*, 76.
[2] a) P. Niu, L. Zhang, G. Liu, H. Cheng, *Adv. Funct. Mater.* **2012**, *22*, 4763–4770; b) Z. Song, T. Lin, L. Lin, S. Lin, F. Fu, X. Wang, L. Guo, *Angew. Chem. Int. Ed.* **2016**, *55*, 2773–2777; *Angew. Chem.* **2016**, *128*, 2823–2827.
[3] a) Y. Ishida, L. Chabanne, M. Antonietti, M. Shalom, *Langmuir* **2014**, *30*, 447–451; b) Q. Cui, J. Xu, X. Wang, L. Li, M. Antonietti, M. Shalom, *Angew. Chem. Int. Ed.* **2016**, *55*, 3672–3676; *Angew. Chem.* **2016**, *128*, 3736–3740.
[4] a) S. Yang, Y. Gong, J. Zhang, L. Zhan, L. Ma, Z. Fang, R. Vajtai, X. Wang, P. Ajayan, *Adv. Mater.* **2013**, *25*, 2452–2456; b) K. Schwinghammer, M. Mesch, V. Duppel, C. Ziegler, J. Senker, B. Lotsch, *J. Am. Chem. Soc.* **2014**, *136*, 1730–1733.
[5] I. Krivtsov, E. Garcia-Lopez, G. Marci, L. Palmisano, Z. Amghouz, J. Garcia, S. Ordonez, E. Diaz, *Appl. Catal. B* **2017**, *204*, 430–439.
[6] Z. Zhou, J. Wang, J. Yu, Y. Shen, Y. Li, A. Liu, S. Liu, Y. Zhang, *J. Am. Chem. Soc.* **2015**, *137*, 2179–2182.
[7] C. Huang, J. Wen, Y. Shen, F. He, L. Mi, Z. Gan, J. Ma, S. Liu, H. Ma, Y. Zhang, *Chem. Sci.* **2018**, *9*, 7912–7915.
[8] Y. Zhang, Z. Zhou, Y. Shen, Q. Zhou, J. Wang, A. Liu, S. Liu, Y. Zhang, *ACS Nano* **2016**, *10*, 9036–9043.
[9] M. Groenewolt, M. Antonietti, *Adv. Mater.* **2005**, *17*, 1789–1792.
[10] a) Y. Li, S. Ouyang, H. Xu, X. Wang, Y. Bi, Y. Zhang, J. Ye, *J. Am. Chem. Soc.* **2016**, *138*, 13289–13297; b) Y. Li, P. Li, J. Wang, Y. Yang, W. Yao, Z. Wei, J. Wu, X. Yan, X. Xu, Y. Liu, Y. Zhu, *Appl. Catal. B* **2018**, *225*, 519–529; c) B. Yuan, Z. Chu, G. Li, Z. Jiang, T. Hu, Q. Wang, C. Wang, *J. Mater. Chem. C* **2014**, *2*, 8212–8215.
[11] a) L. Heymann, S. Bittinger, C. Klinke, *ACS Omega* **2018**, *3*, 17042–17048; b) L. Heymann, B. Schiller, H. Noei, A. Stierle, C. Klinke, *ACS Omega* **2018**, *3*, 3892–3900.
[12] H. Ou, P. Yang, L. Lin, M. Anpo, X. Wang, *Angew. Chem. Int. Ed.* **2017**, *56*, 10905–10910; *Angew. Chem.* **2017**, *129*, 11045–11050.
[13] W. Wang, J. C. Yu, Z. Shen, D. K. L. Chan, T. Gu, *Chem. Commun.* **2014**, *50*, 10148–10150.
[14] J. Zhou, Y. Yang, C. Zhang, *Chem. Commun.* **2013**, *49*, 8605–8607.
[15] M. Stucchi, S. Cattaneo, A. Capella, W. Wang, D. Wang, A. Villa, L. Pratti, *Catal. Today* **2019**, https://doi.org/10.1016/j.cattod.2019.03.022.
[16] a) E. Wirnhier, M. Doblinger, D. Gunzelmann, J. Senker, B. Lotsch, W. Schnick, *Chem. Eur. J.* **2011**, *17*, 3213–3221; b) D. Dontsova, S. Pronkin, M. Wehle, Z. Chen, C. Fettkenhauer, G. Clavel, M. Antonietti, *Chem. Mater.* **2015**, *27*, 5170–5179; c) V. Lau, I. Moudrakovski, T. Botari, S. Weinberger, M. Mesch, V. Duppel, J. Senker, V. Blum, B. Lotsch, *Nat. Commun.* **2016**, *7*, 12165. DOI:10.1038/ncomms12165.
[17] H. Yu, R. Shi, Y. Zhao, T. Bian, Y. Zhao, C. Zhou, G. Waterhouse, L. Wu, C. Tung, T. Zhang, *Adv. Mater.* **2017**, *29*, 1605148.
[18] a) A. Savateev, S. Pronkin, M. Willinger, M. Antonietti, D. Dontsova, *Chem. Asian J.* **2017**, *12*, 1517–1522; b) G. Zhang, L. Lin, G. Li, Y. Zhang, A. Savateev, S. Zafeiratos, X. Wang, M. Antonietti, *Angew. Chem. Int. Ed.* **2018**, *57*, 9372–9376; *Angew. Chem.* **2018**, *130*, 9516–9520.
[19] A. Savateev, S. Pronkin, J. Epping, M. Willinger, C. Wolff, D. Neher, M. Antonietti, D. Dontsova, *ChemCatChem* **2017**, *9*, 167–174.
[20] a) N. El-Gamel, L. Seyfarth, J. Wagler, H. Ehrenberg, M. Schwarz, J. Senker, E. Kroke, *Chem. Eur. J.* **2007**, *13*, 1158–

 © 2019 The Authors. Published by Wiley-VCH Verlag GmbH & Co. KGaA, Weinheim

15213773, 2020, 1, Downloaded from https://onlinelibrary.wiley.com/doi/10.1002/anie.201913331 by KIZ der Universitat Ulm, Wiley Online Library on [19/08/2024]. See the Terms and Conditions (https://onlinelibrary.wiley.com/terms-and-conditions) on Wiley Online Library for rules of use; OA articles are governed by the applicable Creative Commons License

1173; b) L. Seyfarth, J. Sehnert, N. El-Gamel, W. Milius, E. Kroke, J. Breu, J. Senker, *J. Mol. Struct.* **2008**, *889*, 217 – 228.
[21] a) E. Horvath-Bordon, E. Kroke, I. Svoboda, H. Fuess, R. Riedel, S. Neeraj, A. Cheetham, *Dalton Trans.* **2004**, *0*, 3900 – 3908; b) E. Horvath-Bordon, E. Kroke, I. Svoboda, H. Fuess, R. Riedel, *New J. Chem.* **2005**, *29*, 693 – 699.
[22] Y. Zhang, A. Thomas, M. Antonietti, X. Wang, *J. Am. Chem. Soc.* **2009**, *131*, 50 – 51.
[23] a) F. Su, S. Mathew, G. Lipner, X. Fu, M. Antonietti, S. Blechert, X. Wang, *J. Am. Chem. Soc.* **2010**, *132*, 16299 – 16301; b) X. Li, J. Chen, X. Wang, J. Sun, M. Antonietti, *J. Am. Chem. Soc.* **2011**, *133*, 8074 – 8077; c) M. Zhou, P. Yang, S. Wang, Z. Luo, C. Huang, X. Wang, *ChemSusChem* **2018**, *11*, 3949 – 3955; d) A. Savateev, D. Dontsova, B. Kurpil, M. Antonietti, *J. Catal.* **2017**, *350*, 203 – 211; e) A. Savateev, I. Ghosh, B. Konig, M. Antonietti, *Angew. Chem. Int. Ed.* **2018**, *57*, 15936 – 15947; *Angew. Chem.* **2018**, *130*, 16164 – 16176.
[24] I. Krivtsov, M. Ilkaeva, E. Garcia-Lopez, G. Marci, L. Palmisano, E. Bartashevich, E. Grigoreva, K. Matveeva, E. Diaz, S. Ordonez, *ChemCatChem* **2019**, *11*, 2713 – 2724.
[25] a) Y. Shiraishi, S. Kanazawa, Y. Sugano, D. Tsukamoto, H. Sakamoto, S. Ichikawa, T. Hirai, *ACS Catal.* **2014**, *4*, 774 – 780; b) Y. Shiraishi, Y. Kofuji, H. Sakamoto, S. Tanaka, S. Ichikawa, T. Hirai, *ACS Catal.* **2015**, *5*, 3058 – 3066; c) A. Torres-Pinto, M. Sampaio, C. Silva, J. Faria, A. Silva, *Appl. Catal. B* **2019**, *252*, 128 – 137; d) M. Ilkaeva, I. Krivtsov, J. Garcia, E. Diaz, S. Ordonez, E. Garcia-Lopez, G. Marci, L. Palmisano, M. Maldonado, S. Malato, *Catal. Today* **2018**, *315*, 138 – 148.
[26] a) V. W. Lau, D. Klose, H. Kasap, F. Podjaski, M.-C. Pignié, E. Reisner, G. Jeschke, B. Lotsch, *Angew. Chem. Int. Ed.* **2017**, *56*, 510 – 514; *Angew. Chem.* **2017**, *129*, 525 – 529; b) W. Yang, R. Godin, H. Kasap, B. Moss, Y. Dong, S. A. J. Hillman, L. Steier, E. Reisner, J. R. Durrant, *J. Am. Chem. Soc.* **2019**, *141*, 11219 – 11229.
[27] L. Sun, J. Bolton, *J. Phys. Chem.* **1996**, *100*, 4127 – 4134.
[28] H. Kasap, D. S. Achilleos, A. Huang, E. Reisner, *J. Am. Chem. Soc.* **2018**, *140*, 11604 – 11607.
[29] D. Wakerley, M. Kuehnel, K. Orchard, K. Ly, T. Rosser, E. Reisner, *Nat. Energy* **2017**, *2*, 17021.
[30] M. Ilkaeva, I. Krivtsov, E. Bartashevich, S. Khainakov, J. Garcia, E. Diaz, S. Ordonez, *Green Chem.* **2017**, *19*, 4299 – 4304.

Manuscript received: October 18, 2019
Accepted manuscript online: October 29, 2019
Version of record online: November 26, 2019

 © 2019 The Authors. Published by Wiley-VCH Verlag GmbH & Co. KGaA, Weinheim

15213773, 2020, 1, Downloaded from https://onlinelibrary.wiley.com/doi/10.1002/anie.201913331 by KIZ der Universitat Ulm, Wiley Online Library on [19/08/2024]. See the Terms and Conditions (https://onlinelibrary.wiley.com/terms-and-conditions) on Wiley Online Library for rules of use; OA articles are governed by the applicable Creative Commons License

Angewandte Chemie
Eine Zeitschrift der Gesellschaft Deutscher Chemiker

Supporting Information

Water-Soluble Polymeric Carbon Nitride Colloidal Nanoparticles for Highly Selective Quasi-Homogeneous Photocatalysis**

Igor Krivtsov, Dariusz Mitoraj, Christiane Adler, Marina Ilkaeva, Mariana Sardo, Luís Mafra, Christof Neumann, Andrey Turchanin, Chunyu Li, Benjamin Dietzek, Robert Leiter, Johannes Biskupek, Ute Kaiser, Changbin Im, Björn Kirchhoff, Timo Jacob, and Radim Beranek**

anie_201913331_sm_miscellaneous_information.pdf

Experimental Procedures

Materials and synthesis

Melamine (99 %) provided by Sigma Aldrich, KOH and NaOH (Merck, 99 %) were used for the syntheses of the photocatalysts. 4-methoxybenzyl alcohol (4MBA), 4-methoxybenzaldehyde (4MBAL) both with purity of 98% benzyl alcohol (99.8 %), benzaldehyde (99.5 %), glucose (99.5 %) were supplied by Sigma Aldrich while ethanol (99.8 %) and glycerol (99.5 %) were purchased from VWR and all these compounds were used for the photocatalytic tests. Titanium oxysulfate hydrate containing approx. 17 wt% of sulfuric acid ($TiOSO_4 \cdot H_2O \cdot H_2SO_4$) and aqueous solution of H_2O_2 were purchased from Sigma Aldrich and used for photometric determination of H_2O_2.Conventional heptazine-based polymeric carbon nitride (CN) was synthesized for comparison by thermal condensation of 30 g of melamine at 530 °C for 4h, after that the solid was powdered in agate mortar. The solid-state potassium poly(heptazine imide) (K-PHI-S) and water-soluble nanoparticles of potassium poly(heptazine imide) (K-PHI), sodium poly(heptazine imide) (Na-PHI), and mixed sodium-potassium poly(heptazine imide) (K,Na-PHI) were prepared by grinding 1.5 g of melamine with appropriate quantities of KOH, NaOH or a mixture of KOH-NaOH and heating it in a lid-covered crucible at a rate of 5 °C min^{-1} up to 330 °C, then it was kept for 2h at the reached temperature before being withdrawn from the furnace. The obtained solid was powdered and mixed with 100 mL of deionized water. In the case of the K-PHI-S sample, the suspended solid was centrifuged and washed twice with deionized H_2O before being put inside a cellulose membrane with a pore size of 3.5 kDa and dialyzed against H_2O for the purification followed by drying it for 24 h at 80 °C. For the preparation of the K-PHI, Na-PHI and K,Na-PHI samples, the same procedure was implemented with the difference that after the addition of 100 mL of H_2O the insoluble part was filtered out, firstly, by a paper filter and then by a 0.2 μm PTFE syringe filter. Eventually, the solution of the alkali metal poly(heptazine imide) nanoparticles was dialyzed and concentrated by evaporation at 60 °C to a concentration of 5 g L^{-1}, which was determined gravimetrically. In order to obtain solid sample of the water-soluble alkali metal poly(heptazine imide), the solution was gradually evaporated at 60 °C and then dried for 24 h at 80 °C. Table S1 summarizes the synthetic conditions applied for the preparation of the poly(heptazine imide) samples and the yields of the obtained materials.

Characterization

A Mettler–Toledo instrument (TGA/SDTA851^e) was used to investigate the formation of K,Na-PHI from the melamine mixture with KOH/NaOH. For this, a small portion of a precursor containing 1.5 g of melamine, 0.56 g (10 mmol) of KOH and 0.2 g of NaOH (5 mmol) was put in a platinum crucible and heated at a rate of 5 °C min^{-1} up to 330 °C in He atmosphere. Thermal decomposition of the dried alkali metal poly(heptazine imide) samples was carried out using the same equipment, but at a heating rate of 10 °C min^{-1} in O_2 flow (50 mL min^{-1}) from 25 °C to 1000 °C. XRD patterns were obtained using a Pananalytical X'pert PRO diffractometer equipped with a Pixel detector and operating at Cu Kα radiation. FTIR spectra were recorded by means of a Shimadzu IRTracer-100 spectrometer at a resolution of 4 cm^{-1} from the samples powdered and pressed into KBr pellets.

^1H, ^{13}C and ^{15}N magic angle spinning (MAS) solid-state NMR spectra of the K-PHI-S and the dried K,Na-PHI samples were acquired on a Bruker Avance III 400 spectrometer operating at B_0 field of 9.4 T with ^1H, ^{13}C, ^{15}N Larmor frequencies of 400.1/100.6/40.6 MHz, respectively. All experiments were performed on a double-resonance 4 mm Bruker MAS probe, except the ^{15}N cross-polarization MAS (CPMAS) measurements, in which a double-resonance 7 mm Bruker MAS probe was used. Samples were packed into 4 or 7 mm zirconia rotors. Spinning rates between 5 and 15 kHz were employed to record all spectra. ^1H, ^{13}C and ^{15}N chemical shifts are quoted in ppm from: TMS (0 ppm) and α-glycine (secondary reference, C=O at 176.03 ppm and NH_3^+ at 347.6 ppm on the nitromethane scale, respectively). Specifically, the ^{13}C MAS NMR spectra were acquired using a high-power decoupling single pulse sequence with the following conditions: 12 kHz spinning rate, a pulse width of 2.56

μs (45° flip angle) corresponding to 49 kHz, with ^{1}H SPINAL-64 decoupling at 80 kHz, recycle delay (RD) was 60 s. The ^{1}H-^{13}C CPMAS spectra were acquired at a MAS rate of 12 kHz using a ^{1}H 90° pulse length set to 3.2 μs (78 kHz); the CP step was performed with a contact time (CT) of 3500 μs using a 50−100% RAMP shape pulse on the ^{1}H (66 kHz) channel and using a 45 kHz square pulse on the ^{13}C channel; RD was 5 s. During the acquisition, a SPINAL-64 decoupling scheme was employed using a pulse length for the basic decoupling units of 6 μs at a rf field strength of 80 kHz. ^{1}H-^{15}N CPMAS spectra were typically acquired with the following parameters: MAS rate of 5 kHz, ^{1}H 90° pulse length of 4 μs employing a rf field strength of 63 kHz, the CP step was performed with a CT of 2000 μs using a 50−100% RAMP shape on the ^{1}H (57 kHz) channel and using a 34 kHz square shape pulse on the ^{15}N channel; decoupling with SPINAL-64 using a pulse length of 6.8 μs using a rf field strength of 63 kHz was applied, RD was 5 s. All spectra were acquired at ambient probe temperature. MagicPlot Pro software was used for the deconvolution of the chosen spectra. The R^2 values for fitting curves were always higher than 0.97.

In order to perform X-ray photoelectron spectroscopy (XPS), the powder samples K-PHI-S and K,Na-PHI were placed on top of a conductive double-sided carbon tape (Ted Pella Inc., USA) and fixed to the XPS sample holder. The measurements were performed using a UHV Multiprobe system (Scienta Omicron, Germany) with a monochromatic X-ray source (Al Kα) and an electron analyzer (Argus CU) with 0.6 eV energy resolution. Charge compensation during data acquisition was realized by an electron flood gun (NEK 150, Staib, Germany) at 6 eV and 50 μA. The background was subtracted and spectra were calibrated using the C1s peak (284.6 eV) before undergoing fitting using Voigt functions (30:70). A scanning electron microscope JEOL-6610LV equipped with an Oxford Instruments EDX detector was used to collect SEM images of the dry poly(heptazine imide) samples and determine their elemental composition. Particle size distribution of the water-soluble poly(heptazine imide) samples and their zeta-potentials were determined by means of dynamic light scattering (DSL) and electrophoretic mobility methods using a Zetasizer Nano ZS (Malvern Instruments Ltd., UK) operating at a detection angle of 173.5°. Diffusive-reflectance UV-vis spectra of solids were taken by a Shimadzu UV2600 UV-vis spectrophotometer. UV-vis spectra of the poly(heptazine imide) nanoparticles solutions were recorded using a Cary 60 (Agilent Technologies) spectrophotometer. Cyclic voltammogram of the K,Na-PHI material was recorded in the dark in acetonitrile solution of tetrabutylammonium hexafluorophosphate ($TBAFP_6$, 0.1 M) using a SP-300 BioLogic potentiostat (Caix, France) and a three-electrode cell composed of a platinum counter electrode and an Ag/AgCl (sat. KCl) reference electrode. The working electrode was prepared by drop casting of the K,Na-PHI nanoparticles solution on a glassy carbon substrate followed by gelation by adding conc. HCl. The potential values were recalculated and reported with respect to the normal hydrogen electrode (NHE). The images were recorded using the SALVE at 80kV acceleration voltage (where indicated) and the Philips CM20 at 200kV, both in HRTEM mode. The liquid sample was diluted (where indicated) in purified water (10 μl of sample in 1 mL of water), then drop cast onto copper TEM support grids with holey carbon film. The undiluted liquid samples were prepared by dipping of the TEM grid into the solution and drying. The solid samples were sonicated in ethanol and then drop cast onto TEM grids.

Photocatalytic measurements

Selective photocatalytic oxidation reactions of 4MBA to 4MBAL and benzyl alcohol to benzaldehyde were carried out for the K-PHI-S, K-PHI, Na-PHI, and K,Na-PHI samples, CN was used as a reference. For this purpose, the solid samples and the solutions of the poly(heptazine imide) nanoparticles were suspended in 20 mL of water or water-acetonitrile solution of 4MBA (or benzyl alcohol) (0.1 mmol). The pH of water solutions or water-acetonitrile mixture was in the range of 6.5–7.0 and did not undergo noticeable changes after irradiation. The reaction mixture was irradiated for 4 h by a UV LED emitting at 365 nm and producing a photon flux of 40 mW cm^{-2}. The control experiments were carried out in the absence of any photocatalyst under UV-irradiation and in the presence of the K,Na-PHI and CN samples in dark conditions. However, no noticeable reaction took place in such conditions, as the changes in the 4MBA or benzyl alcohol concentrations were below 1 %, and no H_2O_2 was detected after 4 h. The photocatalytic oxidation of 4MBA in the absence of air was performed under the optimal conditions (40 % *vol.*

acetonitrile in the reaction mixture), while purging Ar gas through the system. The samples of 0.1 mL were taken every 30 min and analyzed by an HPLC Shimadzu LC-10ADvp equipped with a UV detector SPD-20A and a reversed phase C18 Nucleosil column. Acetonitrile/water (30/70 vol.) was used as a mobile phase at a flow of 1.2 mL min^{-1} and a column temperature of 60 °C. 4MBA to 4MBAL were detected and quantified at a wavelength of 240 nm, while benzyl alcohol and benzaldehyde were measured at 220 nm. Considering a quasi-homogeneous nature of the irradiated 4MBA (or benzyl alcohol) solutions with the poly(heptazine imide) photocatalysts and the incompatibility of the used HPLC column with some of the organic solvent immiscible with water, which could possibly be used for the organic compounds extraction, the following probe preparation was implemented. The photocatalyst was separated from the reaction medium by means of a salting-out approach. In details, to 0.1 mL of the sample, 0.2 mL of 1M NaCl solution, and 0.8 mL of acetonitrile were added, the salting-out effect resulted in the two-phase system with the photocatalyst in the aqueous phase and 4MBA, 4MBAL (or benzyl alcohol and benzaldehyde) extracted to the organic phase, which was subsequently analysed. The respective volumes of the additives for the probe-preparation were adjusted for the case of acetonitrile/water solutions, as to maintain the H_2O to acetonitrile ratio in the probe constant. The calibration was carried out in the same way giving R^2 values higher than 0.999 for the substrate and the product. The recyclability test was made possible by the precipitation of the photocatalyst after each cycle by adding 0.25 g of NaCl to the reaction mixture in water solution and 0.125 to the reaction mixture in water/acetonitrile medium, following by its centrifugation and re-dispersion in a fresh solution of 4MBA. The selectivity (S) of the reaction was determined by the formula:

$$S_{4MBAL} = \frac{C(4MBAL)}{C_0(4MBA) - C(4MBA)} * 100\%,$$

where C_0(4MBA) is the initial concentration of the substrate, C(4MBA) is the substrate concentration at a given reaction time, and C(4MBAL) is the concentration of the reaction product at a given reaction time. Considering a *quasi*-homogeneous nature of the carried out photocatalytic reaction, the estimation of the quantum yield of the process is more reliable than for the case of heterogeneous systems. For this, the reaction mixture in water(60%)/acetonitrile(40%) medium containing 4MBA (5mM) and the K,Na-PHI photocatalyst having absorbance of 0.1 at 365 nm were put in a quartz cuvette and irradiated with a 365 nm emitting LED for 2 h. After the reaction the concentration of the produced 4MBAL was analysed using the above described HPLC method. The quantum yield (Q) of the process was calculated considering that two electrons are required to be withdrawn from the substrate (4MBA) to oxidize it to 4MBAL (1).

$C_6H_3COH_3CH_2OH + 2h^+ \rightarrow C_6H_3COH_3CHO + 2H^+$ (1)
$O_2 + 2H^+ + 2e^- \rightarrow H_2O_2$ (2)

The photon flux was determined by the formula:

$$\Phi = \frac{\Delta H}{qE},$$

where ΔH is the light power absorbed by the system (W m^{-2}), q is the charge of electron (C) and E is the energy of irradiation (eV).

The quantum yield was determined as:

$$Q = \frac{2\ n(4MBAL)\ N_A}{\Phi t S},$$

where n(4MBAL) is the number of moles of 4MBAL produced, N_A is the Avogadro number, t is the irradiation time in s, and S is the irradiated area of the reactor (m^2)

Hydrogen peroxide concentration was estimated photometrically. Sample of 5 mL of the reaction solution was withdrawn after 4 h of irradiation, to that volume 1 mL of $TiOSO_4$ solution (Ti 1 wt%) in sulfuric acid was added.

The addition of the acidic solution caused the photocatalyst to coalesce, so it could be filtered out through the syringe PTFE 0.2 μm filter. The filtered solution of yellow-coloured titanium peroxocomplex was analysed photometrically using a Cary 60 (Agilent Technologies) spectrophotometer. The absorption at 420 nm was chosen to plot a calibration curve using standard H_2O_2 concentrations and to estimate the concentrations of photocatalytically produced H_2O_2. The selectivity towards the H_2O_2 formation was determined by the formula:

$$S_{H_2O_2} = \frac{C(H_2O_2)}{C_0(4MBA) - C(4MBA)} * 100\%.$$

The photocatalytic hydrogen peroxide production using model lignocellulose-derived substrates such as ethanol, glycerol or glucose was carried out in the same way as that of benzylic alcohols oxidation, however only H_2O_2 concentration was measured after 4 h of irradiation. The control experiments in the absence of photocatalysts or with CN and K,Na-PHI photocatalysts in the dark showed no H_2O_2 formation at such conditions. For the reactions with ethanol and glycerol 1 % wt. solutions of the substrates in water were prepared, while for the reaction with glucose 100 mg of it was dissolved in 20 mL of H_2O.

Theoretical calculations

Periodic Density Functional Theory (DFT) calculations were performed using the Vienna *Ab initio* Simulation Package (VASP) version 5.4.4[1–4] using the projector-augmented wave method[5] to represent the basis set. The exchange-correlation functional by Perdew, Becke, and Ernzerhof was used.[6] The wavefunction was optimized to an accuracy of 10^{-6} eV while geometries were relaxed until the forces reached below $5 \cdot 10^{-2}$ eV Å^{-1}. Gaussian finite-temperature smearing was employed with a smearing width of 0.01 eV. A plane wave energy cut-off of 400 eV and a 2x4x1 Monkhorst-Pack[10] ***k*** grid were found to give converged total energy results. 20 Å of vacuum separated slabs in *z* direction to avoid interaction between periodic images. For implicit solvation calculations, the GLSSA13 solvent model[7] implemented in the VASPsol extension was invoked.[8,9] We assumed typical room temperature bulk solvent dipole moments of 78.4, 36.6, and 32.6 for water, acetonitrile, and methanol, respectively.

Spectroscopic studies

In situ UV-Vis absorption and emission spectra were acquired in a 1cm quartz cell using a JASCO V-780 spectrophotometer and a fluorescence spectrometer (FLS980, Edinburgh), respectively. The data were recorded at room temperature upon irradiation of the sample with at 365 nm. External irradiation with the irradiance of 71 mW / mm^2 at the sample position was provided by a combined mounted LED (M365LP1, THORLABS). The K,Na-PHI sample was diluted in H_2O giving the optical density below 0.8 at 280 nm, and the freeze−pump−thaw method was used to remove oxygen for the measurements.

Results and Discussion

Synthesis

Table S1. Synthetic conditions for the poly(heptazine imide) samples preparation.

Sample name[a]	Melt composition	Sample state	Yield[c]	XRD phase composition[d]
Potassium poly(heptazine imide)				
K-PHI-S1	KOH 5 mmol (0.28 g)	Mostly solid	27 %	PHI and melamine
K-PHI-S2	KOH 7.5 mmol (0.42 g)	Mostly solid	29 %	PHI and melamine
K-PHI-S3	KOH 10 mmol (0.56 g)	Solid and soluble PHI	23-26 %	PHI and melamine
K-PHI-S	KOH 10 mmol (0.56 g)	Dialyzed solid	24-25 %	PHI
K-PHI	KOH 12.5 mmol (0.70 g)	Dialyzed solution	10-11 %	PHI
K-PHI4	KOH 15 mmol (0.84 g)	Dialyzed solution	9 %	PHI
K-PHI5	KOH 20 mmol (1.12 g)	Dialyzed solution	3 %	PHI
Sodium poly(heptazine imide)				
Na-PHI	NaOH 5 mmol (0.2 g)	Dialyzed solution	13 %	PHI
Na-PHI1	NaOH 7.5 mmol (0.3 g)	Dialyzed solution	4 %	PHI
Na-PHI2	NaOH 10 mmol (0.4 g)	Dialyzed solution	negligible	
Potassium-Sodium poly(heptazine imide)				
K,Na-PHI1	KOH 5 mmol (0.28 g) NaOH 5 mmol (0.2 g)	Dialyzed solution	6-9 %	PHI
K,Na-PHI2	KOH 7.5 mmol (0.42 g) NaOH 7.5 mmol (0.3 g)	Dialyzed solution	12-18 %	PHI
K,Na-PHI3	KOH 10 mmol (0.56 g) NaOH 10 mmol (0.4 g)	Dialyzed solution	9-11 %	PHI
K,Na-PHI4	KOH 10 mmol (0.56 g) NaOH 7.5 mmol (0.3 g)	Dialyzed solution	7-9 %	PHI
K,Na-PHI	KOH 10 mmol (0.56 g) NaOH 5 mmol (0.2 g)	Dialyzed solution	31-42 %	PHI

[a] The samples highlighted in grey are chosen for the investigation. [b] The materials were prepared by grinding 1.5 g of melamine with appropriate quantities of KOH, NaOH or a mixture of KOH-NaOH and heating it in a lid-covered crucible at a rate of 5 °C min^{-1} up to 330 °C, then it was kept for 2 h at the reached temperature before being withdrawn from the furnace. [c] The yield was quantified as the mass of the solid obtained after the synthesis (after washing or after dialysis) to the mass of melamine used for the synthesis and multiplied by 100 %. The yields depend on the presence of absorbed moisture in the hydroxide, hence may vary significantly [d] XRD patterns were collected from the dry solid samples, (PHI corresponds to alkali metal poly (heptazine imide) phase).



Figure S1. Tyndall effect observed in the solution of K,Na-PHI nanoparticles

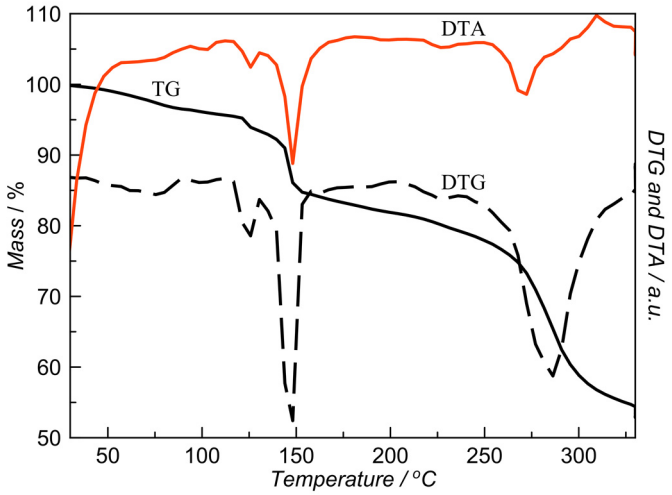

Figure S2. TG, DTG and DTA curves corresponding to the condensation process of melamine in KOH/NaOH mixture under He flow.

XRD analysis

The XRD patterns of the K-PHI-S sample series, obtained at different loadings of KOH in the melt, show that a part of melamine present in the precursor does not undergo the condensation to carbon nitride polymers, which is due to the fact that KOH is solid in this temperature range and it does not provide a liquid medium for melamine dissolution and condensation (Fig. S3 Left). Although the material recovered after the synthesis in KOH (K-PHI-S) was insoluble in water, its purification by washing and centrifugation or filtering was complicated owing to its high dispersibility in it. This is why the solid was dialysed, which allowed to achieve its higher purity (Fig. S3 Left).

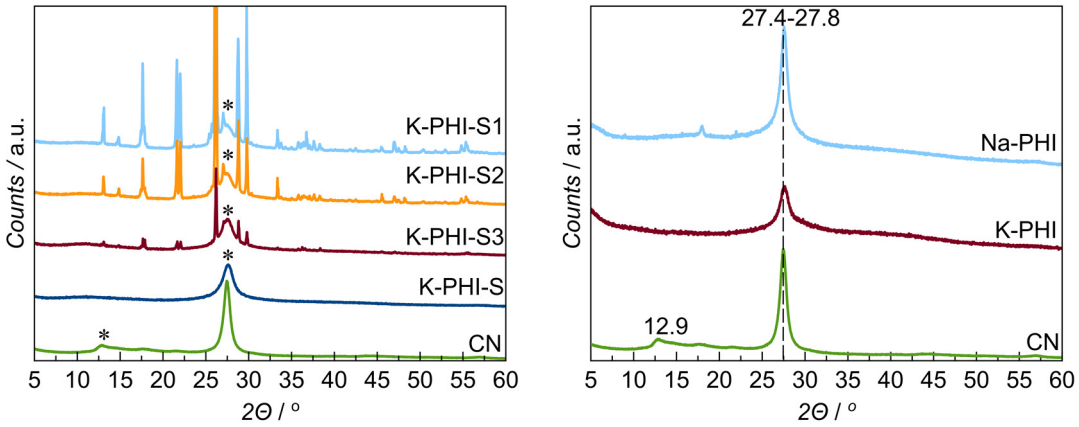

Figure S3. XRD patterns of the K-PHI-S samples (left) and the water soluble K-PHI and Na-PHI samples (right). Asterisk indicates the poly(heptazine imide) or PCN phases, while the other peaks correspond to non-condensed melamine.

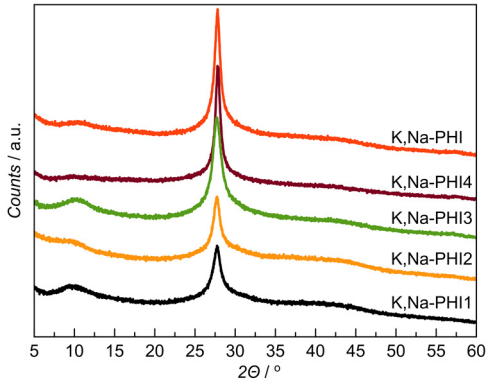

Figure S4. XRD patterns of the K,Na-PHI samples.

FTIR analysis

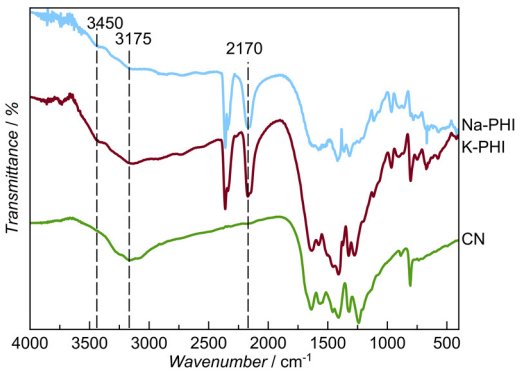

Figure S5. FTIR spectra of the K-PHI and Na-PHI samples in comparison with the CN sample.

TG-DTA analysis

The maximum of thermal decomposition rate of the K-PHI-S and K,Na-PHI samples is observed at about 690 °C (Fig. S6). A clear difference of thermal behaviour of the studied materials could be seen at high-temperature range. K-PHI-S loses 100 % of its initial mass by 800 °C, which it is not the case of K,Na-PHI retaining about 18 % of its initial mass at the same temperature (Fig. S6). The decomposition of the samples might result in the formation of potassium and sodium carbonates, hydroxides or oxides which are all not volatile compounds, however they melt at temperatures above 800 °C and then can be carried away by the gas flow (Fig. S6).

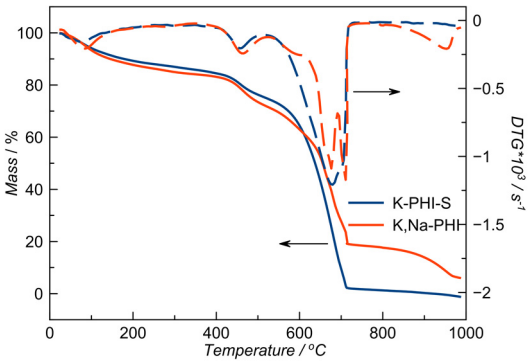

Figure S6. Thermoanalytical curves of the K-PHI-S and K,Na-PHI samples decomposition in O_2 (50 mL min^{-1}).

Elemental analyses

Table S2. Elemental composition of the prepared samples.

Sample name	Elemental composition / wt%[a]	C:N:H[a]	EDX Elemental composition / at% [b]	C:N ratio[b]
K-PHI-S	$C_{29.4}N_{50.5}H_{2.2}$	0.67:1.00:0.61	$C_{35.4}N_{56.1}O_{5.8}K_{2.7}$	0.63
K-PHI	-		$C_{35.6}N_{51.3}O_{8.6}K_{4.5}Ca_{0.1}$	0.69
Na-PHI	-		$C_{33.3}N_{54.2}O_{8.5}Na_{3.8}Ca_{0.2}$	0.61
K,Na-PHI	$C_{27.0}N_{44.4}H_{1.8}$	0.72:1.00:0.56	$C_{34.9}N_{47.8}O_{11.2}K_{2.5}Na_{3.5}Ca_{0.2}$	0.73

[a] On the basis of CHN elemental analysis. [b] Obtained by SEM-EDX method.

NMR study

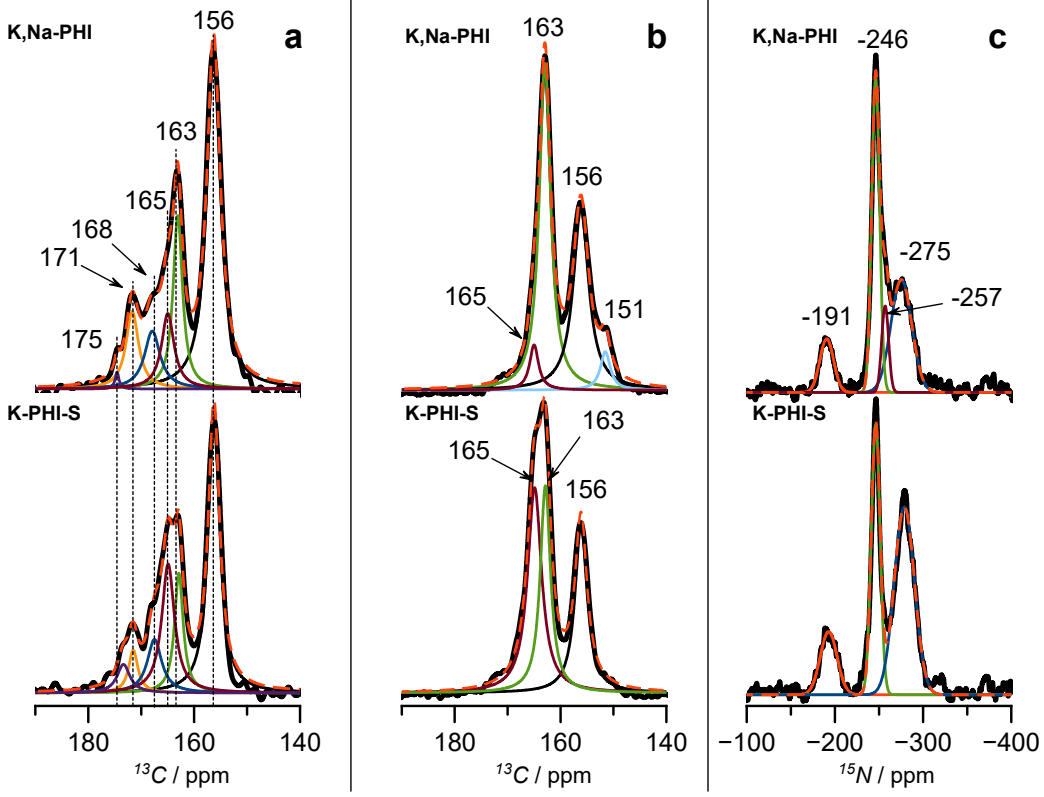

Figure S7. Peak fitting of the a) ^{13}C direct excitation MAS, b) ^{1}H-^{13}C CPMAS, and c) ^{1}H-^{15}N CPMAS solid-state NMR spectra of the K-PHI-S and K,Na-PHI samples. The experimental and fitted curves are represented in solid black and dashed red lines, respectively.

The ^{13}C direct excitation MAS spectra provide a quantitative estimation of the PCN species present in the studied samples (Table S3 and Fig. S7). The peak area of resonance **3** (associated to poly(heptazine) units) is used to estimate the relative amount of nitrile, C≡N (**1**), secondary amines, N=C-NH (**4**), primary amines, N=C-NH_2 (**5**), and oxygenated functional groups, N=C-O^- (**6**), between samples K,Na-PHI and K-PHI-S, by taking the ratios **1:3**, **4:3**, **5:3** and **6:3,** respectively (Table S3). The **6:3** ratio is similar in both materials (*cf.* 0.20 *vs.* 0.24) indicating that the relative amount of the C-O^- species is nearly identical for both. In contrast, the number of -NH_2 groups (**5:3** ratio) in the water-soluble K,Na-PHI decreases with respect to K-PHI-S (*cf.* 0.20 *vs.* 0.50, respectively), suggesting that the KOH/NaOH medium promotes a higher degree of condensation of the -NH_2 groups. Consequently, the formation of heptazine species (Fig. S8) is favoured, resulting in an increased number of N-C=N (**3**) carbons in K,Na-PHI as compared to K-PHI-S (Table S3, Fig. S7). The lower concentration of terminal -NH_2 moieties in K,Na-PHI will likely lead to an overall decrease of the number of hydrogen bonds in the polymer network, thus exerting a direct influence on aggregation and solubility.

Table S3. Estimation of relative concentrations of the PCN species from the deconvoluted ^{13}C MAS NMR spectra

Peak position	Assignment	Contribution of the peak area to the total area of the spectrum (FWHM)		Peak area ratio of the peaks with respect to the area of **3**	
		K-PHI-S	K,Na-PHI	K-PHI-S	K,Na-PHI
122 (**1**)	C≡N	0.13 (6.6)	0.15 (6.6)	0.34	0.35
156 (**3**)	N=C-N (C-N_3)	0.38 (2.6)	0.43 (3.0)	1	1
163 (**4**)	N=C-NH	0.12 (2.0)	0.15 (2.1)	0.32	0.35
165 (**5**)	N=C-NH_2	0.19 (2.9)	0.09 (2.9)	0.50	0.20
168 (**6**)	N=C-O^-	0.09 (3.3)	0.08 (3.5)	0.24	0.20
171-175 (**7**)	C-N^-	0.09 (2.1+2.9)	0.10 (2.9+1.0)	0.24	0.23

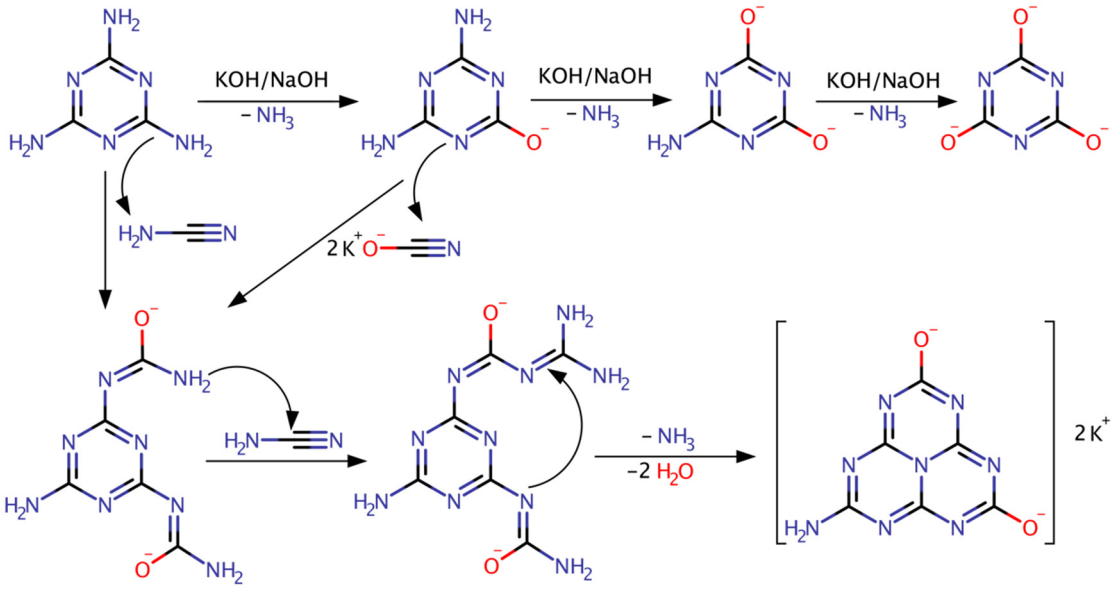

Figure S8. Proposed poly(heptazine imide) condensation pathway in KOH/NaOH melt.

XPS study

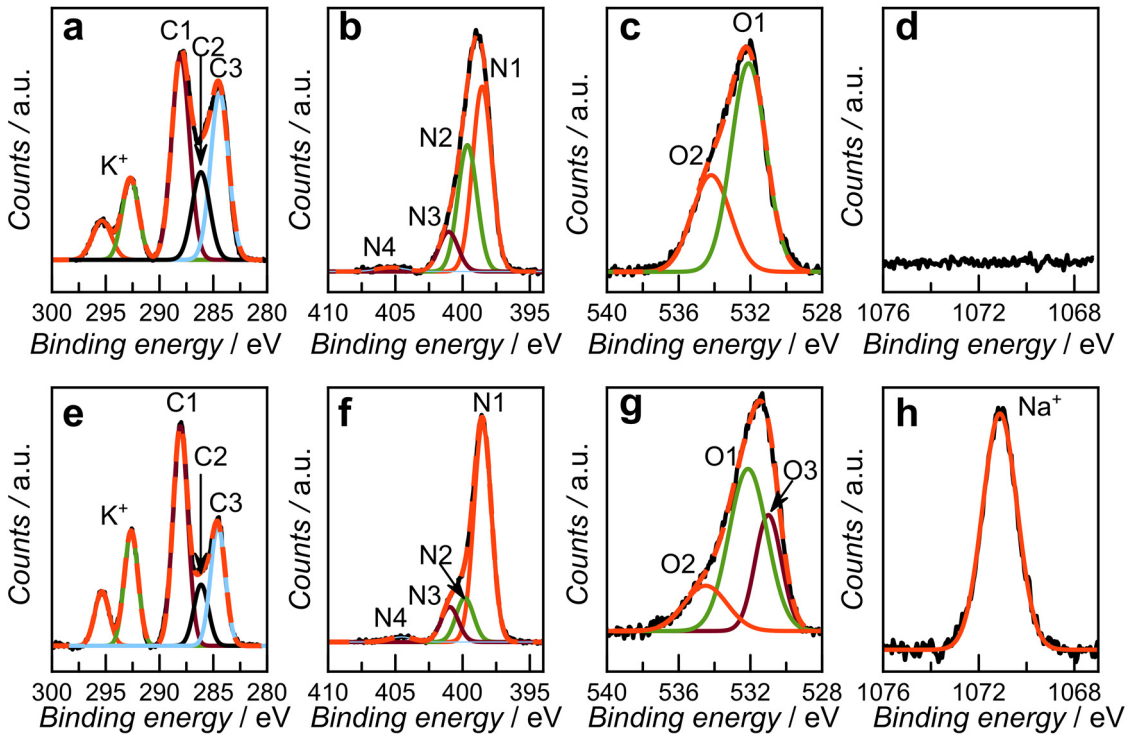

Figure S9. (a, b, c, d) and (e, f, g, h) XP C1s, N1s, O1s and Na1s spectra obtained for the K-PHI-S and K,Na-PHI samples, respectively.

Table S4. XPS data analysis.

Peak	Assignment	Peak position / eV	
		K-PHI-S	K,Na-PHI
C1	N-C=N, C=O	288.0	288.1
C2	C-OH, C-NH_2	286.2	286.1
C3	C-C from carbon tape and adventitious carbon	284.4	284.6
N1	C-N=C, C≡N	398.5	398.5
N2	N-C_3, triazine C-NH_x*	399.6	399.8
N3	C-NH_x	401.0	400.9
N4	N-N	405.3	405.4
O1	O=C-O	532.1	532.1
O2	H_2O	534.2	534.5
O3	HCO_3^-	-	531.0
Ratio between the areas corresponding to the N1:N2:N3 species			
		1:0.68:0.21	1:0.20:0.16

*Peak N2 cannot be assigned solely to the N-C_3 groups, since the ratio between the peak areas of N2:N1 in the K-PHI-S sample of 0.68:1 is far superior to the theoretically possible for the fully condensed polyheptazine structure (*ca.* 0.16:1). We attribute this peak also to the contribution from -NH_x bearing triazine fragments such as melamine.[11,12]

Theoretical study of K,Na-PHI

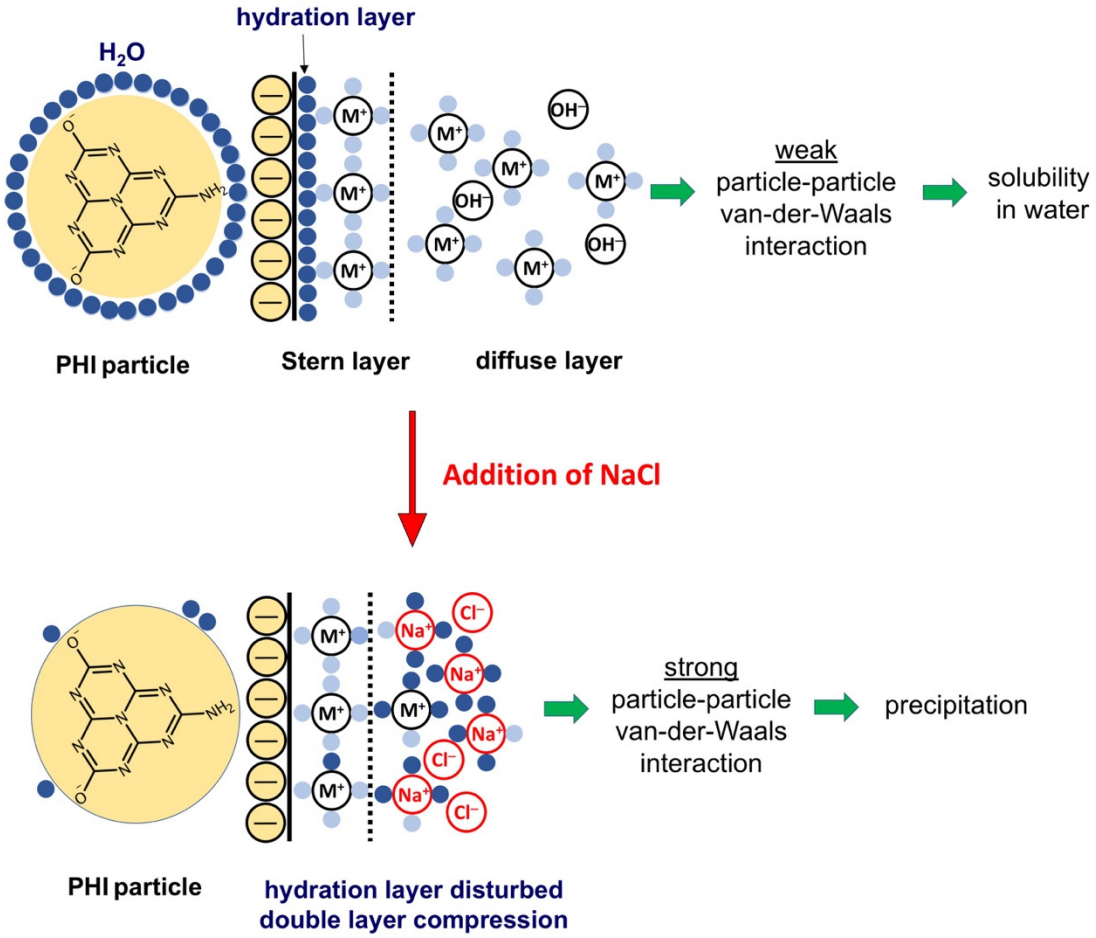

Figure S10. The salting out effect of NaCl addition on the double layer of the K,Na-PHI nanoparticles and their subsequent precipitation. At low ionic strength, the surface of PHI particles is covered with a hydration layer of water molecules, and the electric double layer extends over a relatively large distance, making the inter-particle van-der-Waals attractive forces weak. With increasing Na^+ concentration, due to the addition of NaCl, the hydration layer will gradually be stripped, disturbed as the water molecules hydrate preferentially the Na^+ cations; at the same time, the double layer is compressed due to the more effective screening by Na^+ ions. These effects result in stronger attractive particle-particle van-der-Waals interaction, leading to the coalescence of K,Na-PHI nanoparticles and their precipitation. The process is reversible: after centrifugation and removal of concentrated NaCl solution, the addition of water yields the PHI colloidal particles fully soluble again. M^+ stands for Na^+ or K^+.

The model system used for calculations is shown in Fig. S11 and is based on our experimental characterization; it exhibits a higher degree of condensation than typical carbon nitride model systems based on a periodic arrangement of melon strings but leaves enough boundaries to accommodate some functional groups to represent different N or O containing moieties.

Results of the solvation stabilisation study using the GLSSA13 implicit solvation model are summarized in Table S5. The stability of the model system in water, acetonitrile, and methanol is compared. Two main trends can be extracted from this data: (i) the water environment appears to stabilise the model system more strongly than the other two polar solvents, and (ii) stabilisation improves as a function of the number of oxygen-containing moieties.

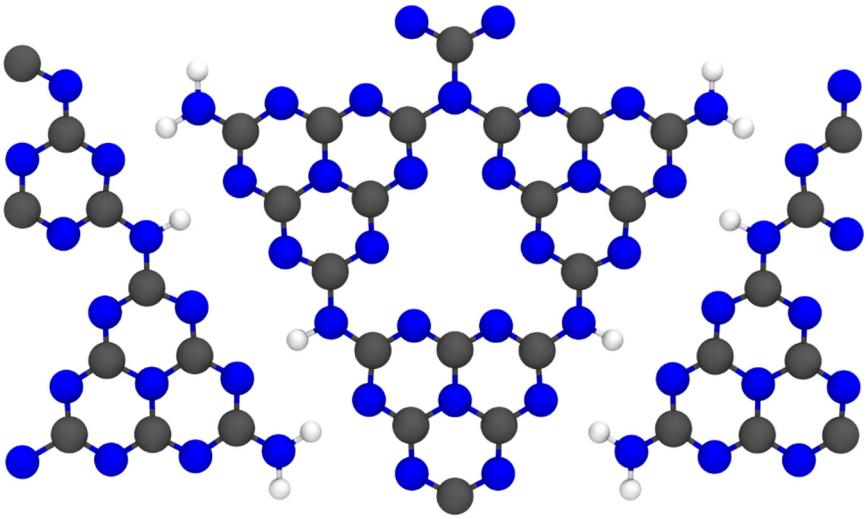

Figure S11. Illustration of one unit cell of the periodic computational carbon nitride model employed in the DFT study. The four -NH_2 groups are subsequently exchanged for -OH for the solvation study.

Table S5. Stabilisation of the carbon nitride model system in different implicit solvent models.

	Stabilization / eV vs. gas phase		
# of NH_2 exchanged	in water	in ACN	in MeOH
0	-1.46	-1.14	-1.10
1	-1.57	-1.24	-1.19
2	-1.66	-1.31	-1.26
3	-1.76	-1.40	-1.34
4	-1.86	-1.48	-1.42

DLS analysis

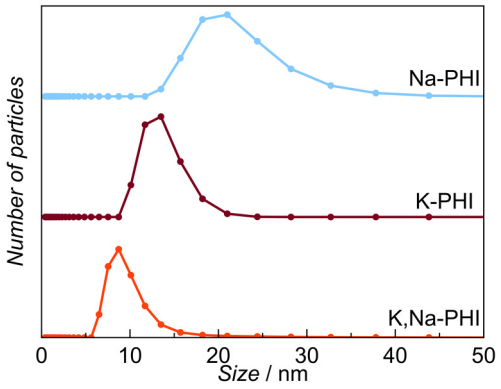

Figure S12. DLS particle size distribution of the poly(heptazine imide) samples.

SEM and TEM investigation

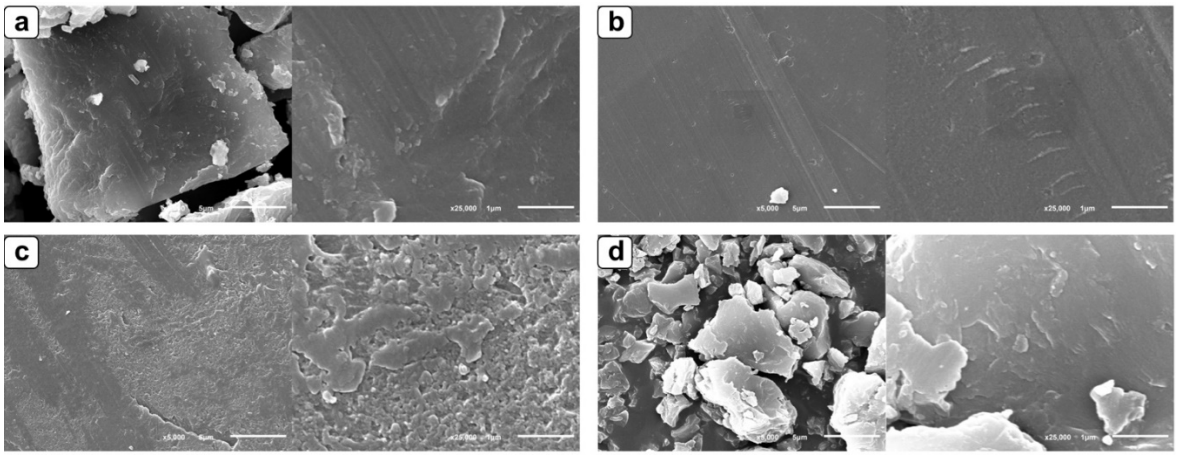

Figure S13. SEM images of the (a) K-PHI-S, (b) K-PHI, (c) Na-PHI and (d) K,Na-PHI samples.

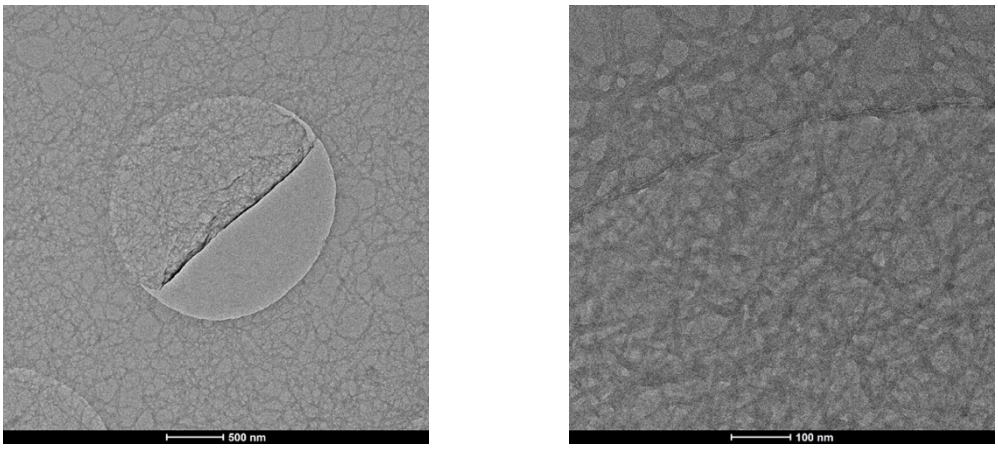

Figure S14. TEM images of the K,Na-PHI sample.

Photocatalytic studies

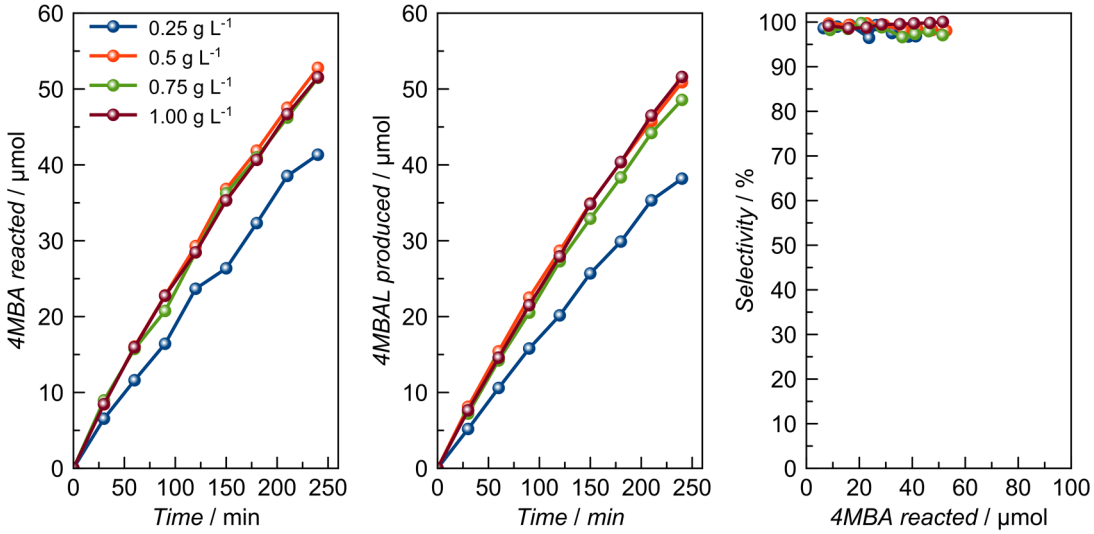

Figure S15. Photocatalytic 4MBA oxidation at different loadings of the K-PHI-S sample (20 mL H_2O, 4MBA 0.1 mmol, LED 365 nm).

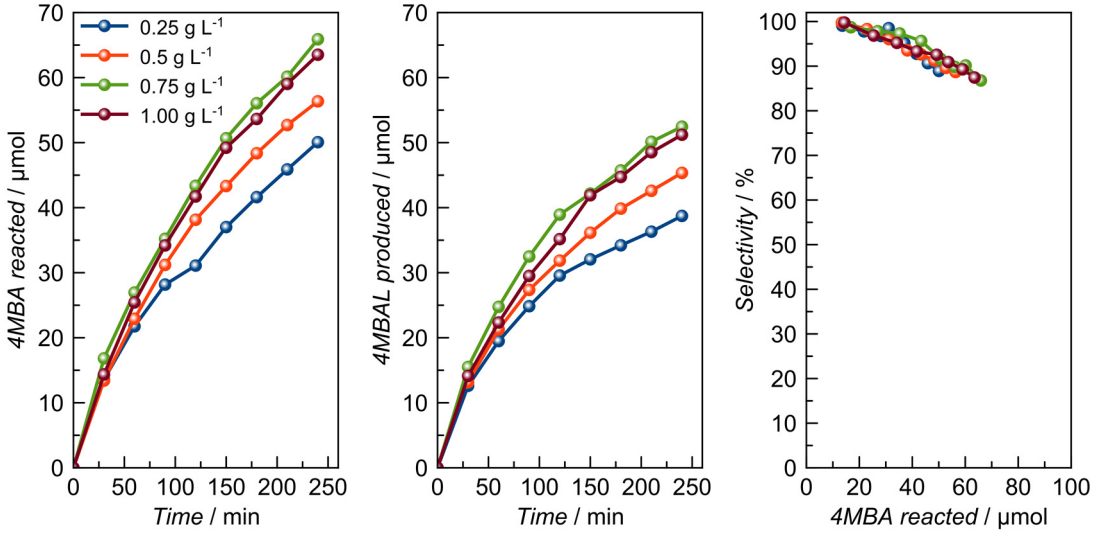

Figure S16. Photocatalytic 4MBA oxidation at different loadings of the K,Na-PHI sample (20 mL H_2O, 4MBA 0.1 mmol, LED 365 nm).

Table S6. Results of photocatalytic oxidation of 4MBA to 4MBAL with the concurrent H_2O_2 production

Sample	4MBA oxidation rate constant *10^3 / min^{-1}[a]	4MBA reacted in 4h / µmol	Selectivity to 4MBAL at 50% of 4MBA conversion / %	Selectivity to 4MBAL after 4 h / %	Selectivity to H_2O_2 after 4 h / %
CN H_2O	-1.4	28	-	≥ 99	97
K-PHI-S H_2O	-2.9	53	97	97	67
K,Na-PHI H_2O	-3.9	64	92	87	48
K,Na-PHI 10 % MeCN	-6.7	82	94	82	51
K,Na-PHI 20 % MeCN	-8.8	88	97	83	62
K,Na-PHI 40 % MeCN	-9.1	86	97	91	76
K,Na-PHI 50 % MeCN	-8.6	87	97	93	74
K,Na-PHI 70 % MeCN	-3.7	56	≥ 99	≥ 99	75
K,Na-PHI 85 % MeCN	-3.7	60	98	98	78

[a] The oxidation rate is quantified considering a pseudo-first order model with R^2 always ≥ 0.98

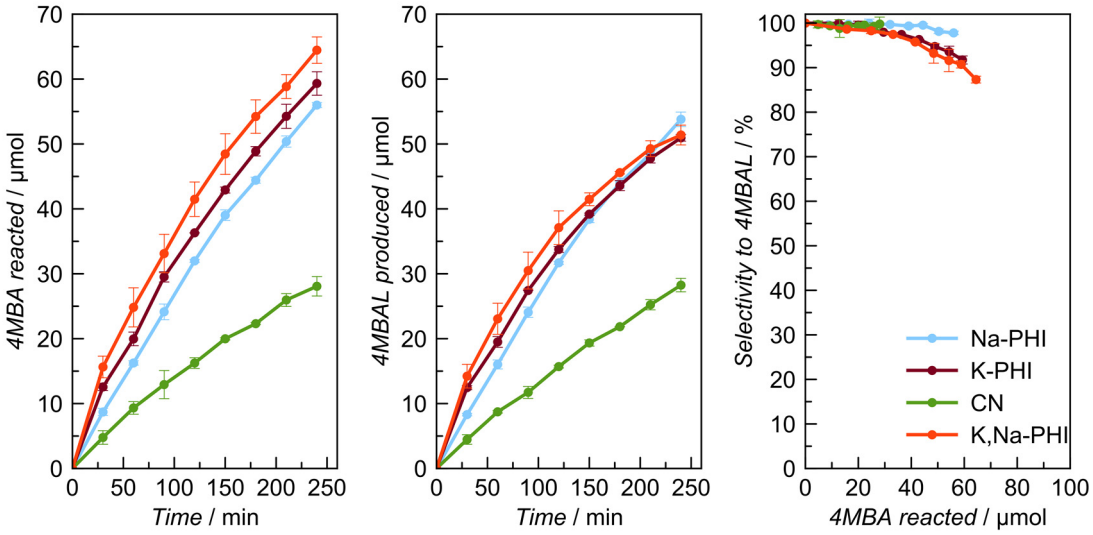

Figure S17. Photocatalytic 4MBA oxidation in the presence of K-PHI and Na-PHI samples (20 mL H_2O, 4MBA 0.1 mmol, LED 365 nm).

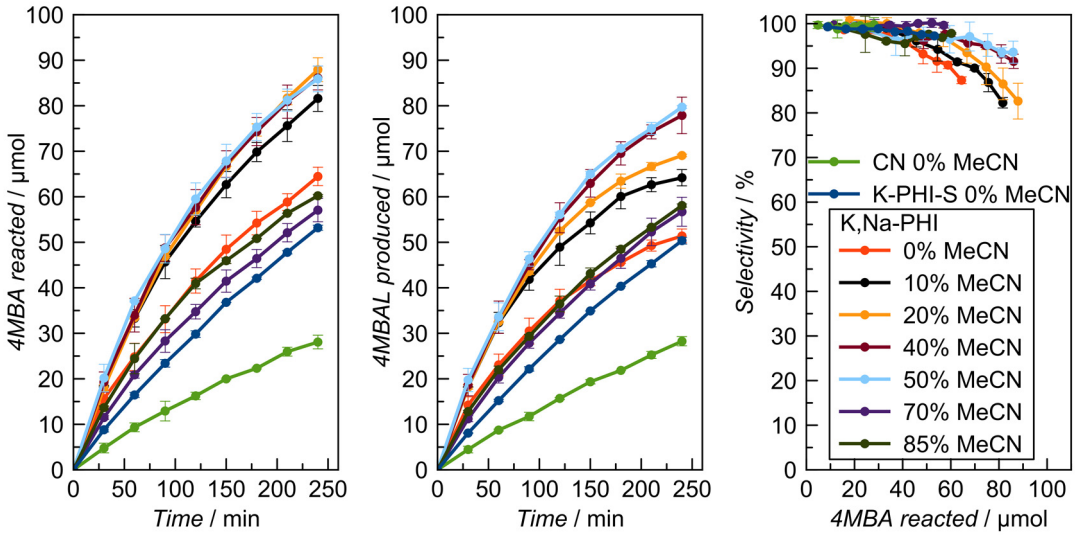

Figure S18. Photocatalytic oxidation of 4MBA in H_2O (20 mL, 4MBA 0.1 mmol, LED 365 nm) and in H_2O/MeCN mixture in the presence of K,Na-PHI (20 mL, X vol% of MeCN, 4MBA 0.1 mmol, LED 365 nm).

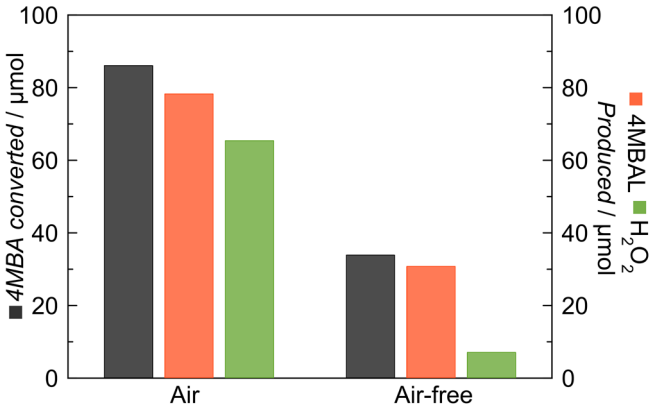

Figure S19. Conversion and selectivity of photocatalytic oxidation of 4MBA towards 4MBAL in air-free atmosphere (0.1 mmol 4MBA, 20 mL, H_2O/MeCN(40 vol.%), 365 nm, 4h) in presence of the K,Na-PHI photocatalyst.

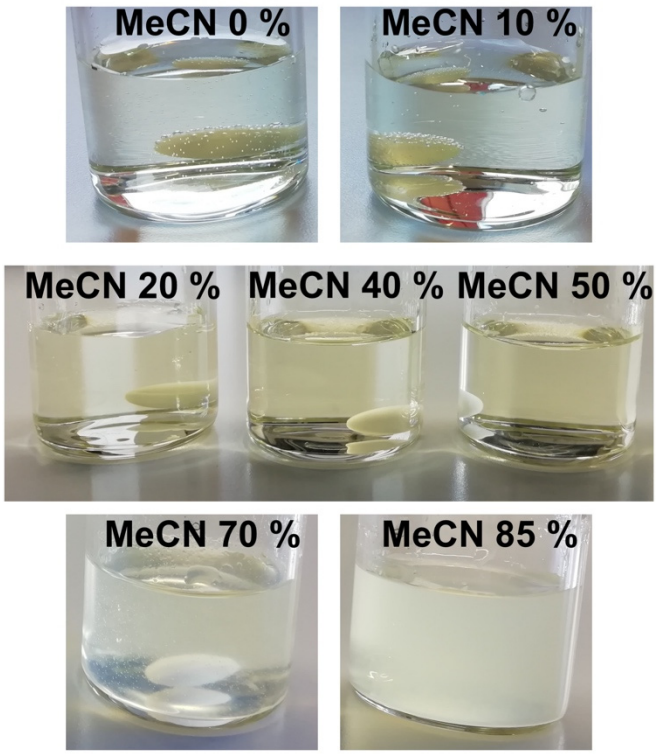

Figure S20. Photographs of the K,Na-PHI sample suspended in 4MBA solutions having varied MeCN vol. %.

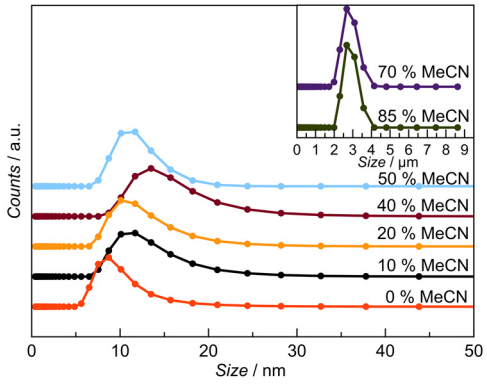

Figure S21. DLS particle size distribution of the K,Na-PHI sample suspended in 4MBA solutions having varied MeCN vol. %.

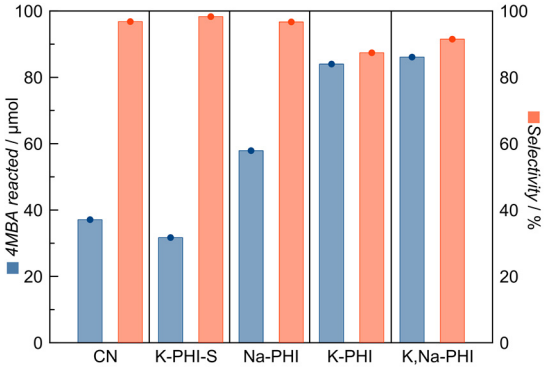

Figure S22. Conversion and selectivity of photocatalytic oxidation of 4MBA towards 4MBAL (0.1 mmol 4MBA, 20 mL, H_2O/MeCN(40 vol.%), 365 nm, 4 h) in presence of different photocatalysts.

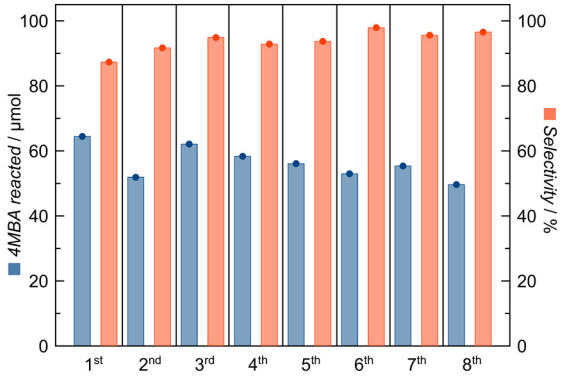

Figure S23. Recyclability test of the K,Na-PHI samples for 4MBA oxidation (20 mL, H_2O, 4MBA 0.1 mmol, LED 365 nm, 4 h of irradiation, 0.25 g of NaCl is added for the photocatalyst recovery).

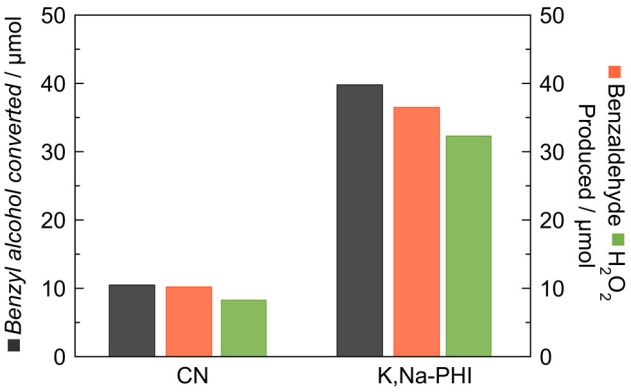

Figure S24. Conversion and selectivity of photocatalytic oxidation of benzyl alcohol towards benzaldehyde (0.1 mmol 4MBA, 20 mL of H_2O, 365 nm, 4 h) in presence of the CN and K,Na-PHI photocatalysts.

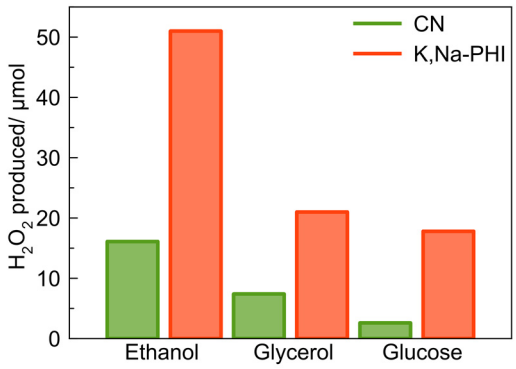

Figure S25. Photocatalytic H_2O_2 production using ethanol, glycerol and glucose as hole scavengers (ethanol and glycerol 1 wt. % solutions in 20 mL of H_2O, glucose 100 mg dissolved in 20 mL of water, 365 nm, 4h) in presence of the conventional CN and the water-soluble K,Na-PHI photocatalysts. The H_2O_2 production was enhanced by the factors of 3.2, 2.8 and 6.8 using ethanol, glycerol and glucose as reducing agents, respectively.

References

1. G. Kresse, J. Hafner, *Phys. Rev. B* **1993**, *47*, 558–561.
2. G. Kresse, J. Hafner, *Phys. Rev. B* **1994**, *49*, 14251–14269.
3. G. Kresse, J Furthmüller, *Comput. Mater. Sci.* **1996**, *6*, 15–50.
4. G. Kresse, J. Furthmüller, *Phys. Rev. B* **1996**, *54*, 11169–11186.
5. G. Kresse, D. Joubert, *Phys. Rev. B* **1999**, *59*, 1758–1775.
6. J. P. Perdew, K. Burke, M. Ernzerhof, *Phys. Rev. Lett.* **1996**, *77*, 3865–3868.
7. D. Gunceler, K. Letchworth-Weaver, R. Sundararaman, K. A. Schwarz, T. A. Arias, *Model. Simul. Mater. Sci. Eng.* **2013**, *21*, 074005.
8. K. Mathew, R. G. Hennig, *ArXiv160103346 Cond-Mat* (2016).
9. K. Mathew, R. Sundararaman, K. Letchworth-Weaver, T. A. Arias, R. G. Hennig, *J. Chem. Phys.* **2014**, *140*, 084106.
10. H. J. Monkhorst, *Phys. Rev. B* **1976**, *13*, 5188–5192.
11. A. P. Dementjev,et al. *Diamond Relat. Mater.* **2000**, *9***,** 1904-1907
12. D. L. Zu, et al. *J. Mater. Sci.* **2007**, *43***,** 689-695

4.5 Water-soluble ionic carbon nitride as unconventional stabilizer for highly catalytically active ultrafine gold nanoparticles

The following article is reprinted without changes from Mohamed M. Elnagar, Johannes Liessem, **Changbin Im**, Dariusz Mitoraj, Ludwig A. Kibler, Christof Neumann, Andrey Turchanin, Robert Leiter, Ute Kaiser, Timo Jacob, Igor Krivtsov, Radim Beranek.

"Water-soluble ionic carbon nitride as unconventional stabilizer for highly catalytically active ultrafine gold nanoparticles." *Nanoscale* 15.47 (2023): 19268-19281, DOI:10.1039/D3NR03375A.

This article is licensed under a Creative Commons Attribution 3.0 Unported Licence. You can use material from this article in other publications without requesting further permissions from the RSC, provided that the correct acknowledgement is given. (CC BY 3.0, https://creativecommons.org/licenses/by/3.0)

Author contributions: Changbin Im performed all the calculations. The manuscript was written through contributions of all authors. All authors discussed the results and commented on the manuscript.

Water-soluble ionic carbon nitride as unconventional stabilizer for highly catalytically active ultrafine gold nanoparticles

4.5.1 Abstract

Ultrafine metal nanoparticles (NPs) hold promise for applications in many fields, including catalysis. However, ultrasmall NPs are typically prone to aggregation, which often leads to performance losses, such as severe deactivation in catalysis. Conventional stabilization strategies (e.g., immobilization, embed- ding, or surface modification by capping agents) are typically only partly effective and often lead to loss of catalytic activity. Herein, a novel type of stabilizers based on water-soluble ionic (K+ and Na+ containing) polymeric carbon nitride (i.e., K,Na-poly(heptazine imide) = K,Na-PHI) is reported that enables effective stabilization of highly catalytically active ultrafine (size of 2-3 nm) gold NPs. Experimental and theoretical comparative studies using different structural units of K,Na-PHI (i.e., cyanurate, melonate, cyamelurate) indicate that the presence of functionalized heptazine moieties is crucial for the synthesis and stabilization of small Au NPs. The K,Na-PHI-stabilized Au NPs exhibit remarkable dispersibility and outstanding stability even in solutions of high ionic strength, which is ascribed to more effective charge delocalization in the large heptazine units, resulting in more effective electrostatic stabilization of Au NPs. The outstanding catalytic performance of Au NPs stabilized by K,Na-PHI is demonstrated using the selective reduction of 4-nitrophenol to 4-aminophenol by $NaBH_4$ as a model reaction, in which they outperform even the benchmark naked Au NPs electrostatically stabilized by excess $NaBH_4$. This work thus establishes ionic carbon nitrides (PHI) as alternative capping agents enabling effective stabilization without compromising surface catalysis, and opens up a route for further developments in utilizing PHI-based stabilizers for the synthesis of high-performance nanocatalysts.

4.5.2 Conclusion

In this work, we demonstrate for the first time that water-soluble ionic (K + and Na + containing) polymeric carbon nitride (K,Na-PHI) can act as a facile, scalable, and highly effective stabilizer in the synthesis of highly catalytically active ultrafine (<3 nm) gold nanoparticles. In the selective reduction of 4-nitrophenol to 4-aminophenol by NaBH 4 employed as a model catalytic reaction, the K,Na-PHI-stabilized Au NPs not only outperform Au NPs stabilized by monomeric structural units of K,Na-PHI (cyanurate, melonate, cyamelurate), but their activity is even superior (TOF higher by the factor of around 1.6) to that of the benchmark naked (i.e., ligand-free) Au NPs electrostatically stabilized by excess $NaBH_4$. These results suggest that K,Na-PHI can provide an effective electrostatic stabilization against the aggregation of Au NPs, without blocking the diffusion of the reactants and products to and from the active sites at the Au catalyst surface. A truly outstanding feature of our K,Na-PHI-stabilized Au NPs is their excellent stability both under ambient conditions (over at least two months), as well as under high ionic strength conditions (up to 0.1 M NaCl solutions) and at elevated temperatures (85 °C for at least 72 hours). Based on our experimental evidence and theoretical calculations, we propose that the strongly enhanced stability of Au NPs stabilized by K,Na-PHI can be explained by the ability of K,Na-PHI to act as a hydrated protective layer that is, due to the more pronounced delocalization of charges, less prone to the double layer compression effects and thus more effectively diminishes the attractive forces between the nano-particles. Moreover, a detailed comparative study using different structural units of K,Na-PHI (cyanurate, melonate, cyamelurate) shows that in particular the presence of functionalized heptazine moieties allowing for better charge delocalization is crucial for the synthesis and more effective stabilization of small Au NPs. This is corroborated by theoretical DFT calculations of Fukui functions which reveal the beneficial effect of the counterion-balanced cyamelurate and cyanamide functional groups in the ionic carbon nitride

on the orbital alignment and electron delocalization, resulting in more effective stabilization of Au NPs. Thus, this work establishes the ionic carbon nitrides (PHI) as alternative capping agents for nanocatalysts that enable effective stabilization without compromising surface catalysis. More generally, it opens up a route for further developments in utilizing PHI-based stabilizers for the synthesis of high-performance ultrafine nanoparticles, especially for applications in which both the stability and the effective transport of species between the interfacial region of nanoparticles and the environment is mandatory.

4.5.3 Contribution to the Conclusion

As a shared First author, I contributed to the theoretical investigation of the stabilization mechanisms of gold nanoparticles (Au NPs) by functionalized carbon nitride species through density functional theory (DFT) calculations. My work involved optimizing the geometries of KCA, KCya, and KMel structures to analyze the impact of conjugation size, the nature of functional groups (cyamelurate and cyanamide), and the role of counterions. By modeling systems with varying numbers of counterions, I demonstrated their critical role in facilitating structural planarization, which enhances -electron conjugation and extends the delocalized electron cloud to functional groups. Additionally, I conducted the Fukui function analysis to elucidate the electronic interactions between the stabilizer and Au NPs, showing how counterions align directional orbitals and improve stabilization. This theoretical insight complemented experimental findings, highlighting that structurally planar species such as KCya, K,Na-PHI, and KMel stabilize Au NPs more effectively than distorted configurations like KCA. My contributions provided a comprehensive understanding of the synergistic effects of functional groups and counterions, advancing the design of effective stabilizers for Au NPs.

Nanoscale

PAPER

View Article Online
View Journal | View Issue

Check for updates

Cite this: *Nanoscale*, 2023, **15**, 19268

Water-soluble ionic carbon nitride as unconventional stabilizer for highly catalytically active ultrafine gold nanoparticles†

Mohamed M. Elnagar, ‡[a] Johannes Liessem,‡[a] Changbin Im,‡[a] Dariusz Mitoraj, [a] Ludwig A. Kibler, [a] Christof Neumann, [b] Andrey Turchanin, [b] Robert Leiter,[c] Ute Kaiser,[c] Timo Jacob, *[a,d,e] Igor Krivtsov *[a,f] and Radim Beranek *[a]

Ultrafine metal nanoparticles (NPs) hold promise for applications in many fields, including catalysis. However, ultrasmall NPs are typically prone to aggregation, which often leads to performance losses, such as severe deactivation in catalysis. Conventional stabilization strategies (*e.g.*, immobilization, embedding, or surface modification by capping agents) are typically only partly effective and often lead to loss of catalytic activity. Herein, a novel type of stabilizers based on water-soluble ionic (K^+ and Na^+ containing) polymeric carbon nitride (*i.e.*, K,Na-poly(heptazine imide) = K,Na-PHI) is reported that enables effective stabilization of highly catalytically active ultrafine (size of ~2–3 nm) gold NPs. Experimental and theoretical comparative studies using different structural units of K,Na-PHI (*i.e.*, cyanurate, melonate, cyamelurate) indicate that the presence of functionalized heptazine moieties is crucial for the synthesis and stabilization of small Au NPs. The K,Na-PHI-stabilized Au NPs exhibit remarkable dispersibility and outstanding stability even in solutions of high ionic strength, which is ascribed to more effective charge delocalization in the large heptazine units, resulting in more effective electrostatic stabilization of Au NPs. The outstanding catalytic performance of Au NPs stabilized by K,Na-PHI is demonstrated using the selective reduction of 4-nitrophenol to 4-aminophenol by $NaBH_4$ as a model reaction, in which they outperform even the benchmark "naked" Au NPs electrostatically stabilized by excess $NaBH_4$. This work thus establishes ionic carbon nitrides (PHI) as alternative capping agents enabling effective stabilization without compromising surface catalysis, and opens up a route for further developments in utilizing PHI-based stabilizers for the synthesis of high-performance nanocatalysts.

Received 11th July 2023,
Accepted 13th November 2023

DOI: 10.1039/d3nr03375a

rsc.li/nanoscale

Open Access Article. Published on 13 November 2023. Downloaded on 7/31/2024 11:34:38 AM.
This article is licensed under a Creative Commons Attribution 3.0 Unported Licence.

Introduction

Ultrafine and highly dispersed metal nanoparticles (NPs) exhibit unique optical, electronic and surface properties, and hold promise for application in various fields, including nanotechnology, optoelectronics, biomedicine, sensing, and catalysis.[1–12] In the field of heterogeneous catalysis, ultrafine (*i.e.*, particles with an average size of *ca.* ≤3 nm) metal NPs often show enhanced catalytic properties that are distinct from their larger counterparts due to the effects of electron energy quantization and surface geometry, *i.e.*, specific surface atom arrangement and coordination.[13,14] For example, ultrafine gold NPs, owing to their large surface area, exposing various surface facets, and a high number of undercoordinated atoms at edge and corner sites, are known to exhibit extraordinary performance in various catalytic conversions, such as CO oxidation, hydrogenation, oxidation of alcohols, coupling reactions, and reduction reactions.[15–19] However, ultrafine metal NPs are thermodynamically and kinetically unstable and tend to aggregate in order to reduce the surface free energy, often resulting in a drastic loss of catalytic performance over time, and thus limiting their practical application.[20,21] Typical strategies to stabilize NPs consist in immobilization on high surface area

[a]*Institute of Electrochemistry, Ulm University, Albert-Einstein-Allee 47, 89081 Ulm, Germany. E-mail: radim.beranek@uni-ulm.de, timo.jacob@uni-ulm.de, krivtsovigor@uniovi.es*
[b]*Institute of Physical Chemistry, Jena Center for Soft Matter (JCSM) and Center for Energy and Environmental Chemistry Jena (CEEC), Friedrich Schiller University Jena, Lessingstr. 10, 07743 Jena, Germany*
[c]*Electron Microscopy of Materials Science, Central Facility for Electron Microscopy, Ulm University, Albert-Einstein-Allee 11, 89081 Ulm, Germany*
[d]*Helmholtz-Institute-Ulm (HIU) Electrochemical Energy Storage, Helmholtzstr. 11, 89081 Ulm, Germany*
[e]*Karlsruhe Institute of Technology (KIT), P.O. Box 3640, 76021 Karlsruhe, Germany*
[f]*Department of Chemical and Environmental Engineering, University of Oviedo, 33006 Oviedo, Spain*

†Electronic supplementary information (ESI) available. See DOI: https://doi.org/10.1039/d3nr03375a

‡These authors contributed equally to this work.

This journal is © The Royal Society of Chemistry 2023

Open Access Article. Published on 13 November 2023. Downloaded on 7/31/2024 11:34:38 AM. This article is licensed under a Creative Commons Attribution 3.0 Unported Licence.

supports, embedding into molecular cage-like materials (*e.g.*, metal–organic frameworks, MOFs), or surface protection by molecules or ions that can act as effective capping agents.[2,22–32] However, all these strategies have also drawbacks. The supported catalysts often exhibit decreased activity as compared to colloidal NPs,[33] and suffer from nanoparticle migration and aggregation, irregular distribution and regrowth, and weak affinity of metal NPs to supports, resulting in increased leaching.[2] The applicability of MOF-embedded metal NPs in catalysis is often limited due to MOF stability issues under catalytic conditions.[34] Finally, the surface capping agents can not only inhibit aggregation but also block the active sites on the NP surface, leading to reduced catalytic activities.[22,23,35] A typical example would be the strongly inhibiting effect of low-weight thiolated polyethylene glycol (HS-PEG) as a stabilizing ligand on the catalytic activity of Au NPs towards the reduction of 4-nitrophenol.[22] Considering the aforementioned aspects, the development of new stabilizers that can effectively stabilize metal NPs without blocking the active sites and the diffusion of the reactants and products to and from the metal surface is of paramount importance in catalysis.

Recently, we reported the first synthesis of fully water-soluble *ionic* polymeric carbon nitride, *i.e.*, potassium and sodium ion-containing poly(heptazine imide) (K,Na-PHI),[36] an ionic member of the polymeric carbon nitride family.[37–43] In aqueous solutions, the K,Na-PHI material can be fully dispersed in form of very small K,Na-PHI colloidal nanoparticles (hydrodynamic diameter ~10 nm) containing a large number of cyanamide and cyamelurate surface moieties, resulting in highly stable *quasi*-homogeneous solutions of K,Na-PHI with no gelation or precipitation over several months.[36] Given the unique features of K,Na-PHI (*i.e.*, water solubility, chemical stability, and ionic nature), we hypothesized that water-soluble K,Na-PHI might open a completely new and attractive possibility to stabilize catalytically active metal NPs. While various promising properties of ionic carbon nitrides, such as their photocatalytic activity and charge storage properties, are well established,[36,37,39,40,44–47] the use of ionic carbon nitrides as stabilizers has not been reported so far. In this contribution, we demonstrate, for the first time, the ability of K,Na-PHI to effectively stabilize ultrafine Au NPs (<3 nm). The stabilized Au NPs exhibit very high catalytic activity in the selective reduction of 4-nitrophenol (4-NP) to 4-aminophenol (4-AP) using $NaBH_4$ as a reducing agent (Fig. 1), a widely used model reaction for evaluating the catalytic activity of nanocatalysts in aqueous media.[22,23,48,49] Moreover, they show robust stability against agglomeration and excellent dispersibility for at least 2 months, as well as excellent accessibility in solution, as demonstrated by turnover frequencies superior to "naked" Au nanoparticles stabilized solely by excess BH_4^- anions. The stabilization effect of K,Na-PHI is elucidated using a comparative analysis employing different structural units of K,Na-PHI (cyanurate, melonate, and cyamelurate) and *ab initio* theoretical calculations, and the dominant role of functionalized heptazine moieties for the stabilization of Au NPs is discussed.

Experimental procedures and computational details

All experimental procedures and computational details are provided in the ESI.†

Results and discussion

Effect of the proposed stabilizers on Au NPs

Water-soluble K,Na-PHI has various functional groups attached to the heptazine units. Our structural analyses and theoretical calculations proposed that K,Na-PHI is characterized by a decreased number of terminal NH_x-groups, as compared to conventional, water-insoluble PCN, that are exchanged with cyamelurate and melonate moieties.[36] Furthermore, an incomplete condensation of the PCN precursor might result in the formation of triazine species within the polymer. Therefore, to obtain a deeper insight into the possible interactions between the Au NPs and K,Na-PHI, we also studied the stabilization effect of potassium melonate (KMel), potassium cyamelurate (KCya), and potassium cyanurate (KCA)

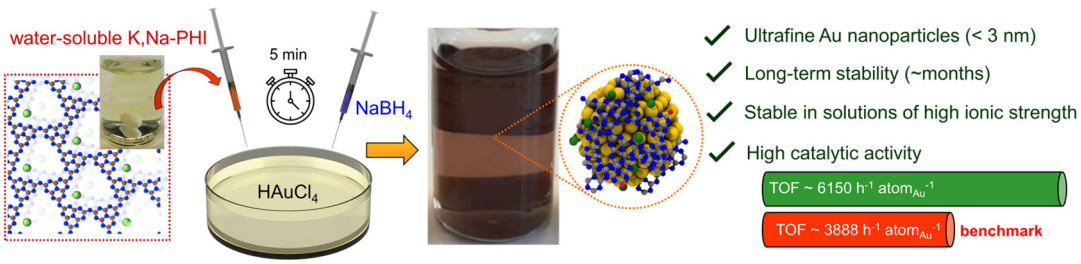

Fig. 1 Concept of effective stabilization of ultrafine Au nanoparticles using water-soluble ionic carbon nitride. The Au NPs are readily obtained by the addition of water-soluble K,Na-PHI into an aqueous solution of $HAuCl_4$ and subsequent reduction by sodium borohydride. The resulting ultrafine Au NPs (size <3 nm) are stable over several months even in solutions of high ionic strength and outperform benchmark "naked" Au NPs stabilized solely by excess $NaBH_4$ in a model catalytic reaction (selective reduction of 4-nitrophenol to 4-aminophenol using $NaBH_4$ as a reducing agent).

Open Access Article. Published on 13 November 2023. Downloaded on 7/31/2024 11:34:38 AM.
This article is licensed under a Creative Commons Attribution 3.0 Unported Licence.

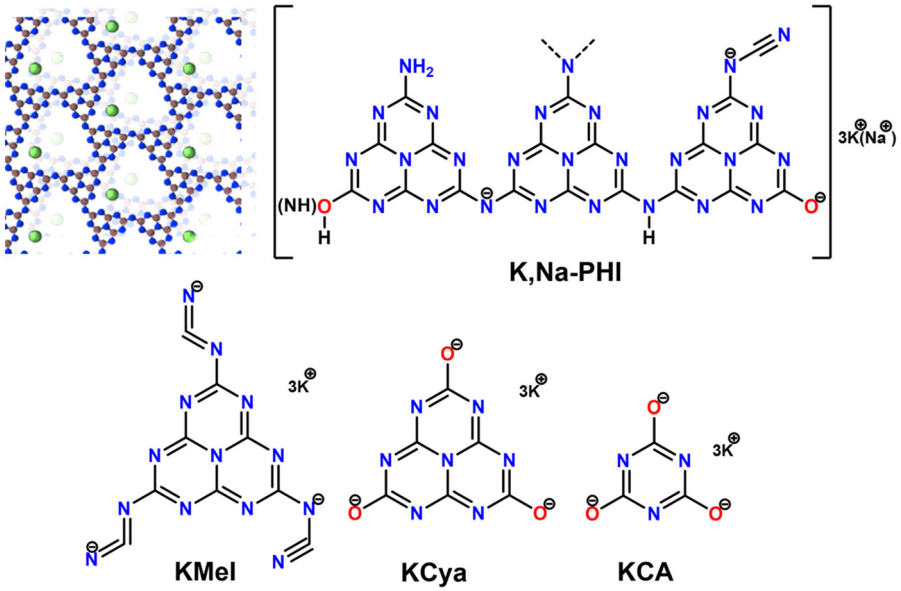

Fig. 2 Stabilizers used in the comparative analysis of the synthesis and catalytic activity of Au NPs. For K,Na-PHI both the typical 3D ionic carbon nitride structure comprising stacks of 2D heptazine-based networks and K^+ and Na^+ cations as well as a schematic structure highlighting the presence of charged surface moieties (*e.g.*, cyanamide and cyamelurate) is shown. For spectroscopic characterization (FTIR and NMR) see ESI, Fig. S1.†

at different concentrations (Fig. 2). For all the proposed stabilizers, $NaBH_4$ was used as a reducing agent for the synthesis of AuNPs. Notably, it is well established that the excess $NaBH_4$ can electrostatically stabilize even very small (~5 nm) colloidal Au NPs without any additional stabilizing agent.[50] Therefore, the "naked" (*i.e.*, ligand-free) Au NPs stabilized by excess $NaBH_4$ represent an ideal benchmark for comparative investigations of the effect of the proposed stabilizers on the size, long-term stability, and catalytic activity of Au NPs. This choice is further substantiated by the fact that though also other weakly binding ligands (*e.g.*, citrate) do allow for good accessibility of active sites on the Au nanoparticle surface, they are typically not able to stabilize Au NPs with sizes below 10 nm when using $NaBH_4$ as a reducing agent,[51–53] prohibiting thus comparative studies in the ultrafine size regime.

A 10-fold excess of $NaBH_4$ with respect to $HAuCl_4$ was selected as the optimum molar ratio of $NaBH_4$: $HAuCl_4$ to produce the benchmark ligand-free Au NPs (denoted as **Au10**) without agglomeration (for details see ESI 2.1†). For a systematic and realistic comparison, the same optimum $NaBH_4$ concentration was also used to fabricate Au NPs in the presence of K,Na-PHI and its monomeric constituents (KMel, KCya, and KCA). In general, the AuNPs stabilized by different concentrations of $NaBH_4$, K,Na-PHI, KMel, KCya, or KCA exhibit different colours and different electronic absorption properties, which is related to their different sizes and the differently pronounced surface plasmon resonance (SPR) effects (see ESI, Fig. S2 and S3,† and the detailed discussion of the optimization studies in ESI 2.1†). For a representative overview, Fig. 3 compares the UV-vis electronic absorption spectra and optical images as well as the average hydrodynamic diameters of **Au10**, **K,NaPHI2**, **KMel0.3**, **KCya0.3**, **KCA0.3** (the sample designations reflect the molar stabilizer : $HAuCl_4$ ratios; for details see ESI, Table S1†) that were obtained at the optimum concentrations for each stabilizer with respect to the smallest achievable size of stable NPs. As presented in Fig. 3a, the SPR peak of Au NPs stabilized by monomeric heptazine-based stabilizers (**K,NaPHI2**, **KMel0.3**, and **KCya0.3**) is less intense and broader than in the case of triazine-based stabilizers (**KCA0.3**) and **Au10**. Moreover, **K,NaPHI2** exhibits a considerably broader band with no discernible plasmonic feature at all, suggesting that most Au NPs are below ~5 nm in size.[54] These trends are consistent with the measurements of the hydrodynamic diameter using dynamic light scattering (DLS, Fig. 3b). In particular, the Au NP samples characterized by a relatively sharp and intense SPR peak show larger hydrodynamic diameters, indicating a larger particle size. More importantly, the inset of Fig. 3b demonstrates that **K,NaPHI2** possesses a very narrow hydrodynamic diameter distribution (3.0 ± 0.6 nm) as compared to other samples. These observations suggest that, although all the investigated triazine- and heptazine-based compounds can stabilize Au NPs, the size as well as the size distribution of the particles strongly depend on the polymerization degree of the stabilizer.

Zeta potential (ζ-potential) is the electric potential (Galvani potential) at the shear plane (*i.e.*, at the interface separating the mobile fluid from the fluid that remains attached to the NP surface), and represents an important indicator of the stability of colloidal suspensions by electrostatic repulsion forces. ζ-Potential is normally influenced by the nature of the NPs and the dispersion medium.[55] We measured the ζ-potential of the prepared suspensions of the Au NPs at the native pH value after dialysis against water to remove the excess $NaBH_4$ hydrolysis products. **Au10** displays a negative

 This journal is © The Royal Society of Chemistry 2023

Open Access Article. Published on 13 November 2023. Downloaded on 7/31/2024 11:34:38 AM.
This article is licensed under a Creative Commons Attribution 3.0 Unported Licence.

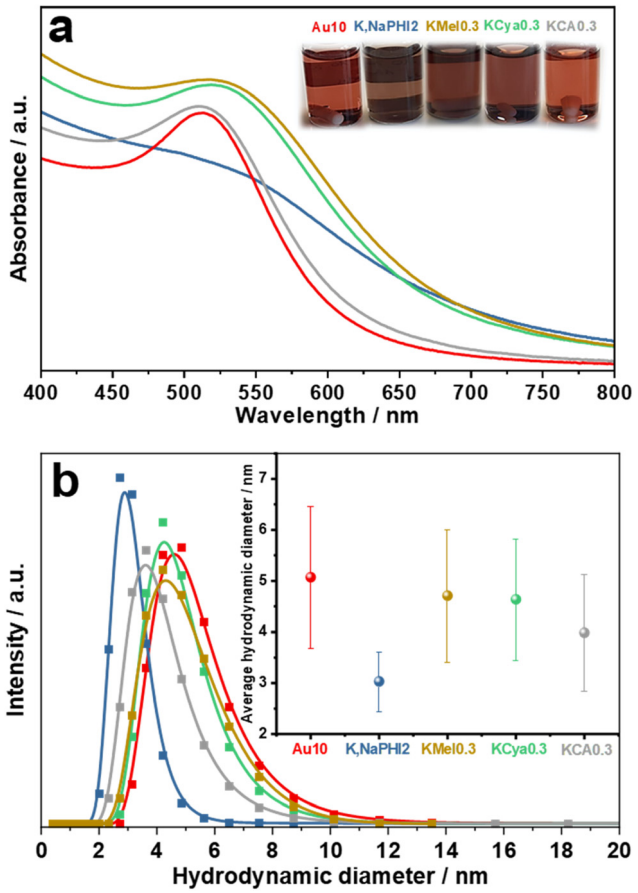

Fig. 3 Optical properties and hydrodynamic diameter of Au NPs: (a) UV-vis electronic absorption spectra and (b) hydrodynamic diameter data determined from the dynamic light scattering (DLS) of **Au10**, **K,NaPHI2**, **KMel0.3**, **KCya0.3**, and **KCA0.3**. The inset in (a) shows the optical images of the samples; the inset in (b) shows the average hydrodynamic diameters. The samples were measured after 1 day of their synthesis. The error bars were constructed as +/− the double of standard deviation (95% confidence interval).

ζ-potential value of −32 ± 1 mV (pH 6.8) because the surface of AuNPs is surrounded by a layer of BH_4^- or $B(OH)_4^-$. Similarly, **K,NaPHI2**, **KMel0.3**, **KCya0.3**, and **KCA0.3** show comparable negative ζ-potential values of −32 ± 2 (pH 6.0), −30 ± 1 (pH 5.7), −31 ± 1 (pH 5.5), and −32 ± 1 mV (pH 5.6), respectively, due to the negativity charged surface moieties (*e.g.*, cyanamide and cyamelurate) of heptazine and triazine-based stabilizers (see Fig. 2). The observed values of ζ-potential of *ca.* −30 mV are in line with the very good stability of NPs.[56]

Next, we analyzed the as-prepared samples using scanning transmission electron microscopy (STEM) as well as high-resolution transmission electron microscopy (HRTEM). The (S)TEM images of **Au10**, **K,NaPHI2**, **KMel0.3**, **KCya0.3**, and **KCA0.3** are shown in Fig. 4. The produced Au NPs with the proposed stabilizers have similar morphology, but the median diameter and the size distributions are different (Fig. 4f and ESI, Fig. S4†). The HAADF-STEM image of **Au10** shows the formation of dispersed Au NPs with a median diameter of around 5.6 nm, which is at least 2.5 times larger than that of **K,NaPHI2**, **KMel0.3**, and **KCya0.3**, but comparable to **KCA0.3**. Furthermore, the estimated particle size distributions reveal that **Au10** and **KCA0.3** have a broader size distribution than **K,NaPHI2**, **KMel0.3**, and **KCya0.3** (ESI, Fig. S4†). Notably, for samples stabilized by monomeric stabilizers (**KMel0.3**, **KCya0.3**, and **KCA0.3**) the observed trends are not fully in line with the trends of hydrodynamic diameters derived from the DLS measurements (compare Fig. 3b and Fig. 4f), which clearly indicates that the hydrodynamic diameter is strongly influenced by the nature of the stabilizer. Most importantly, in contrast to Au NPs stabilized by $NaBH_4$ only (**Au10**) or by cyanurate (**KCA0.3**), only K,Na-PHI (**K,NaPHI2**) and the monomeric *heptazine*-based stabilizers (**KMel0.3**, and **KCya0.3**) provide Au NPs in the ultra-small regime (sub-3 nm). The median diameter of Au NPs stabilized by K,Na-PHI is ~1.7 nm. This size is larger than the estimated cavity size of pol(heptazine imides) (~0.78 nm;[57] for a schematic representation of heptazine cages see ESI Fig. S5†), indicating that Au NPs are not confined in the heptazine cages.

X-ray photoelectron spectroscopy (XPS) analyses were performed to identify the oxidation state of gold and the chemical composition of **Au10**, **K,NaPHI2**, **KMel0.3**, **KCya0.3**, and **KCA0.3**. As shown in Fig. 5, the two distinct peaks centered at 83.6 and 87.3 eV correlate to the spin–orbit doublet of Au $4f_{7/2}$ and $4f_{5/2}$, respectively, demonstrating the presence of metallic Au in the samples.[58] Interestingly, the stabilizers do not significantly affect the binding energy of Au $4f_{7/2}$ and Au $4f_{5/2}$ electrons (ESI, Table S2†), which implies that the stabilizer moieties interact rather weakly with the surface of the Au NPs, most likely *via* electrostatic attractions.

Long-term stability of Au NPs

First, we have investigated the long-term stability of the produced Au NPs against agglomeration under ambient storage conditions. Fig. 6 compares the UV-vis spectra and average hydrodynamic diameters of **Au10**, **K,NaPHI2**, **KCya0.3**, and **KCA0.3** over time. The SPR peak and hydrodynamic diameter of **Au10**, **K,NaPHI2**, and **KCya0.3** did not change significantly over 28 days, indicating high stability against agglomeration (Fig. 6a–c and e). In contrast, **KCA0.3** tends to agglomerate over time, as demonstrated by a sharper SPR peak and larger hydrodynamic diameter after 28 days. Notably, **Au10** possesses a higher tendency to agglomeration after about two months of storage, as indicated by the red-shift of the SPR peak by about 10 nm (inset of Fig. 6a) and the larger hydrodynamic diameter (Fig. 6e). It should be noted that the **K,NaPHI2** shows outstanding stability for at least two months, suggesting that K,Na-PHI is a remarkably effective stabilizer that endows the Au NPs with long-term stability.

Further, we investigated the influence of various concentrations of K,Na-PHI, KCya, and KCA stabilizers on the stability of Au NPs over time (see ESI, Fig. S8a–c and Fig. S9a–f†). Notably, no changes in the UV-vis spectra of the Au NPs stabilized by K,Na-PHI are observed after two months of storage for all the investigated concentrations (ESI, Fig. S8a†). The DLS

Open Access Article. Published on 13 November 2023. Downloaded on 7/31/2024 11:34:38 AM.
This article is licensed under a Creative Commons Attribution 3.0 Unported Licence.

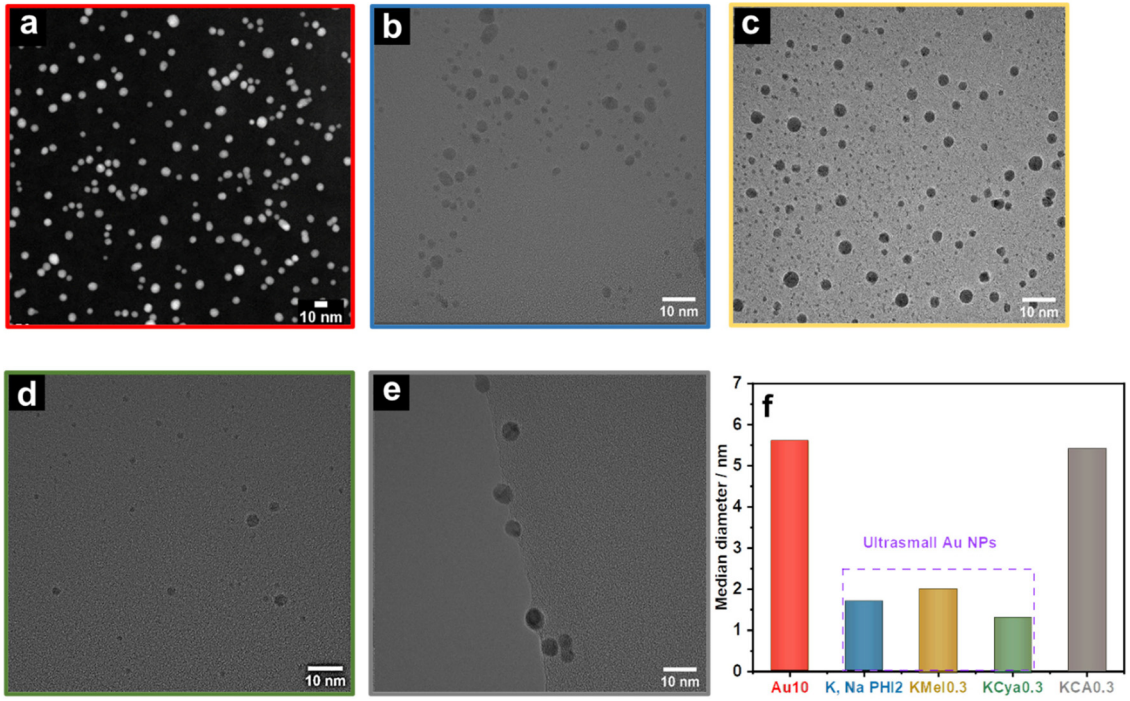

Fig. 4 Size of NPs. HAADF STEM image of (a) **Au10**, and HRTEM images of (b) **K,NaPHI2**, (c) **KMel0.3**, (d) **KCya0.3**, and (e) **KCA0.3**, and their corresponding median diameter (f) derived from the TEM images (for size distribution histograms see ESI, Fig. S4†).

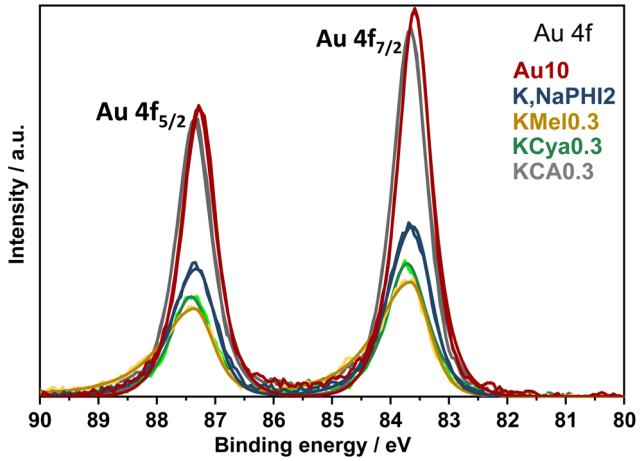

Fig. 5 XPS analysis. High-resolution Au 4f XP spectra of **Au10**, **K,NaPHI2**, **KMel0.3**, **KCya0.3**, and **KCA0.3**. Further details regarding the XPS analysis of all samples are provided in ESI, Fig. S6 and S7.†

measurements demonstrate that the hydrodynamic diameter of Au NPs increases as a function of K,Na-PHI concentration (ESI, Fig. S9a and b†), which suggests that the hydrodynamic diameter is strongly influenced not only by the nature of the stabilizer but also by its amount. Moreover, all the K,Na-PHI stabilized Au NPs are highly dispersed and stable for at least two months except for **K,NaPHI5**, where the hydrodynamic diameter is slightly increasing over time, possibly due to an excessively high amount of the stabilizer. In the case of KCya and KCA-stabilized Au NPs, the stability of the produced Au NPs decreases over time, especially when the molar ratios of the stabilizer with respect to $HAuCl_4$ are ≥10 (see ESI, Fig. S8b, c,† and Fig. 9c–f). The increased tendency to the agglomeration of Au NPs at higher concentrations of KCya and KCA is most likely due to the shorter Debye-length of the electrical double layer as a consequence of the higher ionic strength.[59,60]

Stability of Au NPs at high ionic strength

The stability of metal nanoparticles in solutions of high ionic strength is crucial for their application in catalysis and biology.[61] Therefore, the effect of ionic strength on the stability of **Au10**, **K,NaPHI2**, **KMel0.3**, **KCya0.3**, and **KCA0.3** was investigated by the addition of NaCl at different concentrations (0.001, 0.01, and 0.1 M). The corresponding optical images and average hydrodynamic diameter of the samples are shown in Fig. 7. Remarkably, **K,NaPHI2** and **KMel0.3** are stable and agglomeration-free for at least 6 days even in the presence of 0.1 M NaCl. In contrast, **Au10**, **KCya0.3**, and **KCA0.3** tend to agglomerate over time in the presence of 0.001 and 0.01 M NaCl, as indicated by a larger hydrodynamic diameter and darker brown colour after 6 days of storage. Moreover, the optical images of these samples demonstrate a complete agglomeration in the presence of 0.1 M NaCl after less than 24 h (Fig. 7a). Similar behaviour is well-known for Au NPs stabilized by electrostatic repulsion, such as citrate-capped Au NPs, and can be ascribed to the increased screening of the surface charge and compression of the double layer, resulting in a more attractive particle–particle van der Waals interaction

 This journal is © The Royal Society of Chemistry 2023

Open Access Article. Published on 13 November 2023. Downloaded on 7/31/2024 11:34:38 AM.
This article is licensed under a Creative Commons Attribution 3.0 Unported Licence.

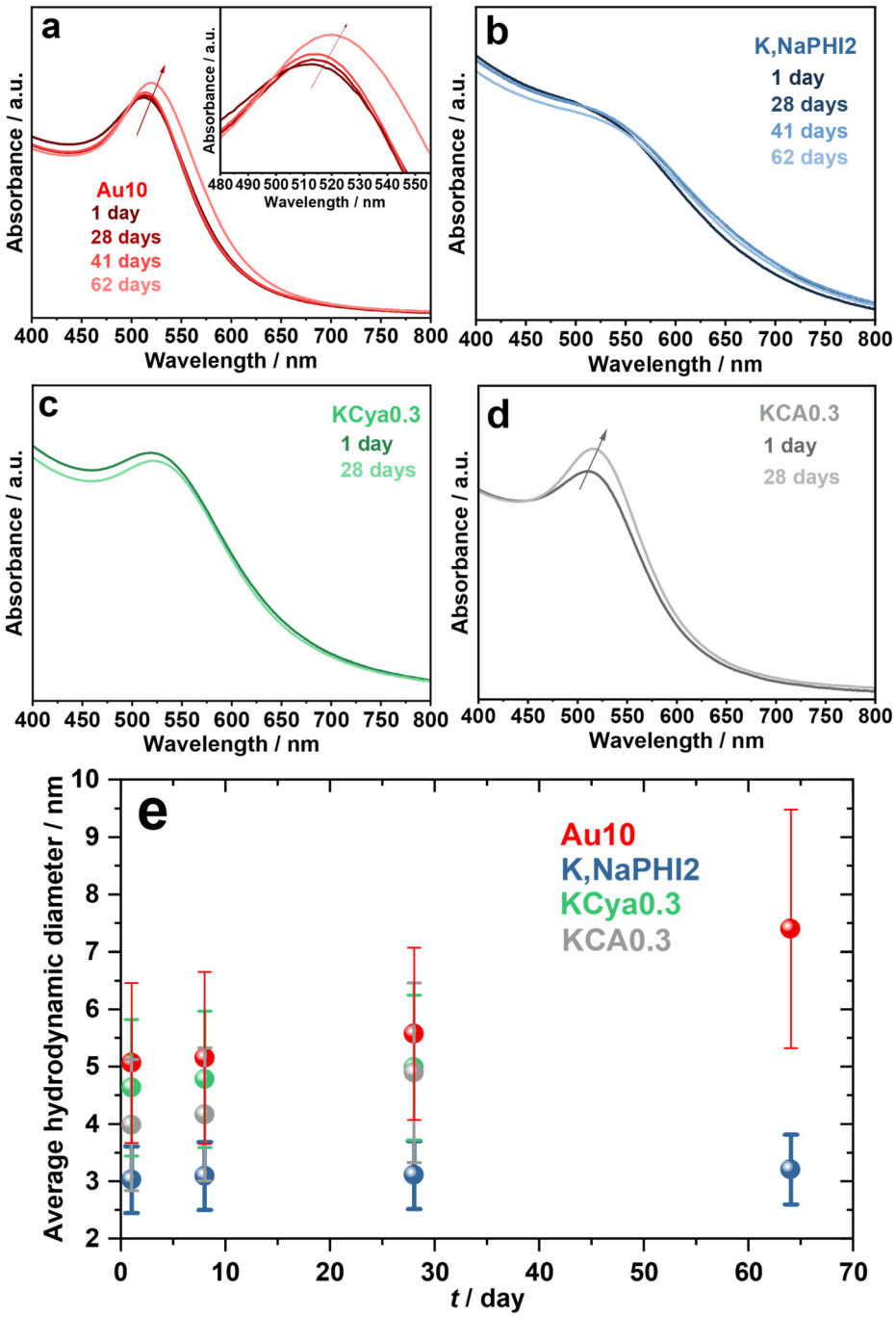

Fig. 6 Long-term stability. (a–d) UV-vis electronic absorption spectra and (e) average hydrodynamic diameter determined from the DLS results of **Au10**, **K,NaPHI2**, **KCya0.3**, and **KCA0.3** as a function of storage time under ambient conditions.

and agglomeration.[62–64] In this context, the strongly enhanced stability of Au NPs stabilized by K,Na-PHI and KMel can be likely explained by the ability of these stabilizers to act as a hydrated protective layer that is, due to the more pronounced delocalization of charges (see the discussion below), less prone to the double layer compression effects and thus more effectively diminishes the attractive forces between the particles at high ionic strength.[59]

Stability of Au NPs at elevated temperature

The thermal stability of colloidal nanoparticles is of paramount importance for practical applications.[65,66] Therefore, **Au10**, **K,NaPHI2**, **KMel0.3**, **KCya0.3**, and **KCA0.3** were heated at 85 °C for 4 h, 8 h, 24 h, 48 h, and 72 h to determine the thermal stability. **Au10** and **KCA0.3** exhibit a notable broadening of the plasmon band, along with a slight red shift of the

Open Access Article. Published on 13 November 2023. Downloaded on 7/31/2024 11:34:38 AM.
This article is licensed under a Creative Commons Attribution 3.0 Unported Licence.

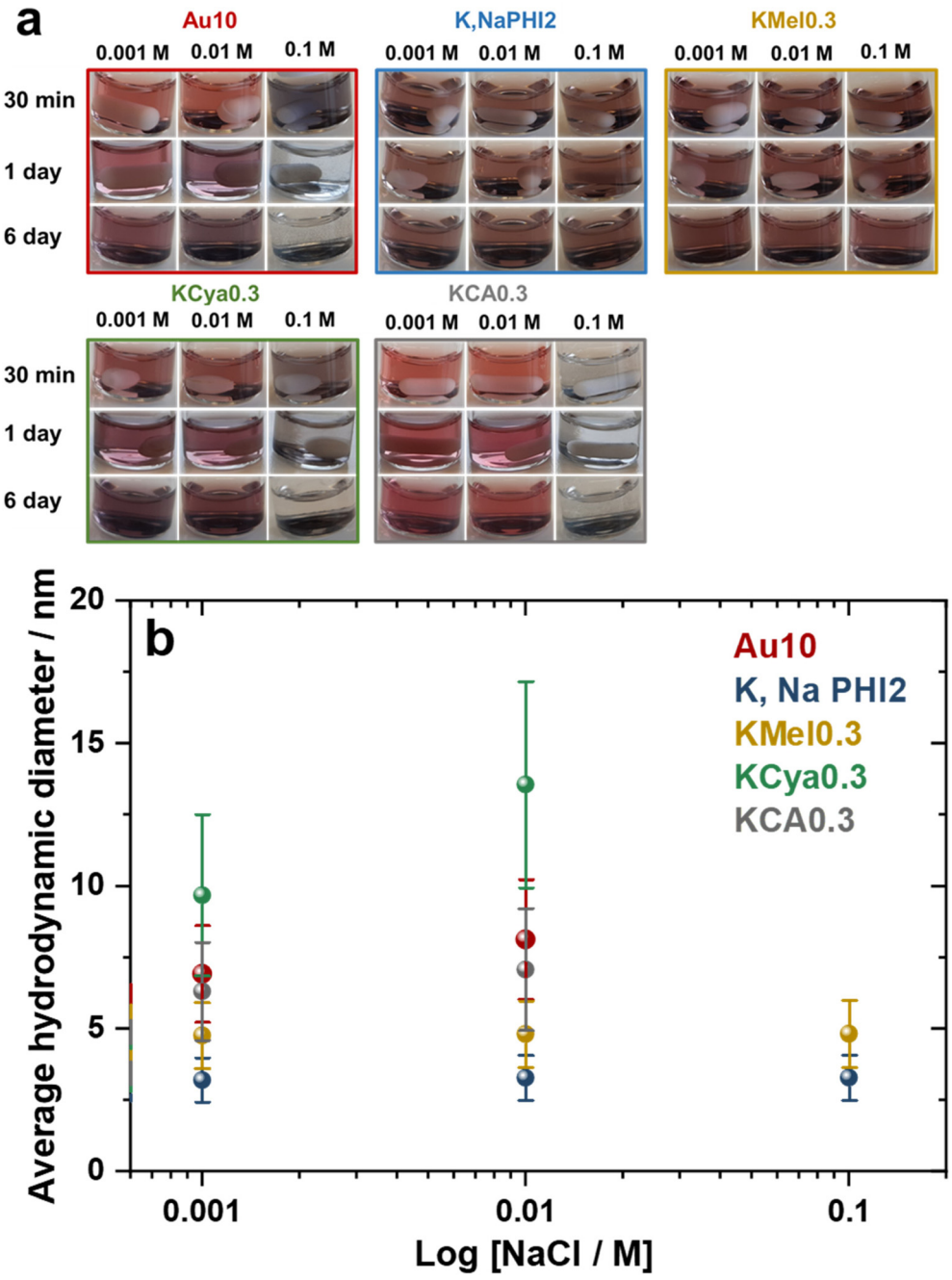

Fig. 7 Stability at high ionic strength. (a) Optical images of **Au10**, **K,NaPHI2**, **KMel0.3**, **KCya0.3**, and **KCA0.3** in the presence of different concentrations of NaCl and (b) the corresponding average hydrodynamic diameter measured 6 days after the addition of NaCl.

maximum, after heating at 85 °C for 4 h and 48 h, respectively (ESI, Fig. S10a and e†). This indicates that at higher temperatures, the nanoparticles experience growth and aggregation, resulting in larger particle sizes due to nanoparticle coalescence.[67] In comparison, the SPR peak of **K,NaPHI2**, **KMel0.3**, and **KCya0.3** did not change considerably after heating at 85 °C even after 72 h, revealing excellent dispersion stability against heating (ESI, Fig. S10b–d†). These results highlight the beneficial effects of the heptazine-based stabilizers that are assumed to form a hydrated protective layer that effectively prevents nanoparticle coalescence and further growth during heating.

Effect of the reductant-derived impurities on the Au NPs stability

It is known that the stabilization mechanism of pristine Au NPs (**Au10**) stabilized by the excess of $NaBH_4$ relies on the formation of a layer (incorporating water molecules) of anions

 This journal is © The Royal Society of Chemistry 2023

Open Access Article. Published on 13 November 2023. Downloaded on 7/31/2024 11:34:38 AM. This article is licensed under a Creative Commons Attribution 3.0 Unported Licence.

(BH_4^-, $B(OH)_4^-$, Cl^-) and cations (Na^+; in a second layer) formed during the reduction of $HAuCl_4$ by $NaBH_4$ on the surface of Au NPs.[50] Hence, to evaluate the true stabilization ability of K,Na-PHI, the prepared suspensions of the Au NPs were dialyzed against water to remove the $NaBH_4$ hydrolysis products. The results unambiguously show that K,Na-PHI can efficiently stabilize ultrafine AuNPs also in the *absence* of the $NaBH_4$ hydrolysis products; for details see ESI, Fig. S11 and S12,† as well as Tables S3 and S4.†

Stabilization mechanism

The studied stabilizers K,Na-PHI, KMel, KCya, and KCA are water-soluble ionic compounds bearing negatively charged functional groups (see Fig. 2). In particular, K,Na-PHI consists of a poly(heptazine imide) network incorporating, apart from NH and $-NH_2$ groups or uncondensed NH_x-including triazine species, also terminal cyanamide $N-C\equiv N^-$ and cyamelurate $C-O^-$ functional groups. We have reported that the dissolved K,Na-PHI has a zeta potential of −31 mV at a pH of 7.5,[36] confirming the negatively charged surface under our reaction conditions. The presence of the negatively charged functional groups on the stabilizers allows for electrostatic stabilization and solubilization of Au NPs in water. The stabilization of the NPs by repulsive electrostatic interactions originates from a diffuse double layer at the surface of NPs coated with charged molecules. Presumably, K,Na-PHI, KMel, KCya, and KCA establish a hydrophilic protective layer around the growing metal nuclei that is permeable to tetrachloroaurate ions (to allow for self-limiting growth) while preventing the diffusional coupling of the particles. A representative model for the electrostatic stabilization of Au NPs by K, Na-PHI is shown in Fig. 8. These considerations are mainly based on the TEM and XPS results revealing that (i) the particle size of Au NPs stabilized by K,Na-PHI is larger than the estimated cavity size of heptazines (ESI, Fig. S5†), excluding the confinement of Au NPs into the heptazine cages, and (ii) the presence of K,Na-PHI does not affect the binding energy of Au $4f_{7/2}$ and Au $4f_{5/2}$ electrons of the Au (0) species, revealing that the stabilizer functional groups only weakly interact with the surface of the Au NPs. Although the stabilization of the Au NPs in water is conditioned by the charged functional groups, the size of the obtained Au NPs depends mostly on the employed stabilizer, *i.e.*, on the monomeric unit and the polymerization degree. Most notably, as compared to the triazine-based stabilizer (KCA), the stabilizers containing heptazine units (K,Na-PHI, KMel, KCya) lead to smaller Au NPs which also exhibit better stability (except for cyanurate) in high ionic strength electrolytes.

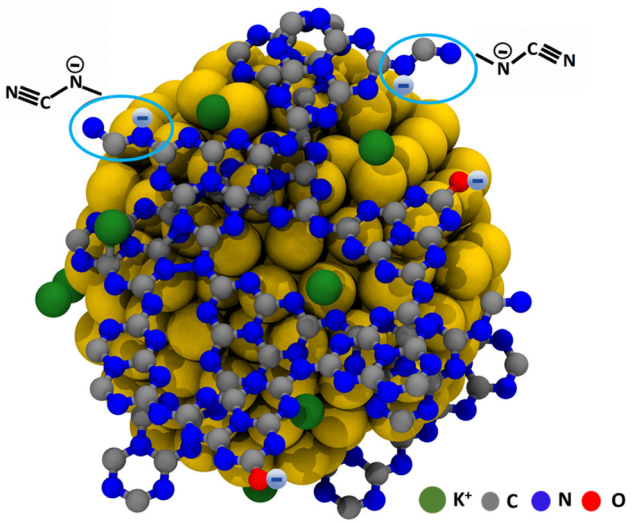

Fig. 8 Schematic representation of the stabilization of Au NPs by K,Na-PHI.

We hypothesized that these beneficial effects of larger heptazine-based stabilizers might be due to the larger charge delocalization in the aromatic system, resulting in more effective electrostatic stabilization of Au NPs which are typically positively charged.[50] To obtain further insight into the stabilization mechanism, we performed density functional theory (DFT) calculations to find the optimized geometry of KCA, KCya, and KMel structures and to investigate the impact of the conjugation size, negatively charged cyamelurate or cyanamide functional groups, and the nature and number of counterions (Fig. 9). Particularly, we modelled the structures with a different number of counterions based on the assumption that the counterions initially stabilize the carbon nitride species and may detach after the stabilization of Au NPs. In addition, we performed a Fukui function analysis of the carbon nitride species to gain a deeper understanding of the stabilization mechanism of Au NPs.[68–71] This analysis provides an estimate of the expected interaction between the stabilizer and Au-NP without the need to directly include the extended Au-NP (having a broad size and shape distribution) into the simulation. More specifically, the electron density of the f^- Fukui function of the carbon nitride represents the electron density for the electrophilic attack from the Au NPs (Fig. 9). The optimized geometries of the carbon nitride species functionalized by the oxygen-containing cyamelurate groups (CA and Cya) reveal a structural out-of-plane deformation near the cyamelurate groups when the counterions are absent. However, in the presence of the counterions, the structures become more planar. In this context, it should be mentioned that the out-of-plane structural distortion translates into a breaking of the π-electron conjugation, which effectively reduces the size of electron delocalization. On the other hand, the cyanamide (NCN^-)-functionalized species (melonate) tends to retain an in-plane structure. The presence of potassium counterions renders the structure even more planar, resulting in an extension of the electron conjugation as compared to the situation without the counterions. Therefore, the primary role of the counterions (potassium) can be understood as facilitating the flattening of the structures with functional groups. Specifically, the electron densities of f^- Fukui functions reveal that the presence of counterions causing the structural flattening leads to an alignment of the directional orbitals from the previously distorted structure into perpendicular π-orbitals within the flat structure. This orbital alignment translates into

Open Access Article. Published on 13 November 2023. Downloaded on 7/31/2024 11:34:38 AM.
This article is licensed under a Creative Commons Attribution 3.0 Unported Licence.

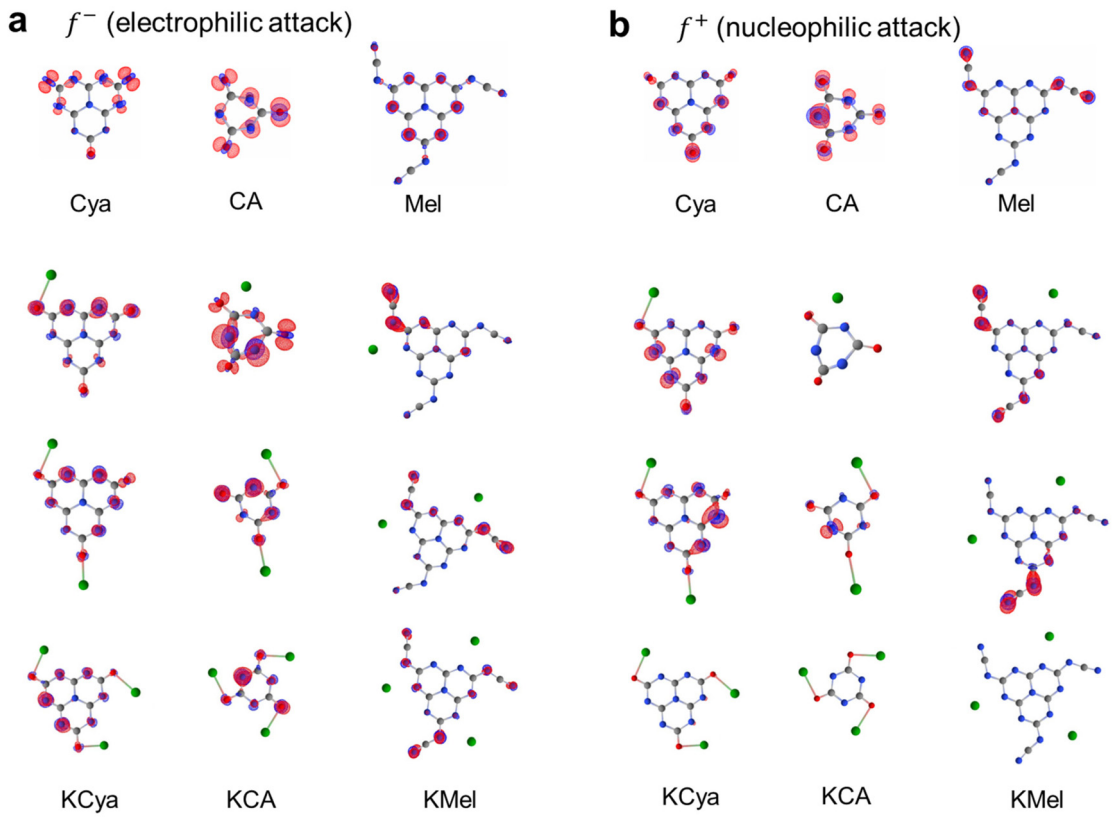

Fig. 9 Theoretical calculations. The electron density from Fukui function (a) negative f^- and (b) positive f^+. The electron density shows the potential frontier reactive site for the respective carbon nitride species. The isosurface value of the electron density is fixed to 0.005787 e Å^{-3} over the structures. The structure is illustrated without the cation (top) and with the different numbers (1–3) of potassium cations (bottom). The blue, the gray, and the green balls stand for N, C, and K atoms, respectively.

an extension of the delocalized electron cloud to the functional groups, facilitating thus the stabilization of the positive surface of Au NPs. The effectiveness of the extended π orbitals in stabilizing Au NPs is supported by the experimental observation that the stabilization (in terms of size and long-term stability) of Au NPs by the structurally more distorted KCA is similar to the case of stabilization solely by $NaBH_4$, while the flatter carbon nitride species, such as KCya, K,Na-PHI, and KMel, can effectively stabilize Au NPs smaller than 3 nm in size (see Fig. 4f and the histograms in ESI, Fig. S4†). In other words, these results suggest that the more effective stabilization of Au NPs by KCya, K,Na-PHI, and KMel as compared to KCA can be attributed to the availability of a delocalized electron cloud with a size equivalent to or larger than the heptazine moiety. In addition, from the analysis of the condensed Fukui function (for details see section 1.5. in ESI†), also known as the dual descriptor, we conclude that this phenomenon is a result of the synergistic effects of the functional groups and the counterions (Fig. 10). The condensed Fukui function describes the local reactivity per atom, and its value is negative at sites prone to the electrophilic attack from an electrophile, and positive at sites preferable for the nucleophilic attack.[68–73] Notably, the condensed Fukui functions for all atoms in structures with the same number of K^+ counterions as the number of functional groups yield all negative values, which corroborates their ability to effectively stabilize the electrophilic Au NPs (Fig. 10). In contrast, the pristine (non-ionic, non-functionalized) heptazine and triazine moieties show positive values of the condensed Fukui functions despite their positive net charge (Fig. S13 and S14 in ESI†), which highlights the significance of the presence of the counterion-balanced cyamelurate and cyanamide functional groups in ionic carbon nitride for the effective stabilization of Au NPs.

Catalytic performance

It is known that strongly interacting stabilizing agents might block the utilization and accessibility of the active sites on the surface of catalytic metal NPs, resulting in catalyst deactivation/poisoning.[22,35] However, the stabilizers that *electrostatically* stabilize Au NPs typically do not interfere significantly with the mass transport processes towards the catalytic surface, thus allowing for high diffusion rates of the reactants and products without completely blocking the active sites.[22,23] As a proof of concept, the catalytic activity of **K,NaPHI2**, **KMel0.3**, **KCya0.3**, and **KCA0.3** was evaluated in the selective reduction of 4-nitrophenol (4-NP) to 4-aminophenol (4-AP) by $NaBH_4$, using the "naked" Au NPs electrostatically stabilized by excess $NaBH_4$ (**Au10**) as a benchmark. The catalytic activity

This journal is © The Royal Society of Chemistry 2023

Open Access Article. Published on 13 November 2023. Downloaded on 7/31/2024 11:34:38 AM.
This article is licensed under a Creative Commons Attribution 3.0 Unported Licence.

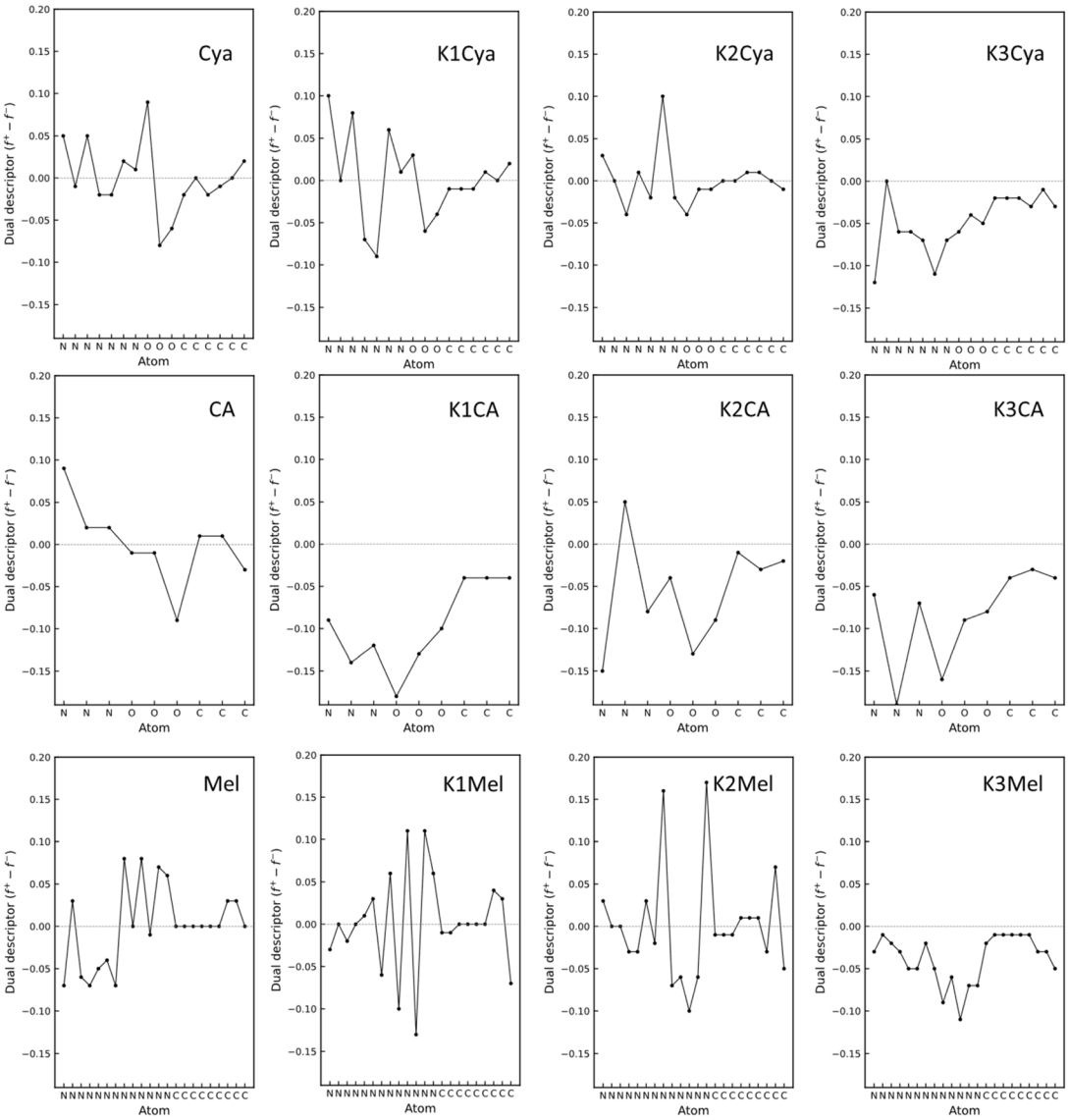

Fig. 10 Condensed Fukui functions. The dual descriptor of the carbon nitride species (Cya, CA, and Mel) in the presence of the different numbers of potassium cations. The negative value corresponds to the electrophilic attack site and the positive value corresponds to the nucleophilic attack site. The values for potassium ions have been excluded in order to emphasize the variations in other atoms. All values, including those for potassium ions, are shown in Table S5 in ESI.†

of all investigated samples was evaluated one day after their synthesis. The catalytic hydrogenation of nitroarenes has been extensively employed as a model reaction to evaluate the activity of Au NP catalysts, and it has the advantage of easy monitoring by UV-vis spectroscopy.[16,22,23,58] As the reaction proceeds after the addition of the catalyst, the absorption peak at 400 nm decreases, while the absorption peak at 300 nm is increasing, showing the conversion of 4-NP to 4-AP (Fig. 11a). The time dependence of the relative absorbance (A_t/A_0%) of the 4-nitrophenolate peak at 400 nm in the presence of **Au10**, **K,NaPHI2**, **KMel0.3**, **KCya0.3**, or **KCA0.3** is shown in ESI, Fig. S15a,† where A_t and A_0 represent the absorbance at the reaction time t and at time t = 0, respectively. An important feature of the reduction of 4-NP catalyzed by ligand-stabilized nanoparticles is the induction period, an initial time interval needed until the reaction takes place.[23] The induction period is related to either the formation of a diffusion pathway through the ligand shell on the NP surface or the restructuring of the NP surface induced by the adsorbed reactant molecules.[22,23,74,75] Interestingly, very short (~2–20 s) induction times are observed for all investigated materials except for **KCA0.3** (~45 s; Fig. S15a†), which indicates that especially the heptazine-based stabilizing agents can *both* effectively stabilize the Au NPs *and* allow for fast diffusion of reactants and products needed for effective surface catalysis.

The rate constants (Fig. 11b) were determined by fitting the data from Fig. S15a† to a pseudo-first-order kinetic model concerning the concentration of 4-NP (Fig. S15b†). The turnover

Open Access Article. Published on 13 November 2023. Downloaded on 7/31/2024 11:34:38 AM.
This article is licensed under a Creative Commons Attribution 3.0 Unported Licence.

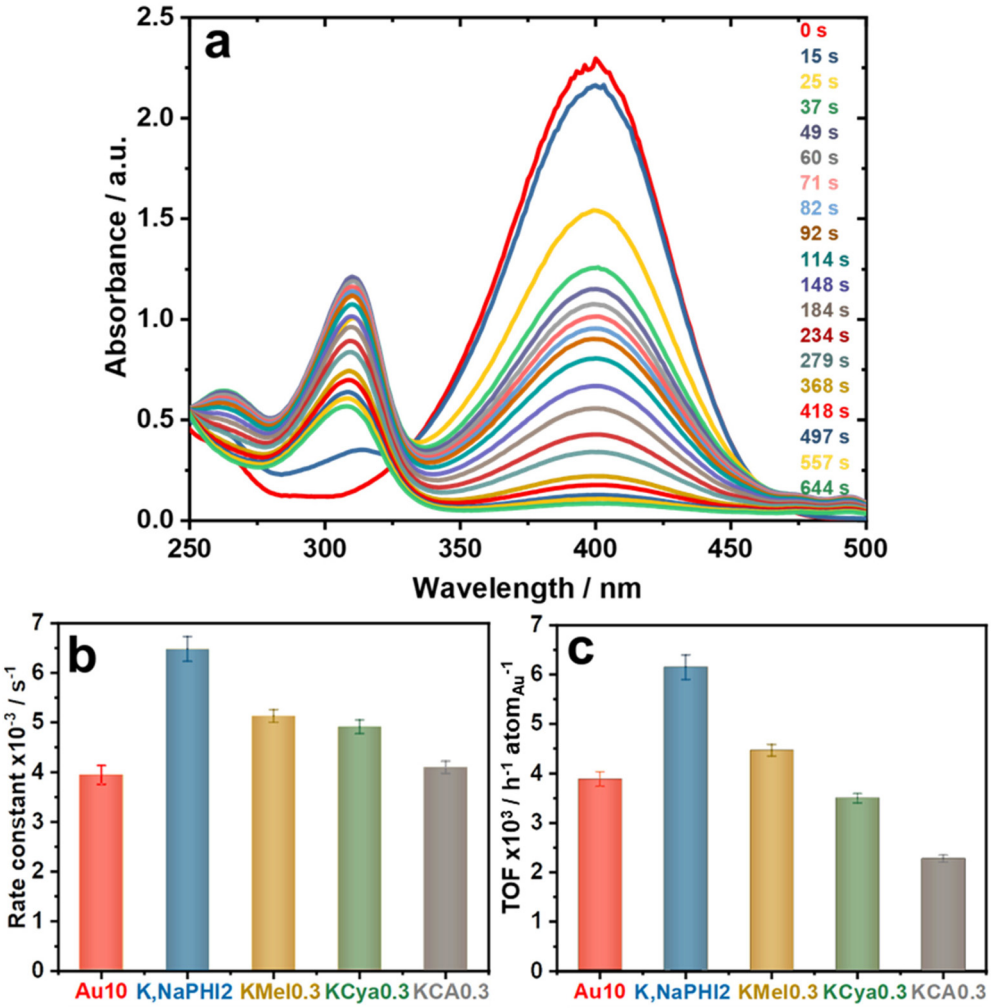

Fig. 11 (a) UV-vis electronic absorption spectra recorded during the reduction of 4-NP in the presence of **K,NaPHI2** catalyst and the calculated (b) rate constant and (c) TOF values for **Au10**, **K,Na PHI2**, **KMel0.3**, **KCya0.3**, and **KCA0.3**. Experimental conditions: 0.1 mL $NaBH_4$ (2.16 mol L^{-1}), 0.3 mL 4-NP (1.2×10^{-3} mol L^{-1}), and 2.5 mL distilled water were mixed into a cuvette at ambient conditions. Then, the UV-Vis spectrum was recorded, followed by the addition of 0.025 mL of AuNP catalyst (1.14 mg L^{-1}) and shaking quickly the cuvette before recording the subsequent spectra.

frequencies (TOF) for investigated samples (Fig. 11c) were calculated using the linear range of substrate conversion at the beginning of the reaction, taking the end of the induction period as time 0. The TOF value is given with respect to one atom of Au, hence its unit is h^{-1} $atom_{Au}^{-1}$. The benchmark sample **Au10** has a TOF value of 3888 h^{-1} $atom_{Au}^{-1}$, which is comparable to the value reported in the literature.[50] Notably, the **K,NaPHI2** catalyst exhibits a remarkably high TOF value of 6149 h^{-1} $atom_{Au}^{-1}$, which is superior to TOFs of the benchmark **Au10** (3888 h^{-1} $atom_{Au}^{-1}$), **KMel0.3** (4464 h^{-1} $atom_{Au}^{-1}$), **KCya0.3** (3498 h^{-1} $atom_{Au}^{-1}$), and **KCA0.3** (2276 h^{-1} $atom_{Au}^{-1}$), as shown in Fig. 11c. The sample **KCA0.3**, comprising a triazine-based stabilizer, possesses the lowest TOF value, which is likely because KCA leads to larger Au NPs. Moreover, among the proposed stabilizers, KCA has the highest density of negatively charged groups where all carbons bear one negatively charged O^- group. Therefore, the AuNPs surface is likely crowded by the stabilizing molecules, partially blocking the surface catalytic activity. The outstanding catalytic performance of the Au NPs stabilized by K,Na-PHI can be, in our view, attributed to two main effects. Firstly, K,Na-PHI favours the formation of ultrasmall Au NPs, allowing for higher specific surface area and more optimal utilization of Au atoms. Secondly, the flexible and extended framework structure of the polymeric K, Na-PHI enables *both* effective stabilization *and* – at the same time – facilitates the diffusion of reactants and products to and from the surface of gold NPs. In this context, it should be noted that $NaBH_4$ at high concentrations is known to increase significantly the ionic strength and thus to induce aggregation of Au NPs.[76] Indeed, under our reaction conditions, both **Au10** and **K,NaPHI2** are prone to aggregation, as apparent by a blue shift of the SPR band (see ESI, Fig. S16†), which can be ascribed to a high concentration of $NaBH_4$ in the reaction solution as $NaBH_4$ is used in a large excess (~600 times the concentration of 4-NP, *i.e.* ~0.1 M). Higher stability against aggregation is expected to be achievable in catalytic reactions operating under optimized conditions with alternative reagents and/or at lower ionic strengths.

 This journal is © The Royal Society of Chemistry 2023

Open Access Article. Published on 13 November 2023. Downloaded on 7/31/2024 11:34:38 AM. This article is licensed under a Creative Commons Attribution 3.0 Unported Licence.

Conclusions

In this work, we demonstrate for the first time that water-soluble ionic (K^+ and Na^+ containing) polymeric carbon nitride (K,Na-PHI) can act as a facile, scalable, and highly effective stabilizer in the synthesis of highly catalytically active ultrafine (<3 nm) gold nanoparticles. In the selective reduction of 4-nitrophenol to 4-aminophenol by $NaBH_4$ employed as a model catalytic reaction, the K,Na-PHI-stabilized Au NPs not only outperform Au NPs stabilized by monomeric structural units of K,Na-PHI (cyanurate, melonate, cyamelurate), but their activity is even superior (TOF higher by the factor of ~1.6) to that of the benchmark "naked" (*i.e.*, ligand-free) Au NPs electrostatically stabilized by excess $NaBH_4$. These results suggest that K,Na-PHI can provide an effective electrostatic stabilization against the aggregation of Au NPs, without blocking the diffusion of the reactants and products to and from the active sites at the Au catalyst surface. A truly outstanding feature of our K,Na-PHI-stabilized Au NPs is their excellent stability both under ambient conditions (over at least two months), as well as under high ionic strength conditions (up to 0.1 M NaCl solutions) and at elevated temperatures (85 °C for at least 72 hours). Based on our experimental evidence and theoretical calculations, we propose that the strongly enhanced stability of Au NPs stabilized by K,Na-PHI can be explained by the ability of K,Na-PHI to act as a hydrated protective layer that is, due to the more pronounced delocalization of charges, less prone to the double layer compression effects and thus more effectively diminishes the attractive forces between the nanoparticles. Moreover, a detailed comparative study using different structural units of K,Na-PHI (cyanurate, melonate, cyamelurate) shows that in particular the presence of functionalized heptazine moieties allowing for better charge delocalization is crucial for the synthesis and more effective stabilization of small Au NPs. This is corroborated by theoretical DFT calculations of Fukui functions which reveal the beneficial effect of the counterion-balanced cyamelurate and cyanamide functional groups in the ionic carbon nitride on the orbital alignment and electron delocalization, resulting in more effective stabilization of Au NPs. Thus, this work establishes the ionic carbon nitrides (PHI) as alternative capping agents for nanocatalysts that enable effective stabilization without compromising surface catalysis. More generally, it opens up a route for further developments in utilizing PHI-based stabilizers for the synthesis of high-performance ultrafine nanoparticles, especially for applications in which both the stability and the effective transport of species between the interfacial region of nanoparticles and the environment is mandatory.

Author contributions

M.E., L.K., I.K., T.J., R.B. and D.M. conceived and supervised the project, J.L., M.E. and I.K. synthesised the materials, characterized them and performed catalytic experiments. C.N. and A.T. performed XPS investigation of the materials and analysed the results. R.L. and U.K. performed TEM-EDX analyses and processed the data. C.I. and T.J. performed the theoretical calculations. M.E. wrote the first draft of the manuscript, and M.E., J.L., C.I., I.K. and R.B. finalized the manuscript with inputs from all authors.

Data availability

All datasets related to this work are available from the repository: **https://doi.org/10.5281/zenodo.8130796**.

Conflicts of interest

There are no conflicts to declare.

Acknowledgements

This work was funded by the Deutsche Forschungsgemeinschaft (DFG, German Research Foundation) – Project No. 364549901 – TRR 234 CataLight (Projects B6, B7, B10, Z2) as well as JA 1972/27-1 and BE 5102/5-1 (Project No. 428764269). Computational resources were provided by the state of Baden–Württemberg through bwHPC and the German Science Foundation (DFG) under Grant No. INST 40/467-1 FUGG. C. N. and A. T. acknowledge financial support of the DFG through a research infrastructure grant INST 275/257-1 FUGG. I. K. acknowledges support by Spanish MCINN (PID2020-113558RB-C41), Gobierno del Principado de Asturias (IDI-2021-000048), and the Alexander von Humboldt Foundation through the Humboldt Research Fellowship.

References

1 N. Wang, Q. Sun and J. Yu, *Adv. Mater.*, 2019, **31**, 1803966.
2 X. Yang, J.-K. Sun, M. Kitta, H. Pang and Q. Xu, *Nat. Catal.*, 2018, **1**, 214–220.
3 Q. L. Zhu and Q. Xu, *Chem*, 2016, **1**, 220–245.
4 L. M. Liz-Marzán, *Langmuir*, 2006, **22**, 32–41.
5 M.-C. Daniel and D. Astruc, *Chem. Rev.*, 2004, **104**, 293–346.
6 V. Karthick, L. Kumar Shrestha, V. G. Kumar, P. Pranjali, D. Kumar, A. Pal and K. Ariga, *Nanoscale*, 2022, **14**, 10630–10647.
7 D. Jaque, L. Martínez Maestro, B. del Rosal, P. Haro-Gonzalez, A. Benayas, J. L. Plaza, E. Martín Rodríguez and J. García Solé, *Nanoscale*, 2014, **6**, 9494–9530.
8 O. J. H. Chai, Z. Liu, T. Chen and J. Xie, *Nanoscale*, 2019, **11**, 20437–20448.
9 H. T. K. Duong, A. Abdibastami, L. Gloag, L. Barrera, J. J. Gooding and R. D. Tilley, *Nanoscale*, 2022, **14**, 13890–13914.
10 M. E. King, M. V. Fonseca Guzman and M. B. Ross, *Nanoscale*, 2022, **14**, 602–611.

Open Access Article. Published on 13 November 2023. Downloaded on 7/31/2024 11:34:38 AM. This article is licensed under a Creative Commons Attribution 3.0 Unported Licence.

11 C. Spedalieri and J. Kneipp, *Nanoscale*, 2022, **14**, 5314–5328.
12 C. Adler, D. Mitoraj, I. Krivtsov and R. Beranek, *J. Chem. Phys.*, 2020, **152**, 244702.
13 J. Yang, M. Yuan, D. Xu, H. Zhao, Y. Zhu, M. Fan, F. Zhang and Z. Dong, *J. Mater. Chem. A*, 2018, **6**, 18242–18251.
14 R. R. Nasaruddin, T. Chen, N. Yan and J. Xie, *Coord. Chem. Rev.*, 2018, **368**, 60–79.
15 L.-W. Guo, P.-P. Du, X.-P. Fu, C. Ma, J. Zeng, R. Si, Y.-Y. Huang, C.-J. Jia, Y.-W. Zhang and C.-H. Yan, *Nat. Commun.*, 2016, **7**, 13481.
16 X. Gou, T. Liu, Y. Wang and Y. Han, *Angew. Chem., Int. Ed.*, 2020, **59**, 16683–16689.
17 H. Yang, Z. Yu, S. Li, Q. Zhang, J. Jin and J. Ma, *J. Catal.*, 2017, **353**, 256–264.
18 Y. Jiang, X. Zhang, X. Dai, W. Zhang, Q. Sheng, H. Zhuo, Y. Xiao and H. Wang, *Nano Res.*, 2017, **10**, 876–889.
19 B. Weng, K.-Q. Lu, Z. Tang, H. M. Chen and Y.-J. Xu, *Nat. Commun.*, 2018, **9**, 1543.
20 A. Mondal and N. R. Jana, *ACS Catal.*, 2014, **4**, 593–599.
21 Y. Wang, J. He, C. Liu, W. H. Chong and H. Chen, *Angew. Chem., Int. Ed.*, 2015, **54**, 2022–2051.
22 S. M. Ansar and C. L. Kitchens, *ACS Catal.*, 2016, **6**, 5553–5560.
23 R. D. Neal, R. A. Hughes, P. Sapkota, S. Ptasinska and S. Neretina, *ACS Catal.*, 2020, **10**, 10040–10050.
24 A. M. Alam and Y. S. Shon, *ACS Appl. Nano Mater.*, 2021, **4**, 3294–3318.
25 Q. L. Zhu and Q. Xu, *Chem*, 2016, **1**, 220–245.
26 J. A. Singh, S. H. Overbury, N. J. Dudney, M. Li and G. M. Veith, *ACS Catal.*, 2012, **2**, 1138–1146.
27 G. González-Rubio, J. Mosquera, V. Kumar, A. Pedrazo-Tardajos, P. Llombart, D. M. Solís, I. Lobato, E. G. Noya, A. Guerrero-Martínez, J. M. Taboada, F. Obelleiro, L. G. MacDowell, S. Bals and L. M. Liz-Marzán, *Science*, 2020, **368**, 1472–1477.
28 J. Feng, C. Gao and Y. Yin, *Nanoscale*, 2018, **10**, 20492–20504.
29 L. E. González García, N. Ninan, J. Simon, R. Madathiparambil Visalakshan, R. Bright, S. K. Wahono, K. Ostrikov, V. Mailänder, K. Landfester, N. Goswami and K. Vasilev, *Nanoscale*, 2021, **13**, 19936–19945.
30 H. R. Moon, D.-W. Lim and M. P. Suh, *Chem. Soc. Rev.*, 2013, **42**, 1807–1824.
31 W. Yuan and C. M. Li, *Langmuir*, 2009, **25**, 7578–7585.
32 W. Yuan, Z. Lu and C. M. Li, *J. Mater. Chem.*, 2011, **21**, 5148.
33 S. Chakraborty, S. M. Ansar, J. G. Stroud and C. L. Kitchens, *J. Phys. Chem. C*, 2018, **122**, 7749–7758.
34 A. Dhakshinamoorthy and H. Garcia, *Chem. Soc. Rev.*, 2012, **41**, 5262.
35 I. A. Safo, C. Dosche and M. Özaslan, *ChemPhysChem*, 2019, **20**, 3010–3023.
36 I. Krivtsov, D. Mitoraj, C. Adler, M. Ilkaeva, M. Sardo, L. Mafra, C. Neumann, A. Turchanin, C. Li, B. Dietzek, R. Leiter, J. Biskupek, U. Kaiser, C. Im, B. Kirchhoff, T. Jacob and R. Beranek, *Angew. Chem., Int. Ed.*, 2020, **59**, 487–495.
37 A. Savateev and M. Antonietti, *ChemCatChem*, 2019, **11**, 6166–6176.
38 H. Schlomberg, J. Kröger, G. Savasci, M. W. Terban, S. Bette, I. Moudrakovski, V. Duppel, F. Podjaski, R. Siegel, J. Senker, R. E. Dinnebier, C. Ochsenfeld and B. v. Lotsch, *Chem. Mater.*, 2019, **31**, 7478–7486.
39 V. W. Lau, I. Moudrakovski, T. Botari, S. Weinberger, M. B. Mesch, V. Duppel, J. Senker, V. Blum and B. v. Lotsch, *Nat. Commun.*, 2016, **7**, 12165.
40 V. W. Lau and B. v. Lotsch, *Adv. Energy Mater.*, 2022, **12**, 2101078.
41 F. K. Kessler, Y. Zheng, D. Schwarz, C. Merschjann, W. Schnick, X. Wang and M. J. Bojdys, *Nat. Rev. Mater.*, 2017, **2**, 17030.
42 C. Im, B. Kirchhoff, I. Krivtsov, D. Mitoraj, R. Beranek and T. Jacob, *Chem. Mater.*, 2023, **35**, 1547–1559.
43 D. Zheng, J. Zhou, Z. Fang, T. Heil, A. Savateev, Y. Zhang, M. Antonietti, G. Zhang and X. Wang, *J. Mater. Chem. A*, 2021, **9**, 27370–27379.
44 C. Li, E. Hofmeister, I. Krivtsov, D. Mitoraj, C. Adler, R. Beranek and B. Dietzek, *ChemSusChem*, 2021, **14**, 1728–1736.
45 C. Adler, S. Selim, I. Krivtsov, C. Li, D. Mitoraj, B. Dietzek, J. R. Durrant and R. Beranek, *Adv. Funct. Mater.*, 2021, **31**, 2105369.
46 C. Adler, I. Krivtsov, D. Mitoraj, L. Santos-Gómez, S. García-Granda, C. Neumann, J. Kund, C. Kranz, B. Mizaikoff, A. Turchanin and R. Beranek, *ChemSusChem*, 2021, **14**, 2170–2179.
47 I. Krivtsov, A. Vazirani, D. Mitoraj, M. M. Elnagar, C. Neumann, A. Turchanin, Y. Patiño, S. Ordóñez, R. Leiter, M. Lindén, U. Kaiser and R. Beranek, *J. Mater. Chem. A*, 2023, **11**, 2314–2325.
48 J. Strachan, C. Barnett, A. F. Masters and T. Maschmeyer, *ACS Catal.*, 2020, **10**, 5516–5521.
49 D. Patra, S. R. Nalluri, H. R. Tan, M. S. M. Saifullah, R. Ganesan and B. Gopalan, *Nanoscale Adv.*, 2020, **2**, 5384–5395.
50 C. Deraedt, L. Salmon, S. Gatard, R. Ciganda, R. Hernandez, J. Ruiz and D. Astruc, *Chem. Commun.*, 2014, **50**, 14194–14196.
51 B. Saini, L. Khamari and T. K. Mukherjee, *J. Phys. Chem. B*, 2022, **126**, 2130–2141.
52 C. Liang, J. Y. Cheong, G. Sitaru, S. Rosenfeldt, A. S. Schenk, S. Gekle, I. Kim and A. Greiner, *Adv. Mater. Interfaces*, 2022, **9**, 2100867.
53 S. Karimi, A. Moshaii and M. Nikkhah, *Mater. Res. Express*, 2019, **6**, 1150f2.
54 I. Hussain, S. Graham, Z. Wang, B. Tan, D. C. Sherrington, S. P. Rannard, A. I. Cooper and M. Brust, *J. Am. Chem. Soc.*, 2005, **127**, 16398–16399.
55 R. J. Hunter, *Zeta Potential in Colloid Science: Principles and Applications*, Academic Press, 1st edn, 1988.
56 A. Carone, S. Emilsson, P. Mariani, A. Désert and S. Parola, *Nanoscale Adv.*, 2023, **5**, 2017–2026.

 This journal is © The Royal Society of Chemistry 2023

Open Access Article. Published on 13 November 2023. Downloaded on 7/31/2024 11:34:38 AM.
This article is licensed under a Creative Commons Attribution 3.0 Unported Licence.

57 H. Schlomberg, J. Kröger, G. Savasci, M. W. Terban, S. Bette, I. Moudrakovski, V. Duppel, F. Podjaski, R. Siegel, J. Senker, R. E. Dinnebier, C. Ochsenfeld and B. v. Lotsch, *Chem. Mater.*, 2019, **31**, 7478–7486.
58 X. Hang, S. Wang, H. Pang and Q. Xu, *Chem. Sci.*, 2022, **13**, 461–468.
59 S. K. Ghosh and T. Pal, *Chem. Rev.*, 2007, **107**, 4797–4862.
60 D. Zopes, B. Stein, S. Mathur and C. Graf, *Langmuir*, 2013, **29**, 11217–11226.
61 Y. Wang, J. E. Q. Quinsaat, T. Ono, M. Maeki, M. Tokeshi, T. Isono, K. Tajima, T. Satoh, S. Sato, Y. Miura and T. Yamamoto, *Nat. Commun.*, 2020, **11**, 6089.
62 E. Boisselier and D. Astruc, *Chem. Soc. Rev.*, 2009, **38**, 1759.
63 R. Pamies, J. G. H. Cifre, V. F. Espín, M. Collado-González, F. G. D. Baños and J. G. de la Torre, *J. Nanopart. Res.*, 2014, **16**, 2376.
64 S. Christau, T. Moeller, J. Genzer, R. Koehler and R. von Klitzing, *Macromolecules*, 2017, **50**, 7333–7343.
65 Y. Wang, J. E. Q. Quinsaat, T. Ono, M. Maeki, M. Tokeshi, T. Isono, K. Tajima, T. Satoh, S. Sato, Y. Miura and T. Yamamoto, *Nat. Commun.*, 2020, **11**, 6089.
66 M. Ranka, P. Brown and T. A. Hatton, *ACS Appl. Mater. Interfaces*, 2015, **7**, 19651–19658.
67 L. M. Farigliano, M. A. Villarreal, E. P. M. Leiva and S. A. Paz, *J. Phys. Chem. C*, 2020, **124**, 24009–24016.
68 A. D. McNaught and A. Wilkinson, *Compendium of chemical terminology*, Blackwell Science Oxford, 1997, vol. 1669.
69 A. J. Cohen, P. Mori-Sánchez and W. Yang, *Chem. Rev.*, 2012, **112**, 289–320.
70 R. R. Contreras, P. Fuentealba, M. Galván and P. Pérez, *Chem. Phys. Lett.*, 1999, **304**, 405–413.
71 W. Yang and R. G. Parr, *Proc. Natl. Acad. Sci. U. S. A.*, 1985, **82**, 6723–6726.
72 P. J. Flory, *Principles of polymer chemistry*, Cornell University Press, 1953.
73 A. Stukowski, *Modell. Simul. Mater. Sci. Eng.*, 2010, **18**, 015012.
74 J. Zeng, Q. Zhang, J. Chen and Y. Xia, *Nano Lett.*, 2010, **10**, 30–35.
75 S. Wunder, Y. Lu, M. Albrecht and M. Ballauff, *ACS Catal.*, 2011, **1**, 908–916.
76 Z. Zhang and Y. Wu, *Langmuir*, 2010, **26**, 9214–9223.

Electronic Supplementary Material (ESI) for Nanoscale.
This journal is © The Royal Society of Chemistry 2023

ELECTRONIC SUPPLEMENTARY INFORMATION (ESI)

Water-soluble ionic carbon nitride as unconventional stabilizer for highly catalytically active ultrafine gold nanoparticles

Mohamed M. Elnagar,[a]‡ Johannes Liessem, [a]‡ Changbin Im,[a]‡ Dariusz Mitoraj,[a] Ludwig A. Kibler,[a] Christof Neumann,[b] Andrey Turchanin,[b] Robert Leiter,[c] Ute Kaiser,[c] Timo Jacob,[a,d,e]* Igor Krivtsov,[a, f]* Radim Beranek[a]*

[a] Institute of Electrochemistry Ulm University, Albert-Einstein-Allee 47, 89081 Ulm, Germany

[b] Institute of Physical Chemistry, Jena Center for Soft Matter (JCSM) and Center for Energy and Environmental Chemistry Jena (CEEC), Friedrich Schiller University Jena, Lessingstr. 10, 07743 Jena, Germany

[c] Electron Microscopy of Materials Science, Central Facility for Electron Microscopy, Ulm University, Albert-Einstein-Allee 11, 89081, Ulm, Germany

[d] Helmholtz-Institute-Ulm (HIU) Electrochemical Energy Storage, Helmholtzstr. 11, 89081, Ulm, Germany

[e] Karlsruhe Institute of Technology (KIT), P.O. Box 3640, 76021, Karlsruhe, Germany

[f] Department of Chemical and Environmental Engineering, University of Oviedo, 33006 Oviedo, Spain

*Corresponding authors: Radim Beranek (radim.beranek@uni-ulm.de), Timo Jacob (timo.jacob@uni-ulm.de), Igor Krivtsov (krivtsovigor@uniovi.es)

1. Materials and Methods	**S2**
1.1 Materials and chemicals	**S2**
1.2 Synthesis	**S2**
1.3 Nitrophenol reduction catalysis	**S6**
1.4 Characterization	**S6**
1.5 Computational details	**S7**
2 Results and discussion	**S8**
2.1 Synthesis of the $NaBH_4$-stabilized Au NPs	**S8**
2.2 Materials characterization	**S13**
2.3 DFT calculations	**S27**
2.4 Catalytic reduction of 4-NP	**S33**

1. Materials and Methods

1.1 Materials and chemicals

Melamine (99 %, Sigma Aldrich), dicyandiamide (99%, Sigma Aldrich), cyanuric acid (98 %, Sigma Aldrich), KOH and NaOH (Merck, 99 %), and potassium thiocyanate (KSCN) (98%, Merk) were used for the synthesis of the stabilizers. Hydrogen tetrachloroaurate ($HAuCl_4.3H_2O$) (49 wt% Au basis, Alfa Aesar) and sodium borohydride ($NaBH_4$) (≥ 96%, Sigma Aldrich) were utilized for the synthesis of Au NPs. All chemicals were used as received without further purification unless otherwise specified.

1.2. Synthesis

1.2.1. Synthesis of the proposed stabilizers

K, Na KPHI. We synthesized the K, Na PHI according to our previously reported method.[1] In brief, 10 mmol KOH (56 g mol^{-1}) and 5 mmol NaOH (40 g mol^{-1}) were ground and mixed with 12 mmol melamine (126 g mol^{-1}). The powder was then heated in a lid-covered crucible at a rate of 5.0 °C min^{-1} up to 330 °C, then it was kept for 2h at the reached temperature before being withdrawn from the furnace. The obtained solid was suspended in 100 mL of deionized water and the insoluble part was filtered out, firstly, by a paper filter and afterward by a 0.2 µm PTFE syringe filter. The obtained solution was dialyzed for several days until neutral pH values, and concentrated by evaporation at 60 °C to a concentration of 5.0 g L^{-1}, which was determined gravimetrically. To obtain solid material of the water-soluble K, Na PHI, the solution was gradually evaporated at 60 °C and then dried for 24 h at 80 °C. The FTIR spectrum shown in **Figure S1a** demonstrates the successful synthesis of K, Na PHI.

Tripotassium melonate. Tripotassium melonate (KMel) was synthesized by a modified procedure described by Schlomberg *et al.* [2] Firstly, the melon polymer was synthesized by dicyandiamide condensation in an open crucible at 550 °C for 4.0 h and the obtained solid was washed with deionized water and dried at 70 °C. Then, 1.5 g of melon polymer was mixed and ground with 3.0 g of KSCN (30.9 mmol, 97 g mol^{-1}). The mixture was heated in a lid-covered crucible at a rate of 5.0 °C min^{-1} up to 550 °C for 4h. The obtained solid was suspended in 50 mL of water, then filtered through a paper filter and through a

syringe 0.2 µm filter to remove solid impurities. The solution was slowly evaporated to a small volume yielding a white powder. The powder was recovered by filtration and washed with ethanol. The FTIR and ^{13}C NMR spectra shown in **Figure S1b,c** demonstrate the successful synthesis of the melonate anion.

Tripotassium cyamelurate. For the synthesis of tripotassium cyamelurate (KCya), 1.0 g of melon was suspended in 1.0 mol L^{-1} solution of KOH and hydrothermally treated in a Teflon-lined stainless-steel autoclave for 16 h at 100 °C. After the treatment, the autoclave was cooled down to room temperature, the solution was filtered through a paper filter to remove undissolved melon and then was slowly evaporated to yield needle-shaped crystals of tripotassium cyamelurate. The ^{13}C NMR spectrum of tripotassium cyamelurate is shown in **Figure S1d.**

Tripotassium cyanurate. Tripotassium cyanurate (KCA) was obtained by stirring KOH and cyanuric acid in a stoichiometric ratio of 3:1 till complete dissolution.

1.2.2. Synthesis of Au NPs

Borohydride-based Au nanoparticle synthesis. Au NPs stabilized by BH_4^- were synthesized using a method similar to that described by Deraedt *et al.*[3], in which Au^{3+} ions are reduced by BH_4^- in an aqueous solution of $HAuCl_4$ and $NaBH_4$. In a typical experiment, the Au NPs stabilized by the proposed stabilizers were synthesized as follows at room temperature (19-22 °C). For the synthesis of each sample, 10 mL of 2.5 × 10^{-4} mol L^{-1} $HAuCl_4 \cdot 3H_2O$ (393.8 g mol^{-1}) was placed in a screw cover glass vial. The solutions were diluted up to 14 mL with deionized water and stirred for 5.0 min. Afterward, 1.0 mL of various concentrations of $NaBH_4$ (5.0 × 10^{-3} mol L^{-1}, 2.5 × 10^{-2} mol L^{-1} , 5.0 × 10^{-2} mol L^{-1} or 1.25 × 10^{-1} mol L^{-1}) was added dropwise under stirring to set the $NaBH_4$:$HAuCl_4$ molar ratios to 2.0, 10, 20, or 50, respectively. Upon addition, an immediate color change was observed, indicating the formation of Au NPs.

Stabilizers-based Au nanoparticle synthesis. Au NPs stabilized by the proposed stabilizers were synthesized using the same aforementioned steps, but with adding the proposed stabilizers and stirring for 5.0 min before the reduction step by $NaBH_4$. For this, various volumes of a specific concentration of the stabilizer (2.5 × 10^{-2} mol L^{-1} in the case of KMel, KCya, or KCA, and 3.0 g L^{-1} in the case of K,Na PHI) were added to have

different $HAuCl_4$: stabilizer ratios. For the reduction step, 1.0 mL of 2.5×10^{-2} $NaBH_4$ ($NaBH_4$:$HAuCl_4$ molar ratio of 10) was added dropwise under stirring. **Table S1** summarizes the final concentrations of $HAuCl_4$, stabilizer, and $NaBH_4$ in the synthesized materials and their corresponding names.

Dialysis step: For reduction of the ionic strength, the Au NPs were put in a cellulose membrane with a pore size of 3.5 kDa and dialyzed against H_2O for about a week.

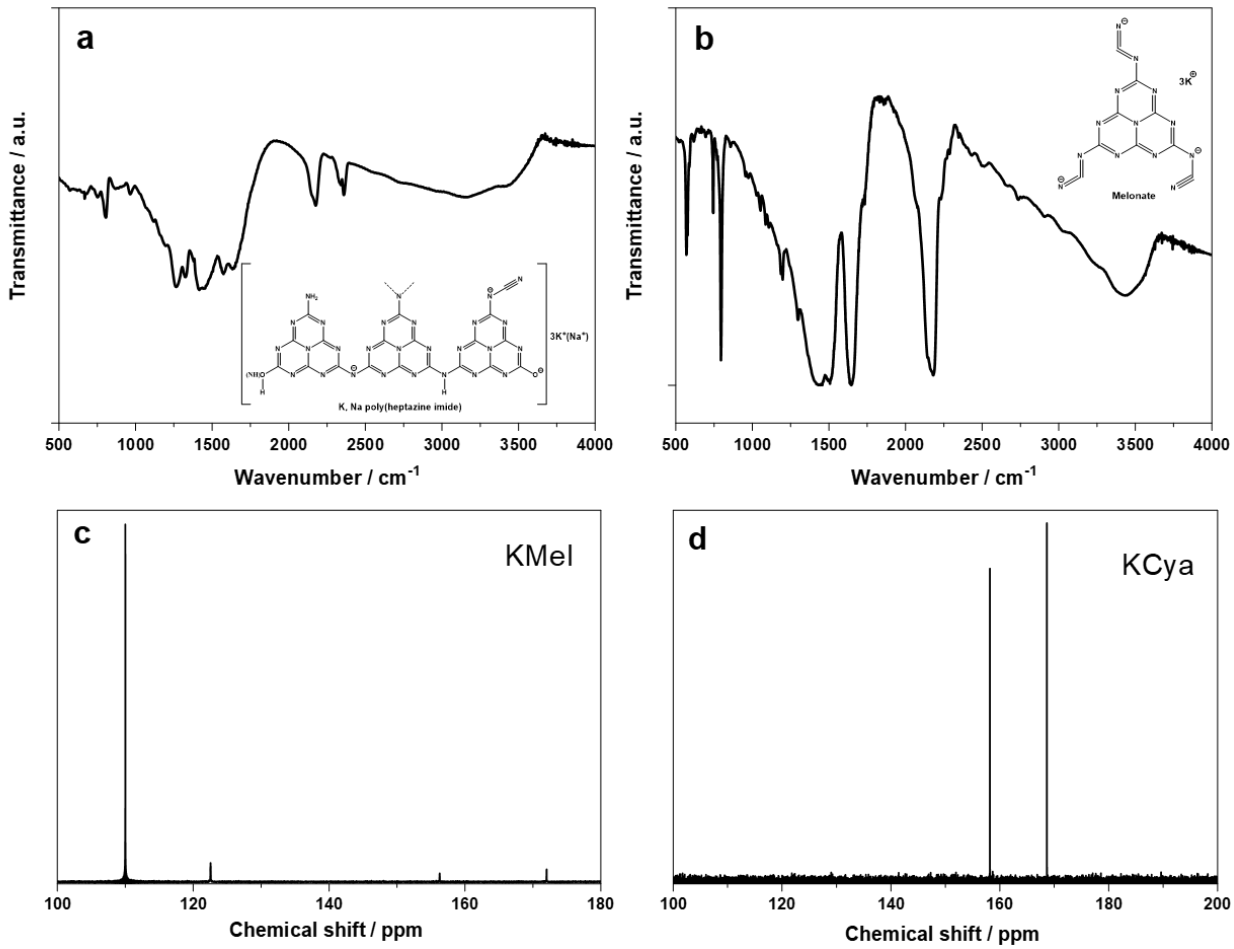

Figure S1. FTIR spectra of (a) K, Na PHI and (b) KMel, and ^{13}C NMR of (c) KMel and (d) KCya.

Table S1. The final concentrations of $HAuCl_4$, stabilizer, and $NaBH_4$ in the synthesized materials and their corresponding names.

Sample name	$HAuCl_4$ concentration / mol L^{-1}	Stabiliser	[Stabilizer : $HAuCl_4$]	$NaBH_4$: $HAuCl_4$ molar ratio
Au2	1.67×10^{-4}	-	-	2
Au10	1.67×10^{-4}	-	-	10
Au20	1.67×10^{-4}	-	-	20
Au50	1.67×10^{-4}	-	-	50
		K, Na PHI / g L^{-1}		
Au10	1.67×10^{-4}	-	-	10
K,NaPHI1	1.67×10^{-4}	1.49×10^{-2}	-	10
K,NaPHI2	1.67×10^{-4}	3.72×10^{-2}	-	10
K,NaPHI3	1.67×10^{-4}	7.43×10^{-2}	-	10
K,NaPHI4	1.67×10^{-4}	1.49×10^{-1}	-	10
K,NaPHI5	1.67×10^{-4}	2.97×10^{-1}	-	10
		KMel/KCya/KCA / mol L^{-1}		
KMel0.1	1.67×10^{-4}	1.67×10^{-5}	1 : 10	10
KMel0.3	1.67×10^{-4}	5.58×10^{-5}	1 : 3	10
KMel1	1.67×10^{-4}	1.67×10^{-4}	1 : 1	10
KMel10	1.67×10^{-4}	1.67×10^{-3}	10 : 1	10
KCya0.1	1.67×10^{-4}	1.67×10^{-5}	1 : 10	10
KCya0.3	1.67×10^{-4}	5.58×10^{-5}	1 : 3	10
KCya1	1.67×10^{-4}	1.67×10^{-4}	1 : 1	10
KCya10	1.67×10^{-4}	1.67×10^{-3}	10 : 1	10
KCA0.1	1.67×10^{-4}	1.67×10^{-5}	1 : 10	10
KCA0.3	1.67×10^{-4}	5.58×10^{-5}	1 : 3	10
KCA1	1.67×10^{-4}	1.67×10^{-4}	1 : 1	10
KCA10	1.67×10^{-4}	1.67×10^{-3}	10 : 1	10

1.3 Nitrophenol reduction catalysis

For the reduction of 4-NP, $NaBH_4$ was added in excess (circa 600 times) compared to 4-NP to ensure pseudo-first-order kinetics. In brief, 0.1 mL $NaBH_4$ (2.16 mol L^{-1}), 0.3 mL 4-NP (1.2×10^{-3} mol L^{-1}), and 2.5 mL deionized water were mixed in a 3 mL quartz cell. Then, the first spectrum was recorded, followed by the addition of 0.025 mL Au NP catalyst (1.14 mg L^{-1}) and shaking the cuvette quickly before recording the subsequent spectra.[4,5] The spectra were taken over a range of 10-15 minutes, where the progress of the reaction was tracked by monitoring the change in intensity of the 4-NP peak at 400 nm as a function of time. The TOF values were calculated considering the reaction data points after the initiation period and from the range that could be fitted with a linear function. The unit of TOF value is h^{-1} $atom_{Au}^{-1}$, as illustrated by the following equation:

$$\frac{mol(4NP)}{mol(Au) \cdot h}$$

1.4 Characterization

UV-vis spectra of the synthesized Au NPs were recorded using a Cary 60 (Agilent Technologies) spectrophotometer. The cuvettes were cleaned using aqua regia between the measurements of different samples. The DLS measurements were performed using Zetasizer Nano ZS (Malvern Instruments Ltd., UK), equipped with a 633 nm solid-state He−Ne laser and operating at a detection angle of 173.5°. The Zeta potential measurements were conducted using a Zetasizer Pro from Malvern Panalytical by Mixed-Mode Measurement phase analysis light scattering (M3-PALS) using a disposable folded capillary cell (DTS1070) in a diameter range of 3.8 nm – 100 µm. Each zeta potential measurement was carried out in triplicate, and the error was quantified as the standard deviation. Analyses were carried out in water (viscosity: 0.8872 Cp; refractive index: 1.33). The TEM images were obtained using the SALVE instrument at 80 kV acceleration voltage and the Philips CM20 at 200kV. For XPS analysis, the measurements were performed using a UHV Multiprobe system (Scienta Omicron, Germany) with a monochromatic X-ray source (Al K_α) and an electron analyzer (Argus CU) with 0.6 eV

energy resolution. Charge compensation during data acquisition was realized by an electron flood gun (NEK 150SC, Staib, Germany) at 6 eV and 50 μA. All samples were prepared by drop-casting on cleaned Si wafers with native oxide. The spectra were afterward calibrated using the Si 2p peak at 99.4 eV. The Au 4f spectra were fitted using the symmetric Voigt function (Gauß-Lorentz, GL) and an asymmetric fit, also based on Voigt functions. The asymmetric fit matches well with the data. The oxygen signal in the elemental composition is not reliable, as also a thin oxidized layer is on top of the Si-substrate. FTIR spectra of the stabilizers were recorded by a Shimadzu IRTracer-100 spectrometer at a resolution of 4 cm^{-1} from the samples powdered and pressed into KBr pellets. ^{13}C NMR spectra of KCya and KMel were acquired with a Bruker Avance III 400 spectrometer after dissolving in D_2O.

1.5. Computational details

All calculations of the carbon nitride model structures were performed using the ORCA package version 5.0.4.[6,7] The PBE0 functional, def2-TZVP basis set, def2/J auxiliary basis set, and DFT-D3 dispersion correction were used.[8–10] Then, the time-dependent DFT calculations of the ground-state geometry were performed using the PBE0 functional to obtain more precise unoccupied orbitals with 50 roots. Fukui functions were calculated to describe the frontier orbitals and the condensed Fukui function was obtained to find local reactivity using the following equations:[11–13]

$$f^+ = \rho_{N+1}(\mathbf{r}) - \rho_N(\mathbf{r}) \text{ for nucleophilic reactions}$$

$$f^- = \rho_N(\mathbf{r}) - \rho_{N-1}(\mathbf{r}) \text{ for electrophilic reactions}$$

The dual descriptor is combined with two Fukui functions to identify the nucleophilic (negative) and the electrophilic (positive) site.

$$f(r) = f^+ - f^-$$

The condensed Fukui functions can also be applied to atomic charges from a Hirshfeld analysis in order to describe the local chemical reactivity.

$$f_k^+ = q_k(N+1) - q_k(N)$$

$$f_k^- = q_k(N) - q_k(N-1)$$

where, $\rho(\mathbf{r})$ is the electron density from DFT calculations and N is the total number of electrons for the system. The condensed Fukui functions are normalized to obtain the dual descriptor.

2. Results and discussion

2.1 Synthesis and characterization of the $NaBH_4$-stabilized Au NPs

The concentration of $NaBH_4$ is a crucial parameter enabling the formation of stable Au NPs and avoiding their immediate precipitation after the synthesis.[3] To optimize the $NaBH_4$:HAuCl ratio, the concentration of $HAuCl_4$ was set as 1.67×10^{-4} mol $L^{-1,}$ and various concentrations of $NaBH_4$ were added (2.0, 10, 20, or 50 $NaBH_4$:$HAuCl_4$ molar ratio to produce **Au2**, **Au10**, **Au20**, or **Au50,** respectively). The optical images of the Au NPs after 24 hours of their synthesis using various $NaBH_4$ concentrations are shown in **Figure S2**. The four suspensions are of different colors, which implies the formation of Au NPs with different particle sizes. Accordingly, one could expect that the particle size is increasing in the sequence of **Au50** > **Au2** > **Au10** or **Au20**.[3] The **Au50** sample turns dark grey after approximately 2.0 h from the synthesis, indicating the rapid agglomeration of the particles.

Figure S3a presents the UV-vis spectra recorded for the synthesized materials on the day of the synthesis and after 21 days of storage at ambient conditions. The **Au10** and **Au20** samples exhibit very similar UV-vis spectra characterized by a narrow surface plasmon resonance (SPR) peak centered at 513 nm. There are no detectable changes in the SPR peak of these samples for at least 21 days (Figure S3a), indicating high colloidal stability. Contrary, the SPR peak for **Au2** is broader and red-shifted to 531 nm, and it becomes even broader and less intense after 21 days, while **Au50** does not show any SPR peak after about 2.0 h from its synthesis (Figure S3a). A complete agglomeration and precipitation of **Au50** is observed after 21 days, so its spectrum could not be recorded. These observations indicate the agglomeration of the Au NPs synthesized using $NaBH_4$:$HAuCl_4$ molar ratios of 2.0 and 50, which is confirmed by the high absorbance intensity in the 600-800 nm range. The stabilization ability of $NaBH_4$ at optimum concentrations is due to the electrostatic stabilization that arises from the presence of a sufficient number of deprotonated anionic species on the surface of NPs.[3] The partial

agglomeration at low $NaBH_4$ concentrations (<10 molar ratio $NaBH_4$:$HAuCl_4$) might be due to the insufficient number of anions (BH_4^-) required for the effective electrostatic stabilization of Au NPs. However, the rapid agglomeration of Au NPs at higher $NaBH_4$ concentration (>20 molar ratio $NaBH_4$:$HAuCl_4$) is induced by the decrease of surface potential that results from the electron injection into the Au NPs upon adding excess $NaBH_4$.[3,14,15] Thus, we have selected $NaBH_4$:$HAuCl_4$ molar ratio 10 as the optimum $NaBH_4$ concentration to produce ligand-free and stable Au NPs.

The effect of K,Na-PHI on the properties of Au NPs was investigated at different PHI concentrations of 1.49×10^{-2}, 3.72×10^{-2}, 7.43×10^{-2}, 1.49×10^{-1}, and 2.97×10^{-1} g L^{-1}, yielding the samples denoted as **K,NaPHI1**, **K,NaPHI2**, **K,NaPHI3**, **K,NaPHI4**, and **K,NaPHI5**, respectively. As shown in Figure S2, the five K,Na-PHI-stabilized Au NPs have a red-brownish colour that is different from that of the **Au10** $NaBH_4$-capped samples, indicating that the addition of K,Na-PHI possibly affects the particle size. Furthermore, the presence of K,Na-PHI, independent of its concentration, leads to a broad peak between 490 nm and 530 nm in the UV-vis electronic absorption spectra, which is in stark contrast to the sharp and intense SPR peak of **Au10** at 513 nm (Figure S3b). This indicates that the average particle size of all K,Na-PHI-stabilized Au NPs might be below 3 nm since larger particles would exhibit a sharper and more intense SPR peak.[16,17]

The effect of KMel, KCya, and KCA on the produced Au NPs has been investigated at different molar ratios (Stabilizer : $HAuCl_4$ = 10, 3, 1, or 0.1) with the corresponding sample designations (Table S1).

As shown in **Figure S2**, the color of the melonate and cyamelurate stabilized Au NPs is comparable to the color of K,NaPHI series except for **KMel10** and **KCya10** which have a reddish and dark grey colors, respectively. On the other hand, the cyanurate stabilized Au NPs exhibit almost the same color as **Au10**, but **KCA10** possesses a reddish color. These macroscopic differences imply that adding 10 molar excess of KMel, KCya, or KCA results in bigger AuNPs, which are expected to be agglomerated, compared to **Au10**. The UV-vis spectra reveal that the particle size of Au NPs varies as a function of the concentration of melonate added (**Figure S3c**). Notably, the particle size of **KMel0.1** and **KMel10** appears to be larger than that of **KMel0.3** and **KMel1**, the SPR peak is sharper and more intense. Furthermore, the SPR peak of **KMel10** is sharper and red-shifted by

about 10 nm than that of **Au10**, which is a clear indication of the beginning of an aggregation phenomenon. In the case of the cyamelurate–stabilized Au NPs, similar behavior is detected for the Au NPs stabilized by 0.1 and 0.3 molar ratio of KCya demonstrated by a less pronounced SPR peak compared to **Au10** (**Figure S3d**). Despite the absorbance of **KCya1** being significantly reduced over the whole spectrum, it displays a sharp SPR peak similar to **Au10,** suggesting a comparable particle size**.** Differently, increasing the concentration of KCya to reach stabilizer:$HAuCl_4$ molar ratio of 10 (**KCya10**) induces the agglomeration of the Au NPs, as revealed by the broadening of the spectrum and the high absorbance intensity at 800 nm. Interestingly, the SPR peak of **KCA0.1** and **KCA0.3** is nearly identical to **Au10** while, the SPR peak of **KCA1** and **KCA10** is red-shifted by approximately 5.0 nm and 18 nm, respectively (**Figure S3e**). These shifts imply that higher concentrations of cyanurate cause the formation of Au NPs with larger particle size.[16]



Figure S2. Optical images of Au NPs stabilized by $NaBH_4$, K,Na PHI, KMel, KCya, and KCA as a function of the concentration of the stabilizer. The code of each sample is shown above its optical image. The concentration of $HAuCl_4$, stabilizer, and $NaBH_4$ in the synthesized materials is listed in Table S1.

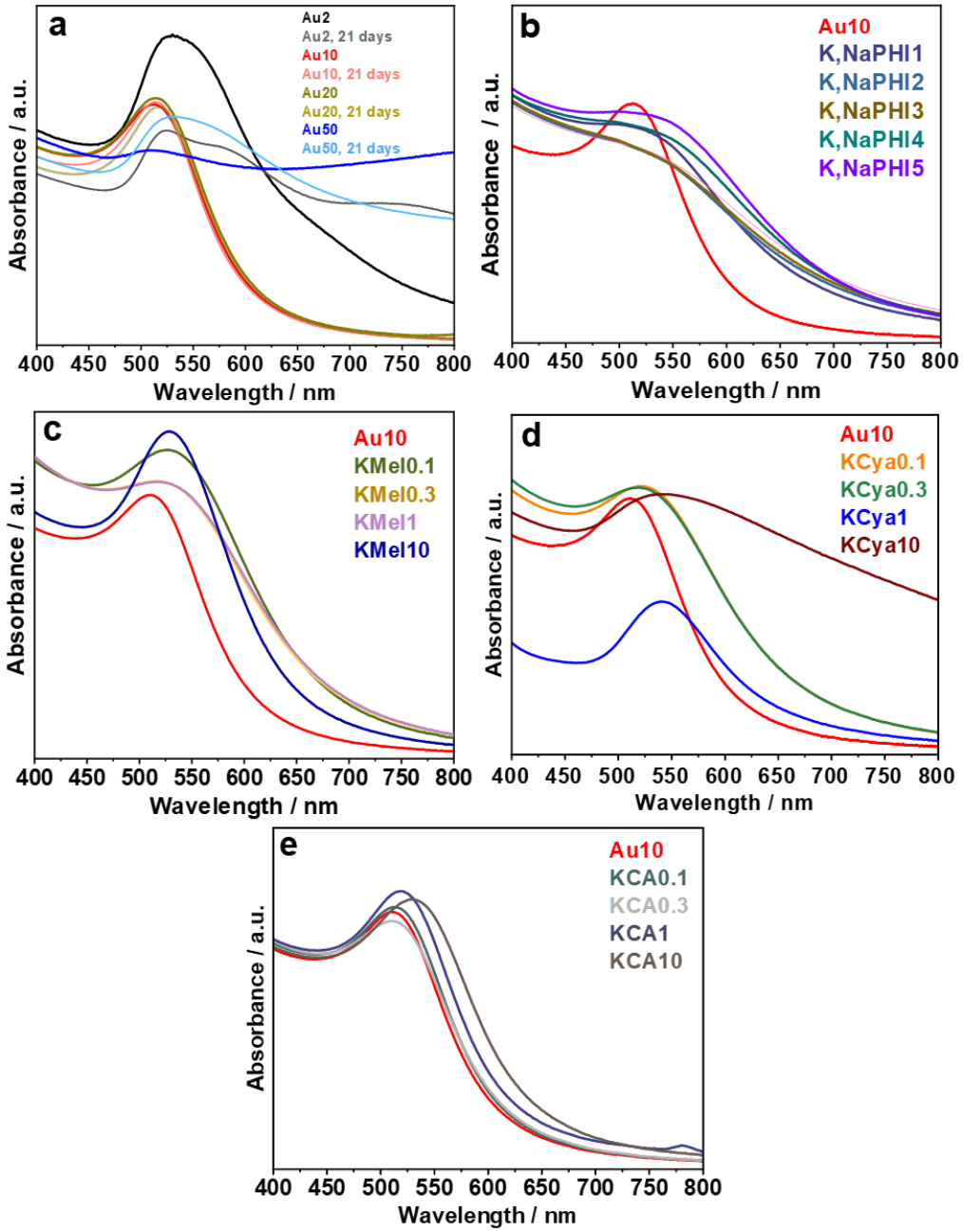

Figure S3. UV−vis absorption spectra of Au NPs stabilized by (a) $NaBH_4$ after synthsis and after 21 days of storage, (b) K,Na-PHI, (c) KMel, (d) KCya, and (e) KCA as a function of the concentration of the stabilizer.

2.2. Materials characterization

Particle size distribution

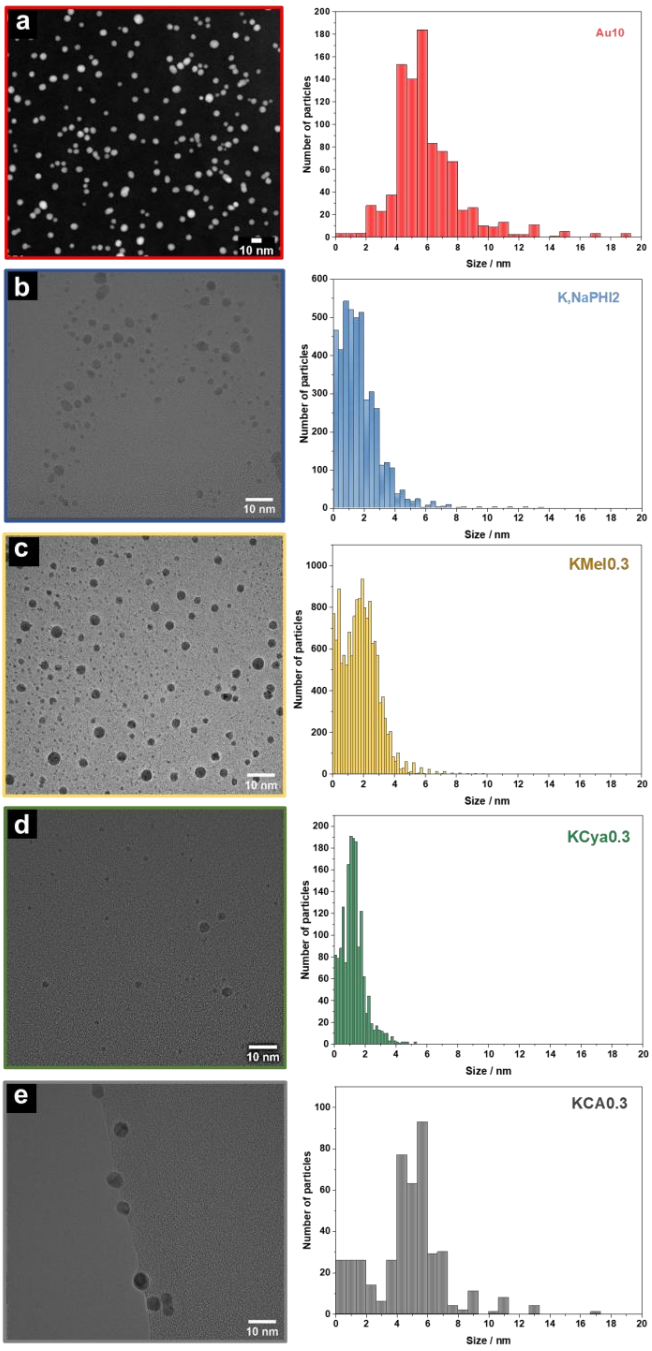

Figure S4. (S)TEM images and particle size distribution derived from the (S)TEM measurements for (a) **Au10**, (b) **K,NaPHI2**, **(**c) **KMel0.3**, (d) **KCA0.3**, and (e) **KCya0.3**.

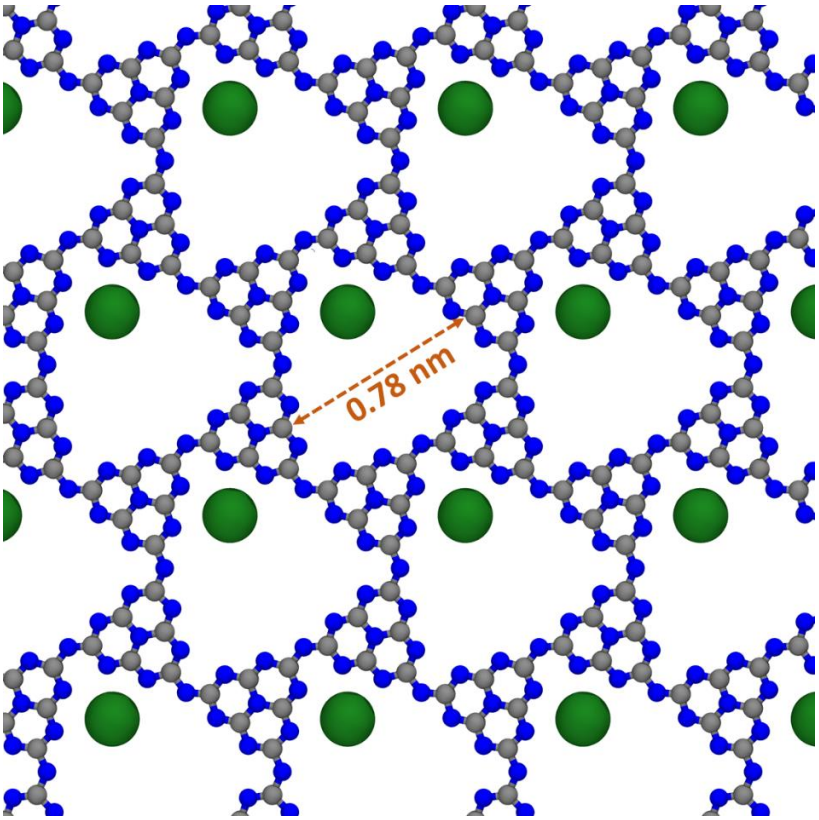

Figure S5. Schematic representation of K, Na-PHI structure highlighting the heptazine cages.

Note on XPS analysis

Figure S6a-e compares XP overview spectra (survey) of all synthesized samples. From the survey spectrum of **Au10**, the peaks corresponding to Au, B, and Na are detected. In addition to these peaks, the peaks of K and N corresponding to the proposed stabilizers are observed. The detection of the carbon peak even in **Au10** might be due hydrocarbon adsorption on the sample or carbonate formation in the basic Au NP suspensions.

The high-resolution spectra of N 1s of the synthesized samples are shown in Figure S7. As expected, **Au10** does not contain any nitrogen peak (Figure S7a). In contrast to this, the N 1s spectrum of **K,NaPHI2** exhibits three bands at 399.1, 400.6, and 405.1 eV which can be assigned to C-N=C and the sum of N-(C3), C-NH-C, as well as the π excitation, respectively (Figure S7b).[1,18,19] The N 1s spectrum of **KMel0.3** is comparable, where the intense peak at 399.3 eV is due to the overlapping of the peaks corresponding to the C-

N=C groups and cyanamide moieties (N≡C), as shown in Figure S7c. Additionally, the peak at 401.2 eV is correlated to the central N atoms in heptazines (N-(C3)). In the N 1s spectrum of **KCya0.3**, one can distinguish two peaks attributed to the C-N=C groups in the heptazines (398.9 eV) and the sum of the N-(C3) and N-C-O$^-$ species (400.6 eV) (Figure S7d). Furthermore, **KCA0.3** exhibits a low-intensity peak centered at 400.6 eV corresponds to the N atoms in deprotonated cyanuric acid (Figure S7e).

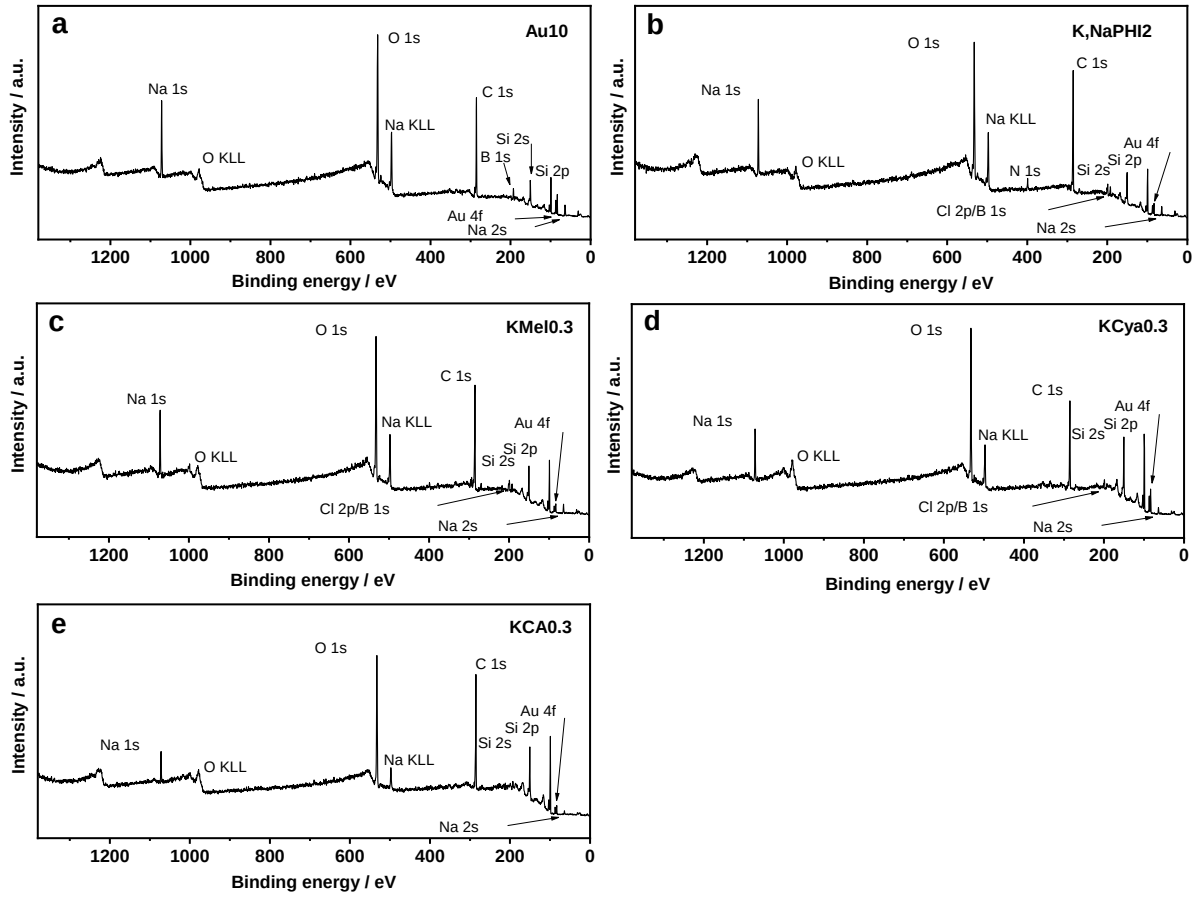

Figure S6. X-ray photoelectron survey spectra of (a) **Au10**, (b) **K,NaPHI2**, (c) **KMel0.3**, (d) **KCA0.3**, and (e) **KCya0.3**.

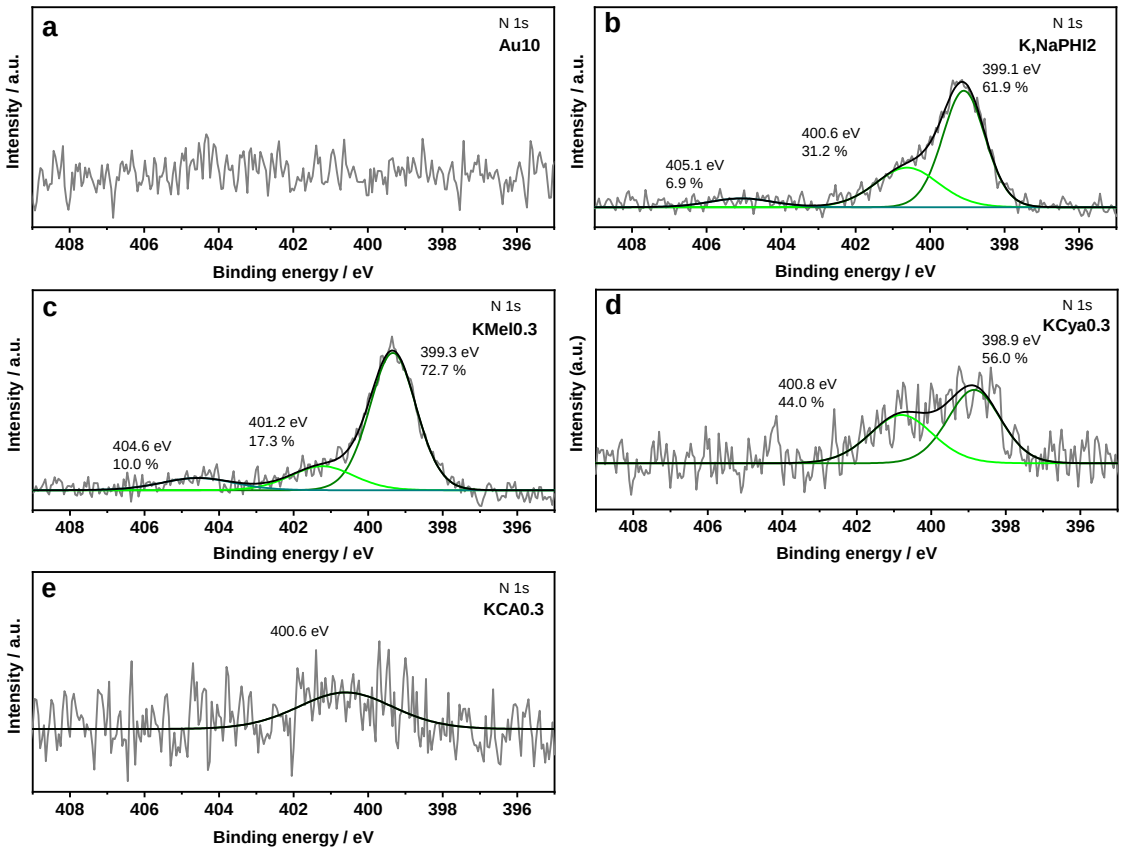

Figure S7. High-resolution N 1s XP spectra of (a) **Au10**, (b) **K,NaPHI2**, **(**c) **KMel0.3**, (d) **KCA0.3**, and (e) **KCya0.3**.

Table S2. Binding energy and full width at half maximum of the Au 4f peaks for the synthesized samples.

Sample		Binding energy / eV	Full width at half maximum / eV
Au10	Au $4f_{7/2}$	83.6	0.7
	Au $4f_{5/2}$	87.3	
K,NaPHI2	Au $4f_{7/2}$	83.6	0.8
	Au $4f_{5/2}$	87.3	
KCya0.3	Au $4f_{7/2}$	83.7	0.8
	Au $4f_{5/2}$	87.4	
KCA0.3	Au $4f_{7/2}$	83.7	0.8
	Au $4f_{5/2}$	87.4	
KMel0.3	Au $4f_{7/2}$	83.7	0.7
	Au $4f_{5/2}$	87.4	

Long-term stability of Au NPs

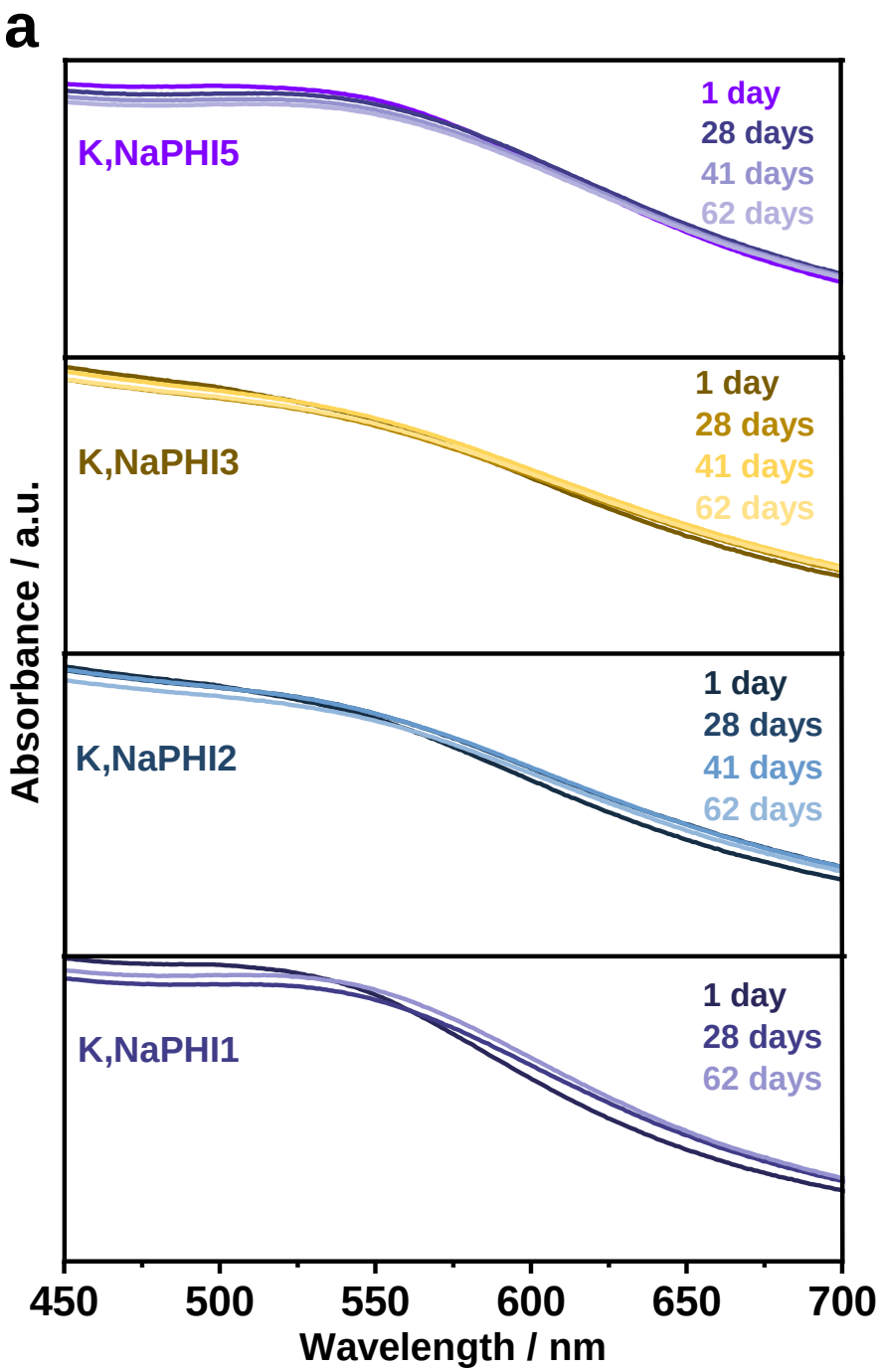

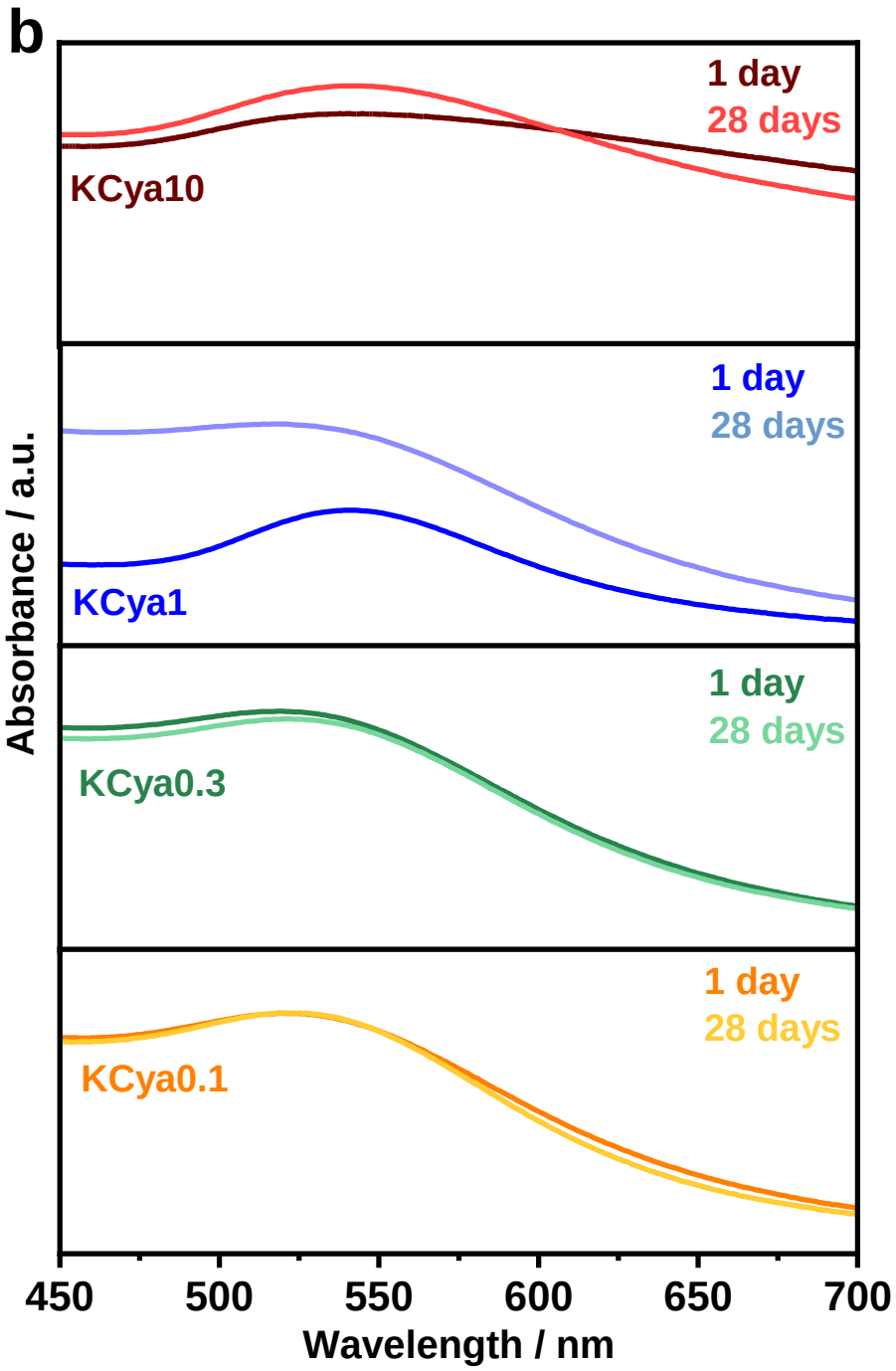
b
1 day
28 days
KCya10
1 day
28 days
KCya1
1 day
28 days
KCya0.3
1 day
28 days
KCya0.1
Absorbance / a.u.
450
500
550
600
650
700
Wavelength / nm

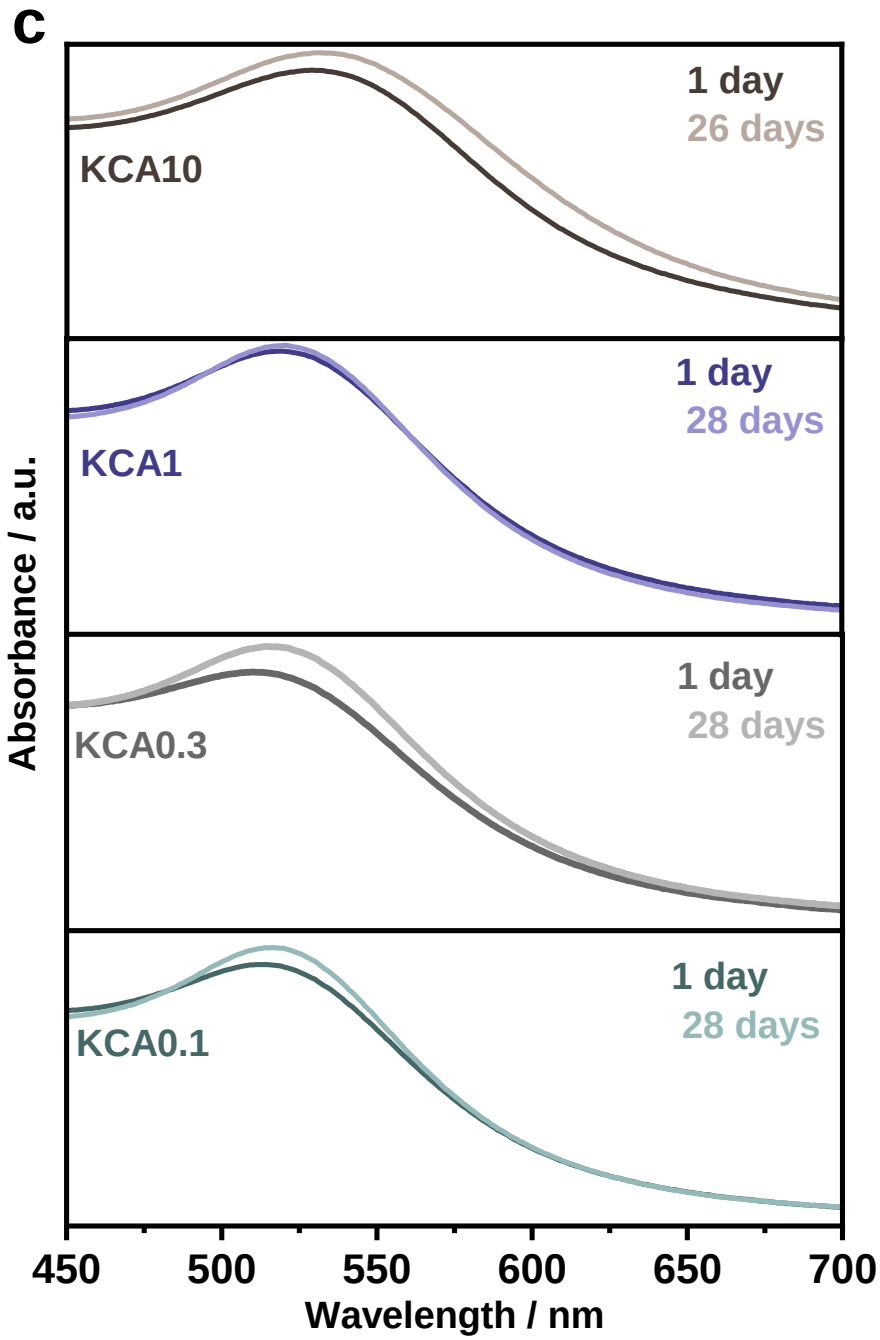

Figure S8. UV−vis absorption spectra of Au NPs produced in the presence of different concentrations of (a) K, Na PHI, (b) KCya, and (c) KCA as a function of the storage time.

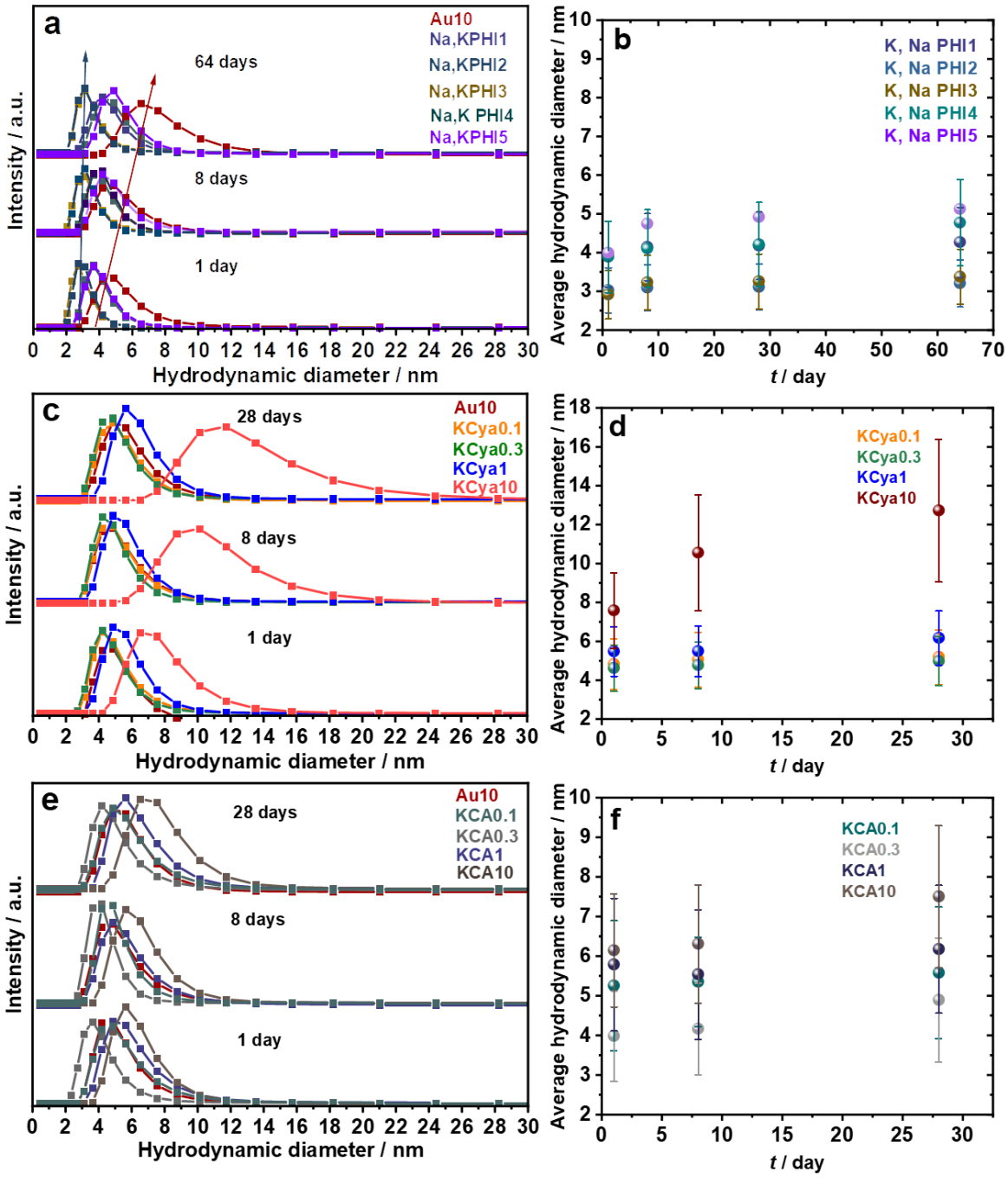

Figure S9. Hydrodynamic diameter determined from the DLS results of Au NPs produced in the presence of different concentrations of (a, b) K, Na PHI, (c, d) KCya, and (e, f) KCA as a function of the storage time.

Stability of Au NPs against heating

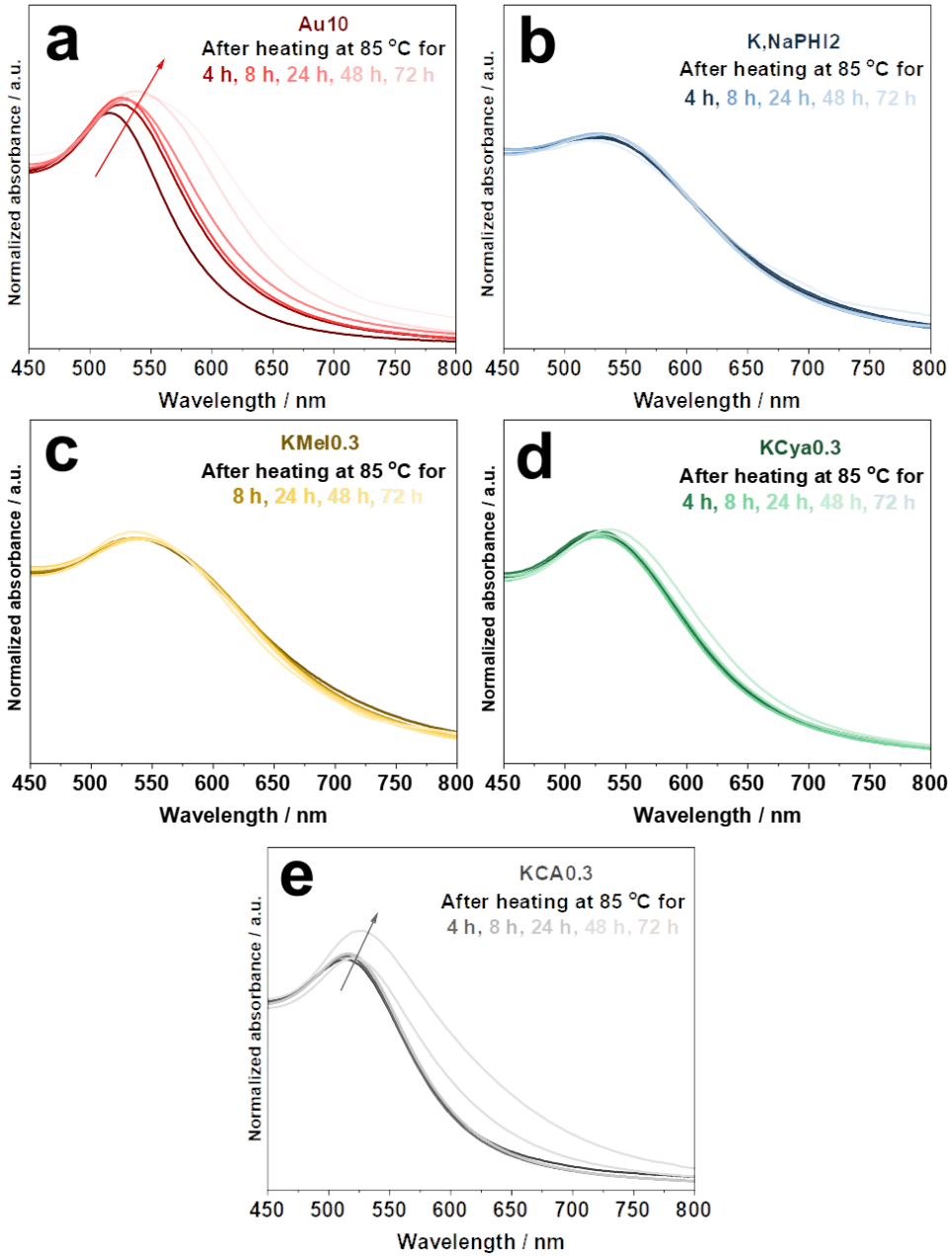

Figure S10. Thermal Stability of Au NPs. (a-e) UV−vis electronic absorption spectra of **Au10**, **K,NaPHI2**, **KMel0.3**, **KCya0.3**, and **KCA0.3** after heating at 85 °C for 4 h, 8 h, 24 h, 48 h, and 72 h.

Note on the effect of reductant-derived impurities on the Au NPs stability

Figure S10 presents the UV-vis spectra, (S)TEM images, and XPS analysis of the **Au10** and the K, Na-PHI-stabilized Au NPs before and after dialysis (_Dial). Upon dialysis, **Au10** is agglomerated as noticed by the broadening of the UV-vis spectrum and the high absorbance intensity at 800 nm (Figure S10a). Similarly, the HAADF-STEM image of **Au10_Dial** reveals that dialysis leads to a complete agglomeration of **Au10 (**Figure S10b,c**)**. This behaviour results from the removal of the excess $NaBH_4$ and consequently, the number of charges around the Au NPs required for electrostatic stabilization is insufficient. In contrast, the UV-vis spectra of the Au NPs stabilized by different concentrations of K, Na-PHI are not significantly changed after dialysis, but the absorbance considerably decreases due to the dilution of the samples during the dialysis process. Furthermore, the average particle size of **K,NaPHI2** is slightly increased after dialysis but it is still below 3 nm, as indicated by the particle size distribution in Figure S11a,b and by comparing the TEM images in Figure S10d,e.

The elemental composition derived from the XPS analysis indicates that the excess $NaBH_4$ from **Au10** and **K,NaPHI2** was removed successfully after dialysis, as demonstrated in Table S3. In the dialyzed samples, no B is detected and the concentration of Na is substantially decreased. The Au $4f_{7/2}$ and Au $4f_{5/2}$ peaks of **Au10** and **K,NaPHI2** are shifted to higher binding energy (by about 0.1 eV) after dialysis (Figure S10f and Table S4). The upshift in the binding energy values after dialysis is due to the change in the chemical environment of the Au NPs into less reductive (removal of the $NaBH_4$ hydrolysis products). On the other hand, dialysis results in no change in the N1s XP spectrum of **K,NaPHI2**.

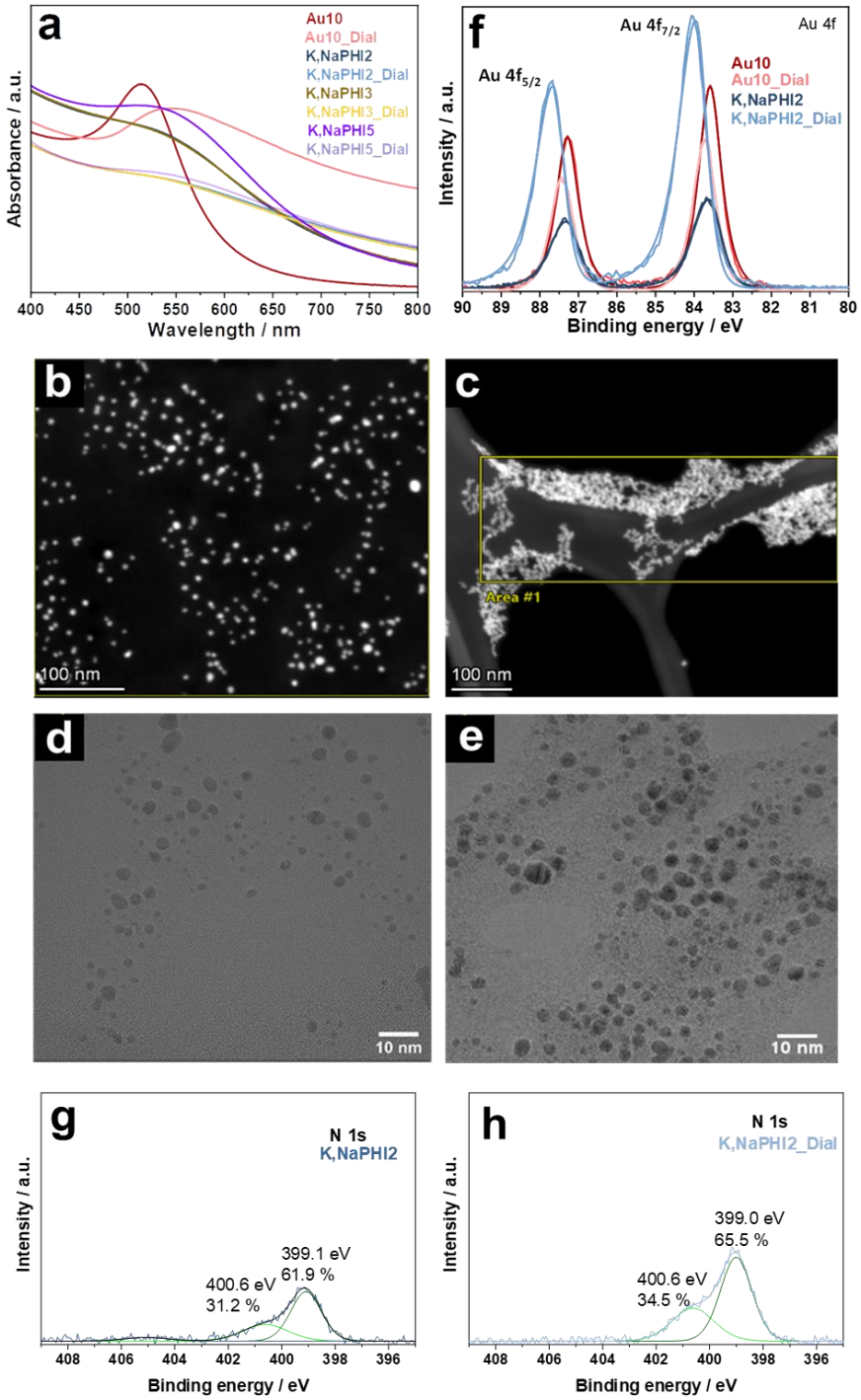

Figure S11. **(a)** UV−vis absorption spectra of **Au10**, **K,NaPHI2**, and **K,NaPHI3** before and after dialysis, HAADF-STEM images of (b) **Au10**, (c) **Au10_Dial**, (d) HRTEM images of **K,NaPHI2**, and **(e) K,NaPHI2_Dial**, (f) XPS spectra of the Au (4f) signal of **Au10** and **K,NaPHI2** before and after dialysis, and (g,h) XPS spectra of the N 1s signal of **K,NaPHI2** before and after dialysis.

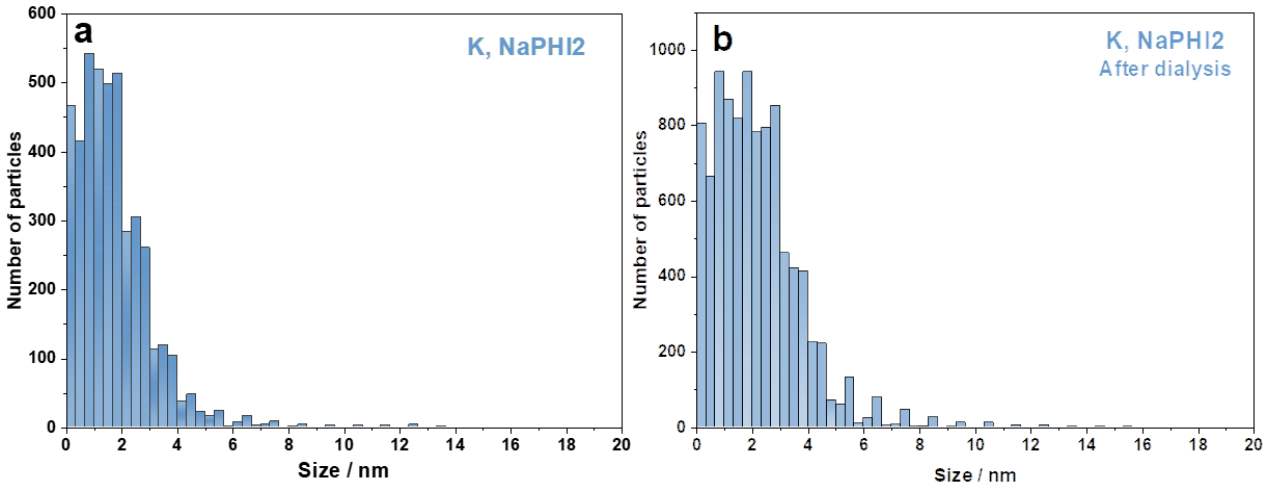

Figure S12. Particle size distribution of **K,NaPHI2** (a) before and (b) after dialysis.

Table S3. Elemental composition derived from the XPS measurements of **Au10** and **K,NaPHI2** before and after dialysis.

Sample	N [%]	Au [%]	Na [%]	B [%]	K [%]	Cl [%]
Au10	-	4	43.1	52.9	-	-
K,NaPHI2	14.2	2	27.9	38.7	3.4	13.7
Au10_Dial	11.8	52.9	35.3	-	-	-
K,NaPHI2_Dial	73.9	19.3	6.8	-	-	-

Table S4. Binding energy and full width at half maximum of the Au 4f for **Au10** and **K,NaPHI2** before and after dialysis.

Sample		Binding energy [eV]	Full width at half maximum [eV]
Au10	Au $4f_{7/2}$	83.6	0.7
	Au $4f_{5/2}$	87.3	
K,NaPHI2	Au $4f_{7/2}$	83.6	0.8
	Au $4f_{5/2}$	87.3	
Au10_Dial	Au $4f_{7/2}$	83.7	0.7
	Au $4f_{5/2}$	87.4	
K,NaPHI2_Dial	Au $4f_{7/2}$	84.0	0.7
	Au $4f_{5/2}$	87.7	

2.3. DFT calculations

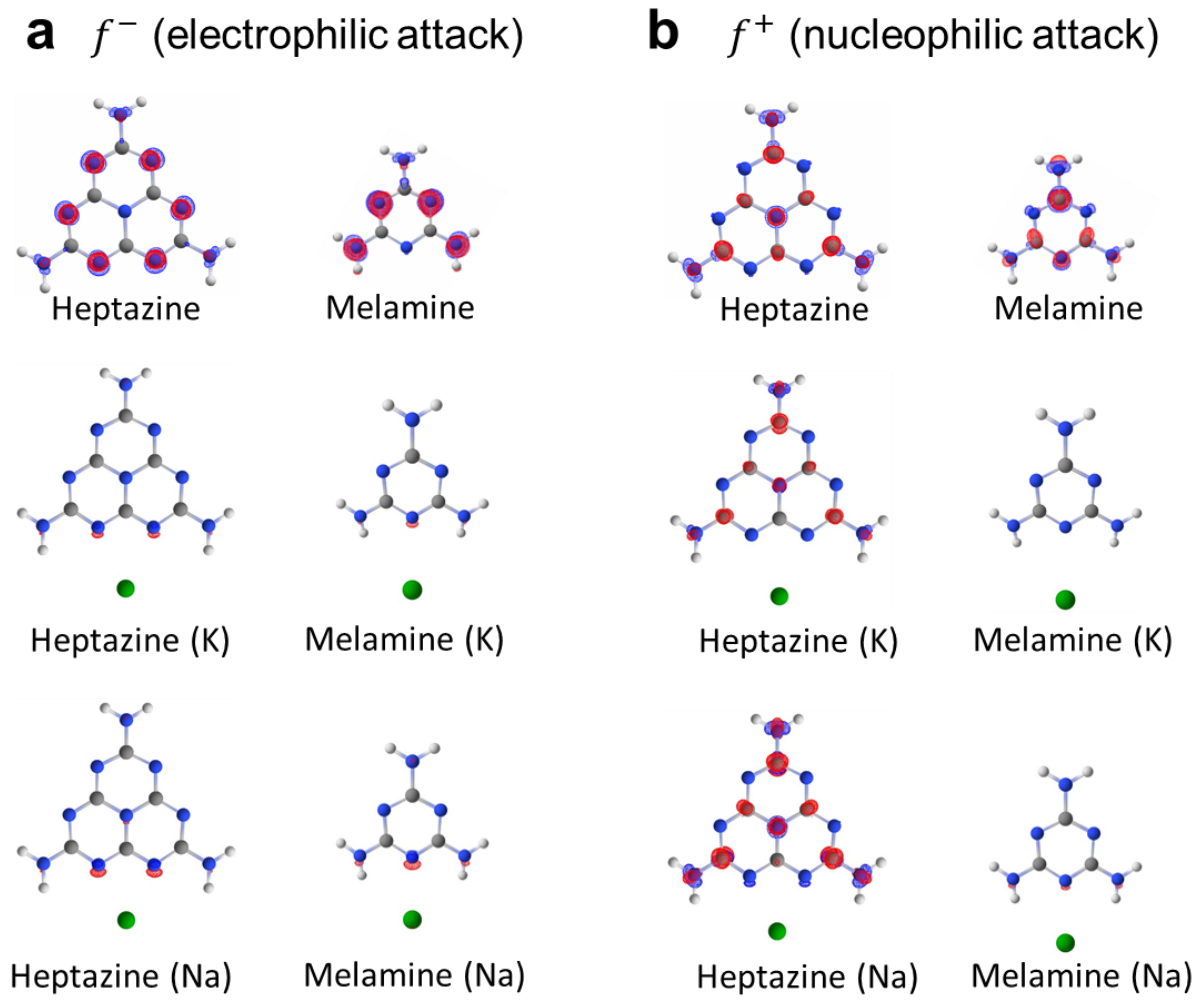

Figure S13. The electron density from Fukui function (a) negative f^- and (b) positive f^+ for (left) heptazine and (right) melamine without the cation (top), with (middle) potassium, and (bottom) sodium.

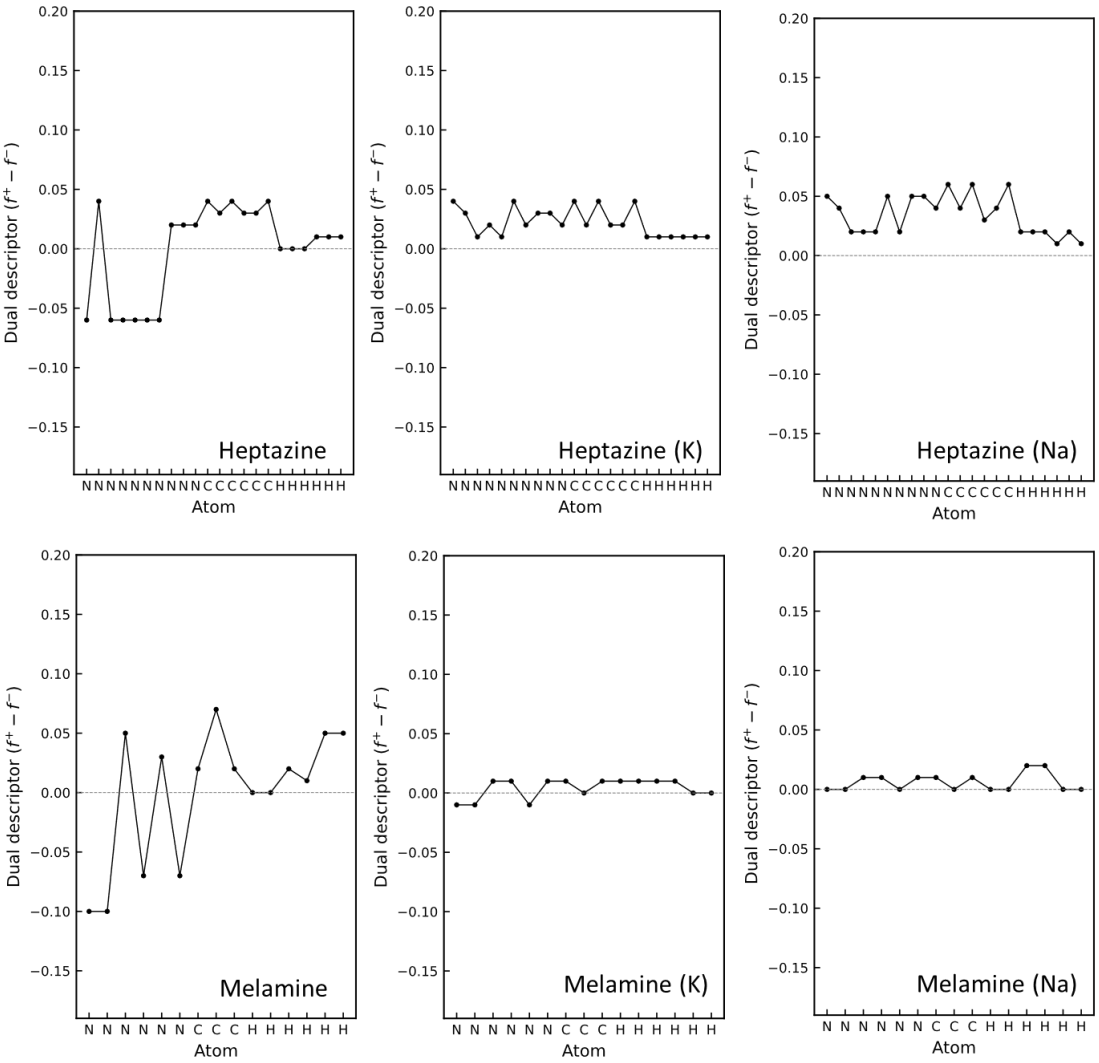

Figure S14. The dual descriptor of heptazine and melamine in the presence of a potassium or a sodium. The negative value corresponds to the electrophilic attack site and the positive value corresponds to the nucleophilic attack site.

Table S5. Fukui function and the dual descriptor from Hirschfeld charge for the carbon nitride species

Cya

Element	Atom Number	*f+*	*f-*	*f0*	*f+-f-*
N	0	-0,10	-0,05	-0,07	-0,05
N	1	-0,01	-0,02	-0,01	0,01
N	2	-0,10	-0,05	-0,07	-0,05
N	3	-0,05	-0,07	-0,06	0,01
N	4	-0,05	-0,07	-0,06	0,02
N	5	-0,08	-0,06	-0,07	-0,01
N	6	-0,07	-0,06	-0,07	-0,01
O	7	-0,19	-0,10	-0,15	-0,08
O	8	-0,09	-0,17	-0,13	0,08
O	9	-0,09	-0,15	-0,12	0,06
C	10	-0,03	-0,05	-0,04	0,02
C	11	-0,02	-0,02	-0,02	0,01
C	12	-0,03	-0,05	-0,04	0,02
C	13	-0,02	-0,03	-0,02	0,00
C	14	-0,02	-0,02	-0,02	0,00
C	15	-0,05	-0,03	-0,04	-0,02

K1Cya

Element	Atom Number	*f+*	*f-*	*f0*	*f+-f-*
N	0	-0,13	-0,03	-0,08	-0,10
N	1	-0,01	-0,01	-0,01	0,00
N	2	-0,11	-0,03	-0,07	-0,08
N	3	-0,04	-0,11	-0,07	0,06
N	4	-0,05	-0,14	-0,10	0,09
N	5	-0,12	-0,06	-0,09	-0,07
N	6	-0,07	-0,06	-0,06	0,00
O	7	-0,11	-0,08	-0,09	-0,02
O	8	-0,07	-0,13	-0,10	0,07
O	9	-0,08	-0,12	-0,10	0,04
C	10	-0,03	-0,04	-0,03	0,01
C	11	-0,02	-0,03	-0,02	0,02
C	12	-0,03	-0,04	-0,03	0,01
C	13	-0,03	-0,02	-0,02	-0,01
C	14	-0,02	-0,02	-0,02	-0,01
C	15	-0,04	-0,02	-0,03	-0,02
K	16	-0,06	-0,05	-0,06	0,00

K2Cya

Element	Atom Number	*f+*	*f-*	*f0*	*f+-f-*
N	0	-0,11	-0,08	-0,09	-0,02
N	1	0,00	0,00	0,00	0,00
N	2	-0,06	-0,10	-0,08	0,04
N	3	-0,07	-0,06	-0,06	-0,01
N	4	-0,06	-0,08	-0,07	0,02
N	5	-0,17	-0,07	-0,12	-0,10
N	6	-0,09	-0,11	-0,10	0,03
O	7	-0,08	-0,12	-0,10	0,05
O	8	-0,05	-0,06	-0,05	0,02
O	9	-0,05	-0,06	-0,06	0,01
C	10	-0,03	-0,03	-0,03	0,00
C	11	-0,02	-0,02	-0,02	0,00
C	12	-0,03	-0,02	-0,02	0,00
C	13	-0,03	-0,02	-0,03	-0,02
C	14	-0,02	-0,02	-0,02	0,00
C	15	-0,03	-0,04	-0,04	0,01
K	16	-0,05	-0,04	-0,05	-0,01
K	17	-0,06	-0,05	-0,06	-0,01

K3Cya0.3

Element	Atom Number	*f+*	*f-*	*f0*	*f+-f-*
N	0	-0,01	-0,13	-0,07	0,12
N	1	0,00	0,00	0,00	0,00
N	2	0,01	-0,05	-0,02	0,07
N	3	-0,01	-0,07	-0,04	0,06
N	4	-0,01	-0,08	-0,04	0,07
N	5	-0,01	-0,12	-0,07	0,11
N	6	0,01	-0,06	-0,02	0,07
O	7	0,00	-0,06	-0,03	0,06
O	8	-0,02	-0,06	-0,04	0,04
O	9	0,00	-0,05	-0,03	0,05
C	10	-0,01	-0,03	-0,02	0,02
C	11	0,00	-0,02	-0,01	0,01
C	12	0,00	-0,02	-0,01	0,02
C	13	0,00	-0,03	-0,02	0,02
C	14	0,00	-0,01	-0,01	0,01
C	15	0,00	-0,03	-0,02	0,03
K	16	-0,02	-0,06	-0,04	0,04
K	17	-0,50	-0,05	-0,27	-0,45
K	18	-0,42	-0,06	-0,24	-0,37

CA

Element	Atom Number	*f+*	*f-*	*f0*	*f+-f-*
N	0	-0,18	-0,09	-0,14	-0,09
N	1	-0,11	-0,09	-0,10	-0,01
N	2	-0,11	-0,09	-0,10	-0,02
O	3	-0,16	-0,17	-0,16	0,01
O	4	-0,16	-0,17	-0,16	0,00
O	5	-0,12	-0,21	-0,17	0,09
C	6	-0,06	-0,05	-0,06	-0,01
C	7	-0,06	-0,05	-0,06	-0,01
C	8	-0,04	-0,07	-0,05	0,03

K1CA

Element	Atom Number	*f+*	*f-*	*f0*	*f+-f-*
N	0	0,02	-0,07	-0,03	0,08
N	1	-0,01	-0,15	-0,08	0,14
N	2	-0,02	-0,14	-0,08	0,13
O	3	-0,02	-0,20	-0,11	0,18
O	4	0,01	-0,12	-0,05	0,12
O	5	-0,02	-0,12	-0,07	0,10
C	6	-0,01	-0,05	-0,03	0,05
C	7	0,00	-0,04	-0,02	0,04
C	8	-0,01	-0,05	-0,03	0,04
K	9	-0,93	-0,06	-0,49	-0,86

K2CA

Element	Atom Number	*f+*	*f-*	*f0*	*f+-f-*
N	0	-0,02	-0,17	-0,10	0,15
N	1	-0,11	-0,06	-0,08	-0,04
N	2	-0,04	-0,12	-0,08	0,08
O	3	-0,04	-0,08	-0,06	0,04
O	4	-0,05	-0,18	-0,12	0,13
O	5	-0,01	-0,10	-0,05	0,09
C	6	-0,02	-0,03	-0,03	0,02
C	7	-0,02	-0,05	-0,04	0,03
C	8	-0,02	-0,04	-0,03	0,03
K	9	-0,06	-0,08	-0,07	0,02
K	10	-0,61	-0,06	-0,34	-0,55

K3CA

Element	Atom Number	*f+*	*f-*	*f0*	*f+-f-*
N	0	0,00	-0,06	-0,03	0,06
N	1	0,00	-0,19	-0,09	0,19
N	2	0,00	-0,07	-0,03	0,07
O	3	0,00	-0,16	-0,08	0,15
O	4	0,00	-0,09	-0,04	0,08
O	5	0,00	-0,08	-0,04	0,08
C	6	0,00	-0,04	-0,02	0,03
C	7	0,00	-0,03	-0,02	0,03
C	8	0,00	-0,04	-0,02	0,03
K	9	-0,32	-0,08	-0,20	-0,24
K	10	-0,32	-0,08	-0,20	-0,24
K	11	-0,32	-0,09	-0,21	-0,24

Mel

Element	Atom Number	*f+*	*f-*	*f0*	*f+-f-*
N	0	-0,03	-0,10	-0,06	0,07
N	1	-0,03	0,00	-0,01	-0,03
N	2	-0,01	-0,07	-0,04	0,06
N	3	-0,02	-0,09	-0,06	0,07
N	4	-0,03	-0,08	-0,06	0,05
N	5	-0,05	-0,09	-0,07	0,04
N	6	0,00	-0,07	-0,04	0,07
N	7	-0,09	-0,01	-0,05	-0,08
N	8	-0,01	-0,01	-0,01	0,00
N	9	-0,09	-0,01	-0,05	-0,08
N	10	-0,06	-0,07	-0,06	0,01
N	11	-0,15	-0,08	-0,11	-0,07
N	12	-0,14	-0,08	-0,11	-0,06
C	13	-0,02	-0,02	-0,02	0,00
C	14	-0,02	-0,02	-0,02	0,00
C	15	-0,03	-0,03	-0,03	0,00
C	16	-0,02	-0,02	-0,02	0,00
C	17	-0,02	-0,02	-0,02	0,00
C	18	-0,03	-0,03	-0,03	0,00
C	19	-0,06	-0,03	-0,05	-0,03
C	20	-0,06	-0,03	-0,05	-0,03
C	21	-0,02	-0,02	-0,02	0,00

K1Mel

Element	Atom Number	*f+*	*f-*	*f0*	*f+-f-*
N	0	-0,03	-0,06	-0,05	0,03
N	1	-0,02	-0,02	-0,02	0,00
N	2	-0,01	-0,03	-0,02	0,02
N	3	-0,02	-0,02	-0,02	0,00
N	4	-0,03	-0,02	-0,03	-0,01
N	5	-0,06	-0,03	-0,05	-0,03
N	6	0,00	-0,06	-0,03	0,06
N	7	-0,07	-0,01	-0,04	-0,06
N	8	-0,03	-0,13	-0,08	0,10
N	9	-0,12	-0,01	-0,07	-0,11
N	10	-0,06	-0,19	-0,12	0,13
N	11	-0,16	-0,05	-0,11	-0,11
N	12	-0,12	-0,06	-0,09	-0,06
C	13	-0,01	-0,02	-0,02	0,01
C	14	-0,01	-0,02	-0,01	0,00
C	15	-0,02	-0,02	-0,02	0,00
C	16	-0,02	-0,02	-0,02	0,00
C	17	-0,02	-0,02	-0,02	0,00
C	18	-0,02	-0,02	-0,02	0,00
C	19	-0,06	-0,02	-0,04	-0,04
C	20	-0,05	-0,02	-0,04	-0,02
C	21	-0,01	-0,08	-0,05	0,07
K	22	-0,03	-0,04	-0,04	0,02

K2Mel

Element	Atom Number	*f+*	*f-*	*f0*	*f+-f-*
N	0	-0,04	-0,01	-0,02	-0,03
N	1	-0,01	-0,01	-0,01	0,00
N	2	-0,02	-0,02	-0,02	0,00
N	3	-0,02	-0,05	-0,04	0,03
N	4	-0,02	-0,05	-0,04	0,03
N	5	-0,05	-0,02	-0,04	-0,04
N	6	-0,01	-0,03	-0,02	0,03
N	7	-0,18	-0,02	-0,10	-0,16
N	8	-0,03	-0,10	-0,06	0,06
N	9	-0,02	-0,08	-0,05	0,06
N	10	-0,05	-0,15	-0,10	0,10
N	11	-0,05	-0,11	-0,08	0,06
N	12	-0,23	-0,06	-0,14	-0,18
C	13	-0,01	-0,02	-0,02	0,01
C	14	-0,01	-0,02	-0,01	0,01
C	15	-0,01	-0,02	-0,01	0,01
C	16	-0,02	-0,01	-0,02	-0,01
C	17	-0,02	-0,01	-0,01	0,00
C	18	-0,03	-0,02	-0,02	-0,01
C	19	-0,01	-0,04	-0,02	0,03
C	20	-0,09	-0,02	-0,06	-0,07
C	21	-0,01	-0,06	-0,04	0,05
K	22	-0,03	-0,04	-0,04	0,01
K	23	-0,02	-0,04	-0,03	0,01

K3Mel

Element	Atom Number	*f+*	*f-*	*f0*	*f+-f-*
N	0	0,00	-0,03	-0,01	0,03
N	1	0,00	-0,01	0,00	0,00
N	2	0,00	-0,02	-0,01	0,02
N	3	0,00	-0,03	-0,01	0,03
N	4	0,00	-0,05	-0,02	0,04
N	5	0,00	-0,05	-0,02	0,05
N	6	0,00	-0,02	-0,01	0,01
N	7	0,00	-0,05	-0,03	0,05
N	8	0,00	-0,09	-0,05	0,09
N	9	0,00	-0,06	-0,03	0,06
N	10	-0,02	-0,13	-0,07	0,11
N	11	-0,02	-0,09	-0,05	0,07
N	12	-0,02	-0,09	-0,05	0,08
C	13	0,00	-0,02	-0,01	0,02
C	14	0,00	-0,01	-0,01	0,01
C	15	0,00	-0,01	-0,01	0,01
C	16	0,00	-0,01	-0,01	0,01
C	17	0,00	-0,01	-0,01	0,01
C	18	0,00	-0,01	-0,01	0,01
C	19	0,00	-0,03	-0,02	0,03
C	20	0,00	-0,03	-0,02	0,03
C	21	0,00	-0,05	-0,03	0,05
K	22	-0,31	-0,04	-0,18	-0,27
K	23	-0,31	-0,03	-0,17	-0,28
K	24	-0,32	-0,03	-0,17	-0,28

hep

Element	Atom Number	*f+*	*f-*	*f0*	*f+-f-*
N	0	-0,04	-0,10	-0,07	0,06
N	1	-0,04	0,00	-0,02	-0,04
N	2	-0,04	-0,10	-0,07	0,06
N	3	-0,04	-0,10	-0,07	0,06
N	4	-0,04	-0,10	-0,07	0,06
N	5	-0,04	-0,10	-0,07	0,06
N	6	-0,04	-0,10	-0,07	0,06
N	7	-0,06	-0,04	-0,05	-0,02
N	8	-0,06	-0,04	-0,05	-0,02
N	9	-0,06	-0,04	-0,05	-0,02
C	10	-0,07	-0,03	-0,05	-0,04
C	11	-0,05	-0,02	-0,03	-0,03
C	12	-0,07	-0,03	-0,05	-0,04
C	13	-0,05	-0,02	-0,03	-0,02
C	14	-0,05	-0,02	-0,03	-0,03
C	15	-0,07	-0,03	-0,05	-0,04
H	16	-0,03	-0,03	-0,03	-0,01
H	17	-0,03	-0,03	-0,03	-0,01
H	18	-0,03	-0,03	-0,03	-0,01
H	19	-0,03	-0,02	-0,03	-0,01
H	20	-0,03	-0,02	-0,03	-0,01
H	21	-0,03	-0,02	-0,03	-0,01

hepK

Element	Atom Number	*f+*	*f-*	*f0*	*f+-f-*
N	0	-0,02	0,02	0,00	-0,03
N	1	-0,03	0,00	-0,01	-0,02
N	2	-0,03	-0,02	-0,02	-0,01
N	3	-0,03	-0,01	-0,02	-0,01
N	4	-0,03	-0,02	-0,02	-0,01
N	5	-0,02	0,02	0,00	-0,03
N	6	-0,03	-0,01	-0,02	-0,01
N	7	-0,04	-0,01	-0,02	-0,03
N	8	-0,04	-0,01	-0,02	-0,03
N	9	-0,04	-0,02	-0,03	-0,02
C	10	-0,04	0,00	-0,02	-0,04
C	11	-0,03	-0,01	-0,02	-0,03
C	12	-0,05	-0,01	-0,03	-0,04
C	13	-0,02	0,00	-0,01	-0,02
C	14	-0,03	-0,01	-0,02	-0,03
C	15	-0,04	0,00	-0,02	-0,04
H	16	-0,02	-0,01	-0,02	-0,01
H	17	-0,02	-0,01	-0,02	-0,01
H	18	-0,02	-0,01	-0,02	-0,01
H	19	-0,02	-0,01	-0,02	-0,01
H	20	-0,02	-0,01	-0,02	-0,01
H	21	-0,02	-0,01	-0,02	-0,01
K	22	-0,36	-0,84	-0,60	0,47

hepNa

Element	Atom Number	*f+*	*f-*	*f0*	*f+-f-*
N	0	-0,03	0,02	-0,01	-0,05
N	1	-0,04	0,00	-0,02	-0,04
N	2	-0,04	-0,02	-0,03	-0,02
N	3	-0,04	-0,02	-0,03	-0,02
N	4	-0,04	-0,02	-0,03	-0,02
N	5	-0,03	0,02	-0,01	-0,05
N	6	-0,04	-0,02	-0,03	-0,02
N	7	-0,05	0,00	-0,03	-0,05
N	8	-0,05	0,00	-0,03	-0,05
N	9	-0,06	-0,02	-0,04	-0,04
C	10	-0,06	0,00	-0,03	-0,06
C	11	-0,05	-0,01	-0,03	-0,04
C	12	-0,07	-0,01	-0,04	-0,06
C	13	-0,03	0,00	-0,02	-0,03
C	14	-0,05	-0,01	-0,03	-0,04
C	15	-0,06	0,00	-0,03	-0,06
H	16	-0,03	-0,01	-0,02	-0,02
H	17	-0,03	-0,01	-0,02	-0,02
H	18	-0,03	-0,01	-0,02	-0,02
H	19	-0,02	-0,01	-0,02	-0,01
H	20	-0,03	-0,01	-0,02	-0,02
H	21	-0,02	-0,01	-0,02	-0,02
Na	22	-0,10	-0,86	-0,48	0,75

mel

Element	Atom Number	*f+*	*f-*	*f0*	*f+-f-*
N	0	-0,05	-0,15	-0,10	0,09
N	1	-0,05	-0,15	-0,10	0,10
N	2	-0,09	-0,04	-0,06	-0,05
N	3	-0,05	-0,12	-0,09	0,07
N	4	-0,08	-0,05	-0,06	-0,03
N	5	-0,05	-0,12	-0,09	0,07
C	6	-0,06	-0,04	-0,05	-0,02
C	7	-0,11	-0,04	-0,08	-0,08
C	8	-0,06	-0,04	-0,05	-0,02
H	9	-0,05	-0,05	-0,05	0,00
H	10	-0,05	-0,05	-0,05	0,00
H	11	-0,07	-0,05	-0,06	-0,02
H	12	-0,06	-0,05	-0,06	-0,01
H	13	-0,08	-0,03	-0,06	-0,05
H	14	-0,08	-0,03	-0,06	-0,05

melK

Element	Atom Number	*f+*	*f-*	*f0*	*f+-f-*
N	0	-0,01	-0,02	-0,01	0,00
N	1	-0,01	-0,02	-0,01	0,00
N	2	0,01	0,02	0,01	-0,01
N	3	-0,01	0,00	0,00	-0,01
N	4	-0,01	-0,02	-0,02	0,00
N	5	-0,01	0,00	0,00	-0,01
C	6	-0,01	0,00	0,00	0,00
C	7	-0,01	-0,01	-0,01	0,00
C	8	-0,01	0,00	0,00	0,00
H	9	-0,02	-0,01	-0,02	-0,01
H	10	-0,02	-0,01	-0,02	-0,01
H	11	-0,02	-0,01	-0,02	-0,01
H	12	-0,02	-0,01	-0,02	-0,01
H	13	-0,01	-0,01	-0,01	0,00
H	14	-0,01	-0,01	-0,01	0,00
K	15	-0,82	-0,89	-0,85	0,07

melNa

Element	Atom Number	*f+*	*f-*	*f0*	*f+-f-*
N	0	-0,02	-0,02	-0,02	0,00
N	1	-0,02	-0,02	-0,02	0,00
N	2	0,01	0,02	0,01	-0,01
N	3	-0,01	0,00	-0,01	-0,01
N	4	-0,02	-0,02	-0,02	0,00
N	5	-0,01	0,00	-0,01	-0,01
C	6	-0,01	0,00	-0,01	-0,01
C	7	-0,01	-0,01	-0,01	0,00
C	8	-0,01	0,00	-0,01	-0,01
H	9	-0,02	-0,02	-0,02	-0,01
H	10	-0,02	-0,02	-0,02	-0,01
H	11	-0,03	-0,01	-0,02	-0,02
H	12	-0,03	-0,01	-0,02	-0,02
H	13	-0,01	-0,01	-0,01	0,00
H	14	-0,01	-0,01	-0,01	0,00
Na	15	-0,77	-0,85	-0,81	0,09

2.4. Catalytic reduction of 4-NP

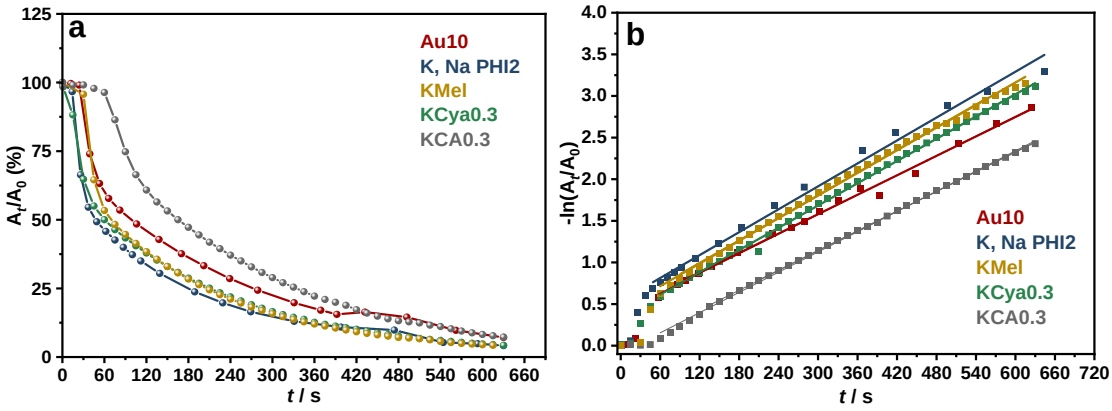

Figure S15. (a) Comparative catalytic conversion of 4-NP with **Au10**, **K,NaPHI2**, **KMel0.3**, **KCA0.3**, and **KCya0.3**. (b) Plots of ln (A_t/A_0) for the absorbance of nitrophenolate anion at 400 nm obtained from the spectra versus time for the reduction of 4-NP catalyzed by the catalysts **Au10**, **K,NaPHI2**, **KMel0.3**, **KCA0.3**, and **KCya0.3**. *Experimental conditions*: 0.1 mL $NaBH_4$ (2.16 mol L^{-1}), 0.3 mL 4-NP (1.2×10^{-3} mol L^{-1}), and 2.5 mL distilled water were mixed into a cuvette at ambient conditions. Then, the UV-Vis spectrum was recorded, followed by the addition of 0.025 mL of AuNP catalyst (1.14 mg L^{-1}) and shaking quickly the cuvette before recording the subsequent spectra.

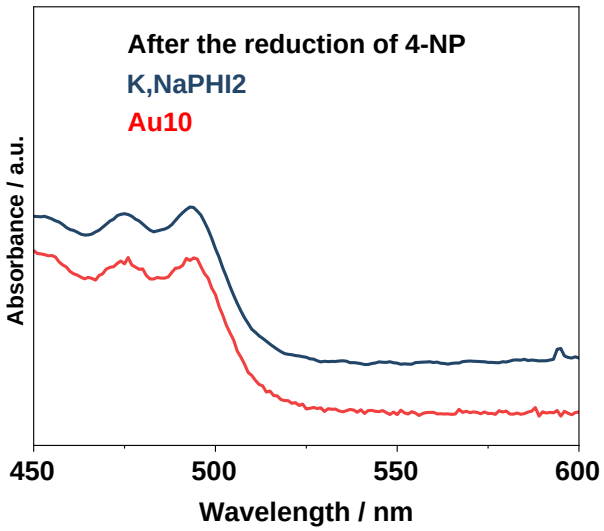

Figure S16. UV−vis electronic absorption spectra of **Au10** and **K,NaPHI2** after the reduction of 4-NP under the reaction conditions specified in the caption of Figure S15.

References

1 I. Krivtsov, D. Mitoraj, C. Adler, M. Ilkaeva, M. Sardo, L. Mafra, C. Neumann, A. Turchanin, C. Li, B. Dietzek, R. Leiter, J. Biskupek, U. Kaiser, C. Im, B. Kirchhoff, T. Jacob and R. Beranek, *Angew. Chem. Int. Ed.*, 2020, **59**, 487-495.

2 H. Schlomberg, J. Kröger, G. Savasci, M. W. Terban, S. Bette, I. Moudrakovski, V. Duppel, F. Podjaski, R. Siegel, J. Senker, R. E. Dinnebier, C. Ochsenfeld and B. v. Lotsch, *Chem. Mater.*, 2019, **31**, 7478–7486.

3 C. Deraedt, L. Salmon, S. Gatard, R. Ciganda, R. Hernandez, M. Mayor and D. Astruc, *ChemComm.*, 2014, **50**, 14194–14196.

4 L. Guardia, J. I. Paredes, J. M. Munuera, S. Villar-Rodil, M. Ayán-Varela, A. Martínez-Alonso and J. M. D. Tascón, *ACS Appl. Mater. Interfaces*, 2014, **6**, 21702–21710.

5 S. García-Dalí, J. I. Paredes, S. Villar-Rodil, A. Martínez-Jódar, A. Martínez-Alonso and J. M. D. Tascón, *ACS Appl. Mater. Interfaces*, 2021, **13**, 33157–33171.

6 F. Neese, *WIREs Computational Molecular Science*, 2012, **2**, 73–78.

7 F. Neese, F. Wennmohs, U. Becker and C. Riplinger, *J. Chem. Phys.*, 2020, **152**, 224108-.

8 J. Heyd, G. E. Scuseria and M. Ernzerhof, *J. Chem. Phys.*, 2003, **118**, 8207–8215.

9 J. P. Perdew, M. Ernzerhof and K. Burke, *J. Chem. Phys.*, 1996, **105**, 9982–9985.

10 C. Adamo and V. Barone, *J Chem Phys*, 1999, **110**, 6158–6170.

11 A. D. McNaught and A. Wilkinson, *Compendium of chemical terminology*, Blackwell Science Oxford, 1997, vol. 1669.

12 R. R. Contreras, P. Fuentealba, M. Galván and P. Pérez, *Chem. Phys. Lett.*, 1999, **304**, 405–413.

13 W. Yang and R. G. Parr, *Proc. Natl. Acad. Sci.*, 1985, **82**, 6723–6726.

14 B. M. Quinn, P. Liljeroth, V. Ruiz, T. Laaksonen and K. Kontturi, *J. Am. Chem. Soc.*, 2003, **125**, 6644–6645.

15 K. B. Male, J. Li, C. C. Bun, S.-C. Ng and J. H. T. Luong, *J. Phys. Chem. C*, 2008, **112**, 443–451.

16 I. Hussain, S. Graham, Z. Wang, B. Tan, D. C. Sherrington, S. P. Rannard, A. I. Cooper and M. Brust, *J. Am. Chem. Soc.*, 2005, **127**, 16398–16399.

17 J. A. Creighton and D. G. Eadon, *J. Chem. Soc., Faraday Trans.*, 1991, **87**, 3881–3891.

18 X. Wang, W. Zhang, X. Gong, X. Hu and X. Yao, *J. Nanopart. Res.*, 2019, **21**, 192.

19 M. Šetka, R. Calavia, L. Vojkůvka, E. Llobet, J. Drbohlavová and S. Vallejos, *Sci. Rep.*, 2019, **9**, 8465.

A Appendix

A.1 Structure–property characteristics: the First-principles calculations

A.1.1 Data Availability

An archive of atomic coordinate files of the investigated structures in the VASP-POSCAR file format is available via Zenodo. (DOI: 10.5281/zenodo.6953396)

A.1.2 Supplementary methods

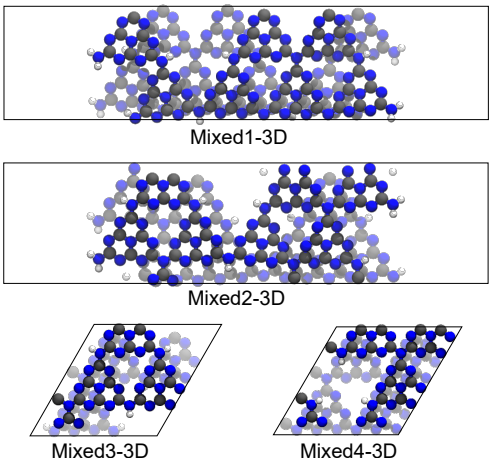

Figure S1: Proposed structures of the mixed motifs used in the study. The structures are composed of the PHI and cg-C_3N_4 structure because of their high DoC (79%–94%). The structures of Mixed1-3D and Mixed2-3D have the edge boundaries which reduce the corrugation. The both Mixed1-3D and Mixed2-3D are distinct from the sequence of the structural motifs. The Mixed3-3D is made of inclusion of PHI structure within cg-C_3N_4 domain to both layers and the Mixed4-3D is constructed of cg-C_3N_4 layer (upper) and PHI layer (bottom), respectively.

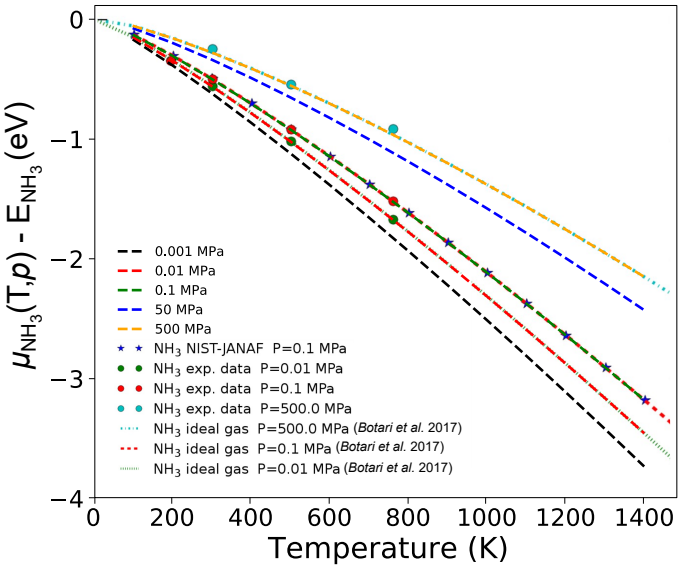

Figure S2: The evaluation of the calculated chemical potential of ammonia used in this study. The reference plots are taken from the NIST-JANAF[194, 195] and the literature.[64, 196] The dotted points ($\mathrm{NH_3}$ NIST-JANAF and $\mathrm{NH_3}$ exp. data) and small dotted lines ($\mathrm{NH_3}$ ideal gas) are taken from the experimental and the literature, respectively. The bold dashed line illustrates the calculated $\Delta\mu_{\mathrm{NH_3}}(\mathrm{T}, p)$ in this study. Then we added two $p_{\mathrm{NH_3}}$ conditions of 0.001 MP and 50 MP to further trace the variations.

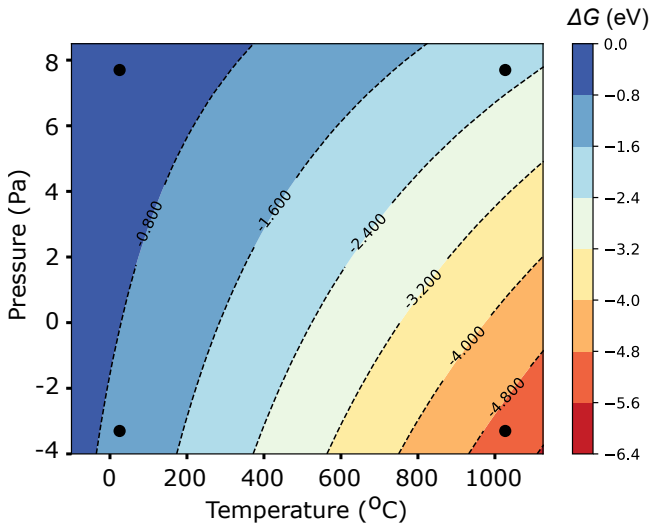

Figure S3: The contour plot of $\Delta\mu_{NH_3}$. The plot is derived from the equation (3.4). The black points is sampled the respective $\Delta\mu_{NH_3}$. (See Figure 8 of red, green, blue, and purple.)

Table S1: Summary of Optical property

Structure	**H-L gap (eV)**	**Structure**	**bandgap (eV)**
h_1	4.62	s-melon-2D	3.62
h_2	3.98	melon-2D	3.68
h_{31}	3.64	PHI-2D	3.32
h_{32}	3.56	$C_9M_{13}H_3$-2D	2.95
h_{33}	3.92	cg-C_3N_4-2D	2.99
h_{34}	3.80	pg-C_3N_4-2D	2.79
h_{41}	3.52	s-melon-3D	3.39
h_{42}	3.71	melon-3D	3.12
h_{43}	3.52	PHI-3D	3.18
h_{44}	3.61	$C_9M_{13}H_3$-3D	2.86
h_{45}	3.46	cg-C_3N_4-3D	2.95
h_{46}	3.65	pg-C_3N_4-3D	2.35
h_{47}	3.59	Mixed1-3D	2.95
h_{48}	3.72	Mixed2-3D	2.88
		Mixed3-3D	2.99
		Mixed4-3D	2.89

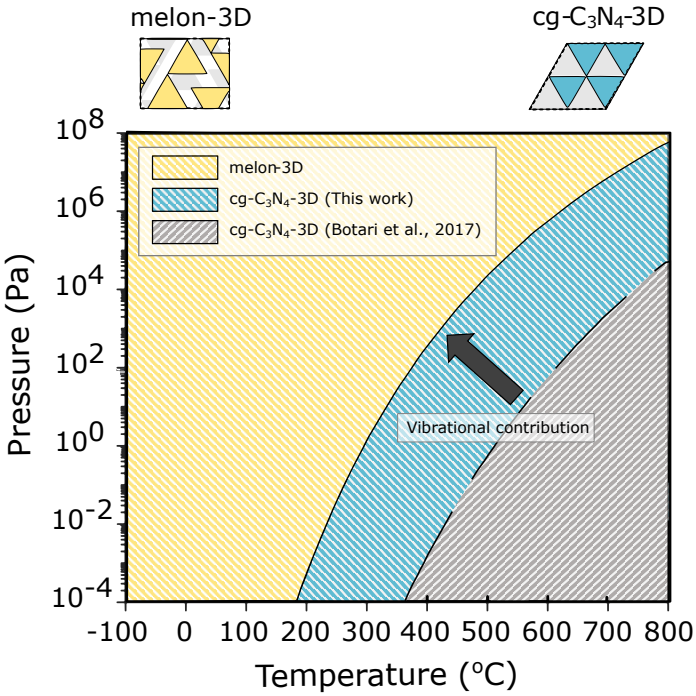

Figure S4: The calculated phase diagram of the normalized free energy of formation between melon-3D and cg-C_3N_4-3D. The inclusion of the vibrational contributions increases the relative stability of of cg-C_3N_4-3D (blue area) to $\Delta\mu_{NH_3}$ direction. The phase diagram of melon structure from the literature is shown in gray area.[64]

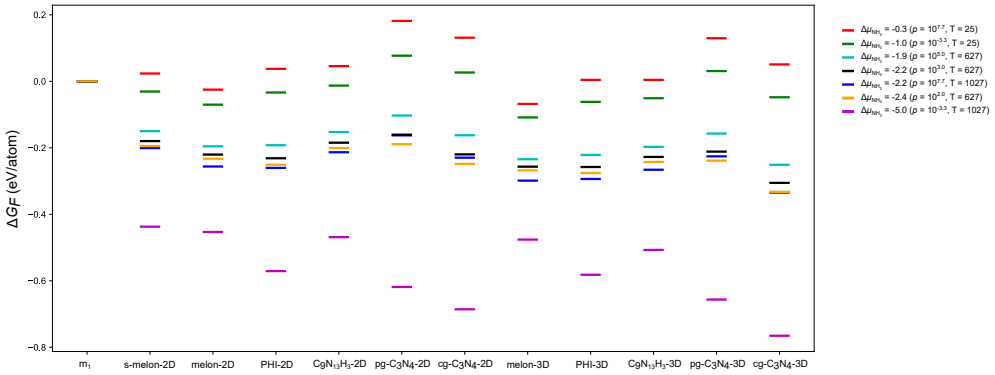

Figure S5: Free energy of formation for 2D and 3D structures with regards to various μ_{NH_3}. The μ_{NH_3} is differentiated from the combination of T and p_{NH_3}. The free energy of formation is normalized to eV/atom due to the different numbers of elements.

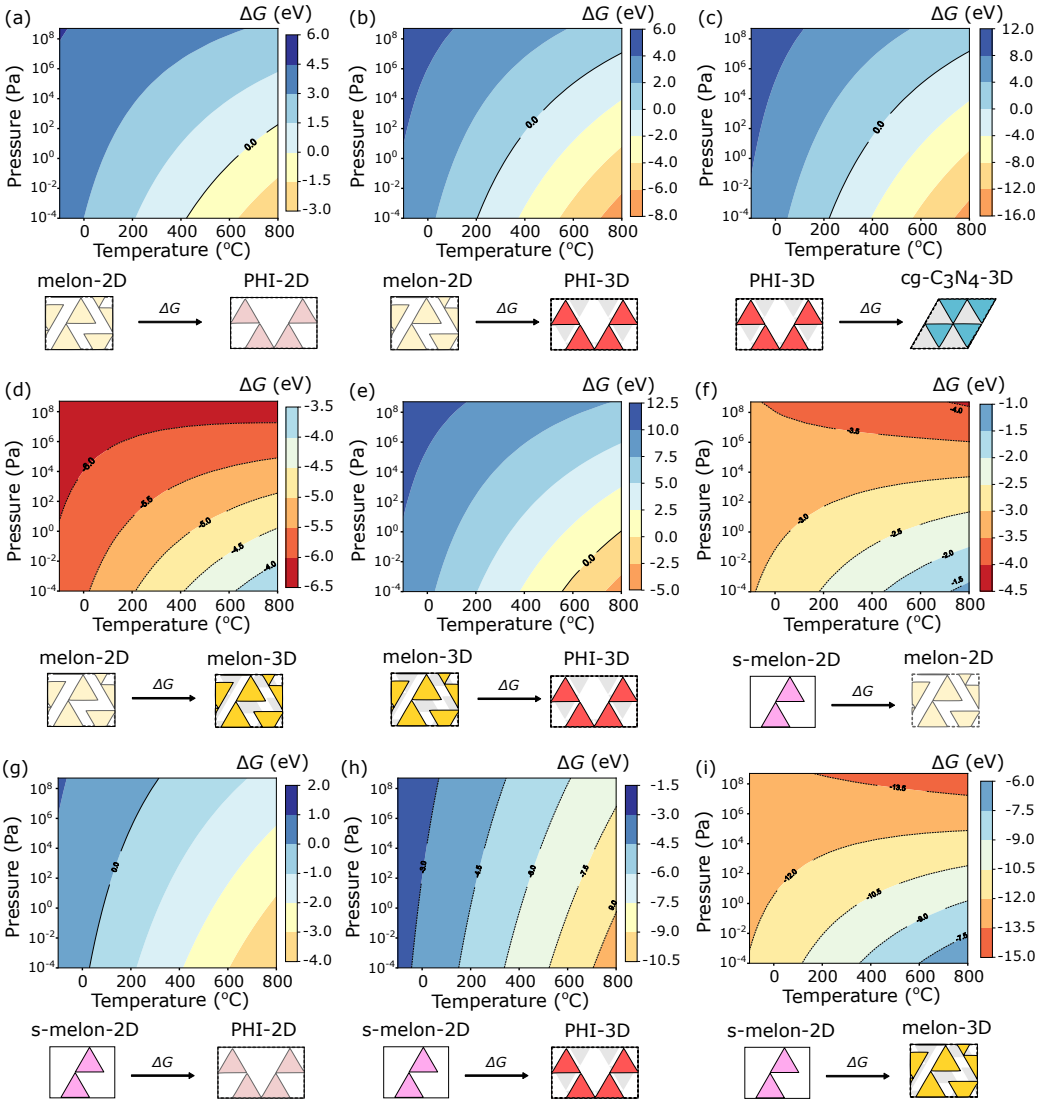

Figure S6: Respective phase diagram of the free energy reaction for 2D and 3D structures. The contour map is used to find spontaneous $\Delta\mu_{NH_3}$ for temperature and p_{NH_3} conditions.

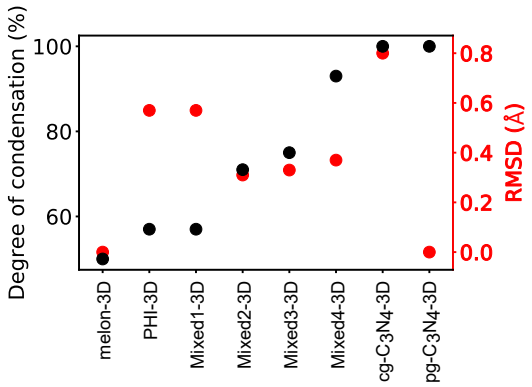

Figure S7: The degree of condensation and RMSD value are plotted with 3D structures.The Mixed structures are composed of PHI and g-C_3N_4 structures (see Figure S1). The RMSD value of 3D structure is obtained from the average of the each layer.

Table S2: Summary of Degree of Corrugation

Structure	**RMSD of out-of-plane (Å)**	**Structure**	**RMSD of out-of-plane (Å)**
h_1	0.01	melon-3D	0.00
h_2	0.08	PHI-3D	0.33
h_{31}	0.20	cg-C_3N_4-3D	0.80
h_{41}	0.20	pg-C_3N_4-3D	0.00
h_{51}	0.25	Mixed1-3D	0.57
Mixed1-2D	0.58	Mixed2-3D	0.57
Mixed3-2D	0.35	Mixed3-3D	0.31
PHI-2D	0.57	Mixed4-3D	0.37
cg-C_3N_4-2D	0.81		

A.2 Structural-electonic-optical properties

A.2.1 Supplementary data

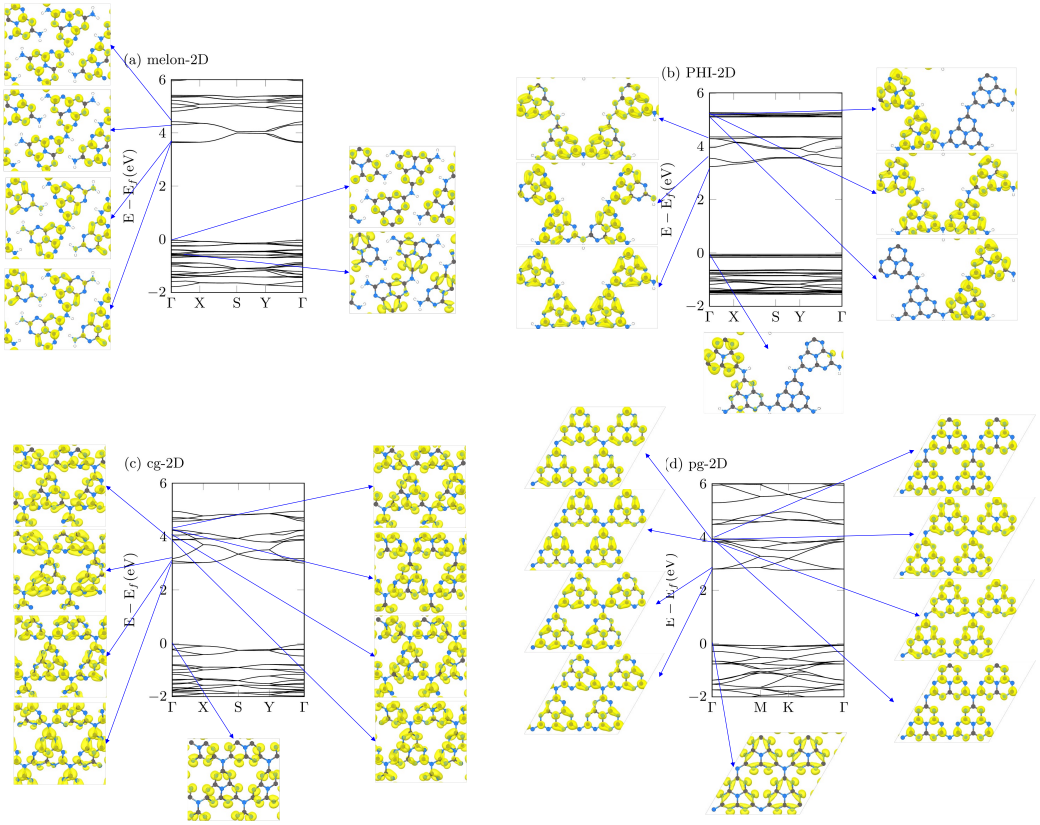

Figure S8: The depiction of electron density in (a) melon, (b) PHI, (c) cg, and (d) pg 2D structures corresponding to the respective energy level at Γ.

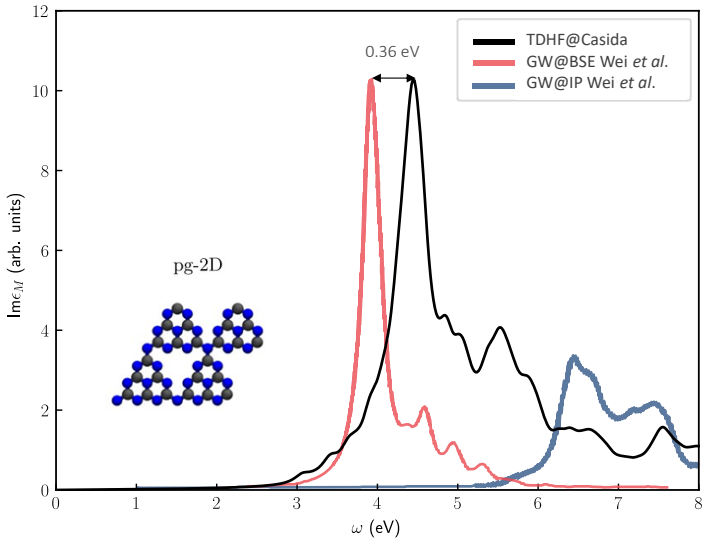

Figure S9: The calculated imaginary part of the dielectric function for pg-2D structure using TD@Casida (black), GW@BSE (red)[125], and GW@IP[125] (blue) calculations. The scissor correction is applied based on the brightest state, which is commonly located around 4 eV.

A.3 Optical properties: *GW*@BSE

Supplementary Information

A.3.1 Supplementary data

Table S3: The lattice parameters of the PCN structures obtained by the CAPZ and PBE functionals.

		Lattice parameters (CA) (Å)			Lattice parameters (PBE) (Å)		
		a	*b*	*c*	*a*	*b*	*c*
2D	melon	16.45	12.57	12	16.42	12.62	12
	PHI	22.29	12.82	12	21.58	12.46	12
	c-gCN	13.28	11.8	12	13.35	11.88	12
	p-gCN	14.15	14.15	12	14.23	14.23	12
3D	melon	16.29	12.45	5.91	16.42	12.62	6.53
	PHI	21.71	12.55	5.6	21.58	12.46	6.51
	c-gCN	13.14	11.81	6.5	13.29	11.84	7.35
	p-gCN	14.13	14.13	6.04	14.23	14.23	6.66

Table S4: Bandgaps of 2D and 3D PCN structures (optimized using PBE functionals) were calculated via independent particle approximations (G_0W_0@IP) and BSE (G_0W_0@BSE) methods, alongside the effective exciton lifetime at 300 K. The (D) and (I) denote the direct and the indirect bandgap, respectively.

	Structure	G_0W_0@IP (eV)	G_0W_0@BSE (eV)	Exiton lifetime $<\tau_{300\mathrm{K}}>$	
				bright	dark
2D	melon	5.44 (D)	3.24	1.87 ps	196.36 ps
	PHI	5.26 (I)	2.03	5.35 ps	633.69 ps
	c-gCN	4.47 (D)	2.63	5.18 ps	63.82 ns
	p-gCN	4.27 (D)	1.97	0.16 ps	747.08 μs
3D	melon	3.82 (D)	3.22	4.61 ps	23.29 ns
	PHI	4.25 (I)	2.53	20.34 ps	289.93 ps
	c-gCN	3.39 (D)	2.67	3.32 ps	2.88 ns
	p-gCN	2.87 (I)	2.00	8.24 ps	31.49 ms

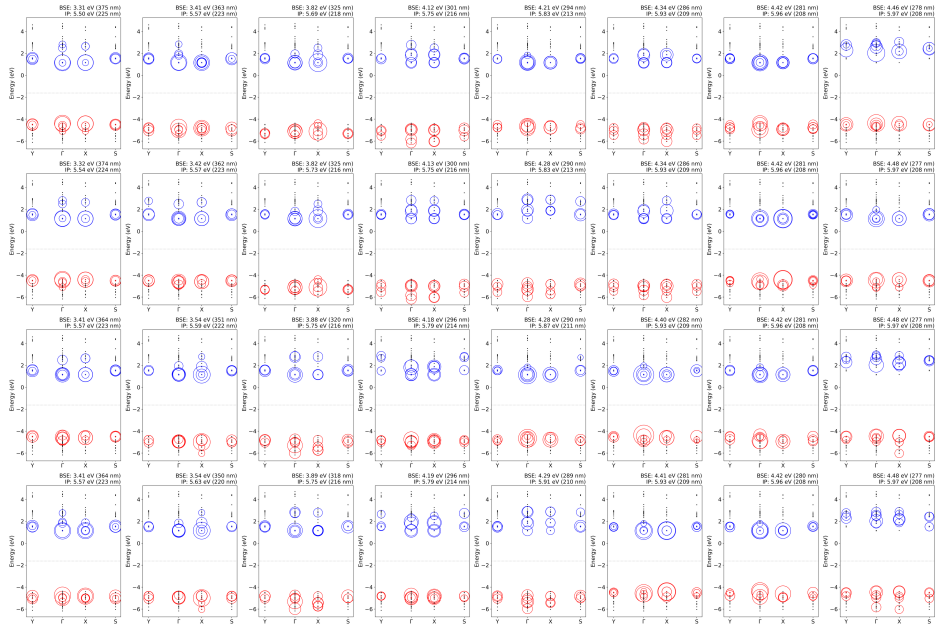

Figure S10: Illustration of the e–h coupling constants corresponding to the 32 excitation energy of melon-2D structure optimized CA (LDA) functionals.

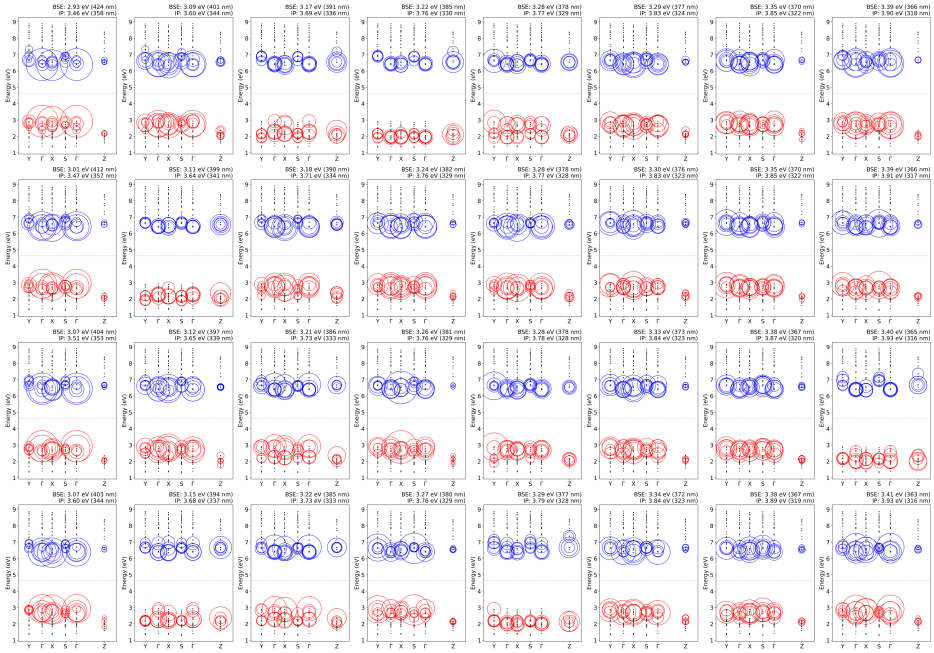

Figure S11: Illustration of the e–h coupling constants corresponding to the 32 excitation energy of melon-3D structure optimized CA (LDA) functionals.

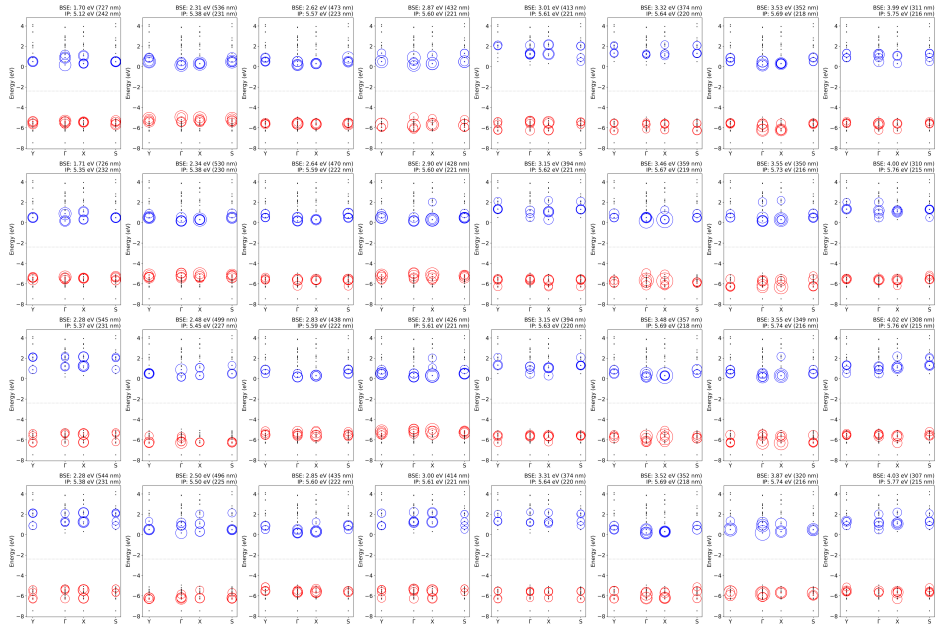

Figure S12: Illustration of the e–h coupling constants corresponding to the 32 excitation energy of PHI-2D structure optimized CA (LDA) functionals.

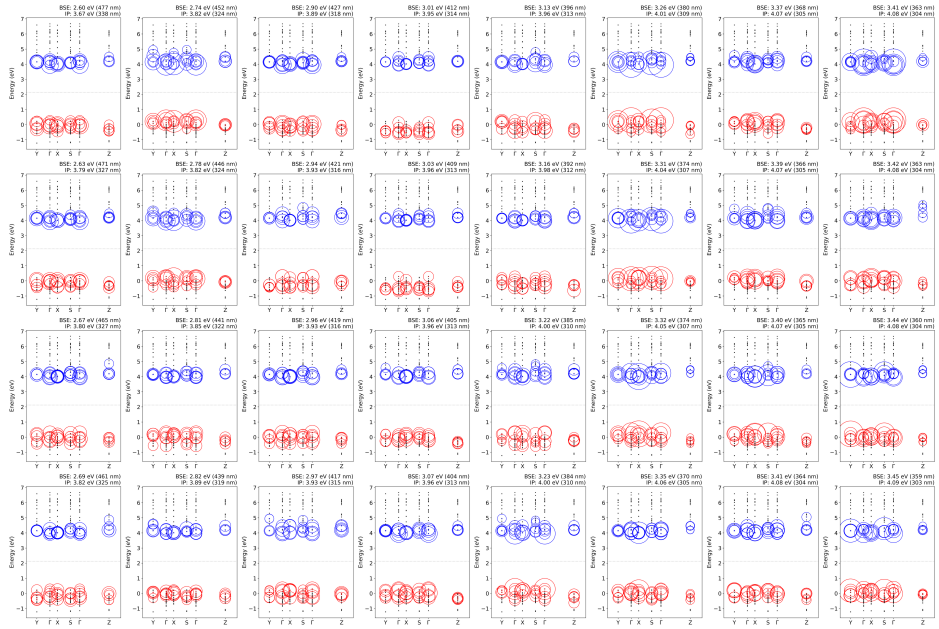

Figure S13: Illustration of the e–h coupling constants corresponding to the 32 excitation energy of PHI-3D structure optimized CA (LDA) functionals.



Figure S14: Illustration of the e–h coupling constants corresponding to the 32 excitation energy of c-gCN-2D structure optimized CA (LDA) functionals.

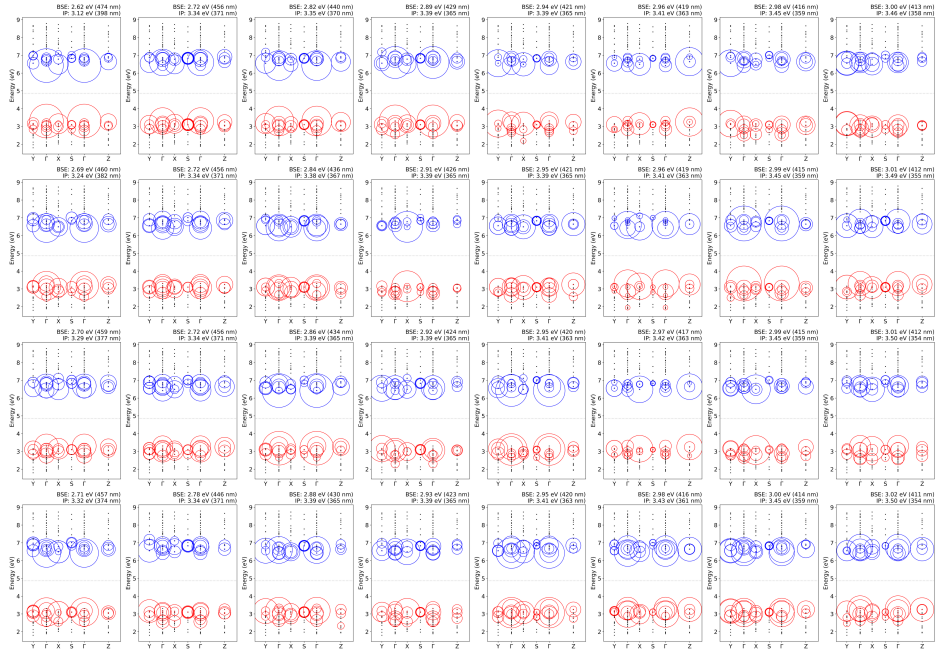

Figure S15: Illustration of the e–h coupling constants corresponding to the 32 excitation energy of c-gCN-3D structure optimized CA (LDA) functionals.

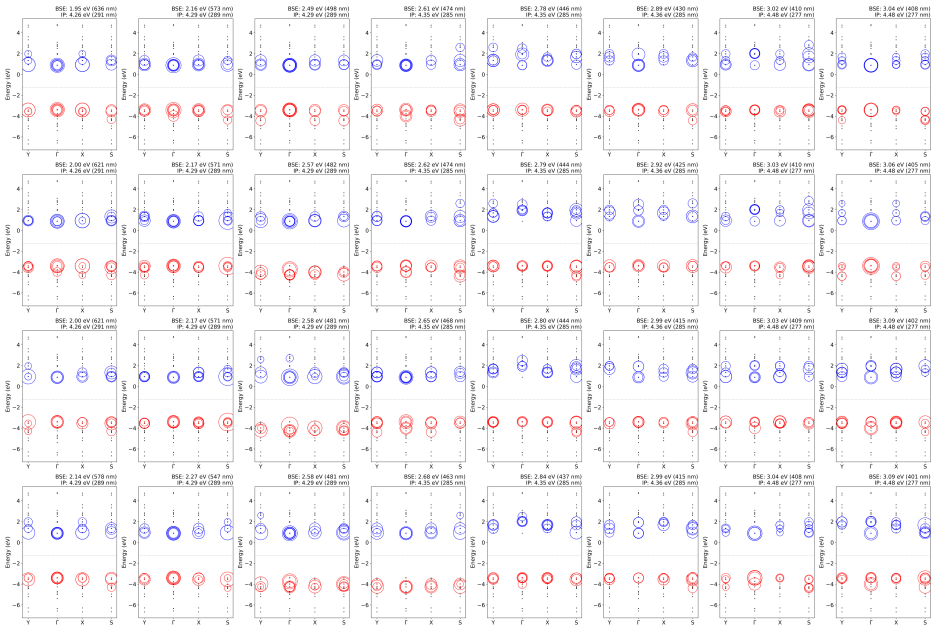

Figure S16: Illustration of the e–h coupling constants corresponding to the 32 excitation energy of p-gCN-2D structure optimized CA (LDA) functionals.

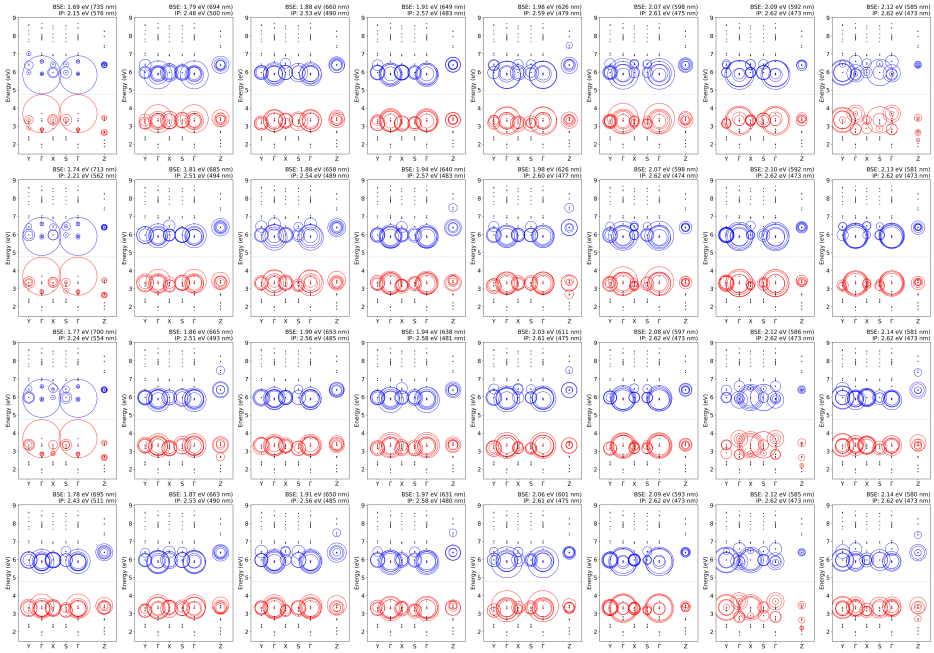

Figure S17: Illustration of the e–h coupling constants corresponding to the 32 excitation energy of p-gCN-3D structure optimized CA (LDA) functionals.

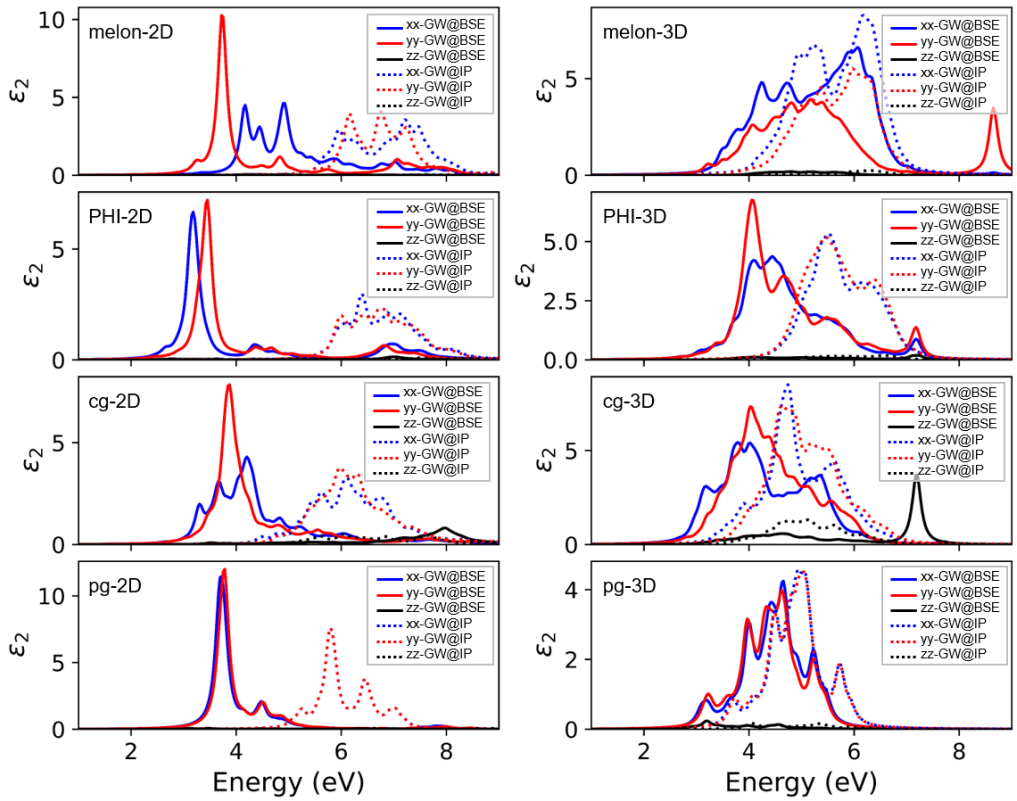

Figure S18: Imaginary part of dielectric functions of the PCN structure optimized with PBE-D3 functionals. The solid and the dashed lines are obtained by the *GW*@BSE and the *GW*@IP respectively.

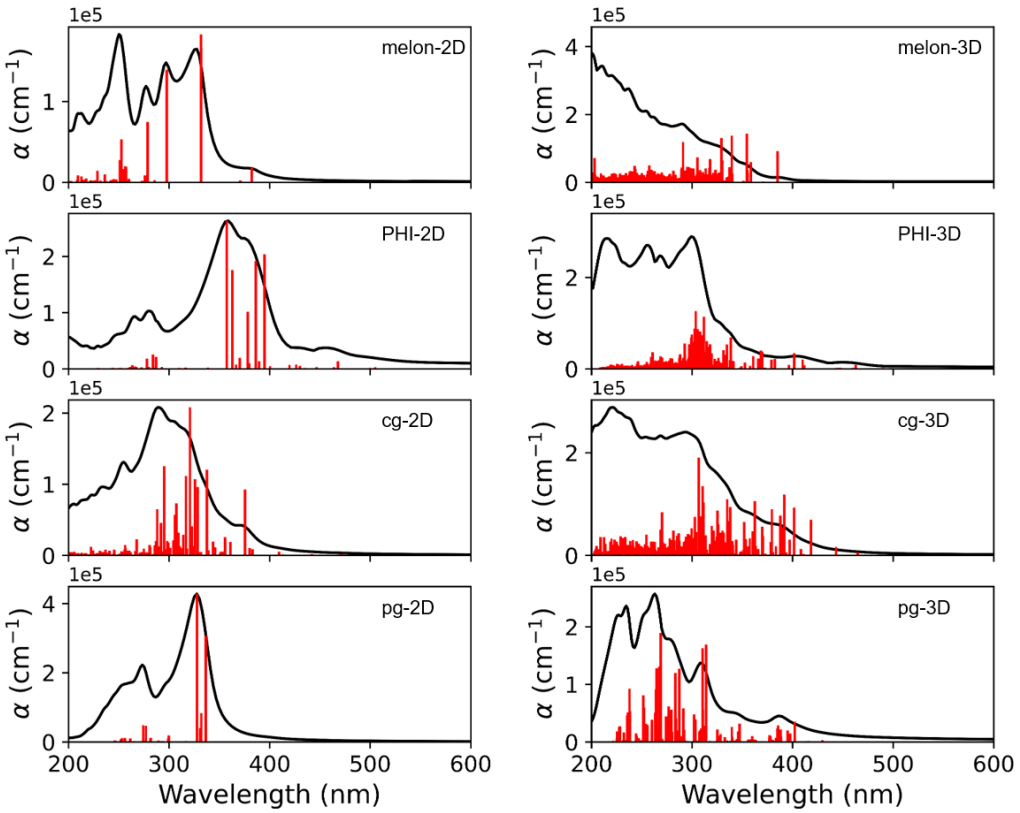

Figure S19: The illustration of the calculated absorption spectra for 2D and 3D PCN models, optimized PBE functionals, along averaged spatial directions. The oscillator strengths in relation to wavelength are presented in red.

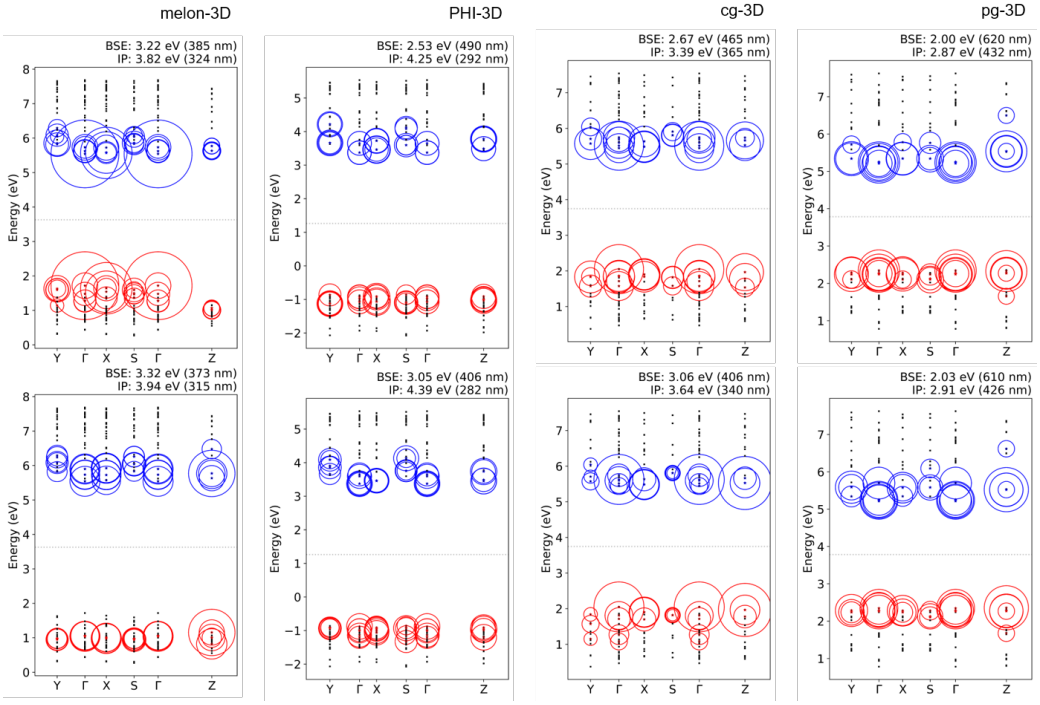

Figure S20: Representaton of eigenvalues (BSE and IP) and coupling coefficients (radius of circles) of bright states for both 2D and 3D PCN structures, optimized by PBE-D3 functionals, corresponding to the absorption edges (top) and interlayer interactions (bottom).

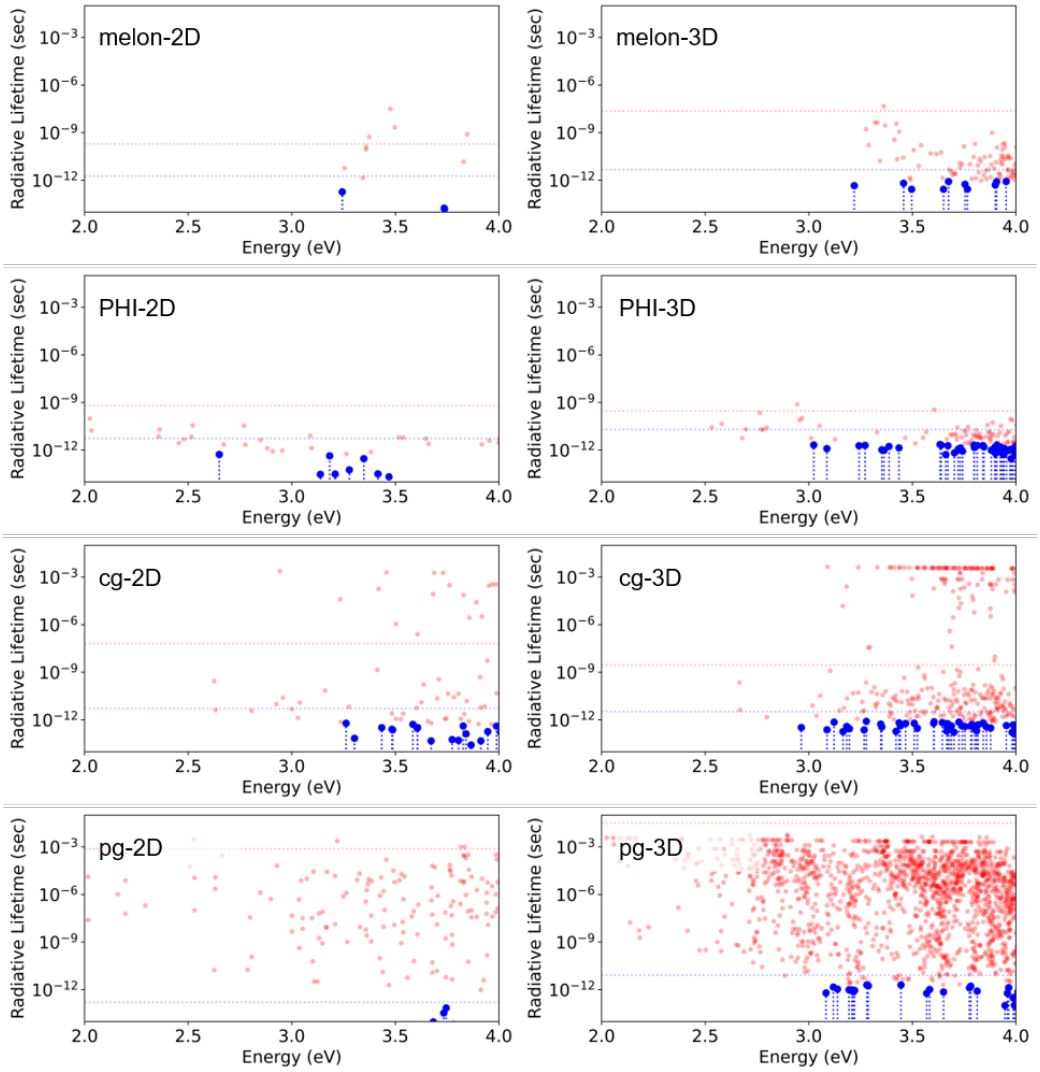

Figure S21: Calculated radiative exciton lifetime of both 2D and 3D PCN structures optimized by PBE-D3 functionals. Bright states are denoted in blue, while dark states are represented in red. Their respective effective lifetime at 300 K are indicated by dashed lines.

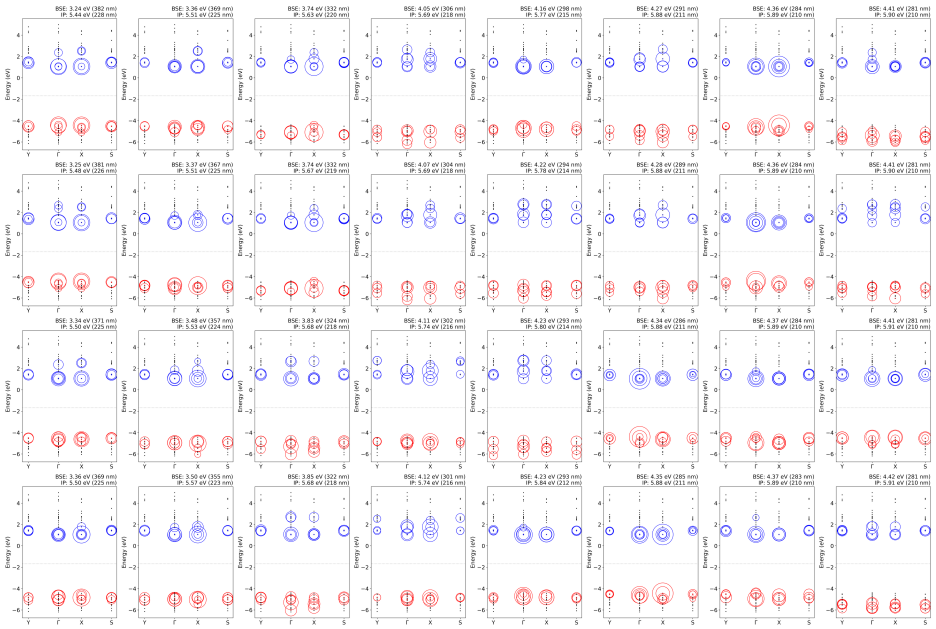

Figure S22: Illustration of the e–h coupling constants corresponding to the 32 excitation energy of melon-2D structure optimized PBE (GGA) functionals.

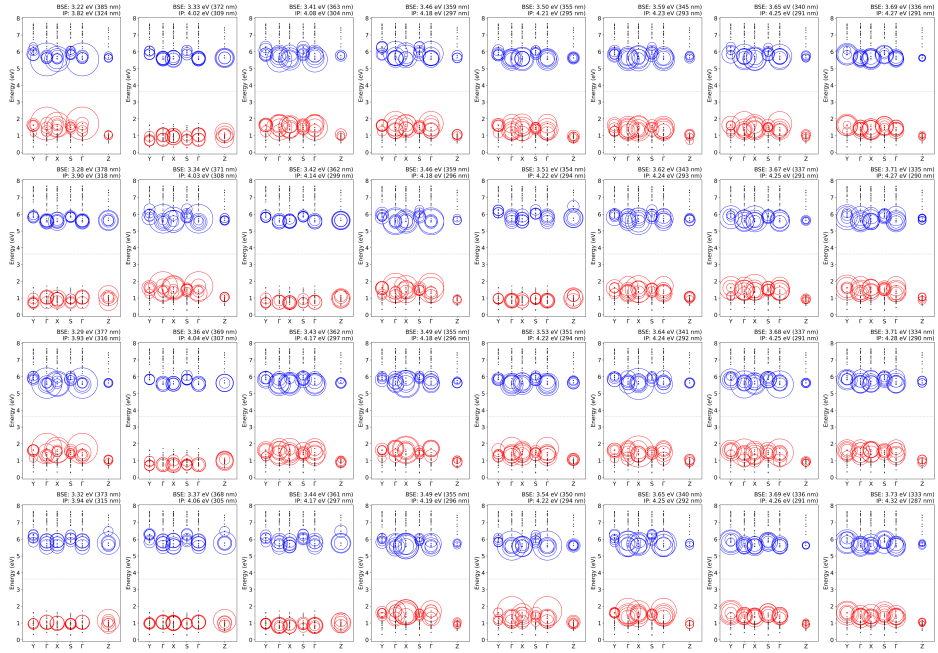

Figure S23: Illustration of the e–h coupling constants corresponding to the 32 excitation energy of melon-3D structure optimized PBE (GGA) functionals.

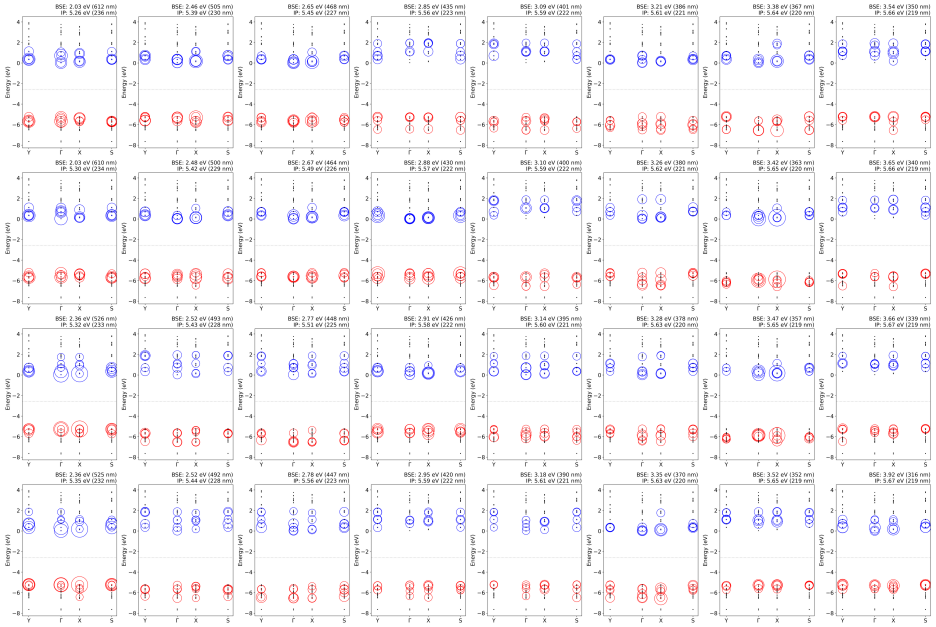

Figure S24: Illustration of the e–h coupling constants corresponding to the 32 excitation energy of PHI-2D structure optimized PBE (GGA) functionals.

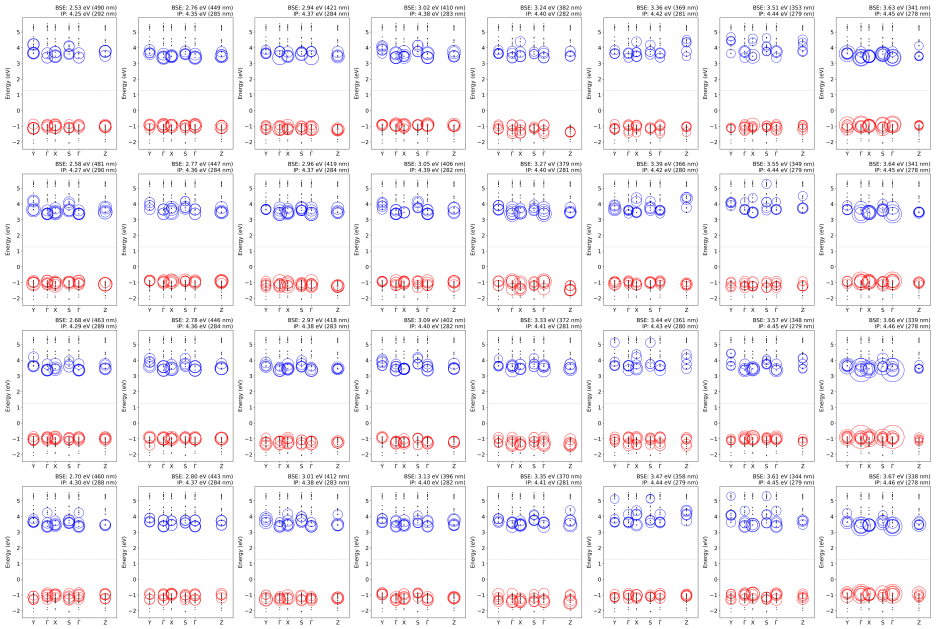

Figure S25: Illustration of the e–h coupling constants corresponding to the 32 excitation energy of PHI-3D structure optimized PBE (GGA) functionals.

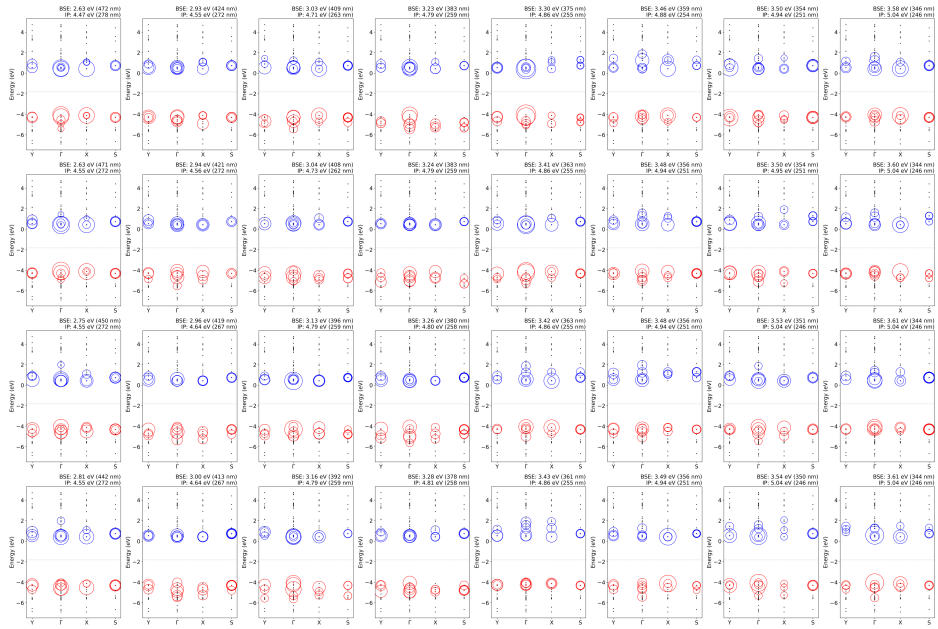

Figure S26: Illustration of the e–h coupling constants corresponding to the 32 excitation energy of c-gCN-2D structure optimized PBE (GGA) functionals.

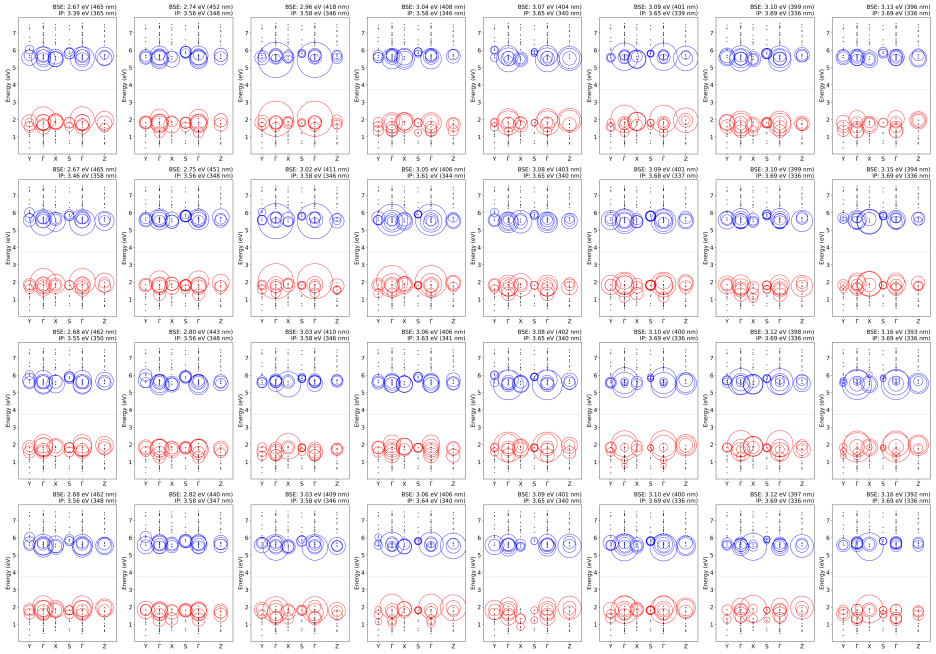

Figure S27: Illustration of the e–h coupling constants corresponding to the 32 excitation energy of c-gCN-3D structure optimized PBE (GGA) functionals.

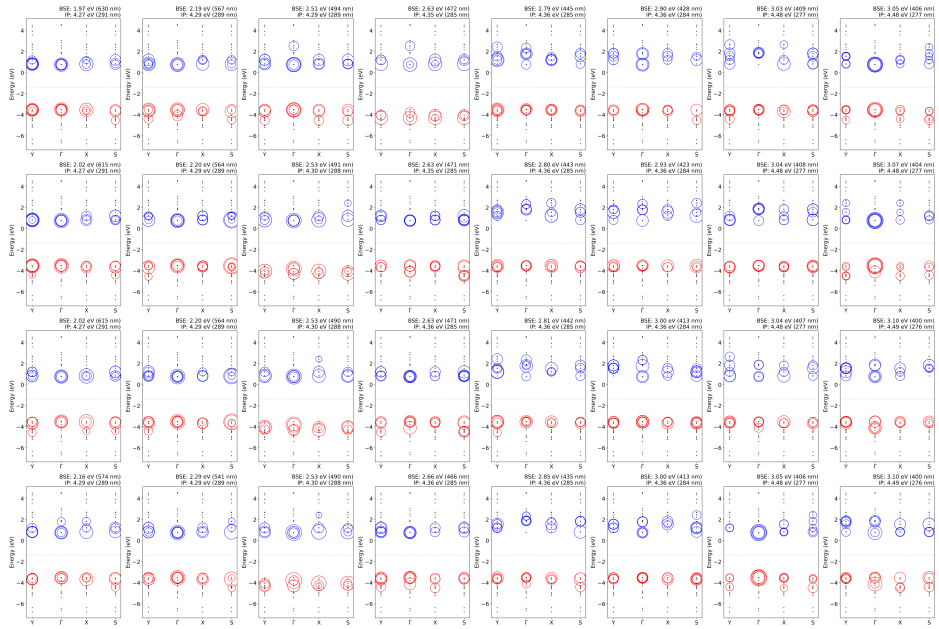

Figure S28: Illustration of the e–h coupling constants corresponding to the 32 excitation energy of p-gCN-2D structure optimized PBE (GGA) functionals.

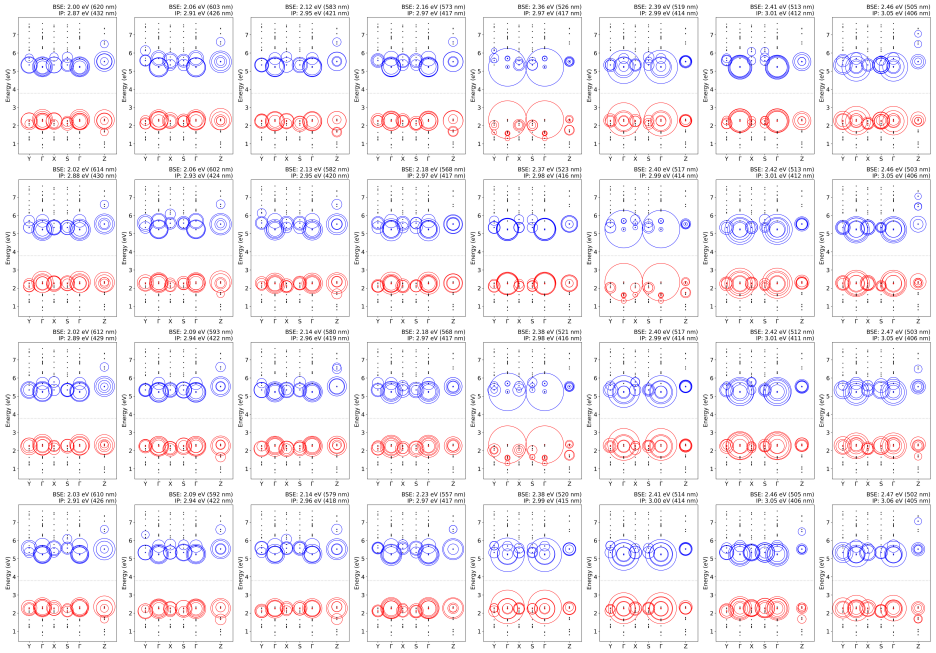

Figure S29: Illustration of the e–h coupling constants corresponding to the 32 excitation energy of p-gCN-3D structure optimized PBE (GGA) functionals.

A.3.2 Modifications of the VASP BSE.F file

This patch can apply to the VASP version of 6.4.1. This patch is based on the patch reported by Bogad *et al.*[197]

Listing A.1: Patchfile for the BSE.F file.

```
--- bse_ori.F  2024-03-03 18:59:44.000000000 +0100
+++ bse_ini.F  2024-03-03 18:59:35.000000000 +0100
@@ -1563,6 +1563,7 @@
       CALL STOP_TIMING("G",IO%IU6,'BSEOSZI')
       IF (IO%IU6>=0) CALL WFORCE(IO%IU6)
     ENDIF
+
  !=======================================================================
  ! deallocation
  !=======================================================================
@@ -2830,7 +2831,7 @@
     INTEGER :: NOMEGA_DIM
     REAL(q) :: OMEGAMAX
     INTEGER :: IU6
-    INTEGER, OPTIONAL :: DESC(DLEN_)
+    INTEGER :: DESC(DLEN_)
   ! local
     INTEGER :: NCV13
     INTEGER K1, K1_LOOKED_UP, K3, ISP
@@ -2842,6 +2843,9 @@
     GDEF       :: CDER_BETWEEN_STATE(3)
     COMPLEX(q) :: CTRANS(3)
     COMPLEX(q) :: CTRANS_SQUARE(3,3)
+    COMPLEX(q) :: ATRANSEL(3)
+    REAL(q)    :: E_AND_ATRANSEL(7,SIZE(R))
+    INTEGER    :: Q_IS_ZERO, N, M
     REAL(q)    :: DKX, DKY, DKZ
```

```
28      COMPLEX(q) :: EPS(NOMEGA_DIM,3,3)
29      REAL(q)    :: OMEGA(NOMEGA_DIM), DOMEGA
30  @@ -2852,6 +2856,9 @@
31      INTEGER I1RES, J1RES, IROW, JCOL
32      INTEGER I1, I2, J1, J2, NLAMBDA
33      REAL(q)    :: RSPIN
34  +#ifdef VASP_HDF5
35  +   CHARACTER(LEN=:), ALLOCATABLE :: PREFIX
36  +#endif
37
38   !  three cases need to be considered
39   !  non-collinear RSPIN=1.0
40  @@ -2874,12 +2881,20 @@
41      NLAMBDA=0
42
43      DOMEGA=R(NCV)/(NOMEGA_DIM-1)
44  +
45      IF (OMEGAMAX>0) THEN
46         DOMEGA=OMEGAMAX/(NOMEGA_DIM-1)
47      ENDIF
48  -
49  +   IF (ABS(WHF%WDES%VKPT(1, NQPOINT)+KPOINT_BSE(1))<=1E-6_q .AND. &
50  +      ABS(WHF%WDES%VKPT(2, NQPOINT)+KPOINT_BSE(2))<=1E-6_q .AND. &
51  +      ABS(WHF%WDES%VKPT(3, NQPOINT)+KPOINT_BSE(3))<=1E-6_q) THEN
52  +      Q_IS_ZERO=1
53  +   ELSE
54  +      Q_IS_ZERO=0
55  +   ENDIF
56   !   loop over column indices (eigenvectors)
57      DO LAMBDA=1, NCV
58  +      ATRANSEL=0
59         ! local storage index in block (J1) and local index of block (J2)
60         J1=   ((LAMBDA-DESC(NB_)*MYCOL-1)/(NPCOL*DESC(NB_)))*DESC(NB_)+1
```

```
61         J2=MOD((LAMBDA-DESC(NB_)*MYCOL-1) ,NPCOL*DESC(NB_))+1
62  @@ -2945,12 +2960,24 @@
63                 ! or  <v_k1,n1| e-iqr |c_k1+q,n3> at finite q
64                 CALL  CDER_BETWEEN_STATES_ROTATED(CDER_BETWEEN_STATE,\
                       \ LATT_CUR, NK1_IN_KPOINTS_FULL_ORIG, ISP, NB1_INTO_TOT\
                       \ , NB3_INTO_TOT)
65                 CTRANS=CTRANS+CDER_BETWEEN_STATE*AMAT(IROW+(JCOL-1)*DESC(\
                       \ LLD_))*WEIGHT
66  +              IF (Q_IS_ZERO==1) THEN
67  +                 ATRANSEL=ATRANSEL+CDER_BETWEEN_STATE*AMAT(IROW+(JCOL-1)*\
    \ DESC(LLD_))*WEIGHT
68  +              ENDIF
69               ENDDO ! I2
70            ENDDO ! I1
71         ENDIF
72
73         ! now sum CTRANS over all nodes for the current LAMBDA
74         CALLMPI( M_sum_z(WHF%WDES%COMM_INTER, CTRANS, 3))
75  +      CALLMPI( M_sum_z(WHF%WDES%COMM_INTER, ATRANSEL, 3))
76  +
77  +      E_AND_ATRANSEL(1, LAMBDA)=R(LAMBDA)
78  +      DO I=1,3
79  +         M=1+I
80  +         N=1+I+3
81  +         E_AND_ATRANSEL(M, LAMBDA)=REAL(ATRANSEL(I))
82  +         E_AND_ATRANSEL(N, LAMBDA)=AIMAG(ATRANSEL(I))
83  +      ENDDO
84
85         DO I=1,3
86            DO J=1,3
87  @@ -3039,19 +3066,25 @@
88      CALL XML_EPSILON_W(DOMEGA, REAL(EPS,q), AIMAG(EPS), NOMEGA_DIM )
89
```

```
 #ifdef VASP_HDF5
-   BLOCK
-      CHARACTER(LEN=:), ALLOCATABLE :: PREFIX
-      IF (LGWLF) THEN
-         PREFIX = "bse"
-      ELSE
-         PREFIX = "tdhf"
-      END IF
-   CALL VH5_WRITE_OPTICAL_TRANSITIONS(IH5OUTFILEID, R_AND_INTENSITY)
-      CALL VH5_WRITE_DIELECTRIC_ENERGIES(IH5OUTFILEID, DOMEGA, NOMEGA_DIM,\
     \  PREFIX)
-      CALL VH5_WRITE_DIELECTRIC_DYNAMIC(IH5OUTFILEID, EPS, PREFIX)
-   END BLOCK
-#endif
-
+    IF (LGWLF) THEN
+       PREFIX = "bse"
+    ELSE
+       PREFIX = "tdhf"
+    END IF
+    CALL VH5_WRITE_OPTICAL_TRANSITIONS(IH5OUTFILEID, R_AND_INTENSITY)
+    CALL VH5_WRITE_DIELECTRIC_ENERGIES(IH5OUTFILEID, DOMEGA, NOMEGA_DIM, \
    \ PREFIX)
+    CALL VH5_WRITE_DIELECTRIC_DYNAMIC(IH5OUTFILEID, EPS, PREFIX)
+#endif
+    CALL XML_VECARRAY("transmatel")
+    CALL XML_FIELD("energy", type="float")
+    CALL XML_FIELD("x_re", type="float")
+    CALL XML_FIELD("y_re", type="float")
+    CALL XML_FIELD("z_re", type="float")
+    CALL XML_FIELD("x_im", type="float")
+    CALL XML_FIELD("y_im", type="float")
+    CALL XML_FIELD("z_im", type="float")
```

```
121 +    CALL XML_ARRAY_REAL(E_AND_ATRANSEL, "(F10.5,' ')")
122 +    CALL XML_CLOSE_TAG ("varray")
123
124    END SUBROUTINE CALCULATE_BSE_OSZI_SCALA
125  #endif
```

A.4 Mechanistic Investigation of HER and ORR on PCNs

A.4.1 Supplementary Information

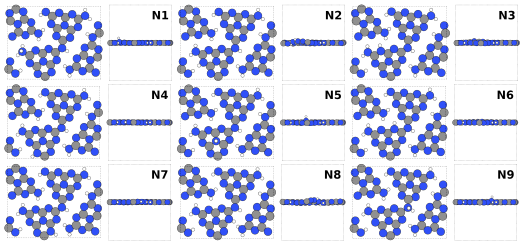

Figure S30: Illustrations of the first hydrogen adsorption sites for top-view (left) and side-view (right) on melon.

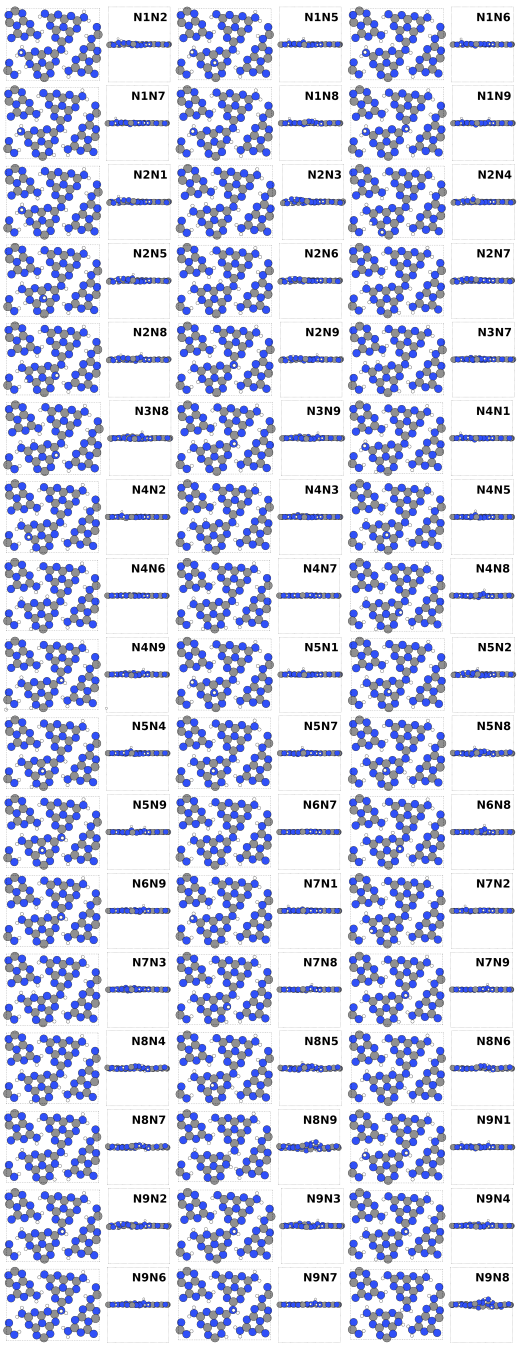

Figure S31: Illustrations of the second hydrogen adsorption sites for top-view (left) and side-view (right) on melon.

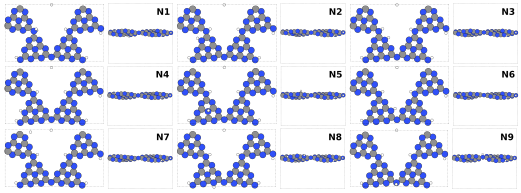

Figure S32: Illustrations of the first hydrogen adsorption sites for top-view (left) and side-view (right) on PHI.

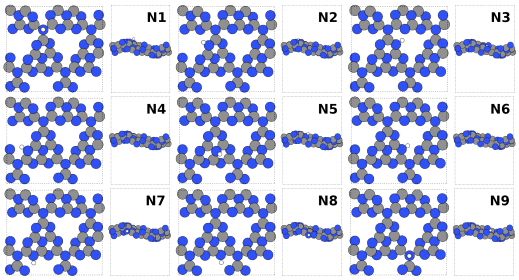

Figure S33: Illustrations of the first hydrogen adsorption sites for top-view (left) and side-view (right) on c-gCN.

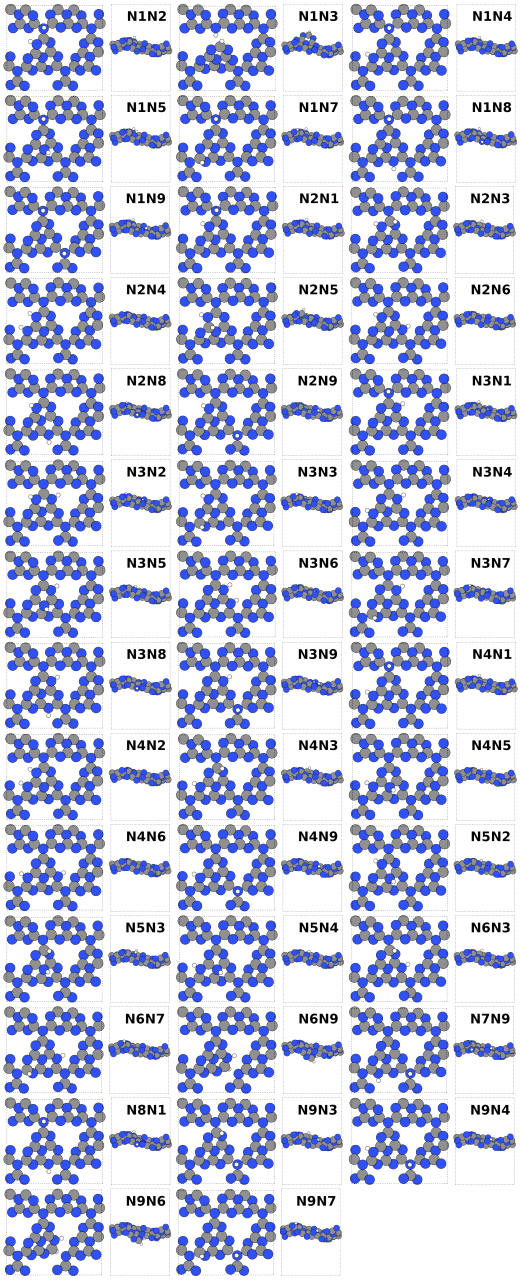

Figure S34: Illustrations of the first hydrogen adsorption sites for top-view (left) and side-view (right) on c-gCN.

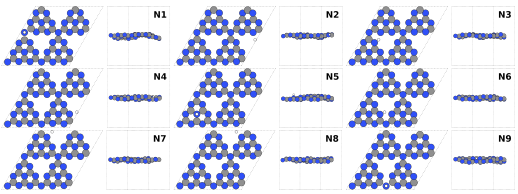

Figure S35: Illustrations of the first hydrogen adsorption sites for top-view (left) and side-view (right) on p-gCN.

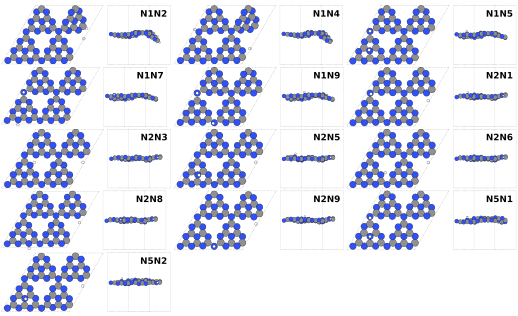

Figure S36: Illustrations of the first hydrogen adsorption sites for top-view (left) and side-view (right) on p-gCN.

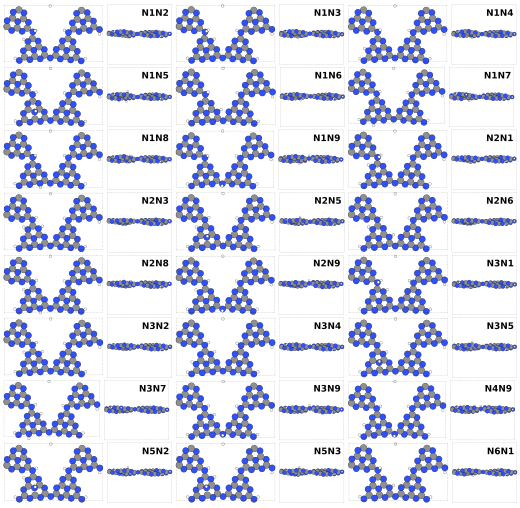

Figure S37: Illustrations of the second hydrogen adsorption sites for top-view (left) and side-view (right) on PHI.

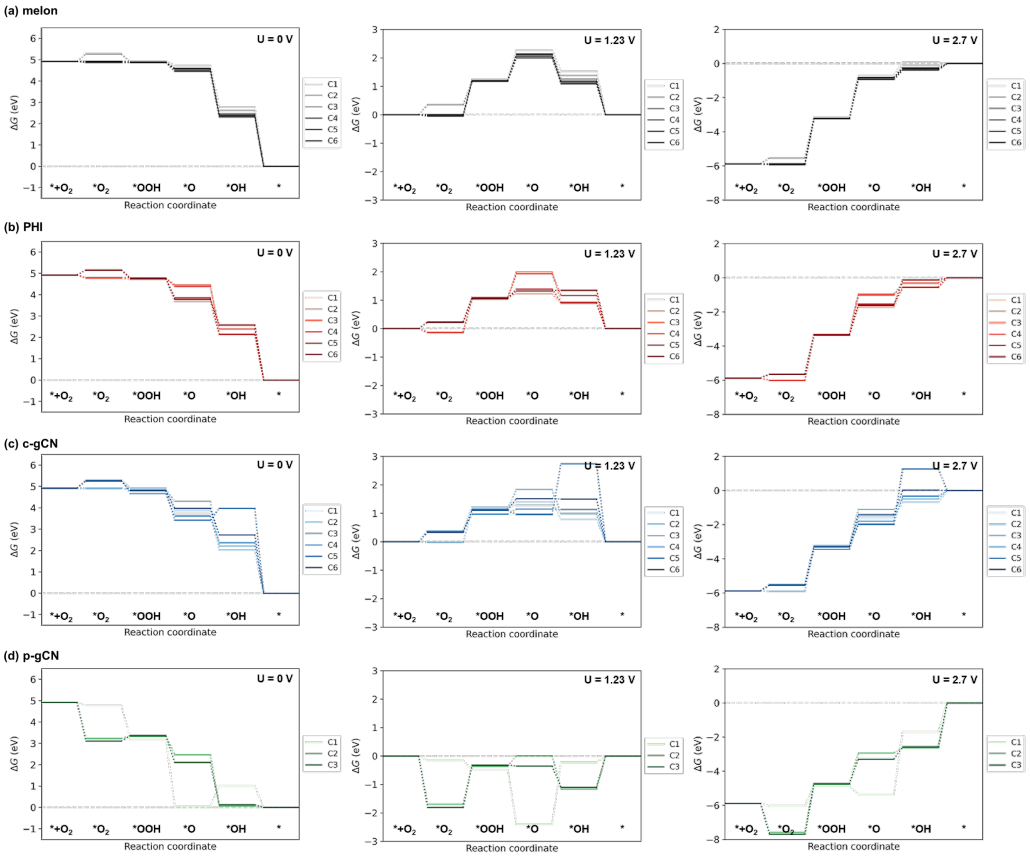

Figure S38: Free energy profiles for the typical ORR process on PCN monolayers: (a) melon, (b) PHI, (c) c-gCN, and (d) p-gCN. The free energy of the intermediates at the investigated active sites is analyzed under applied electrode potentials of $U = 0$, 1.23, and 2.7 V, respectively.

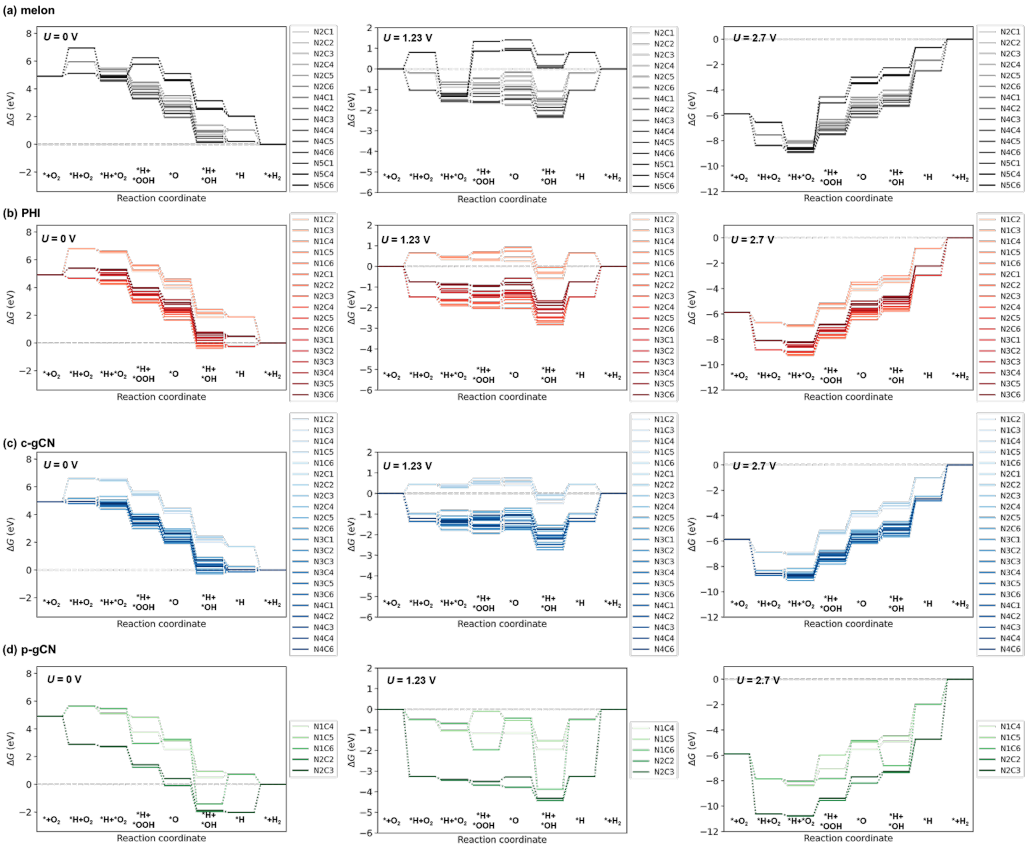

Figure S39: Free energy profiles for the HER-coupled-ORR process on PCN monolayers: (a) melon, (b) PHI, (c) c-gCN, and (d) p-gCN. The free energy of the intermediates at the investigated active sites is analyzed under applied electrode potentials of $U = 0$, 1.23, and 2.7 V, respectively.

Table S5: Free energy of the intermediates for ORR at the active sites of melon monolayer. The ΔG and the potential-determining steps under the simulated electrode potential ($U = 0$ V) are illustrated.

$U = 0$ V	Free energy (eV)					
melon	C1	C2	C3	C4	C5	C6
*+O_2	4.92	4.92	4.92	4.92	4.92	4.92
*O_2	4.91	4.93	5.27	4.87	4.88	4.92
*OOH	4.93	4.91	4.87	4.87	4.88	4.88
*O	4.73	4.55	4.56	4.51	4.46	4.60
*OH	2.76	2.61	2.49	2.36	2.32	2.41
*+H_2O	0.00	0.00	0.00	0.00	0.00	0.00
ΔG_1	-0.01	0.01	0.35	-0.05	-0.04	0.00
ΔG_2	0.01	-0.01	-0.40	0.00	0.00	-0.04
ΔG_3	-0.20	-0.36	-0.31	-0.35	-0.42	-0.29
ΔG_4	-1.96	-1.94	-2.07	-2.16	-2.14	-2.18
ΔG_5	-2.76	-2.61	-2.49	-2.36	-2.32	-2.41
max(ΔG)	0.01	0.01	0.35	0.00	0.00	0.00
Potential-determining step	ΔG_2	ΔG_1	ΔG_1	ΔG_2	ΔG_2	ΔG_1

Table S6: Free energy of the intermediates for ORR at the active sites of melon monolayer. The ΔG and the potential-determining steps under the simulated electrode potential ($U = 1.23$ V) are illustrated.

$U = 1.23$ V	Free energy (eV)					
melon	C1	C2	C3	C4	C5	C6
*+O_2	0.00	0.00	0.00	0.00	0.00	0.00
*O_2	-0.01	0.01	0.35	-0.05	-0.04	0.00
*OOH	1.24	1.22	1.18	1.18	1.19	1.19
*O	2.27	2.09	2.10	2.05	2.00	2.14
*OH	1.53	1.38	1.26	1.13	1.09	1.18
*+H_2O	0.00	0.00	0.00	0.00	0.00	0.00
ΔG_1	-0.01	0.01	0.35	-0.05	-0.04	0.00
ΔG_2	1.24	1.22	0.83	1.23	1.23	1.19
ΔG_3	1.03	0.87	0.92	0.88	0.81	0.94
ΔG_4	-0.73	-0.71	-0.84	-0.93	-0.91	-0.95
ΔG_5	-1.53	-1.38	-1.26	-1.13	-1.09	-1.18
max(ΔG)	1.24	1.22	0.92	1.23	1.23	1.19
Potential-determining step	ΔG_2	ΔG_2	ΔG_3	ΔG_2	ΔG_2	ΔG_2

Table S7: Free energy of the intermediates for ORR at the active sites of melon monolayer. The ΔG and the potential-determining steps under the simulated electrode potential ($U = 2.7$ V) are illustrated.

$U = 2.7$ V	Free energy (eV)					
melon	C1	C2	C3	C4	C5	C6
*+O_2	-5.88	-5.88	-5.88	-5.88	-5.88	-5.88
*O_2	-5.89	-5.87	-5.53	-5.93	-5.92	-5.88
*OOH	-3.17	-3.19	-3.23	-3.23	-3.22	-3.22
*O	-0.67	-0.85	-0.84	-0.89	-0.94	-0.80
*OH	0.06	-0.09	-0.21	-0.34	-0.38	-0.29
*+H_2O	0.00	0.00	0.00	0.00	0.00	0.00
ΔG_1	-0.01	0.01	0.35	-0.05	-0.04	0.00
ΔG_2	2.71	2.69	2.30	2.70	2.70	2.66
ΔG_3	2.50	2.34	2.39	2.35	2.28	2.41
ΔG_4	0.74	0.76	0.63	0.54	0.56	0.52
ΔG_5	-0.06	0.09	0.21	0.34	0.38	0.29
max(ΔG)	2.71	2.69	2.39	2.70	2.70	2.66
Potential-determining step	ΔG_2	ΔG_2	ΔG_3	ΔG_2	ΔG_2	ΔG_2

Table S8: Free energy of the intermediates for ORR at the active sites of PHI monolayer. The ΔG and the potential-determining steps under the simulated electrode potential ($U = 0$ V) are illustrated.

$U = 0$ V	Free energy (eV)					
PHI	C1	C2	C3	C4	C5	C6
*+O_2	4.92	4.92	4.92	4.92	4.92	4.92
*O_2	5.15	5.16	4.77	4.80	5.16	5.14
*OOH	4.77	4.78	4.72	4.79	4.76	4.75
*O	3.84	3.69	4.45	4.39	3.86	3.78
*OH	2.54	2.12	2.16	2.40	2.14	2.58
*+H_2O	0.00	0.00	0.00	0.00	0.00	0.00
ΔG_1	0.23	0.24	-0.15	-0.12	0.24	0.22
ΔG_2	-0.38	-0.38	-0.05	0.00	-0.39	-0.39
ΔG_3	-0.93	-1.10	-0.27	-0.40	-0.91	-0.97
ΔG_4	-1.30	-1.56	-2.29	-1.99	-1.71	-1.20
ΔG_5	-2.54	-2.12	-2.16	-2.40	-2.14	-2.58
max(ΔG)	0.23	0.24	-0.05	0.00	0.24	0.22
Potential-determining step	ΔG_1	ΔG_1	ΔG_2	ΔG_2	ΔG_1	ΔG_1

Table S9: Free energy of the intermediates for ORR at the active sites of PHI monolayer. The ΔG and the potential-determining steps under the simulated electrode potential ($U = 1.23$ V) are illustrated.

$U = 1.23$ V	Free energy (eV)					
PHI	C1	C2	C3	C4	C5	C6
*+O_2	0.00	0.00	0.00	0.00	0.00	0.00
*O_2	0.23	0.24	-0.15	-0.12	0.24	0.22
*OOH	1.08	1.09	1.03	1.10	1.07	1.06
*O	1.38	1.23	1.99	1.93	1.40	1.32
*OH	1.31	0.89	0.93	1.17	0.91	1.35
*+H_2O	0.00	0.00	0.00	0.00	0.00	0.00
ΔG_1	0.23	0.24	-0.15	-0.12	0.24	0.22
ΔG_2	0.85	0.85	1.18	1.23	0.84	0.84
ΔG_3	0.30	0.13	0.96	0.83	0.32	0.26
ΔG_4	-0.07	-0.33	-1.06	-0.76	-0.48	0.03
ΔG_5	-1.31	-0.89	-0.93	-1.17	-0.91	-1.35
max(ΔG)	0.85	0.85	1.18	1.23	0.84	0.84
Potential-determining step	ΔG_2	ΔG_2	ΔG_2	ΔG_2	ΔG_2	ΔG_2

Table S10: Free energy of the intermediates for ORR at the active sites of PHI monolayer. The ΔG and the potential-determining steps under the simulated electrode potential ($U = 2.7$ V) are illustrated.

$U = 2.7$ V	Free energy (eV)					
PHI	C1	C2	C3	C4	C5	C6
*+O_2	-5.88	-5.88	-5.88	-5.88	-5.88	-5.88
*O_2	-5.65	-5.64	-6.03	-6.00	-5.64	-5.66
*OOH	-3.33	-3.32	-3.38	-3.31	-3.34	-3.35
*O	-1.56	-1.71	-0.95	-1.01	-1.54	-1.62
*OH	-0.16	-0.58	-0.54	-0.30	-0.56	-0.12
*+H_2O	0.00	0.00	0.00	0.00	0.00	0.00
ΔG_1	0.23	0.24	-0.15	-0.12	0.24	0.22
ΔG_2	2.32	2.32	2.65	2.70	2.31	2.31
ΔG_3	1.77	1.60	2.43	2.30	1.79	1.73
ΔG_4	1.40	1.14	0.41	0.71	0.99	1.50
ΔG_5	0.16	0.58	0.54	0.30	0.56	0.12
max(ΔG)	2.32	2.32	2.65	2.70	2.31	2.31
Potential-determining step	ΔG_2	ΔG_2	ΔG_2	ΔG_2	ΔG_2	ΔG_2

Table S11: Free energy of the intermediates for ORR at the active sites of c-gCN monolayer. The ΔG and the potential-determining steps under the simulated electrode potential ($U = 0$ V) are illustrated.

$U = 0$ V	Free energy (eV)					
c-gCN	C1	C2	C3	C4	C5	C6
*+O_2	4.92	4.92	4.92	4.92	4.92	4.92
*O_2	5.30	5.30	4.91	5.30	5.25	5.26
*OOH	4.90	4.91	4.85	4.66	4.80	4.81
*O	3.74	3.86	4.29	3.61	3.42	3.98
*OH	2.20	2.02	2.21	2.37	3.97	2.73
*+H_2O	0.00	0.00	0.00	0.00	0.00	0.00
ΔG_1	0.38	0.38	-0.01	0.38	0.33	0.34
ΔG_2	-0.41	-0.40	-0.06	-0.64	-0.46	-0.45
ΔG_3	-1.16	-1.05	-0.55	-1.05	-1.38	-0.83
ΔG_4	-1.53	-1.83	-2.08	-1.24	0.55	-1.24
ΔG_5	-2.20	-2.02	-2.21	-2.37	-3.97	-2.73
max(ΔG)	0.38	0.38	-0.01	0.38	0.55	0.34
Potential-determining step	ΔG_1	ΔG_1	ΔG_1	ΔG_1	ΔG_4	ΔG_1

Table S12: Free energy of the intermediates for ORR at the active sites of c-gCN monolayer. The ΔG and the potential-determining steps under the simulated electrode potential ($U = 1.23$ V) are illustrated.

$U = 1.23$ V	Free energy (eV)					
c-gCN	C1	C2	C3	C4	C5	C6
*+O_2	0.00	0.00	0.00	0.00	0.00	0.00
*O_2	0.38	0.38	-0.01	0.38	0.33	0.34
*OOH	1.21	1.22	1.16	0.97	1.11	1.12
*O	1.28	1.40	1.83	1.15	0.96	1.52
*OH	0.97	0.79	0.98	1.14	2.74	1.50
*+H_2O	0.00	0.00	0.00	0.00	0.00	0.00
ΔG_1	0.38	0.38	-0.01	0.38	0.33	0.34
ΔG_2	0.82	0.83	1.17	0.59	0.77	0.78
ΔG_3	0.07	0.18	0.68	0.18	-0.15	0.40
ΔG_4	-0.30	-0.60	-0.85	-0.01	1.78	-0.01
ΔG_5	-0.97	-0.79	-0.98	-1.14	-2.74	-1.50
max(ΔG)	0.82	0.83	1.17	0.59	1.78	0.78
Potential-determining step	ΔG_2	ΔG_2	ΔG_2	ΔG_2	ΔG_4	ΔG_2

Table S13: Free energy of the intermediates for ORR at the active sites of c-gCN monolayer. The ΔG and the potential-determining steps under the simulated electrode potential ($U = 2.7$ V) are illustrated.

$U = 2.7$ V	Free energy (eV)					
c-gCN	C1	C2	C3	C4	C5	C6
*+O_2	-5.88	-5.88	-5.88	-5.88	-5.88	-5.88
*O_2	-5.50	-5.50	-5.89	-5.50	-5.55	-5.54
*OOH	-3.20	-3.19	-3.25	-3.44	-3.30	-3.29
*O	-1.66	-1.54	-1.11	-1.79	-1.98	-1.42
*OH	-0.50	-0.68	-0.49	-0.33	1.27	0.03
*+H_2O	0.00	0.00	0.00	0.00	0.00	0.00
ΔG_1	0.38	0.38	-0.01	0.38	0.33	0.34
ΔG_2	2.29	2.30	2.64	2.06	2.24	2.25
ΔG_3	1.54	1.65	2.15	1.65	1.32	1.87
ΔG_4	1.17	0.87	0.62	1.46	3.25	1.46
ΔG_5	0.50	0.68	0.49	0.33	-1.27	-0.03
max(ΔG)	2.29	2.30	2.64	2.06	3.25	2.25
Potential-determining step	ΔG_2	ΔG_2	ΔG_2	ΔG_2	ΔG_4	ΔG_2

Table S14: Free energy of the intermediates for ORR at the active sites of p-gCN monolayer. The ΔG and the potential-determining steps under the simulated electrode potential ($U = 0$ V) are illustrated.

$U = 0$ V	Free energy (eV)		
p-gCN	C1	C2	C3
*+O_2	4.92	4.92	4.92
*O_2	4.76	3.23	3.11
*OOH	3.21	3.33	3.37
*O	0.06	2.47	2.11
*OH	1.01	0.07	0.13
*+H_2O	0.00	0.00	0.00
ΔG_1	-0.16	-1.69	-1.81
ΔG_2	-1.55	0.10	0.26
ΔG_3	-3.15	-0.86	-1.26
ΔG_4	0.95	-2.40	-1.98
ΔG_5	-1.01	-0.07	-0.13
max(ΔG)	0.95	0.10	0.26
Potential-determining step	ΔG_4	ΔG_2	ΔG_2

Table S15: Free energy of the intermediates for ORR at the active sites of p-gCN monolayer. The ΔG and the potential-determining steps under the simulated electrode potential ($U = 1.23$ V) are illustrated.

$U = 1.23$ V	Free energy (eV)		
p-gCN	C1	C2	C3
*+O_2	0.00	0.00	0.00
*O_2	-0.16	-1.69	-1.81
*OOH	-0.48	-0.36	-0.32
*O	-2.40	0.01	-0.35
*OH	-0.22	-1.16	-1.10
*+H_2O	0.00	0.00	0.00
ΔG_1	-0.16	-1.69	-1.81
ΔG_2	-0.32	1.33	1.49
ΔG_3	-1.92	0.37	-0.03
ΔG_4	2.18	-1.17	-0.75
ΔG_5	0.22	1.16	1.10
max(ΔG)	2.18	1.33	1.49
Potential-determining step	ΔG_4	ΔG_2	ΔG_2

Table S16: Free energy of the intermediates for ORR at the active sites of p-gCN monolayer. The ΔG and the potential-determining steps under the simulated electrode potential ($U = 2.7$ V) are illustrated.

$U = 2.7$ V	Free energy (eV)		
p-gCN	C1	C2	C3
*+O_2	-5.88	-5.88	-5.88
*O_2	-6.04	-7.57	-7.69
*OOH	-4.89	-4.77	-4.73
*O	-5.34	-2.93	-3.29
*OH	-1.69	-2.63	-2.57
*+H_2O	0.00	0.00	0.00
ΔG_1	-0.16	-1.69	-1.81
ΔG_2	1.15	2.80	2.96
ΔG_3	-0.45	1.84	1.44
ΔG_4	3.65	0.30	0.72
ΔG_5	1.69	2.63	2.57
max(ΔG)	3.65	2.80	2.96
Potential-determining step	ΔG_4	ΔG_2	ΔG_2

Bibliography

[1] F. K. Kessler, Y. Zheng, D. Schwarz, C. Merschjann, W. Schnick, X. Wang, M. J. Bojdys, *Nature Reviews Materials* **2017**, *2*, 1–17.

[2] F. Podjaski, B. V. Lotsch, *Adv. Energy Mater.* **2021**, *11*, 2003049.

[3] A. Gouder, F. Podjaski, A. Jiménez-Solano, J. Kröger, Y. Wang, B. V. Lotsch, *Energy Environ. Sci.* **2023**, *16*, 1520–1530.

[4] J. Liu, Y. Liu, N. Liu, Y. Han, X. Zhang, H. Huang, Y. Lifshitz, S.-T. Lee, J. Zhong, Z. Kang, *Science* **2015**, *347*, 970–974, DOI 10.1126/science.aaa3145.

[5] S. Cao, J. Low, J. Yu, M. Jaroniec, *Adv. Mater.* **2015**, *27*, 2150–2176, DOI 10.1002/adma.201500033.

[6] X. Wang, K. Maeda, X. Chen, K. Takanabe, K. Domen, Y. Hou, X. Fu, M. Antonietti, *Journal of the American Chemical Society* **2009**, *131*, 1680–1681.

[7] K. Schwinghammer, B. Tuffy, M. B. Mesch, E. Wirnhier, C. Martineau, F. Taulelle, W. Schnick, J. Senker, B. V. Lotsch, *Angewandte Chemie International Edition* **2013**, *52*, 2435–2439.

[8] J. Liu, J. Huang, H. Zhou, M. Antonietti, *ACS Applied Materials & Interfaces* **2014**, *6*, 8434–8440.

[9] A. Savateev, M. Antonietti, *ChemCatChem* **2019**, *11*, 6166–6176.

[10] G. Zhang, G. Li, T. Heil, S. Zafeiratos, F. Lai, A. Savateev, M. Antonietti, X. Wang, *Angewandte Chemie International Edition* **2019**, *58*, 3433–3437.

[11] I. F. Teixeira, N. V. Tarakina, I. F. Silva, N. López-Salas, A. Savateev, M. Antonietti, *Advanced Sustainable Systems* **2022**, 2100429.

[12] Z. Ding, X. Chen, M. Antonietti, X. Wang, *ChemSusChem* **2011**, *4*, 274–281.

[13] J. Zhang, M. Grzelczak, Y. Hou, K. Maeda, K. Domen, X. Fu, M. Antonietti, X. Wang, *Chemical Science* **2012**, *3*, 443–446.

[14] C. Wang, Q. Wan, J. Cheng, S. Lin, A. Savateev, M. Antonietti, X. Wang, *Journal of Catalysis* **2021**, *393*, 116–125.

[15] M. A. da Silva, J. Gil, N. V. Tarakina, G. T. Silva, J. Balena, K. Krambrock, M. Antonietti, C. Ribeiro, I. Teixeira, *Chemical Communications* **2022**.

[16] F. Jensen, *Introduction to computational chemistry*, John wiley & sons, **2017**.

[17] V. Balzani, P. Ceroni, A. Juris, *Photochemistry and photophysics: concepts, research, applications*, John Wiley & Sons, **2014**.

[18] C. Cohen-Tannoudji, B. Diu, F. Laloë, *Quantum Mechanics Volume 2*, Hermann, **1986**.

[19] C. Cohen-Tannoudji, B. Diu, F. Laloë, *Quantum mechanics, volume 3: fermions, bosons, photons, correlations, and entanglement*, John Wiley & Sons, **2019**.

[20] D. Golze, M. Dvorak, P. Rinke, *Frontiers in chemistry* **2019**, *7*, 377.

[21] D. Hartree, *The Calculation of Atomic Structures*, J. Wiley, **1957**.

[22] P. Hohenberg, W. Kohn, *Phys. Rev.* **1964**, *136*, B864–B871, DOI 10.1103/PhysRev.136.B864.

[23] W. Kohn, L. J. Sham, *Phys. Rev.* **1965**, *140*, A1133–A1138, DOI 10.1103/PhysRev.140.A1133.

[24] A. D. Beck, *J. Chem. Phys* **1993**, *98*, 5648–6.

[25] D. Langreth, J. Perdew, *Phys. Rev. B* **1977**, *15*, 2884–900.

[26] K.-N. Zhang, X.-T. Hao, *The Journal of Physical Chemistry Letters* **2023**, *14*, 6051–6060.

[27] H. Dong, C. Zhang, J. Yao, Y. S. Zhao, *Aggregate* **2021**, *2*, e103.

[28] P. Liu, **2017**.

[29] P. Xia, M. Antonietti, B. Zhu, T. Heil, J. Yu, S. Cao, *Advanced Functional Materials* **2019**, *29*, 1900093.

[30] Y. Xia, K. Xiao, B. Cheng, J. Yu, L. Jiang, M. Antonietti, S. Cao, *ChemSusChem* **2020**, *13*, 1730–1734.

[31] B. V. Lotsch, M. Döblinger, J. Sehnert, L. Seyfarth, J. Senker, O. Oeckler, W. Schnick, *Chemistry–A European Journal* **2007**, *13*, 4969–4980.

[32] A. Thomas, A. Fischer, F. Goettmann, M. Antonietti, J.-O. Müller, R. Schlögl, J. M. Carlsson, *Journal of Materials Chemistry* **2008**, *18*, 4893–4908.

[33] I. Krivtsov, D. Mitoraj, C. Adler, M. Ilkaeva, M. Sardo, L. Mafra, C. Neumann, A. Turchanin, C. Li, B. Dietzek, et al., *Angewandte Chemie International Edition* **2020**, *59*, 487–495.

[34] D. Mitoraj, I. Krivtsov, C. Li, A. Rajagopal, C. Im, C. Adler, K. Köble, O. Khainakova, J. Hniopek, C. Neumann, et al., *Chemistry–A European Journal* **2021**, *27*, 17188–17202.

[35] V. W.-h. Lau, B. V. Lotsch, *Advanced Energy Materials* **2022**, *12*, 2101078.

[36] J. LIEBIG, *Annalen der Pharmacie* **1834**, *10*, 1–47, DOI `https://doi.org/10.1002/jlac.18340100102`.

[37] L. Gmelin, *Annalen der Pharmacie* **1835**, *15*, 252–258, DOI `https://doi.org/10.1002/jlac.18350150306`.

[38] B. V. Lotsch, W. Schnick, *Chemistry of materials* **2005**, *17*, 3976–3982.

[39] B. V. Lotsch, W. Schnick, *Chemistry of materials* **2006**, *18*, 1891–1900.

[40] F. Goettmann, A. Fischer, M. Antonietti, A. Thomas, *Angewandte Chemie International Edition* **2006**, *45*, 4467–4471.

[41] X. Wang, K. Maeda, A. Thomas, K. Takanabe, G. Xin, J. M. Carlsson, K. Domen, M. Antonietti, *Nature materials* **2009**, *8*, 76–80.

[42] A. Y. Liu, M. L. Cohen, *Science* **1989**, *245*, 841–842.

[43] J Gracia, P Kroll, *Journal of Materials Chemistry* **2009**, *19*, 3013–3019.

[44] X. Li, S. T. Melissen, T. Le Bahers, P. Sautet, A. F. Masters, S. N. Steinmann, T. Maschmeyer, *Chemistry of Materials* **2018**, *30*, 4253–4262.

[45] M. J. Bojdys, J.-O. Müller, M. Antonietti, A. Thomas, *Chemistry–A European Journal* **2008**, *14*, 8177–8182.

[46] G. Algara-Siller, N. Severin, S. Y. Chong, T. Björkman, R. G. Palgrave, A. Laybourn, M. Antonietti, Y. Z. Khimyak, A. V. Krasheninnikov, J. P. Rabe, et al., *Angewandte Chemie International Edition* **2014**, *53*, 7450–7455.

[47] V. W.-h. Lau, I. Moudrakovski, T. Botari, S. Weinberger, M. B. Mesch, V. Duppel, J. Senker, V. Blum, B. V. Lotsch, *Nature communications* **2016**, *7*, 1–10.

[48] S. Melissen, T. Le Bahers, S. N. Steinmann, P. Sautet, *The Journal of Physical Chemistry C* **2015**, *119*, 25188–25196.

[49] S. N. Steinmann, S. T. Melissen, T. Le Bahers, P. Sautet, *Journal of Materials Chemistry A* **2017**, *5*, 5115–5122.

[50] J. P. Perdew, *International Journal of Quantum Chemistry* **1985**, *28*, 497–523.

[51] S. Melissen, T. Le Bahers, S. N. Steinmann, P. Sautet, *The Journal of Physical Chemistry C* **2015**, *119*, 25188–25196.

[52] S. T. Melissen, S. N. Steinmann, T. Le Bahers, P. Sautet, *The Journal of Physical Chemistry C* **2016**, *120*, 24542–24550.

[53] W. Wei, T. Jacob, *Physical Review B* **2013**, *87*, 085202.

[54] R. Godin, Y. Wang, M. A. Zwijnenburg, J. Tang, J. R. Durrant, *Journal of the American Chemical Society* **2017**, *139*, 5216–5224.

[55] W. Yang, R. Godin, H. Kasap, B. Moss, Y. Dong, S. A. Hillman, L. Steier, E. Reisner, J. R. Durrant, *Journal of the American Chemical Society* **2019**, *141*, 11219–11229.

[56] C. Li, E. Hofmeister, I. Krivtsov, D. Mitoraj, C. Adler, R. Beranek, B. Dietzek, *ChemSusChem* **2021**, *14*, 1728–1736.

[57] C. Adler, S. Selim, I. Krivtsov, C. Li, D. Mitoraj, B. Dietzek, J. R. Durrant, R. Beranek, *Advanced Functional Materials* **2021**, *31*, 2105369.

[58] G. Seo, Y. Saito, M. Nakamichi, K. Nakano, K. Tajima, K. Kanai, *Scientific reports* **2021**, *11*, 1–12.

[59] J. Kröger, A. Jiménez-Solano, G. Savasci, P. Rovó, I. Moudrakovski, K. Küster, H. Schlomberg, H. A. Vignolo-González, V. Duppel, L. Grunenberg, et al., *Advanced Energy Materials* **2021**, *11*, 2003016.

[60] Z.-H. Ruan, X.-Y. Gao, Y. Yuan, H.-P. Tan, *Journal of Materials Science* **2021**, *56*, 10382–10392.

[61] H. Dong, Y. Zuo, N. Song, S. Hong, M. Xiao, D. Zhu, J. Sun, G. Chen, C. Li, *Applied Catalysis B: Environmental* **2021**, *287*, 119954.

[62] L. Cheng, H. Zhang, X. Li, J. Fan, Q. Xiang, *Small* **2021**, *17*, 2005231.

[63] J.-Y. Tang, C.-C. Er, L.-L. Tan, Y.-H. Chew, A. R. Mohamed, S.-P. Chai, *Physical Chemistry Chemical Physics* **2022**, *24*, 11124–11130.

[64] T. Botari, W. P. Huhn, V. W. H. Lau, B. V. Lotsch, V. Blum, *Chem. Mater.* **2017**, *29*, 4445–4453, DOI 10.1021/acs.chemmater.7b00965.

[65] G. Kresse, J. Hafner, *Physical review B* **1993**, *47*, 558.

[66] G. Kresse, J. Hafner, *Physical Review B* **1994**, *49*, 14251.

[67] G. Kresse, J. Furthmüller, *Computational materials science* **1996**, *6*, 15–50.

[68] G. Kresse, J. Furthmüller, *Physical review B* **1996**, *54*, 11169.

[69] G. Kresse, D. Joubert, *Physical review b* **1999**, *59*, 1758.

[70] S. Grimme, J. Antony, S. Ehrlich, H. Krieg, *The Journal of chemical physics* **2010**, *132*, 154104.

[71] S. Grimme, S. Ehrlich, L. Goerigk, *Journal of computational chemistry* **2011**, *32*, 1456–1465.

[72] J. P. Perdew, K. Burke, M. Ernzerhof, *Physical review letters* **1996**, *77*, 3865.

[73] A. V. Krukau, O. A. Vydrov, A. F. Izmaylov, G. E. Scuseria, *The Journal of chemical physics* **2006**, *125*, 224106.

[74] F. Neese, *Wiley Interdisciplinary Reviews: Computational Molecular Science* **2012**, *2*, 73–78.

[75] F. Neese, *Wiley Interdisciplinary Reviews: Computational Molecular Science* **2018**, *8*, e1327.

[76] M. Ernzerhof, G. E. Scuseria, *The Journal of chemical physics* **1999**, *110*, 5029–5036.

[77] C. Adamo, V. Barone, *The Journal of chemical physics* **1999**, *110*, 6158–6170.

[78] H. J. Monkhorst, J. D. Pack, *Physical review B* **1976**, *13*, 5188.

[79] A. Togo, L. Chaput, I. Tanaka, G. Hug, *Physical Review B* **2010**, *81*, 174301.

[80] L. Chaput, A. Togo, I. Tanaka, G. Hug, *Physical Review B* **2011**, *84*, 094302.

[81] A. Togo, I. Tanaka, *Scripta Materialia* **2015**, *108*, 1–5.

[82] C. Im, B. Kirchhoff, I. Krivtsov, D. Mitoraj, R. Beranek, T. Jacob, Supporting Dataset for: Investigation of Thermochemical Relationship between Structural and Optical Properties on Photocatalytic Carbon Nitride Materials, **2022**, DOI `10.5281/zenodo.6953396`.

[83] J. Rogal, K. Reuter, Ab initio atomistic thermodynamics for surfaces: A primer, tech. rep., Max-planck-gesellschaft zur foerderung der wissenschaften ev berlin (germany , **2006**.

[84] K. A. Dill, S. Bromberg, D. Stigter, *Molecular driving forces: statistical thermodynamics in biology, chemistry, physics, and nanoscience*, Garland Science, **2010**.

[85] K. Reuter, *Catalysis Letters* **2016**, *146*, 541–563.

[86] Q. Gao, X. Zhuang, S. Hu, Z. Hu, *The Journal of Physical Chemistry C* **2020**, *124*, 4644–4651.

[87] S. Yan, Z. Li, Z. Zou, *Langmuir* **2009**, *25*, 10397–10401.

[88] B. V. Lotsch, W. Schnick, *Chemistry–A European Journal* **2007**, *13*, 4956–4968.

[89] R. C. Dougherty, *The Journal of chemical physics* **1998**, *109*, 7372–7378.

[90] H. Inoki, G. Seo, K. Kanai, *Applied Surface Science* **2020**, *534*, 147569.

[91] J. Liu, H. Wang, M. Antonietti, *Chemical Society Reviews* **2016**, *45*, 2308–2326.

[92] M. Döblinger, B. V. Lotsch, J. Wack, J. Thun, J. Senker, W. Schnick, *Chemical communications* **2009**, 1541–1543.

[93] D. Dontsova, S. Pronkin, M. Wehle, Z. Chen, C. Fettkenhauer, G. Clavel, M. Antonietti, *Chemistry of Materials* **2015**, *27*, 5170–5179.

[94] A. Savateev, S. Pronkin, J. D. Epping, M. G. Willinger, C. Wolff, D. Neher, M. Antonietti, D. Dontsova, *ChemCatChem* **2017**, *9*, 167–174.

[95] Z. Chen, A. Savateev, S. Pronkin, V. Papaefthimiou, C. Wolff, M. G. Willinger, E. Willinger, D. Neher, M. Antonietti, D. Dontsova, *Advanced Materials* **2017**, *29*, 1700555.

[96] L. Lin, W. Ren, C. Wang, A. Asiri, J. Zhang, X. Wang, *Applied Catalysis B: Environmental* **2018**, *231*, 234–241.

[97] H. Schlomberg, J. Kröger, G. Savasci, M. W. Terban, S. Bette, I. Moudrakovski, V. Duppel, F. Podjaski, R. Siegel, J. Senker, et al., *Chemistry of Materials* **2019**, *31*, 7478–7486.

[98] M. Deifallah, P. F. McMillan, F. Cora, *The Journal of Physical Chemistry C* **2008**, *112*, 5447–5453.

[99] A. Savateev, S. Pronkin, M. G. Willinger, M. Antonietti, D. Dontsova, *Chemistry–An Asian Journal* **2017**, *12*, 1517–1522.

[100] A. Schwarzer, T. Saplinova, E. Kroke, *Coordination Chemistry Reviews* **2013**, *257*, 2032–2062.

[101] K. S. Novoselov, A. K. Geim, S. V. Morozov, D.-e. Jiang, Y. Zhang, S. V. Dubonos, I. V. Grigorieva, A. A. Firsov, *Science* **2004**, *306*, 666–669, DOI 10.1126/science.1102896.

[102] *J. Am. Chem. Soc.* **2009**, *131*, 1680–1681, DOI 10.1021/ja809307s.

[103] N. Mendelson, D. Chugh, J. R. Reimers, T. S. Cheng, A. Gottscholl, H. Long, C. J. Mellor, A. Zettl, V. Dyakonov, P. H. Beton, S. V. Novikov, C. Jagadish, H. H. Tan, M. J. Ford, M. Toth, C. Bradac, I. Aharonovich, *Nat. Mater.* **2021**, *20*, 321–328, DOI 10.1038/s41563-020-00850-y.

[104] H. Wang, Z. Du, Z. Cheng, Z. Cao, Y. Ye, Z. Wang, J. Wei, S. Wei, X. Meng, L. Song, Y. Gong, S. Yang, L. Guo, *Adv. Mater.* **2023**, *2301399*, 1–7, DOI 10.1002/adma.202301399.

[105] X. Wang, K. Maeda, A. Thomas, K. Takanabe, G. Xin, J. M. Carlsson, K. Domen, M. Antonietti, *Nat. Mater.* **2009**, *8*, 76–80, DOI 10.1038/nmat2317.

[106] X. Duan, C. Wang, A. Pan, R. Yu, X. Duan, *Chem. Soc. Rev.* **2015**, *44*, 8859–8876, DOI 10.1039/C5CS00507H.

[107] J. An, X. Zhao, Y. Zhang, M. Liu, J. Yuan, X. Sun, Z. Zhang, B. Wang, S. Li, D. Li, *Adv. Funct. Mater.* **2022**, *32*, 2110119, DOI 10.1002/adfm.202110119.

[108] B. Ma, G. Chen, C. Fave, L. Chen, R. Kuriki, K. Maeda, O. Ishitani, T. C. Lau, J. Bonin, M. Robert, *J. Am. Chem. Soc.* **2020**, *142*, 6188–6195, DOI 10.1021/jacs.9b13930.

[109] S. N. Talapaneni, G. Singh, I. Y. Kim, K. AlBahily, A. H. Al-Muhtaseb, A. S. Karakoti, E. Tavakkoli, A. Vinu, *Adv. Mater.* **2020**, *32*, 1–21, DOI 10.1002/adma.201904635.

[110] I. Krivtsov, D. Mitoraj, C. Adler, M. Ilkaeva, M. Sardo, L. Mafra, C. Neumann, A. Turchanin, C. Li, B. Dietzek, R. Leiter, J. Biskupek, U. Kaiser, C. Im, B. Kirchhoff, T. Jacob, R. Beranek, *Angew. Chem. Int. Ed.* **2020**, *59*, 487–495, DOI 10.1002/anie.201913331.

[111] L. Lin, Z. Lin, J. Zhang, X. Cai, W. Lin, Z. Yu, X. Wang, *Nat. Catal.* **2020**, *3*, 649–655, DOI 10.1038/s41929-020-0476-3.

[112] Z. Teng, Q. Zhang, H. Yang, K. Kato, W. Yang, Y. R. Lu, S. Liu, C. Wang, A. Yamakata, C. Su, B. Liu, T. Ohno, *Nat. Catal.* **2021**, *4*, 374–384, DOI 10.1038/s41929-021-00605-1.

[113] Y. Zhao, P. Zhang, Z. Yang, L. Li, J. Gao, S. Chen, T. Xie, C. Diao, S. Xi, B. Xiao, C. Hu, W. Choi, *Nat. Commun.* **2021**, *12*, 1–11, DOI 10.1038/s41467-021-24048-1.

[114] Y. Xu, M. Fan, W. Yang, Y. Xiao, L. Zeng, X. Wu, Q. Xu, C. Su, Q. He, *Adv. Mater.* **2021**, *33*, 1–11, DOI 10.1002/adma.202101455.

[115] H. Ou, S. Ning, P. Zhu, S. Chen, A. Han, Q. Kang, Z. Hu, J. Ye, D. Wang, Y. Li, *Angew. Chem. Int. Ed.* **2022**, *0047*, DOI 10.1002/anie.202206579.

[116] Z. Wang, E. Almatrafi, H. Wang, H. Qin, W. Wang, L. Du, S. Chen, G. Zeng, P. Xu, *Angew. Chem. Int. Ed.* **2022**, *61*, 1–10, DOI 10.1002/anie.202202338.

[117] D. Zhang, P. Ren, W. Liu, Y. Li, S. Salli, F. Han, W. Qiao, Y. Liu, Y. Fan, Y. Cui, Y. Shen, E. Richards, X. Wen, M. H. Rummeli, Y. Li, F. Besenbacher, H. Niemantsverdriet, T. Lim, R. Su, *Angew. Chem. Int. Ed.* **2022**, *61*, DOI 10.1002/anie.202204256.

[118] J. Wu, Z. Liu, X. Lin, E. Jiang, S. Zhang, P. Huo, Y. Yan, P. Zhou, Y. Yan, *Nat. Commun.* **2022**, *13*, DOI 10.1038/s41467-022-34848-8.

[119] W. Xie, K. Li, X. H. Liu, X. Zhang, H. Huang, *Adv. Mater.* **2023**, *35*, 1–8, DOI 10.1002/adma.202208132.

[120] T. Jia, D. Meng, R. Duan, H. Ji, H. Sheng, C. Chen, J. Li, W. Song, J. Zhao, *Angew. Chem. Int. Ed.* **2023**, *62*, 1–9, DOI 10.1002/anie.202216511.

[121] C. Adler, S. Selim, I. Krivtsov, C. Li, D. Mitoraj, B. Dietzek, J. R. Durrant, R. Beranek, *Adv. Funct. Mater.* **2021**, *31*, DOI 10.1002/adfm.202105369.

[122] C. Adler, I. Krivtsov, D. Mitoraj, L. dos Santos-Gómez, S. García-Granda, C. Neumann, J. Kund, C. Kranz, B. Mizaikoff, A. Turchanin, et al., *ChemSusChem* **2021**, *14*, 2170–2179, DOI 10.1002/cssc.202100313.

[123] C. Pulignani, C. A. Mesa, S. A. Hillman, T. Uekert, S. Giménez, J. R. Durrant, E. Reisner, *Angew. Chem. Int. Ed.* **2022**, *61*, e202211587, DOI 10.1002/anie.202211587.

[124] R. Godin, Y. Wang, M. A. Zwijnenburg, J. Tang, J. R. Durrant, *J. Am. Chem. Soc.* **2017**, *139*, 5216–5224, DOI 10.1021/jacs.7b01547.

[125] W. Wei, T. Jacob, *Phys. Rev. B* **2013**, *87*, 1–7, DOI 10.1103/PhysRevB.87.085202.

[126] S. Melissen, T. Le Bahers, S. N. Steinmann, P. Sautet, *J. Phys. Chem. C* **2015**, *119*, 25188–25196, DOI 10.1021/acs.jpcc.5b07059.

[127] G. Zhang, G. Li, Z.-A. Lan, L. Lin, A. Savateev, T. Heil, S. Zafeiratos, X. Wang, M. Antonietti, *Angew. Chem. Int. Ed.* **2017**, *129*, 13630–13634, DOI 10.1002/anie.201706870.

[128] C. Im, B. Kirchhoff, I. Krivtsov, D. Mitoraj, R. Beranek, T. Jacob, *Chem. Mater.* **2023**, *35*, 1547–1559, DOI 10.1021/acs.chemmater.2c02843.

[129] Z. Zhao, Y. Sun, F. Dong, *Nanoscale* **2015**, *7*, 15–37, DOI 10.1039/C4NR03008G.

[130] Z. Chen, A. Savateev, S. Pronkin, V. Papaefthimiou, C. Wolff, M. G. Willinger, E. Willinger, D. Neher, M. Antonietti, D. Dontsova, *Adv. Mater.* **2017**, *29*, 1–8, DOI 10.1002/adma.201700555.

[131] H. Schlomberg, J. Kröger, G. Savasci, M. W. Terban, S. Bette, I. Moudrakovski, V. Duppel, F. Podjaski, R. Siegel, J. Senker, R. E. Dinnebier, C. Ochsenfeld, B. V. Lotsch, *Chem. Mater.* **2019**, *31*, 7478–7486, DOI 10.1021/acs.chemmater.9b02199.

[132] S. N. Steinmann, S. T. Melissen, T. Le Bahers, P. Sautet, *J. Mater. Chem. A* **2017**, *5*, 5115–5122, DOI 10.1039/c6ta08939a.

[133] M. Re Fiorentin, F. Risplendi, M. Palummo, G. Cicero, *ACS Appl. Nano Mater.* **2021**, *4*, 1985–1993, DOI 10.1021/acsanm.0c03317.

[134] B. Schulze Lammers, N. López-Salas, J. Stein Siena, H. Mirhosseini, D. Yesilpinar, J. Heske, T. D. Kühne, H. Fuchs, M. Antonietti, H. Mönig, *ACS Nano* **2022**, *16*, 14284–14296, DOI 10.1021/acsnano.2c04439.

[135] Q. Xie, C. Wang, W. Shen, Y. Fu, Y. Si, *ChemNanoMat* **2023**, DOI 10.1002/cnma.202300102.

[136] M. Feierabend, S. Brem, E. Malic, *PCCP* **2019**, *21*, 26077–26083, DOI 10.1039/C9CP05763C.

[137] S. An, G. Zhang, K. Li, Z. Huang, X. Wang, Y. Guo, J. Hou, C. Song, X. Guo, *Adv. Mater.* **2021**, *33*, 1–9, DOI 10.1002/adma.202104361.

[138] Q. Gao, X. Zhuang, S. Hu, Z. Hu, *J. Phys. Chem. C* **2020**, *124*, 4644–4651, DOI 10.1021/acs.jpcc.0c00411.

[139] Z. Wei, M. Liu, Z. Zhang, W. Yao, H. Tan, Y. Zhu, *Energy Environ. Sci.* **2018**, *11*, 2581–2589, DOI 10.1039/c8ee01316k.

[140] L. Jing, R. Zhu, D. L. Phillips, J. C. Yu, *Adv. Funct. Mater.* **2017**, *27*, DOI 10.1002/adfm.201703484.

[141] Q. Ruan, T. Miao, H. Wang, J. Tang, *J. Am. Chem. Soc.* **2020**, *142*, 2795–2802, DOI 10.1021/jacs.9b10476.

[142] A. J. Rieth, Y. Qin, B. C. Martindale, D. G. Nocera, *J. Am. Chem. Soc.* **2021**, *143*, 4646–4652, DOI 10.1021/jacs.0c12958.

[143] C. Pulignani, C. A. Mesa, S. A. Hillman, T. Uekert, S. Giménez, J. R. Durrant, E. Reisner, *Angew. Chem. Int. Ed.* **2022**, *61*, e202211587, DOI 10.1002/anie.202211587.

[144] P. Kubelka, F. Munk, *Z. Tech. Phys* **1931**, *12*, 259–274.

[145] C Merschjann, T Tyborski, S Orthmann, F Yang, K Schwarzburg, M Lublow, M.-C. Lux-Steiner, T. Schedel-Niedrig, *Phys. Rev. B* **2013**, *87*, 205204.

[146] I. Guilhon, D. S. Koda, L. G. Ferreira, M. Marques, L. K. Teles, *Phys. Rev. B* **2018**, *97*, 1–11, DOI 10.1103/PhysRevB.97.045426.

[147] P. You, C. Lian, D. Chen, J. Xu, C. Zhang, S. Meng, E. Wang, *Nano Lett.* **2021**, *21*, 6449–6455, DOI 10.1021/acs.nanolett.1c01187.

[148] C. Li, C. Adler, I. Krivtsov, D. Mitoraj, R. Leiter, U. Kaiser, R. Beranek, B. Dietzek, *Chem. Commun.* **2021**, *57*, 10739–10742, DOI 10.1039/D1CC03812E.

[149] P. Giusto, B. Kumru, D. Cruz, M. Antonietti, *Adv. Opt. Mater.* **2022**, *10*, 2101965, DOI 10.1002/adom.202101965.

[150] R. Ruger, E. Van Lenthe, Y. Lu, J. Frenzel, T. Heine, L. Visscher, *J. Chem. Theory Comput.* **2015**, *11*, 157–167, DOI 10.1021/ct500838h.

[151] C. Merschjann, S. Tschierlei, T. Tyborski, K. Kailasam, S. Orthmann, D. Hollmann, T. Schedel-Niedrig, A. Thomas, S. Lochbrunner, *Adv. Mater.* **2015**, *27*, 7993–7999, DOI 10.1002/adma.201503448.

[152] G. Chen, Z. D. Zhang, Y. X. Liao, Z. Zhang, Y. Z. You, *Small* **2021**, *17*, DOI 10.1002/smll.202100698.

[153] G. Peng, L. Xing, J. Barrio, M. Volokh, M. Shalom, *Angew. Chem. Int. Ed.* **2018**, *57*, 1186–1192, DOI 10.1002/anie.201711669.

[154] G. Zhang, A. Savateev, Y. Zhao, L. Li, M. Antonietti, *J. Mater. Chem. A* **2017**, *5*, 12723–12728, DOI 10.1039/c7ta03777e.

[155] H. Wang, X. Sun, D. Li, X. Zhang, S. Chen, W. Shao, Y. Tian, Y. Xie, *J. Am. Chem. Soc.* **2017**, *139*, 2468–2473, DOI 10.1021/jacs.6b12878.

[156] D. Y. Qiu, G. Cohen, D. Novichkova, S. Refaely-Abramson, *Nano Lett.* **2021**, *21*, 7644–7650, DOI 10.1021/acs.nanolett.1c02352.

[157] K. L. Corp, C. W. Schlenker, *J. Am. Chem. Soc.* **2017**, *139*, 7904–7912, DOI 10.1021/jacs.7b02869.

[158] J. Kröger, F. Podjaski, G. Savasci, I. Moudrakovski, A. Jiménez-Solano, M. W. Terban, S. Bette, V. Duppel, M. Joos, A. Senocrate, R. Dinnebier, C. Ochsenfeld, B. V. Lotsch, *Adv. Mater.* **2022**, *34*, DOI 10.1002/adma.202107061.

[159] S. Albrecht, L. Reining, R. Del Sole, G. Onida, *Phys. Rev. Lett.* **1998**, *80*, 4510, DOI 10.1103/PhysRevLett.80.4510.

[160] M. Rohlfing, S. G. Louie, *Phys. Rev. Lett.* **1998**, *81*, 2312, DOI 10.1103/PhysRevLett.81.2312.

[161] C. Im, B. Kirchhoff, D. Mitoraj, I. Krivtsov, A. Farkas, R. Beránek, T. Jacob, **2024**, DOI 10.5281/zenodo.10844461.

[162] F. Furche, R. Ahlrichs, *J. Chem. Phys.* **2002**, *117*, 7433–7447, DOI 10.1063/1.1508368.

[163] J. Paier, M. Marsman, G. Kresse, *Phys. Rev. B* **2008**, *78*, 121201, DOI 10.1103/PhysRevB.78.121201.

[164] T. Sander, E. Maggio, G. Kresse, *Phys. Rev. B* **2015**, *92*, 045209, DOI 10.1103/PhysRevB.92.045209.

[165] M Gajdoš, K Hummer, G Kresse, J Furthmüller, F. Bechstedt, *Phys. Rev. B* **2006**, *73*, 045112, DOI 10.1103/PhysRevB.73.045112.

[166] C Rödl, F Fuchs, J Furthmüller, F Bechstedt, *Phys. Rev. B* **2008**, *77*, 184408, DOI 10.1103/PhysRevB.77.184408.

[167] A. Papadopoulos, E Anastassakis, *Phys. Rev. B* **1991**, *43*, 5090, DOI 10.1103/PhysRevB.43.5090.

[168] V. W.-h. Lau, D. Klose, H. Kasap, F. Podjaski, M.-C. Pignié, E. Reisner, G. Jeschke, B. V. Lotsch, *Angew. Chem. Int. Ed.* **2017**, *129*, 525–529.

[169] H. Kasap, C. A. Caputo, B. C. Martindale, R. Godin, V. W.-h. Lau, B. V. Lotsch, J. R. Durrant, E. Reisner, *J. Am. Chem. Soc.* **2016**, *138*, 9183–9192.

[170] C. Merschjann, S. Tschierlei, T. Tyborski, K. Kailasam, S. Orthmann, D. Hollmann, T. Schedel-Niedrig, A. Thomas, S. Lochbrunner, *Adv. Mater.* **2015**, *27*, 7993–7999.

[171] C. Im, B. Kirchhoff, D. Mitoraj, I. Krivtsov, A. Farkas, R. Beránek, T. Jacob, *arXiv preprint arXiv:2403.13685* **2024**.

[172] J. Hafner, *Journal of computational chemistry* **2008**, *29*, 2044–2078.

[173] D. M. Ceperley, B. J. Alder, *Phys. Rev. Lett.* **1980**, *45*, 566–569, DOI 10.1103/PhysRevLett.45.566.

[174] J. P. Perdew, A. Zunger, *Phys. Rev. B* **1981**, *23*, 5048–5079, DOI 10.1103/PhysRevB.23.5048.

[175] A. Tkatchenko, R. A. DiStasio, R. Car, M. Scheffler, *Phys. Rev. Lett.* **2012**, *108*, 236402, DOI 10.1103/PhysRevLett.108.236402.

[176] A. Ambrosetti, A. M. Reilly, J. DiStasio, Robert A., A. Tkatchenko, *The Journal of Chemical Physics* **2014**, *140*, 18A508, DOI 10.1063/1.4865104.

[177] L. Hedin, *Physical Review* **1965**, *139*, A796.

[178] M. van Schilfgaarde, T. Kotani, S. Faleev, *Phys. Rev. Lett.* **2006**, *96*, 226402, DOI 10.1103/PhysRevLett.96.226402.

[179] M. P. Ljungberg, P. Koval, F. Ferrari, D. Foerster, D. Sanchez-Portal, *Physical Review B* **2015**, *92*, 075422.

[180] X. Leng, F. Jin, M. Wei, Y. Ma, *Wiley Interdisciplinary Reviews: Computational Molecular Science* **2016**, *6*, 532–550.

[181] M. Rohlfing, S. G. Louie, *Physical Review B* **2000**, *62*, 4927.

[182] M. Palummo, M. Bernardi, J. C. Grossman, *Nano letters* **2015**, *15*, 2794–2800.

[183] V. Perebeinos, J Tersoff, P. Avouris, *Nano letters* **2005**, *5*, 2495–2499.

[184] J Gracia, P Kroll, *Journal of Materials Chemistry* **2009**, *19*, 3013–3019.

[185] C. Butchosa, P. Guiglion, M. A. Zwijnenburg, *J. Phys. Chem. C* **2014**, *118*, 24833–24842.

[186] Y. Wang, P. Du, H. Pan, L. Fu, Y. Zhang, J. Chen, Y. Du, N. Tang, G. Liu, *Adv. Mater.* **2019**, *31*, 1807540.

[187] X. Wang, S. Blechert, M. Antonietti, *Acs Catalysis* **2012**, *2*, 1596–1606.

[188] H. Schlomberg, J. Kröger, G. Savasci, M. W. Terban, S. Bette, I. Moudrakovski, V. Duppel, F. Podjaski, R. Siegel, J. Senker, et al., *Chem. Mater.* **2019**, *31*, 7478–7486.

[189] P. Zhang, Y. Tong, Y. Liu, J. J. M. Vequizo, H. Sun, C. Yang, A. Yamakata, F. Fan, W. Lin, X. Wang, et al., *Angewandte Chemie* **2020**, *132*, 16343–16351.

[190] J. K. Nørskov, T. Bligaard, A. Logadottir, J. Kitchin, J. G. Chen, S Pandelov, U Stimming, *Journal of The Electrochemical Society* **2005**, *152*, J23.

[191] E. Sargeant, F. Illas, P. Rodriguez, F. Calle-Vallejo, *Journal of Electroanalytical Chemistry* **2021**, *896*, 115178.

[192] M. O. Almeida, M. J. Kolb, M. R. Lanza, F. Illas, F. Calle-Vallejo, *ChemElectroChem* **2022**, *9*, e202200210.

[193] E. Skúlason, G. S. Karlberg, J. Rossmeisl, T. Bligaard, J. Greeley, H. Jónsson, J. K. Nørskov, *Physical Chemistry Chemical Physics* **2007**, *9*, 3241–3250.

[194] M. W. Chase, N. I. S. O. (US), *NIST-JANAF thermochemical tables*, *Vol. 9*, American Chemical Society Washington, DC, **1998**.

[195] NIST-JANAF Table – Ammonia, `http://kinetics.nist.gov/janaf/html/H-083.html`, Accessed: 2021-04-30.

[196] L. Haar, J. S. Gallagher, *Journal of Physical and Chemical Reference Data* **1978**, *7*, 635–792.

[197] R. Bogad, Radiative lifetimes of anisotropic 2D excitons, **2018**.

List of Abbreviations

AI	Artificial Intelligence
HPC	High-Performance Computing
$OLEDs$	Organic Light-Emitting Diodes
$2D$	Two-Dimensional
PCN	Polymeric Carbon Nitride
LDA	Local Density Approximation
ORR	Oxygen Reduction Reaction
HER	Hydrogen Evolution Reaction
SCF	Self-Consistent Field
$fullCI$	Full Configuration Interaction
MP	Møller-Plesset Perturbation Theory
$KS-DFT$	Kohn-Sham Density Functional Theory
DFT	Density Functional Theory
HEG	Homogeneous Electronic Gas
IEG	Inhomogeneous Electron Gas
GGA	Generalized Gradient Approximation
$LSDA$	Local-Spin Density Approximation
E_{xc}	Exchange Energy
PBE	Perdew, Burke, and Ernzerhof
$MCSCF$	Multi-Configurational Self-Consistent Field
$EOM-CC$	Equation-of-Motion Coupled Cluster

$LR-CC$	Linear-Response Coupled Cluster
$TD-DFT$	Time-Dependent Density Functional Theory
$TDHF$	Time-Dependent Hartree-Fock
BSE	Bethe-Salpeter Equation
$FRET$	Förster Resonance Energy Transfer
PVs	Photovoltaics
$OPVs$	Organic Photovoltaics
$LUMO$	Lowest Unoccupied Molecular Orbital
$HOMO$	Highest Occupied Molecular Orbital
SRH	Shockley-Read-Hall
GTO	Gaussian-Type Orbital
PAW	Projector-Augmented Wave
PTI	Poly(triazine imide)
PHI	Poly(heptazine imide)
$VASP$	Vienna Ab initio Simulation Package
DoC	Degree of Condensation
TDA	Tamm-Dancoff Approximation
$PDOS$	Projected Density of States
VBM	Valence Band Maximum
CBM	Conduction Band Minimum
CA	CeperleyAlder Monte-Carlo Correlation
IP	Independent Quasi-Particle
CO_2RR	CO_2 Reduction Reaction
CHE	Computational Hydrogen Electrode
$PECT$	Proton-Coupled Electron Transfer
PDS	Potential-Determining Step
$LR-EF$	Long-Range Electron Transfer

$AuNPs$	Gold Nanoparticles

Curriculum Vitae

Changbin Im

changbin.im@uni-ulm.de
Postdoctoral Associate
Institute of Electrochemistry, Ulm University

RESEARCH FOCUS

- **Computational design of materials and solid/liquid interfaces**:
  — Photo- and electrochemical energy conversion/storage.
- **Mechanistic studies of reactions**:
  — Hydrogen evolution, water splitting, CO_2 conversion, and battery-related reactions.
- **Multi-scale simulations**:
  — (Grand canonical/time-dependent) DFT, post-HF methods (GW, CASSCF, CI), classical MD, ReaxFF, QM/MM, and machine learning potentials.

SKILLS

Computational Software: VASP, ORCA, Gaussian, LAMMPS, GPAW, AMS/ADF
Programming: Python, Fortran, Bash/Shell, Markdown
High-Performance Computing: Cluster management, job scheduling, parallel execution, code compilation
Code Development: Custom script/tools for simulation workflows, data analysis, and machine learning integration
Experimental Literacy: Familiarity with most of *in-situ/ex-situ* characterization techniques

EDUCATION

Doctorate (Dr. rer. nat.) 2018-2025
Thesis: *A Study of Photocatalytic 2D Semiconducting Polymeric Carbon Nitrides*
Insitut für Elektrochemie, Universität Ulm, Germany
Final grade: ***summa cum laude*** (with distinction) (Advisor: Prof. Dr. Timo Jacob)

M.Sc 2011-2013
Department of Polymer Science and Engineering, Inha University, South Korea
GPA: 4.02/4.5
Thesis: Porous Carbon nanofibers for Electrodes of Supercapacitors.
(Advisor: Prof. Hyung-Joon Jin)

B.S 2006-2011
Department of Polymer Science and Engineering, Inha University, South Korea
GPA: 3.82/4.5

EXPERIENCE

Group leader– Theoretical electrochemistry 2024-Present
Institut für Elektrochemie, Universität Ulm, Germany

Research assistant 2025-Present
Helmholtz-Institute Ulm (HIU) Electrochemical Energy Storage, Germany
Karlsruhe Institute of Technology (KIT), Germany

Research Scientist 2022–Present
eSuS Co., Ltd., Gwangju Institute of Science and Technology (GIST), Gwangju, South Korea

Research assistant 2022-2024
Institut für Elektrochemie, Universität Ulm, Germany
- Transregional Collaborative Research Center TRR234 (Catalight)

Research scientist 2013-2017
Research Institute for Solar and Sustainable Energies (RISE),
Gwangju Institute of Science and Technology (GIST), Gwangju, South Korea
(a full-time staff for Benefited Technical Research Personnel for military service of the Korea Army, 03/2013-03/2016)
- Researcher at Division of Energy Storage System, RISE, GIST
- Researcher at Center for cHmeical Energy Storage System (CHESS), RISE, GIST

Research projects (Advisor: Prof. Jaeyoung Lee)
- Synthesis and electrochemical analysis of carbon cathode for lithium-sulfur batteries
- Synthesis and surface investigation of garnet solid electrolytes for all-solid-state Li-ion batteries

Graduate Teaching assistant 2011
Department of Polymer Science and Engineering, Inha University, South Korea
Subject: polymer Chemistry Laboratory (Undergraduate course)

Internship 2009
Openlab program in Department of Chemical engineering, POSTECH, South Korea
Research Scholarship program with grants, POSTECH, South Korea

HONORS AND AWARDS

DAAD Doctoral Scholarship 2018-2022
Graduate Scholarship, Inha University 2011-2012
2009 National College & Graduate Energy Competition, Award, POSTECH 2009
Undergraduate Scholarship, Inha University 2008,2009

PATENTS

1. Jaeyoung Lee*, Jin Won Kim, Changbin Im, Jae Kwang Lee, 'Complex active material for cathode of lithium secondary cell, and preparation method thereof', 10-1592257-0000, Korea, registered (2016).

LIST OF PUBLICATIONS

[1]**C. Im**, M. Stier, and T. Jacob, *In silico design of w-substituted [Mo3S13]2- cluster for the hydrogen evolution reaction*, (2025, In preparation).

[2]D.-Y. Lee, **C. Im**†, S. Kang, T. Jacob, and J. Lee, *Subsurface iron boosting surface ni-rich ni-mo catalyst on efficient hydrogen desorption for anion exchange membrane water electrolysis"*, † (2025, In preparation).

[3]**C. Im**, J. Koenigsdorff, R. Beranek, and T. Jacob, *The origin of catalytic reactivity in hydrogenation-coupled H2O2 production on polymeric carbon nitrides*, (2025, In preparation).

[4]A. Konar, J. Liessem, **C. Im**, D. Mitoraj, P. Sainia, I. Krivtsov, T. Jacob, R. Beranek, and B. Dietzek-Ivanšić, *Spectroscopic investigation of the effect of cations on charge carrier dynamics in water-soluble ionic carbon nitride photocatalysts*, Science Advances (2025, Accepted).

[5]**C. Im**, R. Beranek, and T. Jacob, *Structural influence on exciton formation and the critical role of dark excitons in polymeric carbon nitrides*, Advanced Energy Materials, 2405549 (2025).

[6]**C. Im**, M. M. Elnagar, B. Kirchhoff, D. Mitoraj, I. Krivtsov, A. Farkas, R. Beranek, and T. Jacob, *Unraveling the optical signatures of polymeric carbon nitrides: insights into stacking-induced excitonic transitions*, J. Mater. Chem. C **13**, 8682–8693 (2025).

[7]M. M. Elnagar, J. Liessem, **C. Im**†, D. Mitoraj, L. A. Kibler, C. Neumann, A. Turchanin, R. Leiter, U. Kaiser, T. Jacob, et al., *Water-soluble ionic carbon nitride as unconventional stabilizer for highly catalytically active ultrafine gold nanoparticles*, Nanoscale **15**, †, 19268–19281 (2023).

[8]**C. Im**, B. Kirchhoff, I. Krivtsov, D. Mitoraj, R. Beranek, and T. Jacob, *Structure and optical properties of polymeric carbon nitrides from atomistic simulations*, Chemistry of Materials **35**, 1547–1559 (2023, front cover).

[9]S. Kang, **C. Im**, I. Spanos, K. Ham, A. Lim, T. Jacob, R. Schlögl, and J. Lee, *Durable nickel-iron (oxy) hydroxide oxygen evolution electrocatalysts through surface functionalization with tetraphenylporphyrin*, Angewandte Chemie, e202214541 (2022, front cover).

[10]D. Mitoraj, I. Krivtsov, C. Li, A. Rajagopal, **C. Im**, C. Adler, K. Köble, O. Khainakova, J. Hniopek, C. Neumann, et al., *A study in red: the overlooked role of azo-moieties in polymeric carbon nitride photocatalysts with strongly extended optical absorption*, Chemistry–A European Journal **27**, 17188–17202 (2021).

[11]I. Krivtsov, D. Mitoraj, C. Adler, M. Ilkaeva, M. Sardo, L. Mafra, C. Neumann, A. Turchanin, C. Li, B. Dietzek, R. Leiter, J. Biskupek, U. Kaiser, **C. Im**, B. Kirchhoff, T. Jacob, and R. Beranek, *Water-soluble polymeric carbon nitride colloidal nanoparticles for highly selective quasi-homogeneous photocatalysis*, Angewandte Chemie International Edition **59**, 487–495 (2020).

[12]A. Rajagopal, E. Akbarzadeh, C. Li, D. Mitoraj, I. Krivtsov, C. Adler, T. Diemant, J. Biskupek, U. Kaiser, **C. Im**, M. Heiland, T. Jacob, C. Streb, B. Dietzek, and R. Beranek, *Polymeric carbon nitride coupled with a molecular thiomolybdate catalyst: exciton and charge dynamics in light-driven hydrogen evolution*, Sustainable Energy & Fuels **4**, 6085–6095 (2020).

[13]**C. Im**, D. Park, H. Kim, and J. Lee, *Al-incorporation into Li7La3Zr2O12 solid electrolyte keeping stabilized cubic phase for all-solid-state li batteries*, Journal of energy chemistry **27**, 1501–1508 (2018).

[14]Y. S. Yun, **C. Im**, H. H. Park, I. Hwang, Y. Tak, and H.-J. Jin, *Hierarchically porous carbon nanofibers containing numerous heteroatoms for supercapacitors*, Journal of power sources **234**, 285–291 (2013).

[15]**C. Im**, Y. S. Yun, B. Kim, H. H. Park, and H.-J. Jin, *Amorphous carbon nanotube/mno2/graphene oxide ternary composite electrodes for electrochemical capacitors*, Journal of Nanoscience and Nanotechnology **13**, 1765–1768 (2013).

† = Shared First Authorships

REFERENCES

Prof. Dr. Timo Jacob
Institute of Electrochemistry
Ulm University, Ulm, Germany
Email: timo.jacob@uni-ulm.de

Prof. Dr. Jaeyoung Lee
SDepartment of Environmental Science and Engineering
Gwangju Institute of Science and Technology (GIST), Gwangju, South Korea
Email: jaeyoung@gist.ac.kr

Prof. Dr. Radim Beranek
Institute of Electrochemistry
Ulm University, Ulm, Germany
Email: radim.beranek@uni-ulm.de